

## THESIS / THÈSE

### DOCTOR OF SCIENCES

**Characterization and (U-Th-Sm)/He dating of Moroccan supergene ore deposits**

**New insights to unravel the periods and potential causes of weathering processes.**

Verhaert, Michele

*Award date:*  
2020

*Awarding institution:*  
University of Namur

[Link to publication](#)

#### General rights

Copyright and moral rights for the publications made accessible in the public portal are retained by the authors and/or other copyright owners and it is a condition of accessing publications that users recognise and abide by the legal requirements associated with these rights.

- Users may download and print one copy of any publication from the public portal for the purpose of private study or research.
- You may not further distribute the material or use it for any profit-making activity or commercial gain
- You may freely distribute the URL identifying the publication in the public portal ?

#### Take down policy

If you believe that this document breaches copyright please contact us providing details, and we will remove access to the work immediately and investigate your claim.

# **Characterization and (U-Th-Sm)/He dating of Moroccan supergene ore deposits**

**New insights to unravel the periods and potential causes of  
weathering processes.**

Michèle VERHAERT

Thesis submitted in fulfillment of the requirements  
for the degree of Doctor in Sciences

Faculty of Sciences – Department of Geology  
University of Namur, Belgium

September 2020





## Collaborators



UNIVERSITÉ  
LIBRE  
DE BRUXELLES





*Author*

**Michèle VERHAERT**  
Department of Geology  
University of Namur  
Namur  
Belgium

*Thesis Committee*

**Prof. Dr. Johan YANS** – supervisor  
Department of Geology  
Université de Namur – Belgium

**Prof. Dr. Alain BERNARD** – co-supervisor  
Department of geosciences, environment and  
society  
Université Libre de Bruxelles – Belgium

**Prof. Dr. Cécile GAUTHERON** – co-supervisor  
Department of Earth Sciences  
Université Paris Sud-Saclay – France

**Prof. Dr. Vincent HALLET** - president  
Department of Geology  
Université de Namur – Belgium

**Prof. Dr. Jocelyn BARBARAND**  
Department of Earth Sciences  
Université Paris Sud-Saclay – France

**Prof. Dr. Ir. Eric PIRARD**  
Department of mineral Georesources and geologic  
imagery  
Université de Liège – Belgium

**Prof. Dr. Vinciane DEBAILLE**  
Department of geosciences, environment and  
society  
Université Libre de Bruxelles – Belgium

**Dr. Lhou Maacha**  
Managem Group – Morroco

**Parts of this thesis are based on the following published, accepted and in preparation papers:**

**Verhaert, M.**, Bernard, A., Dekoninck, A., Yans, J., 2016. Characterization and genesis of Cu-Pb-Zn-V-Fe-Mn supergene ore deposits in the area of Bou Arfa (Oriental High Atlas, Morocco). *Geologica Belgica* 19:3-4, 302-304.

**Verhaert, M.**, Bernard, A., Dekoninck, A., Lafforgue, L., Saddiqi, O., Yans, J., 2017. Mineralogical and geochemical characterization of supergene Cu-Pb-Zn-V ores in the Oriental High Atlas, Morocco. *Mineralium Deposita* 52, 1049-1068. doi:10.1007/s00126-017-0753-5.

**Verhaert, M.**, Bernard, A., Saddiqi, O., Dekoninck, A., Essalhi, M., Yans, J., 2018. Mineralogy and genesis of the polymetallic and polyphased low grade Fe-Mn-Cu ore of Jbel Rhals deposit (Eastern High Atlas, Morocco). *Minerals* 8:39. doi:10.3390/min8020039.

Demoulin, A., Barbier, F., Dekoninck, A., **Verhaert, M.**, Ruffet, G., Dupuis, C., Yans, J., 2018. Erosion surfaces in the Ardenne-Oesling and their associated kaolinic weathering mantle, in Demoulin, A. (Ed), *Landscapes and Landforms in Belgium and Luxembourg*. Springer International Publishing, Cham, pp. 63-84. doi:10.1007/978-3-319-58239-9-5.

Poot, J., **Verhaert, M.**, Dekoninck, A., Oummouch, A., El Basbas A., Maacha, L., Yans, J., 2020. Characterization of weathering processes of the giant copper deposit of Tizert (Ighrem inlier, Anti-Atlas, Morocco). *Minerals* 10: 620. doi:10.3390/min10070620.

**Verhaert, M.**, Madi, A., El Basbas, A., Elharkaty, M., Oummouch, A., Oumohou, L., Malfliet, A., Maacha, L., Yans, J., in press. Genesis of As-Pb-rich supergene mineralization: the Tazalaght and Agoujgal Cu deposits (Moroccan Anti-Atlas Copperbelt). *Economic Geology*.

**Verhaert, M.**, Gautheron, C., Vennemann, T., Pinna, R., Mouttaqi, A., Dekoninck, A., Yans, J., in preparation, to be submitted to *Geology*. Goethite (U-Th-Sm)/He dating highlights the early steps of Mn ore formation at Imini, High Atlas, Morocco.

**Verhaert, M.**, Gautheron, C., Vennemann, T., Pinna, R., Saddiqi, O., Madi, A., Maacha, L., Yans, J., in preparation. Unraveling the potential relations between the formation of supergene ores and geodynamics in the Anti-Atlas and High Atlas (Morocco), by goethite (U-Th-Sm)/He dating.

Yans, J., **Verhaert, M.**, Gautheron, C., Antoine, P.-O., Moussi, B., Dekoninck, A., Decrée, S., Chafar, H.R., Hatira, N., Dupuis, C., Pinna-Jamme, R., Jamoussi, F., in preparation, to be submitted to *Minerals*. (U-Th)/He dating of supergene iron (oxyhydr-)oxides of the Nefza-Sejnane district (Tunisia): new insights on mineralization and biostratigraphy of mammals.

## Abstract

Weathering profiles do form when rocks and primary (hypogene) ore bodies are brought to the Earth's surface and exposed to atmospheric conditions. The oxidation of (mostly) sulfides, the dissolution of host rocks, the transport and the (re)concentration of elements enable the precipitation of a wide assortment of secondary (supergene) phases, increase the grade of some metals within the ore, and lead to the formation of supergene ore deposits. The detailed mineralogical, petrological and geochemical characterization of supergene ores, motivated by the growing demand for metals and rare elements that are necessary for the new technologies, targets the identification of eventual economical grades of these elements, in the weathered part of deposits. The ubiquity of iron (oxyhydr-)oxides such as goethite and hematite within supergene environments enables the dating of weathering processes by using the (U-Th-Sm)/He method, while the local occurrence of alunite allows the obtention of crystallization ages through the  $^{40}\text{K}$ - $^{39}\text{Ar}$  dating method. This thesis follows three objectives: 1) defining the paragenetic sequences of supergene base metal deposits and positioning the datable phases within the sequence, 2) dating iron (oxyhydr-)oxides in order to integrate weathering processes in a reliable temporal frame, 3) determining the relative importance of parameters influencing the development of weathering profiles, i.e. climate, which provides water and determines the kinetic of chemical reactions, and geodynamics, which triggers the exhumation of rocks and generates gradients for the progression of fluids. Four sampling areas have been selected to address these issues: 1) three sites of the Eastern High Atlas of Morocco, the Cu site of Jbel Klakh, the Pb-Zn site of Jbel Haouanit, and the Fe-Mn-Cu site of Jbel Rhals, 2) the Mn deposit of Imini, in the Central High Atlas of Morocco, 3) three deposits and several gossans of the Occidental Anti-Atlas of Morocco, the Cu deposits of Tazalaght, Agoujgal and Tizert, and 4) the polymetallic district of Nefza-Sejnane in Northern Tunisia. The vertical distribution of weathering zones, composed from base to top of the hypogene zone (sulfides such as chalcopryrite, pyrite, tennantite, galena, sphalerite), cementation zone (sulfides such as bornite, digenite, chalcocite, djurleite, covellite), oxidized zone (i.e. malachite, azurite, brochantite, olivenite, chenevixite), and leached zone or gossan (iron (oxyhydr-)oxides, mottramite, quartz, calcite) is particularly emphasized in the Cu deposits, but less obvious in the Pb-Zn-Fe-Mn deposits of Jbel Haouanit, Jbel Rhals and Agoujgal. Hand samples of weathered tennantite from Tazalaght and Agoujgal deposits, presenting boxwork textures, also record these transitions at the scale of the sample, reflecting the evolution of fluid-rock interactions with time. The first-order influence of the host rock nature on supergene processes is highlighted in the carbonate-hosted deposits that exhibit a broad panel of oxidized mineral phases of which the precipitation was enabled by an efficient neutralization of the acidic fluids by host rock dissolution. The testing and dating of iron (oxyhydr-)oxides emphasized that the careful selection of samples and their thorough characterization are of the major importance for the acquisition of accurate and meaningful ages. As such, the purest botryoidal goethite samples are considered as the excellent material for (U-Th-Sm)/He dating, while microcrystalline samples are viewed as a second choice. The dating of iron (oxyhydr-)oxides pseudomorphosing pyrite should be avoided. In the High Atlas and Anti-Atlas of Morocco, a correlation between iron (oxyhydr-)oxides and alunite crystallization ages with deformation events of the Late Cretaceous and Cenozoic, related to the Alpine orogeny, suggests that the exhumation of preexisting mineralization and/or of host rocks is a key process required for the formation of supergene ore deposits and gossans. Similar interpretations are propounded in the Tunisian Nefza-Sejnane polymetallic district, where supergene goethite ages indicate the circulation of meteoric fluids in relation with geodynamic events recorded in the area. Therefore, geodynamics is regarded, in the Moroccan Atlas and in Northern Tunisia, as the first-order control for supergene mineralization that generates weathering gradients necessary for the circulation of meteoric fluids. The lack of fit between supergene mineralization ages and Cenozoic (sub)tropical climates in North Africa suggests that climatic parameters only play a secondary role, even if precipitations are required for the circulation of meteoric fluids.

## Résumé

Les profils d'altération météorique résultent de l'exhumation de roches et minerais primaires (hypogènes) et de leur exposition aux agents atmosphériques. L'oxydation de sulfures (principalement), la dissolution des roches hôtes, le transport et la (re)concentration d'éléments chimiques permet la précipitation d'un large assortiment de minéraux secondaires (supergènes), augmente la teneur de certains métaux dans le minerai, et génère la formation de gisements supergènes. La caractérisation minéralogique, pétrographique et géochimique détaillée des minerais supergènes, motivée par la demande croissante en métaux et éléments rares pour les nouvelles technologies, a pour but l'identification de concentrations économiques en ces éléments, dans la partie altérée des gisements métalliques. L'omniprésence des (oxyhydr-)oxydes de fer tels que la goethite et l'hématite dans les environnements supergènes rend possible la datation des processus d'altération météorique par la méthode (U-Th-Sm)/He, alors que la présence locale d'alunite autorise l'obtention d'âges de cristallisation par la méthode  $^{40}\text{K}$ - $^{39}\text{Ar}$ . Cette thèse poursuit trois objectifs : 1) la définition des séquences paragenétiques de gisements métalliques supergènes et le positionnement des phases minérales datables dans ces séquences, 2) la datation des (oxyhydr-)oxydes de fer afin d'intégrer les processus d'altération dans un canevas temporel robuste, 3) la détermination de l'importance relative des paramètres influençant le développement des profils supergènes, que ce soit le climat, qui apporte les fluides nécessaires à l'altération et définit la cinétique des réactions chimiques, ou la géodynamique, qui provoque l'exhumation des roches et génère des gradients pour la progression des fluides. Quatre régions ont été sélectionnées pour répondre à ces questions : 1) trois sites du Haut Atlas Oriental du Maroc, le gîte de cuivre de Jbel Klakh, le gîte plomb-zinc de Jbel Haouanit et le gîte fer-manganèse-cuivre de Jbel Rhals, 2) le gisement de manganèse d'Imini situé dans le Haut Atlas Central du Maroc, 3) trois gisements et plusieurs chapeaux de fer de l'Anti-Atlas Occidental du Maroc comprenant les gisements de cuivre de Tazalaght, Agoujgal et Tizert, et 4) le district polymétallique de Nefza-Sejnane, au Nord de la Tunisie. La distribution verticale de zones d'altération minéralogique, composée, de bas en haut, de la zone hypogène (sulfures tels que la chalcopryrite, pyrite, tennantite, galène, sphalérite), de la zone de cémentation (sulfures tels que la bornite, digénite, chalcocite, djurleite, covellite), de la zone oxydée (*i.e.* malachite, azurite, brochantite, olivénite, chenevixite) et de la zone lessivée ou chapeau de fer ((oxyhydr-)oxydes de fer, mottramite, quartz, calcite), est particulièrement mise en exergue dans les gisements de cuivre, mais moins évidente dans les gisements de plomb-zinc-fer-manganèse de Jbel Haouanit, Jbel Rhals et Agoujgal. Des échantillons de tennantite altérée des gisements de Tazalaght et Agoujgal, présentant des textures en « boxwork » enregistrent aussi cette séquence à l'échelle de l'échantillon, en mettant en évidence l'évolution des interactions fluide-roche avec le temps. L'influence capitale de la nature de la roche hôte de la minéralisation est particulièrement observée dans les gisements contenus dans des roches carbonatées, qui présentent une grande variété de phases minérales oxydées dont la précipitation n'a été possible qu'après une neutralisation efficace de l'acidité des fluides par la dissolution des carbonates de la roche hôte. Les essais analytiques et les datations d'(oxyhydr-)oxydes de fer ont mis l'accent sur l'importance fondamentale de la sélection minutieuse des échantillons et de leur caractérisation approfondie pour l'obtention d'âges corrects, précis et significatifs. Ainsi, les échantillons de goethite botryodale sont considérés comme le matériel idéal pour la datation (U-Th-Sm)/He, alors que les échantillons microcristallins sont relégués en deuxième choix. Il est préférable d'éviter de dater des (oxyhydr-)oxydes de fer pseudomorphosant de la pyrite. Dans le Haut Atlas et l'Anti-Atlas marocains, une corrélation entre les âges de cristallisation des (oxyhydr-)oxydes de fer et de l'alunite, et des périodes de déformations du Crétacé Supérieur et du Cénozoïque suggère que l'exhumation de roches et minerais primaires est un processus clé requis pour le développement de gisements supergènes et de chapeaux de fer. Une interprétation similaire est proposée pour le district polymétallique tunisien de Nefza-Sejnane, où les âges des goethites indiquent la circulation de fluides météoriques en lien avec les événements géodynamiques identifiés dans cette région. Ainsi, la géodynamique est considérée, dans l'Atlas marocain et le Nord de la Tunisie, comme le facteur principal influençant le développement de minéralisations supergènes, conférant les gradients nécessaires à la circulation des fluides météoriques. Le manque de correspondance entre les âges des minéralisations supergènes et les climats cénozoïques (sub)tropicaux du Nord de l'Afrique suggèrent que les paramètres climatiques ne jouent qu'un second rôle dans la création de profils d'altération météorique, même si la présence de précipitations est requise pour assurer la présence de fluides météoriques.

## Remerciements

Je souhaite avant tout remercier mes promoteurs, Johan Yans, Alain Bernard et Cécile Gautheron, pour leur disponibilité, leurs judicieux conseils et leurs encouragements tout au long de ces années de thèse. Merci Johan pour cette expérience et formation de plus de cinq ans. Merci Alain pour votre disponibilité depuis plus de six ans, et pour votre coup d'œil expérimenté sur mes publications. Merci Cécile pour ton accueil lors des missions au sein de GEOPS, pour les innombrables analyses et ton suivi de ce travail.

J'adresse mes remerciements aux membres du Jury pour l'intérêt porté à mon travail ainsi que pour leurs commentaires et suggestions qui ont grandement amélioré le contenu et la forme du présent manuscrit. Merci Eric pour les discussions au sein de conférences, accès au MEB et questions toujours pertinentes. Merci Jocelyn pour tes conseils avisés et ton accueil au sein de GEOPS. Merci Vinciane pour m'avoir permis de réaliser cette étude en participant au Jury FRIA m'ayant accordé cette bourse, et pour ta gentillesse depuis toutes ces années. Merci Monsieur Maacha pour m'avoir donné votre confiance pour travailler sur les sites gérés par Managem, pour m'avoir consacré du temps si précieux, et pour vos questions et commentaires judicieux. Merci Vincent d'avoir présidé ce jury, mais surtout pour vos justes conseils et pour nos nombreuses très agréables discussions.

Merci au FNRS pour les subsides indispensables qui m'ont permis de mener cette thèse dans les meilleures conditions, que ce soit par le biais de ma bourse FRIA ou par les nombreux crédits pour conférences et missions.

Je remercie Gaëtan pour la préparation d'échantillons. Merci à Jeff, Corry et Caroline du Département de Microscopie Electronique pour leur soutien et leur confiance.

Au sein du laboratoire GEOPS, je tiens à remercier Rosella, Fred, Claire, Serge, Gaël, Julius pour leur soutien analytique, mais également Floriane, Maxime, Simon, Mustafa, Ludo, Alexis, Margaux, Maher, Louise, Maxence, Hadrien, Yves, Bertrand, et tous leurs collègues, pour leur accueil chaleureux et tous les bons moments.

Je remercie Torsten Vennemann pour les analyses des isotopes stables ainsi que Pieter L'Hoëst et Annelies Malfliet pour l'acquisition des données en microsonde.

Je tiens à exprimer toute ma reconnaissance à mes collègues marocains, de la société Managem, Lhou Maacha, Mohamed Zouhair et Atman Madi, Mounir Aboulkhir, Abdelmlek Oudjou, Abdelaziz El Basbas, Mohamed Elharkaty, Abdellah Oummouch et Lahcen Oumohou ; de la SACEM, Khalid Ait Ikken, Allal Maali et Abdelali Ait Bendra ; et Omar Saddiqi, Abdellah Mouttaqi et Mourad Essalhi, pour leur accueil et leur aide précieuse sur le terrain, et pour cette découverte du pays magnifique qu'est le Maroc.

Enfin, je souhaiterais remercier tous mes collègues des Départements de Géologie et Géographie pour les magnifiques souvenirs qui resteront à jamais gravés dans ma mémoire. Merci Alan, Julien, Romain, Diego, Aude, Sabine et Flore pour tous les rires et thés partagés au sein de notre sauna, et pour nos liens d'amitié tressés au fil des ans. Merci Augustin pour les aventures marocaines toujours inoubliables. Merci à Ghéreint, Amaël, Djan, Gaëtan, Lorraine, Colette, Vincent, Samantha, Ludovic, Corentin, Valérie, Emilie, Nicolas, Sabine, Catherine, Jérémie, Elisabeth, Sébastien, Florence, Antoine, Sofia, Delphine, Clotilde, Isabelle, Assane, Gary... pour tous ces agréables moments.

Mes derniers remerciements vont à mes parents pour leur soutien indéfectible et à toute épreuve, à ma maman pour son dévouement et ses conseils, à mon papa pour les innombrables relectures en langue anglaise, à ma belle-famille, Marie-France, Eric et Nathan, pour leur gentillesse et leur soutien, à Yuko, et à Alan pour sa compréhension de ma folie et son attention au quotidien.

## Table of contents

<b>Chapter I – Introduction</b>	<b>p. 11</b>
1.1 Interests of supergene ore deposits	p. 14
1.2 Approach and contribution of this work	p. 15
1.3 Structure of the manuscript	p. 16
<b>Chapter II – Weathering processes of metal sulfides hypogene ores: brief state of the art</b>	<b>p. 18</b>
2.1 Structure of supergene profiles in Cu-ore deposits	p. 20
2.2 Factors controlling weathering processes in metal sulfide deposits	p. 21
2.3 Dating weathering processes	p. 23
<b>Chapter III – Geological context of the studied deposits</b>	<b>p. 24</b>
3.1 Geology of Morocco	p. 26
3.2 Moroccan High Atlas	p. 27
3.3 Moroccan Anti-Atlas	p. 31
<b>Chapter IV – Methodology</b>	<b>p. 34</b>
4.1 Sampling strategy	p. 36
4.2 Petrological and mineralogical identification	p. 40
4.3 Geochemistry	p. 43
4.4 Geochronology	p. 45
<b>Chapter V – Characterization of supergene ore deposits</b>	<b>p. 58</b>
5.1 Mineralogical and geochemical characterization of supergene Cu-Pb-Zn-V ores in the Oriental High Atlas, Morocco	p. 63
5.2 Mineralogy and genesis of the polymetallic and polyphased low grade Fe-Mn-Cu ore of Jbel Rhals deposit (Eastern High Atlas, Morocco)	p. 82
5.3 The Tazalaght and Agoujgal Cu deposits, Moroccan Anti-Atlas Copperbelt: Genesis of an As-Pb-rich supergene mineralization	p. 101
5.4 Characterization of weathering processes of the giant copper deposit of Tizert (Ighrem inlier, Anti-Atlas, Morocco)	p. 129
5.5 Summary: metallogeny of Moroccan ore deposits	p. 151
<b>Chapter VI – Timing of weathering processes</b>	<b>p. 152</b>
6.1 Thoughtful selection of samples for (U-Th-Sm)/He dating	p. 157
6.2 Goethite (U-Th-Sm)/He dating highlights the early steps of Mn ore formation at Imini, High Atlas, Morocco	p. 174
6.3 Unraveling the potential relations between the formation of supergene ores and geodynamic in the Anti-Atlas and High Atlas (Morocco), by goethite (U-Th-Sm)/He dating	p. 192
6.4 K-Ar dating of Moroccan alunites	p. 226
6.5 New (U-Th)/He dating of mixed and polyphase alteration processes in the vertebrate-bearing Nefza-Sejnane polymetallic mining district (Tunisia)	p. 232
6.6 Conclusions: implications of Moroccan/ Tunisian GHe and alunite K-Ar ages	p. 248
<b>Chapter VII. General conclusions and perspectives</b>	<b>p. 250</b>
7.1 Characterization of supergene mineralization and profiles	p. 252
7.2 Dating supergene processes	p. 253
7.3 Perspectives	p. 255
<b>Chapter 8. Appendices</b>	<b>p. 257</b>
8.1 Characterization and genesis of Cu-Pb-Zn-V supergene ore deposits in the Oriental High Atlas (Bou Arfa, Morocco) – extended abstract Geologica Belgica (2016)	p. 262
8.2 Characterization and genesis of Cu-Pb-Zn-V supergene ore deposits in the Oriental High Atlas (Bou Arfa, Morocco) – abstract PhD Day UNITER (2016)	p. 263

8.3 The contribution of a Europe-Maghreb cooperation for a better prospection of the mining district of Bou Arfa (Morocco): Supergene Fe-Mn-Cu mineralization at Jbel Rhals – abstract Resources and Innovative Geology (2016)	p. 264
8.4 Characterization and genesis of Pb-Zn-Cu-V supergene ore deposits in the Oriental High Atlas (Bou Arfa, Morocco) – abstract Atlas Georesources International Congress (2017)	p. 265
8.5 Implications of the occurrence of mottramite (PbCu[VO <sub>4</sub> ]) in the Jbel Haouanit Cu-Pb-Zn-V supergene ore deposit (Eastern High Atlas, Morocco) – abstract First West-African Craton and Margins International Workshop (2017)	p. 266
8.6 Chronology of weathering periods by supergene goethite (U-Th)/He dating in the Oriental High Atlas, Morocco – abstract Goldschmidt (2017)	p. 267
8.7 Genesis of the mottramite bearing Jbel Haouanit Cu-Pb-Zn-V supergene ore deposit (Eastern High Atlas, Morocco) – extended abstract SGA (2017)	p. 268
8.8 (U-Th)/He dating of goethite from the gossan of Moroccan supergene ore deposits – abstract Resources for Future Generations (2018)	p. 274
8.9 REE-U-Th-As enrichment in iron (hydr-)oxides from supergene ore deposits of the High Atlas and Anti-Atlas (Morocco) – abstract Conference of the Geological Society of Africa (2018)	p. 275
8.10 The unexpected presence of supergene Cu-Pb-Ca-Zn-Fe arsenates and vanadates in Agoujgal Cu-mine (Anti-Atlas, Morocco) – abstract Geologica Belgica (2018)	p. 276
8.11 Late Miocene to Quaternary mixed hydrothermal/weathering processes in the Nefza-Sejnane polymetallic mining district (Tunisia) viewed by new goethite (U-Th)/He dating – abstract Réunion des Sciences de la Terre (2018)	p. 278
8.12 (U-Th)/He dating of goethite from the gossan of Moroccan supergene deposits – abstract ILEE Research Day (2019)	p. 279
8.13 Expert's report: petrography, mineralogy and geochemistry of the Tazalaght, Agoujgal, Tassrirt and Tizert-Ighrem sites (collaboration UNamur – Managem company)	p. 280
8.14 Erosion surfaces in the Ardenne-Oesling and their associated kaolinic weathering mantle – book chapter (2018)	p. 281
8.15 Localization of collecting sites and samples	p. 303
<b>Chapter 9. References</b>	<b>p. 305</b>

## CHAPTER I

# INTRODUCTION

---



## **Chapter 1**

### **Introduction**

<b>1.1 Interests of supergene ore deposits; examples in Morocco</b>	<b>p. 14</b>
<b>1.2 Approach and contribution of this work</b>	<b>p. 15</b>
<b>1.3 Structure of the manuscript</b>	<b>p. 16</b>

Mineral resources have been extracted and used by mankind since the Stone Age, and are essential to modern civilization for maintaining and improving our quality of life and fundamental to the world's economy, growth and jobs (European Commission 2014, Reich and Vasconcelos 2015). During the last decades, demand increased significantly for base metals such as copper, gold, nickel and iron, but also for cobalt, beryllium, lithium, iodine, tellurium, gallium, rhenium, REEs (Rare Earth Elements) and PGEs (Platinoid Group Elements), among others, due to their use in a wide variety of manufacturing high-tech and energy applications, such as renewable energy devices (tellurium, gallium, indium and germanium for solar applications), high-performance magnets used in wind turbines and electric cars (REE), and liquid crystal displays (LCD) (Reich and Vasconcelos 2015). While the number of materials used across these products considerably increased during recent years, securing reliable, sustainable and undistorted access to some raw materials is a topic of growing concern across the globe (European Commission 2014). Critical raw materials are defined as materials with a high economic importance combined with a high risk associated with their supply. The subcategory of critical elements are metals that are essential for modern societies and subject to the risk of supply restriction, such as gallium, germanium, light and heavy REE. Average crustal abundances of metals are indeed strongly variable. Where Fe, Al, Mg, Ti and Mn are abundantly distributed in the Earth's crust (0.5 to 10%) and only require a small degree of enrichment to make a viable deposit (factors of 4 to 9), base metals such as Cu, Zn and Ni are more sparsely distributed (average crustal abundances of 55-75 ppm) and need to be concentrated by factors in the hundred, and precious metal such as Au and Pt (average crustal abundances of 4-5 ppb) require enrichment factors in the thousands (Robb 2005).

One of the major challenges since the end of the twentieth century revolved around the widespread acceptance that the Earth's natural resources are finite, and that their exploitation should be carried out in a manner that will not detrimentally affect future generations (Robb 2005). This sustainable development concept and challenge requires a better understanding of the Earth's resources, a more efficient recycling of existing resources, and the finding of alternative sources for commodities that are in danger of depletion (Robb 2005). A thorough understanding of the nature, origin and distribution of the world's mineral deposits thus remains a strategic topic. Supergene deposits contribute significantly to the world's supply of base metals (Cu, Zn, Ni, Co) and structural metals (Al, Fe, Ni, V) (Reich and Vasconcelos 2015). This type of deposits forms through the exposition of rocks and primary ore bodies near the Earth's surface and through the oxidation, dissolution, transport and reconcentration of metals. Such processes are highly sensitive to tectonic, climatic and biological forcing (Reich and Vasconcelos 2015). Primary unweathered (fresh) and secondary weathered minerals are called « hypogene » and « supergene », respectively. Among the various minerals that may be encountered in supergene deposits are sulfides, oxides, sulfates, phosphates, oxyhydroxides, carbonates, silicates, native elements, arsenates and vanadates of a wide variety of metals.

In Morocco, mining activities date back to the Antiquity, with the prospecting for copper and silver. A strong recovery of mining activities is recorded since the 1970's, mainly for lead. Natural resources such as phosphate, Ag, Pb, Zn, Ba, Co, Mn, fluorspar, on- and offshore oils are extracted from the subsoil and are thus important for the national economy: the mining sector contributes 3% to the GDP through exports and employs more than 40.000 people (BRPM 2002).

## 1.1 Interests of supergene ore deposits

Boosted by the rise of metal prices since the 2000's, the introduction of modern prospecting tools, and the ever-increasing demand of metals and/or rare earth elements for (new) technologies, the interest of mining industries for supergene deposits is constantly growing (e.g. Hitzman et al. 2003; Boni and Large 2005; Arndt and Ganino 2012). In this context, the near-surface situation (<100m) and softened host rocks of supergene ores enhancing their subsequent relatively easy and fast accessibility and mining are definite advantages over the hypogene, sulfidic mineralization (Cocker 2012; Reich and Vasconcelos 2015). In addition, the oxidation and leaching of rocks and primary ores are major ore forming and ore enriching processes that may result in a two- to ten-folded increase in metal grades for metals such as Cu, Al, Fe, Ni, Mn, U, Au and Zn (Sillitoe 2005; Arndt and Ganino 2012; Reich and Vasconcelos 2015). Apart from the major metal components, supergene ore deposits may also contain economic or near-economic concentrations of trace elements such as critical elements. The enrichment in REE usually ranges from three to ten times, in comparison with hypogene sulfides, but may reach a hundred times in particular cases (Cocker 2012). The resultant highly enriched supergene blanket that forms above the hypogene ore contributes significantly to the overall viability of the mine (Robb 2005; Reich and Vasconcelos 2015). However, the complex mineralogy of supergene ores represents a challenge for the extractive metallurgy and mineral processing (Boni et al. 2009; Reich and Vasconcelos 2015; Choulet et al. 2019). Many supergene blankets remain unmined and unprocessed until the development of viable metallurgical processes (Reich and Vasconcelos 2015). Nevertheless, recent advances in hydrometallurgical acid-leaching, solvent extraction (SX), electron-winning techniques (Choulet et al. 2014; Boni and Mondillo 2015), and leaching by bio-organisms (Zammit et al. 2015) facilitate post-extraction treatments for non-sulfide ores. In the scientific point of view, the particular attraction of supergene ores lies in their formation at the interface between tectonic and climate processes, and in their mineralogical diversity.

Supergene deposits contribute significantly to the world's supply of base metals (Cu, Zn, Ni, Co) and structural metals (Al, Fe, Ni, V) (Reich and Vasconcelos 2015). Giant porphyry Cu deposits such as those of northern Chile, dealing with weathering processes, provide about 70% of the global Cu inventory (Sillitoe 2005; Reich and Vasconcelos 2015). The supergene Zn deposits, providing "calamine" mineralization, focused attention over the past decade since their high-grade ores are easily extracted by open-pit methods (Hitzman et al. 2003; Choulet et al. 2014). The world's most economically important supergene ore deposits are found in Australia, especially in the Hamersley province. There, channel iron deposits supply 40-50% of the iron currently mined in Australia, making this country one of the leading Fe-producing countries along with China and Brazil (Heim et al. 2006a; Danišík et al. 2013; Reich and Vasconcelos 2015). Lateritic profiles, which are chemically stratified weathering zones developed through intensive rock weathering, also contain exploitable reserves of metals such as Fe, Al, Mn, Au, Ni and Co (Vasconcelos 1999). The highly aluminous variety of laterite, bauxites, yield most of the global Al production dominated by Australia, Brazil, China and India (Reich and Vasconcelos 2015). Nickel-rich laterites of Australia, New Caledonia, Brazil, Cuba, Indonesia and the Philippines dominate the global supply of Ni (over 60%) and also provide high contents of Co (Reich and Vasconcelos 2015). Lateritic profiles and supergene enrichment zones also concentrate efficiently precious metal such as Au, Ag and PGEs to economic grades (Reich and Vasconcelos 2015). For instance, gold-bearing laterites of Australia, Africa, Brazil, the Guyana's and India contain free particles of high-purity Au that enables low-cost open-pit mining. Bauxite is also an important source of Ga and REEs. Some metals and metalloids are produced completely as by-products of the refining of major metals: Te is produced from Cu, Re from Mo, In and Ge from Zn, Ga from Al, and Co from Ni (Cocker 2012; Reich and Vasconcelos 2015).

Supergene deposits are perfect analogs of corrosion processes that affect natural and anthropic materials: the apparition of green « verdigris » on copper plumbing pipes and copper and bronze art objects, and of rust on steel tools are examples of weathering. For instance, the green-colored mineral atacamite is massively found in Chilean supergene ore deposits (Reich et al. 2008), but also forms as the green corrosion patina that covers bronze monuments in coastal cities, such as the Statue of Liberty (NY, USA) (Reich and Vasconcelos 2015). Studying the process leading to atacamite formation and dissolution under the exposure of fresh meteoric water in natural environments thus provides insights about the long-term corrosion behavior of bronze objects (Reich and Vasconcelos 2015). Supergene ores also are of great environmental interest since the significant isotopic fractionation of metals from their primary sources to their secondary distal sinks provides natural analogues for the dissolution, transport and subsequent deposition of metals in man-made environments (Reich and Vasconcelos 2015). For instance, large volumes of waste material including waste rock, mill tailings and mineral refinery slags are generated during mining and mineral processing. There, acid mining drainage may lead to the oxidative dissolution of sulfides and to the release of significant amounts of toxic heavy metals (e.g. Pb, Hg) and metalloids (e.g. As, Se) into the environment (Reich and Vasconcelos 2015). The study of natural supergene ore deposits may thus be used to support long-term predictions of how corrosion will affect man-made products in geologic environment, and thus, among others, to explore the rates of oxidation of materials over long timescales and to understand the dispersion of metals in the environment (Renock and Shuller-Nickles 2015).

## **1.2 Approach and contribution of this work**

Supergene metal accumulation are found all over the world, in Europe (e.g. La Calamine, Belgium, Coppola et al. 2008; Upper Silesia, Poland, Górecka et al. 1996), North America (e.g. Heyl 1964; Arizona, USA, Schumer et al. 2019), South America (e.g. Chili, Sillitoe and Mckee 1996; Reich et al. 2008), Asia (e.g. China, Li et al. 2007; Iran, Maghfouri et al. 2018), Oceania (e.g. Australia, Gao et al. 1995; New Caledonia, Iseppi et al. 2018) and Africa (e.g. Morocco, Choulet et al. 2014; Democratic Republic of Congo, Fontaine et al. 2020). Exploration of new supergene targets has been carried out during the last decade in many countries including Morocco. In the Moroccan High Atlas, numerous Cu-Pb-Zn supergene ore deposits described in the 1960'-70's (e.g. Emberger and Pouit 1966) have been (re)studied over the last years (e.g. Choulet et al. 2014). These orebodies were mined in the past, colonial history, but have no more real economic potential due to their small extension and the lack of characterization (e.g. Mouttaqi et al. 2011; Choulet et al. 2014)(Choulet et al. 2014). The Anti-Atlas, known as the "Anti-Atlas copperbelt", also attracts considerable prospecting activity because of the up to two hundred copper and polymetallic occurrences of economic interest (e.g. Bou Azzer, Imiter) and the possibility of finding even more substantial deposits. Regardless of their hypogene ore formation, most of these deposits display evidence of weathering processes.

The first section of this manuscript aims at refining the mineralogical, petrographical and geochemical characterization of Moroccan deposits, and at determining their paragenetic sequences and supergene metallogenies. This topic received little attention for decades, as supergene mineralization was for long left aside as waste. However, the above advantages of such deposits and the development of mineral processing treatment enables the current exploration and mining of such mineralization. Since the complex weathering processes that lead to supergene ore formation occur over a variety of timescales (tens of years to millions of years), and from mineral grain (micron to centimeter) to deposit (meter) and even district (kilometer) scales (Reich and Vasconcelos 2015), the second section of this manuscript is focused on the interpretation of goethite (U-Th-Sm)/He ages recovered in several supergene deposits of Morocco. The purpose of dating weathering products is to constrain when there were favorable geological periods for the development of weathering profiles and metal enrichment

on a regional scale, and to determine the relative importance of the parameters controlling weathering processes, i.e. geodynamics, climate, etc.

### **1.3 Structure of the manuscript**

Chapter 2 is a brief state-of-the-art report on weathering that gathers the concepts needed for the understanding of this manuscript, through defining weathering processes, identifying the major parameters controlling their formation, describing their structure, and discussing the potential dating methods. Chapter 3 presents the geological context of the deposits studied during this thesis, especially focusing on the Moroccan High Atlas and Anti-Atlas geodynamics. Chapter 4 describes the methods used to characterize and date supergene mineralization.

The main sections of this manuscript are the characterization of supergene ore deposits (chapter 5) and the determination of the timing of weathering processes (chapter 6). The majority of data of chapters 5 and 6 is extracted from papers which have been published, accepted, or which are in advanced preparation (Table 1.1). The content of each paper is preserved, but the format is adapted to the size of this manuscript. Each step of the research is introduced by a short paragraph and closed by preliminary conclusions.

Chapter 5 provides an in-depth description of four sampling areas in Morocco, including 1) the Cu-Pb-Zn-V ores of the Jbel Klakh and Jbel Haouanit deposits (Eastern High Atlas), 2) the Fe-Mn-Cu ores of the Jbel Rhals deposit (Eastern High Atlas), 3) the As-Pb-rich Cu deposits of Tazalaght and Agoujgal (Western Anti-Atlas) and 4) the giant Cu deposit of Tizert (Western Anti-Atlas).

Chapter 6 presents ages obtained on supergene mineral phases collected from the above deposits, and aims at determining the potential causes leading to the formation of weathering profiles. In the first subsection, the selection of samples for (U-Th-Sm)/He dating is discussed. Then, the timing of supergene mineralization is presented through: 1) the (U-Th-Sm)/He dating of exceptional goethite from the Imini site, Central High Atlas, Morocco, 2) the (U-Th-Sm)/He dating of iron (oxyhydr-)oxides from the Eastern High Atlas and Western Anti-Atlas, Morocco, 3) the K-Ar dating of alunite from the Eastern High Atlas and Western Anti-Atlas, Morocco, and 4) the (U-Th-Sm)/He dating of iron (oxyhydr-)oxides from North-Tunisia. The last subchapter summarizes the observations and interpretations of these numerous ages, in order to draw conclusions at a regional scale.

Chapter 7 gathers the final conclusions and perspectives.

**Table 1.1. Papers used in this manuscript.**

Sampling site	Location	Chapter	Paper Title
Jbel Klakh and Jbel Haouanit	Eastern High Atlas, Morocco	5.1	Verhaert et al. (2017) <i>Mineralogical and geochemical characterization of supergene Cu-Pb-Zn-V ores in the Oriental High Atlas, Morocco</i> . Mineralium Deposita
Jbel Rhals	Eastern High Atlas, Morocco	5.2	Verhaert et al. (2018) <i>Mineralogy and genesis of the polymetallic and polyphased low grade Fe-Mn-Cu ore of Jbel Rhals deposit (Eastern High Atlas, Morocco)</i> . Minerals
Tazalaght and Agoujgal	Western Anti-Atlas, Morocco	5.3	Verhaert et al. (accepted, in press) <i>The Tazalaght and Agoujgal Cu deposits, Moroccan Anti-Atlas Copperbelt: Genesis of an As-Pb-rich supergene mineralization</i> . Economic Geology
Tizert	Western Anti-Atlas, Morocco	5.4	Poot et al. (2020) <i>Characterization of weathering processes of the giant copper deposit of Tizert (Ighrem inlier, Anti-Atlas, Morocco)</i> . Minerals
Imini	Central High Atlas	6.2	Verhaert et al. (in preparation) <i>Goethite (U-Th-Sm)/He dating highlights the early steps of Mn ore formation at Imini, High Atlas, Morocco</i> . To be submitted in Geology
Jbel Klakh, Jbel Haouanit, Jbel Rhals, Tazalaght, Agoujgal (among others)	Eastern High Atlas and Western Anti-Atlas, Morocco	6.3	Verhaert et al. (in preparation) <i>Unraveling the potential relations between the formation of supergene ores and geodynamic in the Anti-Atlas and High Atlas (Morocco), by goethite (U-Th-Sm)/He dating</i> . To be submitted in Minerals
Nefza-Sejnane	North Tunisia	6.5	Yans et al. (in preparation) <i>New (U-Th)/He dating of mixed and polyphase alteration processes in the vertebrate-bearing Nefza-Sejnane polymetallic mining district (Tunisia)</i> . To be submitted in Minerals
Ardenne	Belgium	7.3	Demoulin et al. (2018) <i>Erosion surfaces in the Ardenne-Oesling and their associated kaolinic weathering mantle</i> .

## CHAPTER II

# WEATHERING PROCESSES OF METAL SULFIDES HYPOGENE ORES: BRIEF STATE OF THE ART

---

## **Chapter 2**

### **Weathering processes of metal sulfides hypogene ores: brief state of the art**

<b>2.1 Structure of supergene profiles in Cu-ore deposits</b>	<b>p. 20</b>
<b>2.2 Key factors controlling weathering processes in metal sulfides deposits</b>	<b>p. 21</b>
<b>2.3 Dating weathering processes</b>	<b>p. 23</b>



This PhD thesis deals with **processes** leading to the weathering of primary (hypogene) metal (Cu, Pb, Zn, Fe, ...) sulfides and to the formation of (non-)sulfide **supergene mineralization**. In accordance with geological and climatic conditions, recurrent oxidation, dissolution, solubilization, remobilization, reconcentration and reprecipitation of elements of economic interest at or near the Earth's surface promote the formation of weathering profiles in ore deposits (Vasconcelos et al. 2015). This chapter aims at outlining a brief state of the art of the knowledge about processes leading to sulfides weathering and (non-)sulfide supergene ore formation, and at presenting the issues discussed in this manuscript. First, the typical structure of Cu supergene profiles is detailed. Then, the key factors controlling weathering processes and leading to the formation of economic metals deposits are presented. Finally, dating methods enabling the determination of the timing of weathering processes are discussed.

## 2.1 Structure of supergene profiles in Cu-ore deposits

In supergene deposits, and especially those presenting copper mineralization, different mineralogical zones are systematically identified, due to the downward, mainly *per descensum*, progression of supergene solutions through times. The typical succession from bottom to top of supergene copper deposits is composed of the 1) primary sulfide zone, 2) secondary sulfides enrichment (cementation) zone, 3) oxidized zone, and 4) leached zone (gossan) (Fig. 2.1.1). These horizons are commonly discernible in outcrops from observable changes in color, mineralogy and texture. Zones of supergene enrichment are also found in the surficial environment above any exposed metal orebody, hosting for instance Pb-, Zn-, Mn-mineralization. The typical pattern of well-defined horizons may however be slightly different, less marked, than for supergene copper deposits.

At the bottom of the section, the primary sulfide zone hosts hypogene, unweathered (fresh) minerals that are commonly sulfides such as chalcopyrite, galena or sphalerite, among others (Fig. 2.1.1). Then, the cementation zone, atop the primary ores, is characterized by the replacement of hypogene sulfides by supergene sulfides, under reduced conditions (Fig. 2.1.1). In the case of copper deposits, secondary sulfides such as bornite, chalcocite and covellite are depleted in iron but enriched in copper, in comparison with chalcopyrite. This zone is separated from the upper horizons by the water table that represent a transition from reduced to oxidizing conditions (e.g. Robb 2005; Arndt and Ganino 2010). The oxidized level commonly hosts a broad spectrum of secondary oxidized minerals such as carbonates, silicates, sulfates, phosphates etc. (Fig. 2.1.1). The leached zone, or gossan, which only contains the skeletal outlines of the original minerals, caps the sequence (Fig. 2.1.1). There, the circulation of fluids leached most metals and only iron (oxyhydr-)oxides, clays and late weathering products occur. The precipitation of oxidized secondary minerals is generally due to the direct precipitation from groundwaters that are saturated with respect to one or more of the components that compose the minerals (Robb 2005). Above the water table, the stability fields of secondary minerals depends essentially on pH, which controls the solubilities of complexing ligands (i.e.  $\text{SO}_4^{2-}$ ,  $\text{CO}_3^{2-}$ ,  $\text{OH}^-$ ,  $\text{PO}_4^{2-}$ ) and determines which complexes are likely to be saturated in the environment (Robb 2005).

Another nomenclature, mostly used in lateritic deposits, may also be applied to sulfide-derived metallic supergene ore deposits. Laterites are defined as the product of intense weathering in humid, warm, intertropical regions of the world (Africa, South America, Australia), and are typically rich in kaolitic clays and Fe-Al (oxyhydr-)oxides (Robb, 2005). Their economic importance lies in their Al and other metals concentrations. Lateritic profiles present a horizontal succession of zones characterized by the retention of a variety of different elements (Robb 2005). The base of a lateritic profile hosts the unaltered/unweathered bedrock, called the protolith (Fig. 2.1.1). Then, atop of the latter, is the

saprolith zone that is composed of highly weathered rocks of which the primary texture and fabric is preserved (Fig. 2.1.1). The laterite (or pedolith), at the upper part of the profile, is characterized by the complete destruction of rock fabric and leaching of all but the most stable elements (Robb, 2005) (Fig. 2.1.1). The regolith encompasses both the saprolith and laterite, i.e. the weathered part of the profile (Fig. 2.1.1).

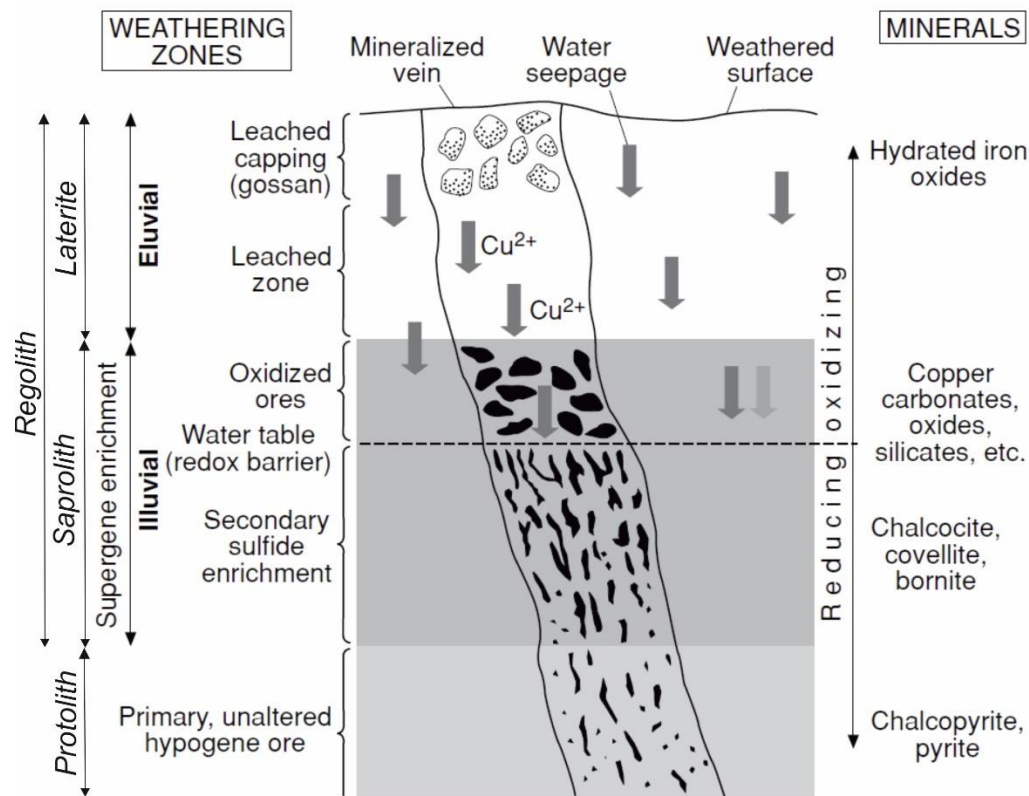


**Figure 2.1.1.** Schematic section through a copper deposit (modified after Robb 2005).

## 2.2 Factors controlling weathering processes in metal sulfides deposits

Following Boni and Mondillo (2015), the development of weathering profiles mostly results from the concurrent actions of leaching fluids, tectonic uplift and brittle fracturing, under wet and warm climates. Several parameters could control the development of such weathering profiles and their variable thickness, mineralogy and physical properties: the mineralogy, chemistry, morphology and structure of the primary ore and of the host rock, the preexistence of fractures and faults, climatic factors that control the temperature, the availability of meteoric water, evapotranspiration rates, the (micro)biological activity, the intensity of leaching and the possible reprecipitation, the tectonic/geodynamic setting that governs the regional uplift of the primary ore, in competition with erosion, and eustatism (Takahashi 1960; Bladh 1982; Sangameshwar and Barnes 1983; Scott et al. 2001; Reichert and Borg 2008; Choulet et al. 2014, 2019; Vasconcelos et al. 2015; Fontaine et al. 2020). Significant weathering and the subsequent formation of supergene mineralization can thus only occur within certain time frames characterized by specific concomitant conditions.

The first factor controlling supergene processes is the parent material, i.e. the country/ wall rocks, and primary ore minerals (Dill 2015). The susceptibility of a primary ore to undergo weathering, the nature of the secondary mineralization and the extension of the weathered profile depends on the nature and amount of hypogene minerals that control the initial acidity of fluids, on the density and extent of

fracturing, and on the neutralizing capacity of host rocks (Takahashi 1960; Bladh 1982; Sangameshwar and Barnes 1983; Scott et al. 2001; Reichert and Borg 2008). The role of the mineral and chemical composition of the host rocks lies in the capacity of carbonates and chlorites to buffer the acidity of mineralizing fluids. Their dissolution in contact with  $H^+$  ions induces the mobilization of alkaline and bicarbonate ions, or the formation of clay minerals such as kaolinite and smectite. The presence of faults and fractures enables a more efficient circulation of fluids and thereby enhance weathering by facilitating water movements and favoring water-rock interactions. By decreasing the cohesion of rocks and ores, the presence of fractures also increases the potential for weathering. In addition, the formation or widening of dissolution cavities also amplifies the permeability and porosity, and provides preferential drains for fluids and spaces (Decrée et al. 2010a) and for more extended secondary mineral precipitation.

The hypogene ore also has a precursor role in the releasing of metals and other species that may influence secondary processes. As highlighted by Bladh (1982), the nature of sulfides, whose stability domains are limited to reduced environments, and their susceptibility to oxidation, determines the sequence of weathering, the consequent availability of metals for transport and the nature of secondary minerals. The weathering of sulfides by fluids percolating *per descensum* induces the release of cations (Cu, Fe, Pb, ...) and ligands ( $SO_4^{2-}$ ,  $CO_3^{2-}$ ,  $OH^-$ ,  $PO_4^{2-}$ , ...). The natural acidity of weathering fluids may be variably amplified during sulfides oxidation: the combination of sulfate, hydrogen anions and atmospheric oxygen results in the formation of sulfuric acid. The generation of such acid solutions mainly depends on the reduced sulfur to metal ratio of sulfides (Chavez 2000): the oxidation of iron-poor sulfides releases modest quantities of acid solutions. At the contrary, the stepwise oxidation of pyrite produces significant amounts of sulfuric acid that may induce, locally, substantial drops of pH and the extensive destruction of sulfides. Moreover, the release and oxidation of ferrous to ferric iron during pyrite dissolution enhance the oxidation of sulfides by catalyzing this process (Chavez 2000; Reichert and Borg 2008).

Environmental factors such as temperature and precipitations directly influence the development of weathering profiles. Wet climates indeed tend to intensify weathering by providing meteoric water, while warmer climates enhance the rate of chemical reactions. Oxidation processes are moreover commonly catalyzed by specialized Fe- and S- oxidizing bacteria.

The local landform, which is shaped by hydrological and pedological processes coupled with the geodynamic evolution of the crust, controls weathering processes (Dill 2015). The importance of geomorphological controls, directly linked with vertical lithosphere movements, at a continental scale, is evidenced by Wyns (2002). To promote the *per descensum* percolation of fluids, and thus the downward progression of a weathering front, uplifts or domings are necessary to exhume rocks and ores to the Earth's surface. However, the preservation of weathering profiles depends on erosion rates: long periods of tectonic (quasi-)stability are thus ideally required. To limit runoff and erosion, but to enhance weathering, long-wavelength lithosphere deformation such as thermal doming, rift shoulder and hot spots are considered to better induce formation and preservation of weathered profiles (Underhill and Partington 1993; Wyns 2002). Since eustasy and isostasy are both related to vertical movements of the lithosphere, they are also involved in the formation of relief, and they may consequently be responsible for weathering processes through the creation of water gradients.

## 2.3 Dating weathering processes

Direct dating of supergene mineralization, which enables determining the timing of weathering processes, is a persistent challenge. However, the acquisition of ages for supergene mineralization is the key to understanding and correlating weathering processes and events of global events such as volcanism, tectonics, and climatic changes (Vasconcelos et al. 2015). Currently, only few dating methods are dedicated to supergene minerals. In the non-exhaustive list below, various constraints limit the use of the methods. For instance, all these methods use minerals that are only found in limited quantities and which do not represent the entire weathering profile; the application of the U-Pb method is restricted to Pb-free environment, which strongly restrains its use. On the contrary, the direct applicability of (U-Th-Sm)/He dating on ubiquitous iron (oxyhydr-)oxides (goethite and hematite) makes the method attractive (e.g. Pidgeon 2003; Shuster et al. 2005).

- Isotopic K-Ar and  $^{40}\text{Ar}/^{39}\text{Ar}$  dating is used to investigate the formation of two types of supergene K-bearing minerals in supergene profiles: K-bearing manganese oxides of the hollandite supergroup, such as cryptomelane (e.g. Vasconcelos et al. 1994; Bonnet et al. 2014); and the alunite and jarosite K-bearing sulfates (e.g. Alpers and Brimhall 1988; Sillitoe and Mckee 1996). The principal issue arises from the omnipresence, in supergene deposits, of muscovite inherited from the parent rocks, which is much older than the supergene mineralization. The second challenge is the multistage formation of Mn oxides in such environments, involving multiple reactivation and precipitation processes and therefore various ages (Vasconcelos et al. 2013).
- The (U-Th)/He or (U-Th-Sm)/He dating method, applied for a long time on minerals such as zircon and apatite, is recently and increasingly used on iron (oxyhydr-)oxides such as supergene goethite and hematite (e.g. Shuster et al. 2005; Riffel et al. 2016). Further information about this method is to be found in chapters 4 and 6 of the present thesis.
- The U-Pb system enables the dating of carbonates to constrain the timing of precipitation, and more precisely of diagenetic and meteoric calcite such as speleothems (e.g. Rasbury et al. 1997; Woodhead et al. 2006).
- The measurement of the accumulated  $^{36}\text{Cl}$  content and the  $^{36}\text{Cl}$ -to-Cl ratios of chlorides such as atacamite provides estimations of surface exposures timing and thus of precipitation ages (Reich et al. 2008).
- Oxygen and hydrogen isotopes, and more precisely their variation over time, are used for dating residual kaolinite (Bird and Chivas 1993).
- Dating using the U-series decay chains and products is applied to date oxides and carbonates originating from supergene environments (Short et al. 1989; Bernal et al. 2006).
- The Rb-Sr dating of Zn silicates and Mn oxides is positively evaluated as a geochronometer for supergene environments (Ruffet et al. 1996; Schneider et al. 2008).
- The palaeomagnetic dating is based on the measurement of the chemical remnant magnetism (CRM) preserved in Fe-bearing minerals (Théveniaut and Freyssinet 1999; Anand and Paine 2002). This method is particularly suitable for areas that underwent tectonic movement leading to a modification of their latitudinal position (e.g. Théveniaut and Freyssinet 1999).
- Apatite fission track (AFT) studies are not directly used to date weathering processes and the precipitation of supergene minerals, but provide information about the thermal history of rocks, leading to the identification of long time events such as uplifts (e.g. Barbarand et al. 2018).

## CHAPTER III

# GEOLOGICAL CONTEXT OF THE STUDIED DEPOSITS

---

## **Chapter 3**

### **Geological context of the studied deposits**

<b>3.1 Geology of Morocco</b>	<b>p. 26</b>
<b>3.2 Moroccan High Atlas</b>	<b>p. 27</b>
<i>3.2.1 The Mesozoic rifting</i>	<i>p. 27</i>
<i>3.2.2 The Cenozoic inversion and uplift</i>	<i>p. 28</i>
<b>3.3 Moroccan Anti-Atlas</b>	<b>p. 31</b>

### 3.1 Geology of Morocco

As stated by (Michard et al. 2017), Morocco is one of the most fascinating nations in the world for studying geology: the country is located at a triple junction between a continent (Africa), an ocean (the Atlantic) and an active plate collision zone (the Alpine belt system). This favourable situation results in the presence of diverse tectonic systems, a varied topography and a wide range of outcropping rocks of Archean to Cenozoic in age. The examination of NW Africa map (Fig. 3.1.1) enables putting Morocco into the geological context, with the identification of five major geological areas (Fig. 3.1.1):

- 1) To the North, the Rif is a collisional mountain belt resulting from the collision of Africa-Eurasia plates and extending along the Mediterranean Sea. It is a part of the North African Rifo-Tellian (Maghrebides) belt. The Rif is constituted of allochthonous units thrust over the edge of the African plate.
- 2) The High Atlas and Middle Atlas belts are parts of the North African intracontinental Atlasic belt extending from Morocco to Tunisia and constituting the deformed foreland of the Rifo-Tellian belt. Meso-Cenozoic autochthonous sediments are there faulted and folded.
- 3) The Moroccan Meseta is a domain of elevated plateaus separated in the Occidental and Oriental Mesetas by the Middle Atlas. This area includes the Missour and High Moulaya intramontane basins. Tabular Meso-Cenozoic formations overlay a Variscan-folded, metamorphized, granitized Paleozoic basement.
- 4) The Anti-Atlas belt, only found in Morocco, is flanked with the Neogene Souss and Ouarzazate Basins shown to the south of the High Atlas borders. In the Anti-Atlas, a Precambrian basement deformed by the Eburnean and Panafrican orogeneses is overlaid by a Paleozoic cover slightly deformed during the Variscan orogeny.
- 5) The South or Saharian area, limited by the South Atlasic Front, is composed of wide plains and desertic plateaus.

The geological history of Morocco starts with the Eburnean orogeny and the formation of the West African Craton around 2 Ga. The Panafrican orogeny then carves the north of the craton, the Anti-Atlas, between 760 and 550 Ma. Further north, between 360 and 290 Ma, the Variscan orogeny affects the Mesetian massifs, the Atlasic basement and the Mauritanides nappes. Finally, the Alpine orogeny induces the formation of the collisional Rif belt and the Atlasic intracontinental belts during the Cenozoic, from 35-40 Ma (Michard et al. 2017).

While, at first sight, the topography of Morocco could be comparable to its Maghrebic neighbours, Algeria and Tunisia, it actually differs in several ways. The elevation is particularly high, in the High Atlas displaying close to 4000 m high massifs (up to 4167 m for Jbel Toubkal), in the Middle Atlas exceeding 3000 m, and in the Anti-Atlas achieving up to 2700 m in Jbel Saghro and 3300m in the Jbel Siroua. The continental basement of Morocco is also much more uplifted than in its neighbouring countries, inducing the outcropping of Paleozoic and Precambrian rocks (Michard et al. 2017).

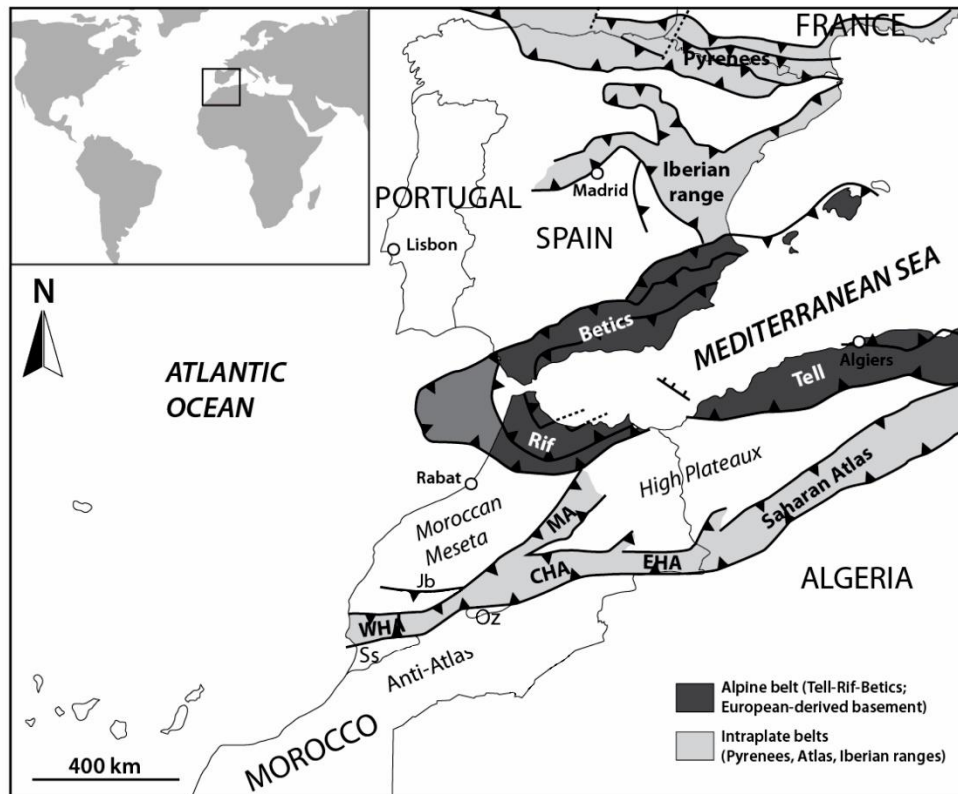


**Figure 3.1.1.** Principal units of Morocco (WHA: Western High Atlas; MA: Middle Atlas; CHA: Central High Atlas; EHA: Eastern High Atlas; SA: Saharan High Atlas; Ss: Souss Basin; Oz: Ouarzazate Basin; Jb: Jebilet front) (modified after Leprêtre et al. 2018).

### 3.2 Moroccan High Atlas

The High Atlas is an intracontinental mountain belt, extending in the WSW to ENE direction, from the Atlantic coast to Algeria where it continues in the so-called “Saharan Atlas” (Fig. 3.1.1.). The Paleozoic substratum of the belt has been deformed through the Panafrican and Hercynian orogenies, and is unconformably overlain by Mesozoic series (Late Triassic clayish formations and evaporites, Early to Middle Jurassic marine carbonates, Late Jurassic to Early Cretaceous detrital sandstones, conglomerates and red clays, Late Cretaceous marls and carbonates) and Cenozoic formations. Its current relief results from two major tectonic events (Mattauer et al. 1977; Frizon de Lamotte et al. 2000, 2008): (1) the Triassic to late Cretaceous pre-orogenic rifting and subsequent filling of the basins, and (2) the Cenozoic basin inversion leading to the shortening of basement and cover units, formation of syn-orogenic basins, and uplift(s) (Teixell et al. 2003; Frizon de Lamotte et al. 2008; Leprêtre et al. 2015) (Fig. 3.2.1). The High Atlas is located at the southern edge of the Variscan Belt (Mattauer et al. 1977; Laville et al. 2004). The reactivation of Variscan tectonic structures played an important role in the subsequent deformation phases, and is attested by the parallelism of the Paleozoic, Mesozoic and Cenozoic Atlasic trends (Bennami et al. 2001; Frizon de Lamotte et al. 2008).

#### 3.2.1 The Mesozoic rifting

The Late Permian-Early Triassic break-up of Pangaea and the opening of the Tethys and Atlantic Oceans triggered the formation, at the NW edge of the African plate, of intracontinental rifts that affected the Variscan basement and induced the thinning of the North African crust (Choubert and Fauve-Muret 1962; Mattauer et al. 1977; Laville and Piqué 1991; Laville et al. 2004). At that time, the Atlasic basin is a channel connected to the Tethys Ocean, but not bound to the Atlantic. During the Triassic, the



distensive context induced the formation of narrow subsident basins separated by horsts, the creation of pull-apart basins, and the development of a mosaic of toppled crustal blocks (El Kochri and Chorowicz 1995; Laville et al. 2004; Sarih 2008). NE-SW and E-W normal faults, along with WNW-ESE and NNE-SSW strike-slip faults circumscribe the basins. During Liassic, a sinistral transform zone induced the division of the Atlasic basin into two trenches that later became the Middle and High Atlas (Mattaueer et al. 1977; Laville et al. 2004). Rifting aborted during late Triassic, and basins were filled by sediments of various origins (Laville et al. 2004). Synrift basins contain a succession of Permian to Triassic red-bed sedimentary rocks (conglomerate, sandstone, siltstone and mudstone), with widespread evaporites and intercalated basaltic and lava flows, followed by Jurassic-Cretaceous carbonates and marls (Giese and Jacobshagen 1992; Frizon de Lamotte et al. 2008). The Atlasic domain was covered by an epicontinental sea with Tethysian dominance during the Liassic period that turned turns to a more Atlantic polarity during late Jurassic (Choubert and Fauve-Muret 1962; Frizon de Lamotte et al. 2008). Triassic rocks are mostly detrital rocks of various grain size and evaporates, with basalt and dolerite flows (Du Dresnay 1965; Verati et al. 2007). The Lower Liassic platform carbonates grade upward into marl, limestone and calcareous turbidite, attesting of a stupendous rise of subsidence probably related to the rifting (Choulet et al. 2014, and references therein). By the end of Jurassic, the sedimentary filling of the basin is followed by a marine regression expressed through the deposition of continental red beds (Frizon de Lamotte et al. 2008). During Late Cretaceous, the deposition of red sandstone and limestone followed by the formation of a carbonate platform brought an end to the emergence of the area and attests of the Late Cenomanian–Turonian transgression event (Frizon de Lamotte et al. 2008). Continental sedimentation is recorded again at the end of Cretaceous, during the Paleocene (Charrière et al. 2005) and until the mid-Eocene (Herbig and Trappe 1994).

The flow of ca. 210–195 Ma basalts and dolerites is related to the Central Atlantic Magmatic Province (CAMP) (Giese and Jacobshagen 1992; Youbi et al. 2003; Knight et al. 2004). Following (Youbi et al. 2003; Frizon de Lamotte et al. 2008), the geochemical signature of these rocks is typical of continental intraplate magmatism, and more precisely of continental tholeiites (flood basalts); their common slight enrichment in incompatible elements implies a potential crustal contamination during rising.

### ***3.2.2 The Cenozoic inversion and uplift(s)***

By the end of Cretaceous, the opening of Atlantic Ocean modified the drifting direction of the African plate from heading E to NE, and made it converge with the Iberian (Eurasian) plate. In response, constraints switched from being extensional to compressional, leading to basin inversion and to shortening of the basement and cover units (Choubert and Fauve-Muret 1962; Mattaueer et al. 1977; Laville and Piqué 1991; Frizon de Lamotte et al. 2000, 2008). Shortening occurred by fracturing and folding the Mesozoic-Cenozoic cover units and the Variscan basement, and sometimes by detachment of cover units from the basement (Giese and Jacobshagen 1992; Frizon de Lamotte et al. 2000, 2008). The Cenozoic uplift occurred at the location of previous rift grabens, by reactivation of former Liassic normal faults as thrusts (Bennami et al. 2001; Teixell et al. 2003; Frizon de Lamotte et al. 2008).

Apart from a first erosional event (Middle/Late Jurassic to Early Cretaceous), four episodes of exhumation are defined in the Eastern High Atlas in relation with the Cenozoic Africa/Eurasia convergence (Leprêtre et al. 2018). These latter will have a significant role in the weathering processes studied in this thesis (see Chapter 6).

The earliest Late Cretaceous deformation events, defined as a thermal doming, are recognized in different domains of Morocco (Froitzheim et al. 2005 and references therein; Saddiqi et al. 2009; Leprêtre et al. 2018; Sehrt et al. 2018) and probably due to mantle-related phenomenon associated to

the Atlantic evolution (Leprêtre et al. 2018). At the beginning of Late Cretaceous, an important erosion phase ( $D_0$ ) associated with kilometer-scale uplift and erosion is affecting mostly the northern flank of the belt, in relation with early compressive events in the Atlas belt (Froitzheim et al. 2005; Domènech et al. 2016; Leprêtre et al. 2018). This wide-scale deformation phase related to the onset of the Africa-Europe convergence affects all NW Africa during Late Cretaceous (Hafid et al. 2006; Frizon de Lamotte et al. 2009; Khomsi et al. 2016; Leprêtre et al. 2018).

The Cenozoic deformation is divided in three steps of uplift (Leprêtre et al. 2015, 2018). The first Cenozoic uplift episode ( $D_1$ ) occurred during late Eocene, between Lutetian and Bartonian (Leprêtre et al. 2015) or between Bartonian and Priabonian (41-35 Ma; Leprêtre et al. 2018) and resulted in ~3 km of erosion. This phase coincides with geodynamic events recognized in Algeria and Tunisia (Frizon de Lamotte et al. 2000; Bracène and Frizon de Lamotte 2002; Khomsi et al. 2016). A second erosion phase ( $D_2$ ) took place during the Early-Middle Miocene (21-17 Ma; Leprêtre et al. 2018), and is related to the setting of nappes and is confined in Morocco (Tesón and Teixell 2008; Leprêtre et al. 2015, 2018). The third Cenozoic deformation phase ( $D_3$ ) is recorded during Late Pliocene-Quaternary (Leprêtre et al. 2015) or during Late Miocene-Early Pliocene (around 10 Ma; Leprêtre et al. 2018). This last uplift episode, which corresponds to the paroxysmal compression phase, when Variscan inherited weak zones were reactivated into reverse faults, overthrusts, and folds, is responsible for the building of the current orogeny and contributes to most of the High Atlas topography building (Morel et al. 2000; Missenard et al. 2006; Leprêtre et al. 2015, 2018). This phase is widely recorded along the whole Atlas area affected by the Africa-Europe convergence.

Two hypotheses are proposed for the deformation of the crust: thin-skin tectonics involving the development of a detachment within Triassic formations (Teixell et al. 2003) and thick-skinned tectonics implying the deformation of the deep crust and highlighting the role of Variscan structures (Frizon de Lamotte et al. 2000). As emphasized by (Choulet et al. 2014), the thick-skinned model most probably prevails in the High Atlas. The current Atlas topography is however not only related to crustal shortening, which is quite modest (15-36 km, Gomez et al. 1996, 2000). While Seber et al. (1996) suggested that a thermal factor may be involved, Ayarza et al. (2005) and Teixell et al. (2005) emitted the hypothesis of the complementary role of asthenospheric processes. Such a thermal anomaly could be related to the Morocco Hot Line, an oblique NE-SW strip of thinned lithosphere observed in Morocco, of which the existence could be explained through the presence of a Mantle plume (Missenard et al. 2006; Frizon de Lamotte et al. 2008). The current High Atlas topography thus results from the concurrent actions of Cenozoic exhumation together with a high asthenospheric heat flow.

Tectonic events		Period / Epoch	Lithostratigraphy and detachment levels	Thickness
Atlasic or Alpine orogeny	<b>INVERSION</b>	Quaternary		100 - 350 m
		Neogene		300 - 1100 m
		Paleogene		400 - 900 m
	<b>POSTRIFT</b>	Cretaceous	Upper	350 - 600 m
			Lower	400 - 600 m
	<b>SYNRIFT</b>	Jurassic	Dogger	500 - +2000 m
			Liassic	
		Triassic		200 - 1500 m
Hercynian or Variscan orogeny	<b>PRERIFT</b>	Carboniferous - Permian		300 m
		Devonian		200 - 350 m
		Silurian		200 - 1000 m
		Ordovician		1000 - 2000 m
		Cambrian		
Pan-African orogeny		Precambrian		?

**Figure 3.2.1.** Synthetic stratigraphic column of the central and eastern High Atlas Mountains, showing the main tectonic events and detachment levels (modified after El Harfi et al. 2006).

### 3.3 Moroccan Anti-Atlas

The Anti-Atlas belt, located on the northern edge of the West African Craton, extends ENE-WSW over more than 600 km, from the Atlantic margin into the African plate (Fig. 3.3.1). The belt culminates at 3200 m at Jbel Siroua and reaches up to 1800 m in altitude in the plateaus (Michard et al. 2017; Sehr et al. 2018). The Anti-Atlas, bounded to the north by the South Atlas fault and the Neogene foreland basins of Souss and Ouarzazate, and to the south by the Tindouf basin, is divided in two by the Anti-Atlas Major Fault (AAMF; Fig. 3.3.1). Numerous irregularly shaped Precambrian basement inliers crop out along the belt axis, surrounded by an up to 10 km Paleozoic sedimentary succession (Fig. 3.3.1). These structures form a NE-SW trending anticline and represent structural culminations of the Variscan fold belt (Helg et al. 2004; Gasquet et al. 2008; Michard et al. 2008).

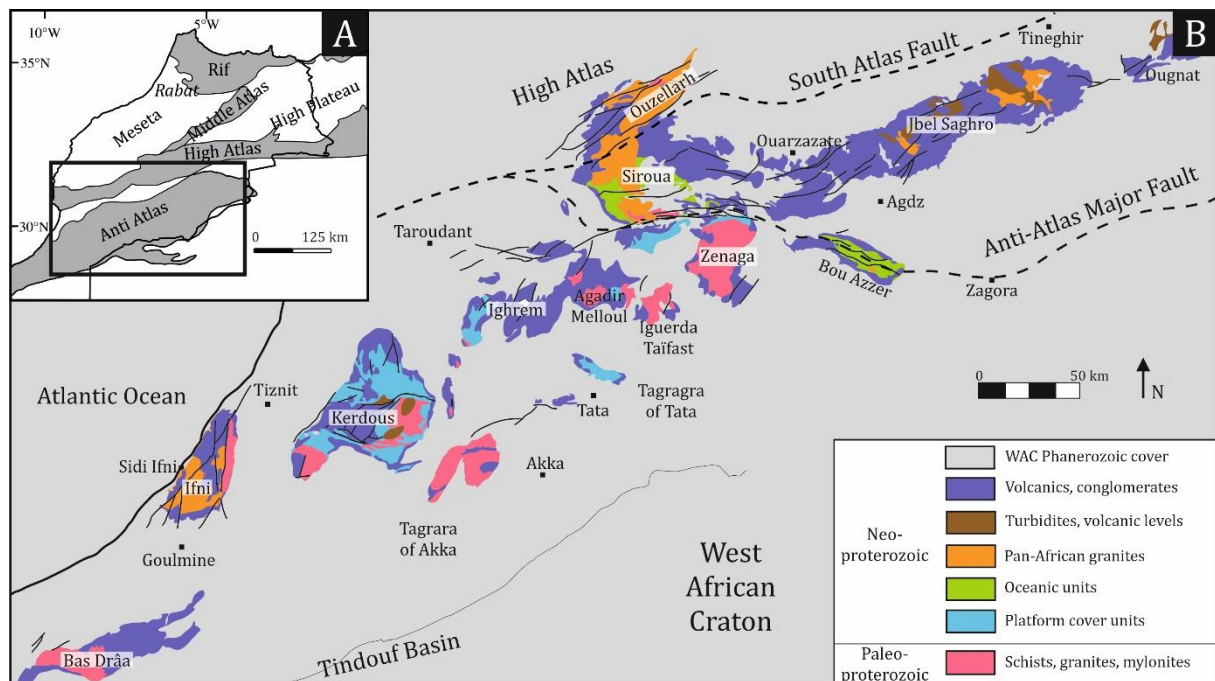


**Figure 3.3.1.** (A) Simplified geologic map of Morocco. (B) Geologic map of the Anti-Atlas highlighting the alignment of Precambrian inliers in the Anti-Atlas (modified after Gasquet et al. 2008 and Ikenne et al. 2017).

The Anti-Atlas has been shaped by the Eburnean, Pan-African, Variscan and Alpine orogenies. Post-Eburnean collapse resulted in the tilting of basement blocks and the filling of continental basins by Upper Ediacarian volcanoclastic formations of the Ouarzazate Group (Gasquet et al. 2008; Soulaïmani et al. 2014).

During the Late Neoproterozoic-Early Cambrian, extension and rifting processes related to the Iapetus Ocean opening triggered the formation of (half-)graben structures later filled by coarse clastic sediments and alkaline basalts of the Tata-Taroudant Group sequence indicating an intracontinental extension (Benssaou and Hamoumi 2003; Soulaïmani et al. 2014). A significant subsidence and the accumulation of fine clastic sediments was subsequently recorded in the Anti-Atlas, during the Cambrian post-rift stage (Helg et al. 2004; Burkhard et al. 2006; Baidder et al. 2008). Several post-Variscan tectonic phases are involved in the exhumation of the Precambrian basement of inliers and the erosion of their Paleozoic cover (Gasquet et al. 2008). (1) Between Late Carboniferous and Early Permian, the Variscan compression caused significant inversion and folding in the Paleozoic basins of the Anti-Atlas, with a NW-SE main direction of shortening (Burkhard et al. 2006; Gasquet et al. 2008; Sehr et al. 2018). This thick-skinned inversion and folding affected the sedimentary cover and the

basement, from the Meseta plateau in the north to Mauritania in the southern part of the Anti-Atlas (Pique et al. 1987; Helg et al. 2004; Burkhard et al. 2006; Michard et al. 2008). (2) Between Late Permian and Early Triassic, the Anti-Atlas was affected by vertical movements triggered by the Tethys and Central Atlantic Oceans opening (Knight et al. 2004; Laville et al. 2004; El Arabi et al. 2006; Sehr et al. 2018). These events confirmed that the Anti-Atlas behaved as a rift shoulder of the Central Atlantic opening (Gouiza et al. 2017). In the Early Cretaceous, cooling of the bedrock continued and erosion locally reached Precambrian rocks (Oukassou et al. 2013). During the Cenomanian-Turonian, a widespread transgression across North-Africa resulted in the flooding of the Anti-Atlas and in its covering by shallow water carbonate deposits that were subsequently nearly completely eroded between the Senonian and the Cenozoic (Frizon de Lamotte et al. 2008; Michard et al. 2008; Leprêtre et al. 2015). (3) On the contrary of the High Atlas where high elevations are related to the Cenozoic convergence of African and Eurasian continents and the induced crustal shortening, the Anti-Atlas was probably less affected by the major Alpine uplift that took place within the Atlas chains (Missenard et al. 2006; Frizon de Lamotte et al. 2009). Following Missenard et al. (2006) and Soulaïmani et al. (2018), the Upper Eocene and Pleistocene exhumation of the Anti-Atlas may ensue from a thermal uplift related to the development and moving of a hot mantle anomaly underneath the belt, along the Moroccan coast, in addition to both plate convergence and lithospheric thinning. This large-scale uplift, which mainly affected the western part of the Anti-Atlas, is associated to an average erosion of 0.08 km/Ma since 30 Ma (Ruiz et al. 2011). Recently, Gouiza et al. (2017) showed that the Anti-Atlas domain has been affected by two episodes of exhumation coinciding with major tectonic and thermal events associated with the Atlantic and Tethys oceans rifting. The first phase resulted in the exhumation of 7.5-10.5 km of crustal rocks by the end of Middle Jurassic, while the second episode led to a 1-3 km subsidence between Late Jurassic and Early Cretaceous and to the exhumation of 2-3.5 km of basement rocks throughout Late Cretaceous and Cenozoic. Overall, episodes of exhumation and subsidence coincide with major thermal and tectonic events in the Anti-Atlas (Gouiza et al. 2017).

The alignment of the Anti-Atlas inliers (Bas Drâa, Ifni, Kerdous, Iggherm, Zenaga, Bou Azzer, J. Saghro and Ougnat; Fig. 3.3.1) follows its highest axis and two major fault zones: Anti-Atlas Major Fault (AAMF) and South Atlas Fault (SAF). They expose the Precambrian metamorphic basement generally hidden under folded Paleozoic rocks (Gasquet et al. 2005; Michard et al. 2017). During the Tonian-Cryogenian, sedimentary series composed of quartzites and limestones were deposited and later deformed and recrystallized during the Pan-African orogeny (686-660 Ma) (Gasquet et al. 2008). To the south of the AAMF, the basement is mainly composed of shales and granites folded and metamorphosed during the Eburnean and Pan-African cycles (Gasquet et al. 2008; Soulaïmani et al. 2014). These rocks are overlaid by a Paleoproterozoic cover and Late Ediacaran volcanoclastic series, slightly deformed and unconformably disposed with the Eburnean and Pan-African series (Anezi and Ouarzazate/Tanalt Group; Fig. 3.3.2) (Soulaïmani and Hefferan 2017; Sehr et al. 2018). To the north of the AAMF (Fig. 3.3.1), the basement is mainly Neoproterozoic and consists of fragments of Cryogenian terrains composed of ophiolites and island arc gneisses that were located at the northern edge of the West African Craton during the paroxysm of the Pan-African orogeny (Hefferan et al. 2014; Soulaïmani et al. 2014; Soulaïmani and Hefferan 2017). As in the south, this domain is covered by the same series of Upper Ediacaran age (Soulaïmani and Hefferan 2017). All these series are unconformably overlaid by Paleozoic sediments up to 12 km thick in both sides of the Anti-Atlas Major Fault (Gasquet et al. 2008; Soulaïmani et al. 2014).

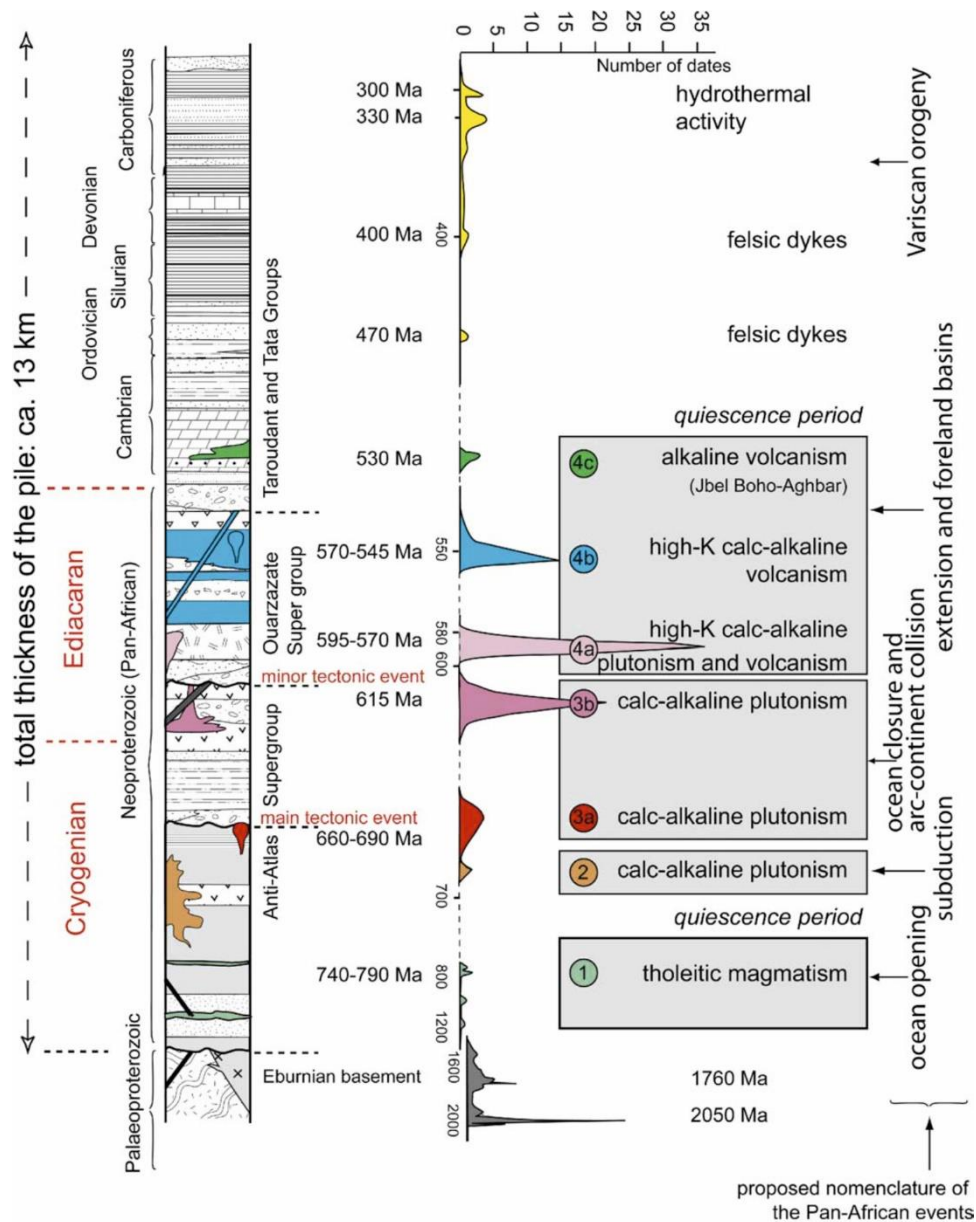


**Figure 3.3.2.** Simplified lithostratigraphy of the Anti-Atlas series with the main tectonic events and U-Pb ages of magmatic episodes (Gasquet et al. 2005).

## CHAPTER IV

# METHODOLOGY

---

## Chapter 4

### Methodology

<b>4.1 Sampling strategy</b>	<b>p. 36</b>
<b>4.2 Petrological and mineralogical identification</b>	<b>p. 40</b>
4.2.1 X-ray diffraction (XRD)	p. 40
4.2.2 Transmitted light microscopy	p. 41
4.2.3 Reflected light microscopy	p. 41
4.2.4 Scanning electron microscopy	p. 41
4.2.5 Electron microprobe microanalysis (EPMA)	p. 42
<b>4.3 Geochemistry</b>	<b>p. 43</b>
4.3.1 Whole rock and mineral investigations	p. 43
4.3.2 Stable isotope geochemistry of oxygen and hydrogen	p. 43
<b>4.4 Geochronology</b>	<b>p. 45</b>
4.4.1 (U-Th-Sm)/He method	p. 45
4.4.1.a Generalities of the method	p. 45
4.4.1.b Goethite and hematite (U-Th)/He method	p. 48
He ejection	p. 49
He diffusivity and retentivity	p. 49
He diffusion in hematite	p. 49
He diffusion in goethite	p. 50
Factors leading to dispersive ages	p. 51
Errors and corrections	p. 52
4.4.1.c Goethite (U-Th-Sm)/He methodology	p. 53
Samples selection	p. 53
Samples preparation	p. 54
Degassing of samples and He measurement	p. 55
Dissolution of samples and U-Th-Sm measurement	p. 56
4.4.2 K-Ar dating of alunite	p. 57



The investigation of rocks and minerals formed during supergene processes requires a broad scope characterization involving field observations, laboratories preparations, mineralogical and geochemical determinations. These analyses lead to a deep understanding of ores petrology, mineralogy, geochemistry and geochronology. This chapter presents all techniques and analytical tools used during this thesis. A particular attention is paid to the selection and characterization of iron (oxyhydr-)oxides (i.e goethite and hematite) for (U-Th-Sm)/He geochronology.

## **4.1 Sampling strategy**

Three sampling campaigns have been successfully organized in relation with this PhD thesis, thanks to the valuable collaborations with local authorities, mining companies and other institutions.

The first one felt in the framework of my master thesis and took place between March 20<sup>th</sup> and 27<sup>th</sup>, 2014, in the area of Bou Arfa, in the oriental High Atlas (Figure 4.1). More than 130 samples have been collected from the old mines of Jbel Klakh (Cu deposit; chapter 5.1), Jbel Haouanit (Pb-Zn deposit, chapter 5.1), and Jbel Rhals (Cu-Fe deposit, chapter 5.2).

The second mission, organized between May 17<sup>th</sup> and 27<sup>th</sup>, 2017, has been focused on the occidental Anti-Atlas: more than hundred samples have been brought back from two mines in operation, Tazalaght (Cu deposit currently in operation, chapter 5.3) and Agoujgal (Cu deposit previously mined, chapter 5.3), and from the mining projects of Tassirt (Cu-Zn deposit) and Tizert (Cu deposit, chapter 5.5).

The third and last field trip, between March 13<sup>th</sup> and 29<sup>th</sup>, 2018, has been divided in two parts. The first week has been dedicated to a Mn deposit in operation in the central Anti-Atlas, Imini, from which we collected around seventy samples of iron (oxyhydr-)oxides. The occidental Anti-Atlas concentrated our attention during the rest of the mission: Tazalaght, Agoujgal, Tassirt, and Tizert-Ighrem sites were revisited for complementary sampling (Figure 4.1). Several gossans have also been explored: Agni, Alous, Assifid, Est-Akka (former Cu deposit), Imi Omagha (Cu-Zn mining project), and Irkhs (Figure 4.1). From all these sites, about 230 samples have been collected. Samples from several mining sites (Bou Arfa Mn deposit, Bouskour) that were housed at the UNamur have also been considered for analyses.

The sites sampled in the Anti-Atlas have been carefully selected. A thorough bibliographic study of supergene mining sites in the Moroccan Atlas has been carried out to draw up an inventory of potential sites and their features (Table 4.1). The initial decisive and critical factors were the presence of primary and secondary metallic mineralization including supergene iron (oxyhydr-)oxides. Then, the selection was focused on deposits that currently were in operation because of the wider set of opportunities on the field: accessibility to the sites, security, existence of information on the surrounding formations and structures, and potential presence of drillings of the primary and secondary ores. The last criterion was the occurrence of uncommon mineral phases (e.g. arsenates), which bring new perspectives to the supergene mineralization.

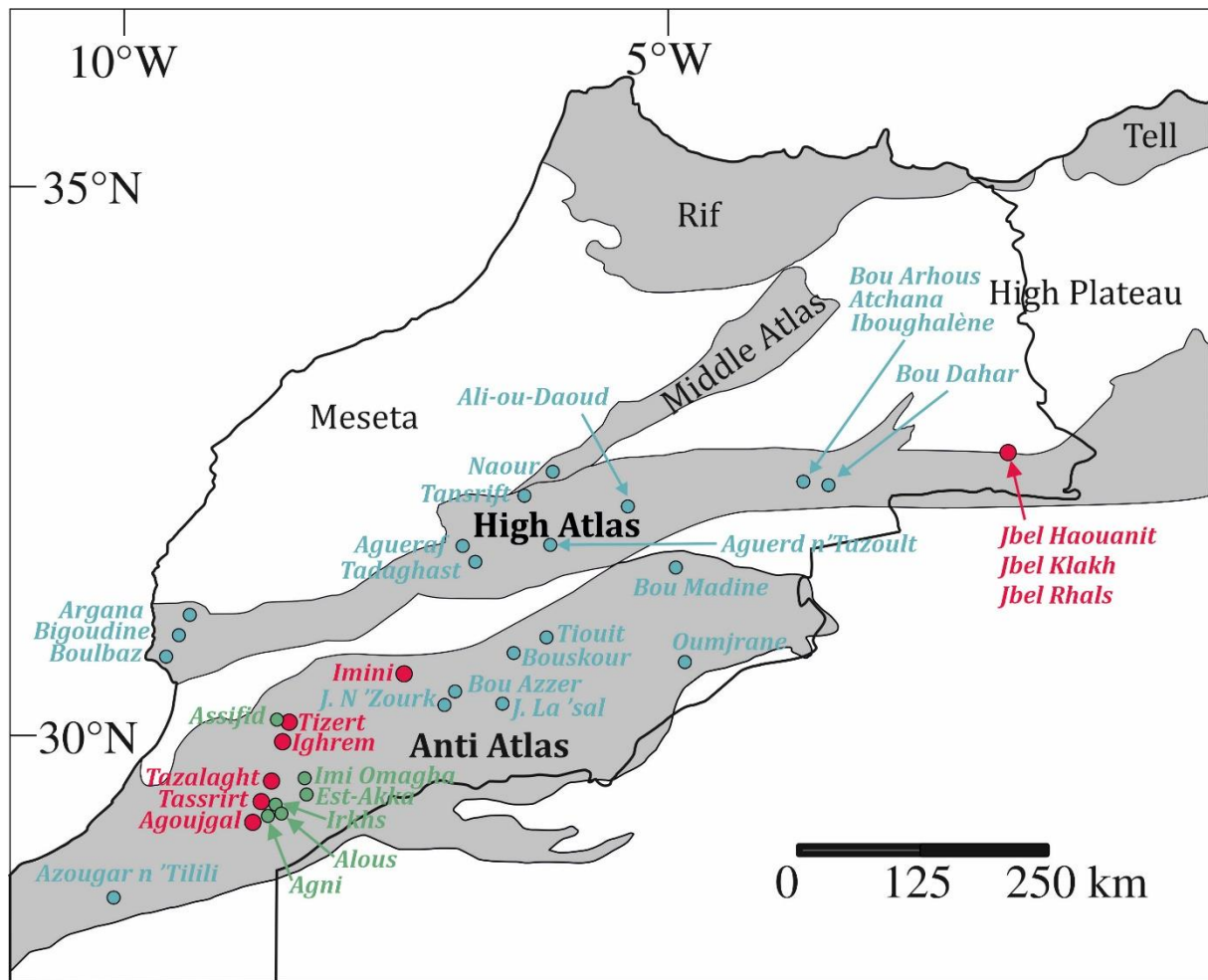


**Figure 4.1.** Non-exhaustive inventory of deposits hosting supergene mineralization in the Moroccan Atlas and Anti-Atlas; (red) sampled deposits, (green) sampled gossan, (blue) other sites not studied here.

**Table 4.1.** Non-exhaustive inventory of deposits hosting supergene ores in the Moroccan Atlas. In grey, sites studied in this PhD.

Region	Site/mine	Mining?	Ore	Gossan	Comments
Oriental High Atlas	Jbel Klakh,		Cu		
	Jbel Haouanit,	Artisanal mining	Pb-Zn	Yes	Relatively easy access
	Jbel Rhals		Cu-Fe-Mn		
Oriental High Atlas	Aït Labbes (Foum Bou Teboul)	Artisanal mining	Pb-Zn	Yes	Already studied by Choulet et al. (2014)
Oriental High Atlas	Tizi n'Firest	Artisanal mining	Pb-Zn	Yes	Only waste rock piles remain; already studied by Choulet et al. (2014)
Oriental High Atlas	Bou Arhous		Pb-Zn		
	Atchana	Managem	Mn	Yes	Many aspects already studied by Choulet et al. (2014)
	Iboughalène		Pb		
Oriental High Atlas	Beni Tajite / Tadjit	Artisanal mining	Pb-Zn	Limited	Lots of sulfides ; already studied by Choulet et al. (2014)

Oriental High Atlas	Bou Dahar	Managem, CADETAF, ...	Pb-Zn	Yes	Numerous mining sites ; already studied by Choulet et al. (2014)
Oriental High Atlas	Tamlalt – Menhououhu	ONHYM + artisanal mining	Fe-Cu-Au	Yes	Au-mineralization: restricted sampling
Oriental High Atlas	Toutia	?	Pb-Zn	?	Little information available
Central High Atlas	Tadaghast	Managem	Pb-Zn	Yes	Already studied by Choulet et al. (2014)
Central High Atlas	Tansrift	Closed	Cu	Yes	Already studied by Ibouh et al. (2013)
Central High Atlas	Ali-ou-Daoud	Managem	Zn-Pb-Fe	Yes	Already studied by Mouguina and Daoudi (2008)
Central Anti-Atlas	Imini	SACEM (ONHYM)	Mn	Yes	Large amounts of botryoidal goethite in the ore; already studied by Dekoninck et al. (e.g. 2016)
Central High Atlas	Aguert n'Tazoult	Artisanal mining + Société des Mines de Tenous (SOMITE)	Zn-Pb	Yes	Already studied by Ibouh and Mouguina (2011)
Central High Atlas	Agueraf	Closed	Cu	Yes	Similar to Jbel Rhals deposit but little information available
Central High Atlas	Naour	Closed	Cu	Limited	Little information available
Occidental High Atlas	Argana				
	Bigoudine	Closed	Cu	Yes	Numerous old mining sites but difficult access and little information available
	Boulbaz				
Oriental Anti-Atlas	Bouskour	Managem – REMINEX	Cu-Pb-Zn-Ag	Yes	Already extensively studied
Oriental Anti-Atlas	Oumjrane	Managem	Cu	Yes	Already extensively studied
Oriental Anti-Atlas	Tiouit	Kefi Mineral's and Roche Invest SPRL	Cu-Au-Ag	Yes	Au-mineralization: restricted sampling
Central Anti-Atlas	Agoujgal	Managem (Akka Gold Mining)	Cu-Ag	Yes	Easy access, large variety of secondary minerals
Central Anti-Atlas	Tazalaght	Managem (Akka Gold Mining)	Cu	Yes	Easy access, large variety of secondary minerals

Central Anti-Atlas	Iourirn	Managem (Akka Gold Mining)	Au-Cu	Yes	Au-mineralization: restricted sampling
Central Anti-Atlas	Bou Azzer	Compagnie de Tifnoute Tirhanimine and Managem	Co-Ni-As-PGE	Yes	Already extensively studied
Central Anti-Atlas	Jbel La'sal (El Graara)	SOMIFER	Cu	Yes	Little information available
Central Anti-Atlas	Jbel n'Zourk	Managem	Cu	Yes	Little information available
Occiden-tal Anti-Atlas	Azougar n'Tilili	Managem	Pb-Zn-Cu-Fe-Au	Yes	Au-mineralization: restricted sampling
Occiden-tal Anti-Atlas	Boumadine	Maya Gold and Silver and ONHYM	Cu-Pb-Zn-Au-Ag-Fe-Sn	Yes	Au-mineralization: restricted sampling

## 4.2 Petrological and mineralogical identification

### 4.2.1 X-ray diffraction (XRD)

Among the numerous analytical techniques that are used to characterize minerals, XRD enables the identification of major crystalline mineral phases, *i.e.* phases that represent more than ~5% of the sample, but also provides additional information about the proportion of minerals in samples and the degree of crystallinity of these phases.

Regular and repeating planes of atoms that form a crystal lattice define the three-dimensional structure of minerals, namely non-amorphous materials. Each mineral diffracts X-rays in a unique way, depending on which atoms constitute the crystal lattice and how these are positioned. When a X-ray beam directed on a sample is diffracted, the interplanar spacing may be determined by applying Bragg's equation (Equ. 4.1):

$$n\lambda = 2d\sin\theta \text{ (Equ. 4.1)}$$

where  $n$  is the order of reflection the diffracted beam,  $\lambda$  is the wavelength of the incident beam,  $d$  is the characteristic distance between crystal planes of a given specimen, and  $\theta$  is the angle between the incident rays and the surface of the specimen.

In an X-ray powder diffractogram generated during the scan, each peak represents a position where the X-ray beam has been diffracted by the crystal lattice. The set of  $d$ -spacings (interplanar spacing), which is unique and exclusive to only one mineral, can easily be calculated from the  $2\theta$  values shown. Comparing this scan with standard reference patterns then allows for identification of the material.

Samples that are analyzed by XRD are first crushed to powder in stainless steel grinding jars in a RETSCHER PM 100 planetary ball mill, in order to ensure the presence of the entire set of representative planes of atoms of the crystal lattice. Powders are sieved to save particles up to 100  $\mu\text{m}$  in size from the rest. Two diffractometers have been used during this study. The first one is a BRUKER X-ray diffractometer equipped with a HI STAR GADDS (General Area Detector Diffraction System)  $\text{CuK}\alpha$  detector (University of Brussels). The second instrumentation consists in a PHILIPS Analytical X-ray diffractometer with a PW3710 BASED  $\text{CuK}\alpha$  detector (University of Namur). Powders were thus in both cases exposed to the monochromatic beam of copper  $\text{K}\alpha$  ray (1,541 Å). The EVA software was used to identify the mineral phases, by comparing the obtained diffractograms with the standard reference patterns of the PDF (Powder Diffraction File) data base.

The ubiquity of iron minerals in many samples made the identification of mineral phases more complex. As a matter of fact, the iron fluorescence with the copper  $\text{K}\alpha$  ray results in a particularly important background.

For a few samples, X-ray powder diffraction has also been performed on clay-fractions that are separated from the bulk rock. Therefore, the isolation of the clayish <2- $\mu\text{m}$ -size fraction is carried out following the Holtzapffel's method (1985). After the crushing of samples, carbonates trapped in the clay-fraction are dissolved by adding HCl to the powder. Samples are suspended in distilled water and beakers are positioned in a centrifuge. Several cycles of gravitational settling and mixing are repeated to allow sedimentation of particles greater than 2  $\mu\text{m}$  diameter and evacuation of all unwanted units (e.g. salts). The clay fraction then forms a stable suspension that can be extracted by pipetting. The solution is centrifuged to concentrate the clay minerals before dropping the suspended sample on glass slides. The determination of clay minerals is based on the knowledge of basal (001) interplanar spacings and their (002), (003), ... harmonics. Clay minerals may also be identified by applying particular

treatments to the slides, since their basal reticular distances are shifting in a characteristic way in accordance with the process. Three glass slides are thus analyzed for each sample. The first slide is air dried. The second is treated with ethylene glycol by a vapor-pressure method, in a vacuum desiccator, for 24 hours. This operation aims to make the smectites swell, as glycol replace water molecules. The third slide is heated at 490°C for two hours in an oven. At that temperature, kaolinite is dehydroxylated, vermiculites and smectites are irreversibly dehydrated, but chlorites are preserved (Thiry *et al.*, 2013).

#### **4.2.2 Transmitted light microscopy**

Since the incident light is transmitted from the source on the opposite side of the specimen to the objective lens, this method of observation is suitable for transparent and translucent minerals, e.g. carbonates and silicates, but is not adequate for oxides, sulfides, and native opaque elements. Transmitted light microscopy has been used to identify the mineral phases of the gangue and host rocks of the deposits and emphasize their structures. For this purpose, some twenty thin sections have been confectioned at the University of Liège. The observation equipment consists in a *Leitz HM-POL* (University of Brussels) and a *Zeiss Axiophot* (University of Namur).

#### **4.2.3 Reflected light microscopy**

Whereas transmitted light microscopes are of little use to anyone wanting to examine opaque minerals, even when ground to a thickness of 30 µm, reflected light microscopes are more appropriate. There, the sample is illuminated from above through the objective. For some samples, immersion liquids have been deposited between the front lens of specific objectives and the surface of the section, to increase the optical resolving power of the microscope. By doing this, contrasts and color shades are emphasized, and some typical characteristics are highlighted. For example, goethite has a darker grey color than hematite when observed “in air”. But, when observing these minerals with crossed nicols and oil, hematite has abundant deep red internal reflections whereas those of goethite are varying in number and light yellow to reddish brown.

The confection of 321 polished sections, from the sawing of rock samples to their mounting in resin and polishing with abrasives, has been carried out at the Universities of Brussels, Paris Sud-Saclay and Namur. The observation of sections has been carried out with a *Zeiss Photomicroscope*, a *Nikon Microphot-FX Epi-U*, and a *Zeiss Axiophot* (Universities of Namur and Brussels). However, many phases and structures are beyond the scope of light microscopy and require the use of scanning electron microscopy.

#### **4.2.4 Scanning electron microscopy**

High spatial resolution information is acquired from scanning electron microscopy (SEM); the use of an energy dispersive spectrometer (EDS, EDX) allows in situ semi-quantitative chemical analysis of minerals. A scanning electron microscope uses a beam of electrons to scan the surface of a sample in order to generate a variety of signals at various depths within the sample (from less than 100 nm to approximately 5 µm into the surface): secondary electrons (SE), back-scattered electrons (BSE), characteristic X-rays and light (cathodoluminescence; CL), absorbed current (specimen current) and transmitted electrons. Such signals deriving from electron-sample interactions contain information about the external morphology of the sample (texture, topography), its chemical composition, its crystalline structure and the orientation of materials of the sample. SE and BSE are most commonly used to create images. BSE belong to the incident electron beam and are reflected after elastic scattering interactions with the sample, while SE originate from conduction or valence bands of the

specimen atoms and are the result of inelastic interactions between the electron beam and the sample. Since SE originate from very close to the specimen surface and BSE from deeper regions of the sample, they carry different types of information. SE provide very high-resolution images of a sample surface and thus information about the morphology and topography, while BSE are most valuable for bringing contrasts in chemical composition out in multiphase samples. The black to white shades of BSE images are related to the atomic number of the atoms present in the sample: heavy elements (high atomic number) reflect electrons more strongly than light elements (low atomic number), and thus appear brighter in the image. BSE are often used in analytical SEM, along with the spectra made from X-rays. X-rays are produced by collisions of the incident electrons with inner shell electrons of the specimen atoms, which result in the release of energy in the form of X-rays with a fixed wavelength related to the difference in energy levels of electrons in different shells for a given element. Thus, each element in a mineral that is excited by the electron beam produce characteristic X-rays. The energy of these X-rays can be measured by Energy-dispersive X-ray spectroscopy (EDS) or Wavelength-dispersive X-ray spectroscopy (WDS) and used to estimate the abundance of elements in the sample and map their distribution.

Back-scattered electron imaging and X-ray analysis require grinding and polishing of the sections surfaces to an ultra-smooth surface. The surface of samples must be electrically conductive, and electrically grounded to avoid the electrostatic charge accumulation. Polished sections are thus coated with an ultrathin coating of carbon, deposited on the samples by high-vacuum evaporation. Samples are mounted rigidly to a specimen holder using a conductive adhesive. Polished sections have been observed with several SEMs: a *JEOL JXA-8600 Superprobe* mounted with an EDS system (University of Brussels), a *JEOL JSM 7500F* with EDS (University of Namur), a *JEOL JSM 6010LV* (University of Namur) and a *Zeiss Sigma 300 FEG* equipped with two Bruker EDS detectors (University of Liège).

#### **4.2.5 Electron microprobe microanalysis (EPMA)**

EPMA is a qualitative and semi-quantitative non-destructive elemental analysis of micro-sized volumes. The method is based on Bragg's equation (Equ. 4.1) and uses monocrystals as monochromators defined by the Holland Circle method. The sample composition is identified by recording WDS spectra (Wavelength Dispersive Spectrometry) since the wavelengths of X-rays is characteristic of emitting phases. The sensitivity lies at the level of tens of ppm, depending on the beam acceleration, the probe current and the mineral matrix. Polished sections of Tazalaght and Imini deposits have been observed with a JEOL Microanalyzer JXA-8530F (JEOL, Tokyo, Japan) field emission electron probe (EPMA) equipped with a high brightness Schottky field emission electron gun (FEG), at the Department of Materials Engineering of KU Leuven.

## 4.3 Geochemistry

### ***4.3.1 Whole rock and mineral investigations***

The investigation of elemental distributions in supergene environments was carried out by the Activation Laboratories (ACTLABS, Ontario, Canada). Their advanced technologies have been used to quantify the chemical composition of host rocks and ores. Elements are classified in different categories: major elements (>1 wt%), minor elements (0.1-1 wt%) and trace elements (<0.1 wt%).

These analyses require the preparation of five grams of powder with a maximum 125 µm grain size. For host rocks and mixed ores, analyses are performed on the whole rock. For selected minerals, crystals are handpicked after coarse grinding. The crushing is performed with a RETSCH PM 100 planetary ball mills (Université de Namur) and stainless-steel grinding mortars. Rare Earth Elements (REE) and most of the trace elements (Cs, Pb, U, Th, Ta, Nb, Hf, Cr, W, Mo, Sn, Bi, Tl, Sb, Pb, In, Ga, Ge, Co, Ni, Cu, Zn, As, Rb, Nb, Ag) have been analyzed by lithium metaborate/tetraborate Fusion Inductively Coupled Plasma Mass Spectrometry (FUS-ICP-MS; Perkin Elmer Sciex Elan 9000 ICP-MS). Major elements oxides (SiO<sub>2</sub>, Al<sub>2</sub>O<sub>3</sub>, Fe<sub>2</sub>O<sub>3</sub>, MnO, MgO, CaO, Na<sub>2</sub>O, K<sub>2</sub>O, TiO<sub>2</sub>, P<sub>2</sub>O<sub>5</sub>) and Sr, Ba, Zr, Be, Sc, V, and Y contents have been quantified by lithium metaborate/tetraborate Fusion Inductively Coupled Plasma Optical Emission Spectrometry (FUS-ICP-OES; Varian Vista 735 ICP). FeO has been quantified by titration, S and SO<sub>4</sub> by combustion infrared detection (ELTRA Instruments). For samples containing high contents of Co, Pb, Zn, Ni, Cu, As, and Mo, Bi, Sb, U, analyses have been carried out with Fusion Inductively Coupled Plasma Sodium Peroxide Oxidation (FUS-Na<sub>2</sub>O<sub>2</sub>) and with Fusion Inductively Coupled Plasma Mass Spectrometry Sodium Peroxide Oxidation (FUS-MS-Na<sub>2</sub>O<sub>2</sub>), respectively, and results quantified in percentages rather than in ppm. Some iron-rich samples required the use of Fusion - X-ray Fluorescence (FUS-XRF) to quantify elements contents. Details concerning all the various manipulations are available at [actlabs.com](http://actlabs.com).

Elements concentrations are frequently compared to reference samples, in order to illustrate enrichments, depletions and anomalies that reflect specific geological processes. The choice of standards depends on the studied type of rock. Here, to highlight supergene geochemical trends, contents have been normalized to Upper Continental Crust (UCC; Taylor and McLennan 1985) considered as a reference for sedimentary rocks. The Post Archean Australian Shale (PAAS; Taylor and McLennan 1985) could also have been used, but the data set is less complete than the UCC. Mineralized sample contents have also been compared to host rocks and hypogene sulfides in order to emphasize enrichment and depletion of elements during weathering.

### ***4.3.2 Stable isotope geochemistry of oxygen and hydrogen***

Iron (oxyhydr-)oxides usually form in equilibrium with the environment. Their oxygen and hydrogen isotopes provide information about their conditions of precipitation and the origin of fluids since they reflect the temperature of formation and the δD and δ<sup>18</sup>O of water. The isotopic signature of water depends, in weathering environments, on the latitude, elevation, continentality and climate. The <sup>18</sup>O/<sup>16</sup>O and D/H (<sup>2</sup>H/<sup>1</sup>H) ratio between heavy and light isotopes only present slight fluctuations and are thus difficult to measure directly. These ratios are thus compared with standards of known ratios such as the Standard Mean Ocean Water (SMOW). The difference (δ) between the sample and the standard value is defined as follows (Equ. 4.2 et 4.3).



$$\delta^{18}\text{O} = \left[ \frac{\frac{\text{sample}^{18}\text{O}}{\text{sample}^{16}\text{O}} - \frac{\text{standard}^{18}\text{O}}{\text{standard}^{16}\text{O}}}{\frac{\text{standard}^{18}\text{O}}{\text{standard}^{16}\text{O}}} \right] \cdot 1000 (\text{‰}) \quad (\text{Equ. 4.2})$$

$$\delta\text{D} = \left[ \frac{\frac{\text{D}_{\text{sample}}}{\text{H}_{\text{sample}}} - \frac{\text{D}_{\text{standard}}}{\text{H}_{\text{standard}}}}{\frac{\text{D}_{\text{standard}}}{\text{H}_{\text{standard}}}} \right] \cdot 1000 (\text{‰}) \quad (\text{Equ. 4.3})$$

Isotopic signatures are fractionated in three ways. Equilibrium fractionation is related to thermodynamic properties of minerals. Kinetic fractionation is due to rates of precipitation that trigger excess or lack of isotopes in particular phases. Biogenic fractionation arises from the metabolic activity of organisms. Fractionation coefficients ( $\alpha$ ), which are temperature-dependent equilibrium constants, reflect the fractionation of isotopes between two phases and enable the use of hydrogen and oxygen isotopes as geothermometers (Equ. 4.4). Oxygen values vary as a linear or sub-linear function, indicating that fractionation decreases when temperature increases (Equ. 4.5, where  $a$  and  $b$  are constants and  $T$  is the temperature).

$$\alpha_{\text{mineral-water}} = \frac{(1000 + \delta_{\text{mineral}}^{18}\text{O})}{(1000 + \delta_{\text{water}}^{18}\text{O})} = \frac{\frac{\text{mineral}^{18}\text{O}}{\text{mineral}^{16}\text{O}}}{\frac{\text{water}^{18}\text{O}}{\text{water}^{16}\text{O}}} \quad (\text{Equ. 4.4})$$

$$1000\ln\alpha_{\text{mineral-water}} = a \cdot 10^6 \cdot T^{-2} - b \quad (\text{Equ. 4.5})$$

The suitability of stable isotopes analyses for goethite and hematite has been demonstrated by (Yapp 1990); both minerals are isotopically indistinguishable at equilibrium. Between 25 and 120°C, the hematite and goethite – water oxygen isotope fractionation is represented by Equ. 4.6. Since only goethite host hydrogen in its structure, which is not the case of hematite,  $\delta^{18}\text{O}$  vs.  $\delta\text{D}$  plots only represent goethite precipitation. The isotopic composition of goethite may be distorted by the common Mn and Al substitutions (Yapp and Pedley 1985). Based on Equ. 4.6, temperature domains and temperatures lines assessing water conditions for goethite precipitation have been estimated (Yapp 1990; Girard et al. 2000).

$$1000\ln\alpha_{\text{goethite-water}} = 1.63 \cdot 10^6 \cdot T^{-2} - 12.3 \quad (\text{Equ. 4.6})$$

Oxygen ( $\delta^{18}\text{O}$ ) and hydrogen ( $\delta\text{D}$ ) isotopic compositions have been determined for goethite samples, at the Institute of Earth Surface Dynamics of the University of Lausanne (Switzerland). Hydrogen and oxygen isotopic compositions are with a Finnigan MAT 253 gas source mass spectrometer (Thermo Fisher Scientific) and are reported in permil (‰), in the typical  $\delta$ -notation relative to the Vienna Standard Mean Ocean Water (VSMOW). According to the method defined by Vennemann et al. (2001), oxygen isotope compositions are obtained using a  $\text{CO}_2$ -laser fluorination line. Between 2 and 3 mg of goethite, crushed from individual grains, are loaded onto small Pt sample holders. After several cycles of pre-fluorination of the chamber, samples are heated with a  $\text{CO}_2$ -laser to yield  $\text{O}_2$ , in the presence of pure  $\text{F}_2$  that acts as a reagent. After purification of the gas, the extracted  $\text{O}_2$  is introduced into the inlet of the mass spectrometer. Oxygen isotope analyzes of the LS-1 quartz standard (in-house-reference material of Lausanne, quartz 18.1‰) are replicated. The hydrogen isotope composition and water content of goethite are determined with a zero-blank auto-sampler and a High-Temperature Conversion Elemental Analyzer (TC-EA) (Thermo Fisher Scientific), according to the method of Bauer

and Vennemann (2014), using between 2 and 3 mg of goethite. In-house reference materials of biotite (G1;  $\delta D = -62 \pm 0.8\text{‰}$ ) and kaolinite (K-17;  $\delta D = -125 \pm 0.9\text{‰}$ ) are used to calibrate the measured isotopic compositions (Bauer and Vennemann, 2014).

## 4.4 Geochronology

### 4.4.1 (U-Th-Sm)/He method

Over the last century, the (U-Th-Sm)/He method has been used to date different mineral phases such as zircon and apatite. The method is based on the production of He during alpha radioactive decay of U, Th and Sm atoms, and on its accumulation and retention within a crystal structure. Since He is a rare gas, its diffusion outside the crystal structure depends on the mineral, the temperature and the crystal size. If He is not lost significantly, the method is considered as a chronometer, while it used as a thermochronometer if He is lost during a particular thermal history.

The first radioisotopic date using a U–He system was produced in 1904 by Rutherford; Strutt (1909) carried out the first tests of U/He on iron-rich minerals. Several decades later, in 1962, Fanale and Kulp defined the first helium isochrones age on the Pennsylvania Cornwall magnetite deposit. The method was later demonstrated to be a reliable chronometer in some cases, but most of the obtained He ages were younger than expected. The potential of (U-Th)/He dating of hematite veins in Germany was studied by Wernicke and Lippolt (1994) and further by Lippolt et al. (1998), who obtained encouraging results. In parallel, the work of Zeitler et al. (1987) and Farley et al. (1996) on apatite opened up new research avenues in the domain of (U-Th)/He dating as a thermochronometer. Advances in the understanding of helium diffusion in different mineral phases such as (oxyhydr-)oxides led to the development of the (U-Th-Sm)/He method, and to the specification of analysis parameters (e.g. Shuster and Farley 2005; Blackburn et al. 2007; Farley and Flowers 2012). Recently, several publications focused on dating hematite and goethite with the purpose of understanding the formation of channels deposits, the source of materials, the formation of a regolith, the quantification of weathering rates, the climatic conditions of the past, the formation of supergene profiles, the formation of lateritic profiles, etc.

#### 4.4.1.a Generalities of the method

Most minerals, including iron (oxyhydr-)oxides, naturally host U, Th and Sm in their crystalline lattice, at different concentration levels ranging from ppb to thousands of ppm (Fig. 4.2). The radioactive decay of  $^{238}\text{U}$ ,  $^{235}\text{U}$ ,  $^{232}\text{Th}$  and  $^{147}\text{Sm}$  to the stable isotopes  $^{206}\text{Pb}$ ,  $^{207}\text{Pb}$ ,  $^{208}\text{Pb}$  and  $^{143}\text{Nd}$ , respectively, triggers the emission of alpha particles and the formation of radiogenic  $^4\text{He}$  atoms (Equ. 4.7, 4.8, 4.9, 4.10; Fig. 4.2).

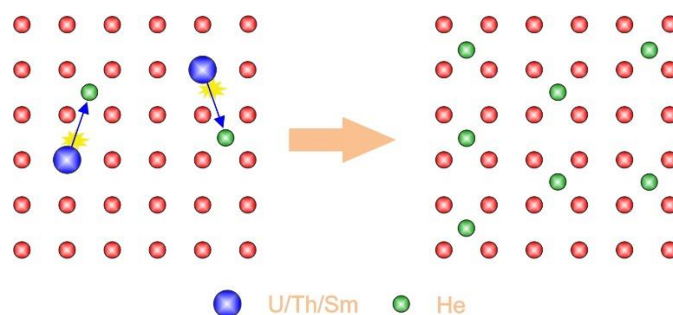
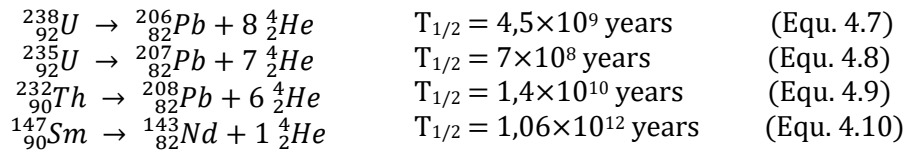


**Figure 4.2.** Schematic representation (not drawn to scale) of the emission of He atoms following the radioactive decay of U, Th and Sm atoms.



The concentration of radiogenic He is proportional to time and to the concentration in U, Th and Sm. Samarium contributes to a negligible proportion to the He budget and is often ignored. For this reason, the method is historically called (U-Th)/He even if the Sm content is currently measured. Both (U-Th)/He or (U-Th-Sm)/He designations may be used. U, Th and Sm contents are often condensed by the effective uranium parameter (eU; Equ. 4.11). The daughter isotope production follows a radioactive decay law (Equ. 4.12).

$$eU = [U] + 0.235[Th] + 0.0075[Sm] \quad (\text{Equ. 4.11})$$

$${}^4\text{He} = 8 \cdot {}^{238}\text{U} (e^{\lambda_{238}t} - 1) + 7 \cdot {}^{235}\text{U} (e^{\lambda_{235}t} - 1) + 6 \cdot {}^{232}\text{Th} (e^{\lambda_{232}t} - 1) + {}^{147}\text{Sm} (e^{\lambda_{147}t} - 1) \quad (\text{Equ. 4.12})$$

where  ${}^4\text{He}$ ,  ${}^{238}\text{U}$ ,  ${}^{235}\text{U}$ ,  ${}^{232}\text{Th}$  and  ${}^{147}\text{Sm}$  refer to present-day amounts,  $t$  is the accumulation time or He age,  $\lambda$  the decay constant ( $\lambda_{238} = 1.55 \times 10^{-10} \text{ yr}^{-1}$ ,  $\lambda_{235} = 9.85 \times 10^{-10} \text{ yr}^{-1}$ ,  $\lambda_{232} = 4.95 \times 10^{-11} \text{ yr}^{-1}$ ,  $\lambda_{147} = 6.54 \times 10^{-12} \text{ yr}^{-1}$ ). Coefficients preceding U, Th and Sm abundances account for the multiple alpha particles emitted within each of the decay series.

The principal parameters that must be considered within the framework of (U-Th-Sm)/He dating are 1) He production, 2) He ejection, and 3) He accumulation into the crystal, which may be affected by He losses by diffusion during a particular thermal history (Farley, 2002). During alpha emission, the alpha particle is emitted with an important kinetic energy of several dozens of MeV (Table 4.2; Ziegler 1977). It travels a dozen microns in the crystal structure and forms a  ${}^4\text{He}$  atom with two electrons of neighboring atoms (Farley et al., 1996; Ketcham et al., 2011). The stopping distance depends on the crystal structure and composition, and to the energy of the emitted particle. Radiogenic atoms of the U-Th decay chains also have a kinetic energy ranging between 65 and 160 eV; the alpha emission results in a recoil movement creating a damage (or amorphous zone) of a few nm (Ketcham et al., 2011).

**Table 4.2.** Characteristic values of the (U-Th-Sm)/He system and mean stopping distances for apatite, hematite and goethite (Ziegler et al., 2010; Ketcham et al., 2011)

Parent isotope	Period (Ga)	Daughter isotope	Number of emitted alpha particles	Mean kinetic energy (MeV)	Mean stopping distance in apatite ( $\mu\text{m}$ )	Mean stopping distance in hematite ( $\mu\text{m}$ )	Mean stopping distance in goethite ( $\mu\text{m}$ )
${}^{238}\text{U}$	4.4683	${}^{206}\text{Pb}$	8	5.36	18.81	13.6	15.5
${}^{235}\text{U}$	0.7038	${}^{207}\text{Pb}$	7	5.94	21.80	15.7	18.0
${}^{232}\text{Th}$	14.05	${}^{208}\text{Pb}$	6	5.85	22.25	16.0	18.4
${}^{147}\text{Sm}$	106	${}^{143}\text{Nd}$	1	2.25	5.93	4.4	5.0

For crystals and grains of a size comparable to that of the mean ejection distance (20  $\mu\text{m}$ ), a part of emitted He may be lost by ejection. Such losses may be evaluated for a dated mineral on the basis of known stopping distances, the kinetic energy of He atoms and grains/crystal size geometry (Farley, 2002). For single and small crystals, a part of He is lost by ejection at the edge of the crystal. In the case of apatite, zircon and titanite, crystals average thousands of microns in length; 5 to more than 70 of He may be lost by ejection (Ehlers and Farley, 2003). Large enough crystals are thus selected for dating in order to limit He losses to 30%. He losses are corrected with an ejection factor ( $F_T$ ) that depends on

the surface-to-volume ratio of the crystal and on the stopping distance of He in the mineral (Farley et al., 1996). However, for large grains and crystals (> 300-400 microns), and for fragments of large grains, such as most iron (oxyhydr-)oxides, He ejection is negligible. Only millimetric-sized crystals and fragments are analyzed to avoid He losses.

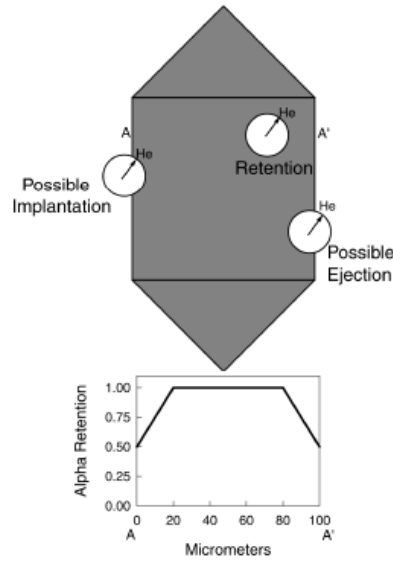


**Figure 4.3.** Effects of alpha stopping distances on He retention. The lower scheme shows the variation of retention from rim to core to rim along the path A-A' (Farley, 2002).

After alpha particle emission, He atoms remain on various vacant sites of the crystal lattice such as interstitial sites, vacancies and radioactive damages. Since He is a noble gas, it does not create chemical bonds. He is thermally active, which means that each atom can move from one site to another, with a diffusion rate depending on temperature (Crank, 1975). He diffusion coefficient within a solid-state with a certain volume follows Arrhenius' equation (Equ. 4.13).

$$\frac{D}{a^2} = \frac{D_0}{a^2} \exp\left(\frac{-E_a}{RT}\right) \quad (\text{Equ. 4.13})$$

where  $a$  is the size of the diffusion domain,  $D$  the diffusion coefficient,  $D_0$  the frequency factor,  $E_a$  the activation energy,  $R$  the universal gas constant, and  $T$  the temperature (K).

The size of diffusion domains ( $a$ ) corresponds to crystal dimensions for minerals such as apatite, zircon and titanite, or to the size of crystallites composing polycrystalline samples such as hematite and goethite. As a function of temperature, He diffuses in various space directions and eventually leaves the crystal. The diffusion within the crystal structure is also impacted by crystal chemistry, vacancies and radioactive damages (Ault et al., 2019). Because of the characteristic He losses with temperature, the (U-Th)/He method was at first mostly used as a thermochronometer: a thermochronometric age records the thermal history of rocks using He diffusion algorithm (Ehlers and Farley, 2003; Ault et al., 2019). The thermal sensitivity of each mineral depends on the diffusion coefficient ( $D_0$  and  $E_a$ ), for a constant diffusion domain ( $a$ ). To quantitatively compare the sensitivity of thermochronometers, Dodson (1973) proposed the notion of closure temperature ( $T_c$ ) that corresponds to the temperature at which 50% of emitted He atoms stay in the crystal for a monotonic cooling. Figure 4.4 presents closure temperatures for different minerals and illustrates all the different existing systems with their respective sensibility.

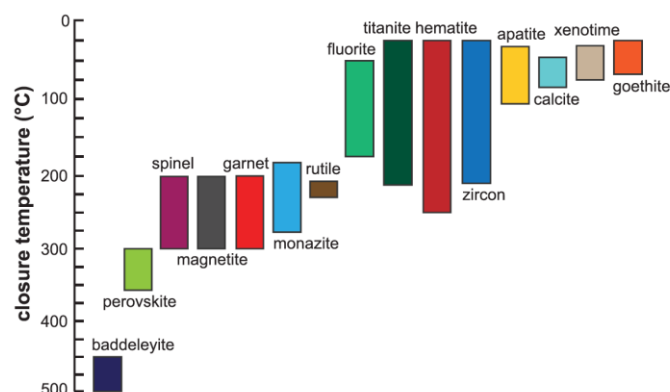


**Figure 4.4.** Closure temperatures for various (U-Th)/He systems (Ault et al., 2019).

The (U-Th)/He method is also used as a chronometer to date mineral crystallization at Earth surface temperature such as in volcanic rocks or supergene mineralization. In this case, the closure temperature notion is less relevant since samples remain in average at the same temperature since crystallization. The condition to use a chronometer is thus that He is retentive at Earth surface temperature for the selected mineral system.

The application of the (U-Th)/He method follows several rules:

- The absence of initial  $^4\text{He}$  in the dated crystal(s) is assumed. Since He concentration in the atmosphere is low (~5 ppm), trapped atmospheric He is unlikely to be significant.
- There is no He contamination in the dated crystal nor U-Th-Sm losses.
- He is retained in the mineral, or the He diffusion behavior is well known.

#### 4.4.1.b Goethite and hematite (U-Th)/He method

Iron oxides minerals are almost ubiquitous in the rocks, sediments and soils accessible on Earth's surface. Among other parameters, their concentration, mineralogy, crystallinity and particle sizes give information about their geological and environmental history. For instance, the degree of structural order and the crystal size are variable and depend on the conditions under which the crystals were formed. Goethite and hematite are the thermodynamically most stable iron oxides at ambient temperature, and are widespread in rocks and soils. The geological occurrence of goethite and hematite is initiated through:

- crystallization of a magma/melt (only hematite),
- precipitation from solutions containing divalent or trivalent iron (e.g. fault systems),
- alteration or weathering of a preexistent mineral phase via dissolution and reprecipitation or through pseudomorphic transformation (e.g. in supergene and lateritic ores),
- transport as a detrital component (Cornell and Schwertmann, 2003; Faivre, 2016). Goethite is thus ubiquitous in small concentrations in consolidated and unconsolidated rocks of any age (minette, oolitic rocks, laterite crusts, bog ores) whereas hematite concentrates in red beds, banded iron formations, laterite crusts and brines.

As already indicated in the previous chapter, although the (U-Th)/He method has been already applied to dating hematite and goethite, only few studies exist and the method is still underexplored due to this relatively young application and to the few laboratories performing such analyses. The frequent dispersion of (U-Th)/He ages, their relatively low precision, their undetermined accuracy related to the absence of standards, the complex nature of goethite samples (e.g. polycrystallinity, poor crystallinity,

presence of multiple diffusion domains, co-existence of several generations), ... are all uncertainties and problems that limited the use of (U-Th)/He method to date hematite and goethite crystallization.

## He ejection

During the selection of fragments from goethite samples, precautions are taken to prevent supplementary uncertainties. In order to avoid any correction due to He loss by ejection, only large crystals ( $> 400 \mu\text{m}$ ) are selected, and the edges of samples are discarded. For goethite and hematite, the ejection factor defined earlier ( $F_T$ ) is considered as null and avoid, given the large size of the sampled constituted of crystallite aggregates.

## He diffusivity and retentivity

Thermally activated He atoms always diffuse in minerals, even at surface temperature, but the amount of diffused He is mostly insignificant if the crystal structure is large ( $>$  microns). Because of the common polycrystalline structure of goethite and hematite, He losses by diffusion may reach up to a few dozen of percent (Shuster et al., 2005; Jonathan A. Heim et al., 2006; Hofmann et al., 2017). The crystallites size is thus one of the most important parameters to know to interpret (U-Th-Sm)/He ages.

In order to determine potential He losses by diffusion, several studies focused on the determination of the diffusion coefficient ( $E_a$ ,  $D_0$ ) and on the assessment of diffusion domains for hematite and goethite. Different experiments have been carried out. The first type of experiment consists of under-vacuum diffusion tests on natural samples to measure, through incremental heating, the degassing with temperature and time of radiogenic  $^4\text{He}$  and of artificial  $^3\text{He}$  that is homogeneously produced by proton irradiation. The spatial concentration of radiogenic  $^4\text{He}$  and of  $^3\text{He}$  are thus measured on the same grain. The amount of radiogenic He in goethite reflects the delicate balance between the production of radiogenic He and the loss of He by thermal diffusion, and is thus related to the time-temperature (t-T) history of the sample. Such  $^4\text{He}/^3\text{He}$  diffusion experiments are thus carried out to remedy diffusion uncertainties and better quantify He losses, identify He retention domains, and thus correct calculated ages to acquire more reliable and accurate data (Farley and Flowers, 2012; Vasconcelos et al., 2013). A second type of experiment consists in Density Functional Theory calculations that enables the quantification of  $D_0$  and  $E_a$  parameters, and the subsequent prediction of He losses (Balout et al., 2017).

**Table 4.3.** Diffusion coefficients and closure temperature obtained for spherical diffusion domains and cooling rates of  $10^\circ\text{C}/\text{Ma}$  (Shuster et al. 2005; Farley, 2018; Balout et al., 2017; Ault et al., 2019), for apatite, hematite and goethite.

Mineral	$E_a$ (kJ/mol)	$\ln(D_0)/a^2$ (ln(s $^{-1}$ ))	a for $D_0$ ( $\mu\text{m}$ )	$D_0$ (cm $^2$ /s)	a ( $\mu\text{m}$ )	$T_c$ ( $^\circ\text{C}$ )
Apatite	121-165	4.8-21.4	60	$4.4 \times 10^{-3}$ - $7.1 \times 10^{-4}$	60	50-120
Goethite	163-178	26-28	0.5	$4.9 \times 10^2$	0.5	51
Hematite	157-170	-	0.1	$5.2 \times 10^{-1}$	0.1	80

## He diffusion in hematite

Following diffusion experiments conducted on hydrothermal hematite presenting large crystallites, hematite is interpreted to be strongly He retentive. Fig. 4.5 presents the evolution of the He fraction retained in a crystal as a function of the holding time, for different temperatures (20, 30, 40, 50 and  $75^\circ\text{C}$ ) and for a  $0.01 \mu\text{m}$ -sized diffusion domain. Following this model, at 20 or  $30^\circ\text{C}$ , He is very well retained in hematite (Farley, 2018; Fig. 4.5). A correction of a few percent needs to be accounted for  $0.1 \mu\text{m}$ -sized crystallites.

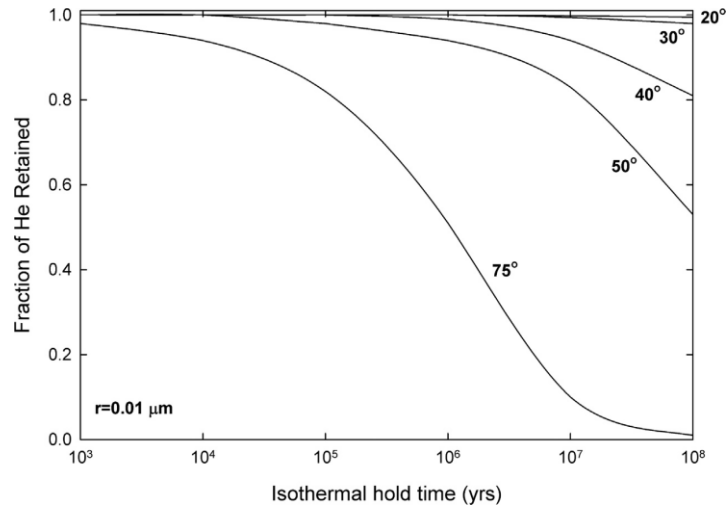


**Figure 4.5.** Retention of He in hematite, with time (Farley, 2018).

### He diffusion in goethite

For goethite, diffusion experiments have been conducted on samples from lateritic soils, where the crystallites size is smaller than for hematite. Since goethite contains water in its crystallite structure, diffusion experiments are more difficult to perform and interpret because of the possible losses of water during the experiments. With such diffusion experiments, Shuster et al. (2005) determine that He losses at surface temperatures can reach up to 30% (Fig 4.6), and that different samples are characterized by different He retentivities.

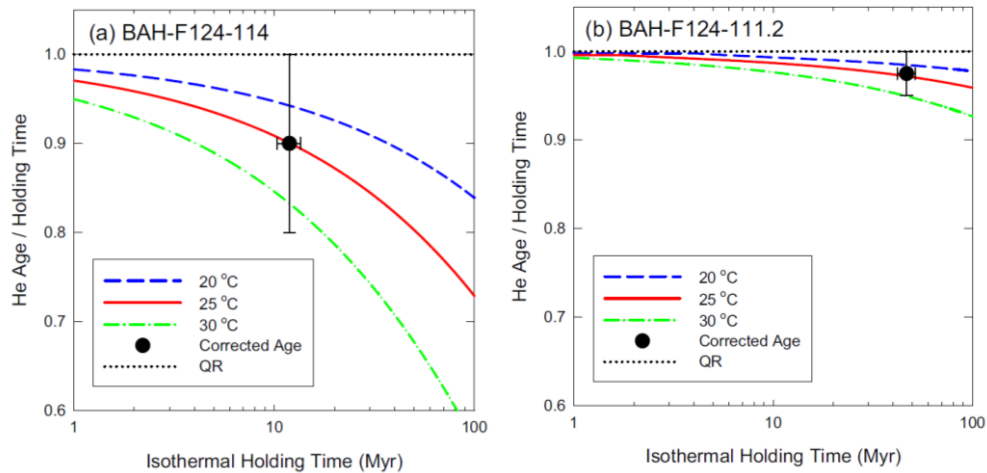


**Figure 4.6.** He retentivity of two supergene goethite samples showing different He retention behaviors (Shuster et al., 2005).

From  $^4\text{He}/^3\text{He}$  diffusion experiments, Deng et al. (2017) calculated He losses of 10, 14, and 18%, and concluded that this variation is not related to crystallite sizes and that, consequently, no correction of this parameter should be applied. They however concluded that a mean correction of 14% may be considered. Other  $^4\text{He}/^3\text{He}$  diffusion experiments on goethite pisoliths (Hofmann et al. 2017) show lower He diffusion losses ranging between 2 and 8%. Consequently, He diffusion and diffusion domain sizes are key parameters to determine the amount of He losses that should be considered for each sample. Up to now, a consensus on He diffusion is still missing, and more diffusion experiments are needed to better characterize He retention in natural goethite. They also observed that events such as solar heat, forest fires, and thunderbolts may reset the system and distort ages (Shuster et al. 2005).

## Factors leading to dispersive ages

Interpretation of goethite and hematite (U-Th-Sm)/He ages may be complex, due to the presence of multiple generations in a single sample (Evenson et al., 2014; Monteiro et al., 2014). The definition of mineral crystallinity encloses the degree of crystalline disorder as well as the size of the crystallites. The crystallinity of goethite and hematite strongly depends on the environment and mode of precipitation: goethite replacing minerals (e.g. pyrite, siderite) are poorly crystallized and enclose many relics, whereas colloform and botryoidal goethite precipitating in cavities and fractures are pure and well crystallized. The association of different sized crystallites is highly frequent in goethite, where it results from successive precipitations and dissolution-reprecipitation processes. Intergrowths between the various generations are very common, making them impossible to separate (Vasconcelos et al., 2013; Monteiro et al., 2014). Ages obtained for such samples are thus an average of all different generations ages.

Secondly, inclusions and relic minerals are often embodied in iron (oxyhydr-)oxides (Fig. 4.7). These relic minerals are commonly presented as “bad neighbors”. When these “neighbors” are He unretentive such as quartz, calcite and muscovite, their presence is tolerable, although in small quantities: their released He is lost by diffusion, and they do not interfere with U-Th-Sm contents since they are not dissolved during the chemical treatment. Problems occur when “mineral neighbors” are He retentive such as zircon, titanite, rutile, ilmenite, apatite, hematite etc. (Fig. 4.7) (Riffel et al., 2016). In this case, He is retained in the sample, is only released with the laser degassing at the same time as He originating from goethite, and thus contribute to the total He content (Fig. 4.7). These minerals and inclusions are however not dissolved during the chemical treatment that focuses on iron (oxyhydr-)oxides dissolution. To resume, these undesired phases add He to the system, but no U and Th; samples then yield older ages than expected (Fig. 4.7). For example, if, for three aliquots of the same sample, ages of 3, 4, and 74 Ma are acquired, the third aliquot has probably been contaminated with an external phase, such as zircon. This issue is more pronounced with iron (oxyhydr-)oxides that replace minerals by pseudomorphose and thus take along many primary impurities and gangue minerals.

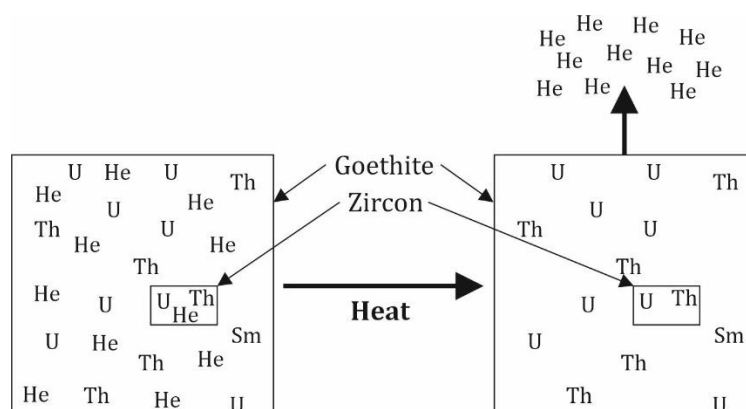


**Figure 4.7.** Influence of “bad neighbors” and inclusions on (U-Th-Sm)/He dating.

Thirdly, the occurrence of U and Th in iron (oxyhydr-)oxides is either due to their adsorption in the lattice, or to their co-precipitation or incorporation in the mineral. Chemical zoning and U-Th concentration gradients may also affect He concentration and result in the acquisition of younger or older ages. The effective uranium parameter highlights variations of both elements in relation with ages.

Finally, substitutions in goethite may influence ages obtained through (U-Th-Sm)/He dating. For instance, it is possible to have a maximum of 33% of aluminum in goethite: as aluminum radius is 17%



smaller than that of iron, having a higher amount of this element would destabilize the crystal lattice (Pinney and Morgan, 2013). This does not come without a price: lattice parameters  $a$  and  $c$  are reduced, and crystallites sizes, thermal stability, solubility, and surface properties of goethite are modified, as well as He diffusion.

To conclude, the interpretation of (U-Th-Sm)/He ages of hematite and goethite samples is complex. Only the selection of well characterized samples permits to access a geological meaning. Disruptions in the system may also lead to the acquisition of older or younger than expected ages.

Several causes may be brought forward to explain younger ages:

- He losses by diffusion in small diffusion domains,
- U and/or Th gain by interactions with weathering fluids,
- dissolution and reprecipitation episodes.

The following causes may contribute to obtaining older ages:

- U and/or Th losses by interactions with weathering fluids,
- gain of He from inclusions and relic minerals.

## **Errors and corrections**

The global analytical error on He measurement ranges between 1 and 5%, while that of U, Th, and Sm varies between 1 and 2%. In the context of goethite (U-Th-Sm)/He dating, He losses by diffusion are the major source of uncertainty and concern, whereas for hematite, He losses by diffusion seem to be insignificant at surface temperatures. Ideally, to quantify diffusion losses,  $^4\text{He}/^3\text{He}$  diffusion experiments should be carried out on the same grain that is used for (U-Th)/He dating (Heim et al., 2006; Vasconcelos et al., 2013). This is however almost impossible; the only conceivable option is to analyse two separate aliquots, which regrettably add supplementary uncertainties (Monteiro et al., 2014). Account taken of all the above, most authors use crystallites sizes to represent the retention domains of hematite and goethite, and correct their results by adding 0 to 20% to measured ages (mostly 10%; e.g. Vasconcelos et al. 2013) and by applying a 10% error to counterbalance He losses by diffusion. The total final correction probably exceeds the effective error, but considers the maximum potential He losses expected for well-crystallized goethite grains. Table 4.4 summarizes the most important parameters presented in some recent publications about (U-Th-Sm)/He dating: type of analyzed material, number of samples and aliquots, dispersion of ages and corrections applied.

**Table 4.4.** Publications on hematite and goethite (U-Th)/He dating and their parameters

Authors	Material analyzed	Number of samples	Number of aliquots	Dispersion of ages	Corrections applied
(Danišík et al., 2013)	Goethite + hematite, drilling, channel iron deposit	8	101	Average	$\pm 1 \delta$ (standard deviation)
(Riffel et al., 2016)	Goethite	11	3/sample	Low	$\pm 1 \delta$ and $\pm 10\%$
(Allard et al., 2018)	Goethite	3	5/sample	Low	$\pm 1 \delta$ and $\pm 10\%$
(Heim et al., 2006)	Goethite	39	73	Good	$\pm 10\%$
(Heim et al., 2006)	Goethite	10	21	High	$^4\text{He}/^3\text{He}$ experiments $\pm 5\%, \pm 10\%, \pm 20\%$
(Pidgeon et al., 2004)	Hematite from laterite	4	1/sample	High	$\pm 1 \delta$
(Farley and Flowers, 2012)	Hematite	1	4	Low	Standard, $\pm 2 \text{ Ma}$
(Deng et al., 2017)	Goethite, drilling, surface of deposit	51		Average	$\pm 2 \delta$
(Ault et al., 2015)	Hematite, fault	10	48	Average	$\pm 1 \delta$
(Shuster et al., 2012)	Goethite, cangas	12	26	High	$\pm 10\%$
(Monteiro et al., 2014)	Goethite, cements in cangas	19	161	Scattered, but in the same range	$\pm 10\%$
(Riffel et al., 2015)	Goethite	45	2/sample	Average	$\pm 10\%$
(Vasconcelos et al., 2013)	Goethite, cements	6	3/sample	Average	$\pm 10\%$
(Shuster et al., 2005)	Goethite	9	30	Good	$^4\text{He}/^3\text{He}$ experiments and modelling
(Evenson et al., 2014)	Hematite and Mn-oxides	9	101	High	$\pm 1 \delta$

#### 4.4.1.c Goethite (U-Th-Sm)/He methodology

##### Samples selection

As very pertinently pointed out by Vasconcelos (1999) for the dating of Mn oxides, the successful dating of supergene materials strongly depends on the careful selection of samples on the field, their subsequent thorough characterization in the laboratories and the thoughtful integration of results in their geological context. Hematite and goethite share very similar features and are thus difficult to distinguish on the field. However, goethite present brown, brownish yellow to orange yellow streak and tints while bright to dark red streak and shades are characteristic of hematite. Mn-oxides are easily differentiated from Fe (oxyhydr-)oxides by their dark grey to black matt appearance. Detailed macroscopic and microscopic investigation of goethite enables to avoid contamination in the dating process and allows the acquisition of accurate and meaningful ages. Details concerning the (pre)selection of hematite and goethite samples for (U-Th-Sm)/He dating are provided in chapter 6.1.

## Samples preparation

Losses of U and Th during ultrasonic cleaning and by volatilization during laser heating are problems that were quite recently identified. Evenson et al. (2014) noticed that samples cleaned in an ultrasonic bath yielded older ages than uncleaned samples and were characterized with lower eU values, even without degassing operations. These issues are probably related to disintegration phenomena and losses of interstitial phases during cleaning. Since these phases are small-sized, He probably diffused to the neighboring crystals, resulting in He deficits and older ages. Danišík et al. (2013) also noticed that goethite heated at high temperatures (1150-1200 °C) yield older ages and present higher Th/U ratios than samples heated at lower temperature. They suggested to heat samples at lower temperatures (500 °C or 930-960 °C), with a less powerful laser or with a furnace equipped with controllable resistance. This would also enable to acquire more reliable ages by not degassing inclusions and neighboring minerals such as rutile and zircon. To prevent these analytical issues, we took care of the different points during sample preparation.

All manipulations required for (U-Th-Sm)/He dating have been performed at the Paris-Sud University, in the GEOPS laboratory. Firstly, goethite samples (Fig. 4.11A) are grinded to keep 0.5 – 1 mm long fragments that are cleaned in milli-Q distilled water in an ultrasonic bath (Fig. 4.11B) to separate goethite needles from loosely adsorbed clay- and silt-size fractions (Fig. 4.11C). This stage is repeated until the water remains clean after ultrasonic treatment, according to the quantity of impurities (Figs. 4.11C, 4.11D). Fragments are then rinsed with pure ethanol in an ultrasonic bath to draw water out of the pores, and left to air dry. An alternative has been considered at Imini: the extraction of very small fragments of different layers of crystallization required the use of a Dremel tool with titanium pins on precisely sawed smooth surfaces. Fragments are selected by handpicking on the basis of their homogeneity, crystallization, coherence and limited porosity under a binocular microscope (Figs. 4.11E, 4.11F, 4.11G). As a first step, three aliquots are usually prepared for each sample, to see if the fragment size is adequate, i.e. if enough He is present (see below). The number of aliquots is later increased, depending on the objectives of the analysis. Each aliquot is measured, photographed, encapsulated into a niobium package (purity 99.9%; Fig. 4.11H), and weighted. As it is very difficult to weight small aliquots without losing parts of the sample, niobium packages are first weighted empty, and then reweighted with the grain inside. During this study, two types of niobium envelopes have been used: first, 0.5-1 mg grains were encapsulated in pure 99.9% niobium foils folded in 4x4mm envelopes. Later, for smallest grains, 0.02-0.08 mg aliquots were put in pure 99.9% 1x1mm niobium tubes that were clamped at both ends.

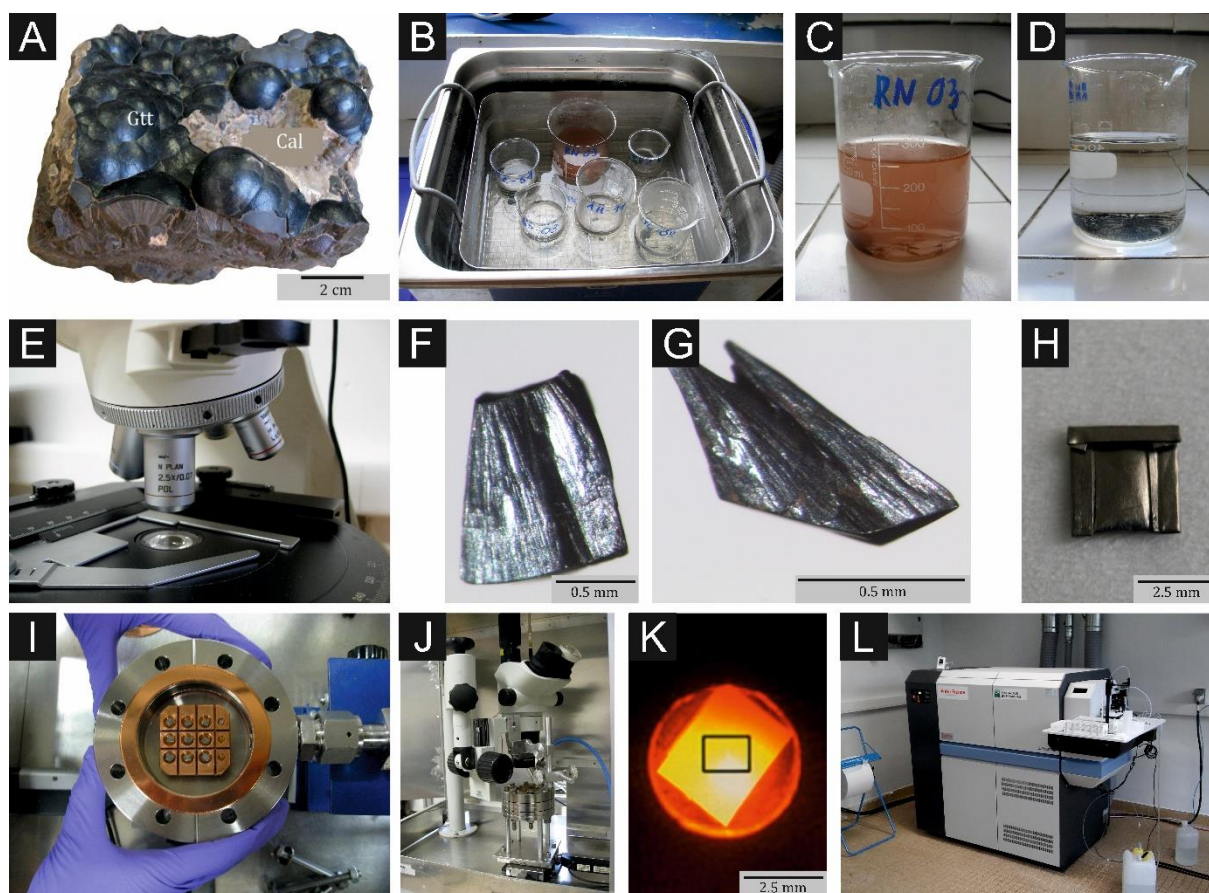


**Figure 4.11.** Principal manipulations required for (U-Th-Sm)/He dating. (A) Ideal goethite sample from Imini deposit: botryoidal, well crystallized, simple to isolate; (B) Ultrasonic cleaning of several samples; (C) Solution with powdery components at the first stage of ultrasonic cleaning; (D) Clean solution at the end of ultrasonic cleaning; (E) Binocular microscope used to select the best goethite fragments for dating; (F and G) Ideal fragments of botryoidal goethite for dating; (H) Niobium envelope enclosing a goethite fragment; (I) Twelve cells plate containing nine goethite samples, a blank, and two Durango apatite samples; (J) Laser and case used for degassing He from goethite fragments; (K) Niobium envelope and goethite fragment heated with the laser; (L) ICP-MS used for quantifying U, Th and Sm contents.

### Degassing of samples and He measurement

The niobium envelopes or tubes are then placed in a vacuum chamber, on a 12 or 49-cells plate, respectively, along with a blank and Durango apatite fragments (Figs. 4.11I, 4.12). Encapsulated samples are one-by-one degassed using a diode Ytterbium laser (Figs. 4.11J, 4.12K) under vacuum for 30 minutes at a temperature below 1000 °C to reach the thermal activation and diffusion of He without losing U and Th. This heating step is once or twice repeated until all  $^4\text{He}$  is degassed. Most goethite grains release low but measurable amounts of He (less than 2% of total  $^4\text{He}$ ) in the second extraction, as observed by Monteiro et al. (2014). The released gas is mixed with a known amount of  $^3\text{He}$ , in the purification line, and separated from most  $\text{H}_2\text{O}$ ,  $\text{CO}_2$ ,  $\text{H}_2$  and Ar using three liquid nitrogen-cooled traps of activated charcoal, a titanium sponge trap heated at  $\sim 850^\circ\text{C}$  and a SAES 701 getter (Fig. 4.12). Helium isotopes ( $^3\text{He}$  and  $^4\text{He}$ ),  $\text{H}_2\text{O}$ ,  $\text{CO}_2$ ,  $\text{H}_2$ , and Ar are measured with a Pfeiffer Prisma Quadrupole mass spectrometer (Fig. 4.12). He results are blank corrected by heating empty niobium envelopes and tubes (= blanks) with the same procedure. In the absence of goethite and hematite standards, Durango apatites, for which ages of formation are well known, are used to calibrate the system.

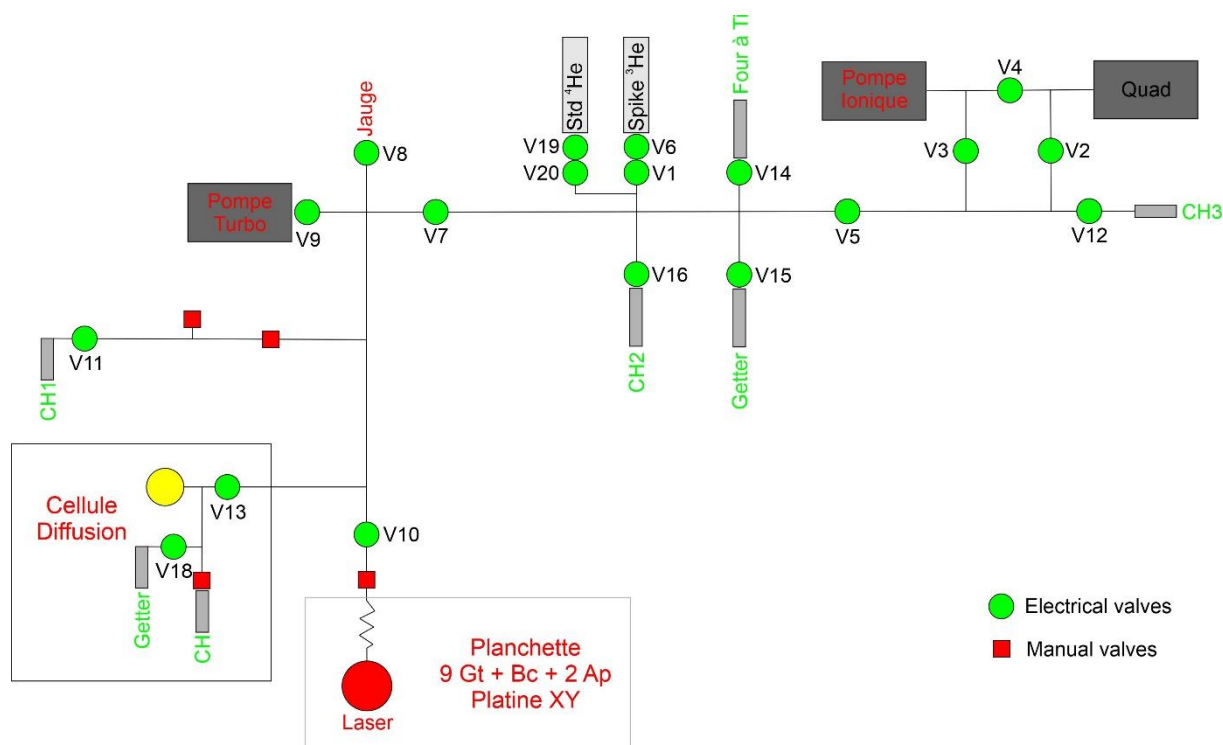


**Figure 4.12.** He extraction line used at Paris Sud University.

### Dissolution of samples and U-Th-Sm measurement

After degassing, aliquots were extracted from the vacuum chamber. The beginning of this second treatment depends on whether aliquots are encapsulated in large Nb envelopes or in small Nb tubes. In the first case, grains are extruded from envelopes that are rinsed with ethanol to recover even small goethite fragments. In the second case, goethite fragments stay in the tubes. The grains, with or without tubes, are transferred into 5 mL Savillex Teflon-capped vials, followed by 100 or 50  $\mu\text{L}$  of 5M  $\text{HNO}_3$  containing known amounts of  $^{230}\text{Th}$  (~4 ppb) and  $^{235}\text{U}$  (~4 ppb),  $^{149}\text{Sm}$  (~4 ppb) and 50  $\mu\text{L}$  of 5N  $\text{HNO}_3$ , 400  $\mu\text{L}$  of 40% concentrated  $\text{HCl}$ , and two drops of 38%  $\text{HF}$ . The tightly closed vials are heated at ~ 100°C overnight. The next day, vials are placed on a hot plate during two hours for complete evaporation. At this stage, if the sample dissolution is not complete, the previous procedure of adding  $\text{HCl}$  and  $\text{HF}$  is repeated. The amount of iron in each aliquot is estimated, based on the weight of the samples and on the proportion by weight of iron in goethite (62.92% following the chemical formula). Depending on the amount of iron present in the sample, a varying quantity of 5M  $\text{HNO}_3$  is added to the solution to set the iron content to 100 ppm. The solution is then heated at 100°C for two hours. After cooling, 1.5 mL of the solution is pipetted and diluted with 1M  $\text{HNO}_3$  to reach a total volume of 3 mL. The solution is taken by an ISI autosampler and  $^{238}\text{U}$ ,  $^{232}\text{Th}$ , and  $^{147}\text{Sm}$  contents are measured using an ELEMENT XR Thermofisher Scientific high-resolution mass spectrometer (Fig. 4.11L).

#### 4.4.2 K-Ar dating of alunite

In mineral deposits containing sulfides, weathering may lead to the formation of sulfate minerals such as alunite and jarosite, which are amenable to radiometric dating K-Ar and  $^{40}\text{Ar}/^{39}\text{Ar}$  methods. The K-Ar dating method is based on the decay of  $^{40}\text{K}$  to  $^{40}\text{Ar}$ . The K-Ar age of alunite is used as a proxy for weathering and supergene enrichment timing, since it is stable only under acidic conditions (Vasconcelos, 1999). Alunite dating has already provided chronology of supergene activity in relation with uplift, such as in the Andes (e.g. Alpers and Brimhall 1988; Sillitoe and Mckee 1996).

Analyses leading to the obtention of K-Ar ages have been performed on six samples of alunite originating from Jbel Klakh (1), Tassirt (4) and Imi Omagha (1), in Actlabs Laboratories (Ontario, Canada).

Samples have been selected on the basis of XRD diffractograms and SEM observations; pure alunite devoid of K-contaminants such as muscovite are selected. The K content of samples confirmed their suitability for radiometric dating. Fragments have been carefully handpicked from crushed samples to select the purest material. At Actlabs laboratories, aliquots have been weighted into Al container, loaded into an extraction unit and degassed at  $\sim 100^\circ\text{C}$  during two days to remove surface gases. Argon is extracted from the sample in double vacuum furnace at  $1700^\circ\text{C}$ . The determination of radiogenic argon content is carried out twice on a MI-1201 IG mass-spectrometer by an isotope dilution method. The spike  $^{38}\text{Ar}$  is introduced to the sample system prior to each extraction. Extracted gases are cleaned up in a two-step purification system. Pure Ar is introduced into the custom-built magnetic sector mass spectrometer (Reinolds type). The test is repeated for each sample to ensure the consistency of the result. Two globally accepted standards (P-207 Muscovite and 1/65 "Asia" rhyolite matrix) are measured for  $^{38}\text{Ar}$  spike calibration. For age calculations, the international values of constants are used following Equ. 4.14, 4.15 and 4.16.

$$\lambda_K = 0.581 \times 10^{-10} \text{y}^{-1} \quad (\text{Equ. 4.14})$$

$$\lambda_\beta = 4.962 \times 10^{-10} \text{y}^{-1} \quad (\text{Equ. 4.15})$$

$$^{40}\text{K} = 0.01167 \text{ (at. \%)} \quad (\text{Equ. 4.16})$$

CHAPTER V

CHARACTERIZATION OF  
SUPERGENE ORE DEPOSITS

---

## Chapter 5

### Characterization of supergene ore deposits

<b>5.1 Mineralogical and geochemical characterization of supergene Cu-Pb-Zn-V ores in the Oriental High Atlas, Morocco</b>	<b>p. 63</b>
5.1.1 Geological setting	p. 63
5.1.2 Materials and methods	p. 64
5.1.3 Results	p. 65
5.1.3.a Petrography of Jbel Klakh samples	p. 65
5.1.3.b Petrography of Jbel Haouanit samples	p. 67
Pb-Zn mineralization	p. 67
Cu and Cu-Pb-V mineralization	p. 68
5.1.3.c Geochemistry of Jbel Klakh	p. 68
5.1.3.d Geochemistry of Jbel Haouanit	p. 69
5.1.4 Discussion	p. 72
5.1.4.a Weathering and neutralization	p. 72
5.1.4.b Jbel Klakh mineralization	p. 73
Primary sulfides zone	p. 73
Secondary sulfides enrichment zone (cementation zone)	p. 73
Oxidized zone	p. 74
Leached zone (gossan)	p. 75
Jbel Klakh paragenesis	p. 75
Geochemistry of the ore	p. 76
5.1.4.c Jbel Haouanit mineralization	p. 77
Pb-Zn mineralization	p. 77
Cu and Ag occurrences	p. 79
Cu-Pb-V occurrences	p. 80
Geochemistry of the ore	p. 80
5.1.5 Conclusion	p. 81
<b>5.2 Mineralogy and genesis of the polymetallic and polyphased low grade Fe-Mn-Cu ore of Jbel Rhals deposit (Eastern High Atlas, Morocco)</b>	<b>p. 82</b>
5.2.1 Geological setting	p. 82
5.2.2 Materials and methods	p. 84
5.2.3 Results	p. 84
5.2.3.a Petrographic characterization	p. 84
Fe-Mn mineralization	p. 86
Cu mineralization	p. 87
5.2.3.b Geochemical characterization	p. 88



Major elements patterns	p. 88
Minor and trace elements patterns	p. 89
Rare Earth Elements patterns	p. 90
<b>5.2.4 Discussion</b>	<b>p. 93</b>
5.2.4.a Hydrothermal alteration and/or weathering of basaltic rocks	p. 93
5.2.4.b Fe-Mn mineralization	p. 94
5.2.4.c Cu mineralization	p. 97
5.2.4.d Late sulfates	p. 98
5.2.4.e Metallogenic model of formation	p. 98
<b>5.2.5 Conclusion</b>	<b>p. 100</b>
<b>5.3 The Tazalaght and Agoujgal Cu deposits, Moroccan Anti-Atlas Copperbelt:</b>	<b>p. 101</b>
<b>Genesis of an As-Pb-rich supergene mineralization</b>	
5.3.1. Geological setting and mining of the deposits	p. 101
5.3.1.a Lithostratigraphic and mineralized units	p. 103
5.3.1.b Ore formation and mining	p. 105
5.3.2. Materials and analytical methods	p. 105
5.3.3. Results	p. 109
5.3.3.a General overview	p. 109
5.3.3.b Ore characterization including SEM semi-quantitative analyses	p. 110
5.3.3.c Bulk rock geochemistry	p. 116
5.3.4. Discussion	p. 119
5.3.4.a Controls of host rocks on the supergene processes	p. 119
5.3.4.b Role of hypogene minerals	p. 120
5.3.4.c Weathering profile and paragenetic sequence	p. 120
5.3.4.d Mechanisms for Cu-arsenates formation	p. 123
5.3.4.e Sequential formation of lead carbonates, sulfates, phosphates, arsenates and vanadates at Agoujgal	p. 125
5.3.5. Conclusion	p. 127
<b>5.4 Characterization of weathering processes of the giant copper deposit of Tizert (Ighrem inlier, Anti-Atlas, Morocco)</b>	<b>p. 129</b>
5.4.1. Geodynamic context	p. 129
5.4.2. Local geologic context	p. 130
5.4.3. Materials and methods	p. 132
5.4.4. Results	p. 133
5.4.4.a Host rocks	p. 133
5.4.4.b Secondary (weathered) mineralization	p. 138
5.4.5. Discussion	p. 142
5.4.5.a Weathering profiles	p. 142
5.4.5.b Paragenesis	p. 143
5.4.5.c Weathering process	p. 144
5.4.5.d Chemical migration during weathering	p. 149
5.4.6. Conclusion	p. 149
<b>5.5 Summary: metallogeny of Moroccan ore deposits</b>	<b>p. 151</b>

Supergene deposits are the subject of a growing interest from mining industries, boosted by the rise of metal prices since the 2000's, the introduction of modern prospecting tools and the ever-increasing demand of metals and/or rare earth elements for (new) technologies (e.g. Hitzman et al. 2003; Boni and Large 2005; Arndt and Ganino 2012). In this context, the near-surface situation (<100m) and softened host rocks of supergene ores, along with their subsequent relatively easy and fast accessibility and mining are definite advantages over the hypogene, sulfidic mineralization (Cocker 2012; Reich and Vasconcelos 2015). An additional benefit of secondary ores is their common higher metal contents, in comparison with primary sulfides (Sillitoe, 2005): the metal-content is commonly 2 to 5 times higher than in the primary minerals (Arndt and Ganino 2010) while the enrichment in REE usually ranges from 3 to 10 times, but may reach 100 times in particular cases (Cocker 2012). Although their complex mineralogy may also represent a challenge for ore processing (Boni et al. 2009; Choulet et al. 2019), recent advances in hydrometallurgical acid-leaching, solvent extraction (SX) and electron-winning techniques (Boni & Mondillo, 2015; Choulet *et al.*, 2014) facilitate post-extraction treatments for non-sulfide ores (e.g. carbonates, such as malachite). In the scientific point of view, the particular attraction of supergene ores lies in their formation at the interface between tectonic and climate processes, and in their mineralogical diversity. Among the various minerals that may be encountered are sulfides, oxides, sulfates, phosphates, oxyhydroxides, carbonates, silicates, native elements, arsenates and vanadates (Reich and Vasconcelos 2015).

In this context, exploration of new supergene targets has been carried out during the last decade in many countries including Morocco. In the Moroccan High Atlas, numerous supergene ore deposits described in the 1960'-70's (Emberger 1969, 1970; Ovtracht 1978) have been (re)studied over the last years (Bruyère et al. 2010; Choulet et al. 2014; Decrée et al. 2008). The Anti-Atlas, known as the "Anti-Atlas copperbelt", also attracts considerable prospecting activity because of the up to two hundred copper and polymetallic occurrences of economic interest and the possibility of finding even more substantial deposits.

This chapter refers to four papers dealing with the mineralogy, petrography, geochemistry and paragenesis of supergene deposits located in the High Atlas and Anti-Atlas of Morocco.

The first paper, co-authored by **Michèle Verhaert**, Alain Bernard, Augustin Dekoninck, Ludovic Lafforgue, Omar Saddiqi and Johan Yans, aims to refine the mineralogy and paragenesis of two Pb-Zn-Cu-V sulfide deposits that underwent significant weathering, in the High Atlas. In the Cu deposit of Jbel Klakh, several stages of supergene mineralization are distinguished: (1) the replacement of hypogene sulfides in the protolith by secondary sulfides in the cementation zone, (2) the formation of oxidized minerals in the saprolite where the environment becomes more oxidizing and neutral, and (3) the precipitation of late carbonates and iron (oxyhydr-)oxides in the laterite. The precipitation of carbonates is related to the dissolution of dolomitic host rocks, which buffers the fluid acidity due to the oxidation of sulfides. In the Jbel Haouanit Pb-Zn deposit, the mineral assemblage is dominated by typical calamine minerals and Cu minerals. Both deposits are thus characterized by specific mineral zonation, from laterite to protolith, related to variations in the mineralogy and ore grades, caused by varying Eh-pH conditions. This study is entitled "*Mineralogical and geochemical characterization of supergene Cu-Pb-Zn-V ores in the Oriental High Atlas, Morocco*" and was published in the journal *Mineralium Deposita* n°52 (pages 1049-1068) in 2017.

The second part of this chapter is based on the paper "*Mineralogy and Genesis of the Polymetallic and Polyphased Low Grade Fe-Mn-Cu Ore of Jbel Rhals Deposit (Eastern High Atlas, Morocco)*", co-authored by **Michèle Verhaert**, Alain Bernard, Omar Saddiqi, Augustin Dekoninck, Mourad Essalhi and Johan Yans, published in the volume 8 of the journal *Minerals* (pages 1-23) in 2018. It focuses on the

mineralogy and paragenesis of the polymetallic Fe-Mn-Cu Jbel Rhals deposit, located in the Oriental High Atlas of Morocco. This study shows that the genesis of this deposit is clearly polyphased, resulting from supergene processes superimposed on hydrothermal phases. The flow of the overlying Permian-Triassic basalts probably generated the circulation of hydrothermal fluids through the sedimentary series, the alteration of basalts and schists, and the subsequent formation of hydrothermal primary ore composed of carbonates (siderite) and Cu-Fe sulfides. Later, several episodes of uplift probably triggered the exhumation of ores and host rocks, generating their weathering and the precipitation of a supergene ore assemblage (goethite, pyrolusite, malachite and calcite). In the Paleozoic basement, Fe-Mn (oxyhydr-)oxides are mostly observed as rhombohedral crystals that correspond to the pseudomorphose of a primary mineral thought to be siderite.

The third section of this chapter deals with the paragenesis and the processes leading to the formation of As-Pb-rich Cu supergene ores in the Anti-Atlas. In Tazalaght's Cu-As deposit, three mineralogical steps are distinguished: (1) the replacement of hypogene sulfides by supergene sulfides in the large cementation zone; (2) the formation of oxidized minerals in a more oxidizing and neutral environment; and (3) the precipitation of iron (oxyhydr-)oxides and quartz in the gossan. In the Cu-As-Pb-V deposit of Agoujgal, the mineralogical units are spatially less confined than at Tazalaght. Both deposits are characterized by As-rich secondary ores that were formed through similar processes, despite some mineralogical and chemical variations highlighting the influence of the host rocks on weathering. The restricted Tazalaght's oxidized mineralization and Agoujgal's cementation zone most likely arise from the contrasting omnipresence of quartzite at Tazalaght that could not enable a fast and effective neutralization of the fluid's acidity, and the large amounts of dolomitic host rocks that could be dissolved at Agoujgal. At both sites, the weathering of tennantite  $((\text{Cu,Fe})_{12}\text{As}_4\text{S}_{13})$  through a boxwork texture records the transition from the cementation zone, the oxidized zone and the gossan, and reflects the fluids evolution with time. This section is based on the paper "*Genesis of As-Pb-rich supergene mineralization: the Tazalaght and Agoujgal Cu deposits (Moroccan Anti-Atlas Copperbelt)*", accepted for publication in the journal *Economic Geology* in 2020. This paper is co-authored by **Michèle Verhaert**, Atman Madi, Abdelaziz El Basbas, Mohamed Elharkaty, Abdellah Oummouch, Lahcen Oumohou, Annelies Malfliet, Lhou Maacha and Johan Yans.

The last paper, co-authored by Julien Poot, **Michèle Verhaert**, Augustin Dekoninck, Abdellah Oummouch, Abdelaziz El Basbas, Lhou Maacha and Johan Yans, aims to characterize the supergene mineral assemblages of the giant Tizert copper deposit, considered as the largest copper resource in the western Anti-Atlas (Morocco), and to determine their formation weathering processes. The Tizert supergene deposit mainly consists in i) a residual patchwork of laterite rich in Fe-oxyhydroxides, ii) a saprolite rich in malachite, or « green oxide zone » where primary structures such as stratification are preserved, and iii) a cementation zone containing secondary sulfides. The abundance of Cu carbonates results from the rapid neutralization of acidic meteoric fluids, due to oxidation of primary sulfides, by carbonate host rocks and chlorite. The unexpected absence of azurite is related to particular environmental conditions. Again, the supergene enrichment is most likely related to episodes of uplift/doming (last event since 30 Ma), which triggered the exhumation of primary/hypogene mineralization, generating their oxidation and the precipitation of secondary/supergene sulfides, carbonates and Fe-oxyhydroxides. This paper is entitled "*Characterization of weathering processes of the giant copper deposit of Tizert (Igherm inlier, Anti-Atlas, Morocco)*" and has been submitted for publication in the journal *Minerals* in 2020.

## 5.1 Mineralogical and geochemical characterization of supergene Cu-Pb-Zn-V ores in the Oriental High Atlas, Morocco

Deposits situated in the Figuig district (south-eastern Morocco) were briefly mined, during the first 50 years of the 20<sup>th</sup> century, for Pb-Zn (Jbel Haouanit), Fe-Mn (Hamarouet and Aïn Beida) and Cu (Jbel Klakh) mineralization hosted in dolomitized Jurassic limestones that form the high reliefs (*Jbels*) (Fig. 1). Since then, these deposits have been poorly investigated. In this study, we focus on two deposits, located at the Jbel Klakh and the Jbel Haouanit (Fig. 1), close to the city of Bou Arfa. No inventory of the various mineral phases of both deposits has been presented. No mineralization model has been proposed to explain the genesis of these ores, and the weathering processes leading to their formation have not been investigated. The purpose of the present study is to characterize the supergene mineral assemblages and their relationships, in order to investigate their formation processes. The observation of the relationships between different types of ore, and between ore and host rocks, results in the identification of several parageneses and a relative chronology of the mineralization. We propose typical cross-sections of the supergene mineralization of both deposits, based on the observation of the vertical distribution of mineral assemblages that define mineralogical zones. Some particular attention is given to the major, minor and rare earth elements contents of these deposits, in order to investigate the geochemical evolution of the supergene mineralizing fluids and to highlight enrichments or depletions in some elements in ore minerals.

### 5.1.1 Geological setting

The Jbel Klakh and Jbel Haouanit mines are located at the northern edge of the Oriental High Atlas (Fig. 5.1.1). This region is characterized by the alternation of high Jurassic carbonate reliefs (*Jbels*) constituted of narrow Triassic to Lower Jurassic-cored anticlines and large plains made of large open Middle Jurassic-cored synclines (Choubert and Fauve-Muret 1962; Frizon de Lamotte et al. 2008). Folds are oriented NE-SW or ENE-WSW. See chapter 5.3.2 for the geodynamic setting.

The Jbel Klakh (32°37'11.28"N; 1°41'13.56"W) and Jbel Haouanit (32°34'30.43"N; 2°26'24.30"W) deposits are respectively located at 28 km eastward and 45 km westward of Bou Arfa (Fig. 5.1.1). Bou Arfa is known for its ancient Mn ore deposit (Fig. 5.1.1), mined from 1923 until 1967. The Jbel Klakh deposit (Fig. 5.1.1) was mined from 1950 to 1971: approximately 246 000 tons of Cu ore have been extracted (Salahane 1978). According to Wadjinny (1998), the exploitation of the Jbel Haouanit mine, until its closure in 1954, yielded 150 000 tons of Pb-Zn ore. Artisanal excavations (32°35'19.63"N; 2°25'3.62"W) are currently exploited at Jbel Haouanit (2.5 km away from the principal mine) for Cu and V ores (Fig. 5.1.1).

In the Bou Arfa area, basement rocks (Fig. 5.1.1) are Precambrian shales, conglomerates, sandstones, and volcanic rocks (Chefchaouni et al. 1963). Cambrian, Ordovician, Silurian and Visean rocks are represented by shale, quartzite and conglomerate with limestone beds (Chefchaouni et al. 1963). Permian to Triassic argillites are sealed by basalt flows, and covered by Liassic, Jurassic and Cretaceous dolomitized limestones, marls and Cretaceous conglomeratic series (Chefchaouni et al. 1963). These formations are overlaid by recent sediments, sand, alluvium and silt (Chefchaouni et al. 1963). Fault systems affecting Triassic, Jurassic and Cretaceous strata are mainly E-W but also NE-SW and WNW-ESE (Chefchaouni et al. 1963; Fig. 5.1.1). They are usually dextral strike-slip faults combined with N-S striking thrusts. Several faults are responsible for sizable gaps, such as the dextral strike-slip fault observed at Jbel Bou Arfa (Fig. 5.1.1). As recognized by Du Dresnay (1965), the stratigraphic succession

of the Bou Arfa series is complex, due to dolomitization and fracturing of the series, scarcity of fossils and lack of marker horizon.

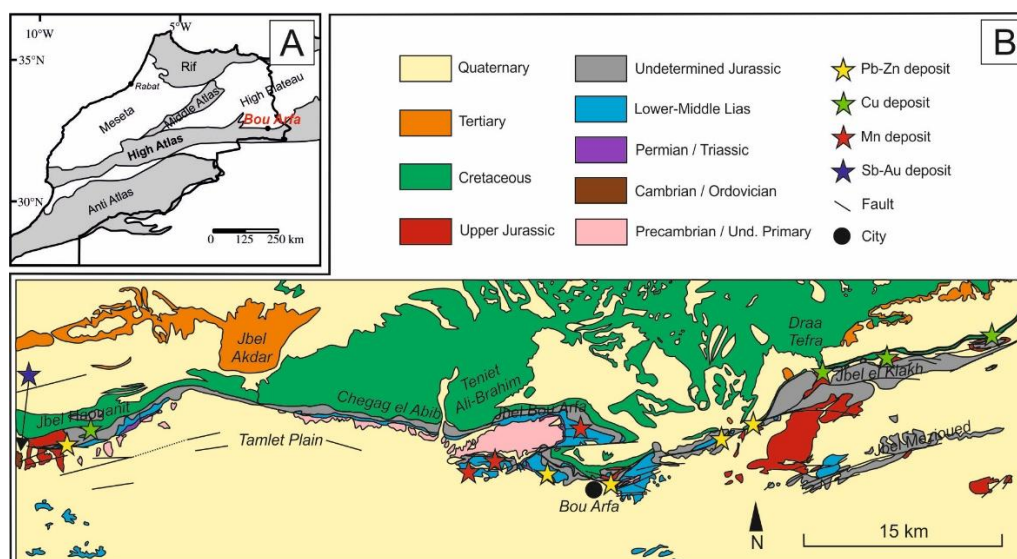


**Figure 5.1.1.** Simplified geologic map of Morocco showing the location of the Bou Arfa mining district. (B) Geology map of the Bou Arfa region showing the location of Jbel Klakh and Jbel Haouanit deposits in Jurassic dolostones (modified from Chefchaouni et al., 1963).

The Jbel Klakh ores are located at 1300–1500 meters in altitude, in two hillocks consisting of a narrow anticline, extending approximately 700 meters. The ores were mostly mined through adits a few tens of meters long. Traces of mining activity also occur in an open-pit excavation of approximately 25 meters deep and 150 meters wide. Ore veins, roughly 0.1 millimeter to 20 centimeters wide, are hosted in strongly fractured Jurassic dolomitized rocks (Chefchaouni et al. 1963). Host rock bedding ranges from 10 centimeters to 1 meter in thickness.

Pb-Zn ores of Jbel Haouanit are also located in anticlines forming hillocks, at 1150–1250 meters in altitude. Mining activities occur over a distance of 600 meters along these structures. The ore was mined in adits 2–3 meters wide, extending several tens of meters. Mineralized veins, 1 millimeter to 20 centimeters in width, are hosted in Jurassic dolomitized rocks (Chefchaouni et al. 1963; Fig. 5.1.1). These limestones are strongly fractured, moderately folded, and lie unconformably over the Paleozoic schistose basement. Bedding is subhorizontal to vertical, and 10 to 50 centimeters thick. The artisanal excavations located 2.5 km away from the principal mine also exhibit mineralized veins hosted by Jurassic dolomitized rocks. These excavations are found over 400 meters along the anticlines, are 1 to 2 meters deep, and host 1 to 5 centimeters wide ore veins. The currently mined Sb-Au ore is hosted in quartz veins cutting Cambrian shale and quartzite (Fig. 5.1.1).

### 5.1.2 Materials and methods

Hundred samples were collected during field work in March 2014: forty-eight come from Jbel Klakh and fifty-two from Jbel Haouanit. Samples were selected within the vertical profile of each site, mostly in adits. As the inclines of Jbel Klakh are no more accessible, some samples of unweathered rocks (especially sulfides) were taken in ore dumps close to the adits entrance. Attention was paid to the nature of the selected samples: gangue, external rims and center of mineralized veins were sampled in order to get an overview of the various secondary minerals.

X-Ray diffraction was carried out on thirty-three Jbel Klakh samples and forty-one Jbel Haouanit samples. Each sample was crushed to powder in agate mortar and then placed onto glass plates. The instrumentation consists of a BRUKER X-Ray diffractometer equipped with a HI STAR GADDS (General Area Detector Diffraction System)  $\text{CuK}_\alpha$  detector (Université Libre de Bruxelles). The EVA software was used with the PDF (Powder Diffraction File) data base in order to identify the major mineral phases. X-Ray diffraction was also carried out on 6 samples containing clays, with a PHILIPS Analytical X-Ray diffractometer (Université de Namur). The isolation of the  $<2\mu\text{m}$  size-fraction and the analyses was performed following Holtzapffel (1985). Analyses were carried out on natural, glycolated and heated ( $490^\circ\text{C}$ ) plates in order to show characteristic shifts of basal reticular distances on  $<2\mu\text{m}$  size-fraction minerals.

Twelve thin sections of host rocks and twenty-two polished sections (twelve of Jbel Klakh and ten of Jbel Haouanit) have been studied using a petrographic polarizing microscope in transmitted light. A JEOL JXA-8600 SUPERPROBE scanning electron microscope (SEM), coupled with a NORAN energy dispersive spectrometer (EDS) (Université Libre de Bruxelles) was used to document textures and to carry semi-quantitative analyses in order to identify selected minerals.

Geochemical analyses were carried out on nineteen samples (seven from Jbel Klakh, twelve from Jbel Haouanit). Crushing was performed with a RETSCH PM 100 planetary ball mills (Université de Namur) in order to obtain the maximum  $125\mu\text{m}$  grain size. Agate grinding mortar were used for the host rocks, whereas stainless steel was used for potentially contaminating minerals. Analyses were performed at the Activation Laboratories (Ontario, Canada). REE and trace elements were analyzed by Fusion Mass Spectrometry (FUS-MS) and major elements by Fusion Inductively Coupled Plasma Optical Emission Spectrometry (FUS-ICP). For one sample particularly rich in Fe (14 HAO 13), contents in major and trace elements were quantified by Fusion-X-ray Fluorescence (FUS-XRF) and by FUS-MS. FeO was quantified by titration. Trace elements V, Sr, Zr and Ba were determined with FUS-ICP. For samples presenting high contents of Cu, Pb, Zn, V, Ag, Mo, In, and Sb, analyses were carried out by Fusion Inductively Coupled Plasma Sodium Peroxide Oxidation (FUS- $\text{Na}_2\text{O}_2$ ) and Inductively Coupled Plasma Optical Emission Spectrometry (ICP-OES). REE contents are normalized to PAAS (Post Archean Australian Shale; Taylor and McLennan 1985), considered as a reference for sedimentary rocks. Major and trace elements contents have been normalized to the UCC (Upper Continental Crust; Taylor and McLennan 1985) to highlight some supergene geochemical trends. Mineralized samples contents are compared and normalized to host rocks, in order to emphasize enrichment and depletion of elements during weathering.

### **5.1.3 Results**

#### **5.1.3.a Petrography of Jbel Klakh samples**

The ores are hosted in dolomitized limestone. Small amounts of finely disseminated Fe (hydr-)oxides occur in most samples. The original limestone has been totally replaced by dolomite, resulting in a xenotopic mosaic of non-planar dolomite, which obliterates the sedimentary textures. Some discrete dolomite rhombs are found, outlined by zoning, as their centers seem to be rich in inclusions. Calcite cement fills the porosity, fractures and intercrystalline spaces of dolomite. Late carbonates (calcite, dolomite, manganocalcite) develop in fractures and cavities; they are often coated with iron (hydr-)oxides (Fig. 5.1.2A). Several faults show tectoglyph structures where iron (hydr-)oxides coat sliding stripes. Next to the ores, heavily weathered marls are constituted of quartz, Fe-rich dolomite and muscovite. The minerals are located in veins having a diameter of between 0.1 cm and 20 cm (Fig. 5.1.2B, 5.1.2C).



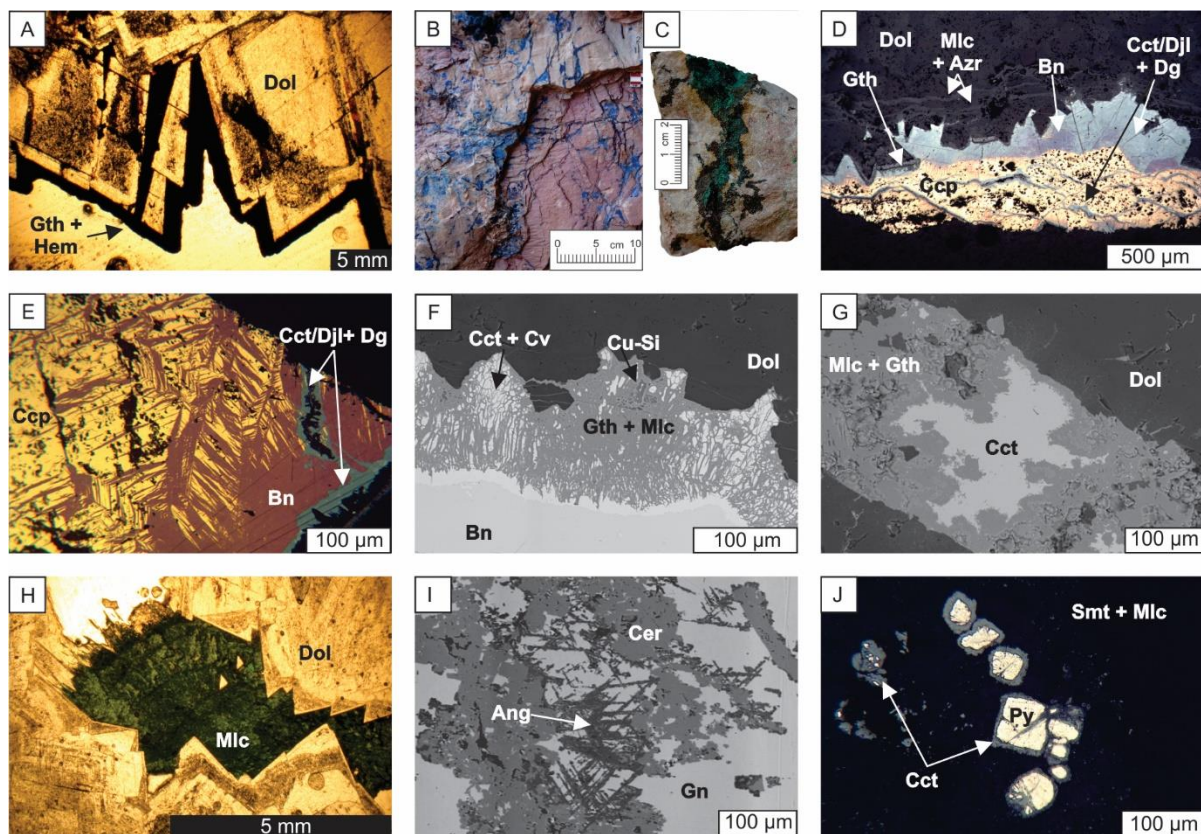


**Figure 5.1.2.** Representative samples of the Jbel Klakh deposit: transmitted light photomicrographs (A, H), field and sample pictures (B, C), reflected light photomicrographs (D, E, J), and SEM microphotographs in backscattered electrons mode (F, G, I). (A) Iron (hydr-)oxides (Gth + Hem) coating dolomite crystals (Dol); (B and C) azurite and malachite veins in dolostone; (D) chalcopyrite (Ccp) and secondary sulfides vein in dolomite (Dol): chalcocite (Cct)/djurleite (Dj), digenite (Dg), bornite (Bn), malachite (Mlc), azurite (Azt), goethite (Gth); (E) bornite (Bn) sparks in chalcopyrite (Ccp), with chalcocite (Cct)/djurleite (Dj)–digenite (Dg) at the edge of the vein; (F) chalcocite (Cct)–covellite (Cv) and an undefined Cu-silicate (Cu-Si) forming a lattice with malachite (Mlc) and goethite (Gth), in the dolostone (Dol); (G) vein of chalcocite (Cct) replaced by malachite (Mlc) and goethite (Gth), in dolomite (Dol); (H) malachite (Mlc) filling cavities between dolomite crystals (Dol); (I) replacement of galena (Gn) by cerussite (Cer), and anglesite (Ang) along its cleavages; (J) replacement of pyrite (Py) by chalcocite (Cct), in a smithsonite (Smt)–malachite (Mlc) gangue.

Cu (and Fe) minerals are found in veins and disseminated in the dolostone. A paragenetic sequence is observed in the mineralized veins, from the center to the edges (Fig. 5.1.2D): 1) chalcopyrite, 2) bornite, 3) digenite – chalcocite and/or djurleite – covellite, and 4) goethite – malachite – azurite – copper silicates. Chalcopyrite is often replaced by bornite along fractures and cleavages, forming sorts of sparks (Fig. 5.1.2E); intergrowths are common between digenite, chalcocite, djurleite and covellite. Chalcocite is intergrown with iron (hydr-)oxides and malachite (Fig. 5.1.2F). This sequence is not systematically observed in all veins, probably due to progressive weathering. In most weathered samples, chalcopyrite is absent, and chalcocite is replaced by malachite (Fig. 5.1.2C, 5.1.2G). At the edges of the veins, malachite is often associated with smithsonite. Concretions of iron (hydr-)oxides are observed onto faces of dolomite crystals, at the contact with secondary sulfides (Fig. 5.1.2D). Numerous veins of calcite, botryoidal goethite, malachite (Fig. 5.1.2C, 5.1.2G), azurite and of a copper hydrated silicate (likely shattuckite;  $\text{Cu}_5[\text{SiO}_3]_4[\text{OH}]_2$ ) are observed in dolostone. Pyrite and chalcopyrite are disseminated in the host rock; their weathering products (i.e. malachite), fill intercrystalline spaces of the dolostone and cavities (Fig. 5.1.2H). Small rare grains have also been identified: barite associated with goethite, brochantite ( $\text{Cu}_4\text{SO}_4[\text{OH}]_6$ ) associated with malachite, quartz, sphalerite, zircon, motttramite ( $\text{PbCu}[\text{VO}_4][\text{OH}]$ ), galena, and stibnite.

The copper deposits are often associated with lead and iron mineralization. Some veins contain large bands of galena weathered in cerussite (Fig. 5.1.2I), which is often associated with covellite. Anglesite is observed in fractures and cleavage plans of galena (Fig. 5.1.2I), but also forms a thin rim around this sulfide. Anglesite is weathered into cerussite. Late dolomite (sometimes ferriferous) and calcite occur at the edge of the veins. In samples characterized by the association of smithsonite and malachite, small crystals of pyrite are replaced by chalcocite (Fig. 5.1.2J). Goethite and hematite are enclosed in large veins, with calcite, dolomite, quartz and kaolinite. Alunite occasionally appear at the edge of these iron (hydr-)oxides veins. Clays are observed in some highly weathered samples: XRD analyses on <2µm fraction indicate the presence of kaolinite, illite, smectite, and mixed-layers with swelling phyllosilicates layers (illite-smectite and kaolinite-smectite).

### **5.1.3.b Petrography of Jbel Haouanit samples**

The mineralized veins are hosted in Jurassic dolostones overlying a schistose Paleozoic basement. As at Jbel Klakh, the replacement of the Jurassic limestone hosting the ores, by dolomite, results in the formation of a xenotopic recrystallized matrix composed of microcrystalline dolomite punctuated by rare iron (hydr-)oxides. Calcite is found as cement in cavities, fractures and intercrystalline pores of dolomite. Some terrigenous residues (quartz, zircon, rutile and ilmenite) as well as other sulfides are found in the host rock of the Cu-Pb-V mineralization.

#### **Pb-Zn mineralization**

The ore veins mostly contain galena (Fig. 5.1.3A) surrounded by lead and zinc weathering minerals (cerussite, anglesite, smithsonite, hydrozincite), which will be here designated as calamine (Fig. 5.1.3B, 5.1.3C). Calamine is white to pale grey or yellow where a small amount of iron is present, but takes a more orange to brown color where the iron content is higher (Fig. 5.1.3C). Cerussite mainly surrounds galena (Fig. 5.1.3B), but also occurs in fractures and along cleavage plans, whereas anglesite only develops in these last two zones. Covellite is often observed at the contact between galena and cerussite/anglesite (Fig. 5.1.3D). Secondary galena is found in cavities of the host rock (Fig. 5.1.3E). Small crystals of pyrite are pseudomorphically replaced by goethite or hematite (Fig. 5.1.3F), which are here commonly enriched in Mo. Smithsonite replaces first sphalerite along cleavage plans and fractures (Fig. 5.1.3G), and later affects the whole crystal, as weathering progresses (Fig. 5.1.3G). Smithsonite encloses anhedral inclusions of a silver sulfide, most likely acanthite (Fig. 5.1.3H). Small grains of stibnite are associated with galena. Large bands of late (ferriferous) dolomite and calcite are also present, while quartz is relatively rare. Large veins of hematite and goethite surround the Pb-Zn ores, sometimes in association with white clayey minerals.



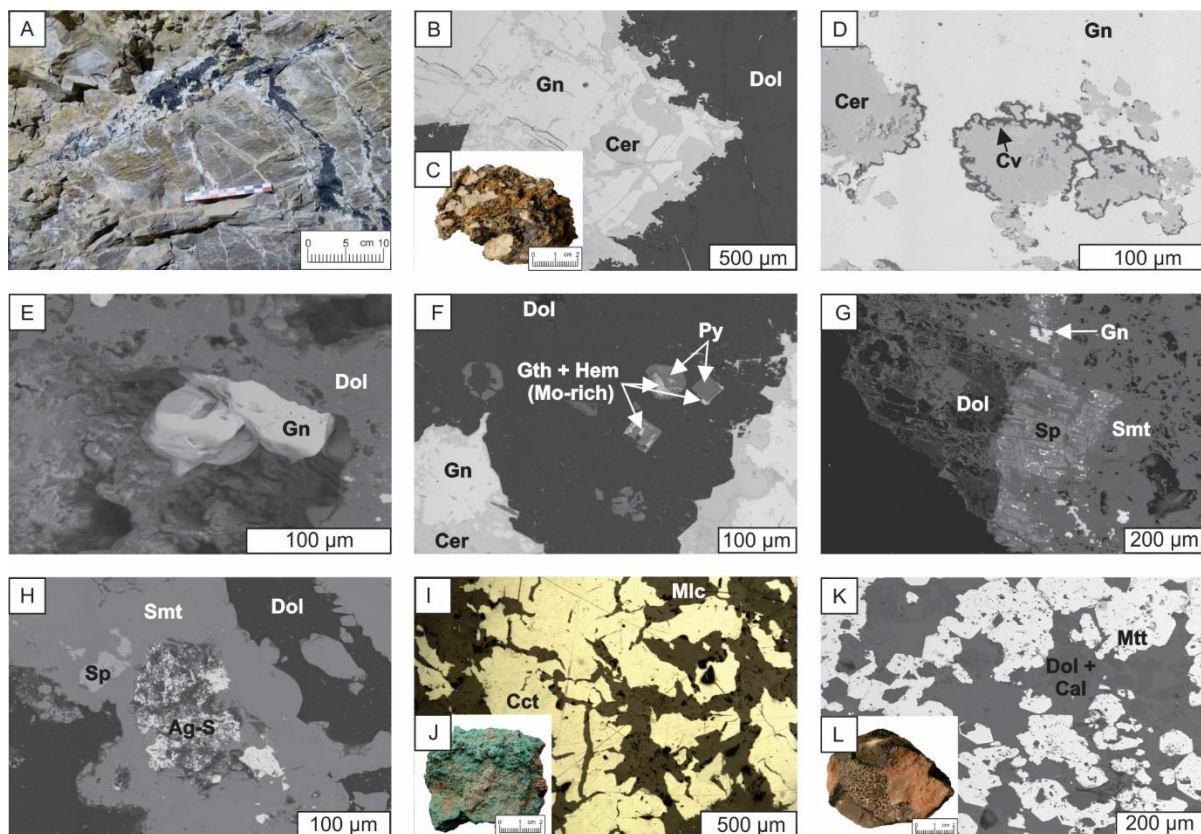


**Figure 5.1.3.** Representative samples of the Jbel Haouanit deposit: field picture (A), samples pictures (C, J, L), reflected light photomicrograph (I), and SEM microphotographs in backscattered electrons mode (B, D, E, F, G, H, K). (A) Veins of galena and calamine in dolostone; (B) replacement of galena (Gn) by cerussite (Cer), surrounded by dolomite (Dol); (C) iron-rich calamine; (D) covellite (Cv) between galena (Gn) and cerussite (Cer); (E) secondary galena in cavities of dolostone (Dol); (F) replacement of pyrite (Py) by Mo-rich iron (hydr-)oxides (Gth + Hem), in dolostone (Dol); (G) sphalerite (Sp) weathered in smithsonite (Smt), close to galena (Gn) and dolomite (Dol); (H) Ag-sulfide inclusion (Ag-S) in smithsonite (Smt) replacing sphalerite (Sp), surrounded by dolomite (Dol); (I) lattice of chalcocite (Cct) and malachite (Mlc); (J) botryoidal malachite; (K) mottramite (Mtt) surrounded by dolomite (Dol) and calcite (Cal); (L) mottramite.

### Cu and Cu-Pb-V mineralization

Copper ores found in artisanal excavations are constituted of highly brecciated chalcocite (Fig. 5.1.3I) weathered in covellite, and later in acicular and botryoidal malachite (Fig. 5.1.3I, 5.1.3J) associated to botryoidal goethite. Covellite often contains silver sulfide inclusions (10 µm), likely acanthite. Small grains of partly oxidized pyrite, barite, copper-lead sulfosalts and phospho-arsenates are disseminated in the ore. Malachite contains numerous small crystals of mottramite. Next to these ores, veins contain euhedral crystals of mottramite (Fig. 5.1.3K, 5.1.3L) surrounded by (ferriferous) calcite, dolomite, and large euhedral crystals of quartz.

#### 5.1.3.c Geochemistry of Jbel Klakh

All Jbel Klakh samples are characterized by a low  $\text{Fe}^{2+}$  (FeO) content (Table 5.1.1). In comparison with the UCC reference, mineralized samples are mostly depleted in mobile (Sr, Ba, U) and immobile (Th, Y, Zr, Hf, V, Cr) elements, and enriched in Mo, Au-related (As, Sb, Ag) and most chalcophile (Pb, Zn, Cu, Co, Ni) elements (Fig. 5.1.4B). All samples are highly enriched in Cu (up to 12000 x UCC), and to a lesser extent in U (Fig. 5.1.4B). Azurite and iron (hydr-)oxides patterns are very similar, as they are both slightly depleted in mobile and immobile elements (Fig. 5.1.4B). Alunite shows positive anomalies in

U, V, Mo, As, Sb and Zn (Fig. 5.1.4B), and is rich in Ge (18.3 ppm) and In (547 ppm) (Table 5.1.1). Malachite pattern shows the highest enrichment in U (38 ppm) (Fig. 5.1.4B; Table 5.1.1). Jbel Klakh samples are depleted in REE when normalized to the PAAS reference, and display flat patterns (Fig. 5.1.4A; Table 5.1.1). Mineralized samples are enriched in REE in comparison to the host rock, and gossan samples are the most enriched samples in REE (Fig. 5.1.4A). The lack of REE fractionation is remarkable (Fig. 5.1.4A), except for alunite, which is characterized by a strong enrichment in LREE relative to HREE.

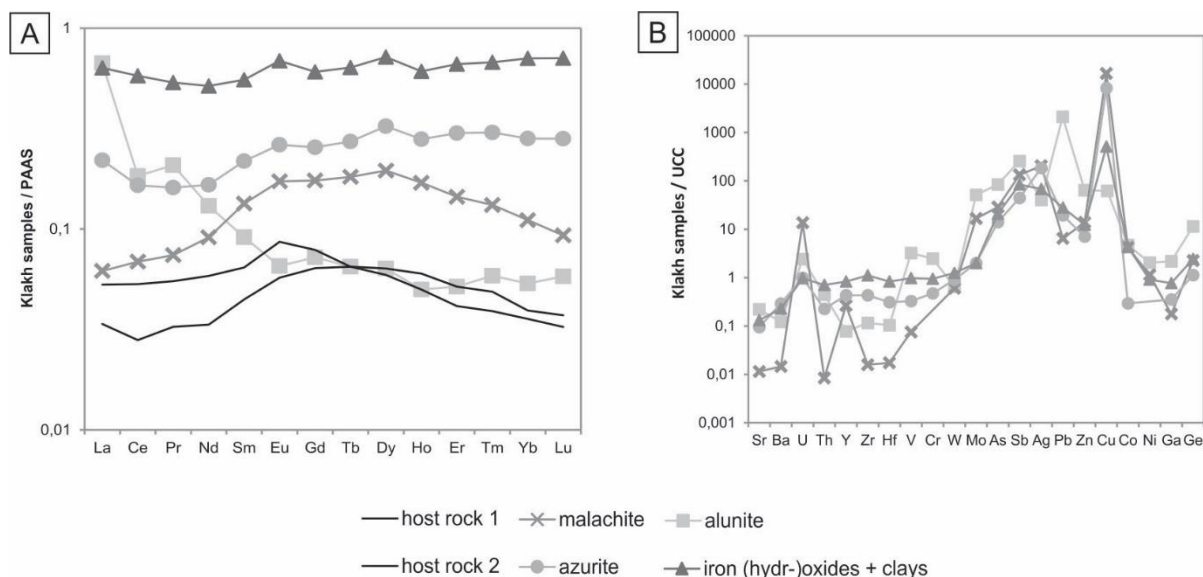


**Figure 5.1.4.** Geochemical data of the Jbel Klakh deposit. (A) REE patterns, with values normalized to the PAAS (Taylor and McLennan 1985); (B) trace elements patterns, with values normalized to the UCC (Taylor and McLennan 1985).

### 5.1.3.d Geochemistry of Jbel Haouanit

All samples are depleted in mobile and immobile elements (exception made for U and V) and enriched in Mo, Au-related and chalcophile elements, when normalized to the UCC reference (Fig. 5.1.5B; Table 5.1.1). Malachite and iron (hydr-)oxides are enriched in V; smithsonite in Ag (up to 10 000 x UCC, 450-550 ppm) and Ge (5-10 x UCC, up to 16.5 ppm) (Fig. 5.1.5B, Table 5.1.1). In comparison to galena, calamine samples are enriched in immobile elements and depleted in mobile elements (Fig. 5.1.5D). Iron (hydr-)oxides are the most enriched samples, besides in U and Ag (Fig. 5.1.5D). Smithsonite is not depleted in U and enriched in Ag and Ge, whereas cerussite is depleted in chalcophile elements, particularly in Sb, Ag and Cu, and enriched in V and Mo (Fig. 5.1.5D). In comparison with PAAS, all samples display flat patterns depleted in REE (Fig. 5.1.5A). All mineralized samples are enriched in REE in comparison to the host rocks. Galena is the most depleted sample in REE (down to  $10^{-2}$  x PAAS) whereas mottramite is the less depleted ( $10^{-0.5}$  x PAAS) (Fig. 5.1.5A; Table 5.1.1). The lack of REE fractionation is remarkable, except for iron (hydr-)oxides which are slightly more enriched in HREE, and for mottramite which displays a weak enrichment in LREE (Fig. 5.1.5A). Galena and mottramite display a negative and a positive Ce anomaly, respectively (Fig. 5.1.5A). In comparison to galena, calamine samples are generally enriched in REE (Fig. 5.1.5C); their patterns are similar, showing positive anomalies in Ce, Eu and Er.

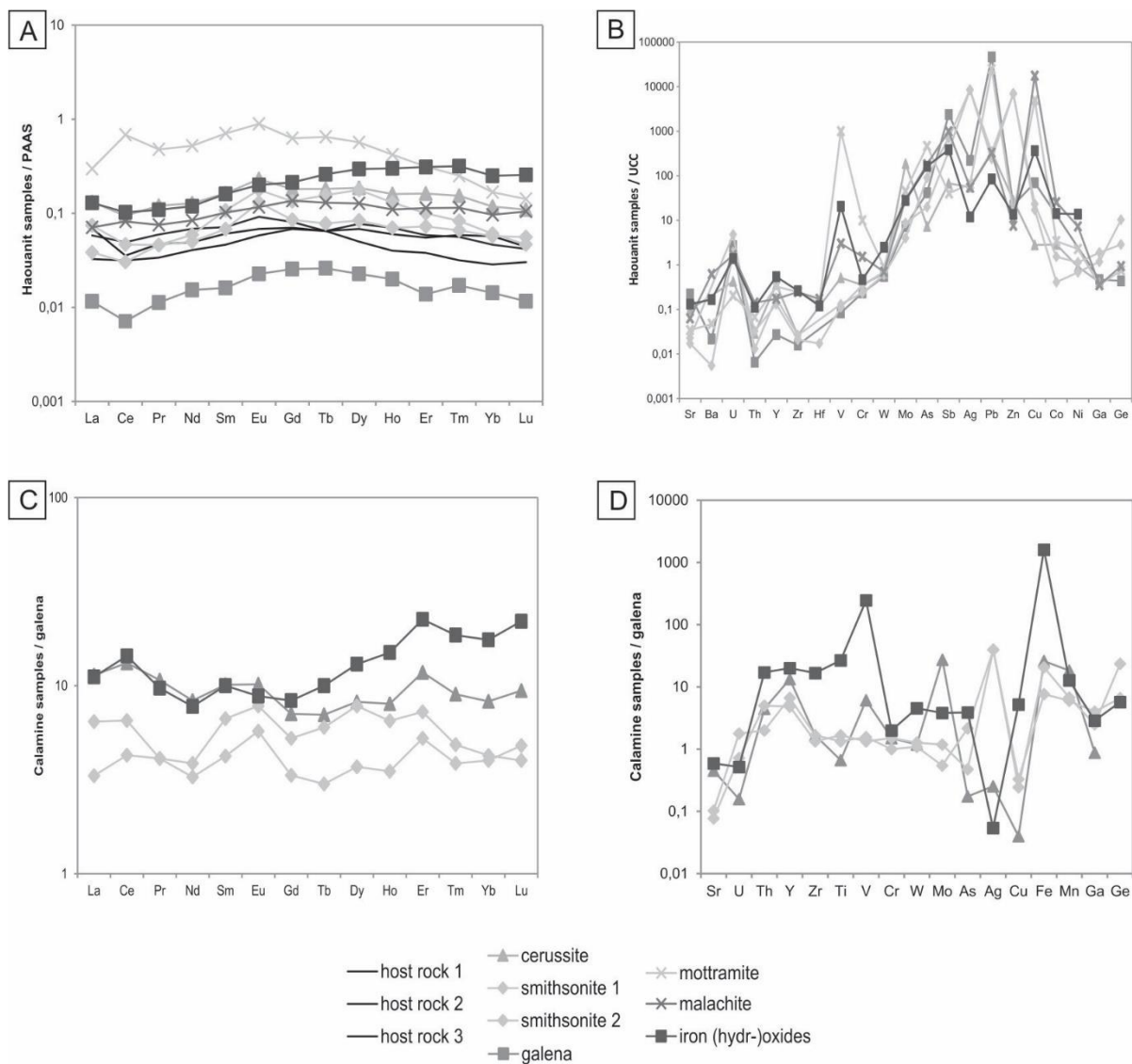


**Figure 5.1.5.** Geochemical data of the Jbel Haouanit deposit. (A) REE patterns, with values normalized to the PAAS (Taylor and McLennan 1985); (B) trace elements patterns, with values normalized to the UCC (Taylor and McLennan 1985); (C) REE patterns, with values normalized to galena; (D) trace elements patterns, with values normalized to galena.

**Table 5.1.1.** Results of geochemical analyses for some Jbel Klakh (KH) and Jbel Haouanit (HT and HAO). Major elements concentrations are listed in %, minor elements and REE are given in ppm. For minor elements, values in bold and marked by one star correspond to contents in %: the detection limit is fixed at 0.01% for V, Zn, Pb, 0.001% for Mo, and 0.005% for Cu; values in bold and marked by two stars are given in ppm; the detection limit is fixed at 3 ppm for Ag, 0.2 ppm for In, and 2 ppm for Sb. Sample 14HAO13 has been analyzed separately, and some contents are quantified with different detection limits (values in italics).

Oxides/ elements	Unit	Detection limit	Jbel Klakh						Jbel Haouanit										
			14KH53A (host rock 1)	14KH53B (host rock 2)	14KH10 (malachite)	14KH23 (azurite)	14KH09 (iron (hydr- joxides))	14KH17 (alunite)	14HT19 (host rock 1)	14HAO18 (host rock 2)	14HAO19 (host rock 3)	14HAO14 (galena)	14HAO17 (cerussite)	14HT13 (smithsonite 1)	14HT16 (smithsonite 2)	14HT07 (motttramite)	14HT05 (malachite)	14HAO13 (iron (hydr- joxides))	
Al <sub>2</sub> O <sub>3</sub>	%	0.01	0.46	0.1	0.1	0.1	10.35	25.69	0.2	0.34	0.19	0.08	0.07	0.07	0.19	0.9	0.61	1.61	
CaO	%	0.01	30.26	30.19	4		0.19	10.53	0.61	30.41	29.93	30.76	0.66	30.09	0.29	0.56	7.64	0.67	12.24
Fe <sub>2</sub> O <sub>3</sub>	%	0.01	0.35	0.06	13.61	0.09	6.52	6.49	0.2	0.28	0.27	< 0.01	0.76	0.61	0.12	0.95	10.36	48.13	
K <sub>2</sub> O	%	0.01	0.13	0.03	< 0.01	0.02	1.6	7.41	0.05	0.09	0.05	0.01	0.02	< 0.01	0.01	0.05	0.09	0.24	
MgO	%	0.01	18.6	20.28	0.47	0.31	6.4	0.43	21.11	20.74	20.82	0.44	20.88	0.55	0.61	0.39	0.45	8.61	
MnO	%	0.001	0.138	0.235	0.044	0.007	0.094	0.006	0.073	0.063	0.068	0.004	0.073	0.027	0.024	0.491	0.014	0.051	
Na <sub>2</sub> O	%	0.01	0.03	0.01	< 0.01	< 0.01	0.06	0.05	0.05	0.03	0.05	< 0.01	0.02	< 0.01	< 0.01	< 0.01	0.01	0.03	
P <sub>2</sub> O <sub>5</sub>	%	0.01	0.02	0.03	< 0.01	0.08	0.11	0.15	0.02	0.02	0.02	0.02	0.03	< 0.01	< 0.01	0.11	0.04	0.31	
SiO <sub>2</sub>	%	0.01	3.03	0.21	0.43	0.18	40.46	6.22	0.34	0.68	0.38	0.11	0.23	0.1	0.4	1.41	5.48	2.94	
TiO <sub>2</sub>	%	0.001/0.01	0.032	0.006	0.004	0.005	0.642	0.111	0.011	0.019	0.011	0.003	0.002	0.004	0.005	0.045	0.058	0.08	
LOI	%		45.26	46.56	29.51	20.16	19.68	37.23	46.59	46.2	45.88	10.41	45.54	35.23	34.83	7.55	26.66	22.37	
Total	%	0.01	98.86	98.7	48.29	21.27	96.67	84.4	99.16	98.42	98.52	11.77	97.73	36.91	36.87	19.56	44.46	96.62	
FeO	%	0.1	0.5	0.9	0.1	0.2	0.2	< 0.1	0.1	< 0.1	< 0.1	0.1	< 0.1	< 0.1	0.1	< 0.1	< 0.1	< 0.1	
V	ppm/%	5	17	6	8	6	104	344	6	< 5	7	9	55	14	12	10.8*	323	2220	
Cr	ppm	20	20	20	< 20	20	80	210	20	20	20	20	30	20	30	850	130	40	
Co	ppm	1	< 1	< 1	72	119	73	80	< 1	< 1	< 1	< 1	49	7	26	58	433	243	
Ni	ppm	20	< 20	< 20	50	70	40	90	< 20	< 20	< 20	< 20	40	30	50	100	320	610	
Cu	ppm/%	10	50	30	41.6*	62.5*	1.27*	1.58*	20	< 10	< 10	1760	70	430	580	12.5*	43.9*	9150	
Zn	ppm/%	30	220	90	980	4640	880	4.48*	< 30	< 30	< 30	1550	0.2*	50.5*	49*	1010	540	970	
Ga	ppm	1	4	3	3	3	13	37	21	14	11	8	7	20	32	6	6	23	
Ge	ppm	0.5/1	0.8	0.7	3.6	2.1	3.9	18.3	< 0.5	< 0.5	< 0.5	0.7	< 0.5	16.5	4.6	1.2	1.5	4	
As	ppm	5	< 5	< 5	43	39	31	126	< 5	< 5	< 5	63	11	136	30	694	272	245	
Rb	ppm	0.1/0.2	4	< 1	< 1	< 1	73	16	1	3	2	< 1	< 1	< 1	< 1	2	2	9	
Sr	ppm	2	33	41	4	3	46	77	30	31	40	78	35	8	6	12	22	46	
Y	ppm	0.5/1	2.4	2.2	5.8	0.7	18.2	1.7	1.5	2.4	3.6	0.6	8	4	2.9	7.2	3.8	12	
Zr	ppm	01-mai	20	4	3	3	211	22	6	9	6	3	5	5	4	47	47	50	
Nb	ppm	0.2/1	0.3	< 0.2	< 0.2	< 0.2	9.6	1.5	< 0.2	< 0.2	< 0.2	< 0.2	< 0.2	< 0.2	< 0.2	3	1.5	< 1	
Mo	ppm/%	2	< 2	< 2	25	< 2	3	77	< 2	< 2	< 2	11	0.031*	6	13	68	44	42	
Ag	ppm	0.5	0.9	0.8	10.2	4.4	3.4	2	< 0.5	< 0.5	< 0.5	11.1	2.8	446**	550**	3.3	2.7	0.6	
In	ppm	0.1/0.2	< 0.1	< 0.1	1.3	0.1	0.9	547**	< 0.1	< 0.1	< 0.1	< 0.1	< 0.1	< 0.1	< 0.1	< 0.1	0.3	< 0.2	
Sn	ppm	1	2	< 1	< 1	< 1	2	< 1	< 1	< 1	< 1	< 1	< 1	< 1	< 1	< 1	< 1	< 1	
Sb	ppm	0.2/0.5	12.3	6.3	26.5	8	16.8	51.5	1.2	1.3	0.7	447**	13.5	141	71.4	8**	157**	77.1	
Cs	ppm	0.1/0.5	0.2	< 0.1	< 0.1	< 0.1	20.4	1.2	< 0.1	0.2	0.2	< 0.1	< 0.1	< 0.1	0.1	0.2	0.3	4	
Ba	ppm	3	14	8	8	235	125	67	5	8	5	12	< 3	< 3	3	26	343	92	
Hf	ppm	0.1/0.2	0.3	< 0.1	0.1	< 0.1	4.8	0.6	0.1	0.2	< 0.1	< 0.1	< 0.1	< 0.1	0.1	0.8	1	0.7	
Ta	ppm	0.01/0.1	0.05	0.02	0.02	0.02	0.81	0.16	0.01	0.04	0.02	0.01	< 0.01	0.02	0.02	0.11	0.11	< 0.1	

<b>W</b>	ppm	0.5/1	1.4	1.4	1.2	1.5	2.5	1.3	1.3	1.1	4	1.1	1.3	1.2	1.4	1.8	1.4	5
<b>Tl</b>	ppm	0.05/0.1	< 0.05	< 0.05	< 0.05	< 0.05	0.31	0.18	< 0.05	< 0.05	< 0.05	< 0.05	< 0.05	0.84	0.13	33	1	0.2
<b>Pb</b>	ppm/%	5	47	32	110	586	474	<b>3.53*</b>	< 5	< 5	< 5	<b>79.8*</b>	<b>0.59*</b>	<b>0.41*</b>	<b>0.58*</b>	<b>42.3*</b>	5610	1450
<b>Bi</b>	ppm	0.1/0.4	< 0.1	< 0.1	< 0.1	< 0.1	0.2	< 0.1	< 0.1	< 0.1	< 0.1	0.8	< 0.1	< 0.1	< 0.1	1.6	1.4	4.9
<b>Th</b>	ppm	0.05/0.1	0.4	0.1	0.09	0.06	7.52	4.74	0.19	0.26	0.25	0.07	0.31	0.14	0.35	0.72	1.52	1.2
<b>U</b>	ppm	0.01/0.1	0.72	0.25	38	0.68	2.7	6.76	0.26	0.17	0.36	7.57	1.19	13.5	5.45	0.57	4.68	3.9
<b>La</b>	ppm	0.05/0.1	2.01	1.28	2.35	0.35	24.1	25.4	1.24	2.21	2.63	0.44	5	1.46	2.83	11.3	2.69	4.9
<b>Ce</b>	ppm	0.05/0.1	4.25	2.24	5.5	0.46	46.3	14.7	2.52	3.94	2.84	0.57	7.53	2.43	3.72	54.6	6.54	8.2
<b>Pr</b>	ppm	0.01/0.05	0.49	0.29	0.66	0.05	4.77	1.85	0.3	0.53	0.42	0.1	1.07	0.41	0.41	4.26	0.67	0.97
<b>Nd</b>	ppm	0.05/0.1	1.87	1.07	2.91	0.29	16.5	4.17	1.3	2.19	1.57	0.49	4.08	1.89	1.6	16.7	2.69	3.8
<b>Sm</b>	ppm	0.01/0.1	0.36	0.25	0.75	0.07	3.1	0.51	0.26	0.4	0.34	0.09	0.91	0.6	0.38	3.95	0.57	0.9
<b>Eu</b>	ppm	0.005/0.05	0.095	0.063	0.19	0.017	0.757	0.072	0.064	0.101	0.075	0.025	0.254	0.195	0.143	0.982	0.128	0.22
<b>Gd</b>	ppm	0.01/0.1	0.37	0.3	0.82	0.06	2.85	0.34	0.32	0.38	0.33	0.12	0.85	0.63	0.4	2.95	0.64	1
<b>Tb</b>	ppm	0.01/0.1	0.05	0.05	0.14	0.01	0.49	0.05	0.05	0.05	0.05	0.02	0.14	0.12	0.06	0.5	0.1	0.2
<b>Dy</b>	ppm	0.01/0.1	0.28	0.26	0.86	0.08	3.16	0.28	0.22	0.34	0.3	0.1	0.82	0.78	0.37	2.5	0.56	1.3
<b>Ho</b>	ppm	0.01/0.1	0.06	0.05	0.17	0.01	0.61	0.05	0.04	0.07	0.06	0.02	0.16	0.13	0.07	0.42	0.11	0.3
<b>Er</b>	ppm	0.01/0.1	0.15	0.12	0.42	0.05	1.92	0.15	0.11	0.17	0.16	0.04	0.47	0.29	0.21	0.91	0.33	0.9
<b>Tm</b>	ppm	0.005/0.05	0.02	0.016	0.054	0.006	0.277	0.024	0.013	0.023	0.024	0.007	0.063	0.034	0.027	0.103	0.047	0.13
<b>Yb</b>	ppm	0.01/0.1	0.11	0.1	0.31	0.04	1.98	0.15	0.08	0.13	0.16	0.04	0.33	0.17	0.16	0.47	0.27	0.7
<b>Lu</b>	ppm	0.002/0.01	0.016	0.014	0.04	0.007	0.305	0.025	0.013	0.018	0.019	0.005	0.047	0.02	0.024	0.061	0.045	0.11

## 5.1.4 Discussion

### 5.1.4.a Weathering and neutralization

The main agents required for weathering are the oxidizing atmosphere and the presence of fluids leaching the primary ore in a vadose or phreatic environment. Tectonic uplift and brittle fracturing are also necessary, to exhume the rocks and trigger their weathering (Boni and Mondillo 2015). A wet and warm climate favors the development of extensive weathering profiles. Dolomitization is also an important parameter to be considered: it is responsible for the high porosity of the host rock, and plays a major role for the percolation of supergene mineralizing fluids.

Sulfides are only stable in reduced conditions; their oxidation releases sulfuric acid, which enhances the weathering processes (Herbert 1999; Domènech et al. 2002). When hypogene minerals are oxidized and leached, cations (Cu, Fe, Pb, ...) and ligands ( $\text{SO}_4^{2-}$ ,  $\text{CO}_3^{2-}$ ,  $\text{OH}^-$ ,  $\text{PO}_4^{2-}$ , ...) are released in acidic fluids that percolate *per descensum* in the primary ore deposit. The acidity of the fluids may be buffered by minerals of the host rocks such as carbonates (Descostes et al. 2002) and chlorites (Brown 1967). They are both dissolved in contact with  $\text{H}^+$  ions, causing, respectively, the release of alkaline and bicarbonate ions (Huminicki and Rimstidt 2008), as well as the formation of clay minerals such as kaolinite and/or smectite. Some silica may also be remobilized, leading to the formation of quartz and other silicates accompanied with metallic elements. Creation and/or widening of karst cavities in the host rock increases permeability and porosity, that provides preferential drains for fluid circulation, as well as spaces for secondary minerals precipitation (Fig. 5.1.30) (Decrée et al. 2010a). The extension of the various types of mineralization depend on the initial acidity, the amount and nature of the hypogene minerals (Scott et al. 2001), as well as the neutralization capacity of the host rocks (Takahashi 1960; Bladh 1982; Sangameshwar and Barnes 1983; Chavez 2000). Local conditions, such as the density and the extent of fracturing, also influence the weathering processes (Borg 2009). Finally, distribution

of the various supergene minerals also depends on the water table level fluctuations, which could be tectonic, climatic, or seasonal in origin (Decrée et al. 2010a).

### 5.1.4.b Jbel Klakh mineralization

Previous authors (Chavez 2000; Robb 2005; De Putter et al. 2010; Arndt and Ganino 2012) described supergene copper deposits. From bottom to top of the profile, they identify: the primary sulfides zone, the secondary sulfides enrichment zone (or cementation zone), the oxidized zone, and the leached zone (or gossan). These zones are also observed at Jbel Klakh, and are discussed separately in this chapter.

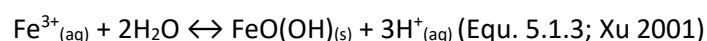
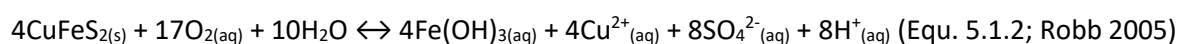
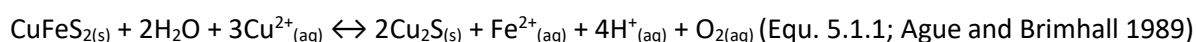
#### Primary sulfides zone

Chalcopyrite, with minor amount of galena and pyrite, are the primary sulfides present in the Jbel Klakh deposit as they precipitated in reduced environments. The presence of supergene smithsonite (Fig. 5.1.2J) and iron (hydr-)oxides indicates that sphalerite and pyrite may also be present as primary minerals, but are completely weathered.

#### Secondary sulfides enrichment zone (cementation zone)

This zone is characterized by the replacement of primary sulfides by other sulfides (Fig. 5.1.2D, 5.1.2E, 5.1.2F), formed by the recombination of metallic cations and  $\text{SO}_4^{2-}$  transported by acidic Cu-rich percolating fluids (Van Langendonck et al. 2013). These secondary sulfides (bornite, digenite, chalcocite, djurleite, and covellite) are well known in the cementation zone. Their occurrence indicates that neutralization of the acidic fluids, during dissolution of the Jurassic host rock, was not sufficient to reach neutral pH conditions and to hinder the fluids from reaching the water table level, where the slightly reduced conditions caused sulfide precipitation. However, secondary sulfides are relatively uncommon at Jbel Klakh: neutralization may have been sufficient to hinder the formation of massive volumes of secondary sulfides.

Chalcopyrite is stable in highly reduced environments (Fig. 5.1.6A), and is progressively transformed in other sulfides (Fig. 5.1.2D, 5.1.2E, 5.1.2F) when conditions become less reduced, as these secondary minerals are more stable (Fig. 5.1.6A) (Ague and Brimhall 1989). At Jbel Klakh, chalcopyrite is successively weathered in bornite, digenite, chalcocite and/or djurleite (Ramdhor 1980), which are Fe-poor Cu sulfides (Fig. 5.1.2D, 5.1.2E, 5.1.2F). Covellite, in fractures and at the edges of chalcocite, is the last secondary sulfide to precipitate, as it is depleted in copper (Chavez 2000). Chalcopyrite may also be directly replaced by chalcocite (Equ. 5.1.1). Released iron (Equ. 5.1.1, 5.1.2) rapidly precipitates in iron (hydr-)oxides (Equ. 5.1.3), when the environment is not acidic enough to have soluble and mobile iron. The assemblage of chalcocite, the main secondary sulfide, and iron (hydr-)oxides (Fig. 5.1.2F), is a typical supergene feature (Van Langendonck et al. 2013). Iron (hydr-)oxides concretions observed onto rhombohedral dolomite crystal faces indicate the direction of fluid percolation (Fig. 5.1.2D). Pyrite is stable in a large pH range but usually transforms in hematite and goethite beyond reduced conditions. Replacement of pyrite by chalcocite (Fig. 5.1.2J) suggests the circulation of Cu-rich fluids. Released iron precipitates in goethite, as  $\text{SO}_4^{2-}$  recombines with copper ions to form chalcocite.





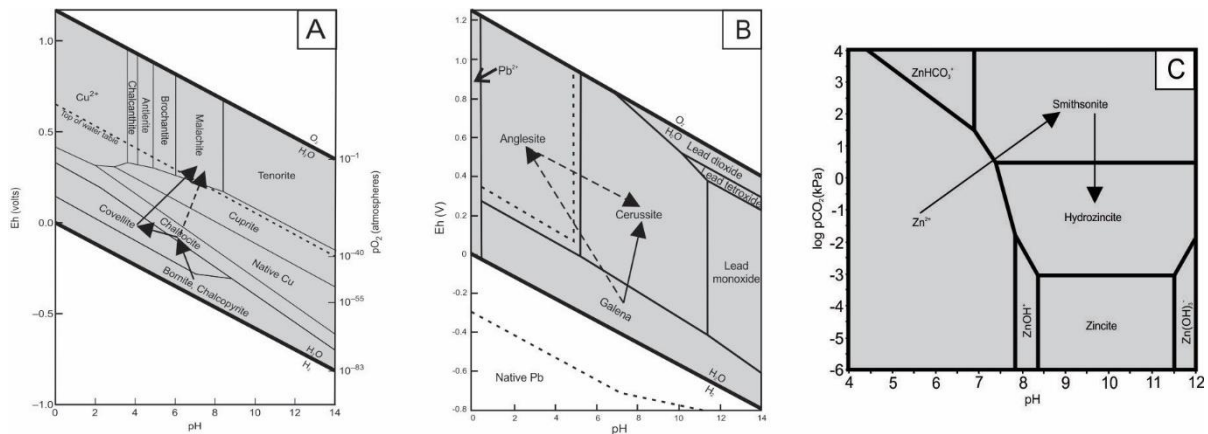


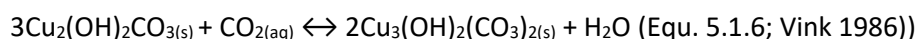
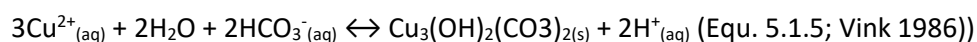
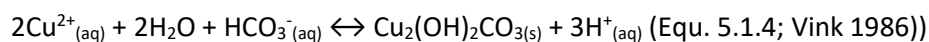
**Figure 5.1.6.** (A) Eh–pH diagram for a part of the system Cu–C–S–Si–O–OH, showing the stability fields of selected copper minerals at 25 °C and 1 atmosphere (modified after Guilbert and Park 1986). As observed at Jbel Klakh, chalcopyrite is firstly weathered in secondary sulfides and later in oxidized minerals. (B) Eh–pH diagram for a part of the system Pb–S–C–O–H, at 25 °C and 1 bar; the assumed activities of dissolved species are:  $Pb = 10^{-6}$  or  $10^{-8}$ ,  $S = 10^{-3}$ ,  $C = 10^{-3}$  (modified after Brookins 1988). At Jbel Haouanit and Jbel Klakh, galena is directly weathered in cerussite, or it is successively replaced by anglesite and afterwards by cerussite. (C) Stability of zinc carbonates in the chemical system Zn–O–H–C in relation to  $pCO_2(g)$  and pH; the activity of zinc is  $a(Zn) = 10^{-5} \text{ mol} \cdot l^{-1}$  (modified after McPhail et al. 2003). Smithsonite is rapidly replaced by hydrozincite under atmospheric  $CO_2$  pressures, as observed at Jbel Haouanit.

## Oxidized zone

The oxidized zone is separated from the cementation zone by the water table level, which represents a transition in the redox conditions (De Putter et al. 2010). It is composed of oxidized minerals such as carbonates, silicates, sulfates, phosphates, oxides. Their formation depends on the pH conditions which control the solubility and activity of cations and complexing ligands. Redox conditions are also highly important, whereas the  $CO_2$  partial pressure controls the precipitation of carbonates. However, most of these minerals formed under near-neutral solutions (Fig. 5.1.6A), after partial or total consumption of pyrite due to oxidation (Reichert and Borg 2008):  $H^+$  ions are no longer released and the activity of sulfate ions decreases.

Carbonates dominate the mineralogy at Jbel Klakh, whereas sulfates and silicates are minor components. Neutralization may have hindered the circulation of highly acidic fluids, and promoted the formation of carbonate minerals. Carbonates (malachite and azurite; Fig. 5.1.2B, 5.1.2H), formed from the recombination of bicarbonate ions and  $Cu^{2+}$ , as copper is a mobile element in oxidized and acidic fluids (Andrew-Jones 1968). Malachite is stable in oxidizing environments (Fig. 5.1.6A), where pH is near neutral to basic (Rose et al. 1958; De Putter et al. 2010). Preliminary neutralization is required for the precipitation of azurite and malachite (Equ. 5.1.4, 5.1.5; Fig. 5.1.6A) in cavities and fractures, and for the impregnation in porosity of the host rock. Azurite is rather found close to chalcopyrite-bearing veins and in deeper zones than malachite, whereas it is associated with chalcocite and goethite in near-surface samples (Fig. 5.1.2C, 5.1.2G). Malachite and azurite are very close in composition, but malachite is more stable under atmospheric conditions. The formation of azurite requires relatively acidic conditions and high carbonate ions activity (Vink 1986). This may appear contradictory, considering that the second condition is typical in near-basic environments (Vink 1986). Azurite precipitates rarely, in more acidic environments than those required for malachite, and if carbonate activity is higher. It is frequently weathered to malachite (Equ. 5.1.6), because of slight variations in the carbonates activity. Transition between these minerals is dependent on slight climatic variations (Vink 1986). At Jbel Klakh, a few Cu-bearing silicates (Fig. 5.1.2F) formed at approximately

the same time from local silica-rich fluids (De Putter et al. 2010). The occurrence of brochantite indicates local, slightly acidic, environments (Chavez 2000).  $\text{Fe}^{2+}$  released from sulfides oxidation is rapidly transformed in  $\text{Fe}^{3+}$ , and precipitates to form goethite and hematite. Lack of copper oxides in Jbel Klakh indicates that fluids may have never reached  $\text{pH} > 8$  (Fig. 5.1.6A).



### **Leached zone (gossan)**

This uppermost zone is only represented by iron (hydr-)oxides; the primary mineralization is completely weathered and other metals leached. Hematite and goethite have large stability ranges, from very acidic to basic pH, in oxidizing and slightly reduced environments. This explains their dominance in the entire sequence of Jbel Klakh supergene mineralization, from the cementation zone to the leached zone. Goethite is the hydrated form of hematite; their respective formation depends on hydration or dehydration reactions. In Jbel Klakh deposit, alunite is observed close to large iron (hydr-)oxides veins. Alunite forms in highly acidic and oxidizing environments. The sulfate complex originates from the weathered sulfides, and aluminum is released at  $\text{pH} < 4$  (De Putter et al. 2002) from the host rock, probably from phyllosilicates present in marls (Robb 2005). Some siliceous and aluminous primary minerals of the Jbel Klakh deposit were involved in the formation of clays (kaolinite, smectite and illite) and quartz. The sources of these clays may be Al- and Si-rich fluids, which precipitated the metals. Kaolinite may be the result of illite or chlorite weathering.

### **Jbel Klakh paragenesis**

A clear sequence of mineralization is observed, from the center to the outer edges of veins: chalcopryite → bornite → digenite → chalcocite/djurleite → covellite → malachite, azurite, copper-bearing silicates → iron (hydr-)oxides. That sequence is not observed as a whole in all samples, as some transitional phases do not precipitate or subsist under very acidic or oxidized conditions. The various supergene minerals are represented in Fig. 5.1.7A. The primary sulfides (chalcopryite, pyrite, galena, and sphalerite) are firstly replaced by secondary sulfides (group 1 in Fig. 5.1.7A: bornite, digenite, chalcocite, djurleite, covellite). Then, they are transformed in sulfates (group 2 in Fig. 5.1.7A: brochantite, anglesite), silicates, carbonates (group 4 in 5.1.7A: malachite, azurite, cerussite, smithsonite). Iron (hydr-)oxides, alunite and clays may form as soon as pH is already partially neutralized, but still acidic (group 3 of Fig. 7A). Late dolomite and calcite form during later stages (group 5 in Fig. 5.1.7A) of supergene weathering.



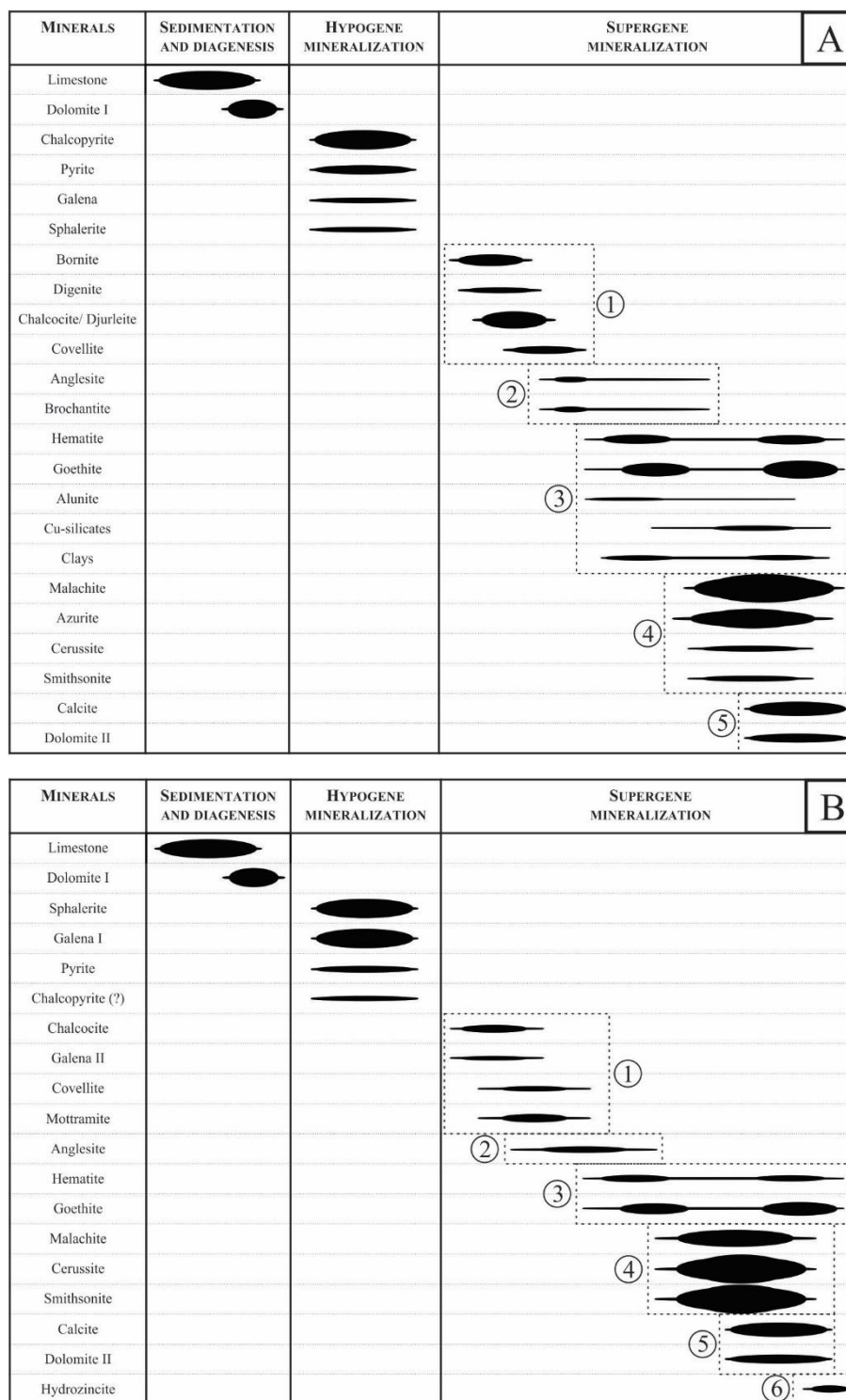


**Figure 5.1.7.** (Paragenetic sequence for the Cu deposit of Jbel Klakh (A) and the Pb-Zn deposit and the Cu(-Pb-V) occurrences of Jbel Haouanit (B). The pH of the fluids increases from left to right, but microenvironments with variable acidity may coexist locally, disturbing this pH evolution on a small scale.

### Geochemistry of the ore

The enrichment in REE of Jbel Klakh secondary minerals, in comparison to the host rocks, is due to the weathering processes. During weathering of the hypogene minerals, REE are mobilized and leached from the upper parts of the profile, before migrating downwards in solution and precipitating in supergene minerals, in relation with the various ligands present in solution (Pagel et al. 1990; Cocker

2012). REE may be adsorbed at the surface of secondary minerals such as clays and iron or manganese (hydr-)oxides, which are characterized by high adsorption capacity, large specific surface, and cation exchange sites (Rose et al. 1958; Yong and Zheng 1993; De Putter et al. 1999; Cocker 2012, 2014).

At Jbel Klakh, remobilized U and REE are concentrated by iron (hydr-)oxides, which is a typical supergene trend (De Putter et al. 1999). LREE are usually enriched in the upper parts of the deposits, whereas HREE are more enriched at greater depth (Lottermoser 1990; Zheng and Lin 1996). A slight REE fractionation, with an enrichment in LREE, is also typically observed in weathering profiles (Zheng and Lin 1996; Brown et al. 2003). REE fractionation tends to be intensified during weathering (Brookins 1989; Leybourne et al. 2006).

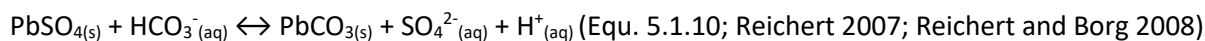
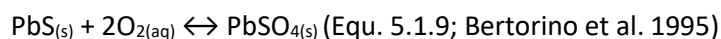
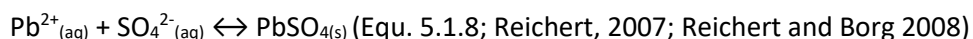
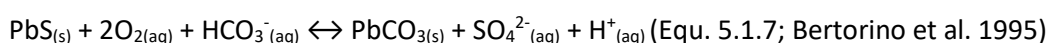
The lack of fractionation in the Jbel Klakh samples (Fig. 5.1.4A) may therefore be a consequence of highly basic pH conditions, possibly related to a significant and rapid neutralization by the host rock. Only alunite shows a strong enrichment in LREE compared to HREE (Fig. 5.1.4A): it precipitates from highly acidic fluids, where LREE are more soluble than HREE (De Putter et al. 1999; Garasic and Jurkovic 2012). The slight negative Ce anomaly of alunite (Fig. 5.1.4A) indicates that this mineral formed in an oxidizing environment.  $Ce^{3+}$  released during weathering is indeed rapidly oxidized in  $Ce^{4+}$  and precipitated, leaving the percolating fluids and the new-formed minerals depleted in Ce (Leybourne et al. 2000, 2006). Mobile elements are preferentially leached and removed by the percolating fluids (Fig. 5.1.4B), unlike immobile elements. Because iron is a relatively immobile element in oxidizing environments, iron (hydr-)oxides precipitate *in situ* and typically concentrate immobile elements and REE, as observed at Jbel Klakh (Fig. 5.1.4B). On the contrary, mobile elements are concentrated in minerals such as malachite, which precipitates from Cu-rich percolating fluids, as Cu is mobile at low pH conditions (Chavez 2000). Therefore, U and Th, which are, respectively, mobile and immobile (Pagel et al. 1990), are correspondingly enriched in malachite and iron (hydr-)oxides. The enrichment of Jbel Klakh samples in chalcophile elements (Fig. 5.1.4B) is related to the occurrence of Cu. Potassium content is high in alunite and some other samples due to the presence of clay assemblages in the entire deposit, while small disseminated barite crystals are responsible for the relatively high content in Ba. All Jbel Klakh samples are characterized by high Sb and Ag contents (Fig. 5.1.4B): these metals are thought to be present in the primary sulfides and/or the host dolostone and released later during weathering. The low content in FeO of Jbel Klakh samples (Table 5.1.1) confirms that only few reduced iron is left in sulfides, and that almost all iron was oxidized during the weathering.

#### **5.1.4.c Jbel Haouanit mineralization**

##### **Pb-Zn mineralization**

In this vein-type ore, the principal primary sulfide is galena (Fig. 5.1.3A, 5.1.3B, 5.1.3D). Before weathering, pyrite (Fig. 5.1.3F) and sphalerite (Fig. 5.1.3G) were likely present, as their weathering products (relics and pseudomorphs) are found in significant quantities. These sulfides are only stable in reduced environments, and leached under slightly acidic and oxidizing conditions in the percolating fluids. The supergene mineral assemblage is dominated by carbonates and iron (hydr-)oxides; the only sulfate is anglesite. When pyrite is weathered,  $Fe^{2+}$  is released and rapidly oxidized into  $Fe^{3+}$ . After several reactions including the formation of gels such as ferrihydrite, iron forms hematite and/or goethite (Xu 2001). In this deposit, hematite is often observed at the center of pyrite pseudomorphs, and goethite at the external rim: goethite precipitates under acidic conditions, whereas hematite forms under neutral pH conditions (Bigham and Murad 1997; Cornell and Schwertmann 2003; Jönsson et al. 2006). Goethite is the hydrated form and commonly replaces hematite.

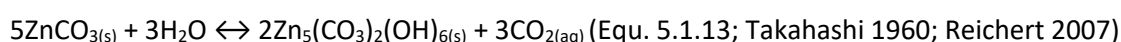
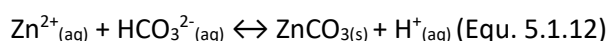
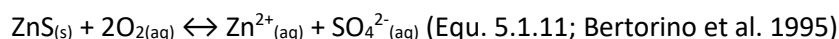
At Jbel Haouanit, galena is commonly oxidized in cerussite (Fig. 5.1.3B, 5.1.3C, 5.1.6B; Equ. 5.1.7), a carbonate stable under slightly acidic to basic conditions (>5 pH units), when  $\text{Pb}^{2+}$  recombines with bicarbonate. An intermediate secondary sulfate, anglesite (Fig. 5.1.6B), may form in acidic environments (<5 pH units), where sulfate ions activity is high. These specific conditions are rarely reached in Pb-Zn supergene deposits, because weathering of galena and sphalerite does not release enough  $\text{H}^+$  ions. The required acidic environments are typically found close to weathered pyrite (Zabinski 1960; Szczerba and Sawłowicz 2009). Pyrite oxidation releases significant amounts of sulfuric acid which may produce, locally, a substantial drop of pH. Moreover, the presence of cerussite around galena (Fig. 5.1.3B) limits the buffering of the acidity (Reichert and Borg 2008), contributes to the formation of microenvironments characterized by pH under 6 and high activity of sulfate ions, causing the precipitation of anglesite (Sangameshwar and Barnes 1983). In the Jbel Haouanit deposit, anglesite develops in fractures and cleavage plans of galena, which constitutes favorable microenvironments; it originates from the association of  $\text{Pb}^{2+}$  from galena and  $\text{SO}_4^{2-}$  from galena and/or pyrite (Equ. 5.1.8), or it may directly replace galena (Equ. 5.1.9). After weathering, when sulfate ions activity drops down and pH increases, anglesite is replaced by cerussite (Equ. 5.1.10), which is more stable in these conditions (Reichert and Borg 2008). The low abundance of anglesite may also be explained by the difficulty to maintain a low pH environment in a deposit hosted by carbonate rocks, whereas the sulfides producing acidity are present in small amounts, and by the leaching of sulfate ions from the weathering zone under slightly acidic conditions. The lead-zinc paragenetic sequence is simple: galena  $\rightarrow$ (anglesite)  $\rightarrow$ cerussite.



Because Pb is an immobile element, galena is replaced *in situ* by its insoluble weathering products which precipitate directly around the sulfide (Fig. 5.1.3B). As cerussite is almost insoluble in non-acidic waters (Garrels 1954), this armoring protects galena from further weathering and oxidation by partially hindering contact (Fig. 5.1.3B) with the oxidizing agents (Hitzman et al. 2003; Reichert and Borg 2008). Sphalerite (Fig. 5.1.3G) and pyrite do not have such a protective layer, and are partly or totally weathered.  $\text{Zn}^{2+}$  ions, which are mobile under acidic conditions (Andrew-Jones 1968), are transported far from the precursor mineral resulting in the lack of any protection layer around sphalerite grains under weathering conditions. The relative resistivity of Jbel Haouanit galena during the oxidation processes, and its subsistence among supergene mineralization, may thus be explained by this armoring effect (Reichert 2007).

At Jbel Haouanit, covellite is often associated with cerussite and anglesite (Fig. 5.1.3D) as well as secondary galena which is found next to cerussite. Those minerals may form when local variations of the water table lead to reduced conditions, which promotes the precipitation of secondary sulfides (Choulet et al. 2014). Cu is mobile in acidic environments and may be transported for a long distance after release from copper sulfide inclusions restricted in the primary sulfides zone of Jbel Haouanit (Ramdohr 1980). The predominant abundance of cerussite suggests a low acidity of the mineralizing fluids. The occurrence of covellite and secondary galena suggests that, locally, slightly reduced conditions prevailed or that the environment was fluctuating between oxidizing and reduced conditions.

When sphalerite undergoes weathering,  $\text{SO}_4^{2-}$  and  $\text{Zn}^{2+}$  ions are released (Equ. 5.1.11). Zinc may afterwards recombine with bicarbonate to form smithsonite (Fig. 5.1.6C; Equ. 5.1.12), as pH reaches neutral values (Reichert 2007). This carbonate is only stable near 7 pH (Fig. 5.1.6C);  $\text{Zn}^{2+}$  is mobile in acidic fluids, but becomes immobile under neutral to basic conditions. Smithsonite is stable under high  $\text{CO}_2$  partial pressures (Fig. 5.1.6C), typically observed in percolating fluids that are not in equilibrium with atmospheric  $\text{CO}_2$ . At the end of the weathering processes, when the environment evolves to arid conditions,  $\text{CO}_2$  pressure returns to atmospheric values. Unstable smithsonite is then progressively replaced by hydrozincite (Fig. 5.1.6C) (Takahashi 1960; McPhail et al. 2003; Reichert 2007) (Equ. 5.1.13), which is stable under low atmospheric  $\text{CO}_2$  pressures (Reichert and Borg 2008).



As no sulfates were observed in sufficient amounts near the mineralization, the sulfate ions released from sulfide oxidation were likely removed by the slightly acidic fluids. Smithsonite and Zn-rich silicates (willemite, hemimorphite) are commonly associated with Pb-Zn supergene deposits, such as “La Calamine” deposits in Belgium (Coppola et al. 2008), but no Zn-silicates were found at Jbel Haouanit. The lack of Zn-rich silicates indicates that the mineralizing fluids did not contain significant amounts of Si, which is rare in calamine deposits (Boni and Mondillo 2015), but consistent with the low content in detritic grains in the host rock dolostone.

Sphalerite, galena and pyrite are the hypogene minerals of the Pb-Zn deposit of Jbel Haouanit (Fig. 5.1.7B). Pyrite is replaced by goethite and hematite (group 3 of Fig. 5.1.7B), galena is weathered in cerussite (group 4 of Fig. 5.1.7B), and locally in anglesite (group 2 of Fig. 5.1.7B). Sphalerite is weathered at the same time as the two other sulfides: smithsonite precipitates under neutral to basic pH conditions (group 4 of Fig. 5.1.7B). Finally, late calcite and dolomite form at the end of this sequence (group 5 of Fig. 5.1.7B). Smithsonite is weathered to hydrozincite when atmospheric conditions are reached (group 6 of Fig. 5.1.7B).

### **Cu and Ag occurrences**

The Cu mineralization (Fig. 5.1.3I, 5.1.3J) observed within some of the small excavations is very similar to that of the highly weathered veins in Jbel Klakh. The significant content of Cu and Fe minerals in these veins suggests that the primary sulfides are chalcopryrite and pyrite. The circulation of acidic, Cu-rich fluids in the Jbel Haouanit deposit triggered the replacement of chalcopryrite in chalcocite, and the remobilization and precipitation of iron in goethite (Fig. 5.1.7B). Covellite then replaces the highly fractured chalcocite (Fig. 5.1.7B), from the edges to the center, when fluids become poorer in Cu. Malachite finally replaces both chalcocite (Fig. 5.1.3I) and covellite (Fig. 5.1.7B), by recombination of dissolved copper and bicarbonate ions. The small  $\text{Ag}_2\text{S}$  inclusions observed in chalcocite and covellite (but also in smithsonite in Jbel Haouanit; Fig. 5.1.3H) are typically found in supergene oxidation zones, and are often associated with low temperature secondary sulfides (Ramdohr 1980). Acanthite is stable up to 179°C, whereas its polymorph argentite only exists beyond this temperature (Ramdohr 1980), which is never reached during supergene processes. The dissolution of Jbel Haouanit sulfides, containing minor amounts of silver, may be the source of this metal. Silver is soluble in  $\text{Ag}_2\text{SO}_4$  or  $\text{Ag}_2\text{CO}_3$  ligands in leached and oxidized zones of weathering profiles, and easily precipitates as a sulfide in the secondary sulfides zone, close to chalcocite (Ramdohr 1980).

## Cu-Pb-V occurrences

Veins of mottramite (Fig. 5.1.3K, 5.1.3L), along with calcite and dolomite, were found in some of the small excavations, close to the Cu mineralization. This mineral is typically found in oxidized zones of vanadium supergene deposits, and may be abundant around Cu-sulfides ores. It is commonly described in deposits from the southern part of Africa (Namibia, Angola, Zambia) (Pelletier 1930; Taylor 1954; Millman 1960; Wartha and Schreuder 1992; Kamona and Friedrich 1994; Boni and Mondillo 2015). This vanadate forms at low temperatures (40–50°C), in arid (Takahashi 1960), acidic and slightly reduced environments (Fig. 5.1.7B), such as the boundary between phreatic and vadose zones (Boni et al. 2007). V is thought to be present in minor quantities in the initial hypogene sulfides and host dolostone of Jbel Haouanit (5–10 ppm; Table 5.1.1). When the host rock is weathered, V is released with other ions. It is probably transported as a calcium metavanadate ( $\text{Ca}[\text{VO}_3]_2$ ) away from its source (Verwoerd 1953; van der Westhuizen 1984; van der Westhuizen et al. 1989) and precipitates by recombination with metal cations in favorable environments. Following Boni et al. (2007), the released Ca may then react with bicarbonate ions to form dolomite and calcite (Fig. 5.1.3K). Once formed, mottramite does not seem to undergo further weathering. Note that descloizite, the Zn analog of mottramite, was not found in this deposit.

## Geochemistry of the ore

As at the Jbel Klakh deposit, the enrichment in REE (Fig. 5.1.5A, 5.1.5C) and trace elements (Fig. 5.1.5B) of Jbel Haouanit secondary minerals (and especially in calamine ores) supports the concentration of some elements in supergene minerals (Cocker 2012). Here again, lack of significant fractionation (Fig. 5.1.5A, 5.1.5C) may be a consequence of basic pH conditions, possibly related to a rapid neutralization of the acidic fluids. However, the slight enrichment in LREE, compared to HREE, of mottramite (Fig. 5.1.5A) indicates that this mineral may have precipitated from slightly more acidic fluids, where LREE are more soluble than HREE (De Putter et al. 1999; Garasic and Jurkovic 2012). Iron (hydr-)oxides of Jbel Haouanit show the reverse trend (Fig. 5.1.5A) and seem to have precipitated from neutral fluids. The positive Ce anomaly of mottramite (Fig. 5.1.5A) suggests that this mineral formed in relation with Eh variations (Leybourne et al. 2000). Iron (hydr-)oxides of Jbel Haouanit are characterized by the highest contents in immobile elements (Fig. 5.1.5B, 5.1.5D), because of their low solubility and their *in-situ* precipitation. All samples are characterized by a high U content, which is typical of this type of deposit, as U is easily leached and accumulated in supergene layers. Higher amounts of U and chalcophile elements in smithsonite, in comparison with cerussite and anglesite (Fig. 5.1.5B, 5.1.5D), are due to the deviation between long circulation of Zn-bearing fluids before precipitation linked to the mobility of Zn, and direct precipitation of cerussite and anglesite around galena related to the immobile character of Pb. The enrichment of sphalerite in Ge is due to the common substitution of this element, involving elements such as Fe, Cu, Ag, to Zn (Cook et al. 2009; Belissont et al. 2014). When Jbel Haouanit sulfides are oxidized, the released Ge accumulates in calamine samples, here particularly in smithsonite (Fig. 5.1.5B, 5.1.5D), by the substitution with Zn in highly oxidizing environments. The high content in V observed in all Jbel Haouanit samples (Fig. 5.1.5B) may be related to the initial occurrence of this element in minor quantities in primary minerals and to the percolation of V-bearing fluids in the entire deposit. The particular enrichment in V of the calamine samples, in comparison to galena (Fig. 5.1.5D), may also indicate that mottramite results from the same weathering step as the other secondary minerals of the Jbel Haouanit deposit.

### 5.1.5 Conclusion

The mineralogical and chemical contents of Jbel Klakh and Jbel Haouanit mineralized veins are different, but the processes responsible for their formation are similar. In both cases, precipitation of supergene minerals is related to the high porosity of the host rocks due to intense diagenetic dolomitization, and subsequent neutralization of the acidic fluids during host rock dissolution. The vertical zoning of the various Pb-Zn-Cu-V mineral assemblage, represented in the vertical cross-sections of both deposits (Fig. 5.1.8), results from the complex physico-chemical processes that took place in the deposits, mainly in relation with pH and Eh variations.

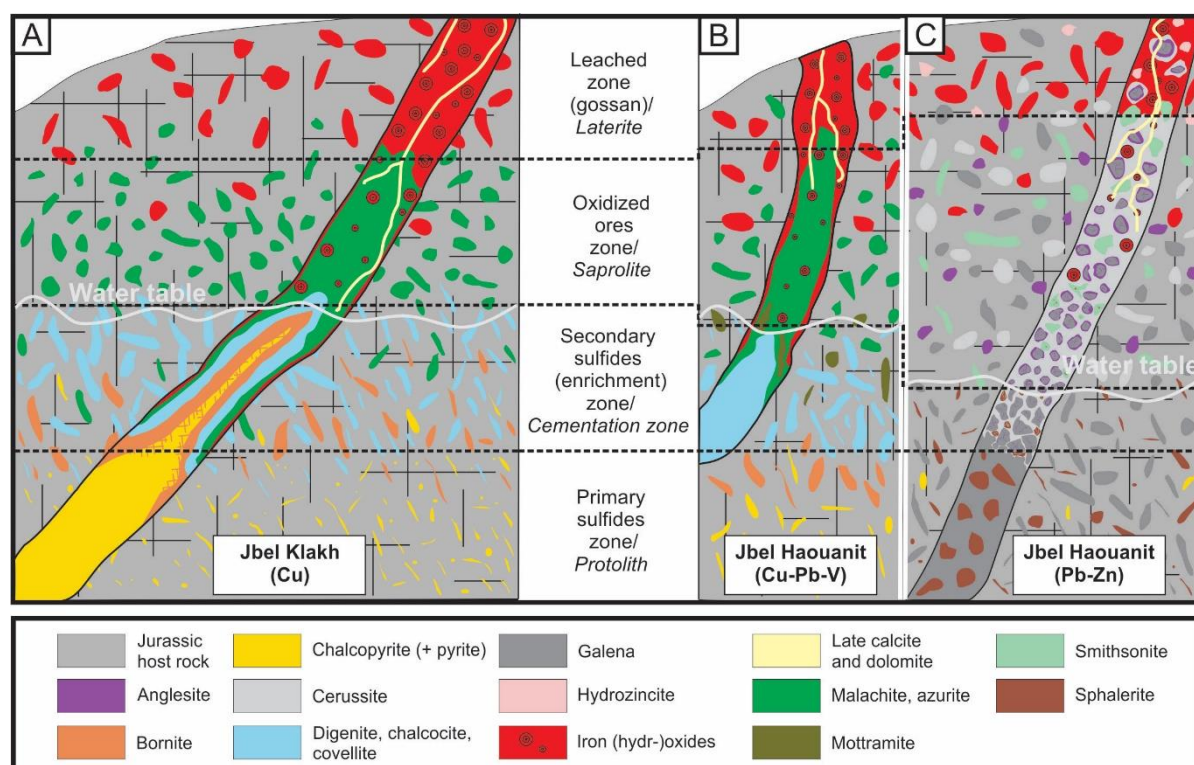


**Figure 5.1.8.** Schematic cross-sections (not at scale) showing the mineralogical zones of the studied supergene ore deposits and the most common mineral phases; (A) Jbel Klakh deposit, (B) Cu(-Pb-V) deposit of Jbel Haouanit, (C) Pb-Zn deposit of Jbel Haouanit (adapted after Webb, 1995 and Robb, 2005).

The weathering of the copper sulfides of Jbel Klakh leads to the development of four mineralogical zones that are distinguished in the vertical cross-section of the deposit (Fig. 5.1.8): the hypogene zone (chalcopyrite, pyrite), the secondary sulfides enrichment zone or cementation zone (bornite, digenite, chalcocite, djurleite, covellite), the oxidized zone (malachite, azurite, brochantite, shattuckite), and the leached zone (iron (hydr)-oxides). The paragenetic sequence at Jbel Haouanit consists of hypogene galena successively replaced by anglesite and cerussite, and sphalerite weathered in smithsonite and hydrozincite. The occurrence of copper minerals and mottramite at Jbel Haouanit indicates that Cu, Pb, V bearing fluids have also circulated through the Jurassic host rocks. Mineralogical zones may also be defined at Jbel Haouanit (Fig. 5.1.8): galena and sphalerite are found in the hypogene zone; mottramite, chalcocite and covellite in the cementation zone; anglesite, cerussite, smithsonite and hydrozincite in the oxidized zone. The leached zone is characterized by iron (hydr)-oxides. Geochemical trends such as the REE-fractionated diagram of alunite and general enrichment in Au-related elements at Jbel Klakh, the REE-V-Ge enrichment of calamine samples and Ag enrichment of smithsonite at Jbel Haouanit, are related to the leaching and concentration, by substitution or adsorption, of some elements during weathering processes.

## **5.2 Mineralogy and genesis of the polymetallic and polyphased low grade Fe-Mn-Cu ore of Jbel Rhals deposit (Eastern High Atlas, Morocco)**

The Jbel Rhals deposit was known as a Cu deposit for centuries and has been shortly exploited during the 19th–20th centuries; some mining activities started up again in 2012. However, there is no mineralogical inventory of the Jbel Rhals deposit, and processes leading to the formation of the various mineral phases have not been investigated yet. The issue of the origin and genesis of these ores has not been raised either. This work presents a petrological, mineralogical, and geochemical synthesis of the Jbel Rhals deposit. We focus our investigation mainly on the supergene processes responsible for the current ore mineralogy, considering that the primary mineralization is not exposed in outcrops or pits, nor in galleries, and that only the oxidation zone of the deposit is accessible. The purpose of this study is to investigate and highlight relationships between mineral associations and host rocks, to identify parageneses, and to propose a metallogenic model in order to explain the genesis of the ores. Special attention is also paid to the potential concentration of some elements classified as “strategic” or “critical” raw materials by the European Union (Light Rare Earth Elements (LREE), Heavy Rare Earth Elements (HREE), Y, In) in supergene mineral phases.

### ***5.2.1 Geological setting***

The Jbel Rhals deposit is located at the northern edge of the Oriental High Atlas (Fig. 5.2.1). See chapter 5.3.2 for the geodynamic setting.

The Jbel Rhals ore deposit (32°20'40.6" N; 1°58'40.6" W), elevated between 1200 and 1300 m in altitude, is located at 20 km south of the city of Bou Arfa, in the Figuig province of Morocco (Fig. 5.2.1). The deposit is situated in a Precambrian-Liassic inlier, at the base of a 200 m high cliff (Fig. 5.2.2a), eastward of the Tamlet plain which is filled with various Quaternary materials, and south of Jurassic-Cretaceous reliefs hosting supergene Cu-Pb-Zn-V ore deposits (Fig. 5.2.1) (Verhaert et al. 2017). The place is also known as “Guelb en Nahas”, which means the “Copper Hill” in Arabic, referring to some ancient mining activities by Portuguese miners for copper ores. The Cu mineralization has been somewhat mined during the 20<sup>th</sup> century, but received little attention since closure of the deposit until 2012, when a project of mining recovery was submitted. Ores were/are mined in shafts and subhorizontal galleries of several tens of meters long and about two meters high, driven into the Paleozoic basement rocks (Fig. 5.2.2b). The shafts are not accessible anymore. The stratigraphic succession of the entire area (mapped by Chefchaoui et al. (1963)) is complex: the intense fracturing and moderate folding of the series disrupt the sedimentary structures arrangement, and most original features are no more apparent. Several NE-SW normal faults are observable in the deposit area (Fig. 5.2.1), one of which, close to the ores, triggers a pluri-decametric displacement in the Triassic-Jurassic series.

The basement is constituted of Paleozoic shales that are successively covered by Triassic conglomerates, Triassic silty layers, and Jurassic dolomitized series (Fig. 5.2.2a). Permian-Triassic basalts are found between the basement and Triassic-Jurassic series (Fig. 5.2.2a). The several meters thick Fe-Mn ore is confined to the Paleozoic shales, right under the Permian-Triassic basalts (Fig. 5.2.2a), while Cu-mineralized veins extend from the Paleozoic shales (and the Fe-Mn ore) to the Triassic conglomerates. The thickness of the shale beds ranges from 1 centimeter to several decimeters. Stratification is subvertical in the Paleozoic shales (Fig. 5.2.3a), but horizontal in the Triassic and Sinemurian formations.



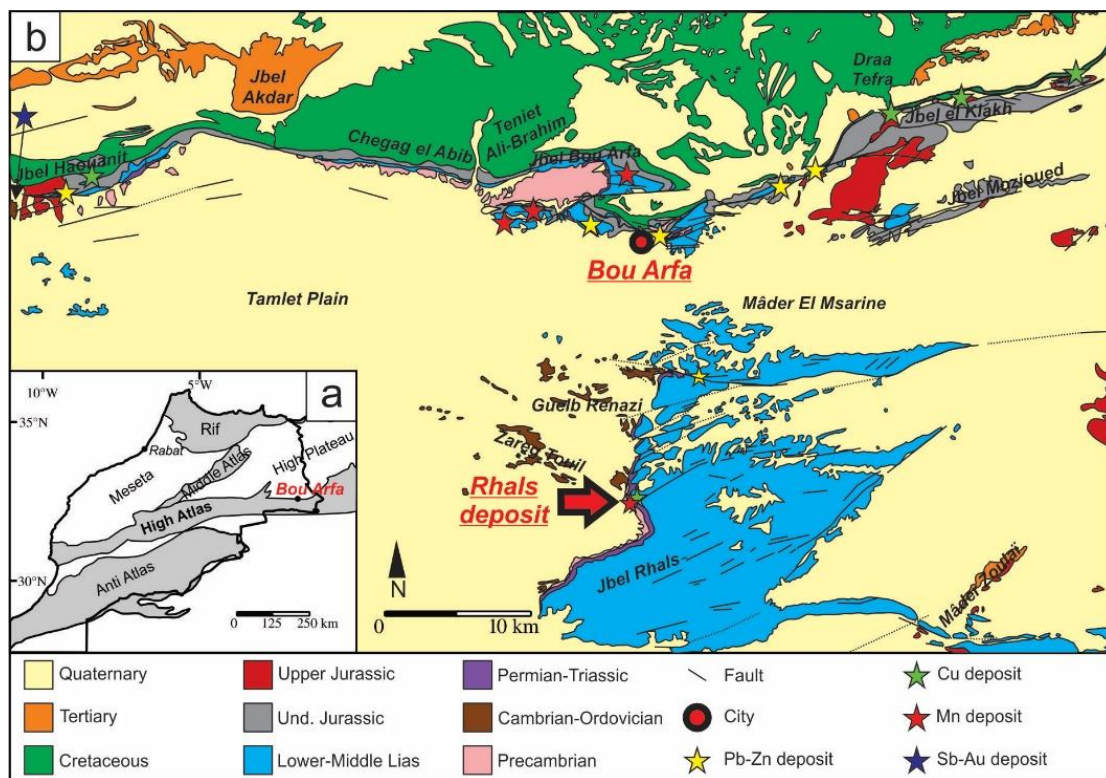


**Figure 5.2.1.** (a) Simplified geologic map of parts of Morocco and location of Bou Arfa; (b) Synthetic geologic map of the Bou Arfa region generalized according to the ages of units and showing the location of the Jbel Rhals ore deposit (modified from Chefchaouni et al., 1963).

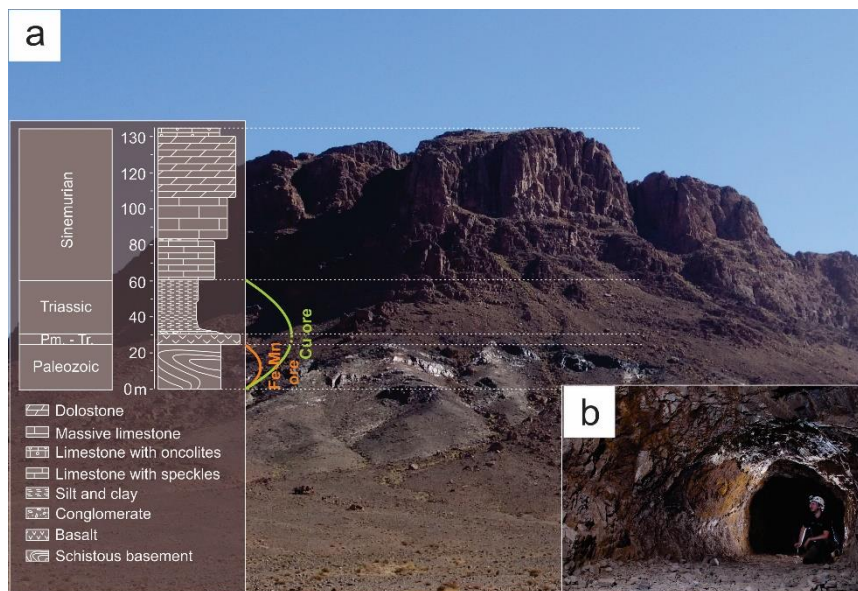


**Figure 5.2.2.** (a) Field view of Jbel Rhals and stratigraphic log of the observed units (modified after Lafforgue (2016)); (b) mining gallery showing Fe-Mn mineralization.



## **5.2.2 Materials and methods**

Thirty samples were collected in March 2014. X-Ray diffraction was carried out on twenty-one samples in order to identify the major mineral phases of the ore, using a BRUKER X-ray diffractometer (Bruker, Billerica, MA, USA) with a HI STAR GADDS (General Area Detector Diffraction System) CuK $\alpha$  detector. One thin section of the “freshest” basalt was observed in transmitted light mode with a LEITZ HM-POL petrographic polarizing microscope (Microscope Central, Feasterville, PA, USA). Twenty-one polished sections were observed on a ZEISS PHOTOMICROSCOPE reflection microscope (Carl Zeiss AG, Oberkochen, Germany), and with a JEOL JXA-8600 SUPERPROBE scanning electron microscope (SEM) (JEOL, Tokyo, Japan) coupled to an energy dispersive electron spectrometer (EDS).

Geochemical analyses were performed on eighteen samples in Activation Laboratories (Ancaster, ON, Canada). REE (Rare Earth Elements) and most of the trace elements were analyzed by Fusion Mass Spectrometry (FUS-MS) (Perkin Elmer Sciex Elan 9000 ICP-MS; Sciex AB, Singapore); Sr, Ba, Zr, and V contents were quantified by Fusion Inductively Coupled Plasma Optical Emission Spectrometry (FUS-ICP) (Varian Vista 735 ICP; Agilent, Santa Clara, CA, USA). Major elements of host rocks, basalts and Cu-mineralized veins were analyzed by FUS-ICP, while contents of iron-rich samples were evaluated with Fusion-X-ray Fluorescence (FUS-XRF) (Panalytical Axios Advanced XRF; PANalytical, Almelo, The Netherlands). FeO was quantified by titration. For samples containing high contents of Mo, Cu, Co. and Ni, analyses were carried out with Fusion Inductively Coupled Plasma Sodium Peroxide Oxidation (FUS-Na<sub>2</sub>O<sub>2</sub>), and results quantified in percentages rather than in ppm. Afterwards, REE contents were normalized to those of the PAAS (Post Archean Australian Shale; Taylor and McLennan 1985), considered as a reference for sedimentary rocks, while major and trace elements contents have been normalized to those of the UCC (Upper Continental Crust; Taylor and McLennan 1985). Mineralized samples contents have also been compared and normalized with those of host rocks, in order to highlight potential enrichments or depletions in particular elements.

## **5.2.3 Results**

### **5.2.3.a Petrographic characterization**

The Jbel Rhals deposit hosts two types of mineralization located in different veins. On the one hand, Fe-Mn minerals are restrained in decimetric-scaled veins hosted in Paleozoic schists, and overlaid by basalts. On the other hand, Cu minerals are found in veins of millimetric scale cutting Paleozoic schists, Fe-Mn ores, and Triassic conglomerates.

Host rocks and basalts underwent significant fracturing and severe alteration and weathering. Paleozoic schists (Fig. 5.2.3a) are mainly composed of quartz, muscovite and chlorite; rare single (La, Ce, Nd) phosphate grains are observed associated to quartz (Figure 5.2.4f). In some places, the schisteous protolite has been almost completely altered/weathered to clays (probably illite). Triassic conglomerates, composed of quartz and muscovite, experienced a circulation of iron-rich fluids, which turned their original whitish color to a red tint (Fig. 5.2.5g), and caused the rimming of some quartz grains with goethite. Basalts are strongly altered/weathered: the basalt considered on the field as “the freshest”, meaning “poorly weathered”, actually lost much of its primary minerals and textures (Fig. 5.2.3b), while the most altered/weathered one is composed of three layers of different colors and compositions (Fig. 5.2.3c). In the poorly weathered sample, plagioclase laths are still recognizable, but ferromagnesian minerals are intensively altered/weathered (Fig. 5.2.3d). Secondary quartz and clays are identified, along with chlorite presenting variable proportions of Al and Fe. Skeletal crystals of ilmenite and hematite, exsolution lamellae of hematite and pyrophanite in ilmenite (Fig. 5.2.3d,

5.2.3e), and fine hematite dendrites are also observed. Most altered/weathered basalt is composed of a greenish clay-rich layer, a red-brown iron-rich layer and a white layer (Fig. 5.2.3c, 5.2.3f). The white part is mostly composed of quartz, with some calcite and chlorite (Fig. 5.2.3h). Quartz, chlorite, clays and calcite are present in the greenish layer, along with some rutile laths (Fig. 5.2.3g), euhedral apatite and scarce small grains of pyrite. Different grain shapes suggest that some minerals are relics of original/primary ones (Fig. 5.2.3g), but weathering/alteration made their identification impossible. For instance, the clayey losangic sections observed in Figure 5.2.3g are thought to be relics of pyroxenes or olivines. Less common relics are associated to high porosities in the red-brown layer (Fig. 5.2.3j) where quartz, chlorite, clays, and a mix of calcite, goethite and pyrolusite are identified (Fig. 5.2.3g). Goethite and pyrolusite are often associated together and form concentric structures, where they are respectively located at the center and at the external rim (Fig. 5.2.3i). Zircon and (La, Ce, Nd) phosphates have been observed in the poorly weathered basalt, close to quartz, and in the altered/weathered sample, associated with pyrolusite.

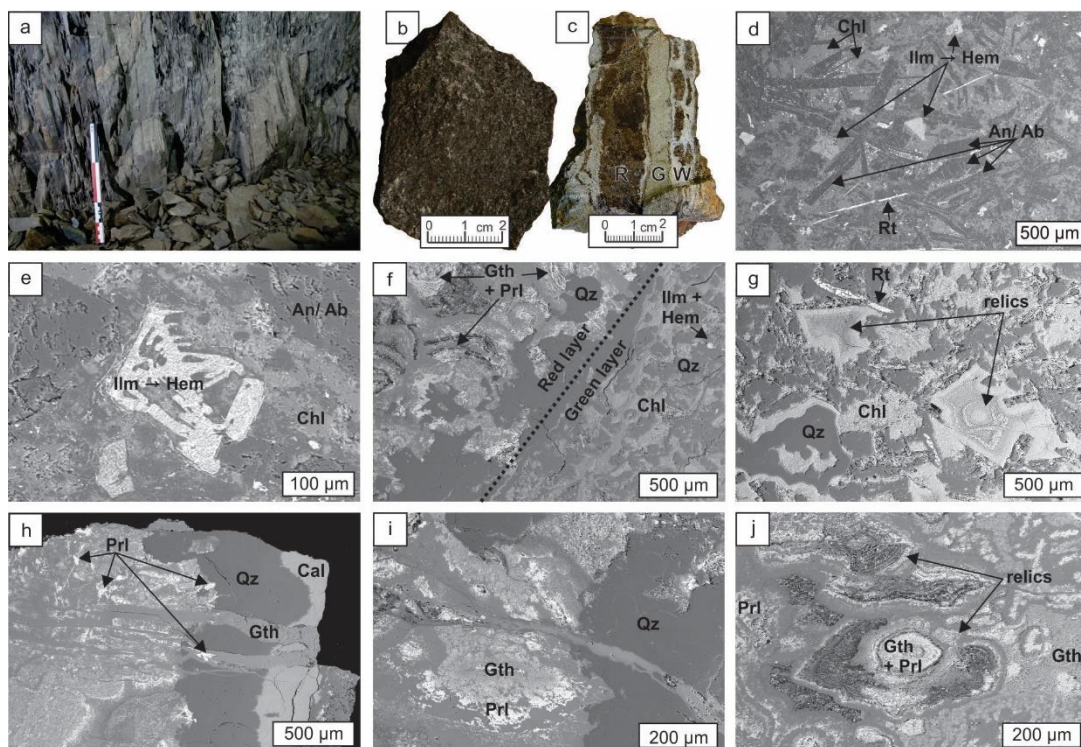


**Figure 5.2.3.** Host rocks (d – j: SEM (Scanning Electron Microscope) photomicrographs, in backscattered electrons mode). (a) Paleozoic schistoseous host rock (the scale is 30 cm long); (b) Permian-Triassic poorly weathered basalt; (c) most altered/weathered basalt composed of three different layers: red (R), green (G) and white (W); (d) poorly weathered basalt, with albite (Ab) and anorthite (An) laths, rutile (Rt), chlorite (Chl), and ilmenite (Ilm) weathered in hematite (Hem); (e) skeletal ilmenite (Ilm) presenting exsolution lamellae of hematite (Hem), in the poorly weathered basalt; (f) transition between the red and the green altered/weathered layers of the basalt, with goethite (Gth), pyrolusite (Prl), chlorite (Chl), quartz (Qz) and ilmenite-hematite (Ilm + Hem); (g) quartz (Qz), chlorite (Chl), rutile (Rt) laths, and relics of primary minerals in the green part of most altered/weathered basalt; (h) border between red and white parts of the most altered/weathered basalt, with quartz (Qz), calcite (Cal), goethite (Gth), and pyrolusite (Prl); (i) transition between the red and the white layers of the most altered/weathered basalt, with quartz (Qz), goethite (Gth), pyrolusite (Prl); (j) goethite (Gth) and pyrolusite (Prl) forming concentric structures in relation to relics of primary minerals, in the red part of most altered/weathered basalt.

## Fe-Mn mineralization

The main minerals are goethite, hematite and pyrolusite; they are either powdery and poorly crystalline, pseudomorphosing a preexistent rhombohedral mineral (Fig. 5.2.4b), and/or forming collomorph structures (Fig. 5.2.4j). Powdery iron oxihydroxides are yellow, red, or even (dark) brown. At Jbel Rhals, rhombohedral goethite sometimes shows a yellow iridescence that is due to a fine layer of iron oxihydroxides coating the surfaces of crystals (Fig. 5.2.4a). Late sulfates such as jarosite ( $\text{KFe}_3(\text{SO}_4)_2(\text{OH})_6$ ), melanterite ( $\text{FeSO}_4 \cdot 7\text{H}_2\text{O}$ ) and ferricopiapite ( $\text{Fe}_5(\text{SO}_4)_6\text{O}(\text{OH}) \cdot 20\text{H}_2\text{O}$ ) developed as coatings on the walls and roof of certain galleries (Fig. 5.2.4l).

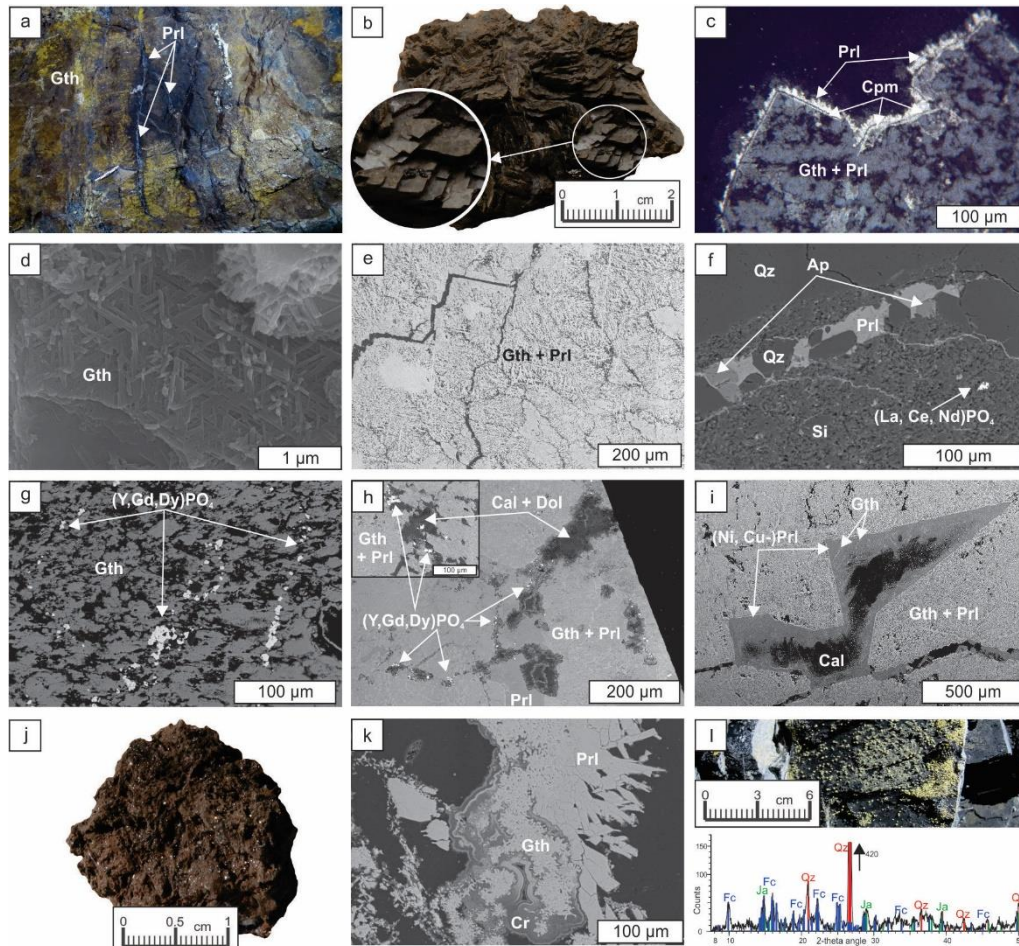


**Figure 5.2.4.** Fe-Mn mineralization (c: reflected light photomicrograph; d – l, k: SEM photomicrographs, in backscattered electrons mode). (a) Pyrolusite (Prl) veins in iridescent goethite (Gth); (b) rhombohedral goethite; (c) acicular pyrolusite (Prl) and cryptomelane (Cpm) at the surface of goethite (Gth) intermixed with pyrolusite (Prl); (d) goethite (Gth) crystallites highlighting the pseudomorphose of siderite along cleavages; (e) cleavages of primary minerals preserved in the intermixed goethite (Gth) and pyrolusite (Prl); (f) apatite (Ap) and quartz (Qz) in a pyrolusite (Prl) vein cutting quartz (Qz) and unidentified silicates (Si), where a (La, Ce, Nd) phosphate is observed; (g) accumulation of (Y, Gd, Dy)PO<sub>4</sub> in goethite (Gth); (h) (Y, Gd, Dy)PO<sub>4</sub> on the edges of calcite (Cal) and dolomite (Dol) crystals, close to pyrolusite (Prl), in the intermixed goethite (Gth) and pyrolusite (Prl); (i) calcite (Cal) observed as triangle-shaped sections of rhombohedrons, undergoing weathering and replacement by Ni- and Cu-rich pyrolusite ((Ni, Cu-)Prl) and goethite (Gth), in the intermixed goethite (Gth) and pyrolusite (Prl); (j) goethite with collomorph structures; (k) pyrolusite (Prl), goethite (Gth), and cryptomelane (Cr) growing in a cavity and forming collomorph structures; (l) yellowish jarosite (Ja) and ferricopiapite (Fc) (with X-Ray diffraction pattern) coating the Paleozoic schisteous host rock.

Goethite often shows an unusual habitus denoting the pseudomorphose of a precursor mineral, characterized by rhombohedral dark brown to black crystals (Fig. 5.2.4b – 5.2.4e), with relatively well-preserved cleavages and fractures often punctuated by Mn oxides. Pyrolusite is often intermixed with goethite (Fig. 5.2.4c – 5.2.4e), but is also growing as laths on goethite crystals (Fig. 5.2.4c), and is observed in veins getting through goethite. Other Mn oxihydroxides are noticed, but their identification is difficult due to their common intermixing and small dimensions; we nevertheless suspect the presence of lithiophorite and cryptomelane commonly observed in weathering deposits in Morocco (Dekoninck et al. 2016a) (Figure 5.2.4c, 5.2.4k). Quartz is present as large euhedral zones and sometimes as late euhedral crystals growing on goethite and coated by pyrolusite laths. Euhedral apatite is occasionally found in pyrolusite veins (Fig. 5.2.4f). In the intermixed goethite-pyrolusite, calcite is progressively replaced by Ni- and Cu-rich pyrolusite and goethite, from the outer rim and through cleavages (Fig. 5.2.4i). Some samples also host collomorph structures involving Fe and Mn (hydr-)oxides (Fig. 5.2.4j). In most cases, botryoidal goethite grows toward the center of cavities, which are subsequently filled with several generations of pyrolusite laths, goethite needles, and supposed cryptomelane and lithiophorite (Fig. 5.2.4k). (Y, Gd, Dy) phosphates are evidenced in the powdery, rhombohedral, and collomorph samples, edging some quartz veins, forming “veins” in goethite (Fig. 5.2.4g) and aggregates close to calcite, dolomite, and pyrolusite (Fig. 5.2.4h). Very small scarce grains of pyrite and galena have been observed in goethite.

### **Cu mineralization**

The schisteous basement (Fig. 5.2.5a, 5.2.5b), the Fe-rich ore (Fig. 5.2.5d – 5.2.5f) and the Triassic conglomerates (Fig. 5.2.5g – 5.2.5i) are cut by numerous Cu-mineralized veins. Within schists, veins are mainly filled with goethite, but malachite and a hydrated Cu-silicate (probably chrysocolla, yet formal identification of this mineral was not possible due to its relative scarcity) are also observed (Fig. 5.2.5b, 5.2.5c). The veins cutting through goethite and pyrolusite contain calcite, acicular malachite growing from the center to the edges of veins (Fig 5.2.5f), and sometimes Cu- (and Ni-) silicates (Fig. 5.2.5e). Malachite, growing from the edges to the center of veins (Fig. 5.2.5h), is the main mineral within veins intersecting conglomerates, but cuprite, tenorite, a hydrated Cu-silicate (probably chrysocolla) (Fig. 5.2.5i), and pyrite relics are noticed at their center.



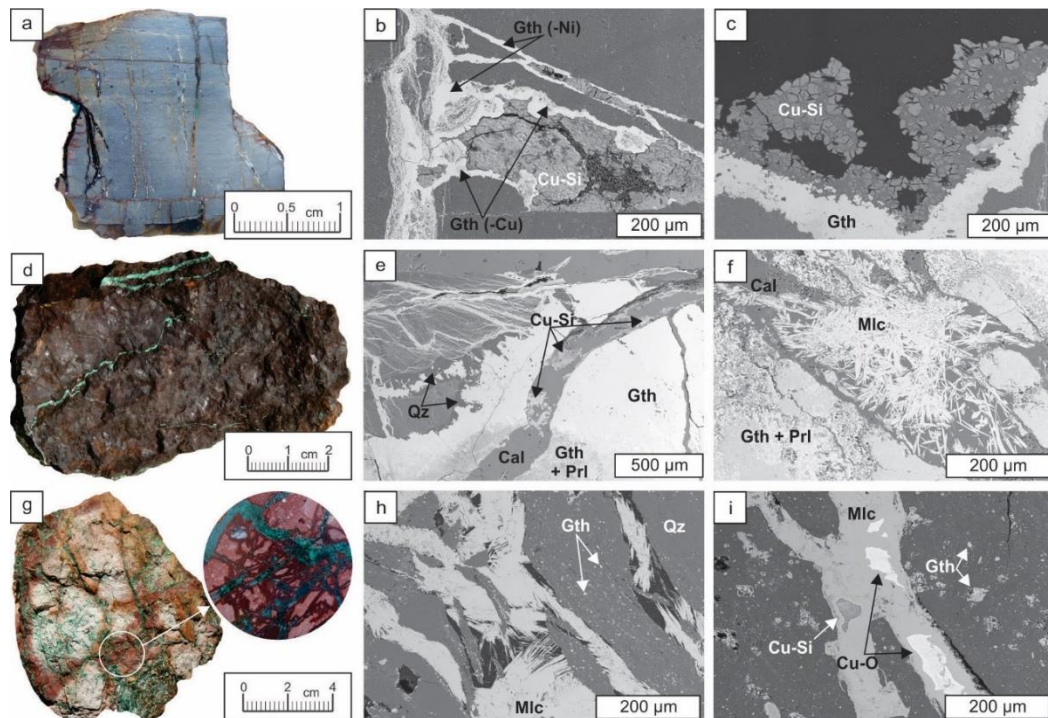


**Figure 5.2.5.** Cu mineralization (b, c, e, f, h, i: SEM photomicrographs, in backscattered electrons mode). (a) Cu-veins in Paleozoic schist (polished section); (b) hydrated Cu-silicate (Cu-Si) in Ni- or Cu-rich goethite vein (Gth (-Ni) and Gth (-Cu)); (c) hydrated Cu-silicate (Cu-Si) covering goethite (Gth); (d) Cu-mineralized veins in goethite (and pyrolusite); (e) Cu-silicates of various compositions (Cu-Si) in a calcite (Cal) vein cutting quartz (Qz) and the intermixed goethite (Gth) and pyrolusite (PrI); (f) acicular malachite (Mlc) in calcite (Cal) vein cutting goethite (Gth) and pyrolusite (PrI); (g) Cu-mineralized veins in iron-rich Triassic conglomerate; (h) acicular malachite (Mlc) vein cutting through iron-rich conglomerate composed of quartz (Qz) and goethite (Gth); (i) hydrated Cu-silicate (Cu-Si) and Cu-oxides (Cu-O) in malachite (Mlc) veins cutting goethite (Gth)-rich conglomerate.

### 5.2.3.b Geochemical characterization

Contents of major, minor or trace, and rare earth elements (REE) of host rocks and mineralization are presented in Table 5.2.1.

#### Major elements patterns

Host rocks and mineralization have similar major element contents (Fig. 5.2.6a), but  $\text{Fe}_2\text{O}_3$  and  $\text{MnO}$  are obviously subject to strong variations. In comparison to the fresh host rock, the altered/weathered schist is slightly depleted in all major elements. Major elements contents of the green part of the altered/weathered basalt are very close to those of the poorly weathered sample, unlike the red part, which is depleted in  $\text{SiO}_2$ ,  $\text{TiO}_2$ ,  $\text{Al}_2\text{O}_3$ ,  $\text{Na}_2\text{O}$ , and enriched in  $\text{Fe}_2\text{O}_3$ ,  $\text{MnO}$ ,  $\text{CaO}$ . The fresh host rock, the poorly weathered basalt, and the green altered/weathered basalt are quite rich in their  $\text{FeO}$  content, which is not the case for the red altered/weathered basalt.

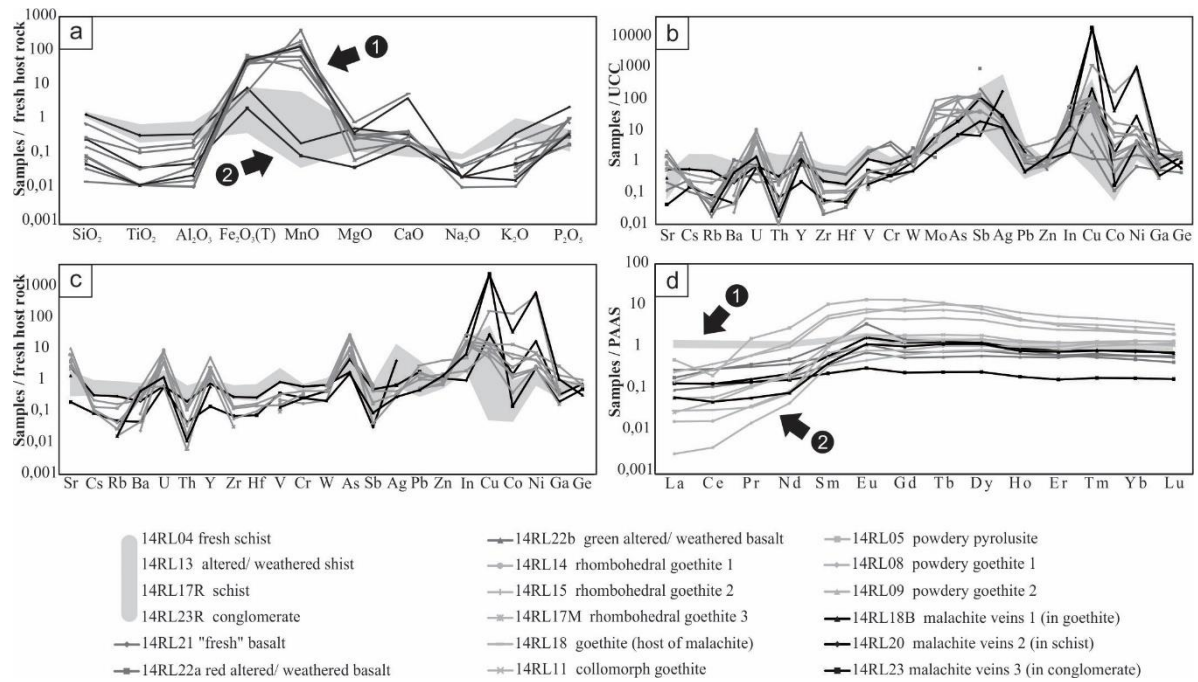


**Figure 5.2.6. Geochemical data:** (a) major elements patterns, with values normalized to the host rock (fresh schist). A distinct divergence is observed between the copper veins in schists and conglomerates (group 2), and the others (group 1); (b) trace elements patterns, with values normalized to the UCC (Upper Continental Crust) [18]; (c) trace elements patterns, with values normalized to the host rock (fresh schist); (d) REE patterns, with values normalized to the PAAS [18]. A distinction is observed between the host rocks (no REE fractionation; group 1), and the mineralized samples (REE fractionation; group 2). The shaded areas indicate the major elements (a), minor elements (b,c), and REE (d) contents of the host rocks (schists and conglomerate).

### Minor and trace elements patterns

Many values are below the detection limit (e.g., Ta, Nb, Tl, Bi). Host rocks and basalts have higher amounts of Zr and Th than mineralized samples, but are depleted in U, Y, Mo, As, In, Cu, Co., and Ni. The fresh schist, the altered/weathered schist, and gangue minerals of the Fe-Mn mineralization display the highest contents in Rb (respectively 179, 117, and 162 ppm), Nb (respectively 17.3, 7.5, and 9.3 ppm), and Zr (respectively 152, 84, and 101 ppm). Goethite hosting malachite veins is very rich in Cu, Co and Ni (respectively 2.92%, 0.268%, 3.48%), but in this particular case, the enrichment is considered as contamination from the hosted veins during sampling (Fig. 5.2.5d). Most samples are enriched in U and depleted in Th, when contents are normalized to those of the UCC (Fig. 5.2.6b); the more they are rich in U, the less they are in Th. The greenish altered/weathered basalt profile is very similar to that of the poorly weathered basalt, while the red part is more comparable to the mineralized samples. Both altered/weathered basalts are depleted in Co, in comparison to the poorly weathered basalt, but enriched in Cu and Ni. Mineralized samples are enriched in chalcophile elements, but contents in Co and Ni are somewhat variable. All mineralized samples (beside 14RL23), and particularly powdery oxihydroxides, are enriched in Y, as well as goethite 14RL18 reaching 179 ppm. Fe-Mn mineralization have similar profiles punctuated by enrichments in U, Y, Mo, As, Sb, Ag, In, Cu, Co, Ni, Ga, and depletions in Rb, Ba, Th, Zr, Hf, V, Cr. Cu-mineralized veins have very similar patterns regarding minor elements, but divergent values for Co and Ni. As the fresh host rock only differs from the UCC at the level of Sr, As, Sb, Ag, and Cu, almost no difference is observed between normalization to the schist (Fig. 5.2.6c) and to the UCC (Fig. 5.2.6b).

## Rare Earth Elements patterns

Normalization of REE contents of all samples to PAAS (Fig. 5.2.6d) highlights some significant trends. Host rocks, and more particularly fresh schist, have logically similar flat profiles close to that of the PAAS. All mineralized samples are characterized by a fractionation, with a depletion in LREE ( $\text{La/Lu}$  between 0.19 and 111.41), but there are significant individual differences between Fe-Mn powdery samples (average  $\text{La/Lu} = 10.78$ ), pseudomorphosing (average  $\text{La/Lu} = 1.57$ ) and collomorph Fe-Mn samples (average  $\text{La/Lu} = 2.13$ ), and Cu veins (average  $\text{La/Lu} = 93.50$ ). Poorly crystalline powdery samples present the highest contents in REE (average  $\Sigma\text{REE} = 264.82$  ppm; five to ten times higher than other samples) and are quite rich in Nd, Gd, Dy, and Sm. Powdery pyrolusite displays a negative Ce anomaly ( $\text{Ce/Ce}^* = 0.23$ ). Both poorly weathered and altered/weathered basalts have similar profiles. In comparison to the poorly weathered basalt, the goethite-rich red altered/weathered sample is enriched in MREE and presents a positive Eu anomaly ( $\text{Eu/Eu}^* = 2.75$ ), while the clayey green altered/weathered basalt is depleted in all REE and particularly in LREE. An interesting similarity is noticed between basalts and mineralized samples, particularly the malachite veins: they all show REE fractionation with a slight LREE depletion (respectively, for basalts and the Cu mineralization: average  $\text{La/Lu} = 31.15$  and  $31.17$ ;  $\Sigma\text{REE} = 58.16$  and  $34.66$ ), unlike host rocks (average  $\text{La/Lu} = 105.91$  and  $\Sigma\text{REE} = 211.41$ ). Malachite veins display a very slight positive anomaly in Eu ( $\text{Eu/Eu}^* = 1.84, 1.95$  and  $1.30$ ) similar to basalts, which is not the case of other samples. A division may be observed between malachite veins: those getting through conglomerate are strongly depleted in REE and do not present any fractionation, counter to those cutting goethite and schist showing a slighter depletion.

**Table 5.2.1.** Results of geochemical analyses for selected samples of host rocks and mineralized samples (W/A = weathered and/or altered). Major elements concentrations are listed in %, minor elements and Rare Earth Elements (REE) are given in ppm. For minor elements, values in bold and marked with an asterisk (\*) correspond to contents in %: the detection limit is fixed at 0.01% for Ni and Cu, and 0.001% for Co and Mo. The Eu and Ce anomalies (Eu/Eu\* and Ce/Ce\*) are calculated with PAAS (Post Archean Australian Shale)-normalized values (Taylor and McLennan 1985).

Oxides/Elements	Detection Limit	Host Rocks				Basalts			Fe-Mn Mineralization								Cu-Mineralization		
		14RL04 (Fresh Schist)	14RL13 (W/A Schist)	14RL17R (Host Schist of Goethite)	14RL23R (Conglomerate Host of Malachite)	14RL21 (Fresh Basalt)	14RL22A (Red W/A Basalt)	14RL22B (Green W/A Basalt)	14RL05 (Powdery Pyrolusite)	14RL08 (Powdery Goethite)	14RL09 (Powdery Goethite)	14RL11 (Colloform Goethite)	14RL14 (Rhomboidal Goethite)	14RL15 (Rhomboidal Goethite)	14RL17M (Rhomboidal Goethite)	14RL18 (Goethite Host of Malachite)	14RL18B (Malachite in Goethite)	14RL20 (Malachite in Schist)	14RL23 (Malachite in Conglomerate)
Al <sub>2</sub> O <sub>3</sub> (%)	0.01	18.84	8.79	15.23	5.00	13.14	0.70	11.86	2.77	3.31	1.32	4.31	0.19	0.30	0.75	0.20	0.41	6.63	0.92
CaO (%)	0.01	0.87	0.07	0.19	0.20	5.57	26.45	2.54	0.19	0.17	0.38	0.26	0.36	0.38	0.16	4.72	3.44	0.30	0.15
Fe <sub>2</sub> O <sub>3</sub> (%)	0.01	1.06	0.43	9.08	1.68	4.80	15.76	2.99	6.63	39.15	49.13	44.81	69.85	62.97	75.38	41.79	54.59	8.62	2.16
K <sub>2</sub> O (%)	0.01	3.81	2.45	3.82	1.14	0.22	0.05	0.05	0.56	0.68	0.26	0.15	0.04	<0.01	0.08	0.11	0.06	1.44	0.18
MgO (%)	0.01	2.11	0.34	1.22	0.25	5.73	5.37	4.68	0.25	0.71	0.66	0.13	0.54	0.69	0.60	1.67	0.80	1.11	0.08
MnO (%)	0.001	0.156	0.028	0.935	0.006	0.921	4.441	0.279	60.940	7.391	21.220	29.150	10.33	16.150	4.502	23.020	19.840	0.030	0.013
Na <sub>2</sub> O (%)	0.01	1.01	0.07	0.09	0.07	2.98	0.05	0.74	0.04	0.04	<0.01	<0.01	0.01	<0.01	<0.01	0.02	0.02	0.02	0.02
P <sub>2</sub> O <sub>5</sub> (%)	0.01	0.17	0.02	0.08	0.03	0.14	<0.01	0.19	0.05	0.13	0.06	0.03	0.17	0.05	0.07	0.18	0.06	0.38	0.03
SiO <sub>2</sub> (%)	0.01	58.13	85.67	65.44	88.22	44.42	16.73	54.21	16.28	39.58	8.86	3.45	4.44	2.02	4.78	0.84	2.77	77.56	14.93
TiO <sub>2</sub> (%)	0.01	0.88	0.53	0.59	0.18	1.07	0.03	0.95	0.09	0.11	0.03	< 0.01	0.01	0.01	0.01	0.01	0.01	0.29	0.03
LOI (%)		4.67	1.59	4.29	2.03	9.79	28.72	6.88	10.45	8.17	12.27	11.66	12.41	12.91	11.36	15.90	11.94	3.14	25.09
Total (%)	0.01	91.70	99.99	100.96	98.81	88.78	98.30	85.37	98.25	99.44	94.19	93.95	98.35	95.48	97.69	88.44	93.94	99.52	43.61
FeO (%)	0.1	6.0	0.1	1.7	<0.1	8.7	<0.1	12.4	<0.1	<0.1	<0.1	<0.1	<0.1	<0.1	<0.1	<0.1	<0.1	2.6	<0.1
V (ppm)	5	142	195	140	333	237	51	197	23	51	48	14	34	18	28	16	20	125	55
Cr (ppm)	20	110	60	80	50	280	30	360	40	50	<20	<20	20	<20	<20	<20	30	70	30
Co (ppm/%)	1	20	1	19	1	19	2	7	53	138	102	277	8	24	30	0.268 *	702	31	3
Ni (ppm/%)	20	70	<20	120	50	70	30	200	490	310	310	530	200	160	170	3.48 *	4.54 *	1230	170
Cu (ppm/%)	10	180	10	150	9480	30	50	190	1600	1860	2790	2530	950	2480	1200	2.92 *	43.9 *	5160	44.5 *
Zn (ppm)	30	70	<30	40	<30	50	<30	40	110	70	70	70	50	80	60	300	100	80	<30
Ga (ppm)	1	29	17	24	8	20	9	20	82	42	12	14	30	10	5	12	32	10	6
Ge (ppm)	1	3	3	3	2	3	1	3	2	3	<1	<1	2	<1	<1	<1	1	2	2
As (ppm)	5	6	<5	9	21	<5	<5	<5	36	138	180	37	168	66	54	124	10	11	28
Rb (ppm)	2	179	117	162	57	7	4	2	23	31	8	5	<2	<2	3	5	3	55	9
Sr (ppm)	2	74	24	138	57	74	537	43	283	220	776	496	205	339	176	476	105	196	15
Y (ppm)	1/0.5	33	27	35	26	19	24	16	69	179	90	38	61	32	48	88	21	26	5
Zr (ppm)	5	152	84	101	40	94	4	100	19	22	9	<5	<5	<5	5	<5	<5	45	11
Nb (ppm)	1	17	8	9	3	9	5	7	<1	2	<1	<1	<1	<1	<1	<1	<1	3	1
Mo (ppm/%)	2	<2	11	3	7	<2	2	<2	10	64	0.013 *	48	74	64	32	6	3	<2	10
Ag (ppm)	0.5	2.0	3.9	1.3	27.6	1.5	<0.5	1.1	<0.5	<0.5	0.9	0.7	<0.5	<0.5	<0.5	0.6	0.6	8.4	1.4
In (ppm)	0.1	0.1	<0.1	0.2	1.9	0.1	0.8	<0.1	0.2	1.5	3.0	1.8	1.4	1.7	1.5	0.5	0.7	0.1	2.6
Sb (ppm)	0.2	40.7	30.7	2.3	2.7	17.3	179.0	41.4	26.2	28.2	18.5	8.0	22.7	7.2	7.4	1.7	3.8	1.3	21.1
Cs (ppm)	0.5	7.8	3.1	7.6	3.7	0.5	0.9	1.2	1.1	1.8	0.9	<0.5	<0.5	<0.5	<0.5	0.8	<0.5	2.6	0.7
Ba (ppm)	1	527	353	437	151	353	615	142	297	123	148	146	45	13	25	302	243	114	25
Hf (ppm)	0.2	3.9	2.1	2.8	0.9	2.2	0.2	2.3	0.6	0.7	0.4	<0.2	<0.2	<0.2	<0.2	<0.2	<0.2	1.1	0.3
Ta (ppm)	0.1	1.4	1.0	1.1	0.6	0.6	0.2	0.5	<0.1	<0.1	0.3	0.3	<0.1	0.3	0.3	0.3	<0.1	0.6	0.1
W (ppm)	1	4	5	4	4	1	5	2	<1	2	3	2	1	2	3	2	1	3	2



Ti (ppm)	0.1	0.9	0.6	0.7	0.5	0.1	<0.1	<0.1	<0.1	0.8	0.9	1.6	<0.1	0.1	<0.1	0.5	0.7	0.3	<0.1
Pb (ppm)	5	16	65	5	28	15	21	46	19	29	17	26	9	9	8	48	8	<5	30
Bi (ppm)	0.1	0.1	11.8	<0.1	2.1	<0.1	<0.1	<0.1	<0.1	1.0	0.1	<0.1	<0.1	<0.1	<0.1	<0.1	<0.1	<0.1	1.1
Th (ppm)	0.1	16.8	8.8	11.0	3.6	2.4	0.1	2.7	1.9	2.4	0.6	<0.1	<0.1	<0.1	0.3	0.1	0.2	3.6	0.8
U (ppm)	0.1	3.1	6.4	2.3	5.3	0.6	2.1	1.1	27.0	11.8	17.2	11.2	29.3	24.8	11.8	2.0	4.0	2.1	1.9
La (ppm)	0.1	54.7	37.2	41.1	35.8	10.6	6.9	3.5	18.5	9.3	5.5	1.0	0.6	0.1	2.2	1.1	2.3	4.9	5.0
Ce (ppm)	0.1	111.0	77.6	103.0	73.1	23.3	22.4	8.9	16.2	30.7	22.4	3.7	1.3	0.3	4.8	2.4	3.8	10.2	10.3
Pr (ppm)	0.01	12.10	9.37	10.00	8.17	2.95	3.35	1.25	14.10	5.46	5.56	0.94	0.33	0.13	1.04	0.31	0.52	1.48	1.26
Nd (ppm)	0.1	42.3	38.0	39.2	31.7	12.3	15.9	5.8	91.4	31.0	39.3	7.3	2.7	1.4	5.9	2.4	2.5	7.14	5.14
Sm (ppm)	0.1	8.2	8.4	9.1	6.8	3.3	6.4	2.1	59.4	26.5	31.5	6.0	3.0	1.9	4.0	5.5	2.2	3.3	1.3
Eu (ppm)	0.05	1.75	1.77	2.21	1.68	1.26	3.93	0.80	15.10	7.41	8.92	2.05	0.89	0.52	1.18	5.29	1.28	1.85	0.34
Gd (ppm)	0.1	6.6	5.5	8.2	5.0	3.5	7.0	2.6	63.4	41.0	34.8	8.9	3.9	3.0	6.3	21.7	4.8	6.0	1.1
Tb (ppm)	0.1	1.0	0.9	1.3	0.8	0.6	1.0	0.4	8.8	8.1	6.0	1.5	0.8	0.6	1.1	3.8	0.9	1.0	0.2
Dy (ppm)	0.1	6.0	5.1	6.8	4.7	3.6	4.9	2.7	36.4	42.0	29.3	8.3	4.6	3.7	6.7	19.5	5.2	5.6	1.1
Ho (ppm)	0.1	1.1	0.9	1.2	0.8	0.7	0.8	0.6	4.7	6.7	4.4	1.4	1.0	0.8	1.3	3.1	0.8	0.9	0.2
Er (ppm)	0.1	3.3	2.6	3.4	2.2	1.8	1.8	1.6	9.7	15.6	10.5	3.7	2.9	2.3	3.6	7.5	2.2	2.4	0.5
Tm (ppm)	0.05	0.48	0.39	0.46	0.33	0.28	0.23	0.26	1.13	1.98	1.40	0.51	0.50	0.43	0.55	1.02	0.33	0.34	0.07
Yb (ppm)	0.1	3.2	2.6	2.9	2.1	1.7	1.4	1.7	6.6	11.8	8.4	3.3	3.8	3.2	3.9	6.2	2.3	2.1	0.5
Lu (ppm)	0.01	0.49	0.38	0.43	0.30	0.26	0.18	0.24	0.87	1.47	1.16	0.47	0.59	0.52	0.58	0.85	0.30	0.31	0.07
La/Lu		111.4	99.2	95.1	118.2	41.4	37.6	14.4	21.3	6.3	4.7	2.1	1.0	0.2	3.8	1.3	7.7	15.8	70.0
ΣREE (ppm)		255.2	193.2	232.5	176.2	67.5	80.0	33.1	360.2	246.1	217.5	51.0	27.7	19.4	44.3	85.5	30.6	49.3	27.5
Eu/Eu *		1.12	1.21	1.19	1.34	1.74	2.75	1.62	1.15	1.05	1.26	1.31	1.21	1.02	1.10	2.26	1.84	1.95	1.30
Ce/Ce *		0.99	0.96	1.17	0.98	0.96	1.07	0.98	0.23	0.99	0.93	0.88	0.67	0.60	0.73	0.94	0.80	0.87	0.94

### **5.2.4 Discussion**

As already stressed by many authors, the understanding of supergene deposits formation and the identification of the hypogene ores are complicated by the overprinting of weathering processes over primary ores, and by the lack of data on supergene (and sometimes hydrothermal) fluid chemistry leading to difficulties in quantifying pH, Eh, and geochemical signatures of these fluids. However, as emphasized by (Ramdohr 1980), textural relations and structures of newly formed mineralization allow reasonably accurate deductions about the nature of original minerals and the character of the fresh/unweathered deposits.

At Jbel Rhals, a sequence of mineralization is highlighted by successive intersects of supergene mineralized veins: pyrolusite veins cut through goethite, unidentified silicates and quartz veins go through goethite and pyrolusite, and fine calcite and malachite veins pass through goethite, pyrolusite and silicates. Goethite is the first supergene minerals to precipitate; pyrolusite (probably followed by lithiophorite and cryptomelane) forms later, under more oxidizing conditions (Fig. 5.2.7). The Fe-Mn oxihydroxides forming rhombohedral minerals seem to replace a primary mineral, thought to be a carbonate (probably siderite—see below). Their precipitation is followed by the filling of cavities and fractures with minerals forming collomorph structures, and finally by poorly crystalline powdery minerals. Malachite, calcite, and probably chrysocolla precipitate later, in thinner veins that cross through Fe-Mn ores. Sulfates observed on some walls formed recently, and most probably are related to ongoing mining activities.

#### **5.2.4.a Hydrothermal alteration and/or weathering of basaltic rocks**

The Jbel Rhals host rocks, especially basalts, show evidence of extensive alteration and/or weathering, as attested by the various secondary products, the few preserved primary minerals (Fig. 5.2.3d – 5.2.3g), and the mineralogical and chemical variation of the layered most altered/weathered basalt (Fig. 5.2.3c). Some secondary minerals may result from low-temperature hydrothermal alteration (e.g., chlorite, albite and clays), while others from weathering processes (e.g., goethite and pyrolusite), but mixing of these mineral phases get the determination even more complicated in terms of origin, and the understanding of their formation processes more complex.

Weathering of basalts usually follows the next sequence: glass–plagioclases–ferromagnesian minerals—Fe and Ti oxides (Macaire and Perruchot 1988; Dekayir and El-Maataoui 2001). When the glass proportion is significant, that component being particularly susceptible to weathering, the weathering sequence is modified as follows: glass–ferromagnesian minerals–plagioclases–Fe and Ti oxides (Ludden and Thompson 1979; Karrat et al. 1998). Plagioclases and Fe-Ti oxides are the only primary minerals remaining in Jbel Rhals basalts (Fig. 5.2.3d), which suggests that weathering followed the second sequence described above. Preservation of Fe-Ti oxides during weathering is quite common, as observed by (Nesbitt and Wilson 1992; Dekayir and El-Maataoui 2001). The relatively close TiO<sub>2</sub> contents of the greenish layer and the parent basalt endorse that Ti-oxides tend to be immobile during weathering of Jbel Rhals ore and that they were moderately dissolved and transported (Nesbitt and Wilson 1992; Sanematsu et al. 2011; Maulana et al. 2014). Exsolution lamellae of hematite (and pyrophanite) in ilmenite are primary, and the skeletal shape of crystals reflects their fast growth under supercooling (Fig. 5.2.3e).

The layered structure of the altered/weathered basalt (Fig. 5.2.3c) and the mineralogical and geochemical segregation in the three layers (Fig. 5.2.3f) suggest a sequential weathering of primary minerals and reflect various environments of precipitation. The red layer, rich in  $\text{Fe}^{3+}$ , Mn, Ca, and mobile elements such as U (Fig. 5.2.6, Table 5.2.1), is mostly composed of goethite and pyrolusite (Fig. 5.2.3h – 5.2.3j) that may result from alteration/weathering of ferromagnesian minerals such as pyroxenes and olivines (Kamel et al. 1996; Dekayir and El-Maataoui 2001; Daoudi and Pot de Vin 2002). The greenish layer, composed of quartz, calcite, chlorite, clays (Fig. 5.2.3g) and rich in Si and Al (Table 5.2.1), is thought to concentrate alteration/weathering products of the dissolution of feldspars (Kamel et al. 1996; Dekayir and El-Maataoui 2001; Daoudi and Pot de Vin 2002), and (relics of) primary minerals, resulting in a relative enrichment in immobile elements (e.g., Th, Zr, Ti). Chlorite and clays are typical features of the hydrothermal alteration of basalts, and are here frequently observed as pseudomorphs after primary minerals, as stressed by (Kamel et al. 1996; Torres-Alvarado et al. 2007). Albite is thought to be formed from the low-temperature hydrothermal alteration of anorthite. The conservation of original minerals fabrics and the filling of spaces created by dissolution with associated clays and Fe oxihydroxides (Fig. 5.2.3h, 5.2.3j) imply that the alteration/weathering took place under isovolumetric conditions (Hamidi et al. 1997; Morey and Setterholm 1997). The various undetermined and mixed silicates observed in veins cutting through schist and Fe-Mn mineralization are also thought to be the result of the alteration/weathering of basalts and from the percolation of derived fluids (Torres-Alvarado et al. 2007). The white layer is made of quartz (Fig. 5.2.3h, 5.2.3i) that precipitated later than minerals of the two other layers, from Si-rich fluids circulating through voids fractures, probably under acidic conditions.

The geochemical features (REEs, major and minor elements) of the greenish layer are very close to those of the parent basalt, which is not the case of the red part (Fig. 5.2.6). The latter is much closer in composition to the Fe-Mn mineralization. This variance reflects the successive steps of weathering of the primary minerals, the subsequent partition of elements, and their precipitation into specific mineral phases, under particular conditions. Respectively, the very low and slightly high FeO contents of the red and greenish layers also indicate that minerals of the red part formed under oxidizing conditions, while reducing conditions prevailed during precipitation in the greenish layer. The (slight) positive Eu anomalies of basalts, and especially of the red altered/weathered layer, are related to the decoupling of Eu from other REE, because of its presence as trivalent (under surface conditions) or divalent (in reduced environments and at elevated temperatures and pressures) cations (Sverjensky 1984; Lewis et al. 1997). The positive anomaly of the poorly weathered basalt is related to the incorporation of Eu in plagioclase during magmatic processes (Alderton et al. 1980). As plagioclase is absent from most altered/weathered layers, Eu is supposed to be incorporated in a secondary phase, hydrothermal or supergene, by adsorption on clay minerals and/or co-precipitation with Fe oxihydroxides (Lewis et al. 1997; Dawood et al. 2004; Leybourne et al. 2006). According to (Sverjensky 1984; Michard 1989; Leybourne et al. 2006; Torres-Alvarado et al. 2007), positive Eu anomalies related to the predominance of  $\text{Eu}^{2+}$  in hydrothermal fluids are indeed typically found in associated ore deposits.

### **5.2.4.b Fe-Mn mineralization**

The unusual rhombohedral crystals of Jbel Rhals goethite denote the pseudomorphosis of a former mineral. This hypogene mineral is thought to be siderite, although this mineral has not been observed at Jbel Rhals, probably owing to the high degree of weathering and the extreme instability of this mineral under oxidizing conditions (Fig. 5.2.7a) (Kholodov and Butuzova 2008). Pseudomorphosis of goethite and pyrolusite after siderite is common in supergene environments (Ramdohr 1980; Kholodov

and Butuzova 2008) and has been documented in many places, e.g., at Akjouit (Mauritania; Ramdohr 1980), Lake George (USA; Skala and Hollabaugh 2012), Errachidia (Morocco; Makkoudi 1995), Ljubija (Bosnia; Garasic and Jurkovic 2012), Schwarzwald (Germany; Markl et al. 2006), and Granada (Spain; Torres Ruiz 1983). Besides the rhombohedral characteristic of the pseudomorphs, other diagnostic indications of the initial presence of siderite at Jbel Rhals are cleavages, the Mn content, and the dark-brown color. Relatively well-preserved 120°-orientated cleavages and fractures of the primary carbonate are forming a “box-work pattern” (Fig. 5.2.4d) and are punctuated with goethite and pyrolusite, as described by Skala and Hollabaugh (2012) in Colorado (USA). The intermixing of goethite and pyrolusite, the development of pyrolusite laths at the surface of goethite and quartz crystals, in cavities and veins cutting goethite, also support the hypothesis of primary siderite at Jbel Rhals. Siderite usually contains a significant amount of Mn (1–3%) that can be released during weathering and be available for later Mn oxides formation (Hamidi et al. 1997; Garasic and Jurkovic 2012). The close association of goethite and pyrolusite is thus related to the release of the Mn that crystallizes as small aggregates of pyrolusite arranged within the network of goethite (Torres Ruiz 1983). The supposed hypogene siderite is probably of hydrothermal origin: siderite typically forms in reduced environments from solutions containing little dissolved sulfur but a lot of bicarbonate ions (Kholodov and Butuzova 2008). Some small scarce sulfide grains such as chalcopyrite, pyrite, and galena, observed in the ore, are strengthening this hypothesis, as hydrothermal siderite is commonly accompanied by such sulfides as that concentrate the little dissolved sulfur present in solution (Kholodov and Butuzova 2008; Decrée et al. 2008; Palinkaš et al. 2016).

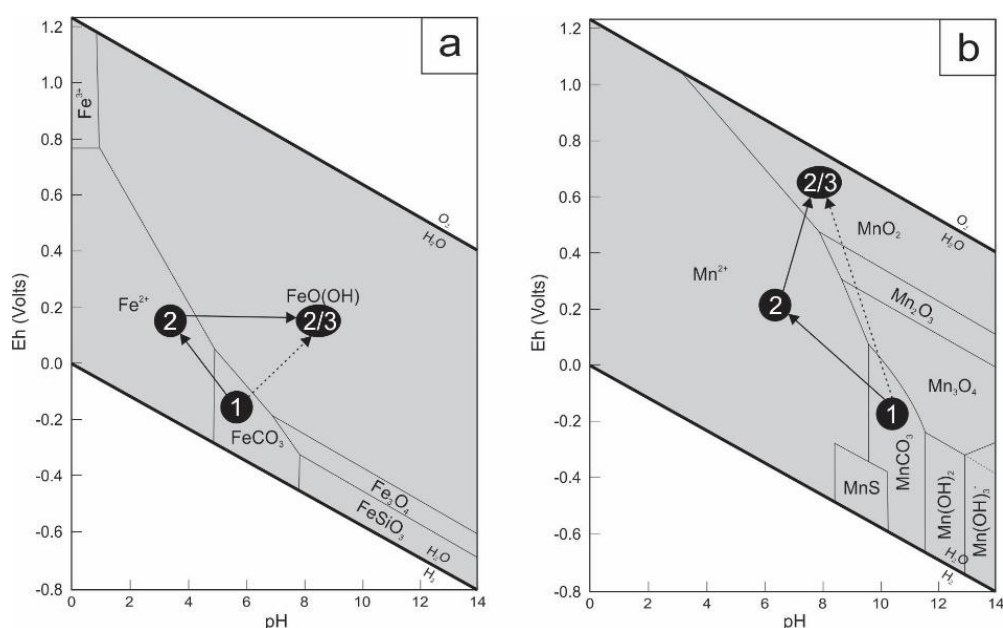


**Figure 5.2.7.** (a) Eh–pH diagram for a part of the Fe–C–Si–O–H system, showing the stability fields of selected iron minerals at 25 °C and 1 atmosphere (modified after Brookins (1988)). Siderite (1) may be directly weathered in goethite (2), or it may be leached first, leading to the presence of aqueous  $\text{Fe}^{2+}$  (2) and later to the precipitation of goethite (3); (b) Eh–pH diagram for a part of the Mn–C–S–O–H system showing the stability fields of selected manganese minerals at 25 °C and 1 atmosphere (modified after Brookins (1988)). Rhodochrosite may be directly weathered in pyrolusite (2), or is firstly leached, leading to the presence of aqueous  $\text{Mn}^{2+}$  (2) and later to the precipitation of pyrolusite (3).

Goethite is the most common and most stable Fe oxyhydroxide under atmospheric conditions (Fig. 5.2.7a), and is widely observed in gossan of ore deposits. Hematite, present in minor proportions at Jbel Rhals, is thought to have precipitated shortly before goethite but to have turned into goethite as the latter is more stable under oxidizing conditions (Fig. 5.2.7a). It is also possible, but quite unlikely,

that hematite formed during hydrothermal processes, and that small amounts have been preserved from weathering. Large euhedral quartz is supposed to have formed during hydrothermal phases. The fine quartz veins cutting mineralization and basalts, and the small crystals observed at the surface of various minerals precipitated during the last stages of weathering.

In supergene environments, manganese oxide minerals are represented by pyrolusite, cryptomelane, todorokite, nsutite, and other poorly defined phases (Post 1999; Bruyère et al. 2010; Dekoninck et al. 2016a). Pyrolusite, which is only stable under strongly oxidizing conditions and at neutral to basic pH (Fig. 5.2.7b), is the most common Mn oxide at Jbel Rhals. Two generations of pyrolusite are recognized: the first precipitated with goethite, in pseudomorphose of siderite (Figure 5.2.4b – 5.2.4e), while the second formed later, during the last stages of weathering, at the surface of goethite crystals (Fig. 5.2.4c), in cavities, and in veins cutting through goethite. Such early and late pyrolusite have already been observed in the Mn Imini district, 500 km southwestward (Dekoninck et al. 2016a). Collomorph structures filling cavities and including goethite, pyrolusite and cryptomelane (Fig. 5.2.4j, 5.2.4k) are thought to be contemporary of the second generation of pyrolusite, and to have precipitated from successive generations of supergene fluids of various compositions with increasing O<sub>2</sub> content to allow Mn(IV) in the form of pyrolusite. The small amount of these structures does not allow further conclusions about their genesis to be drawn. Later precipitation of Mn oxides, in comparison to Fe oxihydroxides, is due to the greater solubility of Mn in oxidizing fluids, and to its greater resistance to oxidation. The presence of Mn oxides (particularly pyrolusite) suggests that highly oxidizing conditions were reached, particularly in the vicinity of fissures and cavities (Koppi et al. 1996).

Enrichment in U but depletion in Th of the Fe-Mn mineralized samples, in comparison to host rocks and basalts of Jbel Rhals (Fig. 5.2.6b, 5.2.6c), is a typical supergene trend and is related to a selective U vs. Th mobilization during weathering processes. Soluble and mobile U in supergene fluids is preferentially leached and accumulated in neoformed minerals (oxyhydroxides), while immobile Th is retained in weathering-resistant minerals or incorporated in rapidly precipitating minerals (Braun et al. 1990; Pagel et al. 1990; Nicaise et al. 1996; De Putter et al. 2002). The concentration of U in Fe-Mn oxihydroxides and clays is related to the high specific surface of these minerals and the subsequent important adsorption capacity (Decrée et al. 2010a), but also to the neoformation of discrete minerals at the interface between Fe-Mn oxihydroxides and clays, and fluids (Kamineni et al. 1986; Koppi et al. 1996; Nicaise et al. 1996; De Putter et al. 2002). In the same trend, host rocks are rich in immobile Zr, Rb, Nb, while mineralized samples are rich in Y, Mo, As, Sb, In, and chalcophile elements that may be adsorbed on Fe-Mn oxihydroxides (as observed in other Fe-Mn mineralization; Decrée et al. 2013) and clays or incorporated into supergene minerals. Enrichment of As is related to the adsorption of this element by Fe oxihydroxides, in the form of arsenate or FeAsO<sub>4</sub>, in oxic environments (Farmer and Lovell 1986; Dawood et al. 2004).

The slightly negative Ce anomaly of poorly crystalline pyrolusite is the only noteworthy feature observed in Figure 5.2.6d. Ce anomaly results from oxidation of this element to Ce<sup>4+</sup> and to its subsequent decoupling from the other REE which maintain their trivalent ionic states and are leached by circulating water (Bau and Dulski 1996). Oxidation to Ce<sup>4+</sup> is restricted to strongly oxidizing environments, and is usually observed in the most weathered part of the profiles, for Fe-Mn oxihydroxides patterns (Ludden and Thompson 1979; Pracejus et al. 1990; Cotten et al. 1995). The lack of a general negative Ce anomaly at Jbel Rhals might indicate that the tetravalent Ce was incorporated in other mineral phases than pyrolusite, or that pyrolusite precipitated under unusually low pH conditions, as Ce<sup>4+</sup> is unstable below pH 4 and 5 (Brookins 1988; Leybourne et al. 2006).

The low-grade enrichment in REE and the preferential intake of HREE+Y (Fig. 5.2.6) of Fe-Mn oxyhydroxides are typical features of supergene deposits associated to igneous rocks (Nesbitt and Wilson 1992; Castor and Hendrick 2006) and have been correlated with the presence of secondary phosphates close to weathered basalts in French Polynesia (Cotten et al. 1995) and in Hawaii (Fodor et al. 1992). The highest REE + Y content of the amorphous, poorly crystalline, powdery Fe oxyhydroxides (Fig. 5.2.6) is related to (1) the trapping of (M)REE by these minerals, under acid conditions, by coprecipitation and adsorption processes (Leybourne and Johannesson 2008; Cocker 2012), (2) the sorption of REE onto the surface of clays that are common in powdery samples (Coppin et al. 2002; Ayora et al. 2015), (3) the presence of (Y, Gd, Dy) phosphates in the ore. The occurrence of multiple REE, whether La-Ce-Nd or Y-Gd-Dy (Y being usually considered with HREE to which it is chemically and physically similar), within a single mineral, is due to the similar ionic radii and trivalent oxidation state of these elements, and to the subsequent common substitution of REE for each other into crystal structures (Castor and Hendrick 2006). The origin of REE may be the dissolution of minerals observed in the parent rock (monazite, allanite, ...), or the release of trace concentrations present in primary and/or hydrothermal apatite, calcite, dolomite, feldspars, ..., (Banfield 1989; Castor and Hendrick 2006; Ayora et al. 2015). Here, MREE enrichment suggests that REEs originate from the weathering of primary phosphate minerals, and particularly of apatite (Hannigan and Sholkovitz 2001; Köhler et al. 2005). (La, Ce, Nd) phosphates are only observed in host rock (Fig. 5.2.4f) and basalts, close to primary minerals, and are therefore supposed to be primary minerals that resisted weathering (Ayora et al. 2015). The low mobility of LREE may also have caused the rapid precipitation of LREE phosphates, close to parent rocks, while more mobile HREE were more importantly leached (Lottermoser 1990; Göb et al. 2011). The proximity of (Y, Gd, Dy) phosphates with Fe-Mn ore (Fig. 5.2.4g), quartz veins, calcite, pyrolusite and cavities (Fig. 5.2.4h) suggests that these minerals are supergene, in agreement with the observations of (Banfield 1989; Lottermoser 1990; De Putter et al. 1999), suggesting that HREE phosphates are generally concentrated in fissure fillings and voids, along with minerals precipitating during the late stages of weathering.

#### 5.2.4.c Cu mineralization

The small amount of Cu mineralization in veins does not allow extensive conclusions about their genesis to be drawn. Goethite, malachite, chrysocolla, and Cu-oxides are observed in veins cutting through the Paleozoic schisteous basement (Fig. 5.2.5a – 5.2.5c), the intermixed goethite-pyrolusite (Fig. 5.2.5d – 5.2.5f), and Triassic conglomerates (Fig. 5.2.5g – 5.2.5i). Textures and sequences highlighted in these veins suggest that these minerals are of supergene origin. Cu-oxides and hydrated silicates (Fig. 5.2.5i) formed prior to and later than malachite, respectively; euhedral malachite needles precipitated prior to calcite, which is filling the cavities (Fig. 5.2.5f). Goethite precipitated in these veins before Cu-minerals (Fig. 5.2.5b), but is younger than the Fe-Mn intermixed ore. Late precipitation of carbonates indicates that during most of the weathering, acid conditions hindered the formation of these phases, and that higher pH values were only reached during the latest stages. The source of Cu may be Cu-sulfides that formed during hydrothermal processes, and were rapidly weathered to malachite, oxides and silicates when Eh increased. Some scarce grains of strongly weathered pyrite and the occurrence of Ni-rich goethite strengthen the hypothesis that Cu-, Fe- (and Ni-) sulfides existed in the primary ore.

The similar REE, major and minor elements patterns of the Cu and Fe-Mn mineralization (Fig. 5.2.6) may imply that the precipitation of these phases is related to the same supergene event(s); Fe and Mn were mobilized and precipitated during the first stages of supergene precipitation, while chalcophile elements remained in solution and precipitated later. The geochemical differences between the veins

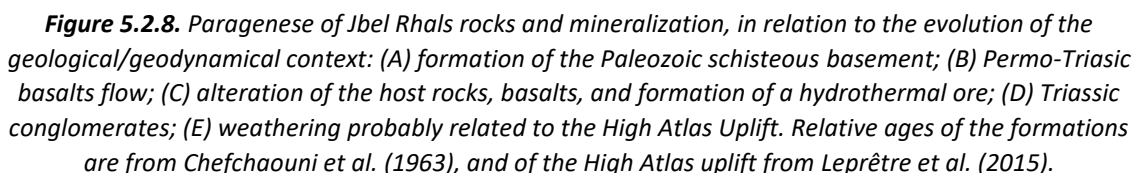
cutting schists and goethite, and those cutting conglomerates, notably for Co. and Ni contents (Fig. 5.2.6), suggest that two generations of Cu-mineralized veins are present at Jbel Rhals. Veins cutting through conglomerates are thought to have formed later. Their REE pattern shows no fractionation, close to the host conglomerate, and their depletion in Y contrasts with other mineralized samples, confirming this hypothesis (Fig. 5.2.6c, 5.2.6d).

#### **5.2.4.d Late sulfates**

Late sulfates (jarosite, melanterite and ferricopiapite) developed locally as coatings on galleries walls and roofs (Fig. 5.2.4l) are supposed to be recent and related to mining activities. Their occurrence may indicate the initial presence of pyrite that would have been destabilized by strongly acid conditions prevailing at a very local scale.

#### **5.2.4.e Metallogenic model of formation**

The textural, mineralogical and geochemical observations listed above suggest that the studied rocks underwent several episodes of transformation, and that the various minerals observed in the ores result from weathering events superimposed on hydrothermal altered rocks and hydrothermal siderite-based metal sulfide veins (Fig. 5.2.8). The polyphased metallogenic history of Jbel Rhals polymetallic deposit is characterized by (1) the circulation of hydrothermal fluids shortly after the basalts flows, which triggered some hydrothermal alteration and the precipitation of associated minerals, and (2) the later circulation of oxidizing fluids that activated weathering of the ores and their environment (Fig. 5.2.8). The presence of basalts, whose Permian/Triassic flow are related to the Central Atlantic Magmatic Province (CAMP), supports the hypothesis of early hydrothermal ore formation at Jbel Rhals (Palinkaš et al. 2016). The hydrothermal hypogene ores are then considered to be late Permian to Triassic in age and to have been induced by the thermal heat flow and events triggered by the Permian-Triassic rifting of the Central Atlantic, just as suggested in other mineral deposits of North Africa (Kamel et al. 1996; Cheilietz et al. 2010; Margoum et al. 2015; Bouabdellah and Margoum 2016; Bouabdellah et al. 2016). Among multiple outcomes, these hydrothermal processes may be responsible for the alteration of basalts, and for the formation of secondary phases such as chlorite and clays, siderite and sulfides. Altered rocks and mineralization were later subjected to supergene processes that are probably related to the Cenozoic High Atlas orogeny. Several episodes of uplift (defined by Frizon de Lamotte et al. 2000, 2008; Leprêtre et al. 2015) generated the exhumation of series and ores and promoted their exposition to oxidizing atmospheric conditions and meteoric water, leading to their weathering. Intense fracturing of host rocks facilitated infiltration and percolation of mineralizing fluids, which were in addition not hindered by the previously altered basalt. The lack of carbonates in the host rocks prevented buffering of the fluids acidity and led to the precipitation of minerals stable under acidic conditions, such as goethite. Fe-Mn oxihydroxides precipitated first, and were later cut by Cu-mineralized veins.



99



et al. 2013). Clays and chlorite precipitation is considered to be related to feldspars alteration/weathering. Siderite and sulfides, goethite and hematite, formed under respectively reduced (hydrothermal) or oxidized (supergene) conditions, are thought to be related to the alteration/weathering of ferromagnesian minerals that may release large quantities of Fe (Hamidi et al. 1997; Daoudi and Pot de Vin 2002). Basalts are therefore regarded as one of the metal sources at Jbel Rhals, other sources being for instance the altered/weathered host rocks.

### **5.2.5 Conclusion**

The Jbel Rhals polymetallic deposit has a polyphased metallogenic history, with mineralization resulting from supergene processes superimposed over hydrothermal alteration. The supergene phases constitute the major mineralization currently observed (goethite, hematite, pyrolusite, cryptomelane, malachite, Cu-oxides and silicates, calcite, dolomite, REE(PO<sub>4</sub>), late sulfates, quartz, clays, silicates) whereas little is left of the hydrothermal mineralization (siderite and minor sulfides). The flow of basalts into the Paleozoic schisteous basement, during Permian-Triassic, the subsequent circulation of hydrothermal fluids through basalts and host rocks, and the formation of the primary deposit, are related to the same geotectonic settings that are part of the intracontinental rifting stage. These hydrothermal processes triggered the alteration of schists and basalts, the leaching of some elements as iron from rocks through fluid–rock interaction, and the formation of a hydrothermal mineral assemblage presumably composed of siderite and sulfides that precipitated from high temperature fluids. During the Cenozoic Era, several episodes of uplift recorded in the High Atlas enabled the exhumation of basalts, host rocks, and hypogene ores, their subsequent weathering, and the formation of a supergene ore from oxidizing low temperature surface-derived fluids. Hydrothermal siderite has thereby been replaced, sometimes “in situ”, by Fe-Mn oxihydroxides (goethite, pyrolusite), while dissolved sulfides were notably later involved in the malachite formation. These supergene processes are also related to the enrichment in HREE, Y, and mobile elements such as U in secondary minerals.

### **5.3 The Tazalaght and Agoujgal Cu deposits, Moroccan Anti-Atlas Copperbelt: Genesis of an As-Pb-rich supergene mineralization**

The major source of arsenic, the sulfosalt tennantite, is a widespread hypogene mineral in supergene deposits, where it co-exists with common base metal sulfides. The oxidation and dissolution of such primary minerals under oxidizing (near-)surface conditions result in the mobilization and release of ions and elements trapped in the crystalline structure including, for instance in tennantite, As, Sb, Cu, Fe, S, Zn, Pb, Hg, Ag, Cd, Co, Mn and Bi (George et al. 2017). The subsequent recombination of elements leads to the formation of thermodynamically more stable phases. The widespread occurrence of As-bearing minerals and compounds in mine environments may lead to high arsenic concentrations in mine tailings and waste rocks piles, even before mineral processing operations (Paktunc and Bruggeman 2010). Since arsenic is a toxic, highly soluble and mobile element, over a wide pH range and thus in many environments, it is crucial to understand its behavior in near-surface situations in order to minimize its release to surroundings. In general, arsenates are known for their relatively low solubility and high stability, which makes them particularly attractive since they effectively immobilize elements such as arsenic and heavy potentially toxic elements by trapping them into their structure (Kocourková et al. 2011; Göb et al. 2014). As stressed by Keim et al. (2018), studies on the presence and behavior of sulfosalts and arsenates are surprisingly scarce, given their widespread occurrence and the major environmental risks related to their weathering.

In this contribution, we present results focusing on the weathering of hypogene sulfides and sulfosalts into oxidized mineral phases, at the copper deposits of Tazalaght and Agoujgal, located in the occidental Anti-Atlas. Along with their classical hypogene and supergene mineral associations, they contain a wide range of rare base metals minerals, including arsenates that represent challenges for ore processing. As such, the presence of arsenates at Tazalaght has only been discovered after a strong increase of arsenic in the ore concentrate (Tijani and Quajhain 1992; Asladay 2002). The present study identifies an extensive variety of secondary minerals, with many that have not previously been reported from the deposits. Since the mineralization is hosted in different rocks, mostly carbonates at Agoujgal and quartzites at Tazalaght, deposits present various weathering products and thereby document the formation processes of more exotic supergene copper ore deposits. Both Tazalaght and Agoujgal samples have the potential to provide insight into the development of a secondary mineral association from a primary sulfide, and present the opportunity to describe in detail a boxwork texture derived from tennantite and hosting various arsenates. The investigation of these secondary associations contributes to understand the geochemical processes of the supergene zone and the mobility of As and other heavy metals in near-surface environments, aside from providing critical information for ore processing.

#### ***5.3.1. Geological setting and mining of the deposits***

Tazalaght and Agoujgal deposits are situated in the Anti-Atlas, at the contact between Precambrian and Cambrian formations, and between inliers and cover formations (Fig. 5.3.1, 5.3.2, 5.3.3; Maddi et al., 2011).

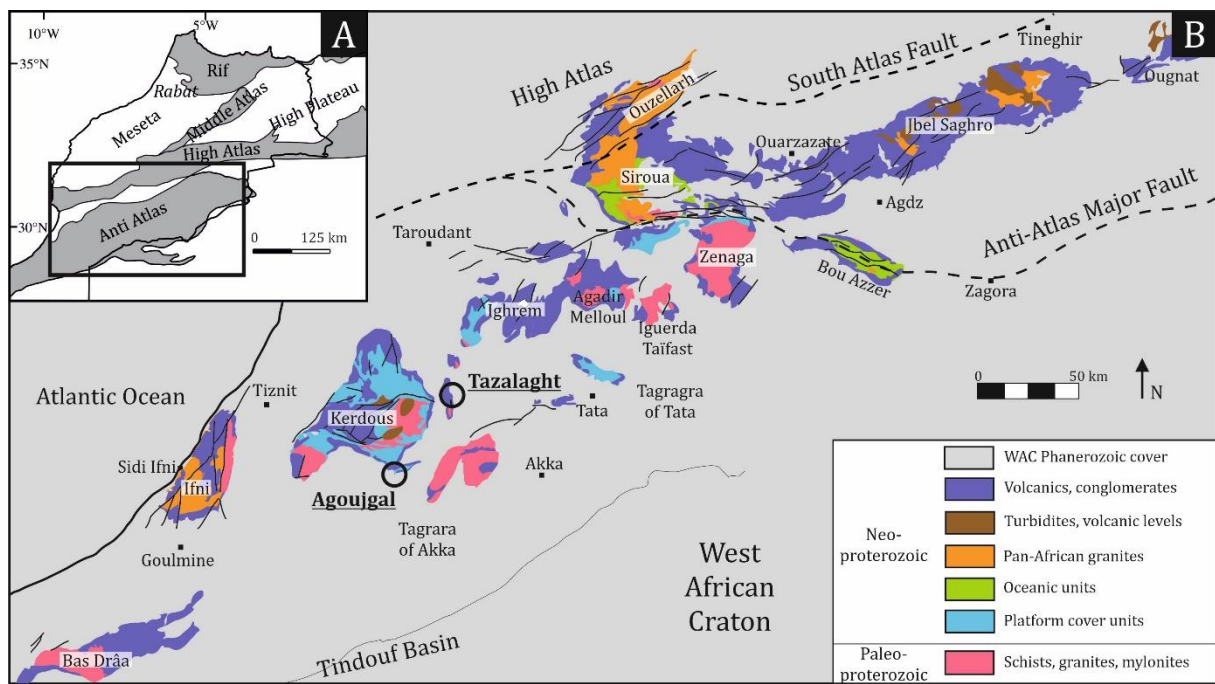


**Figure 5.3.1.** (A) Simplified geologic map of Morocco. (B) Geologic map of the Anti-Atlas showing the location of Tazalaght and Agoujgal deposits, and highlighting the alignment of Precambrian inliers in the Anti-Atlas (modified after Gasquet et al., 2008 and Ikenne et al., 2017).

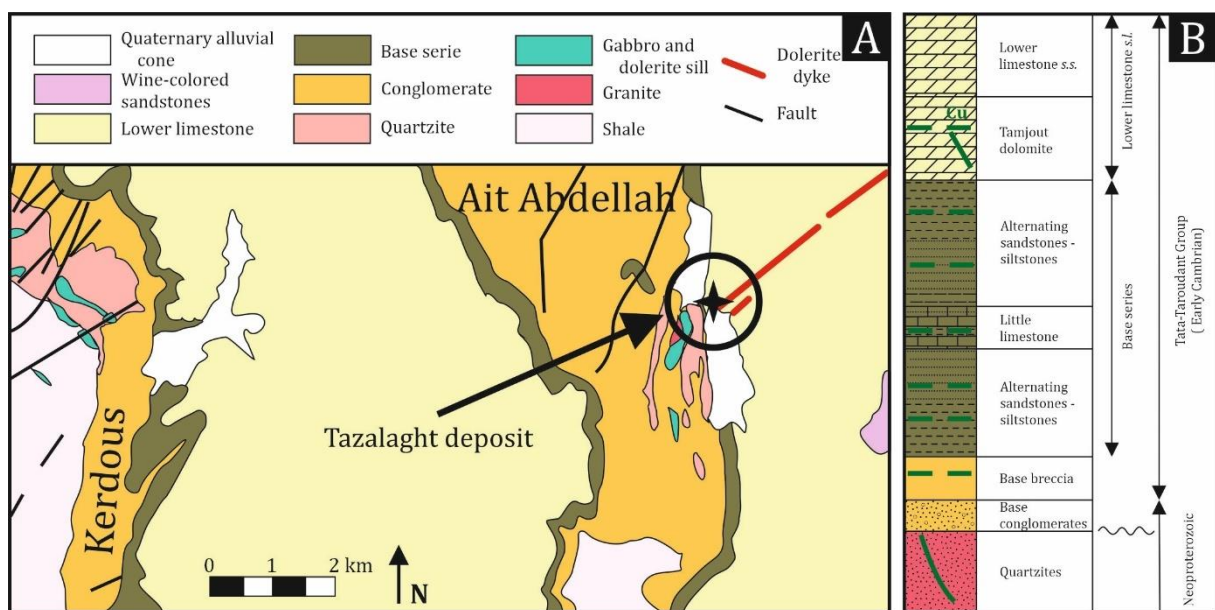


**Figure 5.3.2.** (A) Geologic map of Ait Abdellah and the east of Kerdous inliers, showing the location of Tazalaght deposit (modified after El Basbas et al., 2012). (B) Stratigraphic column of Tazalaght deposit, indicating the Cu-rich layers (modified after El Basbas et al., 2012).

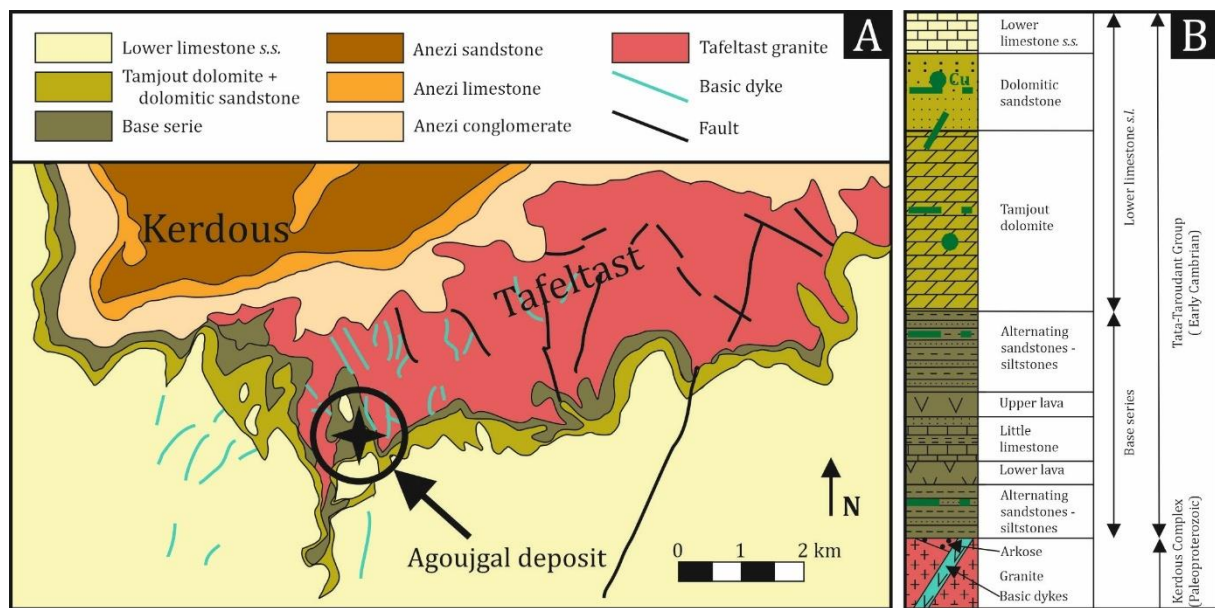


**Figure 5.3.3.** (A) Geologic map of Tafeltast and the south of Kerdous inliers, showing the location of Agoujgal deposit (modified after Maddi et al., 2012). (B) Stratigraphic column of Agoujgal deposit, indicating the Cu-richest layers (modified after Maddi et al., 2012).

### 5.3.1.a Lithostratigraphic and mineralized units

The small village of Tazalaght, 40 km east of Tafraout city, hosts a hundred meters-deep active open-pit quarry (Fig. 5.3.2, 5.3.4A). The quarry is situated at the eastern edge of the Aït Abdellah inlier, east of the Kerdous inlier, at an altitude of approximately 1800 m (Fig. 5.3.2A). The Paleoproterozoic basement (Talat Zegket Formation) is successively unconformably overlain by Early-Middle Neoproterozoic quartzites and metapelites (Azaghar Formation), Late Neoproterozoic ignimbrites and volcano-detrital rocks (Aït Abdellah Formation), conglomerates (Ouarzazate Group) and Early Cambrian formations (Tata Group) (Massacrier 1980). The lithostratigraphic sequence of the deposit is composed of Paleoproterozoic quartzites and conglomerates probably representing a succession of palaeoshoals and palaeobasins, Neoproterozoic conglomerates, Cambrian quartzitic breccias and alternating sandstones and siltstones of the “Base Serie”, and Cambrian carbonates of the “Lower Limestone Series” including the thick “Tamjout dolomite” layer (Massacrier, 1980; Asladay, 2002; El Basbas et al., 2011; Fig. 5.3.2B). Numerous NNW-SSE and NNE-SSW fractures affect the area (Asladay 2002; El Basbas et al. 2011). The primary mineralization mainly occurs in quartzites and quartzitic breccia, at the contact between the basement and cover formations, and in the Base Serie. Sulfides comes under two different forms. In the quartzite, narrow veins and lenses seem to be controlled by fractures, while disseminated or laminated stratiform sulfides occur in the sandstone and siltstones of the Base Serie and in Tamjout dolomite (Asladay 2002; El Basbas et al. 2011).

The 60 meters deep open-pit quarry of Agoujgal is located 46 km south of Tafraout (Fig. 5.3.3, 5.3.4B). The deposit is situated at an altitude of 1300 m, in the small Tafeltast inlier, at the southeastern angle of the Kerdous inlier (Fig. 5.3.3A). The Paleoproterozoic and Early Neoproterozoic basement of the Kerdous inlier is unconformably overlain by the Late Neoproterozoic volcano-detrital Anezi and Ouarzazate formations (Hassenforder 1987). The Tafeltast basement is composed of an Eburnean granite ( $2046 \pm 3$  Ma; Hassenforder et al. 2001) intersected by numerous basic dykes ( $1741 \pm 10$  Ma; Youbi et al. 2013; Fig. 5.3.3A). The Tata-Taroudant Group formations related to the Early Cambrian transgression evolve from detrital towards carbonate terms with volcanic episodes, with, from base to top, alternating siltstones and sandstones of the “Base Serie” and the “Lower Limestones s.l.”



composed of the “Tamjout dolomite”, dolomitic sandstones, and the “Lower Limestones s.s.” (Fig. 5.3.3B). The Tata-Taroudant formations recorded two types of deformation : an ENE-WSW monoclinical structure moderately dipping to the SSE, and N-S, E-W and NE-SW fractures mostly developed in dolomite (Maddi et al. 2011). The primary Cu mineralization, considered as stratiform, occurs in the sandstone-siltstone of the Base Serie, the dolomite, and the dolomitic sandstone. The secondary mineralization resulting from weathering processes fills fractures and cavities in the dolomite, and is associated with cements in sandstones and microconglomerates.

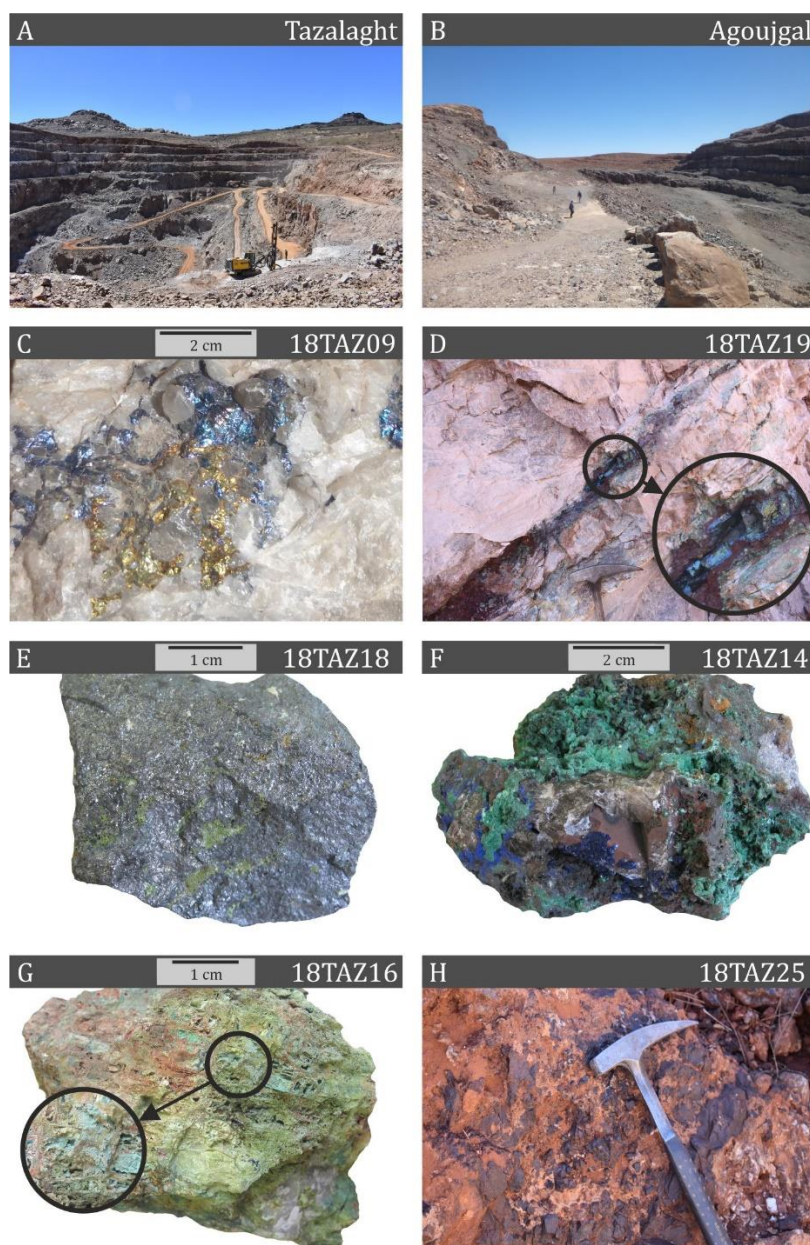


**Figure 5.3.4.** Field pictures of Tazalaght and Agoujgal, and representative Tazalaght's samples pictures. (A) Tazalaght open-pit quarry; (B) Agoujgal open-pit quarry; (C) Primary sulfides (chalcopyrite, bornite) filling cavities in quartzite; (D) Secondary sulfides (bornite, chalcocite), malachite, and goethite, in stratabound vein in Tamjout dolomite; (E) Slightly weathered tennantite; (F) Malachite and azurite filling cavities in quartzite; (G) Cu-arsenates (mostly olivenite) replacing tennantite with a boxwork texture, in cavities in quartzite; (H) Gossan hosting massive goethite, in quartzite.

### **5.3.1.b Ore formation and mining**

The origin, age and genesis of Tazalaght and Agoujgal's primary ores is a matter of debate. Some authors propose 1) a syngenetic origin in relation with the infracambrian transgression and contemporary with the sedimentation (Emberger and Pouit 1966; Pouit 1966), 2) an epigenetic origin related to hydrothermal processes, where mineralizing solutions deposited metals at favorable levels (Chazan 1954; Fauvelet 1973; Maddi et al. 2011) or 3) a mix of hydrothermal fluids and brines (Asladay et al. 1998). Following Clauer and Leblanc (1977), the syngenetic mineralization may also have been remobilized and precipitated as veinlets after hydrothermal processes related with the terminal Triassic-Jurassic magmatism. The syngenetic hypothesis relates the mineralization and the Late Precambrian palaeogeography: copper is thought to concentrate where the transgressive Base Serie thickness is inferior to 50 meters. Much later, weathering processes triggered the oxidation of sulfides and the copper enrichment of the upper formations such as the Base Serie and the Tamjout dolomite (El Basbas et al. 2011).

Since 2011, MANAGEM and its subsidiary Akka Gold Mining (AGM) mine Tazalaght's deposit. The economic copper ore, estimated at 3,000,000 tons with a copper grade of 1.5% (El Basbas et al. 2011), is concentrated in the quartzite, sandstone and siltstone. Agoujgal's deposit was mined between 2007 and 2016 by AGM with an annual production of 600,000 tons of ore with a grade of 1.6% of copper and 20g/t of silver (Maddi et al., 2011). The current reserves, mostly hosted in Tamjout dolomite, are estimated at 5,000,000 tons of ore (Maddi et al., 2011). The economic ores are concentrated in a zone of a few hundred meters long and ten meters thick, in relation with the basement paleorelief (Maddi et al. 2011). Sulfides (mainly chalcopyrite, chalcocite, bornite and covellite) and oxidized ores (malachite and azurite) are currently mined at Tazalaght, as previously at Agoujgal. Rarer sulfides and sulfosalts such as tennantite (up to 2% at both deposits) and galena (up to 1% at Agoujgal) are included in the ore, but the geographically restricted As-richest zones are avoided. These heterogeneous sulfidic and oxidized ores are treated separately. Sulfides are treated by flotation, while oxides are extracted by sulfidation prior to flotation treatment. Whereas the presence of Ag is valorizing the concentrate, As, Pb and Sb are unwelcome elements in both the treatment and the product. The final product is a 20% Cu concentrate, with tolerable contents of 1% As, 5% Pb, 20 ppm Sb and 300 g/t Ag.

### **5.3.2. Materials and analytical methods**

During two field campaigns, in May 2017 and March 2018, hundred samples have been collected from Tazalaght, and ninety-eight from Agoujgal. X-Ray diffraction has been carried out on eighty samples from Tazalaght and seventy-one from Agoujgal in order to identify the major mineral phases of the ores, using a Philips Analytical X-ray diffractometer (Table 5.3.1). Seven thin section of host rocks have been observed in transmitted light mode with a Zeiss Axiophot petrographic polarizing microscope (Carl Zeiss AG, Oberkochen, Germany). Eighty-seven and eighty-four polished sections, from Tazalaght and Agoujgal, respectively, have been observed on a Zeiss Axiophot reflection microscope (Carl Zeiss AG, Oberkochen, Germany), with a Jeol JSM-7500F scanning electron microscope (SEM) (JEOL, Tokyo, Japan) coupled to an energy dispersive X-ray spectrometer (EDS) and with a Zeiss Sigma 300 FEG scanning electron microscope (Carl Zeiss AG, Oberkochen, Germany) equipped with two Bruker EDS detectors (Bruker Corporation, Massachusetts, USA) (Table 5.3.1). Three polished sections of copper arsenates from Tazalaght have also been observed with a JEOL Microanalyzer JXA-8530F (JEOL, Tokyo, Japan) field emission electron probe (EPMA) equipped with a high brightness Schottky field emission electron gun (FEG), at the Department of Materials Engineering of KU Leuven (Leuven, Belgium). Geochemical analyses have been performed on six samples of Tazalaght and nineteen of Agoujgal, in

Activation Laboratories (Ancaster, ON, Canada) (Tables 5.3.1, 5.3.2). Minerals as pure as possible were manually handpicked, crushed and sieved. Details concerning the subsequent various manipulations are available at [actlabs.com](http://actlabs.com). REE (Rare Earth Elements) and most of the trace elements (Cs, Pb, U, Th, Ta, Nb, Hf, Cr, W, Mo, Sn, Bi, Tl, Sb, Pb, In, Ga, Ge, Co, Ni, Cu, Zn, As, Rb, Nb, Ag) have been analyzed by lithium metaborate/tetraborate Fusion Inductively Coupled Plasma Mass Spectrometry (FUS-ICP-MS) (Perkin Elmer Sciex Elan 9000 ICP-MS; Sciex AB, Singapore); Sr, Ba, Zr, Be, Sc, V, and Y and major elements contents have been quantified by lithium metaborate/tetraborate Fusion Inductively Coupled Plasma Optical Emission Spectrometry (FUS-ICP-OES) (Varian Vista 735 ICP; Agilent, Santa Clara, CA, USA). FeO has been quantified by titration, S and SO<sub>4</sub> by combustion infrared detection (ELTRA Instruments, Haan, Germany). For samples containing high contents of Sb, Co, Pb, Zn, Ni, Cu, As, and Mo and Bi, analyses have been carried out with Fusion Inductively Coupled Plasma Sodium Peroxide Oxidation (FUS-Na<sub>2</sub>O<sub>2</sub>) and with Fusion Inductively Coupled Plasma Mass Spectrometry Sodium Peroxide Oxidation (FUS-MS-Na<sub>2</sub>O<sub>2</sub>), respectively, and results quantified in percentages rather than in ppm. Afterwards, major and trace elements contents have been normalized to those of the UCC (Upper Continental Crust; Taylor and McLennan, 1985), considered as a reference for sedimentary rocks.

**Table 5.3.1.** Summary of analyses performed on Tazalaght and Agoujgal As-bearing samples.

Sample number	Description	Host rock	Location		Elevation	XRD	SEM	Geochem. analyses	EPMA
			Lat (°N)	Long (°W)	(m)				
<u>Tazalaght</u>									
17 TAZ 06A	Co-arsenates	Quartzite	29°44'54"	8°43'24"	1832	x	x		
17 TAZ 06B	Co-arsenates	Quartzite	29°44'54"	8°43'24"	1832		x		
17TAZ07C	Co-arsenates	Quartzite	29°44'54"	8°43'24"	1832	x	x	x	
17 TZ 09A	Co-Cu-arsenates and carbonates	Quartzite	29°44'55"	8°43'27"	1834	x	x		
18 TAZ 06	Cu-arsenates and carbonates	Quartzite	29°44'53"	8°43'19"	1841	x	x	x	
18 TAZ 16 A	Cu-arsenates and carbonates	Quartzite	29°44'50"	8°43'22"	1852	x	x	x	x
18 TAZ 16 B	Cu-arsenates and carbonates	Quartzite	29°44'50"	8°43'22"	1852	x	x	x	
18 TAZ 16 C	Cu-arsenates and carbonates	Quartzite	29°44'50"	8°43'22"	1852	x	x		
18 TAZ 18 A	Tennantite	Quartzite	29°44'49"	8°43'22"	1850	x	x	x	
18 TAZ 18 B	Slightly weathered tennantite	Quartzite	29°44'49"	8°43'22"	1850	x	x		
18 TAZ 18 C	Slightly weathered tennantite	Quartzite	29°44'49"	8°43'22"	1850	x	x		
18 TAZ 18 D	Slightly weathered tennantite	Quartzite	29°44'49"	8°43'22"	1850	x	x		
18 TAZ 18 E	Slightly weathered tennantite	Quartzite	29°44'49"	8°43'22"	1850	x	x	x	x
18 TAZ 18 F	Slightly weathered tennantite	Quartzite	29°44'49"	8°43'22"	1850	x	x		x
18 TAZ 18 G	Slightly weathered tennantite	Quartzite	29°44'49"	8°43'22"	1850	x	x		
18 TAZ 18 H	Slightly weathered tennantite	Quartzite	29°44'49"	8°43'22"	1850	x	x		
<u>Agoujgal</u>									
17 AG 16	Cu-arsenates and vanadates	Sandstone	29°23'26"	9°1'18"	1320	x	x	x	
17 AG 26	Mottramite	Sandstone	29°23'29"	9°1'24"	1286	x	x	x	
18 AG 01	Mottramite	Sandstone	29°23'29"	9°1'24"	1287	x	x	x	
18 AG 02A	Pb-phosphates, carbonates and sulfates	Sandstone	29°23'29"	9°1'24"	1287	x	x	x	
18 AG 02B	Pb-phosphates, arsenates, and mottramite	Sandstone	29°23'29"	9°1'24"	1287	x	x	x	
18 AG 03A	Galena and miwed Pb-weathering products	Sandstone	29°23'29"	9°1'24"	1287	x	x	x	
18 AG 03B	Galena and miwed Pb-weathering products	Sandstone	29°23'29"	9°1'24"	1287		x		
18 AG 04	Pb-sulfates and Fe-oxides	Sandstone	29°23'29"	9°1'24"	1287	x	x	x	
18 AG 05	Cerussite	Sandstone	29°23'29"	9°1'24"	1287	x	x		
18 AG 05A	Cerussite	Sandstone	29°23'29"	9°1'24"	1287		x		
18 AG 05B	Pb arsenates, phosphates, and Fe-oxides	Sandstone	29°23'29"	9°1'24"	1287		x		
18 AG 06A	Slightly weathered galena	Sandstone	29°23'29"	9°1'24"	1287	x	x	x	
18 AG 06BA	Pb-phosphates, carbonates, arsenates and sulfates	Sandstone	29°23'29"	9°1'24"	1287	x	x		
18 AG 06BB	Pb-carbonates and sulfates	Sandstone	29°23'29"	9°1'24"	1287		x		
18 AG 06C	Pb-carbonates and arsenates	Sandstone	29°23'29"	9°1'24"	1287	x	x	x	
18 AG 06D	Pb-carbonates and sulfates	Sandstone	29°23'29"	9°1'24"	1287	x	x		
18 AG 07	Mottramite and Fe-oxides	Sandstone	29°23'29"	9°1'23"	1292	x	x	x	



18 AG 08	Pb-carbonates and sulfates	Sandstone	29°23'29"	9°1'23"	1292	x	x	x
18 AG 09	Pb-phosphates, carbonates, arsenates and sulfates	Sandstone	29°23'29"	9°1'23"	1292	x	x	x
18 AG 10	Pb-phosphates, carbonates and sulfates	Sandstone	29°23'29"	9°1'23"	1292	x	x	x
18 AG 11	Mottramite and secondary Pb-phases	Sandstone	29°23'29"	9°1'23"	1292	x	x	
18 AG 18	Cu-arsenates	Sandstone	29°23'29"	9°1'23"	1292	x	x	x
18 AG 23A	Slightly weathered tennantite	Sandstone	29°23'37"	9°1'13" <sup>2</sup>	1321	x	x	x
18 AG 23AB	Slightly weathered tennantite	Sandstone	29°23'37"	9°1'13" <sup>2</sup>	1321	x	x	
18 AG 23B	Slightly weathered tennantite	Sandstone	29°23'37"	9°1'13" <sup>2</sup>	1321	x	x	x
18 AG 23C	Slightly weathered tennantite	Sandstone	29°23'37"	9°1'13" <sup>2</sup>	1321	x	x	
18 AG 23D	Slightly weathered tennantite	Sandstone	29°23'37"	9°1'13" <sup>2</sup>	1321	x	x	
18 AG 24A	Cu-Fe-arsenates	Sandstone	29°23'34"	9°1'17"	1307	x	x	x
18 AG 24B	Cu-Fe-arsenates	Sandstone	29°23'34"	9°1'17"	1308	x	x	x
18 AG 24BB	Cu-Fe-arsenates	Sandstone	29°23'34"	9°1'17"	1309	x	x	
18 AG 24C	Cu-arsenates	Sandstone	29°23'34"	9°1'17"	1310	x	x	x
18 AG 24CB	Cu-arsenates	Sandstone	29°23'34"	9°1'17"	1311	x	x	
18 AG 25	Cu-arsenates	Sandstone	29°23'34"	9°1'17"	1312	x	x	

### 5.3.3. Results

#### 5.3.3.a General overview

Quartzite (quartz and <5% chlorite), quartzitic breccia (coarse quartz grains cemented by cryptocrystalline quartz, muscovite and chlorite), alternating sandstones and siltstones of the Base Serie (finely crystallized quartz, muscovite and chlorite cut by veins hosting coarser grains of the same minerals) and Tamjout dolomite (dolomite and 5% quartz) host Tazalaght's mineralization. The mineralized rocks of Agoujgal are the alternating sandstones and siltstones of the Base Serie, the dolomitic sandstone and Tamjout dolomite. These formations overlay a strongly fractured, altered and/or weathered granite mostly composed of quartz, muscovite, biotite and microcline.

A typical mineralogical zonation appears in Tazalaght deposit, in relation with depth, highlighting the progressive *per descensum* weathering of ores. The primary sulfide zone (~100-80 m deep) hosting unweathered mineral phases (Fig. 5.3.4C) and the secondary sulfide zone or cementation zone (~80-70 m deep) corresponding to the groundwater table fluctuation level (Fig. 5.3.4D) constitute the bottom units of the sequence. The much-diversified oxidized zone (~70-20 m deep) concentrates phases such as carbonates (malachite and azurite), oxides (cuprite, tenorite, goethite, hematite, ...) and arsenates (olivenite, conicalcite, chenevixite) (Fig. 5.3.4E, 5.3.4F, 5.3.4G). Close to the surface, the leached zone or gossan (20-0 m deep) is almost only constituted of iron (oxyhydr-)oxides (Fig. 5.3.4H). Even if the mineral zonation with depth of Agoujgal is far less marked than at Tazalaght, it is possible to distinguish zones where primary sulfides, secondary sulfides, oxidized minerals (Fig. 5.3.5A-5.3.5E) and iron (oxyhydr-)oxides (Fig. 5.3.5F) are concentrated.

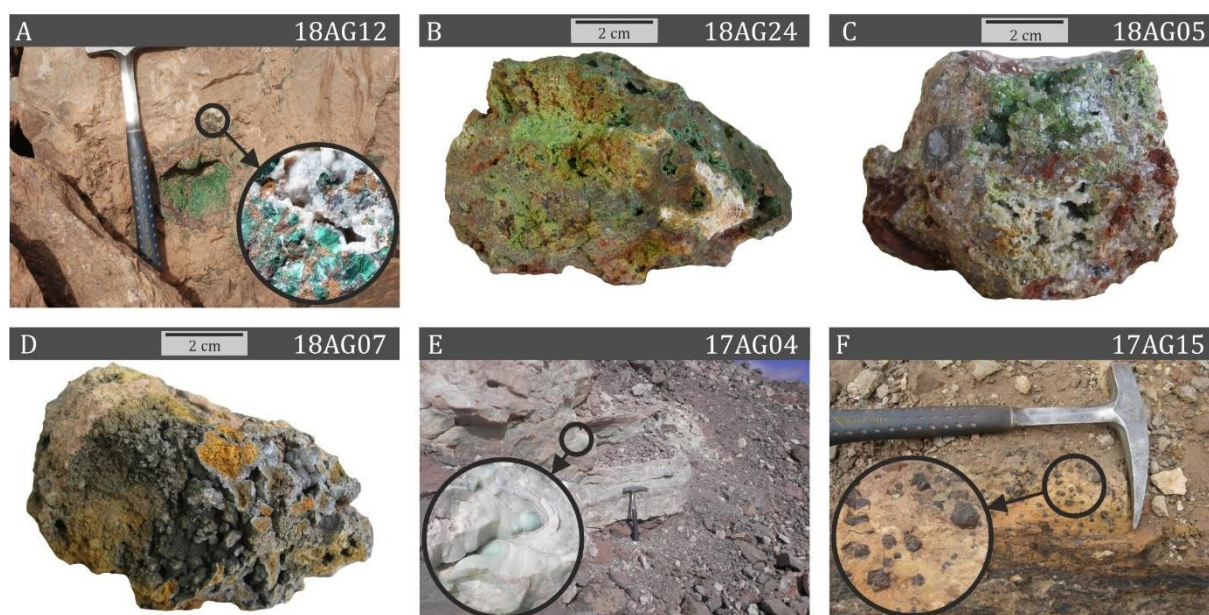


**Figure 5.3.5.** Agoujgal's representative samples pictures. (A) Malachite filling cavities in Tamjout dolomite, sometimes covered by late calcite; (B) Cu-arsenates and malachite; (C) Supergene lead minerals; (D) Mottramite covering botryoidal and earthy goethite; (E) Goethite and hematite pseudomorphing stratabound euhedral goethite; (F) Late massive greenish calcite.

### 5.3.3.b Ore characterization including SEM semi-quantitative analyses

The most common primary sulfide of Tazalaght, chalcopyrite, is hosted with minor bornite by quartzite or its quartz veins (Fig. 5.3.4C, 5.3.6A), or I stratabound in sandstones-siltstones of the Base Serie and in Tamjout dolomite. Rarer tennantite is always associated with chalcopyrite and bornite and contains significant varying concentrations of Zn (2.2-3.8%), Sb (1.4-2%), Fe (3-5.7%) and Co (0.6-5.2% close to Co-arsenates), according to SEM analyses. Scarce chlorite veins enclose dolomite replaced by calcite and Mn-goethite, but also chalcopyrite and very scarce galena, sphalerite, arsenopyrite, Co-gersdorffite ((Co,Ni)AsS) and star-shaped grains of an unidentified Mo-oxide. At Agoujgal, chalcopyrite and pyrite (Fig. 5.3.6B) are the most represented hypogene sulfides, along with minor tennantite and galena. In the Base Serie, dolomitic sandstone and Tamjout dolomite, euhedral pyrite encloses gangue minerals such as monazite ((Ce,La,Nd)PO<sub>4</sub>), apatite, rutile/anatase, calcite, dolomite and chlorite. Chalcopyrite and covellite sometimes fill cavities and fractures in unweathered pyrite (Fig. 5.3.6B). Massive chalcopyrite is concentrated at the center of veinlets and cavities in carbonate formations, in a gangue of calcite, dolomite, chlorite and talc. Tennantite fills cavities in the dolomitic sandstone, always in association with chalcopyrite, at the contrary of galena which occurs alone in such cavities. Agoujgal's tennantite concentrates 2.4-3.2% of Zn, 3-5% of Fe, and up to 1.3% of Pb. Very scarce and small sulfides such as cobaltite (CoAsS), bismuthinite (Bi<sub>2</sub>S<sub>3</sub>), galena (with 1.9% of Bi), sphalerite (with 1.6% of Bi), arsenopyrite (FeAsS), tennantite (Cu<sub>6</sub>Cu<sub>4</sub>(Fe,Zn)<sub>2</sub>As<sub>4</sub>S<sub>13</sub>), matildite (AgBiS<sub>2</sub>), greenockite (CdS), kobellite (Pb<sub>22</sub>Cu<sub>4</sub>(Bi, Sb)<sub>30</sub>S<sub>69</sub>) and acanthite (Ag<sub>2</sub>S) are present in one sample at the contact between pyrite and the gangue.

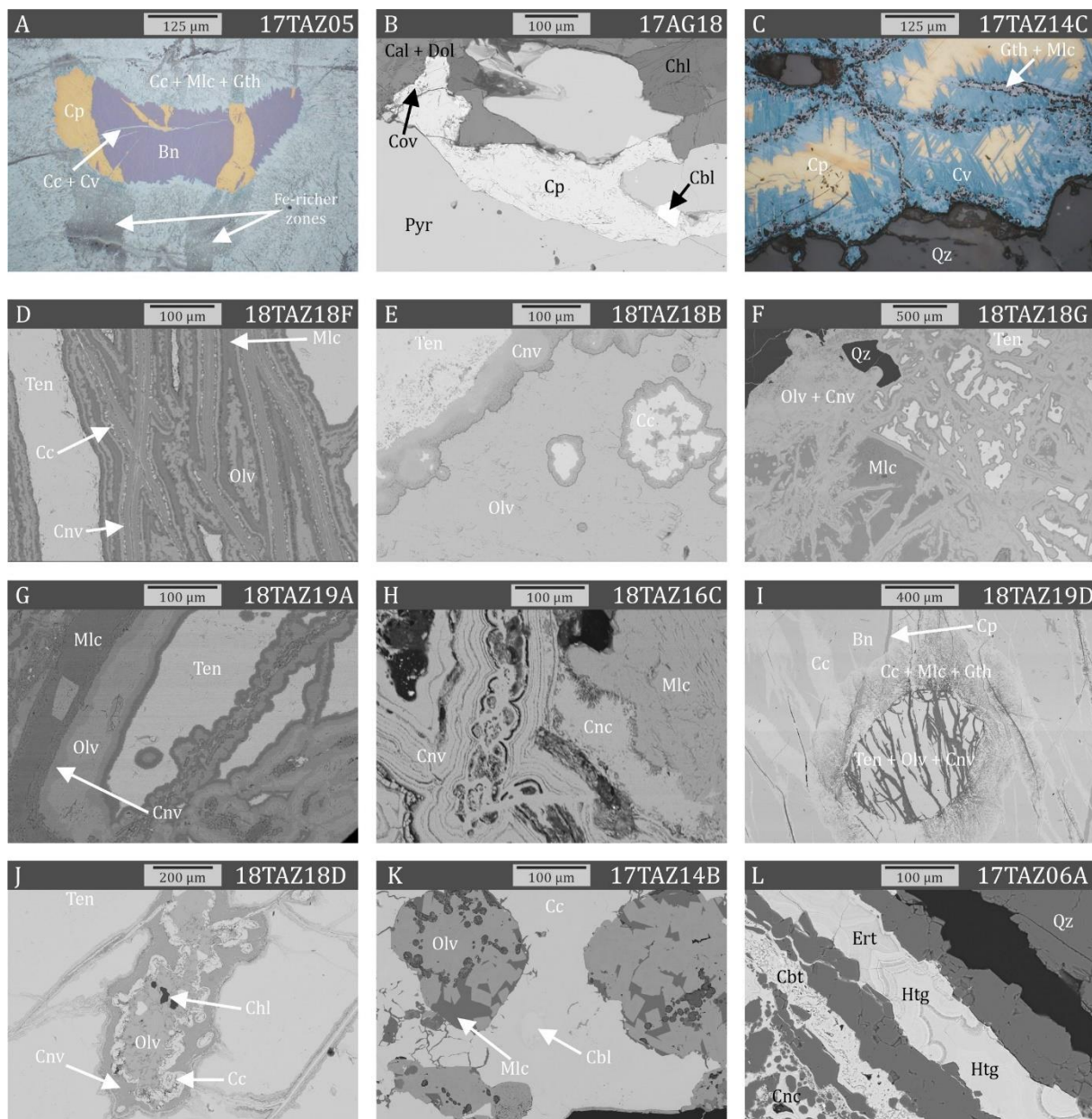


**Figure 5.3.6.** Representative samples of Tazalaght and Agoujgal deposits: reflected light microphotographs (A, C), SEM microphotographs in back scattered electrons mode (B, D – L). (A) Weathering of chalcopyrite and bornite in chalcocite, malachite, and goethite forming a boxwork texture; (B) Chalcopyrite weathered to covellite, filling cavities and fractures in euhedral pyrite, along with minor cobaltite; (C) Weathering of chalcopyrite in covellite, and filling of fractures by goethite and malachite; (D) Tennantite slightly weathered along fine veinlets filled with the successive chenevixite, chalcocite, malachite, and olivenite; (E) Massive replacement of tennantite by chenevixite and olivenite; (F) Strongly weathered tennantite, replaced by olivenite and chenevixite along veinlets, and by malachite filling the cavities; (G) Weathering of tennantite into malachite, chenevixite, and olivenite; (H) Successive precipitation of chenevixite, conicalcrite, and malachite in cavities resulting from tennantite dissolution; (I) Tennantite weathered to chenevixite and olivenite, surrounded by bornite and chalcopyrite weathered to chalcocite, malachite, and goethite; (J) Weathering of tennantite and formation of secondary chalcocite, olivenite, and chenevixite around gangue minerals such as chlorite; (K) Olivenite and malachite included in a gangue of chalcocite including cobaltite grains; (L) veins of erythrite, heterogenite and cobaltlotharmeyerite cutting through the quartzite and conicalcrite; (Cp = chalcopyrite, Bn = bornite, Cc = chalcocite, Cv = covellite, Mlc = malachite, Gth = goethite, Qz = quartz, Hem = hematite, Ten = tennantite, Olv = olivenite, Cnv = chenevixite, Chl = chlorite, Cnc = conicalcrite, Cbl = cobaltite, Cbt = cobaltlotharmeyerite, Ert = erythrite, Htg = heterogenite).

At Tazalaght, secondary sulfides mixed with oxidized phases mostly fill irregular fractures in the primary chalcopyrite, but also in quartzite and quartzitic breccia, and result from weathering of stratabound hypogene sulfides in sandstones-siltstones of the Base Serie and in Tamjout dolomite (Fig. 5.3.4D). Several weathering successions exist for chalcopyrite (and bornite) at Tazalaght, which may either be 1) replaced by secondary bornite along fractures and then by other sulfides, or 2) progressively and successively replaced by chalcocite, covellite, goethite and malachite, or 3) directly replaced by covellite, with some goethite and malachite (Fig. 5.3.6C). Most samples of the cementation zone are thus composed of chalcocite, malachite, goethite and covellite, which form a boxwork texture typical of supergene deposits (Fig. 5.3.6A). Goethite occurs at the center of the veinlets brecciating chalcocite, while malachite and rarer covellite are present at the edges. As weathering expands, chalcocite is completely replaced by covellite, malachite and goethite. Cu- and/or Ag- sulfides, probably stromeyerite ( $\text{AgCuS}$ ) and acanthite ( $\text{Ag}_2\text{S}$ ) are often observed close to covellite and chalcocite. The initial occurrence of weathered chalcopyrite or bornite is indicated by iron-rich zones where chalcopyrite was present: more iron is released from its weathering, and more goethite consequently forms *in situ* (Fig. 5.3.6A). Only few secondary sulfides are observed at Agoujgal, in association with oxidized phases. Consistently to what is observed at Tazalaght, chalcopyrite mostly forms a boxwork texture with chalcocite (and djurleite ( $\text{Cu}_{31}\text{S}_{16}$ )), malachite and goethite. Covellite, stromeyerite and acanthite occur in most weathered samples.

The oxidized zone of Tazalaght extends into the quartzite, quartzitic breccia, Base Serie, Tamjout dolomite and in veins cutting all these layers. The most common minerals are botryoidal malachite and prismatic azurite associated with iron (oxyhydr-)oxides (Fig. 5.3.4F). Malachite encloses gangue minerals such as quartz and monazite, and infiltrates into sheets and coats radial aggregates of chlorite. According to SEM semi-quantitative analyses, Tazalaght's malachite contains varying proportions of As (1.6-2.1%), Fe (1.8-4.6%) and Sb (0.3-1%). The rarer mineral phases found in the oxidized zone are cuprite and tenorite hosting cubic grains of alunite, Cu-silicates mostly represented by chrysocolla, and colloform structures composed of successive asbolane ( $(\text{Ni},\text{Co})_{2-x}\text{Mn}(\text{O},\text{OH})_{4.n}\text{H}_2\text{O}$ ), heterogenite ( $\text{CoO}(\text{OH})$ ) and malachite. Although tennantite and arsenates arising from its weathering are omnipresent at Tazalaght, their concentration is restricted to strongly fractured areas that are rich in iron (oxyhydr-)oxides. There, complex structures mostly involve several generations of malachite, olivenite ( $\text{Cu}_2\text{AsO}_4(\text{OH})$ ), conichalcite ( $\text{CaCu}(\text{AsO}_4)(\text{OH})$ ) and chenevixite ( $\text{Cu}_2\text{Fe}_2(\text{AsO}_4)_2(\text{OH})_4(\text{H}_2\text{O})$ ) (Fig. 5.3.4G). The most common weathering texture of Tazalaght's tennantite is the development of oxidized minerals along fractures (Fig. 5.3.6D), where different sequences are possible: 1) chenevixite concentrated at the center of the veinlets is successively followed by the chalcocite-malachite association, olivenite, and malachite (Fig. 5.3.6D); 2) olivenite is at the center of the veinlets, and chenevixite at the edges; 3) tennantite is directly in contact with successive generations of malachite followed by chenevixite, and olivenite. According to SEM analyses, Tazalaght's olivenite concentrates Ca (0.3-1.9%), Fe (0.5-5.5%), Zn (1.1-4.4%) and Sb (1-2.1%), while chenevixite is rich in Sb (2.6-4.6%) and Zn (2.1%). The contact between tennantite and olivenite is often punctuated by chenevixite (Fig. 5.3.6E). As weathering continues, fractures widen, cavities are filled with secondary phases, and arsenates develop until complete replacement of tennantite (Fig. 5.3.6E, 5.3.6F, 5.3.6G). Textures indicating the replacement of tennantite along cleavage planes and fractures are frequently highlighted at the macroscopic and microscopic scales: in Fig. 5.3.6H, chenevixite precipitated along former cleavage planes, and cavities were later filled by conichalcite and malachite. Arsenates are rarely weathered, once formed. Rarer mineral associations and structures also occur in Tazalaght's oxidized zone. For instance, rounded masses of tennantite, olivenite, chenevixite and malachite are very locally surrounded or intersected by chalcopyrite, bornite and the chalcocite-malachite-goethite boxwork association (Fig. 5.3.6I). In tennantite, arsenates and chalcocite develop around gangue



minerals. For instance, quartz grains and chlorite are successively surrounded by olivenite, chalcocite, chenevixite, and again chalcocite (Fig. 5.3.6J). A recent blasting operation in Tazalaght's quartzite brought to light a small restricted area rich in Co-bearing minerals. Clusters of Co-malachite (0.8-1.8% of Co) host euhedral Co-olivenite (0.4-5% of Co and 0.7-1.9% of Ni) in a matrix of chalcocite where small cobaltite (with 0.3-2.7% of Ni) grains are identified (Fig. 5.3.6K). Erythrite ( $\text{Co}_3(\text{AsO}_4)_2 \cdot 8(\text{H}_2\text{O})$ ) veinlets are there intersected by heterogenite veinlets, and coated with conichalcite. Veins with cobaltlotharmeyerite ( $\text{Ca}(\text{Co,Fe,Ni})_2(\text{AsO}_4)_2 \cdot 2(\text{H}_2\text{O, OH})$ ) are intersected and coated by heterogenite and erythrite (Fig. 5.3.6L). In this area, erythrite concentrates Cu (0.1-1.2%), Fe (0.5-1.1%), Zn (2%) and Ni (1.6-2%), heterogenite is rich in Cu (1.4-2.8%), Mn (0.2-2.2%), Ni (3.1-7.1%) and As (0.2-2.4%), conichalcite contains Zn (0.2-2.5%), Co (1-2.5%) and Ni (0.3-3%), and cobaltlotharmeyerite includes Zn (0.3-1.5%), according to SEM analyses. The rare replacement of euhedral Zn-rich olivenite by malachite, in a matrix of conichalcite and chenevixite, is highlighted in the EPMA diagram of Fig. 5.3.7A and 5.3.7B: Zn and As concentrations drop at the edge of crystals undergoing weathering, while Cu, O, and C contents rise, before entering in malachite domain.

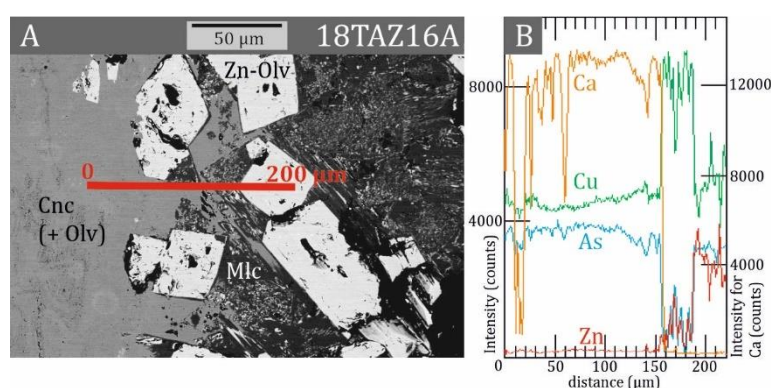


**Figure 5.3.7.** (A) SEM microphotograph in back scattered electrons mode, with EPMA line analysis on Tazalaght Cu arsenates, cutting the transition between conichalcite, malachite, and Zn-rich olivenite. (B) Evolution of Cu, As, Zn, and Ca intensities with distance, showing a strong increase in Cu coupled to a drop of As when entering the Zn-olivenite domain. Ca fluctuates in conichalcite (probably mixed with malachite or goethite), and drops in olivenite. Zn fluctuates in olivenite, indicating different Zn-enrichment zones in the crystals.

The oxidized mineralization of Agoujgal is principally composed of copper minerals concentrated in veins and veinlets in the Base Serie, in clusters and impregnations in dolomite, and in cavities in the dolomitic sandstone (Fig. 5.3.5A). Malachite, the most common mineral in the oxidized zone, is often coated by goethite, hematite, and later calcite and quartz (Fig. 5.3.5A). Chalcocite, covellite, cuprite, tenorite, acanthite and stromeyerite relicts are variably embodied in malachite, as well as anhedral mottramite grains ( $\text{PbCu}(\text{VO}_4)(\text{OH})$ ) and gangue minerals such as chlorite, quartz, apatite, monazite and rutile/anatase. Almost no azurite is found at Agoujgal. Cu-silicates, probably chrysocolla, rarely replace malachite. Tennantite is more weathered than at Tazalaght, but the numerous arsenates deriving from its weathering (Fig. 5.3.5B) also concentrate in relatively restricted areas. Tennantite is generally surrounded by a thin layer of Ag-rich chalcocite (1.9-3.6% of Ag) that occasionally hosts small barite grains, followed by several arsenates of which the sequence varies (Fig. 5.3.8A). For instance, chalcocite might be in contact with euhedral Fe-rich olivenite grains cemented by Fe-Ca-rich olivenite. In the absence of chalcocite, tennantite is directly surrounded by malachite followed by chenevixite. In the most weathered samples, the replacement of tennantite is completed by 1) malachite (and rare brochantite) hosting euhedral conichalcite and olivenite (Fig. 5.3.8B), or 2) by massive Zn-rich olivenite cemented by Zn-rich conichalcite, or 3) only by massive olivenite. Between slightly weathered tennantite and completely oxidized zones, Ag-rich chalcocite, chenevixite, acanthite and pseudomorphs hosting goethite and Zn-rich conichalcite are successively coated with Fe-Ca-Cu-arsenates (possibly barahonaite  $((\text{Ca,Cu,Na,Fe,Al})_{12}\text{Fe}_2(\text{AsO}_4)_8(\text{OH,Cl})_x \cdot n\text{H}_2\text{O})$  or lukrahnite

( $\text{Ca}(\text{Cu,Zn})(\text{Fe,Zn})(\text{AsO}_4)_2(\text{OH},\text{H}_2\text{O})_2$ ), Zn-rich olivenite and Zn-rich conicalcrite (Fig. 5.3.8C, 5.3.8D). At Agoujgal, according to SEM analyses, olivenite variably concentrates Ca (0.1-1.3%), Fe (0.8-4%) and Zn (1.1-4.7%), conicalcrite is rich in Zn (0.7-1.5%) and Fe (1.4-2.6%), and malachite contains As (2.3-3.7%), Fe (1.6-3.7%), Zn (1.2-4.9%) and Sb (1-1.9%). Malachite and conicalcrite frequently fill fractures in Tamjout dolomite, at the edges and at the center of the veins, respectively, but malachite might also be precursor to the arsenate (Fig. 5.3.8E). Ghosts of primary minerals are highlighted by goethite and conicalcrite (Fig. 5.3.8F). Iodargyrite and native silver have been once identified in conicalcrite, close to barite, while globular aggregates of beaverite ( $\text{PbCu}(\text{Fe,Al})_2(\text{SO}_4)_2(\text{OH})_6$ ) formed on one occasion at the surface of this arsenate. The former presence of tennantite is confirmed in most weathered samples with the precipitation of weathering products along particular directions, similarly to what was observed at Tazalaght. Cleavages planes are highlighted by 1) conicalcrite (Fig. 5.3.8G), 2) goethite and yukonite ( $\text{Ca}_3\text{Fe}(\text{AsO}_4)_2(\text{OH})_3 \cdot 5\text{H}_2\text{O}$ ), 3) goethite and (phosphatian) arseniosiderite (1.4-2.5% of P and 1.8-1.9% of Cu) (Fig. 5.3.8H), or 4) only goethite. Malachite, conicalcrite or residual quartz fill in cavities. Later mottramite (with 1.2-2% of As and 0.2-0.9% of Fe) occasionally crystallize at the surface of samples, in cavities or between conicalcrite needles (Fig. 5.3.8I).

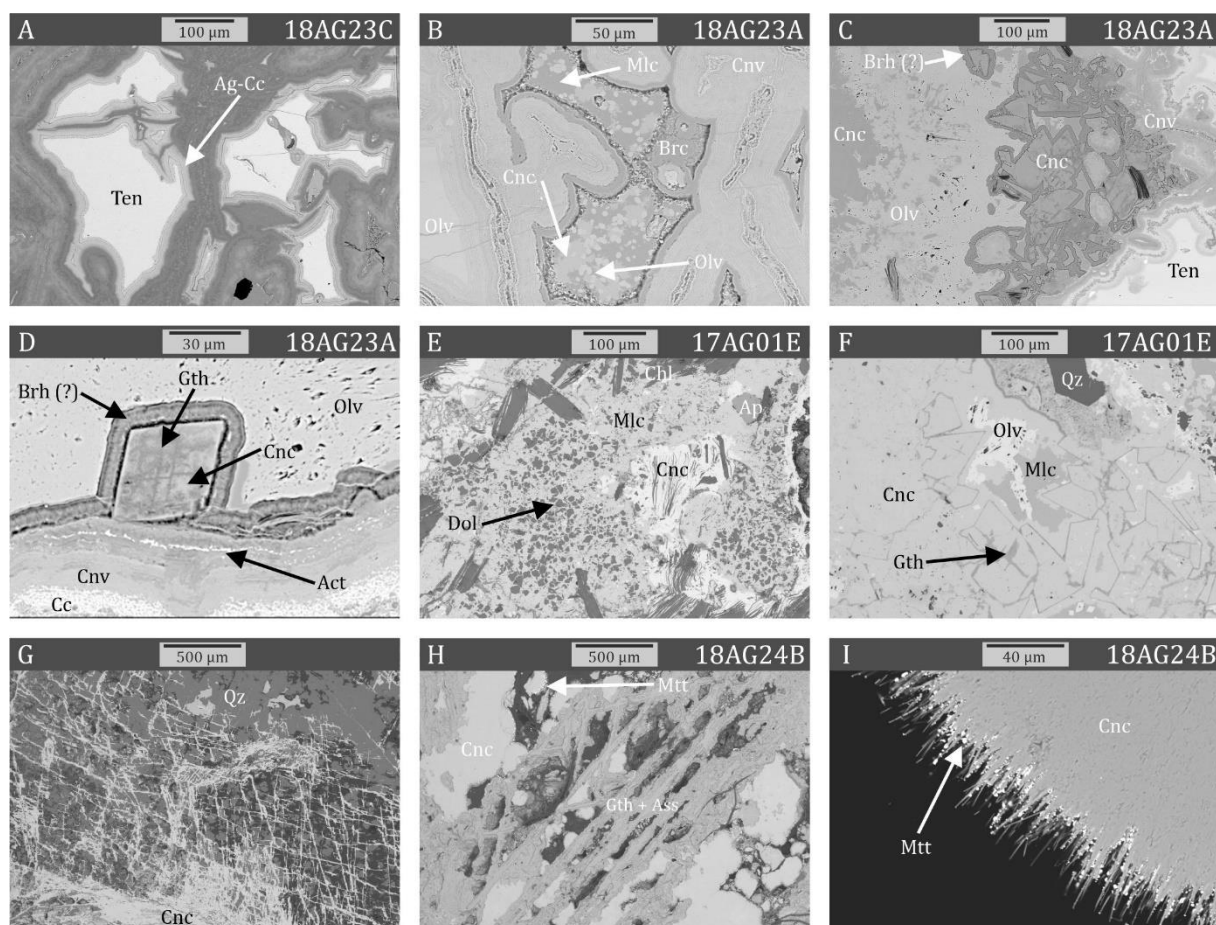


**Figure 5.3.8.** Representative samples of Agoujgal's Cu-mineralization: SEM microphotographs in back scattered electrons mode. (A) Tennantite weathered to Ag-rich chalcocite and Fe- or Fe-Ca-rich olivenite; (B) Complete replacement of tennantite through veins by chenevixite and olivenite; and filling of cavities by malachite, brochantite, and euhedral olivenite and conicalcrite; (C and D) Ghosts of primary minerals filled by conicalcrite and goethite, and coated by successive barahonaite (or lukrahnite), olivenite, and conicalcrite, close to tennantite edged by acanthite and chalcocite; (E) Conicalcrite and malachite surrounding chlorite and dolomite; (F) Small mottramite grains coating conicalcrite needles; (G) Conicalcrite replacing a primary mineral along cleavage planes, in a gangue of quartz; (H) Goethite and arseniosiderite replacing a primary mineral along cleavage planes, with cavities filled by conicalcrite; (I) Small mottramite grains coating conicalcrite needles; (Ten = tennantite, Ag-Cc = Ag-rich chalcocite, Olv =

*olivenite*, *Mlc* = malachite, *Cnc* = conicalcrite, *Brc* = brochantite, *Brh* = barahonaite (or lukrahnite), *Cnv* = chenevixite, *Gth* = goethite, *Act* = acanthite, *Cc* = chalcocite, *Qz* = quartz, *Chl* = chlorite, *Ap* = apatite, *Dol* = dolomite, *Ca* = calcite, *Ass* = arseniosiderite, *Mtt* = mottramite, *Cdf* = calcio-duftite).

The presence of lead minerals is a particularity of Agoujgal's deposit (Fig. 5.3.5C). Primary galena is mostly replaced by anglesite, cerussite and covellite (Fig. 5.3.9A). This classical Pb-assemblage is occasionally intersected by malachite veins. More exotic secondary lead minerals are also identified. Phosphohedyphane ( $\text{Ca}_2\text{Pb}_3(\text{PO}_4)_3\text{Cl}$ ) fills cavities in cerussite, encloses plumbojarosite ( $\text{PbFe}_6(\text{SO}_4)_4(\text{OH})_{12}$ ) clusters, intersects associated quartz, osarizawaite ( $\text{PbCuAl}_2(\text{SO}_4)_2(\text{OH})_6$ ) and plumbojarosite (Fig. 5.3.9B), or fills ghosts of former minerals later coated with calcio-duftite (( $\text{Pb,Ca}$ ) $\text{CuAsO}_4(\text{OH})$ ). Osarizawaite here contains elevated proportions of Fe (3.8-7%) and locally up to 3.9% of P, while plumbojarosite, calcio-duftite and phosphohedyphane concentrate 1.7-2.9% of Cu, up to 2.7% of Zn, and 0.9-2.1% of As, respectively. Cerussite is sometimes associated with euhedral calcio-duftite and malachite replacing primary minerals, or embodied with mimetite ( $\text{Pb}_5(\text{AsO}_4)_3\text{Cl}$ ) in anhedral calcio-duftite (Fig. 5.3.9C). Large clusters of mimetite are associated with arsenopyrite weathered to Fe-rich gartrellite ( $\text{Pb}(\text{Cu,Fe})_2(\text{AsO}_4, \text{SO}_4)_2(\text{CO}_3, \text{H}_2\text{O})_{0.7}$ ). Very locally, euhedral mimetite is replaced and coated by calcio-duftite and conicalcrite (Fig. 5.3.9D) that embody calcio-volborthite ( $\text{CaCu}(\text{VO}_4)(\text{OH})$ ). In cavities, complex structures of successive mineral layers contain Fe-rich gartrellite, yukonite and goethite that are all intersected by conicalcrite, calcio-duftite and ultimately mottramite (Fig. 5.3.9E). There, conicalcrite concentrates Pb (1.6-5%), Fe (0.3-1.1), P (up to 0.6%) and V (up to 1.5%), Fe-rich gartrellite is rich in Ca (0.3-1.3%), Zn (1.1-1.5%) and Fe (8.5-11.8), and yukonite contains up to 1.8% of Cu.

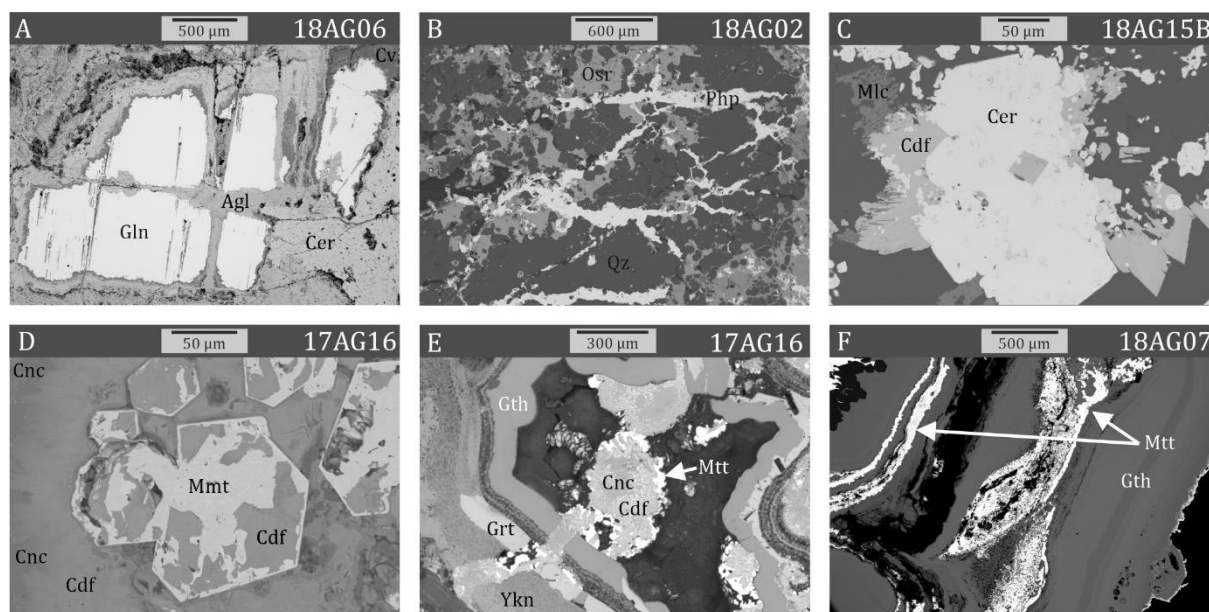


**Figure 5.3.9.** Representative samples of Agoujgal's Pb-mineralization: SEM microphotographs in back scattered electrons mode. (A) Galena successively weathered to covellite, anglesite and cerussite; (B) Phosphohedyphane cutting osarizawaite and quartz; (C) Euhedral calcio-duftite in cerussite, close to malachite; (D) Euhedral mimetite replaced and surrounded by successive generations of conicalcrite and calcio-duftite; (E) Filling of cavities by successive yukonite, gartrellite, goethite, conicalcrite, calcio-duftite, and mottramite; (F) Successive generations of botryoidal mottramite and goethite; (Gln = galena, Agl = anglesite, Cer = cerussite, Cdf = calcio-duftite, Mmt = mimetite, Grt = Fe-gartrellite, Osr = osarizawaite, Php = phosphohedyphane, Qz = quartz, Mlc = malachite, gth = goethite, Mtt = mottramite).



Tazalaght's gossan mostly hosts iron (oxyhydr-)oxides pseudomorphosing rhombododecahedral pyrite. Several generations of hematite and goethite are identified, with suspected replacements of hematite by goethite, and vice versa. Powdery goethite, hematite and Mn oxides containing variable proportions of Mn, Fe, Zn, Cu, Co, Ni and Si are found in fractures where water is currently leaking. In Agoujgal's gossan, goethite and hematite frequently pseudomorphose cubic and dodecahedral pyrite (Fig. 5.3.5F). Hematite generally concentrates at the center of the pseudomorphs, while goethite is restricted at the edges. Dodecahedral pseudomorphs follow the stratification of the Base Serie (Fig. 5.3.5F) and embody gangue minerals and rare iodargyrite. Botryoidal goethite and mottramite are present at the very bottom of the quarry, associated with powdery goethite, hematite and Mn oxides. Successive generations of goethite and mottramite are overlapping (Fig. 5.3.5D, 5.3.9F); the first generation of mottramite usually includes gangue minerals while the second is very pure. A greenish late calcite coats and intersects the host rocks and supergene mineralization, frequently leading to their brecciation (Fig. 5.3.5E).

### 5.3.3.c Bulk rock geochemistry

The REE, major and trace elements concentrations of Tazalaght and Agoujgal samples are presented in Table 5.3.2. Most Tazalaght and Agoujgal samples display low REE contents. Tazalaght samples are rich in Cu (up to 60.3 %) and As (up to 5.2 %). Co-bearing arsenates concentrate Co (up to 15 %) and Ni (up to 2.8 %). Tennantite and Cu-arsenates are rich in Zn (up to 5.9 %) and in Sb (up to 1.5 %); the sulfosalt also contains up to 2700 ppm of Ag. The normalization of tennantite and Cu arsenates contents to those of the UCC highlights enrichments in U, As, Sb, Ag, Pb, Zn, and Cu (Fig. 5.3.10A). Agoujgal ores are rich in As (up to 13.8 %), Cu (up to 48 %), and Pb (up to 78.4 %). Tennantite contains up to 1.8% of Zn, 5700 ppm of Sb, and 2260 ppm of Ag. The enrichment in V and Y is restricted to Cu-vanadates samples (up to 7.2 % and 1770 ppm, respectively), which also concentrate Zn (up to 1.9 %). Mo is found at the highest rates in secondary Pb ores (max. 2190 ppm), while the Bi content reaches a peak in Cu-vanadates and Cu-arsenates (max. 1580 ppm). The normalization of Agoujgal samples contents to those of the UCC shows up enrichments in U, Y, V, Mo, Bi, As, Sb, Ag, Pb, Zn and Cu (Fig. 5.3.10B). An interesting trend is the Pb-enrichment of supergene Cu-arsenates (1.8-23.1%) in comparison with the very low Pb content of tennantite (40-60 ppm). In a similar way, all secondary Pb ores are much richer in As (0.1-2.2 %) than galena (50 ppm) (Fig. 5.3.10C).

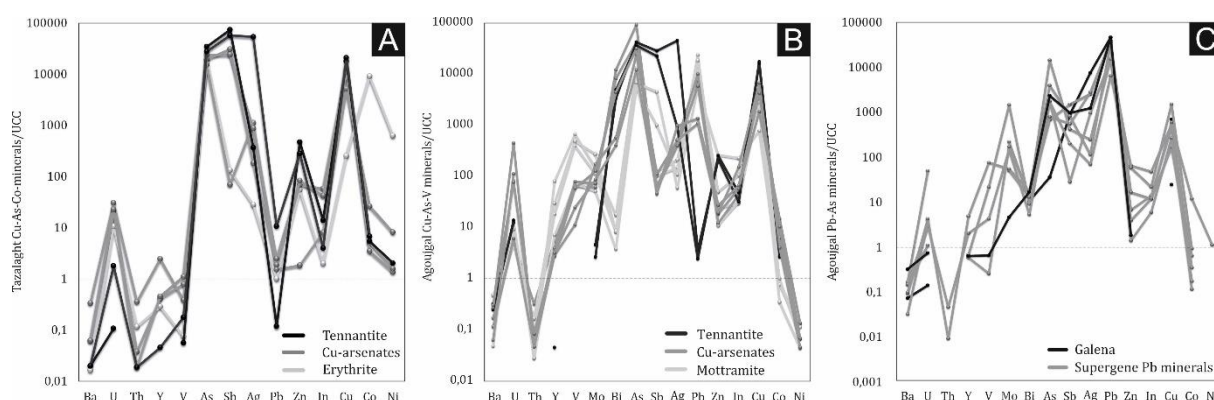


**Figure 5.3.10.** Geochemical data of sulfosalts, arsenates and sulfates of Tazalaght and Agoujgal deposits. (A) Trace elements patterns of Tazalaght Cu-As-Co minerals, with values normalized to the UCC (Taylor and McLennan, 1985); (B) Trace elements patterns of Agoujgal Cu-As-V minerals, with values normalized to the UCC (Taylor and McLennan, 1985); (C) Trace elements patterns of Agoujgal Pb-As minerals, with values normalized to the UCC (Taylor and McLennan, 1985).

**Table 5.3.2.** Results of geochemical analyses for tennantite, Cu-arsenates, Cu-vanadates, and supergene Pb ores of Tazalaght and Agoujgal. Minor elements and REE are listed in ppm. For minor elements, values in italics correspond to very rich samples, and have been quantified in % and here given in ppm for more clarity.

Oxide/ Element	Samples																								
	Tennantite 18 AG 23A	Tennantite 18 AG 23B	Cu-arsenates 18 AG 24A	Cu-arsenates 18 AG 24B	Cu-arsenates 18 AG 24C	Cu-vanadates 17 AG 16	Cu-vanadates 17 AG 26	Cu-vanadates 18 AG 07	Cu-vanadates 18 AG 01	Cu-arsenates 18 AG 18	Galena 18 AG 06A	Supergene Pb ore 18 AG 02A	Supergene Pb ore 18 AG 02B	Supergene Pb ore 18 AG 03A	Supergene Pb ore 18 AG 04	Supergene Pb ore 18 AG 06C	Supergene Pb ore 18 AG 08	Supergene Pb ore 18 AG 09	Supergene Pb ore 18 AG 10	Tennantite 18 TAZ 18A	Tennantite 18 TAZ 18E	Cu-arsenates 18 TAZ 06	Cu-arsenates 18 TAZ 16A	Cu-arsenates 18 TAZ 16B	Erythrite 17 TAZ 07C
FeO	4.4	2.7	<0.1	<0.1	0.3	<0.1	<0.1	<0.1	<0.1	0.7	<0.1	<0.1	<0.1	<0.1	<0.1	0.4	0.3	<0.1	<0.1	0.9	1.6	0.8	0.5	<0.1	0.7
SiO <sub>2</sub>	0.76	4.33	4.49	0.55	1.42	2.45	3.97	13.82	26.74	1.5	0.41	7.73	11.8	0.21	5.38	42.17	0.2	1.03	0.12	0.03	1.2	34.2	0.12	0.13	16.14
Al <sub>2</sub> O <sub>3</sub>	0.01	<0.01	2.56	0.14	1.2	1.87	0.93	1.14	3.66	0.94	<0.01	1.84	4.51	0.02	1.17	0.05	0.01	0.35	0.02	<0.01	0.85	6.98	0.35	0.21	2.37
Fe <sub>2</sub> O <sub>3</sub>	0.65	1.06	41.5	22.02	39.44	20.54	8.51	56.62	13.09	13.34	0.03	27.51	10.02	12.59	65.11	6.6	10.53	3.97	0.57	0.96	0.48	5.16	12.59	10.45	2.06
MnO	0.015	0.01	0.491	0.127	0.134	0.196	0.046	0.021	0.108	0.16	0.003	0.013	0.032	0.005	0.027	0.027	0.004	0.037	0.005	0.004	0.007	0.004	0.004	0.005	0.05
MgO	0.16	0.04	3.46	0.11	0.6	1.48	0.18	0.38	2.06	1.07	<0.01	0.2	0.83	<0.01	0.26	0.04	<0.01	0.18	0.02	<0.01	0.14	0.17	0.08	0.04	2.56
CaO	1.07	1.97	7.33	10.72	8.68	8.3	1.58	0.44	1.45	9.46	0.03	1.3	1.23	0.08	0.51	1.41	0.06	5.9	1.2	0.02	0.1	0.29	0.83	4.96	0.63
Na <sub>2</sub> O	<0.01	<0.01	0.04	0.03	0.05	0.02	0.02	0.04	0.14	0.03	<0.01	0.07	0.09	<0.01	0.05	0.02	<0.01	0.02	<0.01	<0.01	0.01	0.03	<0.01	<0.01	0.01
K <sub>2</sub> O	<0.01	<0.01	<0.01	<0.01	0.03	0.01	0.11	<0.01	0.45	0.01	<0.01	0.01	0.82	<0.01	0.08	<0.01	<0.01	0.05	<0.01	<0.01	0.07	0.66	<0.01	<0.01	0.03
TiO <sub>2</sub>	0.001	<0.001	0.362	<0.001	0.042	0.06	0.023	0.043	0.127	0.043	<0.001	0.02	0.139	<0.001	0.031	<0.001	<0.001	0.008	0.001	<0.001	0.017	0.072	<0.001	<0.001	0.011
P <sub>2</sub> O <sub>5</sub>	0.02	0.01	2.06	1.27	1.23	1.23	1.18	0.9	1.54	1.29	0.02	3.38	1.07	0.17	1.71	1.05	0.13	14.38	2.82	0.01	0.09	0.22	0.13	0.33	0.25
LOI	11.27	10.43	8.95	6.09	8.17	7.13	4.54	9.02	5.09	5.74	1.57	25.71	10.52	14.74	12.13	4.83	15.53	4.71	13.54	16.59	13.17	8.1	14.46	11.61	19.28
S	9.07	7.29	0.11	0.04	0.11	0.06	0.04	0.03	< 0.01	0.03	8.92	7.39	1.69	0.53	1.46	0.04	0.87	0.18	0.52	26.3	21.5	0.56	0.06	0.08	0.02
SO <sub>4</sub>	N.D.	N.D.	N.D.	N.D.	N.D.	N.D.	N.D.	N.D.	N.D.	N.D.	N.D.	23.2	5.02	1.55	4.14	0.16	2.56	0.51	1.53	N.D.	N.D.	N.D.	N.D.	N.D.	N.D.
Sr	14	30	71	38	176	82	28	24	42	44	77	58	39	26	42	61	43	162	59	<2	12	237	4	13	45
Ba	179	138	150	35	167	95	147	27	178	64	41	83	266	52	92	18	83	55	180	11	11	184	34	34	9
U	34.5	39.0	1260.0	313.0	217.0	14.6	37.1	231.0	25.6	17.2	0.4	8.5	13.1	8.1	140.0	11.2	3.1	12.0	2.1	0.3	5.0	85.6	58.9	63.2	29.8
Th	<0.05	<0.05	0.5	<0.05	0.9	3.47	0.31	0.3	0.9	0.5	<0.05	0.5	1.8	<0.05	<0.05	<0.05	<0.05	0.1	<0.05	<0.05	0.2	3.8	0.4	0.2	1.24
Y	1	<1	64	61	70	118	1770	156	403	87	<1	45	660	<1	15	13	<1	108	14	<1	1	54	9	10	6.3
Zr	<1	<1	147	32	64	57	217	43	188	60	3	20	261	<1	22	5	<1	10	3	3	10	84	27	11	9
Hf	<0.1	<0.1	2.2	0.4	1.1	1.2	2.5	0.6	1.7	1.0	<0.1	0.3	2.4	<0.1	0.4	<0.1	<0.1	0.3	<0.1	<0.1	0.2	2.4	0.2	<0.1	0.4
Sc	2	2	19	7	41	16	124	13	31	15	<1	2	51	<1	2	2	<1	5	<1	2	2	3	7	4	<1
V	<1	<1	1221	6242	2657	6960	71810	7701	42540	8484	<1	464	52380	<1	2349	28	<1	8166	71	6	19	41	84	119	8
Cr	<20	20	40	40	30	50	400	130	250	30	<20	30	270	<20	50	100	<20	80	<20	<20	<20	<20	<20	<20	<20
W	<0.5	<0.5	6.0	2.0	3.0	<0.5	5.8	3.0	5.0	3.0	<0.5	2.0	2.0	<0.5	2.0	2.0	<0.5	<0.5	<0.5	<0.5	<0.5	<0.5	<0.5	<0.5	1.7
Mo	7	4	260	190	130	91	220	77	170	110	<2	220	410	330	2190	260	76	83	7	<2	26	1780	710	450	190
Bi	437.0	637.0	74.7	576.0	53.0	1580	2.3	0.5	1.1	1070	1.4	0.7	1.1	1.6	1.2	1.7	1.7	2.3	2.2	20.7	10.5	93.8	129.0	55.0	10.2
As	62800	54600	36400	47300	18000	138000	19600	10100	8000	62800	54	2600	10100	1020	2600	21800	1200	5900	3500	51900	41900	22800	29100	36000	29400
Sb	5700	4500	22.2	11.2	9.2	11.9	20.6	900	200	12.7	182.0	5.7	25.4	300	40.5	83.8	111.0	164.0	194.0	14800	11500	13.9	6200	4800	26.7
Ag	2260	45.7	25.4	19.9	48.8	24.6	7.4	3.0	5.5	26.2	379.0	48.2	10.6	128.0	3.5	12.4	139.0	5.8	61.9	18.4	2700	56.0	9.2	44.0	1.4
Pb	61	42	18400	99200	23100	127000	401000	95200	236000	170000	790000	266000	314000	659000	110000	260000	669000	597000	784000	2	183	26	32	42	17

Zn	15300	18100	1320	1380	1930	850	1720	18600	3570	870	<30	480	790	280	4630	4170	100	1180	130	33500	20000	130	4840	5870	3900
In	1.6	2.4	2.9	7.6	3.3	1.6	1.5	11.4	5.3	2.2	<0.1	0.7	1.6	0.6	2.4	1.1	0.3	0.6	<0.1	0.7	0.2	0.4	2.9	2.1	0.1
Cu	438000	413000	46300	167000	106000	102000	134000	19600	63400	135000	17500	11700	70800	4210	13500	37700	6720	14900	620	449000	528000	130000	307000	282000	6280
Co	46	47	253	69	177	141	14	17	13	107	<1	2	6	11	203	16	3	6	<1	92	116	450	59	87	155000
Ni	<20	<20	<20	<20	30	30	<20	<20	<20	20	<20	<20	<20	<20	50	<20	<20	<20	<20	90	<20	360	60	70	27600
Ga	<1	<1	4	1	2	17	2	14	9	3	<1	4	6	<1	4	1	<1	2	<1	<1	1	5	2	2	4
Ge	<0.5	<0.5	1.0	<0.5	<0.5	2.4	1.5	44.0	8.0	<0.5	<0.5	<0.5	<0.5	<0.5	3.0	1.0	<0.5	<0.5	<0.5	<0.5	<0.5	<0.5	<0.5	<0.5	0.6
La	0.9	0.3	57.1	13.9	171.0	917.0	62.1	9.7	36.2	119.0	0.1	30.3	145.0	0.2	26.5	9.0	0.1	24.8	0.2	0.2	0.8	10.1	0.9	0.8	3.59
Ce	1.6	0.3	64.6	4.1	187.0	1530.0	11.0	7.6	28.9	233.0	0.1	9.2	43.3	0.4	7.3	17.7	0.3	12.4	0.3	<0.05	0.9	23.1	0.4	0.8	7.87
Pr	0.18	<0.01	10.4	5.27	30.5	156.0	18.3	2.89	13.1	28.2	<0.01	7.97	24.1	0.05	3.66	2.42	<0.01	6.75	0.05	<0.01	0.1	2.8	0.32	0.28	1.08
Nd	0.8	0.2	42.3	26.3	112.0	511.0	98.3	14.9	65.0	112.0	<0.05	36.0	105.0	0.2	13.4	10.9	0.2	32.8	0.2	<0.05	0.4	10.9	1.7	1.5	4.71
Sm	0.2	<0.01	10.0	7.1	19.8	61.8	34.8	5.3	21.7	21.9	<0.01	6.9	30.6	<0.01	3.1	2.7	<0.01	9.9	<0.01	<0.01	0.2	2.6	0.9	0.6	1.47
Eu	0.0	0.0	4.21	1.93	6.33	8.22	11.8	1.46	6.24	4.95	0.0	1.42	8.82	0.0	0.74	0.75	0.0	2.38	0.0	0.0	0.0	0.33	0.29	0.2	0.233
Gd	0.2	<0.01	11.6	9.6	15.6	33.8	91.0	10.1	36.7	19.5	<0.01	7.4	57.8	<0.01	3.3	3.7	<0.01	12.0	<0.01	<0.01	0.2	5.7	1.6	1.4	1.59
Tb	<0.01	<0.01	1.8	1.5	2.5	4.03	19.6	2.1	6.9	2.7	<0.01	1.0	11.1	<0.01	0.5	0.5	<0.01	2.0	<0.01	<0.01	<0.01	1.6	0.4	0.3	0.24
Dy	0.2	<0.01	11.4	9.4	15.3	20.8	169.0	16.0	52.7	16.3	<0.01	6.1	84.0	<0.01	3.0	2.3	<0.01	12.2	0.3	<0.01	0.2	11.2	2.4	2.1	1.21
Ho	<0.01	<0.01	2.3	2.1	3.0	4.06	44.3	4.1	12.7	3.3	<0.01	1.2	20.1	<0.01	0.6	0.4	<0.01	2.6	0.1	<0.01	<0.01	2.2	0.5	0.4	0.25
Er	0.1	<0.01	7.0	5.9	9.2	10.7	138.0	12.6	36.7	9.2	<0.01	3.1	58.0	<0.01	1.5	1.2	<0.01	7.3	0.5	<0.01	<0.01	5.8	1.2	1.3	0.74
Tm	<0.005	<0.005	0.93	0.71	1.31	1.31	19.6	1.87	4.89	1.2	<0.005	0.36	7.88	<0.005	0.18	0.15	<0.005	1.06	0.09	<0.005	<0.005	0.73	0.19	0.2	0.106
Yb	<0.01	<0.01	7.3	4.9	9.6	7.43	125.0	11.5	31.3	7.2	<0.01	1.8	49.2	<0.01	1.0	1.0	<0.01	5.8	0.6	<0.01	<0.01	4.2	1.2	1.3	0.64
Lu	0.01	<0.005	1.24	0.76	1.38	1.02	18.00	1.78	4.52	1.02	<0.005	0.26	7.52	<0.005	0.15	0.15	<0.005	0.88	0.09	<0.005	0.01	0.58	0.16	0.18	0.093

N.D.: no data

Major elements oxides are expressed in %.

Minor elements and REE are listed in ppm. Values in *italics* have been quantified in % and are here given in ppm for more clarity.

### **5.3.4. Discussion**

The development of weathering profiles mostly results from the concurrent actions of leaching fluids, tectonic uplift and brittle fracturing, under wet and warm climates (Boni and Mondillo 2015). The typical succession from bottom to top of supergene copper deposits, composed of the 1) primary sulfide zone, 2) secondary sulfides enrichment (cementation) zone, 3) oxidized zone, and 4) leached zone (gossan), has already been described by many authors (e.g. De Putter et al., 2010; Taylor, 2011; Arndt and Ganino, 2012; Verhaert et al., 2017). The extension of the weathered profile depends on the initial acidity of fluids, the nature and amount of hypogene minerals, the neutralizing capacity of host rocks, and the density and extent of fracturing (Takahashi 1960; Bladh 1982; Sangameshwar and Barnes 1983; Scott et al. 2001; Reichert and Borg 2008; Choulet et al. 2019; Fontaine et al. 2020). Even though some authors (Boni and Mondillo 2015; Choulet et al. 2019) suggest, mostly for Zn deposits, the influence of low temperature hydrothermal fluids predating the strictly supergene phases, nothing here indicates that this is the case at Tazalaght or Agoujgal.

#### **5.3.4.a Controls of host rocks on the supergene processes**

The nature of secondary mineral phases and the extension of mineralogical zones strongly depend on the composition of primary sulfides and host rocks where carbonates and chlorites may buffer the acidity of mineralizing fluids. Their dissolution in contact with  $H^+$  ions induces the mobilization of alkaline and bicarbonate ions, or the formation of clay minerals such as kaolinite and smectite. At Tazalaght, most of the mineralization is hosted in quartzite and quartzitic breccia, with very low carbonates and chlorite concentrations. Their low buffering capacity is responsible for the contrast between the limited extension of the oxidized zone and the much larger secondary sulfides zone. The relative abundance of secondary sulfides suggests that the neutralization of weathering fluids was not sufficient to reach neutral pH conditions and to jeopardize their access to the water table level. The slightly acidic and reduced conditions prevailing in that zone triggered sulfide precipitation and prevented the formation of oxidized phases.

On the contrary, Agoujgal's mineralization is mostly hosted by dolomitic sandstone and dolomite that contain carbonates in sufficient quantities to allow the neutralization of acidic fluids. The oxidized zone is thus much more extended than at Tazalaght, while its secondary sulfides zone is uneven and limited in space, due to the sufficient buffering of weathering fluids through carbonates dissolution and to the subsequent rapidly prevail of oxidizing conditions. The higher degree of weathering and the larger amount of supergene products at Agoujgal, in comparison with Tazalaght, also indicate a more intense acidic leaching and a subsequent more efficient acidity buffering. The formation or widening of dissolution cavities in carbonate rocks most probably increased both their permeability and porosity, and provided preferential drains for fluids and spaces (Decrée et al. 2010a) for more extended secondary mineral precipitation (Fig. 5.3.5A) than at Tazalaght. For instance, the precipitation of malachite amounts of economic significance by the recombination of bicarbonate and  $Cu^{2+}$  ions in cavities, fractures, and porosity of the host rock was only possible after the neutralization of acidic fluids (Fig. 5.3.4F). At Agoujgal, close to the granite, the mineralization is hosted by alternating sandstones and siltstones that contribute to a lesser extent to the buffering of the fluids acidity. There, the slightly more acidic conditions were optimal for the formation of Cu-Pb arsenates and sulfates.

### 5.3.4.b Role of hypogene minerals

The hypogene ore has a precursor role in the releasing of metals and other species that may influence secondary processes. At Tazalaght and Agoujgal, primary minerals are sulfides whose stability domains are limited to reduced environments. As highlighted by Bladh (1982), the nature of sulfides and their susceptibility to oxidation determines the sequence of sulfides weathering, the consequent availability of metals for transport and the nature of secondary minerals. The weathering of sulfides by fluids percolating *per descensum* induces the release of cations (Cu, Fe, Pb, ...) and ligands ( $\text{SO}_4^{2-}$ ,  $\text{CO}_3^{2-}$ ,  $\text{OH}^-$ ,  $\text{PO}_4^{2-}$ , ...). The natural acidity of weathering fluids may be variably amplified during sulfides oxidation: the combination of sulfate, hydrogen anions and atmospheric oxygen results in the formation of sulfuric acid. The generation of such acid solutions mainly depends on the reduced sulfur to metal ratio of sulfides (Chavez 2000): the oxidation of iron-poor sulfides releases modest quantities of acid solutions. At the contrary, the stepwise oxidation of pyrite produces significant amounts of sulfuric acid that may induce, locally, substantial drops of pH and the extensive destruction of sulfides. Moreover, the release and oxidation of ferrous to ferric iron during pyrite dissolution enhance the oxidation of sulfides by catalyzing this process (Chavez 2000; Reichert and Borg 2008). The more intense weathering of Agoujgal's area, in comparison with Tazalaght, most probably results from the large amounts of pyrite in the hypogene ore. The presence of  $\text{Fe}^{2+}$ -bearing silicates such as biotite in Agoujgal's granite also probably contributed to the generation, close to this magmatic unit, of acidic solutions and to the precipitation of Cu-Pb arsenates and sulfates that require (slightly) acidic environments. At Tazalaght, although only small amounts of tennantite remain, the omnipresence of arsenates confirms that the sulfosalt was one of the major components of the hypogene ore, along with chalcopryite, bornite and pyrite (Fig. 5.3.4C, 5.3.4D, 5.3.6A). Two main hypogene sulfides are present at Agoujgal: stratabound euhedral pyrite, and chalcopryite associated with minor galena and tennantite, in veins and lenses. The very scarce other sulfides (e.g. bismuthinite, matildite) most probably result from local variations in the mineralizing fluids. At both sites, the varying Zn and Sb contents of tennantite ensue from the common substitution of these elements for Cu and As (Nickel et al. 2007; George et al. 2017).

### 5.3.4.c Weathering profile and paragenetic sequence

In the cementation zone of both deposits, chalcopryite is successively weathered to bornite, chalcocite and covellite when conditions become less and less reduced (Fig. 5.3.11, 5.3.12B) (Ague and Brimhall 1989). The much rarer direct replacement of chalcopryite by chalcocite or covellite suggests the circulation of Cu- and Fe-depleted fluids and probably slightly more oxidizing conditions (Fig. 5.3.6B, 5.3.6C, 5.3.12B). As weathering continues, released Fe and Cu precipitate close to the sulfides, in iron (oxyhydr-)oxides and malachite (Fig. 5.3.4F), leading to the formation of a typical supergene boxwork texture, as previously observed in quite similar Cu supergene ores (Fontaine et al. 2020). There, chalcocite and minor covellite are brecciated by a lattice of malachite and goethite veinlets (Fig. 5.3.6A).

Minerals	Hypogene	Supergene		
	Primary sulfides	Secondary sulfides	Oxidized zone	Leached zone
Pyrite	████████			
Chalcopyrite	████████			
Galena	=====			
Tennantite	=====			
Rare other sulfides	=====	= arsenopyrite, cobaltite, bismuthinite, sphalerite, matildite, greenockite, kobellite		
Bornite		----		
Chalcocite/djurleite		=====	=====	
Covellite		=====	=====	
Acanthite + stromeyerite		-----	=====	
Malachite			████████████████████	
Chrysocolla			-----	
Ag-chalcocite			-----	
Barite			-----	
Olivinite			=====	
Conichalcite			████████████████████	
Chenevixite			=====	
Barahonaite/Lukrahnite			-----	
Brochantite				-----
Native Ag			-----	
Yukonite			=====	
Arseniosiderite			=====	
Anglesite			=====	
Cerussite			-----	
Phosphohedyphane			-----	
Plumbojarosite			=====	
Fe-osarizawaite			=====	
Calcio-duftite			-----	
Mimetite			=====	
Fe-gartrellite			-----	
Calcio-volborthite			-----	
Mottramite				=====
Iodargyrite			-----	
Hematite			████████████████████	=====
Goethite			-----	=====
Powdery Mn oxides				-----
Quartz			=====	=====
Calcite			=====	=====
Beaverite				---

**Figure 5.3.11.** Paragenetic sequence for Agoujgal and Tazalaght deposits. The fluids pH increases from left to right, but microenvironments with variable acidity may coexist locally, disturbing this pH evolution on a small scale. The dotted lines indicate the rare occurrence of some minerals of which the stability domains limits are difficult to precise. “Rare other sulfides” stands for arsenopyrite, cobaltite, bismuthinite, shalerite, greenockite, kobellite and gersdorffite.

Above the water table denoting a transition from reduced to oxidized conditions, the oxidized zone of Tazalaght hosts carbonates, silicates, arsenates and oxides (Fig. 5.3.11, 5.3.12B). At Agoujgal, the wider variety of secondary minerals including carbonates, sulfates, silicates, arsenates, phosphates, vanadates, oxides, and sporadically halides (Fig. 5.3.11) denote their formation under strongly varying chemical conditions, over an appreciable pH range (Fig. 5.3.12A), and from solutions of complex compositions (Radková et al. 2017). Supergene minerals involving copper are ubiquitous at both deposits, since its high mobility and solubility in oxidized and acidic fluids enable its transport as a cation over long distances before precipitation (Verhaert et al. 2017). At the contrary, lead minerals are confined in small areas of Agoujgal’s deposit, since lead behaves as an immobile element in oxidized environments. In most cases, galena is replaced *in situ* by an armoring of insoluble weathering products that partially hinders contact with oxidizing agents and thus protects the sulfide from further

weathering (Hitzman et al. 2003; Reichert and Borg 2008). The broader stability of malachite under atmospheric conditions is responsible for its predominance over azurite, although they share very close chemical compositions. Malachite precipitation requires low  $\text{CO}_2$  partial pressures ( $P_{\text{CO}_2} < 10^{-2}$ ), restricted copper activities ( $a_{\text{Cu}} < 10^{-2}$ ), oxidizing and neutral to basic pH conditions, and thus preliminary neutralization of the acidity (Vink 1986; De Putter et al. 2010; Howell 2014). The formation of azurite necessitates a more acidic environment and higher carbonate ion activities and  $\text{CO}_2$  partial pressures (Vink 1986). The quite late and scarce occurrence of unidentified copper silicates at Tazalaght and of brochantite and chrysocolla at Agoujgal suggests the local circulation of slightly acidic fluids, maybe resulting from the dissolution of chalcocite (Chavez 2000).

In the uppermost gossan, most mobile elements are leached from the primary mineralization, and almost only iron (oxyhydr-)oxides remain (Fig. 5.3.4H, 5.3.11). Agoujgal gossan is very similar to that of Tazalaght, considering the ubiquity of iron (oxyhydr-)oxides, i.e. hematite and goethite, pseudomorphosing pyrite (Fig. 5.3.4H, 5.3.5F). The numerous pseudomorphs and the low amount of late botryoidal goethite suggest the *in situ* oxidation and replacement of pyrite, under semi-arid and arid climate conditions. The mere presence of goethite and hematite not only in the leached zone, but also in the entire supergene profile of both deposits, arises from their large stability ranges extending from very acidic to basic pH and from oxidizing to slightly reduced environments (Verhaert et al. 2018). Along with some botryoidal goethite, calcite and mottramite are the last phases that precipitated in significant amounts at Agoujgal (Fig. 5.3.11). The late greenish calcite of Agoujgal, which owes its color from the absorption of remaining aqueous copper, formed at the very end of the sequence, after efficient carbonate rocks dissolution and a strong increase in pH conditions (Fig. 5.3.5E) (Howell 2014). At Tazalaght, the poorly crystallized iron and manganese (oxyhydr-)oxides precipitating in fractures are probably very recent. Their high Zn, Cu, Co and Ni concentrations arise from the incorporation of these metal ions in the crystalline lattice, and/or to their adsorption as oxides behave as high-surface-area substrates (Manceau et al. 1992; Dong et al. 2000; Feng et al. 2007; Decrée et al. 2010b).

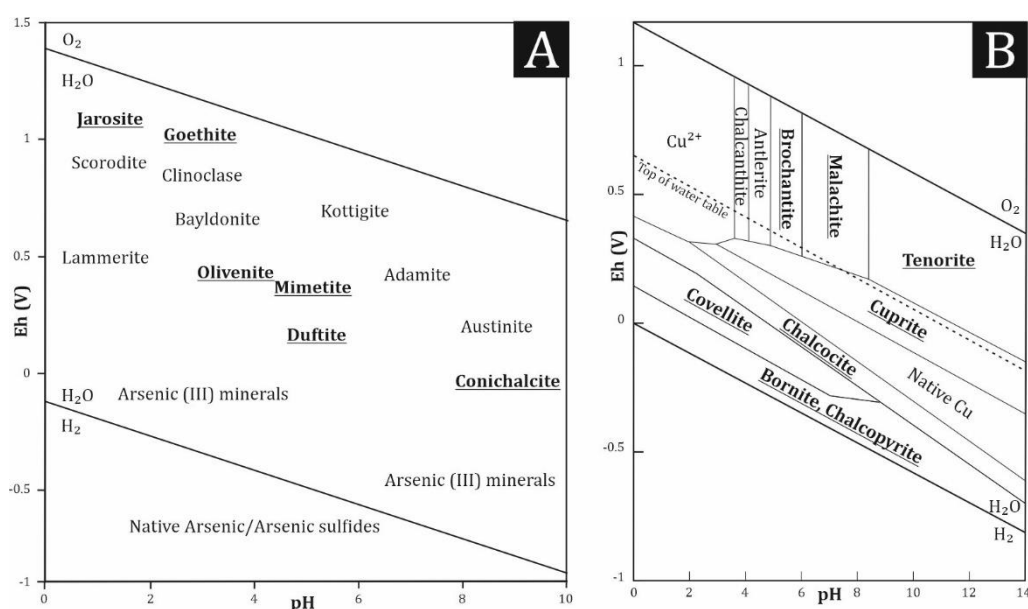


**Figure 5.3.12.** (A) Schematic Eh-pH diagram showing relative stability fields for common arsenate and arsenite mineral species, highlighting the stability of jarosite group minerals under strongly acidic and oxidizing conditions, of olivenite, mimetite, and duftite under slightly acidic conditions, and of conicalcrite under neutral to slightly basic conditions (modified after Howell, 2014). (B) Eh-pH diagram for a part of the Cu-C-S-Si-O-OH system, showing the stability fields of selected copper minerals at 25°C and 1 atm (modified after Guilbert and Park, 1986).



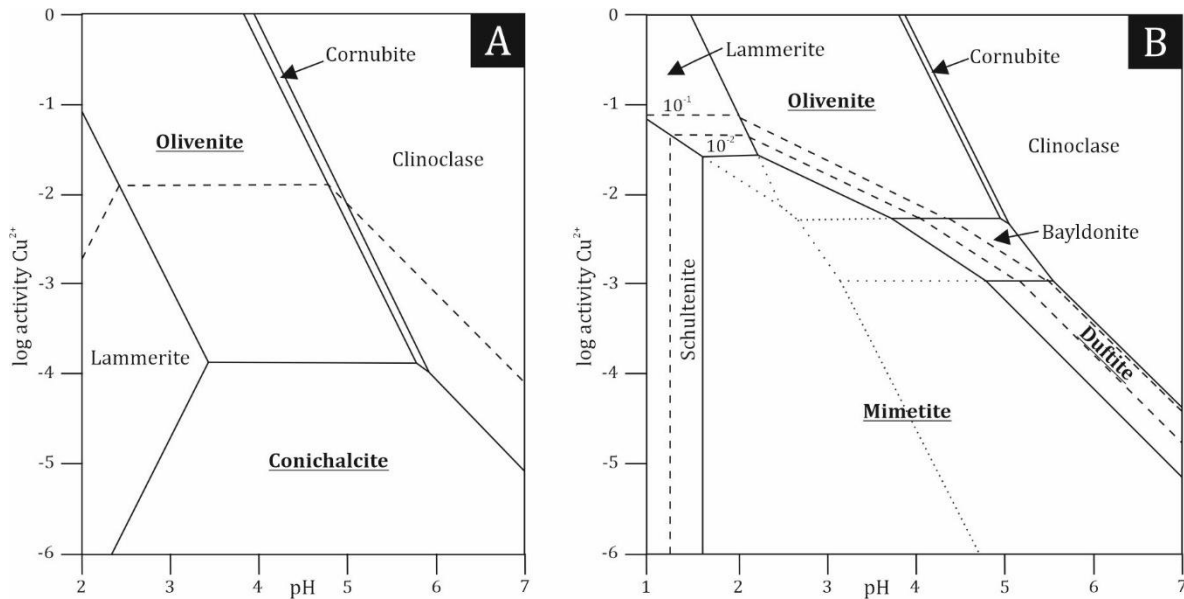


**Figure 5.3.13.** (A) Eh-pH diagram for a part of the Cu-Ca-As-P-O-H system, showing the stability fields of selected Cu arsenates at 25°C and 1 atm (modified after Magalhães et al., 1988). The assumed activities of dissolved species are  $a_{\text{Ca}^{2+}} = 10^{-5}$  (full lines) and  $10^{-3}$  (dashed lines). As observed at Tazalaght and Agoujgal, adding even small amount of Ca will strongly modify the stability field of olivenite and conichalcite and favor the precipitation of the latter. (B) Eh-pH diagram for a part of the Cu-Ca-Pb-As-P-O-H system, showing the stability fields of selected Cu and Pb arsenates at 25°C and 1 atm (modified after Inegbenebor et al., 1989). The assumed activities of dissolved species are for the full lines  $a_{\text{Pb}^{2+}} = 10^{-7}$  and  $a_{\text{Cl}^-} = 10^{-3}$ . The dotted lines give information about the phase boundaries in the absence of chloride ion, while the dashed lines indicate the effects of the increase of its activity ( $a_{\text{Cl}^-} = 10^{-2}$  and  $10^{-1}$ ). As observed at Agoujgal, the occurrence of olivenite, mimetite, conichalcite or Duftite, is mostly related to the activities or their metal components.

#### 5.3.4.d Mechanisms for Cu-arsenates formation

At Tazalaght and Agoujgal, the precipitation of various secondary minerals and the common association of arsenates and carbonates such as malachite (Fig. 5.3.4G) suggest that their formation arise from varying physical-chemical conditions of the environment, i.e. pH (acidity) and Eh (redox potential), and complex evolving aqueous concentrations (Magalhães et al., 1988; Fig. 5.3.12A, 5.3.12B). The nearly coeval occurrence of arsenates and malachite (Fig. 5.3.8B) also results from the wide pH stability ranges of these phases (Magalhães et al. 1988; Gołębiowska et al. 2006). Some As-oxidized specimens enclose relics of primary tennantite (Fig. 5.3.6D-5.3.6G, 5.3.6J), others are completely weathered and contain no remnant of the primary ore (Fig 5.3.6H). The weathering of tennantite is similar at Tazalaght and Agoujgal, in terms of processes, but secondary resultant phases vary since arsenates are sensitive to Eh and pH changes (Bowell 2014). The oxidation of tennantite mostly results in an open cellular boxwork pattern (Fig. 5.3.6F) where several weathering stages are easily identified, which reflects a stepwise change of the oxidation potential of fluids interacting with the hypogene material (Nickel et al. 2007; Keim et al. 2018). Similarly to what was noticed at the Bari Lo prospect (Australia) and in the Schwarzwald (Germany) (Nickel et al. 2007; Keim et al. 2018), arsenates firstly form an irregular network of veinlets that follow crystallographic planes such as cleavage planes (Fig. 5.3.6H) or that are curved without any particular directions (Fig. 5.3.6D). Then, veinlets widen into larger veins by dissolving, brecciating and isolating tennantite remnants (Fig. 5.3.6F). Ultimately, arsenates and oxidized phases completely replace the primary sulfosalt and fill cracks, cavities and fractures into the host rocks and the neighboring mineralization (Fig. 5.3.6F). At Tazalaght and Agoujgal, the boxwork cell walls consist of intergrown arsenates, while cells are filled



with various oxidized minerals including malachite, olivenite, conichalcite, hematite and goethite, or left empty.

Two sequences of tennantite oxidation are identified at Tazalaght: 1) Zn-tennantite → chalcocite later weathered to malachite → Zn-olivenite → Sb-chenevixite → malachite, or 2) Zn-tennantite → chalcocite later weathered to malachite → Sb-chenevixite → Zn-olivenite (Fig. 5.3.11). Olivenite and chenevixite, of which the association has already been observed by Frost et al. (2014), occur in a wide variety of forms, often intergrown, as rims around tennantite or as cell walls (Fig. 5.3.6D-5.3.6G). The presence of at least two generations of olivenite is substantiated by its less common occurrence as euhedral crystals surrounded by malachite (Fig. 5.3.6K), aside from its association with chenevixite. Conichalcite rarely inserts before malachite, as a cavity-filling phase (Fig. 5.3.6H). The eventual initial precipitation of chalcocite along the veins and around gangue minerals, before or together with arsenates (Fig. 5.3.6D, 5.3.6J), has also been observed by Nickel et al. (2007) and by Keim et al. (2018). The local coexistence of arsenates and chalcocite reflects relatively high oxygen fugacity, but an Eh potential that is not sufficient to directly weather the sulfide (Keim et al. 2018). At Agoujgal, tennantite is successively weathered into copper sulfides, several generations of arsenates, carbonates and oxides, often resulting in specimens composed of earthy arsenate aggregates mixed with powdery goethite and hematite (Fig. 5.3.5B). Following the formation of chalcocite at the contact with tennantite (Fig. 5.3.8A), the development of the oxidizing front continues with the precipitation of euhedral olivenite and conichalcite, and with a second generation of olivenite, conichalcite, and malachite (Fig. 5.3.8A-5.3.8F). Beside this general and most common sequence, goethite, yukonite and arseniosiderite form the skeleton of pseudomorphs that are later filled with conichalcite, malachite, mottramite and late quartz, indicating the *in situ* replacements of previous minerals (Fig. 5.3.8G, 5.3.8H). Calcium and iron arsenates such as yukonite typically form from  $\text{Ca}^{2+}$  rich fluids, under oxidizing, neutral pH conditions (Gołębiewska et al. 2006; Radková et al. 2017). The relative immobility of Fe and mobility of Cu in supergene fluids explain the rapid precipitation of iron arsenates along cleavage planes and fractures and the later precipitation of copper phases. The rare inverse weathering sequence consisting of successive malachite, olivenite and conichalcite suggests local variations of Eh-pH conditions at Agoujgal.

The presence of clinoclase was expected at both sites. Under atmospheric conditions, malachite takes predominance over azurite, and clinoclase is usually predicted to be more stable than olivenite (Bowell 2014). However, at Tazalaght and Agoujgal, the formation of olivenite was by all accounts favored by a lower pH (pH 2 – 6), at the expense of clinoclase which precipitates under more neutral conditions (pH > 4; Fig. 5.3.13A) (Bowell 2014). Conichalcite is a common associate of olivenite at Agoujgal, but is rare in the oxidized zone of Tazalaght. Its occurrence at Agoujgal is related to the dissolution of carbonate rocks and to the ensuing presence of reasonably small amounts of  $\text{Ca}^{2+}$  in a neutral solution, which tends to extend the thermodynamic stability field of conichalcite upon that of olivenite (Fig. 5.3.13A) (Magalhães et al. 1988; Gołębiewska et al. 2006). The relative scarcity of carbonate rocks at Tazalaght and the consequent low  $\text{Ca}^{2+}$  activity promoted the precipitation of olivenite and limited the stability field of conichalcite (Gołębiewska et al. 2006) (Fig. 5.3.11, 5.3.13A). At Tazalaght, the local Co-enrichment of olivenite and malachite results from the weathering of scarce cobaltite grains, together with chalcopyrite, bornite and tennantite (Fig. 5.3.6K). The local singular occurrence of heterogenite, cobaltlotharmeyerite, erythrite and asbolane, atypical in this quite restricted mineralization, is supposed to derive from the weathering of scarce Co-, Mn-, Ni-bearing sulfides (Fig. 5.3.6K, 5.3.6L). The high Ni and Mg contents of erythrite are related to its solid solution with annabergite and hornesite, respectively.

Tazalaght and Agoujgal deposits share major geochemical trends, even if they differ on some base metal contents. Tazalaght ores concentrate Cu, As, Co and Zn, while Cu, As, Pb, V and Zn are the elements most found at Agoujgal. The varying Fe, Sb, Ag, Pb and Zn contents arise from the adsorption and intake of these elements into the crystalline structure of minerals. The contrasting Zn- and Sb-enrichment of olivenite and iron arsenates, respectively, is a characteristic trend of both deposits. The Zn initially present in tennantite is mostly included in olivenite, but has also been transported by weathering solutions away from its source, since Zn is a more mobile element than Cu (Keim et al. 2018). Olivenite commonly contains Zn, as it forms an unlimited solid solution with its Zn-analog adamite (Bowell 2014). However, Zn never prevails over Cu in Tazalaght and Agoujgal arsenates, and the Zn content is insufficient to form adamite. The fluids that circulated in the oxidized zone of both deposits were thus characterized by much higher Cu than Zn concentrations, which is corroborated by the fact that chalcopyrite, bornite and tennantite are very common in the primary ore, whereas sphalerite is only rarely recorded. Ionic Sb is less mobile than As, S, Cu, and Zn, which explains its direct coprecipitation, substitution and/or adsorption in/onto supergene minerals, i.e. iron arsenates such as chenevixite and oxides (Radková et al. 2017). The enrichment in U but depletion in Th of Tazalaght and Agoujgal oxidized ores is a typical supergene trend related to a selective mobilization during weathering processes. Soluble and mobile U is preferentially leached and accumulated in newformed minerals while immobile Th is retained in weathering-resistant minerals or rapidly incorporated in new-formed minerals (Braun et al. 1990; Pagel et al. 1990; Nicaise et al. 1996; De Putter et al. 2002). Even though Agoujgal's tennantite is locally rich in Ag, arsenates and other weathering products only sparsely incorporate this element. After its release during the dissolution of tennantite, Ag is removed as soluble ions and complexes, and reprecipitated as distinct mineral phases (Keim et al. 2016). The precipitation of acanthite and stromeyerite grains between the Ag-rich sulfosalt and chalcocite has already been observed by Keim et al. (2018) in Germany. Native Ag and acanthite, which concentrate Ag in the oxidized ore of Agoujgal are typical of temperate climates (Guilbert and Park 1986) and are more likely to precipitate due to redox processes (Keim et al. 2016). Their association with barite crystals has already been notified by Stevko and Ozdin (2012) in the weathered Jasenie-Soviansko base metals deposits (Slovak Republic). Barite formed by recombination of sulfate from tennantite and Ba possibly derived from the dissolution of host rocks and gangue elements. The formation of iodargyrite, which is rare at Agoujgal and only associated with oxidized copper and iron minerals, is only possible in semi-arid to arid environments with elevated iodine concentration (Boyle 1997; Golebiowska et al. 2010; Keim et al. 2016). The absence of chlorargyrite at Agoujgal, which is usually more common in supergene environments and is an indicator of slightly moister climates (Boyle 1997), is probably related to low Cl concentrations in the mineralizing fluids.

#### **5.3.4.e Sequential formation of lead carbonates, sulfates, phosphates, arsenates and vanadates at Agoujgal**

At Agoujgal, the weathering sequence of galena follows varying schemes, the most common being: 1) galena → (covellite →) anglesite → cerussite (→ phosphohedyphane). However other sequences are also identified: 2) Fe-osarizawaite and plumbojarosite → phosphohedyphane → calcio-duftite; 3) mimetite → phosphohedyphane ↔ calcio-duftite → malachite; 4) calcio-duftite → cerussite → malachite; 5) mimetite → calcio-duftite → conichalcite (Fig. 5.3.11). These sequences suggest rapid and subtle variations in the activity of ions in aqueous solutions, involving the nearly coeval precipitation of carbonates, sulfates, phosphates and arsenates. Anglesite and cerussite commonly replace galena *in situ* (Fig. 5.3.9A), while sulfates and phosphates encrust former minerals or precipitate in veins (Fig. 5.3.9B). Anglesite forms if acidic conditions prevail (< 5 pH units) and if sulfate ion activity is high, while cerussite precipitates under slightly acidic (> 5 pH units) to basic conditions

after the buffering of the acidity. At Agoujgal, the relative scarcity of anglesite is probably related to the low amount of  $H^+$  ions released during galena weathering, to the subsequent relatively low acidity of fluids, and to the difficulty to maintain a low pH environment in a carbonate-hosted deposit (Szczerba and Sawłowicz 2009). The formation of covellite between galena and anglesite (Fig. 5.3.9A) results from the local occurrence of reduced conditions and to the probable presence of copper-rich inclusions in galena, and/or to the ubiquity of mobile copper-rich fluids in the entire deposit (Choulet et al. 2014). At Agoujgal, the formation of phosphohedyphane with the last phases of the secondary mineralization (Fig. 5.3.9B) results from the incompatibility and instability of base metal phosphates with sulfide ions (Nriagu 2011). Poorly soluble lead phosphates are the most thermodynamically stable lead minerals under supergene geochemical conditions, over a wide pH range; their formation requires only limited amounts of free phosphate ions that could most probably result here from gangue apatite dissolution (Cotter-Howells et al. 1994; Cotter-Howells 1996; Nriagu 2011; Keim and Markl 2015; Shevade et al. 2017). The anglesite – cerussite – lead phosphates sequence has also been observed in roadside systems (Nriagu 2011). The transformation of lead sulfates into phosphates, such as the precipitation of phosphohedyphane after osarizawaite and plumbojarosite, has also been observed by Cotter-Howells (1996). These phases share close compositions: beaverite and plumbojarosite form a solid solution with replacement of  $Fe^{3+}$  ions by  $Cu^{2+}$  or  $Zn^{2+}$  ions, or both, and only differ from osarizawaite in the Al content (Scott 1987). Such lead sulfates, stable in acidic environments and generally considered as mature Pb phases (Davis et al. 1993), frequently occur in the supergene oxidized zone of Pb-Zn deposits (Scott 1987). Sulfate complexes and metal ions involved in sulfates precipitation originate from hypogene sulfides while Ca and Al most probably derive from carbonates and phyllosilicates of the host rocks, respectively. Beaverite efflorescences are probably related to the recent post-mining extensive oxidation of ores. As stressed by Dill (2015, and references therein), supergene mineral assemblages that completely differ from the principal mineral association can grow in poorly ventilated mining galleries, shafts, and dumps, as a result of post mining oxidation. At Agoujgal, such surface encrustations may result from evaporation processes during the dry season, after sulfide oxidation inducing the circulation of acid mine drainage waters during more humid periods (Jambor et al. 2000; Harris et al. 2003). The stability fields of jarosite type minerals such as plumbojarosite, anglesite and cerussite suggest that several Pb-mineralizing events took place at Agoujgal. At least two events are clearly separated: an initial acidic event associated with the preliminary oxidation of sulfides, and a subsequent carbonate event after much of the (partial) neutralization of the acidity (Leverett et al. 2005).

The lead arsenates mimetite and calcio-duftite also occur at Agoujgal, in association with copper oxidized phases such as malachite, conicalcite, calcio-volborthite and mottramite (Fig. 5.3.9E). The spatially-limited occurrence of mimetite pseudomorphs suggests that this arsenate may replace galena during the first stages of weathering (Leverett et al. 2005; Sejkora et al. 2009) and implies the small-scale circulation of weakly saline fluids characterized by low  $Cu^{2+}$  activities (Inegbenebor et al. 1989). The replacement of mimetite by calcio-duftite is related to a drop of the Cl content, a small pH increase and a rise of  $Ca^{2+}$  and  $Cu^{2+}$  activities (Fig. 5.3.13B) while its later substitution by conicalcite ensues from a drop of  $Pb^{2+}$  activity and a rise of pH (Inegbenebor et al. 1989; Howell 2014). The rare association of phosphohedyphane and duftite, which seem to precipitate in similar pH and Eh conditions at Agoujgal, has been described by Kampf et al. (2006). The sequential precipitation of copper minerals after less soluble and more stable lead arsenates that are less dispersed in the secondary ore indicates an increase of  $Cu^{2+}$  activities during weathering and the later circulation of highly mobile copper rich fluids. The contrasting low and high Pb amounts of tennantite and Cu-arsenates, respectively, coupled to the low and high As content of galena and supergene Pb ores indicate the relatively simultaneous

weathering of galena and tennantite at Agoujgal, resulting in the mixing of fluids and in the precipitation of mixed secondary ores containing various base metals (Fig. 5.3.10B, 5.3.10C).

The occurrence of late mottramite irregularly scattered in Agoujgal oxidized ores, as veins cutting the entire oxidized mineralization, overgrowing walls of dissolution cavities, and precipitating with late botryoidal goethite (Fig. 5.3.5D) corroborates the observation of Boni et al. (2007) that vanadates such as mottramite often form during late phases in the supergene history. The absence of mottramite at Tazalaght arises from the absence of lead in the primary mineralization. As previously proposed by Schweltnus (1945), Verwoerd (1953), van der Westhuizen et al. (1989), and Boni et al. (2007), mottramite forms by recombination of V mobilized from host rocks and/or sulfides, with residual Cu and Pb amounts deriving from primary sulfides. According to van der Westhuizen et al. (1989) and Boni et al. (2007), mottramite is thought to precipitate under arid, slightly acidic and reduced conditions that are typically found at the boundary between the phreatic and the vadose zones of carbonates karsts. However, Dill et al. (2013) suggest that vanadates are most stable under strongly oxidizing and neutral pH conditions. The association of mottramite and goethite at Agoujgal implies that the hypothesis of Dill et al. (2013) is more adequate in this case. The slight enrichment in As of mottramite arises from the common partial substitution of V by As, and to the existence of isomorphic solid solutions between adellite (i.e. conichalcite) and descloizite groups (Gołębiewska 2005; Frost et al. 2014).

### **5.3.5. Conclusion**

Tazalaght and Agoujgal deposits are characterized by diversified copper secondary ores, including Cu-Pb arsenates. Even if some differences exist in terms of mineralogical and chemical contents between the two ore deposits, the processes responsible for the formation of these supergene ores are very similar. At both sites, the oxidation of base metal sulfides and tennantite resulted in an acidic environment and in the mobilization of several ions. The recombination of cations and ligands led to the formation of a wide assortment of phases ranging from sulfides stable in reduced conditions to carbonates such as malachite that obviously prefer oxidizing conditions and neutral pH levels. The precipitation of supergene oxidized phases, at Agoujgal, and in a lesser extent at Tazalaght, was made possible through an efficient neutralization of the acidic fluids by host rock dissolution.

The supergene processes led, at Tazalaght, to the development of four mineralogical zones clearly distinguished in any vertical cross-section of the deposit, from base to top: the hypogene zone (chalcopyrite, pyrite, tennantite), the large cementation zone (bornite, chalcocite), the oxidized zone (malachite, azurite, olivenite, chenevixite), and the leached zone (goethite, hematite). The only exotic phases at Tazalaght are scarce Co-sulfides and Co-arsenates. These four types of mineral associations are also identified at Agoujgal, but are less confined in spatially-limited zones. The hypogene zone is composed of chalcopyrite, pyrite, and tennantite; the very limited cementation zone hosts small volumes of chalcocite, mostly; the much-diversified oxidized zone is principally constituted of malachite, olivenite, conichalcite, and yukonite; the gossan is made of hematite and goethite. Along with the copper mineralization, galena is weathered to a broad set of Pb-phases reflecting the circulation of fluids of complex and varying composition, including the carbonate cerussite, the sulfates anglesite, osarizawaite, plumbojarosite, beaverite, the phosphate phosphohedyphane, and the arsenates mimetite and calcio-duftite. The vanadate mottramite is ubiquitous in the secondary mineralization, indicating the circulation of V-rich fluids in the deposit.

The difference between the secondary assemblages of both deposits clearly demonstrates the influence of the host rocks nature on supergene processes/neoformations. At Tazalaght, the quartzitic host rocks could not fast enough neutralize the fluids acidity to develop in a larger way the oxidized

mineralization. The scarcity of Ca-phases, and in particular Ca-arsenates, is related to the scarcity of carbonate rocks in this deposit. The fluids acidity must have been slowly buffered over a long period of time at Tazalaght. On the contrary, the extensive oxidized zone of Agoujgal and the omnipresence of Ca-minerals such as conichalcite and yukonite are due to the large amount of carbonate host rocks in the deposit. The common association of Cu, Pb, Fe, Ca- arsenates, sulfates, phosphates, vanadates, and oxides is particular and reflects a much more complex physical-chemical evolution of the mineralization, in relation with pH and Eh variations. The fluids acidity must have been initially quickly buffered at Agoujgal, as almost no secondary sulfides are present, leading to the precipitation of large amounts of carbonates. However, many fluctuations are supposed to have caused the formation of successive generations of carbonates, arsenates and sulfates, among others.

Both Tazalaght and Agoujgal provided samples that enabled the description of a boxwork texture derived from tennantite. The textures and mineral assemblages of single hand specimens record the transition from the fresh ore (tennantite), the cementation zone (chalcocite), the oxidation zone (arsenates and malachite), and finally the gossan (goethite and hematite). As evidenced by the secondary arsenates assemblage, boxwork textures are useful tools reflecting the evolution of fluid-rock interactions with time.



#### 5.4 Characterization of weathering processes of the giant copper deposit of Tizert (Ighrem inlier, Anti-Atlas, Morocco)

The Tizert site (western Anti-Atlas, Morocco) is considered as the largest copper deposit in the western Anti-Atlas (Oummouch et al. 2017). This deposit was discovered in 1969. Using a series of galleries, the site was first studied between 1970 and 1975 by the Bureau des Recherches Pétrolières et Minières (BRPM), which estimated the reserves to 1,062,000 t with 2.3% Cu and 65 g/t Ag (Asladay et al. 1998). Since 2011, exploration studies have been carried out by the Managem group; the resources are now estimated to 56,820,000 t with 1.03% Cu and 23g/t Ag (Oummouch et al. 2017). Other copper deposits are currently mined in this part of the Anti-Atlas, especially in Neoproterozoic to Early Cambrian rocks: the Tazalaght mine (reserves 260,000 t with 1.89% Cu; Asladay et al. 1998; Verhaert et al. in press), the Ouansimi mine (reserves 1,087,000 t with 2.63% Cu) (Annich 2002; El Basbas et al. 2019) and the Agoujgal mine (reserves 5,000,000 t with 1% Cu and 20 g/t Ag) Verhaert et al. in press). In their pioneering characterization of the Tizert deposit, Oummouch et al. (2017) mainly i) highlight mineralogical phases observed in this area, focusing on primary (hypogene) mineral phases, and ii) evaluate its potential for possible exploitation (grades and tonnage). In this study, we complete the primary mineralization data proposed by Oummouch et al. (2017), by characterizing the supergene mineral assemblages, in order to determine their formation processes and identify possible enrichment associated to weathering in the Tizert giant Cu deposit.

#### 5.4.1. Geodynamic context

See chapter 3.3 for the geodynamic setting of Tizert deposit.

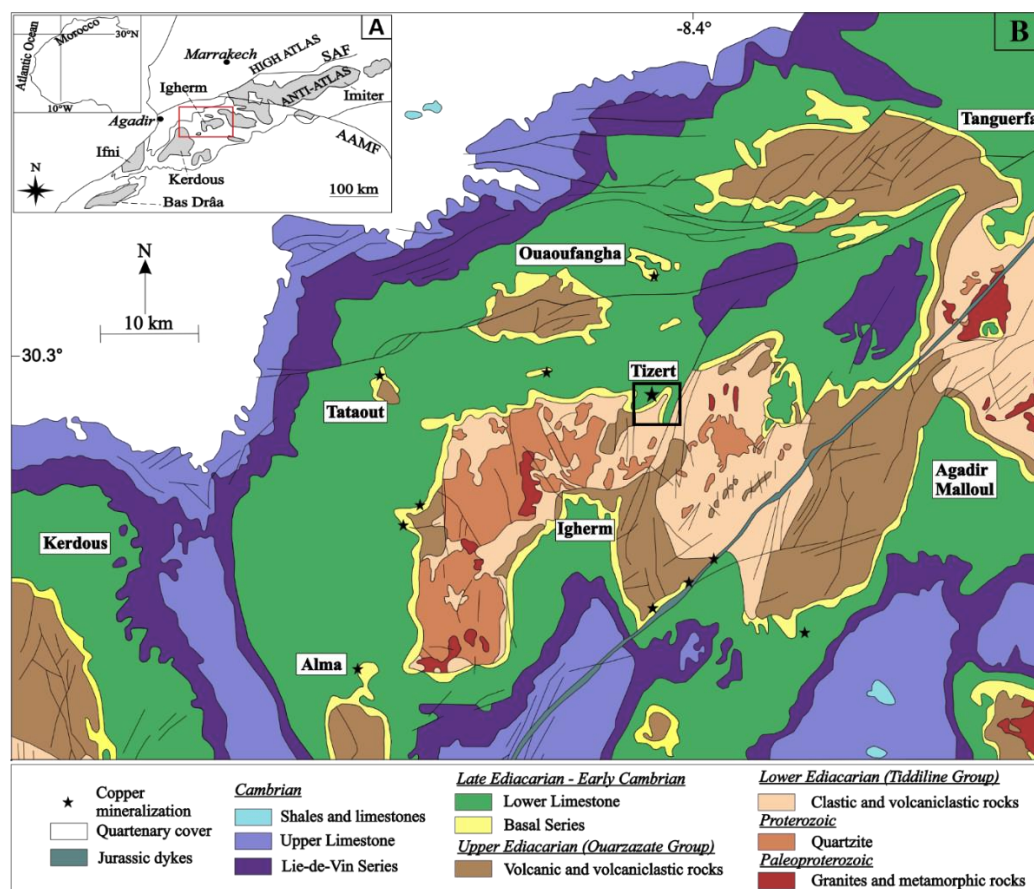


**Figure 5.4.1.** (a) General map of the Anti-Atlas; (b) Simplified geological map of the Igherm inlier (Modified after Oummouch et al. 2017).

### 5.4.2. Local geologic context

The Tizert copper deposit is located at the northern edge of the Iggherm inlier, which is composed of Paleoproterozoic to Lower Cambrian formations (Fig. 5.4.1b). Mineralization is mainly carried by malachite [ $\text{Cu}_2\text{CO}_3(\text{OH})_2$ ] and secondary sulfides such as chalcocite II ( $\text{Cu}_2\text{S}$ ) or covellite ( $\text{CuS}$ ). According to Oummouch *et al.* (2017), silver is represented by minerals such as stromeyerite ( $\text{CuAgS}$ ), eugenite ( $\text{Ag}_{11}\text{Hg}_2$ ) or chlorargyrite ( $\text{AgCl}$ ).

The Proterozoic basement is mainly composed of metamorphic rocks (orthogneiss and migmatites) and granitic intrusions formed during the Eburnean orogeny. These granites, dated at  $2050 \pm 6$  Ma (U-Pb on zircons), are porphyritic, mylonitized and generally weathered; their chemical composition is close to a subalkaline peraluminous adamellite (rich in Ba, Sr, Zr and REE) (Aït Malek *et al.* 1998). The Tonian-Cryogenian limestones and quartzites (Lkest and Taghdout Group) have been deformed and recrystallized during the Pan-African orogeny (Gasquet *et al.* 2008). In the Lower Ediacaran, late orogenic clastic and volcanoclastic series were deposited and deformed by a second event around 600 Ma (Thomas *et al.* 2004); this is the Tiddiline Formation (Fig. 5.4.2), which constitutes the oldest rocks outcropping in the Tizert region. The second part of the Ediacaran is characterized by late to post-orogenic collapses leading to an accumulation of nearly 2 km of conglomerates, volcanic and volcanoclastic rocks from the Ouarzazate Group (600-560 Ma), unconformably disposed with Eburnean and Pan-African series (Thomas *et al.* 2002; Walsh *et al.* 2012). This group, such as the Tiddiline series, is very small or absent in the Tizert area (Oummouch *et al.*, 2017).

The Adoudou Formation (Fig. 5.4.2) unconformably overlies the Ouarzazate Supergroup with an angular unconformity of up to  $20^\circ$  (Thomas *et al.* 2002). It was deposited between the Late Ediacaran and the Early Cambrian [between  $550 \pm 3$  Ma and  $521 \pm 7$  Ma, according to Gasquet *et al.* (2005) and between  $561 \pm 1$  and  $524.84 \pm 0.09$  Ma according to Maloof *et al.* (2010)], The Adoudou Formation, forming the base of the Taroudant Group (Maloof *et al.*, 2010), was deposited during a major marine transgression from west to southeast; sedimentary units are thicker and carbonates more abundant in the western part (Benssaou and Hamoumi 2003). It is generally divided into two members (Fig. 5.4.2): the Tabia and the Tifnout Members (Maloof *et al.* 2006). The Tabia Member corresponds to the “Basal Series” and is composed of different units, from base to top: (1) a massive Basal Conglomerate consisting of fluvial sandstones, coarse silico-clastic debris and silts; (2) peritidal carbonates, dolostones and silts; (3) sandstones and silts (grey - purple - greenish) (Benssaou and Hamoumi 2003; Maloof *et al.* 2006). The thickness of this “Basal Series” varies in the Tizert region from absent to 100 m thick (Oummouch *et al.*, 2017).

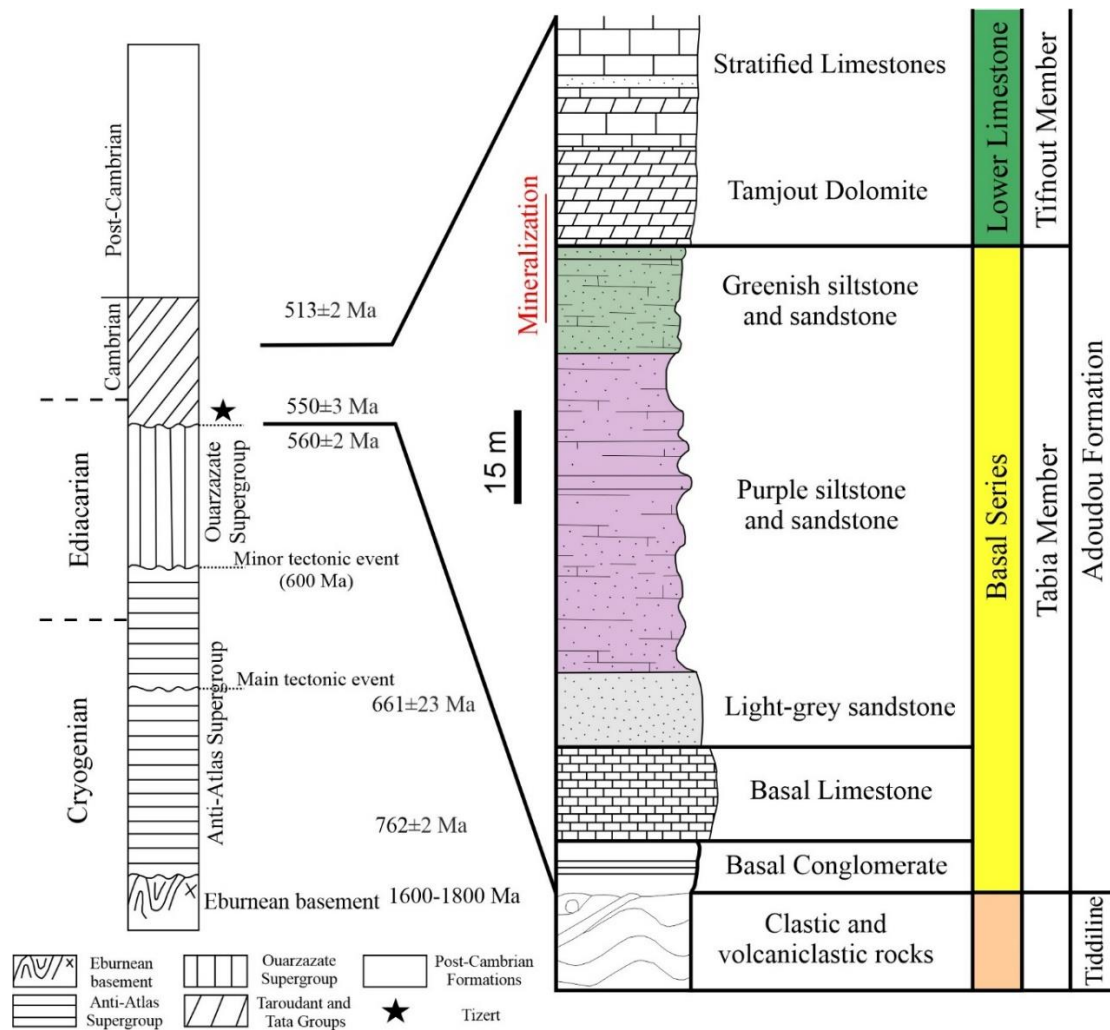


**Figure 5.4.2.** Simplified lithostratigraphy of the Anti-Atlas (left) and major geological units observed in the Tizert deposit (right) (Modified from Gasquet et al. 2005; Boudzoumou et al. 2012; Oummouch et al. 2017).

The upper part of the Adoudou Formation is defined by the Tifnout Member. Its base consists of a 50-200 m thick dolostone, the Tamjout Dolomite, generally described as a partially silicified stromatolite dolostone formation (Benssaou and Hamoumi 2003; Oummouch et al. 2017). Above this massive dolostone, the Tifnout Member is composed of parasequences (metric scale) composed of marls, dolostones and siltstones at the base, and also micritic and grainstone carbonates (Maloof et al. 2006, 2010). Trachytic and andesitic flows, dated at  $534 \pm 10$  Ma on the Jbel Boho syenites, may also occur within the Tifnout Member (Maloof et al., 2006). The Tizert Cu mineralization is mainly located at the base of the Tamjout Dolomite and in the upper part of the Tifnout Member (Fig. 5.4.2; Oummouch et al., 2017). Above the Adoudou Formation lies the "Lie-de-Vin" series, which are associated with a tilting in the Anti-Atlas margin (Maloof et al., 2005). They are composed of purplish silts/argillites formed by an increased supply of silico-clastic sediments to the basins, and of dolomitic limestones (Soulaïmani et al. 2003; Maloof et al. 2006; Oummouch et al. 2017). These series do not outcrop in the Tizert region.



### 5.4.3. Materials and methods

Fifty-five samples were collected in March 2018, twenty-three from surface and others from three boreholes (C1, C15 and 75; Fig. 5.4.3). Samples from surface are labeled “TIZ X” (e.g. TIZ 15), when boreholes samples are labeled for example C15C8, where 15 is the number of the borehole and 8 the number of the sample. X-Ray Diffraction was carried out on forty-five samples in order to identify the major mineral phases. XRD analyzes of powdered samples were performed using X-Ray Panalytical X’Pert Pro diffractometer and a PHILLIPS PW3710 (CuK $\alpha$  radiation) at the PC2 platform (UNamur), operating at 40kV and 30mA. Some samples containing clays were also analyzed by XRD. The isolation of the < 2 $\mu$ m size fraction and the analyzes were performed following Holtzapffel (1985) methodology.

Seventeen polished sections (mineralized samples) and fourteen thin sections were prepared at the Geology Department of the University of Namur and at the Laboratorio Petrografico (OMT di Canepa Pierluigi), respectively. They have been studied using a petrographic polarizing microscope in transmitted and reflected light. A JEOL JSM 7500F scanning electron microscope (SEM), coupled with an energy dispersive spectrometer (EDS), was used to carry semi-quantitative analyzes in order to identify some mineral phases at the Microscopy Service of the University of Namur.

Geochemical analyzes were carried out on twenty-five samples (thirteen from surface et twelve from boreholes). Crushing was performed with a RETSCH PM 100 planetary ball mills (University of Namur) in order to obtain the maximum 125  $\mu$ m grain size. Agate crushing mortar was used for most samples except for iron oxides, where a stainless-steel mortar was used to avoid contamination. The various analyzes were carried out by Activation Laboratories Ltd (Actlabs, Canada). Rare earth elements were analyzed by FUS-MS (Fusion Mass Spectrometry) and major elements by FUS-ICP (Fusion Inductively Coupled Plasma Optical Emission Spectrometry). The reduced iron (FeO) was determined by titration. Trace elements were also analyzed by FUS-MS; in some cases, Cu and Pb were quantified in percents rather than in ppm, by FUS-Na<sub>2</sub>O<sub>2</sub> (Fusion Inductively Coupled Plasma Sodium Peroxide Oxidation). Major, trace and rare earth elements are normalized to the composition of the upper continental crust (UCC, Taylor and McLennan, 1985) to highlight geochemical trends. Host rocks, mineralized and weathered samples are compared to show possible enrichment or depletion for each element.

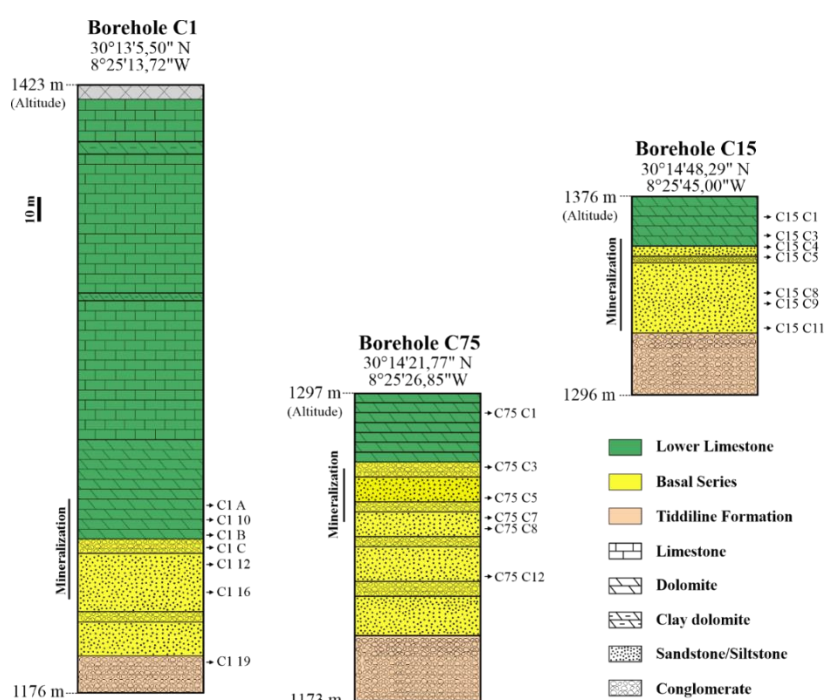


**Figure 5.4.3.** Schematic representation of studied boreholes (C1, C15 and C75) with different analyzed samples.

## 5.4.4. Results

### 5.4.4.a Host rocks

The petrography, mineralogy and geochemistry of the host rocks play a crucial role in the formation of weathered ores (Verhaert et al. 2017). In the Tizert area, most of host rock (Tamjout Dolomite and the Basal Series - without the Basal Conglomerate) were collected at the Issedrin section, few kilometers NW of Tizert main deposit.

Other host rock samples were collected from three boreholes of the Tizert site (C1, C15 and C75; Fig. 5.4.3) in order to allow chemical comparison with weathered samples. In the boreholes, lithologies equivalent to those of the Issedrin section were analyzed: Tamjout Dolomite (C75C1), red sandstone (C75C3), purplish siltstone (C75C8) and greenish siltstone (C75C12). It is important to highlight that some of the host rocks, considered as “fresh”, are slightly mineralized by a very low proportion of primary sulfides. Table 5.4.1 shows geochemical analyzes for all these host rocks.

*Tamjout Dolomite* - It is a relatively pure dolostone made up of dolomite, calcite, quartz and muscovite. Calcite and quartz are mainly observed in nodules and veins. The presence of galena in one Tamjout Dolomite sample of the Issedrin site is confirmed by geochemical analyzes (e.g. TIZ 45, Table 5.4.1) and will be describe in the primary mineralization section (see below). There is no other observation of primary sulfides in the Issedrin site. The grades of Ag (0.6 ppm), As (5 ppm) and Cu (30 ppm) for the borehole sample (C75C1) are relatively high in comparison with the UCC while Pb (5 ppm) is quite depleted (Table 5.4.1) although no primary sulfide was observed in this sample. The Tamjout Dolomite (surface and borehole, Fig. 5.4.4A) is depleted in REE. The sample (C75C1) from Tizert borehole and the TIZ 45 sample from the Issedrin section are thus weakly mineralized. All the other samples from boreholes and from the Issedrin section are considered as “fresh” (= not mineralized).

*Basal Series* – The Basal Series contains sandstones, siltstones and conglomerates showing various colours (light-grey, purplish, greenish and red) and limestone (“Petit Calcaire”). The upper part is characterized by a light-grey sandstone (TIZ 44) made of quartz, muscovite, chlorite (Fig. 5.4.5A) and feldspars (mostly orthoclase and albite). The carbonate content is quite low (Ca content of 0.4% and LOI 1.4%). This rock, like most samples from Basal Series, show an Ag content (1,1 ppm) similar to the one observed in the Tamjout Dolomite (Table 5.4.1). REE profile is quite the same as the PAAS, except for HREE, the latter being slightly depleted (Fig. 5.4.4A). Purplish and greenish siltstones are mostly observed in the upper and central part of the series. Purplish siltstones are made up of quartz, muscovite, chlorite, feldspars and hematite. Grain size is relatively small (max. 0.15 mm) and the matrix is mainly composed of hematite and quartz, whereas the cement is slightly carbonated. SiO<sub>2</sub> content (58.7%) is lower than the light-grey sandstone (75.5%), while Fe<sub>2</sub>O<sub>3</sub> is higher (5.9%) mostly due to hematite (responsible of the purple coloration) and chlorite. The Al<sub>2</sub>O<sub>3</sub>, K<sub>2</sub>O and TiO<sub>2</sub> contents are the highest among host rocks (Table 5.4.1). REE pattern shows slight but not significative enrichment for surface samples, which is not observed in the boreholes (Fig. 5.4.4A).

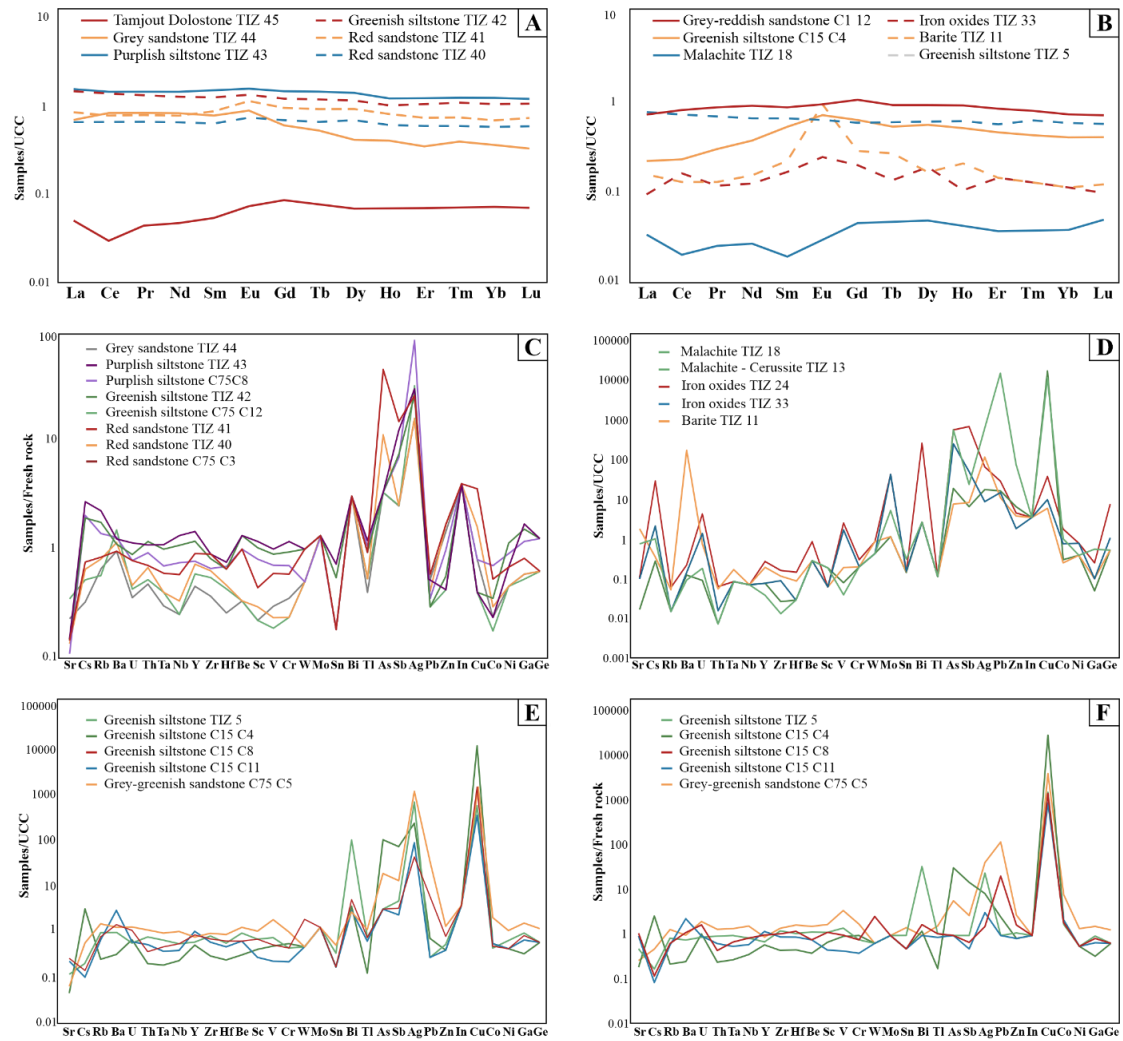


**Figure 5.4.4.** Geochemical data: (A) REE patterns for fresh rocks (Tamjout Dolomite and Basal Series), with values normalized to UCC; (B) REE patterns for weathered samples with values normalized to UCC; (C) trace elements patterns for weathered greenish siltstone/sandstone, with values normalized to UCC; (D) with values normalized to fresh greenish siltstone; (E) trace elements patterns for fresh host rocks (Basal Series), with values normalized to UCC (Upper Continental Crust); (F) trace elements patterns for main mineral phases in Tamjout Dolomite; with values normalized to UCC.

**Table 5.4.1.** Results of geochemical analyzes for selected samples of host rocks and mineralization/weathered rocks. Major elements are listed in % while minor elements and REE are listed in ppm; except for values with an asterisk (\*) which are in %. LOD = Limit of Determination.

Oxides/Elements		Host rocks											Mineralization														
		Tamjout Dolomite TIZ45	Grey sandstone TIZ44	Purplish siltstone TIZ43	Greenish siltstone TIZ42	Red sandstone TIZ41	Red sandstone TIZ40	Conglomerate C1 11	Tamjout Dolomite C75C1	Red sandstone C75C3	Purplish siltstone C75C8	Greenish siltstone C75C12	Iron oxides (Dolomite) TIZ33	Iron oxides (Dolomite) TIZ24	Malachite (Dolomite) TIZ 18	Malachite (Conglomerate) TIZ14	Malachite/Cerussite (Dolomite) TIZ13	Barite in quartz (Dolomite) TIZ11	Greenish siltstone TIZ5	Grey-reddish sandstone C1 12	Conglomerate C1 16	Greenish siltstone C15C4	Conglomerate C15C5	Greenish siltstone C15C8	Greenish siltstone C15C11	Greenish siltstone C75C5	
SiO <sub>2</sub> (%)	0.01	0.91	75.55	62.86	62.86	61.15	78.87	61.52	0.61	45.04	65.05	65.05	5.81	7.98	1	59.24	6.4	37.69	66.58	47.56	65.14	41.06	55.94	59.49	56.15	56.98	
Al <sub>2</sub> O <sub>3</sub> (%)	0.01	0.31	11.25	16.79	16.79	12.01	10.73	13.91	0.14	9.57	15.31	15.31	0.62	1.29	0.08	13.16	0.02	1.06	14.4	11.1	12.11	4.82	9.16	13	10.09	18.04	
Fe <sub>2</sub> O <sub>3</sub> (%)	0.01	0.21	0.61	1.91	1.91	3.22	0.97	2.76	0.11	1.19	3.9	3.9	30.93	60.18	0.11	3.09	< 0.01	0.83	1.21	1.52	1.05	0.01	1.18	1.1	1.22	2.57	
MnO (%)	0.01	0.27	0.013	0.012	0.012	0.122	0.013	0.075	0.458	0.271	0.023	0.023	0.061	0.091	0.036	0.062	0.009	0.174	0.025	0.271	0.15	0.036	0.195	0.175	0.309	0.015	
MgO (%)	0.01	20.48	1.35	2.5	2.5	3.81	0.66	5.26	21.31	7.83	2.86	2.86	11.61	1.28	1.26	5.39	0.18	8.75	2.82	5.6	3.6	0.53	4.22	3.86	5.87	3.1	
CaO (%)	0.01	29.58	0.4	0.37	0.37	4.81	0.21	1.51	29.77	12.3	1.00	1.00	19.42	14.45	7.96	0.39	0.29	13.78	0.76	7.16	4.63	6.1	8.63	5.98	7.56	0.48	
Na <sub>2</sub> O (%)	0.01	0.03	1.83	0.61	0.61	0.08	0.11	1.92	0.02	0.04	0.28	0.28	0.02	0.03	0.01	1.09	< 0.01	0.02	1.12	0.08	1.22	0.03	0.05	0.64	0.29	0.06	
K <sub>2</sub> O (%)	0.01	0.09	4.92	6.39	6.39	4.68	5.72	2.26	0.04	2.89	5.79	5.79	0.1	0.29	0.01	1.91	< 0.01	0.32	4.6	3.19	2.81	1.34	2.75	3.82	3	6.73	
TiO <sub>2</sub> (%)	0.001	0.013	0.243	0.622	0.622	0.4	0.233	1.007	0.007	0.403	0.513	0.513	0.014	0.07	0.003	1.332	0.001	0.053	0.414	0.354	0.707	0.27	0.528	0.645	0.246	0.64	
P <sub>2</sub> O <sub>5</sub> (%)	0.01	0.09	0.1	0.15	0.15	0.12	0.11	0.17	0.07	1.11	0.11	0.11	0.04	0.32	0.03	0.12	0.12	0.29	0.16	1.29	0.21	0.53	1.13	0.1	0.12	0.25	
LOI (%)		46.14	1.44	3.72	3.72	8.7	1.96	4.84	46.26	18.07	3.92	3.92	29.54	14.63	30.01	6.16	21.65	19.3	4.67	13.87	5.78	11.04	12.02	5.61	11.98	6.07	
<b>Total (%)</b>	0.01	98.36	99.37	99.04	99.04	100.1	100.0	99.35	99.02	98.82	100.1	100.1	98.19	100.6	40.6	96.84	28.79	82.29	97.75	92.67	98.84	65.98	95.86	95.75	97.4	95.17	
FeO (%)	0.1	0.2	1.5	1.5	2.8	0.9	0.4	3.7	0.2	0.1	1.2	0.3	< 0.1	< 0.1	< 0.1	4.4	0.2	< 0.1	0.9	0.6	1.3	0.2	< 0.1	1.2	0.5	0.2	
S (%)	0.001	0.05	-	-	-	-	-	-	-	-	0.005	-	-	-	0.021	0.041	1.16	-	-	-	-	-	-	-	-	-	
SO <sub>4</sub> (%)	0.05	-	-	-	-	-	-	-	-	-	-	-	-	-	-	-	-	7.8	-	-	-	-	-	2.6	-	-	
Sc (ppm)	1	< 1	3	16	14	6	4	24	< 1	4	11	3	1	1	3	18	3	1	10	6	10	6	12	10	4	15	
Be (ppm)	1	< 1	< 1	4	4	3	< 1	1	< 1	1	3	< 1	1	3	< 1	1	< 1	< 1	3	2	2	< 1	1	2	2	4	
V (ppm)	5	15	32	107	96	64	25	177	5	33	76	20	209	313	10	140	< 5	24	85	54	64	56	94	59	26	210	
Cr (ppm)	20	< 20	30	100	80	50	20	90	< 20	50	60	< 20	< 20	30	< 20	100	< 20	< 20	40	80	70	50	50	40	20	90	
Co (ppm)	1	1	4	3	6	9	5	25	< 1	7	12	3	15	35	6	45	20	5	8	12	12	9	7	9	10	37	
Ni (ppm)	20	< 20	< 20	30	50	30	< 20	50	< 20	< 20	40	< 20	40	40	< 20	70	< 20	< 20	< 20	< 20	< 20	< 20	< 20	< 20	< 20	50	
Cu (ppm/%*)	10/0.005	70	20	< 10	10	90	40	40	30	180	20	< 10	280	1070	46.4*	2.28*	31.9*	170	1.51*	4*	40	30.7*	2.24*	3.86*	9290	4.23*	
Zn (ppm)	30	40	< 30	30	40	120	110	240	< 30	70	70	< 30	150	370	530	140	5990	310	40	90	100	30	30	60	< 30	100	
Ga (ppm)	1	1	11	29	26	14	10	17	1	11	20	9	2	5	< 1	16	11	2	17	14	15	6	11	15	12	28	
Ge (ppm)	1	< 1	1	2	2	1	1	1	< 1	< 1	2	< 1	2	14	< 1	2	< 1	< 1	1	< 1	1	< 1	< 1	1	< 1	2	
As (ppm)	5	16	< 5	< 5	< 5	68	17	5	< 5	28	< 5	< 5	419	1000	32	< 5	930	13	< 5	9	11	164	166	5	< 5	30	
Rb (ppm)	2	2	74	253	198	94	91	65	< 2	68	156	64	2	8	< 2	55	< 2	7	114	81	86	30	72	87	80	178	

Sr (ppm)	2	85	80	38	53	51	47	56	57	52	38	122	41	45	7	28	307	731	44	94	88	17	62	98	85	24
Y (ppm)	1	2	10	32	26	20	16	13	1	25	17	13	2	7	2	16	1	5	14	31	23	12	40	20	24	18
Zr (ppm)	2	6	70	171	155	171	120	148	4	230	126	104	20	36	6	128	3	26	164	171	419	60	120	141	120	188
Mo (ppm)	2	< 2	< 2	< 2	< 2	< 2	< 2	< 2	< 2	< 2	< 2	< 2	73	72	< 2	< 2	9	< 2	< 2	< 2	< 2	< 2	3	< 2	< 2	2
Ag (ppm)	0.5	1.6	1.1	1.5	1.3	1.3	0.8	4	0.6	1.8	4.2	1.6	< 0.5	3.7	1	36.4	34.5	6.5	36.3	12.9	4.1	12.6	4.2	2.3	4.7	62.5
In (ppm)	0.2	< 0.2	< 0.2	< 0.2	< 0.2	< 0.2	< 0.2	< 0.2	< 0.2	< 0.2	< 0.2	< 0.2	< 0.2	< 0.2	< 0.2	< 0.2	< 0.2	< 0.2	< 0.2	< 0.2	< 0.2	< 0.2	< 0.2	< 0.2	< 0.2	
Sn (ppm)	1	< 1	1	4	3	1	1	1	1	1	3	1	< 1	1	< 1	1	2	< 1	2	1	2	1	1	1	1	3
Sb (ppm)	0.5	0.6	< 0.5	2.5	1.5	3	0.5	< 0.5	< 0.5	1.2	1.4	< 0.5	11.3	151	1.5	0.7	5.4	1.9	1	0.6	0.6	15.5	1.5	0.7	0.5	2.8
Cs (ppm)	0.5	< 0.5	1.5	12.6	8.9	3.5	3	3	< 0.5	3.5	9.4	2.4	< 0.5	< 0.5	< 0.5	3	< 0.5	< 0.5	5.5	3.6	3.7	2.1	3.3	4.4	4.5	11.9
Ba (ppm)	2	13	524	614	621	526	633	651	11	334	707	827	67	143	80	1844	60	106000	573	8298	638	188	5449	841	1723	737
Hf (ppm)	0.2	< 0.2	1.5	4.4	3.8	3.8	2.7	3.2	< 0.2	11.5	4	2.5	0.2	1	< 0.2	3	< 0.2	0.6	3.5	3.3	8.8	1.5	2.6	3.9	2.9	5.4
Ta (ppm)	0.1	< 0.1	0.3	1.1	1	0.6	0.4	0.4	< 0.1	0.6	0.7	0.4	< 0.1	< 0.1	< 0.1	0.4	< 0.1	0.2	0.7	0.5	0.6	0.2	0.3	0.5	0.4	1
W (ppm)	1	< 1	< 1	2	2	2	< 1	< 1	< 1	< 1	< 1	< 1	< 1	2	< 1	< 1	< 1	2	1	< 1	2	1	< 1	4	< 1	< 1
Tl (ppm)	0.1	< 0.1	0.3	0.9	0.7	0.4	0.4	0.4	< 0.1	0.3	0.8	0.4	0.1	0.1	< 0.1	0.3	< 0.1	< 0.1	0.6	0.5	0.6	0.1	0.4	0.6	0.5	0.9
Pb (ppm/%)	5/0.01	316	6	9	< 5	10	7	< 5	< 5	15	6	5	287	551	316	21	29.6*	213	< 5	10	< 5	13	< 5	107	< 5	622
Bi (ppm)	0.4	< 0.4	< 0.4	< 0.4	< 0.4	< 0.4	< 0.4	< 0.4	< 0.4	< 0.4	< 0.4	< 0.4	< 0.4	37.8	< 0.4	< 0.4	0.4	< 0.4	14	6.2	< 0.4	0.5	1.4	0.7	0.4	< 0.4
Th (ppm)	0.1	0.2	5.1	11.7	12.6	7.5	7.3	2.8	< 0.1	8	9.9	5.6	0.2	0.8	< 0.1	2.1	< 0.1	0.7	8.8	6.8	8.4	2.3	2.7	4.2	6	12.5
U (ppm)	0.1	1.3	1	3.2	2.5	2.2	1.3	1.1	0.7	2	2.2	1.2	4.5	13.8	0.3	0.7	0.6	2.4	1.7	2.5	2.2	2	1.7	3.2	1.8	3.8
La (ppm)	0.1	1.9	26	58.1	56.2	31.8	24.5	8.3	1.1	26.5	32.3	28.3	3.4	6.9	1.2	11.5	1	5.7	28.8	27	46.5	8.1	18.3	10.4	33.6	35.6
Ce (ppm)	0.1	2.5	65.7	114	109	61.4	52	19.3	1.5	58.6	59.5	58.7	12.4	11.1	1.5	26.1	0.9	9.9	56.9	63.9	94.1	17.8	42.7	22.7	72.4	64.9
Pr (ppm)	0.05	0.39	7.25	12.7	11.6	6.91	5.81	2.37	0.2	6.87	6.25	6.21	1	2.02	0.21	3.33	0.17	1.1	6.03	7.63	10.3	2.58	5.81	2.49	6.71	6.75
Nd (ppm)	0.1	1.5	26.1	45.6	40.1	24.5	20.6	9.5	0.9	26.2	22.4	22.8	3.8	8.4	0.8	13.3	0.8	4.7	20.6	28.5	35.8	11.6	27	10.1	23.3	23.4
Sm (ppm)	0.1	0.3	4.3	8.3	6.9	4.8	3.5	2.1	0.2	5.3	4.1	3.8	0.9	1.9	0.1	3.1	0.2	1.2	3.6	4.8	6.8	2.9	8.3	2.2	4.5	4.2
Eu (ppm)	0.05	0.08	0.96	1.7	1.45	1.23	0.8	0.56	< 0.05	1.19	0.86	0.86	0.26	0.43	< 0.05	0.93	0.06	0.99	0.68	1.02	1.59	0.77	2.3	0.61	1.22	0.85
Gd (ppm)	0.1	0.4	2.8	6.8	5.6	4.4	3.2	2.1	0.2	4.7	3.2	2.9	0.9	1.9	0.2	3.3	0.1	1.3	2.7	4.9	5.2	2.9	10.6	2.9	4.7	3.4
Tb (ppm)	0.1	< 0.1	0.4	1.1	0.9	0.7	0.5	0.4	< 0.1	0.7	0.5	0.4	0.1	0.3	< 0.1	0.6	< 0.1	0.2	0.4	0.7	0.8	0.4	1.7	0.6	0.8	0.5
Dy (ppm)	0.1	0.3	1.8	6.1	5	4	3	2.4	0.1	4	3.2	2.5	0.8	1.4	0.2	3.5	< 0.1	0.7	2.6	4	4.7	2.4	8.5	4	5	3.3
Ho (ppm)	0.1	< 0.1	0.4	1.2	1	0.8	0.6	0.5	< 0.1	0.8	0.7	0.5	0.1	0.2	< 0.1	0.7	< 0.1	0.2	0.6	0.9	0.9	0.5	1.4	0.8	1	0.7
Er (ppm)	0.1	0.2	1	3.5	3	2.1	1.7	1.6	< 0.1	2.2	2	1.4	0.4	0.6	0.1	1.9	< 0.1	0.4	1.6	2.4	2.7	1.3	3.3	2.3	2.6	2.2
Tm (ppm)	0.05	< 0.05	0.16	0.5	0.44	0.3	0.24	0.26	< 0.05	0.32	0.3	0.21	0.05	0.09	< 0.05	0.28	< 0.05	0.05	0.25	0.32	0.37	0.17	0.36	0.32	0.38	0.35
Yb (ppm)	0.1	0.2	1	3.4	2.9	1.9	1.6	1.9	< 0.1	2	2.1	1.5	0.3	0.4	0.1	1.8	< 0.1	0.3	1.6	2	2.5	1.1	2	2.1	2.3	2.5
Lu (ppm)	0.01	0.03	0.14	0.51	0.45	0.31	0.25	0.29	0.01	0.33	0.33	0.22	0.04	0.05	0.02	0.27	< 0.01	0.05	0.24	0.3	0.37	0.17	0.28	0.3	0.33	0.41

For trace elements, Ag (1.5 to 4.2 ppm for the drilling sample) and Sb enrichment are well marked (Fig. 5.4.4C). The greenish siltstone (TIZ43) is made up of quartz, chlorite, muscovite, dolomite and feldspars. Like in the purplish siltstone, grain size does not exceed 0.15 mm and the cement is slightly carbonated. The proportion of chlorite is much higher than in other rocks of the Issedrin section and is at the origin of the greenish coloration. Cu content is very low (< 10 ppm), SiO<sub>2</sub> content is quite similar to the purplish siltstone (Table 5.4.1), Ag and Sb grades are well marked (Fig. 5.4.4C) and REE pattern (Fig. 5.4.4A) show a slight enrichment compared to PAAS. The composition of major elements in the greenish siltstone from borehole (e.g. C75C12) is quite different, mainly due to a lower proportion of chlorite, a higher proportion of quartz and the presence of microconglomerate clasts.

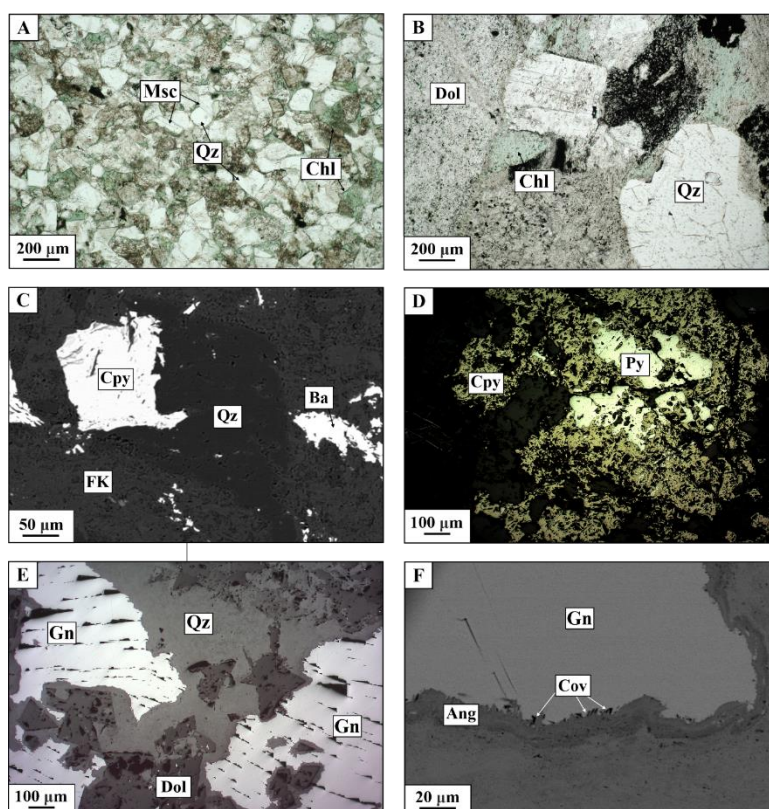


**Figure 5.4.5.** Representative samples and observations of the host rocks: (a) Abundance of chlorite (Chl, Qz = quartz, Msc = muscovite) in light-grey sandstone (TIZ 44); (b) Red sandstone (TIZ 41); (c) Chalcopyrite (Cpy) and barite (Ba) in coarse grey sandstone (TIZ S19); (d) Pyrite (Py) and chalcopyrite (Cpy) in Basal Conglomerate (TIZ S10); (e) Galena (Gn) in Tamjout Dolomite (TIZ 45); (f) Galena (Gn), covellite (Cov) sticks and anglesite (Ang) in Tamjout Dolomite (TIZ 45).

In the central part of the Basal Series, red sandstone (e.g. TIZ 41, Fig. 5.4.5B) is composed of dolomite, quartz, muscovite, chlorite and orthoclase. Grain size can reach 2 mm for quartz, while chlorite and orthoclase do not exceed 0.5 mm. The proportion of carbonates (cement and matrix) is higher than in other sandstones and siltstones of the Basal Series. The enrichments in As, Ag and Sn are significant (Fig. 5.4.4C, respectively 45, 26 and 15 times UCC values). In addition, a slight enrichment in Cu can be observed, such as in the Tamjout Dolomite. The composition of this red sandstone is variable, especially regarding the proportion of chlorite and carbonates (e.g. TIZ 40, lower proportions), which are generally balanced by SiO<sub>2</sub> (quartz) content.

The lower part of the Basal Series also contains a Basal Limestone, the so-called “Petit Calcaire”. This rock (e.g. TIZ 39) is actually a calcareous dolostone composed of dolomite, quartz, calcite and fluorapatite. This unit has a relatively small thickness (a few meters) and it is not observed in the three studied boreholes. Samples of PIII conglomerate (Basal conglomerate in Fig. 5.4.3; e.g. sample C1 19

in Table 5.4.1) were also analyzed by XRD. This rock is composed of quartz, calcite, hematite, albite, muscovite, apatite, orthoclase and chlorite and is transitional between the Basal Series and the Tiddiline Formation.

Oummouch et al. (2017) described the primary mineralization to be composed of sulfides such as chalcopyrite, pyrite, bornite I, chalcocite I and galena. These primary sulfides were observed in samples TIZS5 (sandstone), S6 (grey sandstone), S10 (conglomerate) and S19 (coarse sandstone). Bornite (e.g. TIZS6) and chalcopyrite (e.g. TIZ S5 and S19, Fig. 5.4.5C) are mostly observed separately, exception made of some samples (e.g. TIZ S10, Fig. 5.4.5D). These primary sulfides are disseminated in the host rock (sandstone and conglomerate of the Basal Series, and Lower Limestone) and are difficult to observe in subsurface samples due to weathering. SEM analyzes reveal low values (<0.5%) of As, Pb (except for galena), Zn and other chalcophile elements in Cu-sulfides. The Tamjout Dolomite (TIZ 45) shows a very slight mineralization characterized by the presence of galena (Fig. 5.4.5E and 5.4.5F). This primary sulfide, such as pyrite and chalcopyrite, is relatively homogeneous and does not contain huge amounts of other metals. Only low variations in terms of Ag (1.6 – 0.6 ppm), Pb (316 – 5 ppm) and As (16 – 5 ppm) can be mentioned between TIZ 45 (poorly mineralized) and C75C1 (fresh) dolostone, which are probably related to low content of Ag, or even As, in the galena.

#### **5.4.4.b Secondary (weathered) mineralization**

*Tamjout Dolomite* – Malachite is the predominant secondary mineral in the Tamjout Dolomite. Various weathered samples were analyzed; malachite (Cu 31.6 wt.%) and cerussite (Pb 29.6 wt.%) could be almost completely isolated from one sample (TIZ 13), except for a small amount of quartz (6.4 wt.%, Table 5.4.1). These samples also show relatively high content in Zn (5990 ppm), As (930 ppm), Sr (307 ppm) and Ag (34,5 ppm). Chalcocite II is a minor component (1.2 wt.% S in this sample; Table 5.4.1). The REE pattern is similar to the “fresh” Tamjout Dolomite. The Tamjout Dolomite sample (TIZ 45) shows, in low proportions, some secondary mineralization such as anglesite, cerussite and covellite surrounding galena (Fig. 5.4.5F). Pb-arsenates are also locally observed.



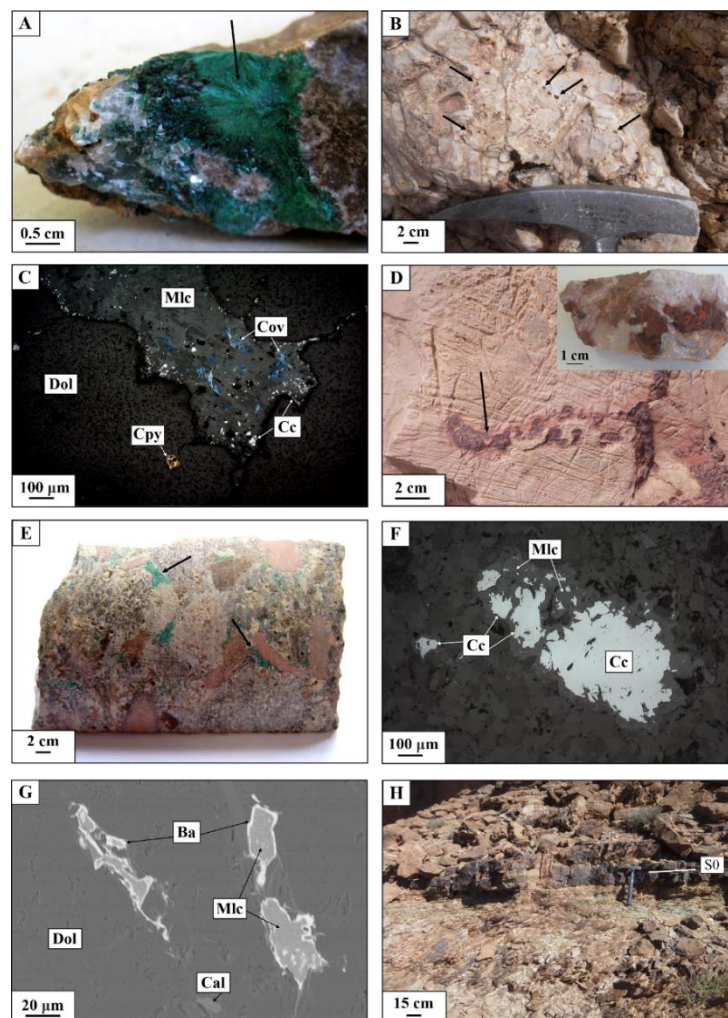


**Figure 5.4.6.** Representative samples and observations of the Tizert deposit: (a) Malachite (Mlc) and calcite (Cal) in Tamjout Dolomite (TIZ 18); (b) Pyrite dissolution ghosts in quartz veins in Tamjout Dolomite; (c) Malachite (Mlc), chicken-wire chalcocite (Cc), covellite (Cov) and chalcopyrite (Cpy) in Tamjout Dolomite (C15 C1); (d) Hematite in Tamjout Dolomite (TIZ 33); (e) Malachite in matrix of Basal Conglomerate (TIZC15 C5); (f) Malachite and chalcocite in greyish red sandstone in Basal Series (C1 12); (g) Malachite surrounded by barite (Ba) in greyish red sandstone from Basal Series (C1 12); (h) Stratification plan (SO) in Tamjout Dolomite.

Malachite with some calcite could be isolated (TIZ 18, Fig. 5.4.6A). In this sample, secondary sulfides such as covellite or chalcocite II are rare, as confirmed by the very low S content ( $\sim 0.02\%$ ; Table 5.4.1). An enrichment in Zn (530 ppm), Pb (316 ppm) and As (32 ppm) is observed, while Ag content (1 ppm, probably linked to galena) is low compared to previous sample (TIZ 13). REE profile is similar to all other Tamjout Dolomite samples (Fig. 5.4.4B). Low proportions of kaolinite have been identified for some borehole samples (TIZ C15 C3, TIZ C1 A and B). In the upper part of the Tamjout Dolomite some cubic remnants of pyrite (Fig. 5.4.6B), locally pseudomorphosed in iron-oxyhydroxides are observed in quartz veins.

SEM and transmission microscopy analyses of the upper part of the Tamjout Dolomite (e.g. TIZC15 C1) close to the Lower Limestone level (Fig. 5.4.2) reveal the presence of malachite, chicken-wire chalcocite II and covellite, and residual primary chalcopyrite (Fig. 5.4.6C). Chalcocite II and covellite are observed within malachite (mostly on the edges). The EDS analysis shows small proportions of As in malachite ( $\sim 1\%$ ). Residual chalcopyrite with chalcocite II on the edge is also observed.

Hematite and goethite associated to calcite, dolomite and quartz are identified within the weathered Tamjout Dolomite. The composition of these samples is mainly controlled by  $\text{Fe}_2\text{O}_3$ ,  $\text{MgO}$ ,  $\text{CaO}$  and  $\text{SiO}_2$ .



(e.g. TIZ24 and TIZ33; Fig. 5.4.6D; Table 5.4.1). V is enriched in some weathered samples (TIZ 24 and TIZ33, 313 and 209 ppm, respectively) compared to fresh rocks. Enrichments in Cu (1070 and 280 ppm), As (1000 and 419 ppm), Pb (551 and 287 ppm), Zn (370 and 150 ppm), Sb, Mo, Bi and U are highlighted (Table 5.4.1, Fig. 5.4.4D). No significant enrichment in Ag is detected in iron oxides. The REE pattern is flat and depleted compared to PAAS values (Fig. 5.4.4B). Iron oxyhydroxides are not frequent in the Tamjout Dolomite compared to widespread malachite. In most samples of the Tizert deposit, Pb content is correlated to As and Zn enrichments (e.g. TIZ 13, TIZ 18, TIZ 24, TIZ 33 and TIZ 45; Table 5.4.1).

*Basal Series* – In the Tizert deposit, most of the mineralization is located in the greenish siltstone of the Basal Series (Oummouch et al., 2017). Most samples located in the central and lower parts of the Basal Series are generally less affected by weathering and thus have lower Cu content. Surface and boreholes samples were therefore analyzed in this part of the Basal Series. For most of them, secondary Cu-mineralization is disseminated. For example, sample TIZ 5 contains malachite and chemical analysis reveals 1,5 wt.% Cu (whole rock) and 36,3 ppm of Ag (up to 700 x UCC, Table 5.4.1, Fig. 5.4.4D). Ba content is similar to the UCC, while Pb and As are under the detection limit (< 5 ppm). Other samples (e.g. TIZC15 C8 and C11, Fig. 5.4.4E and 5.4.4F) display higher Cu content (up to 4%) with variable Ag, As, Pb and Ba content (whole rock, Table 5.4.1). No major Ag-Pb-As-bearing secondary mineral phases have been identified in these rocks. Only few iron oxides are observed in chalcocite II and could explain slight variations of Pb and As. In most cases, chalcocite II is surrounded by malachite; rare fluorapatite is concentrated near malachite. Variations for most minor and trace elements in greenish siltstones are generally not consistent with fluctuations of the Cu grade (except for As in malachite). However, high Ag values are usually related to high Pb, As and Zn contents (e.g. TIZC75 C5). REE profile is similar to “fresh” greenish siltstones (Fig. 5.4.4B).

Conglomerates and microconglomerates also host Cu mineralization mainly represented by malachite in the matrix (Fig. 5.4.6E). The matrix of these samples shows up to 2.3% of Cu and low Ba enrichment resulting from the common presence of barite (e.g. TIZC15 C5 and TIZ14; Fig. 5.4.6E; 5549 and 1844 ppm, respectively; Table 5.4.1).

Many mineral phases, including secondary mineralization, are identified in greyish red sandstones (e.g. TIZC1 12, Fig. 5.4.6F and 5.4.6G): quartz, dolomite, malachite, chalcocite II, hematite, feldspars, apatite (1.3% P<sub>2</sub>O<sub>5</sub>), muscovite and barite. It is a sandstone rich in carbonates (low SiO<sub>2</sub> content, 47.6%, Table 5.4.1), in which malachite can be surrounded by a rim of barite (Fig. 5.4.6G). The edge of chalcocite II is replaced by malachite (Fig. 5.4.6G) and hematite. Bornite is also identified inside and outside malachite. Cu content for this sample is about 4 wt.%, in addition to Ba, Ag and Zn enrichments. However, Pb and As concentrations are very low (10 and 9 ppm, respectively). REE profile is again similar to all samples from the Basal Series, with a slight depletion in LREE (Fig. 5.4.4D). Various mineral phases are identified, such as quartz, muscovite, dolomite, apatite, kaolinite, chlorite, hematite, goethite and calcite. Rare phosphates are rich in Y (O 63.8%, P 18.1% and Y 13.5 %) and HREE (Dy 1.9%, Gd 0.8%, Yb 0.9% and Er 1.1%) (TIZC15 C9). Oummouch et al. (2017) described Ag-bearing minerals, such as stromeyerite (CuAgS), eugenite (Ag<sub>11</sub>Hg<sub>2</sub>), arquerite (Ag,Hg), chlorargyrite (AgCl) or native Ag. These minerals are not identified in this study, except in the greenish-grey sandstone (TIZC75 C7), where associated S, Ag and Cu could be attributed to stromeyerite embodied in malachite. Some barite (surrounding malachite) and anatase (TiO<sub>2</sub>) are also highlighted.

Some clays are observed in the weathered Basal Series and rarely in the Tamjout Dolomite. These are mainly kaolinite (e.g. TIZC1 A), illite, smectites (e.g. TIZC15 C11), chlorite (swelling or not, e.g. TIZ 14, TIZC1 16) and interstratified clays (mostly illite-smectite, e.g. TIZC1 12-16). Table 5.4.2 summarizes the mineral phases observed in the studied samples.

**Table 5.4.2.** Mineral phases observed in the different samples of Tizert deposit (H = Host rocks, W = weathered rocks, XXX = major, XX = frequent, X = minor).

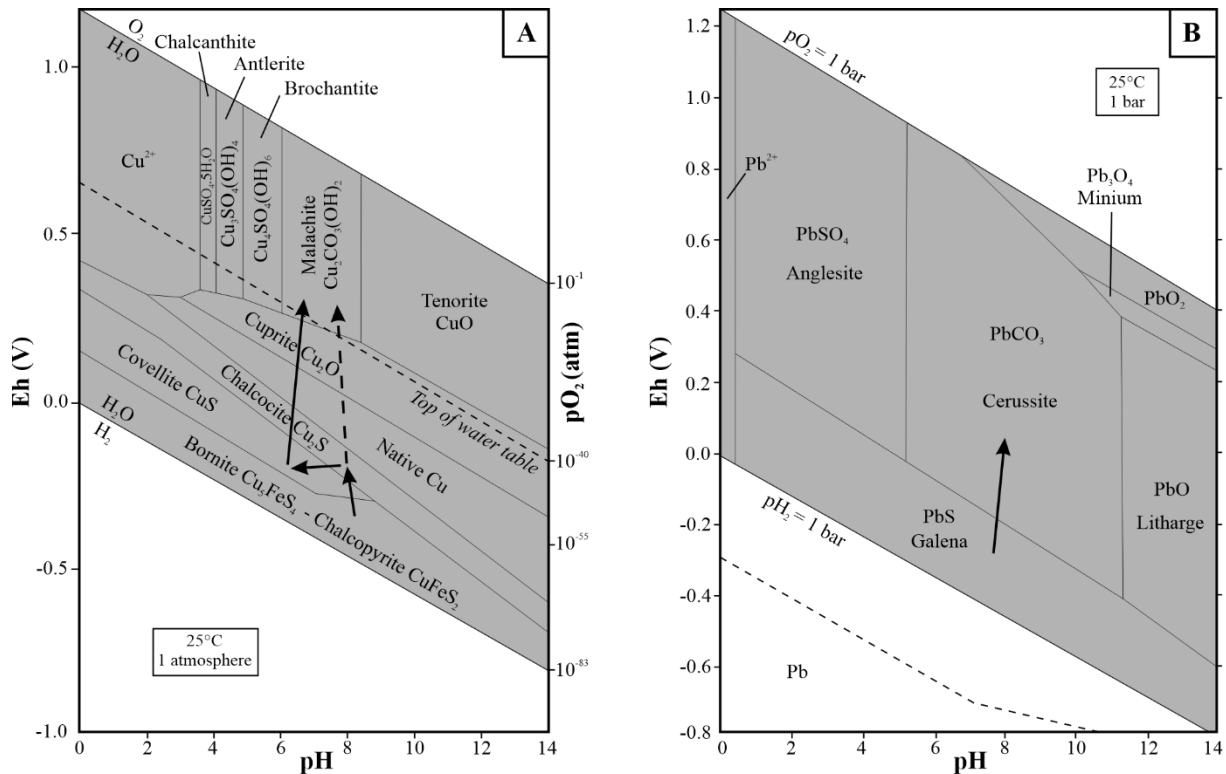
Weathering profile	Mineral phases	Issedrin cross-section (F)							Boreholes (F)				Tamjout Dolomite (W)					Basal Series (W)													
		Tamjout Dolomite TIZ 45	Greyish sandstone TIZ 44	Purplish siltstone TIZ 43	Greenish siltstone TIZ 42	Red sandstone TIZ 41	Red sandstone TIZ 40	"Petit Calcaire" TIZ 39	Tamjout Dolomite C75 C1	Red sandstone C75 C3	Purplish siltstone C75 C8	Greenish siltstone C75 C12	Malachite-cerussite TIZ 13	Malachite TIZ 18	Iron oxides TIZ 24	Iron oxides TIZ 33	Malachite (LW) C15 C1	Greenish siltstone TIZ 5	Conglomerate TIZ 14	Grey-red sandstone C1 12	Conglomerate C1 16	Greenish siltstone C15 C4	Conglomerate C15 C5	Greenish siltstone C15 C8	Grey-greenish sandstone C15 C9	Greenish siltstone C15 C11	Grey-greenish sandstone C75 C5	Grey-greenish sandstone C75 C7			
Laterite	Goethite																														
	Hematite	XXX							XXX				XX XXX XXX					X X X X													
	Kaolinite	X X																X X													
	Smectites																	X X													
	Illite												X																		
	I-S clays																	X													
Saprolite	Cerussite												XXX																		
	Malachite												XXX					XXX XX XX													
	Y-Phosphate																	XX XX XX													
	Rutile												X					X													
	Stromeyerite																	XX													
	Chalcocite												XX					XX													
	Covellite												XX					XX													
Protolith/Primary mineralization	Bornite																	XX XX													
	Barite																	XX													
	Chalcopyrite												X					XX													
	Galena	X																													
	Quartz	XX	XXX	XXX	XXX	XXX	XXX	XX	XX	XXX	XXX	XXX	X	XX	XX	XX	XX	XXX	XXX	XXX	XXX	XXX	XXX	XXX	XXX	XXX	XXX	XXX	XXX	XXX	
	Dolomite	XXX	X	X	X	XX	XX	XXX	XXX	XX	X	X			XX	XXX		X		XX	XXX		XXX	XX	XX	XX					
	Muscovite	X	XX	XX	X	X	X		X	X	X	X				X		X	X	X	XX	XX		XX	X	X	X	X	X		
	Chlorite		XX	X	XX	X	X			X	X	XX						XX	XXX	XX	XX	XX		XX	XX	XX	XX	XX	XX		
	Feldspars		XX	XX	XX	XX	XX			XX	XX	XX						XX	XX	XX	XX		XX	XX	X	X	X	X	X		
	Calcite	X							XX	X					XX X					X											
	Apatite		X															XX X													

## **5.4.5. Discussion**

### **5.4.5.a Weathering profiles**

The presence of an oxidizing environment and fluids leaching the primary ore are the main factors leading to weathering (Choulet et al. 2014; Boni and Mondillo 2015; Verhaert et al. 2017; Sillitoe 2019). Other factors such as uplift of the area and fracturing enable the exhumation and subsequent weathering of host rocks and mineralization (Boni and Mondillo, 2015). The structure, the porosity and the permeability of the host rocks and the presence of faults/fractures facilitate the percolation of meteoric waters and therefore control the flow of supergene fluids (Borg 2009; Choulet et al. 2014). In addition, the nature of the host rocks (e.g. limestone or dolostone) influences neutralization processes of acidic fluids (Widdowson 2008; Boni and Mondillo 2015; Ciantia and Castellanza 2016).









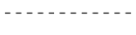
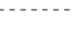






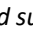
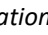
The weathering profile can be separated into different zones. The upper part of the weathering profile generally referred to as laterite, gossan or leaching zone is rarely conserved in the Tizert deposit (Fig. 5.4.9) and is limited to few subsurface samples in which iron oxyhydroxides are abundant (e.g. TIZ24, 33 and 36). Under this leaching zone, the oxidation zone (saprolite, Fig. 5.4.9), also defined as the "green oxide zone" is separated from the cementation zone by the water table level (Reich and Vasconcelos 2015). The limit between the cementation and the oxidation zone reflects the transition from a reducing to an oxidizing environment allowing the formation of secondary carbonates such as malachite that are stable under oxidizing conditions and for a neutral to basic pH (Fig. 5.4.7A) (Robb 2005; De Putter et al. 2010; Verhaert et al. 2017). Other minerals such as cerussite (Fig. 5.4.7B;  $\text{PbCO}_3$ , e.g. TIZ13), sulfates (barite, e.g. TIZ11) or phosphates may also be formed (Robb 2005), as it is the case at Tizert (Fig. 5.4.5C and 5.4.6G). The cementation zone (saprolite, Fig. 5.4.9) is characterized by the replacement of primary sulfides by other secondary sulfides (Verhaert et al. 2017). At Tizert, chalcopyrite and bornite I are replaced by chalcocite II, bornite II and covellite, which are stable under more reducing and lower pH conditions (Fig. 5.4.7A). These secondary minerals are formed by recombination of metal cations and sulfate ions transported by acidic fluids (Van Langendonck et al. 2013). The presence of these sulfides indicates that neutralization of the fluids was not sufficient to reach a neutral pH and that these solutions were able to reach the level of the groundwater table as redox barrier (Robb 2005; Verhaert et al. 2017). The main Cu minerals are found in the "green oxide zone" (mainly malachite) and in the cementation zone (covellite and chalcocite II). In this part of the weathering profile, also called saprolite, the stratification ( $S_0$ ) and schistosity are preserved (Fig. 5.4.6H). This further indicates that weathering is almost not completed in the Tizert deposit.



**Figure 5.4.7.** (a) Eh-pH diagram of the system Cu-C-S-Si-O-OH showing stability fields of Cu-minerals at 25°C and 1 atm (modified from Guilbert and Park 1986); (b) Eh-pH diagram of the system Pb-S-C-O-OH showing the stability fields of Pb-minerals at 25°C and 1 bar (modified from Brookins 1988).

### 5.4.5.b Paragenesis

The mineralizing sequence (Fig. 5.4.8) observed in the Tizert copper deposit is as follows: chalcocite - pyrite - bornite I – chalcocite I - galena → bornite II → chalcocite II/covellite → malachite/cerussite → hematite, goethite. Primary sulfides (Fig 5.4.5C to 5.4.5F; chalcocite I, pyrite, galena, chalcocite I and bornite I) are initially replaced by secondary sulfides (Fig 5.4.6C and 5.4.6F; chalcocite II, covellite and bornite II) in the cementation zone. Isolated bornite (e.g. TIZS6) is primary while it also could be secondary in some other samples (e.g. TIZC1 12). Covellite has a smaller stability range than bornite and chalcocite is formed after chalcocite II or directly from chalcocite (in some cases chalcocite II is not observed) since this Cu-depleted sulfide is the last secondary sulfide to precipitate (Chavez 2000). The presence of covellite reflects slight variations in the groundwater table leading to more reducing conditions (Choulet et al. 2014; Sillitoe 2019). Malachite forms when pH rises (neutral to basic); this mineral is more abundant in the Lower Limestone because fluid neutralization has been more efficient in carbonate rocks. Barite is identified as primary along with primary sulfides (e.g. TIZS19, Fig. 5.4.5C) and as a secondary mineral forming a rim around malachite (e.g. TIZ C1 12, Fig. 5.4.6G). Barite may precipitate in a large field of pH and Eh under supergene conditions (Hanor 2019). At Tizert, the Ba required for the formation of supergene barite probably originates from sandstones and siltstones of the Basal Series that contain a significant quantity of this element (Table 5.4.1, 500 - 800 ppm). As previously proposed by Oummouch et al. (2017), we confirm the two origins (primary and secondary) for barite at Tizert.

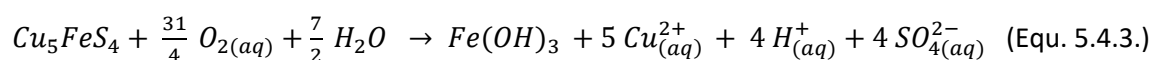
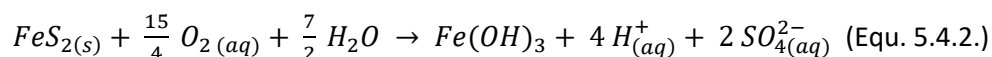
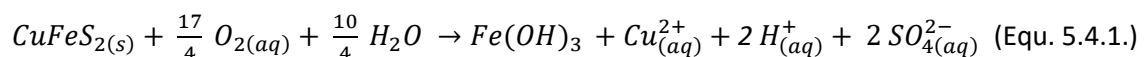
MINERALS	HYPOGENE*	SUPERGENE MINERALIZATION	
		CEMENTATION ZONE	SAPROLITE AND LATERITE
Chalcopyrite*			
Bornite I*			
Bornite II			
Pyrite*			
Galena*			
Chalcocite I*			
Chalcocite II			
Covellite			
Stromeyerite I*			
Stromeyerite II			
Malachite			
Cerussite			
Barite I			
Barite II			
Hematite/Goethite			
Clays			

**Figure 5.4.8.** Paragenetic sequence of the Tizert deposit (hypogene and supergene mineralization; \*observed by Oummouch et al. 2017)

### 5.4.5.c Weathering process

Weathering processes are responsible for the *in situ* supergene enrichment of copper and other elements such as zinc, silver or gold in many near-surface deposits (Reich and Vasconcelos 2015; Robb 2005). For the Tizert copper deposit, it is mainly an enrichment in Cu and, to a lower extent, in Ag (Oummouch et al. 2017). This statement is attributed to three main processes: (1) oxidation of primary sulfides, (2) *per descensum* transport of acidic solutions and (3) neutralization of acidic fluids, leading to the formation of secondary minerals.

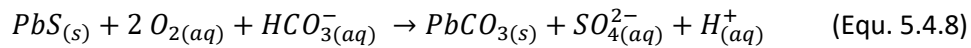
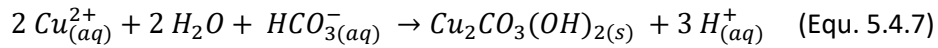
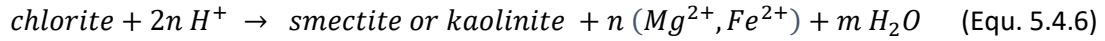
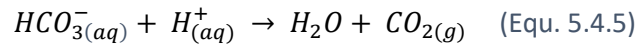
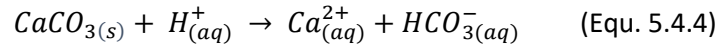
The first step leading to enrichment is the oxidation of the primary sulfides like chalcopyrite, pyrite or bornite I (Fig. 5.4.9, Equ. 5.4.1 to 5.4.3):



The oxidation of hypogene minerals leads to the production of  $\text{H}^+$  ions (decrease in pH) in the weathering zone as well as the release of  $\text{SO}_4^{2-}$  ions, which will reinforce the weathering process, and other ligands ( $\text{CO}_3^{2-}$ ,  $\text{PO}_4^{3-}$ , ...) and metallic cations ( $\text{Cu}^{2+}$ ,  $\text{Fe}^{2+}$ , ...) (Domènech et al. 2002; Reich and

Vasconcelos 2015; Sillitoe 2019). The hypogene orebody was leached from  $\text{Cu}^{2+}$  cations that led to a slight enrichment in Fe and to the formation of hematite or goethite in the upper part of the weathering profile (Robb 2005). Such concentration is mainly due to the very low mobility of iron, which is therefore not transported by supergene fluids (Verhaert et al. 2017). Other elements (like Pb and Zn) with low mobility can also be concentrated in these lateritic Fe oxides, as it is the case in Tizert (e.g. TIZ24 and TIZ 33, Fig. 5.4.6D).

Transport is an important step in the enrichment process; once oxidized and leached, the metals, here mainly Cu and Ag, are transported *per descensum* by acidic fluids over a distance of several tens or even hundreds of meters due to the high mobility of copper (Reich and Vasconcelos 2015; Arrobas et al. 2017; Verhaert et al. 2017; Sillitoe 2019). Then, neutralization of acidic fluids is necessary to allow the precipitation of secondary minerals that require neutral pH conditions such as malachite or cerussite (Equ. 5.4.7 and 5.4.8, Fig. 5.4.6A, 5.4.6C, 5.4.6E, 5.4.6F and 5.4.6G). This neutralization (Equ. 5.4.4 to 5.4.6) involves carbonates (Descostes et al. 2002) such as those from the Tamjout Dolomite and/or chlorites (Brown 1967), the latter being widely available in sandstones and siltstones of the Basal Series (Fig. 5.4.5A and 5.4.5B). The presence of smectite and/or kaolinite in some samples (e.g. TIZ3, TIZC1 C and TIZC1 10) confirms that part of the fluid has been locally neutralized by chlorites (Brown 1967). However, significant amounts of chlorite are still present in the weathering profile. This, in addition to the relative abundance of malachite suggests that acidic fluids were mainly neutralized by carbonates in the Lower Limestone (especially Tamjout Dolomite) and that the chlorite-rich upper part of the Basal Series only slightly contributed to the neutralization of acidic fluids.



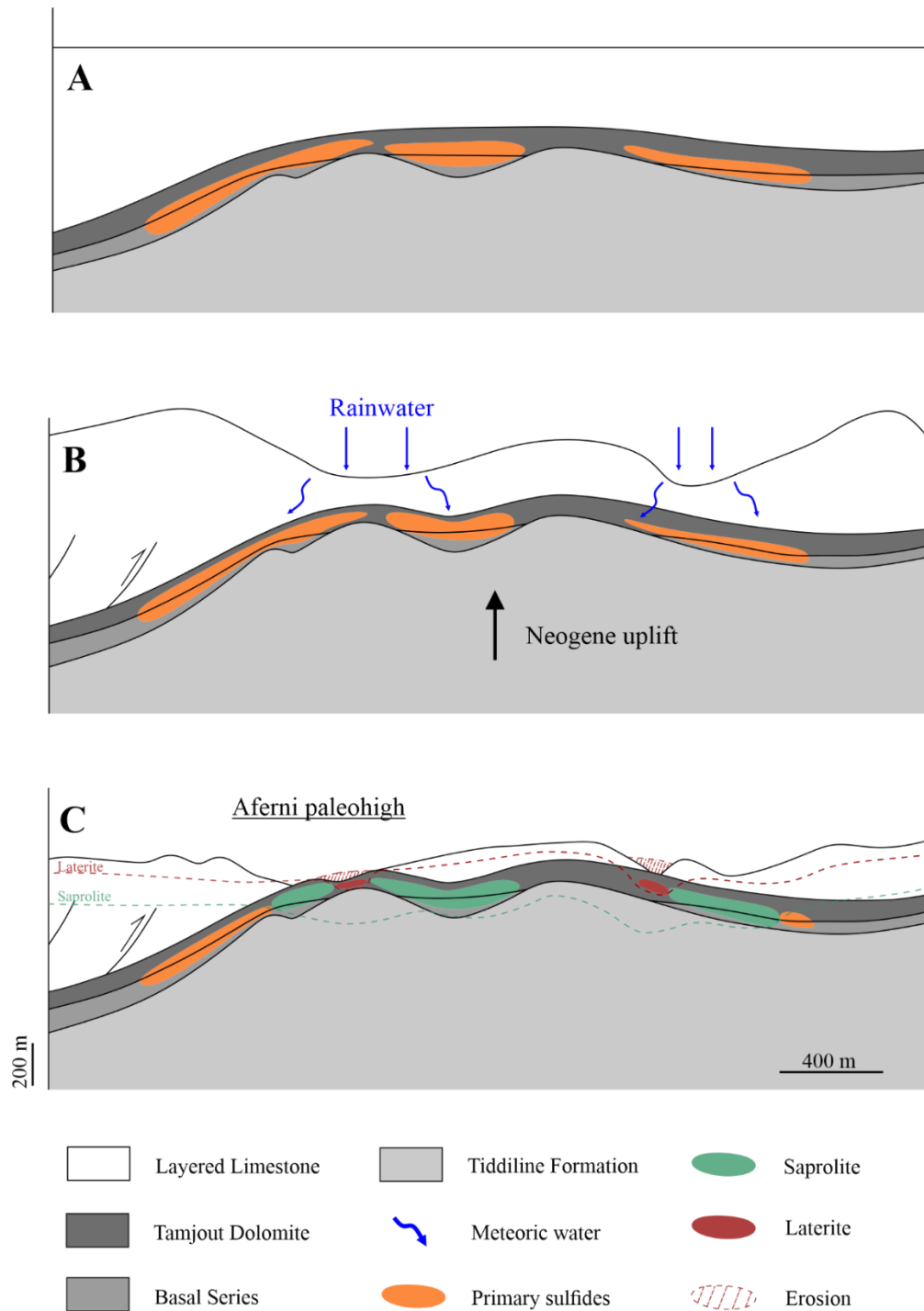


**Figure 5.4.9.** Schematic representation of the weathering model for the supergene Tizert deposit: (a) initial situation (pre-~30 Ma), with fresh primary (hypogene) ore well developed along basin margins adjacent to the basement paleohighs, see Oummouch et al. (2017) for details; (b) initiation of weathering during Neogene uplift(s); (c) current situation, with weathering profile (laterite s.s. – saprolite – primary sulfides) (Modified from Oummouch et al. 2017).

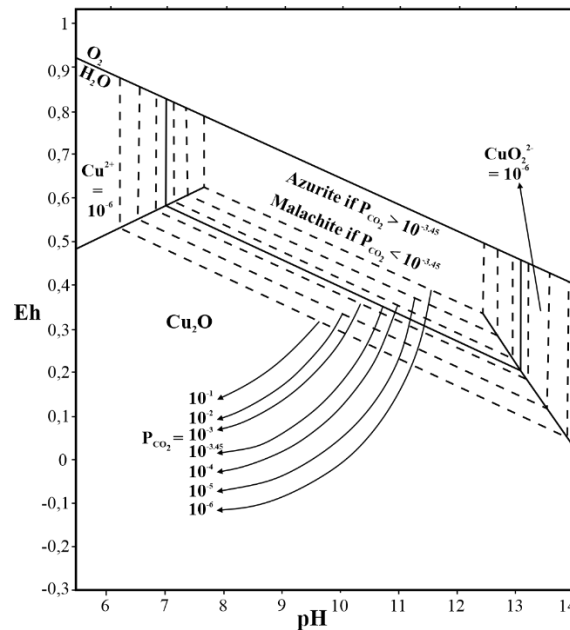


**Figure 5.4.10.** Eh-pH diagram of the system Cu-O-H-CO<sub>2</sub> at 25°C and 1 atm. total pressure. Total dissolved copper 10<sup>-6</sup> mol. The diagram shows the stability fields of malachite and azurite as a function of P<sub>CO<sub>2</sub></sub>. Equilibrium is reached at P<sub>CO<sub>2</sub></sub> = 10<sup>-3.45</sup> atm. with corresponding pH = 6.95, pH = 13.05 and Eh = 0.67 – 0.0592pH (straight lines) (modified from Vink 1986).

Azurite and malachite have very similar chemical compositions. Malachite is more often observed than azurite because it is more stable under atmospheric conditions (Verhaert et al. 2017). The absence or the very low occurrence of azurite at Tizert can be explained by several factors. The formation of this mineral requires slightly acidic conditions with high carbonate ion activity, while malachite precipitates under neutral to slightly basic pH (Vink 1986). In addition, azurite often recrystallizes into malachite when the activity of carbonate ions slightly varies. However, no pseudomorphosed malachite was observed at Tizert, suggesting that malachite was the only secondary carbonates to precipitate during weathering processes. The transition from malachite to azurite is very sensitive to slight chemical variations in the environment (Vink 1986). In the Cu-O-H-CO<sub>2</sub> system (Fig. 5.4.10), the balance between azurite and malachite is reached for a CO<sub>2</sub> partial pressure of 10<sup>-3.45</sup> atm, close to atmospheric pressure; both minerals may coexist at such pressure and at pH levels ranging from 6.95 to 13.05 (Vink 1986). At Tizert, such chemical conditions were not reached and jeopardized the neoformation of azurite. Hence, azurite remains absent (or rarely observed according to Oummouch et al. 2017).

The absence/scarcity of azurite is quite common in supergene copper deposits of Morocco such as the Jbel N'Zourk deposit (Central Anti-Atlas), for which a similar mineralogical assemblage (except for some Cu-oxides) in the same host rocks (Basal Series – Tamjout Dolomite) is observed (Clavel and Leblanc 1971; Maacha et al. 2011b), and the Jbel La'Sal deposit (Maacha et al. 2011a; Bourque et al. 2015) in Bou Azzer - El Graara inliers (Table 5.4.3), or elsewhere in the world (e.g. Luiswishi deposit, DRC) (Fontaine et al. 2020). On the contrary, other deposits located in the Anti-Atlas such as Agoujgal, Tazalaght or Ouansimi (Table 5.4.3; Asladay et al. 1998; El Basbas et al. 2011; Managem et al. 2012; Basbas et al. 2019; Verhaert et al. in press) show higher proportions of azurite, even in quite similar host rocks than at Tizert. This is also the case in the Yangla deposit (China; Du et al. 2020) and the Tsumeb deposit (Namibia; Miller 2008). Even if such mineralization are located in the same host rocks, the local geodynamic context (especially fracturing and weathering depth) of each deposit may have been slightly different and may have locally displayed higher local pCO<sub>2</sub> allowing azurite formation. The presence of azurite in supergene Cu-deposits may be related to the formation of carbonic acid (high pCO<sub>2</sub>) with favorable climatic conditions during weathering. However, this assertion requires further



investigation, especially by dating supergene minerals formed under weathering processes/periods in order to integrate them in the local/global geological context (Lippolt et al. 1998; Vasconcelos 1999).

**Table 5.4.3.** Supergene malachite and azurite occurrences in some Cu-deposits in Morocco and around the world

Deposits	Localisation	Host rocks	Mineralization	References
Jbel N'Zourk	Bou Azzer - El Graara and Zenaga inliers (Morocco)	Basal Series - Tamjout Dolomite	Cu-oxides, <u>malachite</u> and <u>rare traces of azurite</u> . Primary sulfides rarely observed, similar as Tizert	Clavel & Leblanc (1971); Maacha et al. (2011)
Tazalaght	Aït Abdallah inlier (Morocco)	Quartzite "XII" to Lower Limestone	Cu-sulfides, <u>malachite and azurite</u>	Asladay et al. (1998); El Basbas et al. (2011)
Jbel La'Sal	Bou Azzer - El Graara inliers (Morocco)	Lower part of Cambrian cover	<u>Malachite</u> , chalcocite, native Cu, chrysocole and cuprite	Maacha et al. (2011)
Ouansimi	Ouansimi - Kerdous inliers (Morocco)	Basal Series - Lower Limestone	Pyrite, chalcopryrite, bornite, covellite, cuprite, chalcocite, <u>malachite</u> , <u>azurite</u> and native Cu	Baoutoul et al. (2013), El Basbas et al. (2020)
Agoujgal	Kerdous inlier (Morocco)	Basal Series - Tamjout Dolomite - Agoujgal Limestone	Chalcopryrite, pyrite bornite, chalcocite, covellite, <u>malachite</u> , <u>azurite</u> , galena, sphalerite, Fe-oxides	Asladay et al. (1998); Maddi et al. (2011)
Luiswishi	High-Katanga (DRC)	Neoproterozoic siliciclastic and carbonate sedimentary rock	Chalcopryrite, carrollite, pyrite, <u>malachite</u> , heterogenite, bornite, chalcocite and goethite	Fontaine et al. (2020)
Yangla	Saniang Region (China)	Metamorphic rocks	Pyrite, chalcopryrite, pyrrhotite, molybdenite, galena, sphalerite, <u>azurite</u> , <u>malachite</u>	Du et al. (2020)
Tsumeb	Northern Namibia	Otavi Group : limestone and dolomite	<u>Malachite</u> , <u>azurite</u> , wulfenite, diopside, galena, tennantite, pyrite, chalcopryrite, digenite, djurleite, ...	Miller (2008)

The Tizert area experienced several geodynamic events during its geological history. The last major uplift, which probably led to weathering of the deposit, was initiated around 30 Ma, with an average erosion rate of 0.08 km/Ma (Ruiz et al. 2011). Consequently, the Meso-Cenozoic cover of this area has mostly been eroded and the Lower Cambrian terrains probably remained under a cover of sediments until the Neogene (Leprêtre et al. 2015), prior to their exposure to surface/weathering conditions. The lowermost Cambrian is mainly characterized by Lower Limestone series, with notably the Tamjout Dolomite (Fig. 5.4.3 and 5.4.4) that displays a relatively high porosity and thus allows an efficient permeability, where supergene fluids are able to percolate. Moreover, the Basal Series were deposited in an extensional context, in basins delimited by normal faults that are not observed in Tamjout Dolomite and overlying limestones (Oummouch et al. 2017). Such fault systems also facilitate the percolation of supergene fluids within the Basal Series and have an impact on the depth of weathering. In addition, the occurrence of primary mineralization is generally related to the varying thickness of the Basal Series (0 to 100 m) associated with paleohighs (Oummouch et al. 2007).

#### 5.4.5.d Chemical migration during weathering

Most of the primary and secondary mineralization is concentrated in the greenish siltstone of the Basal Series: Cu-enrichment is the highest, followed by Ag and Pb (up to 100 times compared to fresh rocks). Moreover, no major depletion in metals has been identified in weathered rocks.

Other elements are slightly enriched in the weathered ore, such as As, which is generally higher in malachite-rich samples. Such high As contents are generally associated to Pb, Zn and Ag enrichments. However, the source of As is not clearly identified. As could originate from fresh rocks since primary sulfides such as pyrite, galena and chalcopyrite are devoid of this metal. Moreover, the presence of arsenopyrite (not observed) is not excluded. Oummouch et al. (2017) determined an average grade of 23 g/t of Ag in the deposit. However, only one sample displays an Ag-mineral (stromeyerite, TIZC75 C7). By taking an average of weathered samples (oxides, secondary sulphides, etc.), the Ag content reaches ~13 ppm (from 0.5 to 62.5 ppm). No correlation could be made between the Ag content, the nature of the rock and the mineral phases. In the Tizert deposit, galena shows low Ag content (< 5 %). However, high Ag concentrations in galena have been identified in many deposits: in Morocco, Imiter deposit (Anti-Atlas) (Pasava 1994; Borisenko et al. 2013) and Tighza polymetallic district (Hercynian Belt, Central Morocco) (Marcoux et al. 2015), and elsewhere around the world, as example the Broken Hill deposits (Morland and Webster 1998; Walters 1998). At Tizert, the absence of chlorargyrite which was observed by Oummouch et al. (2017) could be explained by its very local formation due to anthropogenic influences (Dill et al. 2013; Dill 2015), even if chlorargyrite also forms naturally under arid and tropical climates (Boyle 1997; Golebiowska et al. 2010; Alfieris et al. 2013). Native silver is stable under reduced conditions (Keim et al. 2016) and is therefore rarely observed in the weathering zone.

Enrichment in V, Cu, Zn, As, Mo, Sb, U, Pb and Bi are related to Fe-oxyhydroxide (e.g. TIZ24 and TIZ33, Fig. 5.4.6D). In general, Fe-oxides concentrate immobile elements, such as U and REE (De Putter et al. 1999; Verhaert et al. 2017). The highest U content of Tizert's Fe-oxyhydroxides, generally associated with a Th depletion, is a typical supergene trend and is often related to the mobilization of U and Th during weathering processes. Mobile and soluble U in supergene fluids is preferentially leached and accumulated in neoformed oxyhydroxide minerals, while Th remains less sensitive to weathering phases or is rapidly assimilated by the first precipitating mineral phases (Braun et al. 1990; Pagel et al. 1990; Verhaert et al. 2018). However, in these Fe-oxyhydroxides concentrated in Tamjout Dolostone REE are depleted compared to the UCC. Finally, the main chalcophile elements (Pb, Zn, Cu) and the elements generally associated with Au (Sb, As) are enriched.

#### 5.4.6. Conclusion

At Tizert, the hypogene mineralization consisting of pyrite, chalcopyrite, chalcocite I, bornite I and galena, was affected by weathering processes leading to the formation of a secondary, supergene mineralization, mainly represented by malachite, covellite, bornite II and chalcocite II. The supergene mineralization is mainly hosted (in percentage and volume) in weathered greenish siltstones of the Basal Series, with a significant Cu enrichment compared to the fresh rocks. In addition, high Cu content can also be observed in the greyish-red conglomerates and sandstones of the Basal Series, as well as in the Tamjout Dolomite Formation, to a lower extent.

The Tizert giant copper deposit is mainly represented by the "green oxide zone" hosting significant amounts of malachite. This abundance of Cu carbonates is explained by the rapid neutralization of acidic supergene fluids by host rocks mainly composed of dolostones ("Lower Limestone" - Tamjout

Dolomite Formation). In addition, chlorites of the Basal Series sandstones also played a role in this neutralization and resulted in the neoformation of smectites and/or kaolinite in weathered rocks. The absence of azurite at Tizert, which is quite common in supergene deposits, is due to low CO<sub>2</sub> partial pressure and high pH conditions. Laterite s.s. is rarely observed in this deposit and iron oxyhydroxides are only observed in few spots ("patchwork" laterite).

Besides Cu, only Ag is enriched during weathering processes, when slight enrichments in As, Zn, Zn, Ba or Pb are observed. The mineralization is relatively disseminated and homogeneous in the entire deposit, which could be a major advantage for potential mining.

## 5.5 Summary: metallogeny of Moroccan ore deposits

The mineralogical and chemical contents of Jbel Klakh, Jbel Haouanit, Jbel Rhals, Tazalaght, Agoujgal and Tizert supergene ores are different, but the processes responsible for their formation are quite similar. The oxidation of base metal sulfides resulted in an **acidic environment** and triggered the mobilization of ions. The recombination of cations and ligands led to the formation of a wide assortment of phases ranging from sulfides stable in reduced conditions to carbonates such as malachite that obviously prefer oxidizing conditions and neutral pH levels. The precipitation of supergene oxidized phases, at Jbel Klakh, Jbel Haouanit, Agoujgal and Tizert, and in a lesser extent at Tazalaght, was made possible through an efficient neutralization of the acidic fluids by host rock dissolution. Both carbonate minerals and chlorite were involved in such processes.

The supergene processes led, at Jbel Klakh, Tazalaght, Tizert, and moderately at Jbel Haouanit and Agoujgal, to the development of four **mineralogical vertical zones** clearly distinguished in any vertical cross-section of the deposits, from base to top: the hypogene zone (mostly chalcopryrite, pyrite, tennantite, galena, sphalerite), the cementation zone (bornite, digenite, chalcocite, djurleite, covellite), the oxidized zone (*i.e.* malachite, azurite, brochantite, olivenite, chenevixite), and the leached zone (iron (oxyhydr-)oxides, mottramite, quartz, calcite). The formation of such vertical sequences results from the complex physico-chemical processes that took place in the deposits and reflects pH and Eh variations. The Jbel Rhals polymetallic deposit is a peculiar case: it owns a polyphased metallogenic history composed of supergene processes superimposed over hydrothermal alteration and does not show any vertical zoning.

The influence of the **host rocks and primary mineralization nature** on supergene processes/neoformations is clearly highlighted through the difference between the secondary assemblages of carbonate-hosted (Jbel Klakh, Jbel Haouanit, Agoujgal, Tizert) and other deposits (Jbel Rhals, Tazalaght). Quartzitic host rocks such as those hosting Tazalaght ores can not fast enough neutralize the fluids acidity, and the precipitation of a large oxidized mineralization including carbonates is (partly) jeopardized. On the contrary, carbonate host rocks allow the quick buffering of the fluids acidity, the precipitation of large amounts of oxidized mineral phases such as carbonates, and the formation of extensive oxidized zones. The common association of Cu, Pb, Fe, Ca, Zn-carbonates, arsenates, sulfates, phosphates, vanadates, and oxides in supergene deposits reflects complex physical-chemical evolution of the mineralizing fluids, in relation with pH and Eh variations. The vanadate mottramite is ubiquitous in supergene ores, indicating the common circulation of V-rich fluids in such environments. Geochemical enrichments in particular elements are related to the leaching and concentration, by substitution or adsorption, of such elements during weathering processes.

The formation of supergene ores in the High Atlas and Anti-Atlas of Morocco is presumably related to **exhumation and uplift processes** during Cenozoic. Dating supergene mineral phases that are present in all deposits, such as iron (oxyhydr-)oxides, could (or not) validate this assumption. This will be the aim of the data described in Chapter 6 (see below).

CHAPTER VI

TIMING OF WEATHERING PROCESSES

## Chapter 6

### Timing of weathering processes

<b>6.1 Thoughtful selection of samples for (U-Th-Sm)/He dating</b>	<b>p. 157</b>
First tests	p. 158
<b>6.2 Goethite (U-Th-Sm)/He dating highlights the early steps of Mn ore formation at Imini, High Atlas, Morocco</b>	<b>p. 174</b>
6.2.1 Geological setting	p. 174
6.2.2 Study site and methods	p. 175
6.2.3 Results and interpretations	p. 176
6.2.3.a Chronology of Imini's goethite precipitation	p. 176
6.2.3.b Composition of the mineralizing fluids	p. 177
6.2.3.c Paragenetic and geodynamical implications	p. 178
6.2.4 Conclusions	p. 179
6.2.5 Data Repository – Supplementary material	p. 179
6.2.5.a Samples and analytical methods	p. 179
Sampling strategy	p. 179
Petrological characterization	p. 181
Geochemical characterization	p. 181
Stable isotope geochemistry	p. 182
(U-Th-Sm)/He dating	p. 182
6.2.5.b Additional results and interpretations	p. 183
Characterization	p. 183
Stable isotope geochemistry	p. 188
(U-Th-Sm)/He dating	p. 188
<b>6.3 Unraveling the potential relations between the formation of supergene ores and geodynamic in the Anti-Atlas and High Atlas (Morocco), by goethite (U-Th-Sm)/He dating</b>	<b>p. 192</b>
6.3.1 Geological setting	p. 192
6.3.1.a Anti-Atlas (Tazalaght, Agoujgal, Tassrirt, Irkhs, Tizert, Assifid and Ighrem sites)	p. 192
6.3.1.b High Atlas (Jbel Rhals, Jbel Haouanit and Jbel Klakh sites)	p. 194
6.3.2 Materials and analytical methods	p. 194
6.3.3 Results	p. 201
6.3.3.a Mineralogical characterization	p. 201
6.3.3.b Geochemical characterization	p. 204
6.3.3.c (U-Th-Sm)/He data	p. 213
6.3.3 Discussion	p. 220

6.3.4.a Selection and characterization of most reliable samples for (U-Th-Sm)/He dating	p. 220
6.3.4.b Composition of fluids and mineralizing events	p. 221
6.3.4.c Role of geodynamic during weathering periods	p. 222
High Atlas	p. 222
Anti-Atlas	p. 222
6.3.5 Conclusion	p. 225
<b>6.4 K-Ar dating of Moroccan alunite</b>	<b>p. 226</b>
6.4.1 Geologic context	p. 226
6.4.2 Methodology	p. 227
6.4.3 Results	p. 228
6.4.4 Discussion	p. 230
<b>6.5 New (U-Th)/He dating of mixed and polyphase alteration processes in the vertebrate-bearing Nefza-Sejnane polymetallic mining district (Tunisia)</b>	<b>p. 232</b>
6.5.1. Geological setting	p. 232
6.5.2. Materials and methods	p. 234
6.5.3. Results	p. 236
6.5.4. Discussion	p. 239
6.5.4.a (U-Th)/He age significance using petrographic examination of goethite	p. 239
6.5.4.b Age of the meteoric Fe-fluids in the Nefza-Sejnane district	p. 239
Late Tortonian weathering event ( $8.6\pm0.9$ Ma)	p. 239
Late Pleistocene weathering event ( $0.8\pm0.2$ Ma)	p. 240
Stratigraphic frame of the Nefza-Sejnane district	p. 240
Significance of the weathering periods at a regional scale	p. 243
Revision and refined age of the mammalian fauna in the Douahria Fe-deposit	p. 244
6.5.5. Conclusion	p. 246
<b>6.6 Conclusions: implications of Moroccan and Tunisian GHe and K-Ar ages</b>	<b>p. 248</b>

Regionally, in accordance with geological and climatic conditions, recurrent dissolution, solubilization, remobilization, reconcentration and reprecipitation of elements of economic interest at or near the Earth's surface promote the formation of weathering profiles in ore deposits (Vasconcelos et al. 2015). Several parameters control the development of such weathering profiles: 1) the mineralogy and morphology of the primary ore (see chapter 6.3), 2) the structure of the host rock and the preexisting fractures and faults, 3) the nature of the host rock (see chapter 6.3), 4) climatic factors that control the temperature, the availability of meteoric water, evapotranspiration rates, the (micro)biological activity, the intensity of leaching and the possible reprecipitation, 5) the tectonic/geodynamic setting that governs the regional uplift of the primary ore, in competition with erosion, and 6) eustatism (Reichert and Borg 2008; Choulet et al. 2014; Vasconcelos et al. 2015). Significant weathering and the subsequent formation of supergene mineralization can thus only occur within certain time frames characterized by specific concomitant conditions. Since the formation of supergene mineralization generally lasts (tens of) Ma, information about the tectonic and climatic history of specific locations/areas can be recorded and preserved in secondary mineral phases. Supergene ore deposits thus provide direct access to complete sections through the weathered crust and help in understanding the timing of weathering processes. While the mineralogical-geochemical parameters and genesis of supergene ores is usually well understood and defined (e.g. Choulet et al. 2014; Verhaert et al. 2017; Verhaert et al. in press), the timing of secondary ore precipitation and the role of the above-named parameters are still matter of debate. Until now, temporal context of ore formation has mostly been studied using K-Ar and Ar-Ar methods on Mn oxides (e.g. Vasconcelos et al. 1994).

This chapter refers to three papers dealing with the chronology of supergene ore deposits through (U-Th-Sm)/He dating of iron (oxyhydr-)oxides. The first subchapter deals with the selection and characterization of iron (oxyhydr-)oxides, which strongly affect the successful character of dating (chapter 6.1). With numerous supergene Cu-Pb-Zn-V ore deposits/sites and a well-characterized geodynamic frame (Frizon de Lamotte et al. 2008; Gouiza et al. 2017; Leprêtre et al. 2018), the Moroccan Anti-Atlas (chapters 6.2, 6.3, 6.4) and High Atlas (chapters 6.3, 6.4) constitute natural laboratories to explore and understand the potential relations/causes between oxidation processes and local/regional uplifts and/or climatic events. Similarly, the formation of Tunisian Fe-Mn-LREE-U-Pb ores is tentatively related to geodynamic and climatic events (chapter 6.5).

The second section of this chapter is based on a paper, entitled *“Goethite (U-Th-Sm)/He dating highlights the early steps of Mn ore formation at Imini, High Atlas, Morocco”*, co-authored by **Michèle Verhaert**, Cécile Gautheron, Torsten Vennemann, Rosella Pinna, Abdellah Mouttaqi, Augustin Dekoninck and Johan Yans. This study will be submitted for publication to the journal *Geology*. This paper presents (U-Th-Sm)/He dating of botryoidal goethite, combined with  $\delta^{18}\text{O}$  and  $\delta\text{D}$  stable isotopes analyses, at the Imini Mn ore deposit, High Atlas, Morocco. It highlights early Fe mineralization following dolomite dissolution, prior to Mn oxides, which is consistent with the limiting range of the Cenomanian-Turonian host rock. The remarkable purity, crystallinity and large dimensions of Imini's goethite crystallites enable the high reproducibility of (U-Th-Sm)/He ages through an efficient He retention in the crystalline lattice. Precipitation rates for goethite are moreover estimated. The Cretaceous GHe (goethite (U-Th-Sm)/He) ages that correspond with the onset of the Africa-Eurasia convergence and the resulting Late Cretaceous-Cenozoic Atlasic doming, suggests that surface deformation (at least partly) controls the precipitation of goethite at Imini.

The second paper composing the third subchapter is co-authored by **Michèle Verhaert**, Cécile Gautheron, Torsten Vennemann, Rosella Pinna, Omar Saddiqi, Otman Maddi, Lhou Maacha and Johan Yans. This study, entitled *“Unraveling the potential relations between the formation of supergene ores and geodynamics in the Anti-Atlas and High Atlas (Morocco), by goethite (U-Th-Sm)/He dating”*, will be



submitted for publication in the special volume "*Supergene evolution of polymetallic Deposits, including non laterite Fe and Mn ores*" of the journal *Minerals*. This study confronts (U-Th-Sm)/He dating of different types of iron (oxyhydr-)oxides samples from the Anti-Atlas and the High Atlas (Morocco) to determine which types provide the best results. While botryoidal goethite is judged as the best material for (U-Th-Sm)/He method, pyrite-pseudomorphosing samples are the worst material as they commonly include intermixed goethite and hematite generations and inherited host rocks minerals. The divergent textures of botryoidal and pseudomorphosing samples, along with their  $\delta^{18}\text{O}$ ,  $\delta\text{D}$ , eU and minor elements contents, highlight their various formation process: from the circulation of mineralizing fluids and *in situ*, respectively. Both in the Anti-Atlas and in the High Atlas, GHe ages match with Late Cretaceous and Cenozoic erosional phases. Consequently, it is proposed that the exhumation of primary mineralization and rocks is a key process required for the formation of supergene ore deposits, and that it could ensue from, and be driven by, uplift and erosional phases. Differential deformation between studied sites is tentatively proposed to explain the absence of relation between iron (oxyhydr-)oxides sampling localization and GHe ages.

The fourth section focuses on the K-Ar dating of alunite originating from some deposits studied in chapter 6.3, to provide more information on the timing of weathering processes in these deposits, and to tentatively confirm the relation between supergene mineralization and geodynamic events.

The third paper entitled "*(U-Th)/He dating of supergene iron (oxyhydr-)oxides of the Nefza-Sejnane district (Tunisia): new insights on mineralization and biostratigraphy of mammals*" constitutes the fifth subchapter. The co-authors Johan Yans, **Michèle Verhaert**, Cécile Gautheron, Pierre-Olivier Antoine, Béchir Moussi, Augustin Dekoninck, Sophie Decrée, Ridha Chaftar, Nouri Hatira, Christian Dupuis, Rosella Pinna-Jamme and Fakher Jamoussi present here, for the first time in Tunisia, supergene goethite (U-Th)/He ages, from various localities/deposits of the mining district of Nefza-Sejnane (Tunisia), which highlight direct dating of significant weathering periods during late Tortonian and late Pleistocene. These weathering events are most likely associated to favorable conditions that combine i) wet climate, displaying sufficient meteoric water, and ii) regional exhumation, due to large-scale vertical lithospheric movements enhancing the percolation of fluids. Matched with previous works, these results refine the stratigraphic frame of the Fe-Mn-LREE-U-Pb-Zn and clay deposits in the district, confirming the influence of meteoric fluids circulation during the late Cenozoic. The authors moreover propose a taxonomic and stratigraphic revision of the classical mammals from the Fe-rich Douahria locality.

The last subchapter aims to combine the conclusions of the previous subchapters and to propose hypotheses at large scales.

## 6.1 Thoughtful selection of samples for (U-Th-Sm)/He dating

As very pertinently pointed out by Vasconcelos (1999) for the dating of Mn oxides, the successful dating of supergene materials strongly depends on the careful selection of samples on the field, their subsequent thorough characterization in the laboratories and the thoughtful integration of results in their geological context. Detailed macroscopic and microscopic investigation of iron (oxyhydr-)oxides enables to avoid dating contaminated and impure samples and allows the acquisition of accurate and meaningful ages.

On the field, samples containing iron (oxyhydr-)oxides are sampled massively, mostly in the gossans of supergene deposits, but also in the oxidized zones and in the host rocks. Much attention is paid to their environment of formation, i.e. if they precipitated in veins, fractures, faults, cavities, by pseudomorphose or by impregnation of host rocks. Hand-sized samples are preferred but cm-sized samples are also collected. Back to the laboratories, samples are photographed from every angle and thoroughly examined. A first selection is made on the basis of the macroscopic aspect of samples: visibly impure samples are discarded (i.e. powdery samples and mixed phases that are too small to be separated). Then, X-ray diffraction is then carried out to verify the composition of samples: major phases must be goethite and/or hematite. A third and last selection is based on the observation with reflection optical microscopes and scanning electronic microscopes of polished sections of the remaining set of samples. The objective of this last stage is to retain only pure, datable samples that should deliver reliable ages of precipitation. Particular attention is thus paid to discard samples that present one of the characteristics listed below. Tables 6.1.1 and 6.1.2 gather the information of all samples preselected during this thesis for (U-Th-Sm)/He dating, from Tunisia-Belgium-France, and Morocco, respectively. All these samples have once been considered for dating, but only a few were actually dated. The rejection of samples is based on the following problems that were discovered as the thesis proceeded:

- presence of powdery phases (e.g. Fig. 6.1.4C, 6.1.4L)
- presence of poorly crystallized phases (e.g. Fig. 6.1.1P, 6.1.3N)
- presence of excessively porous material (e.g. Fig. 6.1.2O, 6.1.5L)
- variation of phases at a small scale: rim vs center of pseudomorphs (e.g. Fig. 6.1.1E)
- mixing of (several generations of) hematite and goethite (e.g. Fig. 6.1.2T, 6.1.2K, 6.1.3O, 6.1.4N, 6.1.4V, 6.1.5E, 6.1.5G)
- mixing with Mn oxides (datable phase), pyrite (e.g. Fig. 6.1.1E, 6.1.1F), malachite (e.g. Fig. 6.1.2D, 6.1.2E), mottamite (potential datable phase; e.g. Fig. 6.1.3I)
- omnipresence of quartz (e.g. Fig. 6.1.1P, 6.1.2I, 6.1.2K; 6.1.5Q), clays (e.g. Fig. 6.1.4I, 6.1.4J), calcite (e.g. Fig. 6.1.3M), dolomite (e.g. Fig. 6.1.2K, 6.1.2O 6.1.3V, 6.1.5Q), ...
- presence of gangue minerals such as apatite, zircon, ... (e.g. Fig. 6.1.3C)
- presence of lamellar crystals (only concerns hematite; e.g. Fig. 6.1.1Q-6.1.1X, 6.1.5P)
- presence of small crystallites (<100-200nm; see Chapter 6.3)
- limited quantity of datable material (e.g. Fig. 6.1.2F)

Ever since the start of this thesis, it was clear that the presence of powdery, poorly crystallized or excessively porous phases in samples is highly problematic since these poorly He-retentive phases that experienced significant He losses are disintegrated during cleaning. It was also obvious that the concentration of silicates and carbonates in iron (oxyhydr-)oxides, even if these minerals are (probably) not He-retentive, is not ideal, even if the occurrence of a few crystals is tolerated. The first analyses have been performed on lamellar hematite; obviously, these very thin crystals are not sufficiently He-

retentive and should be avoided (see below). Then, the testing of goethite and hematite pseudomorphosing (mostly) pyrite brought to light several issues (see Chapter 6.3). First, these samples are not at all homogeneous at the scale of the pseudomorph, and strong variations occur between the rim and the center. The presence of remaining pyrite is not so much of an issue but its complex replacement by generations of iron (oxyhydr-)oxides makes it difficult to separate. However, the common presence of gangue minerals such as zircon and apatite, inherited from the host rock during the replacement of pyrite, is a major issue: these very small crystals are only identified through SEM analyses, and are impossible to extract. Their presence may induce severe undesirable consequences such as the obtention of completely erroneous ages. Finally, the main problem of such samples is the mixing of several generations of hematite and goethite, in the entire pseudomorph; hydration and dehydration processes are most probably responsible for the replacement of hematite by goethite, and *vice versa*. The resulting interspersed phases of different generations provide meaningless mixed ages. The testing of fine botryoidal and microcrystalline goethite associated with supergene mineralization provided good results as long as it is not mixed with (potentially) datable phases such as Mn oxides, mottramite and malachite (see Chapter 6.3). The dating of such mixed phases would again deliver uninterpretable pointless ages. Ultimately, large botryoidal goethite was tested for (U-Th-Sm)/He dating; as the purest unmixed material, it provided promising results (see Chapter 6.2). On the basis of the previously listed criteria, botryoidal goethite appears to be the ideal material for (U-Th-Sm)/He, while iron (oxyhydr-)oxides pseudomorphosing pyrite seem to be the worst examples. This hypothesis will be further discussed in chapter 6.3.

### First tests

The first attempts of (U-Th)/He dating of this thesis were carried out in 2016 on samples originating from Tunisia, France (Vosges massif), Belgium (Stavelot massif) and Morocco (Ouarzazate area). The Tunisian ages are discussed in chapter 6.7. The Belgian, French and Moroccan ages of this study set (Table 6.1.1) could however not be widely discussed, neither published, as they do not have much geological meaning in relation with their context.

The lamellar hematite sampled in Saphoz, in the Vosges massif, was particularly problematic (samples 14SPZ45 and 14SPZ51; Fig. 6.1.1Q – 6.1.1X; Table 6.1.3). The degassing of the very thin lamellae took a very long time; instead of the usual two or three heating steps, four to seven were necessary. Even after seven heating steps, the quantity of degassed He was still strongly rising for some aliquots. The dissolution of aliquots and the measuring of U and Th contents provided an explanation to this difficult He degassing. The U content of these aliquots, up to ten times higher than that of the other grains, suggests the presence of inclusions. The ages of these aliquots are thus discarded. For the three remaining aliquots, the degassing was almost complete. The ages and He content, however, strongly vary: 389.5 and 27656 nccSTP/g, 135.3 and 117115 nccSTP/g, 12.0 Ma and 8336 nccSTP/g (Table 6.1.3). Moreover, the 389.5 Ma age is impossible to consider as an age of precipitation, since the mineralization is hosted in Visean rocks (346.7-330.9 Ma). This highlights that, besides inclusions, there is another issue with Saphoz samples. It is supposed that the hematite lamellae composing Saphoz samples are too thin (Fig. 6.1.1S, 6.1.1T, 6.1.1X) to ensure proper retention of He, and that He losses with time were variable but considerable.

The botryoidal hematite of Ouarzazate (sample 15AH11; Fig. 6.1.5O; Table 6.1.3) provides ages of 382.2, 527.4, 483.9 and 533.1 Ma, the last three being concordant. The host rock is Late Neoproterozoic to Early Cambrian in age; the very old ages could be considered, since these three aliquots also give quite concordant ages. However, U concentrations vary, which could imply the presence of inclusions or of other mineral phases even if no issues were noticed during the degassing. Microscopically, structures indicating the hydration of hematite to goethite are observed, suggesting

that ages could represent averages of several iron (oxyhydr-)oxides generations. Such old ages, which were not expected, are difficult to relate with the regional geological context. Additional samples should be sampled and dated to confirm/infirm/refine these preliminary results.

Samples 15TDP03 and 15RN03 were both sampled in the Stavelot massif, in Belgium, in quartz veins (Fig. 6.1.1K – 6.1.1N; Table 6.1.3). It was not expected to acquire divergent ages for both samples composed of lamellar hematite. The ages obtained for sample 15TDP03, 531.7, 542.0, 696.8 and 943.1, are erroneous: the host rock is Ordovician in age (485.4 – 443.8 Ma) (Table 6.1.3). Such unlikely ages are thus difficult to explain. The low U and Th contents do not support the hypothesis of the presence of inclusions, neither do the old ages uphold the theory of He losses. The final option would be the presence of a mineral that releases He but that is not dissolved and that does not provide U and Th. From the four aliquots of sample 15RN03, however, three are relatively concordant in ages (157.0, 54.4, 121.6, 148.4) and U contents. Such young ages match with the Ordovician age of the host rock. The younger grain is characterized with the highest U, Th and Sm contents, probably highlighting the presence of an unwanted inherited mineral. However, both Stavelot samples are characterized by very thin hematite lamellae that are probably not much He retentive. Supplementary sampling and dating could help to consider these three concordant ages.

**Table 6.1.1. Iron (oxyhydr-)oxides samples from Tunisia, Belgium and France, (pre-)selected for (U-Th-Sm)/He dating.**

Area	Site	Age host rock	Sample	Type	Figure	X R D	RM	SEM	Geo-chem.	Isot.	(U-Th-Sm)/He	Quality	Comments
Tunisia	Tamra mine	Pliocene	14TAM07	Poorly crystallized goethite and hematite	6.1.1A, 6.1.1B	X	X	X		X	Nov 2015	Poor	Mixed phases, with Mn oxides
			14MnTAM	Goethite	6.1.1C, 6.1.1D	X	X	X			Nov 2015	Medium	Rim of sample = ok Center = mixed phases
	Bou Kchiba mine	<Oligocene	14BK09	Goethite in pseudomorphosis of pyrite	6.1.1E, 6.1.1F	X	X	X			Nov 2015	Poor	Mixed phases, presence of pyrite
			14BK11	Euhedral botryoidal goethite	6.1.1G, 6.1.1H	X	X	X			Nov 2015	Very good	Very pure rim
	Ouechtata	Triassic	14OU03	Goethite in pseudomorphosis of pyrite	Idem 6.1.1E, 6.1.1F	?	?	?		X	Nov 2015	Good	/
			13OULI	Euhedral goethite	/	?	?	?			2013	Good	/
	Oued Belif	Tortonian	14OB02	Goethite in vein	6.1.1I, 6.1.1J	X	X	X			Nov 2015	Poor	Presence of too much quartz
	Nefza		13NEFZA	Goethite in vein	/	?	?	?			2013	Good	/
Belgium-Stavelot	Tier Del Preu	Ordovician	15TDP03	Hematite in a quartz vein	6.1.1K, 6.1.1L		X	X			Sept 2016	Medium	Pure lamellar hematite, with quartz
	Regnié		15RN03	Hematite in a quartz vein	6.1.1M, 6.1.1N		X	X			Sept 2016	Medium	Pure lamellar hematite, with quartz
Belgium	Transinne	Miocene	TRANS	Goethite in pseudomorphosis of pyrite	6.1.1O, 6.1.1P		X	X			Discarded	Bad	Too much silicates
France-Vosges	Saphoz	<Viséan	15SPZ04	Hematite-quartz-dolomite-rhodochrosite breccia	6.1.1Q, 6.1.1R, 6.1.1T		X	X			Discarded	Bad	Too small hematite lamellae
			14SPZ08	Botryoidal hematite	6.1.1U	X	X	X			Discarded	Bad	Too small hematite lamellae
			14SPZ45	Hematite in red jasper	6.1.1V	X	X	X			Sept 2016	Poor	Small hematite lamellae
			14SPZ51	Hematite	6.1.1W, 6.1.1X	X	X	X			Sept 2016	Poor	Small hematite lamellae

**Table 6.1.2. Iron (oxyhydr-)oxides samples from Morocco (pre-)selected for (U-Th-Sm)/He dating.**

Site	Age host rock	Sample	Type	Figure	XRD	RM	SEM	Geo-chem.	Isot.	(U-Th-Sm)/He	Quality	Comments
Bou Arfa – Jbel Rhals	Jurassic	14RL14	Goethite in pseudomorphosis of siderite	6.1.2A, 6.1.2B	X	X	X	X		2017	Medium	Mixed with minor Mn oxides; small crystallites
		14RL15	Goethite in pseudomorphosis of siderite	6.1.2C	X	X	X	X		2017	Medium	Mixed with minor Mn oxides; small crystallites
		14RL17	Goethite in pseudomorphosis of siderite	/	X	X	X	X		Discarded	Poor	Mixed with Mn oxides; small crystallites; powdery phases
		13RL02A	Goethite mixed with supergene phases	6.1.2D	X	X	X			Discarded	Bad	Mixing with malachite, Mn oxides etc
Bou Arfa – Jbel Klakh	Jurassic	14KH10	Goethite in vein	6.1.2E	X	X	X			Discarded	Bad	Poorly crystallized, mixed with malachite
		14KH12	Hematite plating on fault filling materials	6.1.2F	X	X	X			Discarded	Bad	Too small crystals, presence of gangue minerals
		14KH50	Goethite in a vein with Mn-oxides	6.1.2G, 6.1.2H	X	X	X			2017-2019	Poor	Several successive generations of goethite
		14KH52B	Microcrystalline goethite in a fracture	6.1.2I		X	X			Discarded	Bad	Too much quartz
Bou Arfa – Jbel Haouanit	Jurassic	13HAO05	Hematite and goethite in a vein at the surface	6.1.2J		X	X			Discarded	Bad	Mixed phases and omnipresence of quartz and clays
		14HAO04	Hematite and goethite in a vein	Idem 6.1.2J		X	X			Discarded	Bad	Mixed phases and omnipresence of quartz and clays
		14HAO05A	Hematite and goethite in a vein	6.1.2K		X	X			Discarded	Bad	Mixed phases and omnipresence of quartz and clays
		14HAO05B	Hematite and goethite in a vein	Idem 6.1.2K		X	X			Discarded	Bad	Mixed phases and omnipresence of quartz and clays
		14HAO10	Botryoidal goethite covering preexistent supergene phases	/		X	X			Discarded	Medium	Mixed phases – not enough material
		14HT02	Microcrystalline goethite associated with motttramite	6.1.2L, 6.1.2M	X	X	X	X	X	2017-2019	Medium	Mixed with motttramite
		14HT07	Microcrystalline goethite associated with motttramite	Idem 6.1.2L, 6.1.2M	X	X	X	X	X	2017-2019	Medium	Mixed with motttramite
Bou Arfa – Jbel Mokhta	Jurassic	13BOU09A	Hematite and goethite in pseudomorphosis of pyrite	6.1.2N		X	X			Discarded	Bad	Poorly crystallized, presence of gangue minerals
		13BOU09B	Hematite and goethite in pseudomorphosis of pyrite	6.1.2O		X	X			Discarded	Bad	Poorly crystallized, presence of gangue minerals
Bouskour	Jurassic	15BOU03	Goethite in pseudomorphosis of pyrite	6.1.2P		X	X			Discarded	Poor	Mixed with supergene phases such as malachite, poorly crystallized

Bouskour	Jurassic	15BOU04	Microcrystalline goethite	6.1.2Q		X	X		Discarded	Poor	Mixed with supergene phases such as malachite, poorly crystallized
		15BOU05	Microcrystalline goethite	6.1.2R		X	X		Discarded	Poor	Mixed with supergene phases such as malachite, poorly crystallized
Agoujgal	Late Proterozoic	17AG09B	Microcrystalline goethite	6.1.2S, 6.1.2T	X	X	X	X	Discarded	Poor	Mixed of excessively porous hematite-goethite generations
		17AG09D	Microcrystalline goethite	6.1.2U, 6.1.2V	X	X	X		Discarded	Poor	Mixed of excessively porous hematite-goethite generations
		17AG09E	Goethite and hematite in pseudomorphosis of pyrite	6.1.2W	X	X	X		Discarded	Bad	Mixed of excessively porous hematite-goethite generations
		17AG14A	Goethite and hematite in pseudomorphosis of pyrite	/	X	X	X		Discarded	Bad	Omnipresence of quartz in a poorly crystallized material
		17AG14B	Goethite and hematite in pseudomorphosis of pyrite	6.1.2X, 6.1.3A	X	X	X	X	2017-2019	Medium	Limited mixing of hematite and goethite
		17AG14D	Goethite and hematite in pseudomorphosis of pyrite	/	X	X	X	X	Discarded	Bad	Omnipresence of quartz and gangue minerals in a poorly crystallized material
		17AG14E	Goethite and hematite in pseudomorphosis of pyrite	6.1.3B, 6.1.3C	X	X	X		Discarded	Poor	Omnipresence of gangue minerals in mixed hematite-goethite generations
		17AG14F	Goethite and hematite in pseudomorphosis of pyrite	Idem 6.1.3B, 6.1.3C	X	X	X		Discarded	Poor	Omnipresence of gangue minerals in mixed hematite-goethite generations
		17AG14G	Goethite and hematite in pseudomorphosis of pyrite	Idem 6.1.3B, 6.1.3C	X	X	X	X	Discarded	Bad	Omnipresence of gangue minerals in mixed hematite-goethite generations
		17AG15	Goethite and hematite in pseudomorphosis of pyrite	6.1.3D, 6.1.3E	X	X	X	X	2017-2019	Medium	Limited mixing of hematite and goethite
		17AG25A	Botryoidal goethite	6.1.3F, 6.1.3G	X	X	X	X	2017-2018	Poor	Powdery material, presence of gangue minerals
		17AG26	Botryoidal goethite associated with mottramite	6.1.3H	X	X	X	X	2017-2019	Medium	Mixed with mottramite
		18AG07	Botryoidal goethite associated with mottramite	6.1.3I	X	X	X	X	2018-2019	Medium	Mixed with mottramite
Tazalaght	Late Proterozoic	17TAZ01A	Goethite and hematite in pseudomorphosis of pyrite	6.1.3J, 6.1.3K	X	X	X	X	2017-2019	Medium	Limited mixing of hematite and goethite
		17TAZ01C	Botryoidal goethite	6.1.3L, 6.1.3M	X	X	X	X	2017-2019	Good	Pure goethite
		17TAZ03	Powdery goethite and Mn-oxides	6.1.3N	X	X	X	X	Discarded	Bad	Omnipresence of gangue minerals in poorly crystallized material
		17TAZ15	Goethite and hematite in pseudomorphosis of pyrite	6.1.3O, 6.1.3P				X	Discarded	Bad	Mixing of several hematite-goethite generations
		17TAZ16	Goethite and hematite in pseudomorphosis of pyrite	6.1.3Q, 6.1.3R				X	2017-2018	Poor	Mixing of several hematite-goethite generations

Tazalaght	Late Proterozoic	17TZ04B	Lamellar hematite	6.1.3S, 6.1.3T				X	2017-2018	Medium	Platy hematite composed of undersized crystallites	
		18TAZ23	Microcrystalline goethite associated with calcite	6.1.3U, 6.1.3V	X	X	X	X	Discarded	Poor	Omnipresence of quartz in a poorly crystallized material	
		18TAZ25	Goethite and hematite in pseudomorphosis of pyrite	Idem 6.1.3J, 6.1.3K	X	X	X	X	Discarded	Poor	Mixing of several hematite-goethite generations	
		18TAZ26	Microcrystalline goethite	6.1.3W	X	X	X	X	Discarded	Poor	Omnipresence of quartz in an excessively porous material	
		18TAZ27	Botryoidal goethite	6.1.3X	X	X	X	X	X	2018-2019	Good	Pure goethite
Tassirt	Late Proterozoic - Cambrian	17TAS01D	Goethite and hematite in pseudomorphosis of pyrite	6.1.4A, 6.1.4B	X	X	X		2017-2019	Good	Fairly pure goethite	
		17TAS07	Powdery iron (oxyhydr-oxides)	6.1.4C	X	X	X	X	Discarded	Bad	Poorly crystallized material	
		17TAS10A	Goethite and hematite in pseudomorphosis of pyrite	Idem 6.1.4D, 6.1.4E					Discarded	Poor	Omnipresence of quartz and gangue minerals in mixed hematite-goethite generations	
		17TAS10B	Goethite and hematite in pseudomorphosis of pyrite	6.1.4D, 6.1.4E	X	X	X	X	2017-2019	Medium	Limited mixing of hematite and goethite	
		17TAS10C	Goethite and hematite in pseudomorphosis of pyrite	Idem 6.1.4D, 6.1.4E	X	X	X	X	2017-2019	Medium	Limited mixing of hematite and goethite	
		17TAS10D	Goethite and hematite in pseudomorphosis of pyrite	6.1.4F					Discarded	Poor	Omnipresence of quartz and gangue minerals in mixed hematite-goethite generations	
		18TAS01B	Microcrystalline goethite	/	X	X	X	X	Discarded	Bad	Omnipresence of quartz and gangue minerals in mixed hematite-goethite generations	
		18TAS01D	Botryoidal goethite	6.1.4G, 6.1.4H	X	X	X	X	X	2018-2019	Good	Pure goethite
		18TAS02	Botryoidal hematite	6.1.4I, 6.1.4J	X	X	X	X	Discarded	Bad	Omnipresence of gangue minerals and clays	
		18TAS03	Botryoidal hematite	Idem 6.1.4I, 6.1.4J	X	X	X	X	Discarded	Bad	Omnipresence of gangue minerals and clays	
		18TAS04	Botryoidal hematite	Idem 6.1.4I, 6.1.4J	X	X	X		Discarded	Bad	Omnipresence of gangue minerals and clays	
		18TAS07	Goethite and hematite in pseudomorphosis of pyrite	6.1.4K	X	X	X	X	Discarded	Poor	Omnipresence of quartz and gangue minerals in mixed hematite-goethite generations	
		18TAS11	Powdery iron (oxyhydr-oxides)	Idem 6.1.4L	X	X	X	X	Discarded	Bad	Poorly crystallized material	
		18TAS78	Powdery iron (oxyhydr-oxides)	6.1.4L	X	X	X	X	Discarded	Bad	Poorly crystallized material	
Tizert	Late Proterozoic	17TIZ01A	Microcrystalline goethite	6.1.4M	X	X	X	X	2017-2019	Medium	Limited presence of quartz	



Tizert	Late Proterozoic	17TIZ01B	Microcrystalline mixed goethite and hematite	/	X	X	X	X	Discarded	Poor	Mixed hematite-goethite generations
		17TIZ01C	Microcrystalline mixed goethite and hematite	6.1.4N	X	X	X		Discarded	Bad	Excessively porous material
		17TIZ01D	Microcrystalline mixed goethite and hematite	Idem 6.1.4N	X	X	X		Discarded	Poor	Mixed hematite-goethite generations
		17TIZ03	Botryoidal goethite	6.1.4O, 6.1.4P	X	X	X	X	2017-2019	Good	Mixed hematite-goethite generations
		17TIZ05	Botryoidal goethite	/	X	X	X		Discarded	Poor	Omnipresence of gangue minerals in undersized fragments
		17TIZ06	Powdery iron (oxyhydr-)oxides	Idem 6.1.4N	X	X	X	X	Discarded	Bad	Poorly crystallized material
Ighrem	Late Proterozoic	17IG01	Botryoidal goethite	6.1.4Q	X	X	X	X	2017-2019	Perfect	Pure goethite
		18IG02	Botryoidal goethite	6.1.4R	X	X	X	X	2018-2019	Perfect	Pure goethite
		18IG03	Goethite and hematite in pseudomorphosis of pyrite	6.1.4S, 6.1.4T	X	X	X	X	Discarded	Poor	Omnipresence of quartz and calcite in mixed hematite-goethite
Assifid	Late Proterozoic - Cambrian	18ASS01A	Botryoidal goethite	Idem 6.1.4U	X	X	X	X	2018-2019	Perfect	Pure goethite
		18ASS01B	Botryoidal goethite	6.1.4U	X	X	X	X	2018-2019	Perfect	Pure goethite
		18ASS02	Goethite and hematite in pseudomorphosis of pyrite	6.1.4V	X	X	X	X	Discarded	Poor	Omnipresence of quartz and calcite in mixed hematite-goethite generations
		18ASS03	Microcrystalline goethite	/	X	X	X	X	Discarded	Poor	Mixing of several hematite-goethite generations
Irkhs	Late Proterozoic	18IR01	Botryoidal goethite	6.1.4W, 6.1.4X	X	X	X	X	2018-2019	Perfect	Pure goethite
		18IR02	Botryoidal goethite	6.1.5A	X	X	X	X	Discarded	Poor	Omnipresence of quartz in an excessively porous material
		18IR04	Botryoidal goethite brecciated by calcite	6.1.5B, 6.1.5C	X	X	X		Discarded	Poor	Omnipresence of clays in undersized fragments
		18IR05	Microcrystalline goethite	/	X	X	X		Discarded	Bad	Excessively porous material
		18IR07	Goethite and hematite in pseudomorphosis of pyrite	6.1.5D, 6.1.5E	X	X	X	X	Discarded	Bad	Mixing of excessively porous hematite-goethite generations
Est Akka	Late Proterozoic	18EA01	Goethite and hematite in pseudomorphosis of pyrite	6.1.5F, 6.1.5G	X	X	X	X	Discarded	Medium	Omnipresence of quartz and calcite in mixed hematite-goethite generations
		18EA02	Microcrystalline goethite	/	X	X	X	X	Discarded	Medium	Omnipresence of quartz and calcite in mixed hematite-goethite generations
		18EA03	Goethite in pseudomorphosis of pyrite	6.1.5H	X	X	X		Discarded	Medium	Omnipresence of quartz in porous mixed hematite-goethite generations
Agni	Late Proterozoic	18AGN01	Microcrystalline goethite	6.1.5I	X	X	X		Discarded	Poor	Omnipresence of quartz
		18AGN02	Microcrystalline hematite	6.1.5J	X	X	X		Discarded	Poor	Omnipresence of quartz
Imi Omagha	Late Proterozoic - Cambrian	18IM03	Powdery iron (oxyhydr-)oxides	6.1.5K	X	X	X	X	Discarded	Bad	Poorly crystallized material
		18IM05A	Goethite and hematite in pseudomorphosis of pyrite	/	X	X	X	X	Discarded	Poor	Omnipresence of quartz and calcite in mixed hematite-goethite generations

Imi Omagha	Late Proterozoic - Cambrian	18IM05B	Botryoidal goethite	6.1.5I	X	X	X		Discarded	Medium	Undersized fragments containing gangue minerals
Alous	Late Proterozoic	18AL02	Vein and quartz filling fractures	6.1.5M	X	X	X		Discarded	Poor	Omnipresence of quartz
		18AL03	Powdery iron (oxyhydr-)oxides	Idem 6.1.5K	X	X	X		Discarded	Bad	Poorly crystallized material
		18AL05	Vein and quartz filling fractures	6.1.5N	X	X	X	X	Discarded	Poor	Omnipresence of quartz
		18AL06	Powdery iron (oxyhydr-)oxides	Idem 6.1.5K	X	X	X	X	Discarded	Bad	Poorly crystallized material
Ouarzazate	< Pc III	15AH11	Botryoidal hematite	6.1.5O		X	X		Sept 2016	Good	Pure hematite with few Mn oxides
	< Pc III	15BT03	Hematite in a vein	6.1.5P		X	X		Discarded	Bad	Too much quartz
Imini	Cenomanian-Turonian	15SOU01	Hematite-goethite lumps	6.1.5Q	X	X	X		Discarded	Bad	Too much calcite and dolomite
Imini-Plateaux	Cenomanian-Turonian	15PL02	Botryoidal goethite	/	X	X	X	X	2017-2019	Perfect	Pure goethite
		18PL02A	Powdery hematite and goethite	/	X				Discarded	Bad	Poorly crystallized material
		18PL02B	Botryoidal goethite	6.1.5R, 6.1.5S	X	X	X	X	2018-2019	Perfect	Pure goethite
		18PL07	Botryoidal goethite	6.1.5T, 6.1.5U	X	X	X	X	2018-2019	Perfect	Pure goethite
		18PL07B	Botryoidal goethite	Idem 6.1.5U	X	X	X		Discarded	Good	Pure goethite
		18PL20	Botryoidal goethite	Idem 6.1.5U	X	X	X		Discarded	Good	Pure goethite
		18PL25	Botryoidal goethite	6.1.5V, 6.1.5W	X	X	X	X	2018-2019	Perfect	Pure goethite
		18PL27	Botryoidal goethite	6.1.5X	X	X	X	X	Discarded	Good	Pure goethite
		18TIF01	Botryoidal goethite	6.1.6A, 6.1.6B	X	X	X	X	2018-2019	Perfect	Pure goethite
Imini-Tifersine	Cenomanian-Turonian	18TIF05	Botryoidal goethite	Idem 6.1.6B	X	X	X	X	Discarded	Good	Pure goethite
		18TIF12	Mixed Mn oxides and goethite	Idem 6.1.6B	X				Discarded	Good	Pure goethite
		18TIF16	Brechified botryoidal goethite	/	X				Discarded	Good	Pure goethite
		18TIF20	Botryoidal goethite	6.1.6C, 6.1.6D	X	X	X	X	2018-2019	Perfect	Pure goethite
Imini- Far West	Cenomanian-Turonian	18FAR02	Botryoidal goethite	6.1.6E, 6.1.6F	X	X	X	X	2018-2019	Perfect	Pure goethite
		18FAR02A	Botryoidal goethite	6.1.6G, 6.1.6H	X	X	X	X	2018-2019	Perfect	Pure goethite
		18FAR02B	Botryoidal goethite	/	X	X	X		Discarded	Good	Pure goethite

Imini- Far West	Cenomanian- Turonian	18FAR02C	Powdery hematite and goethite	/	X		X	Discarded	Good	Poorly crystallized material
		18FAR03	Botryoidal goethite	Idem 6.1.6E, 6.1.6F	X	X	X	Discarded	Good	Pure goethite
		18FAR07X	Botryoidal goethite	Idem 6.1.6G, 6.1.6H	X	X	X	Discarded	Good	Pure goethite
		18FAR15	Botryoidal goethite	Idem 6.1.6E, 6.1.6F	X	X	X	Discarded	Good	Pure goethite
		18FAR17	Botryoidal goethite	Idem 6.1.6G, 6.1.6H	X	X	X	Discarded	Good	Pure goethite
		18FAR18	Botryoidal goethite	Idem 6.1.6E, 6.1.6F	X	X	X	Discarded	Good	Pure goethite

**Table 6.1.3.** First attempts of (U-Th)/He dating on iron (oxyhydr-)oxides of this study.

Site	Nature	Protolite	Name	Heating steps	<sup>4</sup> He sample (ccSTP)	± s (ccSTP)	U (ng)	Th (ng)	weight (mg)	<sup>4</sup> He (nccSTP/g)	± s (nccSTP/g)	<sup>238</sup> U (ppm)	<sup>232</sup> Th (ppm)	eU (ppm)	Th/U	Age (Ma)	± s (Ma)
Saphoz (Vosges, France)	Lamellar hematite	Visean	SPZ45-1a	7	8.32E-08	4.16E-09	205.87	0.07	3.01	27656	2.77E-04	68.39	0.02	68.40	0.00	<b>3.3</b>	<b>0.3</b>
			SPZ45-1b	4	1.34E-07	6.70E-09	2.84	0.02	0.37	362115	3.62E-03	7.68	0.04	7.69	0.01	<b>389.5</b>	<b>39.0</b>
			SPZ45-2	4	4.45E-08	2.23E-09	2.72	0.02	0.38	117115	1.17E-03	7.15	0.06	7.17	0.01	<b>135.3</b>	<b>13.5</b>
			SPZ45-3	7	1.00E-07	5.00E-09	14.52	0.01	0.21	476170	4.76E-03	69.14	0.06	69.16	0.00	<b>56.9</b>	<b>5.7</b>
			SPZ51-1	4	1.30E-08	6.50E-10	8.96	0.04	1.56	8336	8.34E-05	5.74	0.03	5.75	0.00	<b>12.0</b>	<b>1.2</b>
Ouarzazate (Morocco)	Botryoidal hematite	Pc III	AH11-1	2	1.26E-07	6.29E-09	1.97	0.01	0.27	465797	4.66E-03	7.30	0.03	7.31	0.00	<b>527.4</b>	<b>52.7</b>
			AH11-2	2	1.26E-07	6.32E-09	2.16	0.01	0.14	902817	9.03E-03	15.42	0.06	15.44	0.00	<b>483.9</b>	<b>48.4</b>
			AH11-3	3	7.47E-08	3.73E-09	1.62	0.01	0.17	439283	4.39E-03	9.50	0.03	9.51	0.00	<b>382.2</b>	<b>38.2</b>
			AH11-4	3	8.59E-08	4.29E-09	1.33	0.01	0.13	660392	6.60E-03	10.24	0.09	10.26	0.01	<b>533.1</b>	<b>53.3</b>
Tier Del Preux (Stavelot, Belgium)	Lamellar hematite	Ordovician	TDP03-1	3	6.49E-09	3.25E-10	0.10	0.04	0.21	30908	3.09E-04	0.48	0.19	0.52	0.39	<b>531.7</b>	<b>53.2</b>
			TDP03-2	2	8.24E-09	4.12E-10	0.12	0.07	0.23	35818	3.58E-04	0.54	0.30	0.61	0.56	<b>542.0</b>	<b>54.2</b>
			TDP03-3	2	9.12E-09	4.56E-10	0.19	0.13	0.43	21215	2.12E-04	0.43	0.30	0.51	0.68	<b>396.8</b>	<b>39.7</b>
			TDP03-4	2	7.68E-09	3.84E-10	0.07	0.05	0.19	40397	4.04E-04	0.35	0.28	0.42	0.82	<b>943.1</b>	<b>94.3</b>
Régnié (Stavelot, Belgium)	Lamellar hematite	Ordovician	RN03-1	2	4.21E-09	2.10E-10	0.22	0.19	0.17	24743	2.47E-04	1.28	1.13	1.55	0.88	<b>157.0</b>	<b>15.7</b>
			RN03-2	2	5.45E-09	2.72E-10	0.82	0.55	0.37	14719	1.47E-04	2.20	1.48	2.56	0.67	<b>54.4</b>	<b>5.4</b>
			RN03-3	2	5.98E-09	2.99E-10	0.40	0.28	0.43	13911	1.39E-04	0.93	0.64	1.08	0.69	<b>121.6</b>	<b>12.1</b>
			RN03-4	2	7.47E-09	3.73E-10	0.41	0.30	0.40	18673	1.87E-04	1.02	0.74	1.20	0.72	<b>148.4</b>	<b>14.8</b>

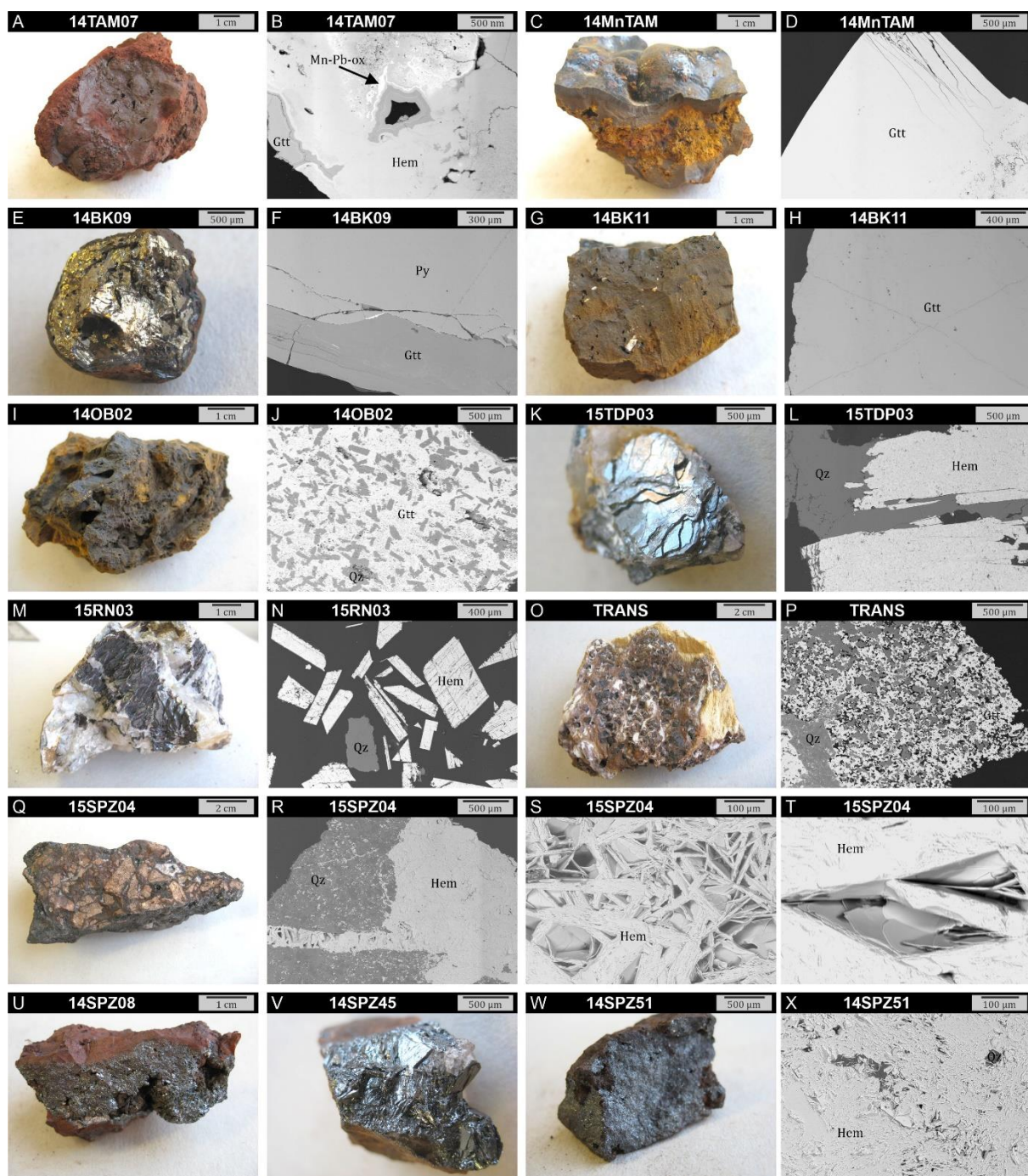


**Figure 6.1.1.** Representative iron (oxyhydr-)oxides samples from Tunisia, Belgium and France, (pre-)selected for (U-Th-Sm)/He dating.



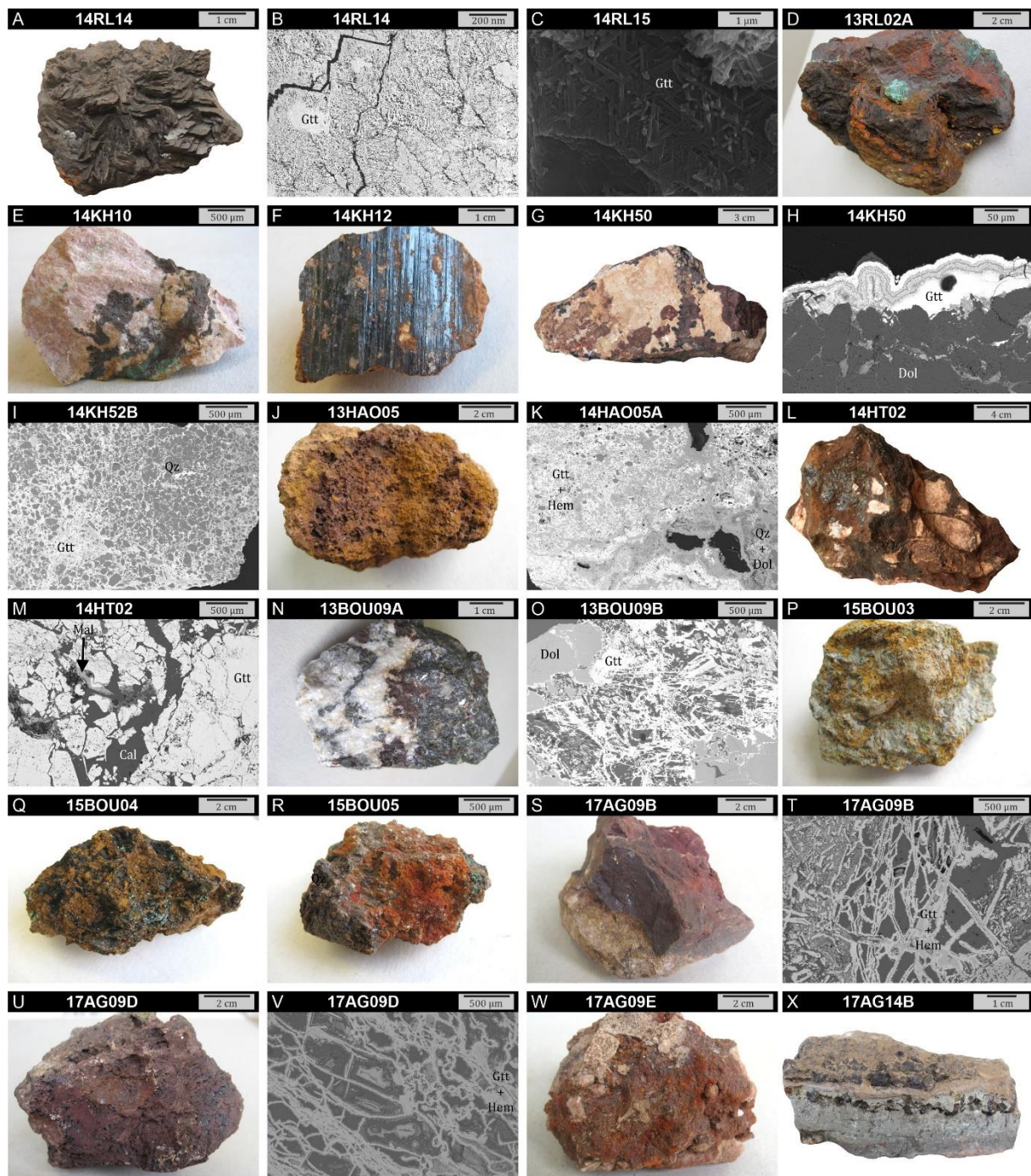


**Figure 6.1.2.** Representative iron (oxyhydr-)oxides samples from Morocco, (pre-)selected for (U-Th-Sm)/He dating (part 1/5).



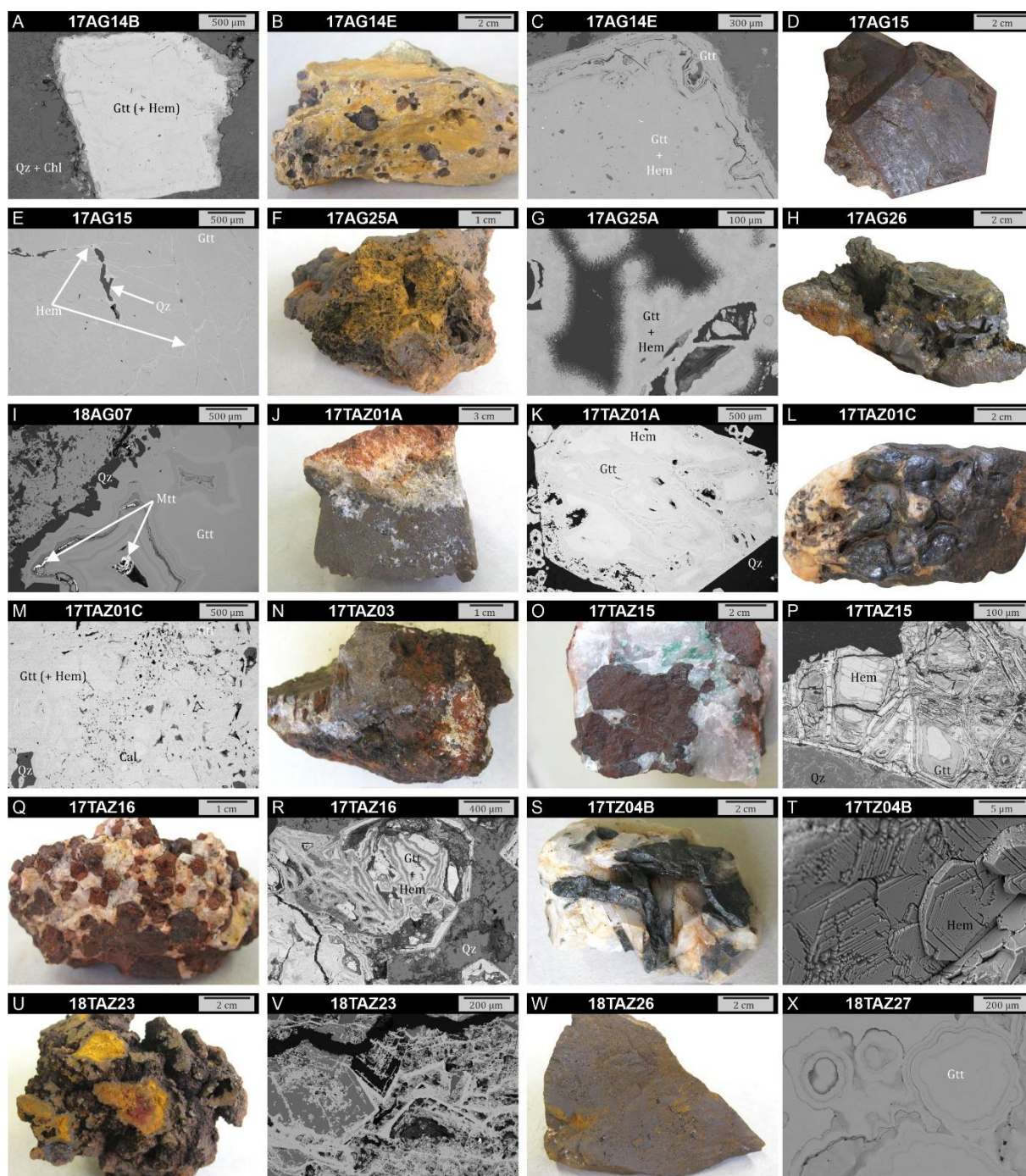


**Figure 6.1.3.** Representative iron (oxyhydr-)oxides samples from Morocco, (pre-)selected for (U-Th-Sm)/He dating (part 2/5).



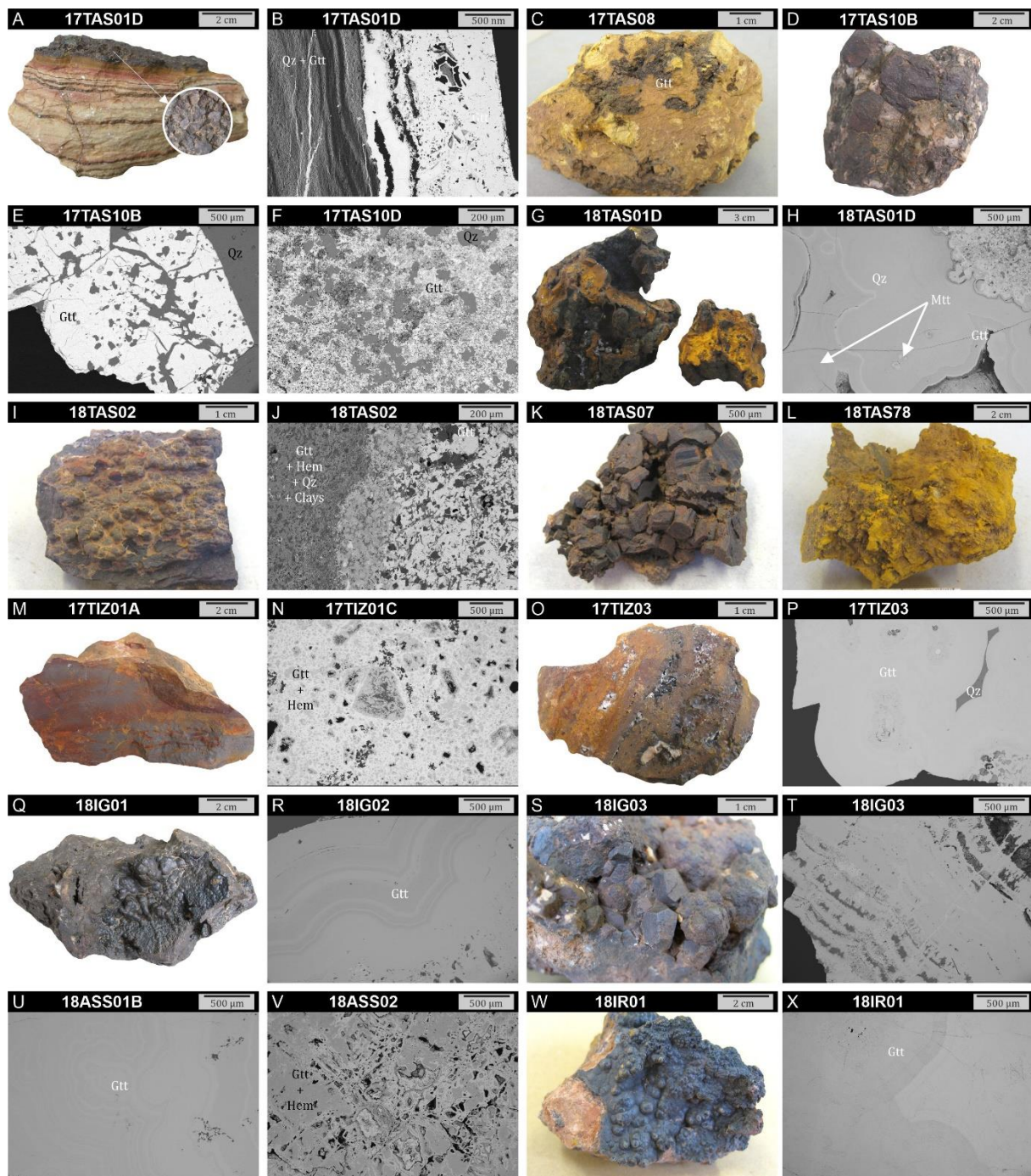


**Figure 6.1.4.** Representative iron (oxyhydr-)oxides samples from Morocco, (pre-)selected for (U-Th-Sm)/He dating (part 3/5).



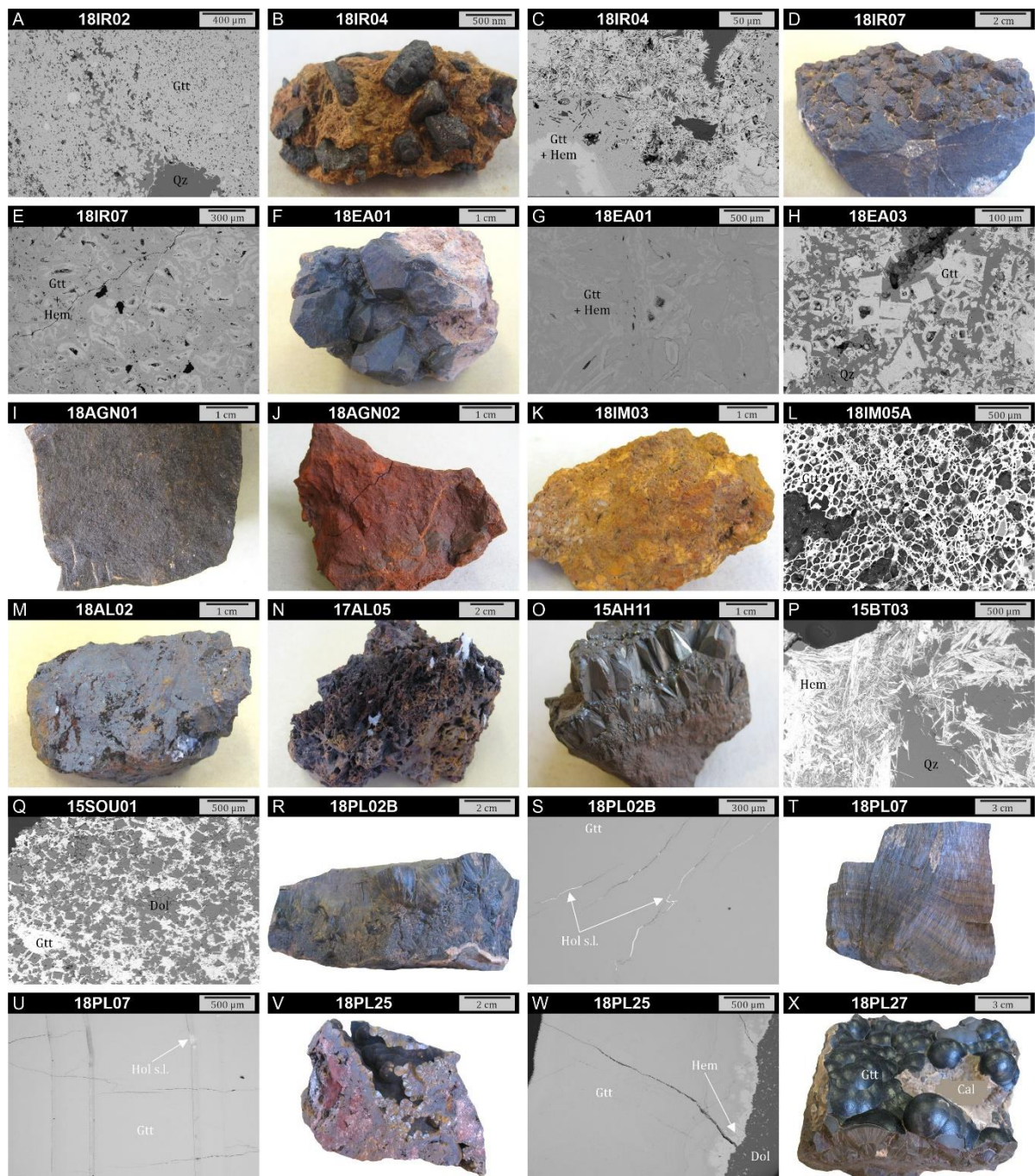


**Figure 6.1.5.** Representative iron (oxyhydr-)oxides samples from Morocco, (pre-)selected for (U-Th-Sm)/He dating (part 4/5).



**Figure 6.1.6.** Representative iron (oxyhydr-)oxides samples from Morocco, (pre-)selected for (U-Th-Sm)/He dating (part 5/5).

## 6.2 Goethite (U-Th-Sm)/He dating highlights the early steps of Mn ore formation at Imini, High Atlas, Morocco

The present study aims to provide clues to a better understanding of weathering processes and of the genesis of metallic ore deposits. The High Atlas Mountains of Morocco host a great number of metallic ore deposits, whose formation processes are likely related to geodynamic events (Bouabdellah and Slack 2016). The Imini district (southern High Atlas) presents high Mn grades that enabled the production of concentrates for steel and chemistry industries since the early 20<sup>th</sup> century (Gutzmer et al. 2006). The timing of precipitation of these Mn ores remains controversial, although several metallogenic models have been proposed to explain their formation (Force et al. 1986; Rhalmi et al. 1997; Gutzmer et al. 2006; Dekoninck et al. 2016a). The occurrence of goethite in the western and northern parts of the district was briefly mentioned by Pouit (1966), Lesavre (1975), Beaudoin et al. (1976) and Thein (1990). However, the processes leading to the formation of goethite, at Imini, are unknown. In this study, we aim to show that goethite (U-Th-Sm)/He (GHe) dating is an efficient tool for determining the temporal context of ore formation. This method is based on the production of He during the radioactive decay of U, Th and Sm, and on its accumulation within goethite crystallites (Shuster et al. 2005; Ault et al. 2019). Because of the ubiquity of goethite in various surface environments and of the high He retentivity in this mineral, the GHe method knows a growing interest (e.g. Vasconcelos et al., 2015). Here, GHe ages are produced in a Mn ore deposit where the well-known host rock age demonstrates the strength of the methodology. The detailed petrological and geochemical characterization reveals the structure, composition and paragenetic relations of goethite, while  $\delta D$ - $\delta^{18}O$  analyses refine the knowledge about the composition of the mineralizing fluids. The numerous (U-Th-Sm)/He goethite ages, together with analyses of stable isotopes and local geological constraints, bring concrete indications and restrictions on the initial steps of mineralization in the Imini district in its regional geodynamic context. Moreover, the acquisition of ages for several successive goethite generations allows the calculation of precipitation rates.

### 6.2.1 Geological setting

The Imini district lies in the western part of the Ouarzazate foreland basin, which hosts Triassic to Miocene sedimentary sequences (Fig. 6.2.1A). The ore-bearing Cenomanian-Turonian dolostone unconformably lies on Lower Cretaceous and Triassic red beds, folded Paleozoic schists to the north and east, and Precambrian volcanic rocks to the south (Fig. 6.2.1B) (Thein 1990; Gutzmer et al. 2006). Overall, the host carbonates are successively overlaid by Senonian sandy red beds, marine Eocene and lacustrine Miocene sediments. This sequence forms monoclinical plateaus, slightly inclined toward the south and limited to the north by the South Atlas Front (Leprêtre et al. 2015). The main structural features of the area are an E-W anticline, an E-W fault hosting vein-type barite deposits, and two main fault systems inherited from the Triassic-Jurassic rift system and/or formed during the Cenozoic Atlasic uplift (Fig. 6.2.1B) (Frizon de Lamotte et al. 2000). The ten meters thick host dolostone is subdivided into three sedimentary facies: Late Cenomanian pink sandy dolostone ( $S_1$ ), Late Cenomanian white bioclastic dolostone ( $S_2$ ) and Early Turonian cherty fossiliferous dolostone ( $S_3$ ) (Rhalmi et al. 1997, 2000) (Fig. 6.2.1C). An early diagenetic dolomitization triggered the formation of massive microspar and its subsequent replacement by rhombs of pseudosparitic dolomite, and erased the characteristic initial sedimentary textures (Force et al., 1986; Rhalmi et al., 1997). The Cenomanian transgression, recorded through the flooding of the former fluvial environment, is followed by shallowing upward of the platform during the Cenomanian-Turonian (Thein 1990; Rhalmi et al. 2000). After the Turonian, karstification processes induced the development of one to ten meters long karst cavities along the  $S_2$  (Gutzmer et al. 2006). The Imini Mn deposits form lenses aligned in a WSW-ENE direction over 25 km



(Fig. 6.2.1B). The ores are concentrated in 1 to 2.5 m thick stratabound layers defined as C<sub>1</sub>, C<sub>2</sub> and C<sub>3</sub> (Fig. 6.2.1C) (Gutzmer et al. 2006). Layers C<sub>1</sub> and C<sub>2</sub> are found in the S<sub>1</sub> and the lowermost part of the S<sub>2</sub>, and contain the economic Mn-bearing pyrolusite ore (Gutzmer et al. 2006). The top of the S<sub>2</sub> hosts the C<sub>3</sub> layer that contains goethite and hollandite group minerals (Gutzmer et al. 2006; Dekoninck et al. 2016a).

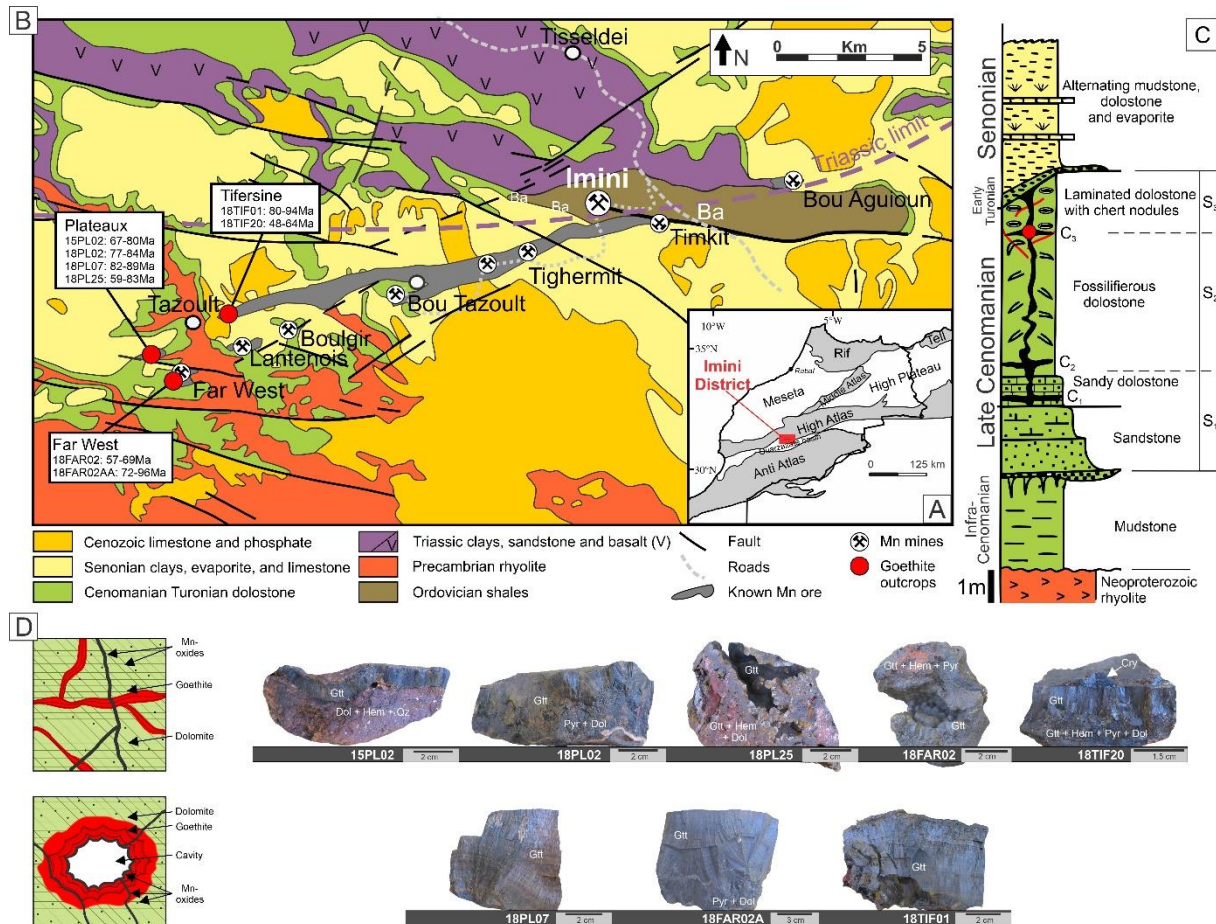


**Figure 6.2.1.** (A) Simplified structural map of Morocco. (B) Geological map of the Imini district showing the location of Far West, Tifersine and Plateaux deposits, and highlighting the (U-Th-Sm)/He goethite ages (modified after Lalaoui et al., 1991; Dekoninck et al., 2016a). (C) Detailed stratigraphic log of the western part of the district (modified after Gutzmer et al., 2006; Dekoninck et al., 2016a). The three sedimentary systems (S<sub>1</sub>, S<sub>2</sub>, S<sub>3</sub>) and the stratabound Mn ore layers (C<sub>1</sub>, C<sub>2</sub>, C<sub>3</sub>) originate from Rhalmi et al. (2000) and Gutzmer et al. (2006), respectively. (D) Schematic representations and pictures of the eight He dated goethite samples dated, divided as cavity-filling or fracture-filling samples.

## 6.2.2 Study site and methods

Nineteen, twenty and thirty-four samples have been collected from three goethite-rich deposits located in the western part of the district, respectively: Far West (FAR), Tifersine (TIF), and Plateaux (PL). Botryoidal goethite, the most common iron phase in the C<sub>3</sub>, forms geodes in large dissolution (karstic) cavities, or veinlets by filling fractures (Fig. 6.2.1D). Both varieties of goethite present accretionary growth bands that indicate direct precipitation of successive generations of goethite, without any intersect (Fig. 6.2.1D, 6.2.2). The variation in brownish tints between successive layers of the colloform structures is due to porosity variations of the radiating crystals (Fig. 6.2.1, 6.2.2). Goethite never replaces the dolostone fabric and is not substituted by any Fe or Mn minerals, but is coated and intersected by later Mn oxides (Fig. 6.2.1D). Eight botryoidal goethite samples have been selected for (U-Th-Sm)/He dating and  $\delta D$ - $\delta^{18}O$  analyses, on the basis of X-ray diffraction, scanning

electron microscopy and geochemical investigations (Fig 6.2.1D; Table 6.2.1). (U-Th-Sm)/He dating has been performed on five aliquots of each of five fracture-filling goethite (18FAR02, 15PL02, 18PL02, 18PL25, 18TIF20), without targeting particular generations. In order to allow the calculation of precipitation rates, three to six aliquots of three generations (0.8 to 1.5 cm apart) have been extracted from three large cavity-filling goethite samples (18FAR02A, 18PL07, 18TIF01), and dated with a high spatial resolution (Fig. 6.2.2). All methods and additional samples descriptions are reported in the Data Repository.

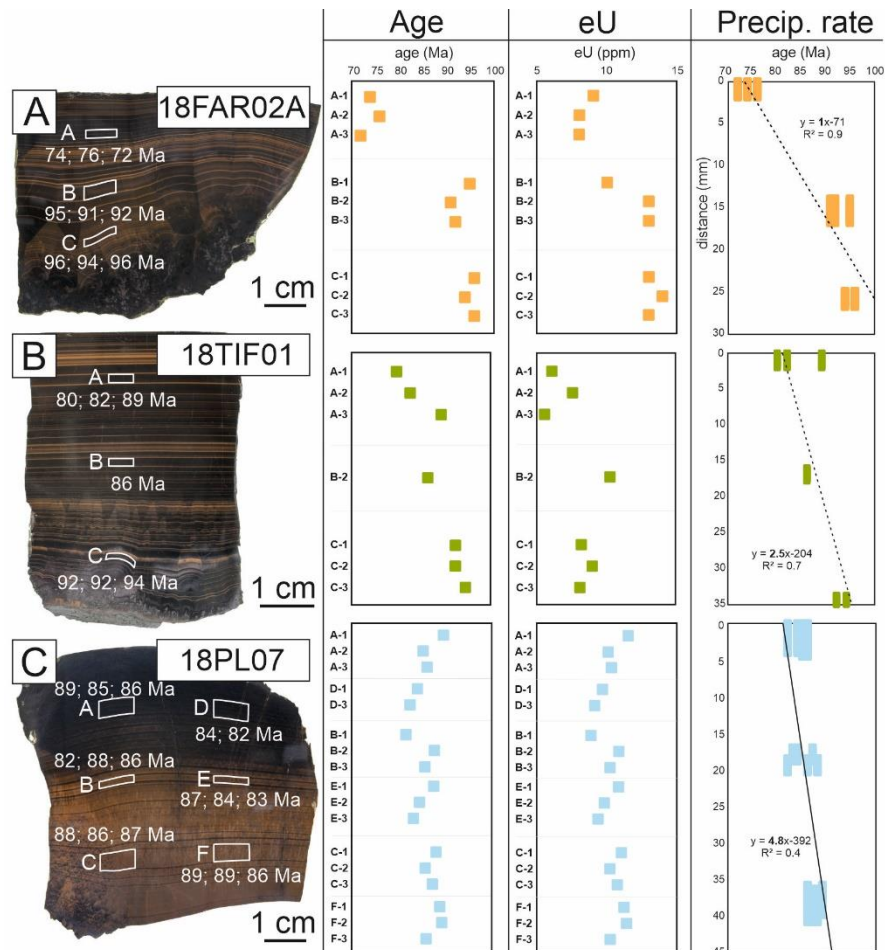


**Figure 6.2.2.** Large botryoidal goethite samples (A) 18FAR02A, (B) 18TIF01 and (C) 18PL07, and comparison of ages, effective uranium contents and calculated precipitation rates.

## 6.2.3 Results and interpretations

### 6.2.3.a Chronology of Imini's goethite precipitation

(U-Th-Sm)/He results are listed in table 6.2.6. The mean ages of cavity-filling goethite samples range from  $96 \pm 6$  to  $72 \pm 4$  Ma, while fracture-filling goethite specimens present younger ages varying between  $85 \pm 5$  and  $48 \pm 3$  Ma (Fig. 6.2.1, 6.2.2). The very high reproducibility of Imini's goethite ages, around 3.5%, and the highly consistent effective uranium (eU) values ( $eU = [U] + 0.235[Th] + 0.0075[Sm]$ ; Ault et al., 2019) suggest a quantitative He retention in the crystalline lattice, and no system reopening after goethite crystallization. The (U-Th-Sm)/He dating of goethite usually implies the consideration of corrections to compensate He diffusive losses due to the common small size of crystallites (e.g. Shuster et al., 2005; Heim et al., 2006). However, at Imini, the age corrections are constrained by the maximum age range of the host rock (100.5–89.8 Ma): the precipitation of goethite must postdate dolomitization. A maximum 3 to 4% He diffusion correction is thus applied to the raw

ages, and a 5% uncertainty is considered. This correction, much lower than the usual 2 to 30% value (e.g. Shuster et al., 2005; Heim et al., 2006; Vasconcelos et al., 2013; Hofmann et al., 2017), arises from the substantially large Imini's goethite crystallites (>100 nm) that enable a remarkably high He retention. The purity, homogeneity, and efficient crystallization of Imini's goethite also contribute to yielding statistically reproducible ages that require few corrections (see Data Repository for additional details).

The high-resolution dating of three generations of 1) 18FAR02A delivers ages of  $95 \pm 6$  Ma,  $93 \pm 5$  Ma, and  $74 \pm 4$  Ma, 2) 18TIF01 shows ages of  $93 \pm 6$  Ma,  $86 \pm 5$  Ma, and  $84 \pm 5$  Ma, and 3) 18PL07 yields ages of  $85 \pm 5$  Ma,  $85 \pm 5$  Ma, and  $87 \pm 5$  Ma (Fig. 6.2.2A, 6.2.2B, 6.2.2C). The decrease of GHe ages from the center outwards confirms that ages decline as a function of goethite growth, demonstrate the evolution of the mineralizing fluid and the precipitation of goethite through time (Fig. 6.2.2). By comparing ages with the distance between dated generations, goethite precipitation rates are estimated at 1, 2.5 and 4.8 mm/Ma, with correlation coefficients ( $R^2$ ) of 0.9, 0.7 and 0.4 (Fig. 6.2.2). Discrepancy between age populations of sample 18FAR02A reveals the fast precipitation of goethite around 90 Ma, and the much slower formation of thinner layers around 70 Ma (Fig. 6.2.2A). A short precipitation time is also suggested for the similar-aged thick layers of sample 18PL07. GHe ages of cavity-filling goethite suggest the precipitation shortly after the dolostone formation and the circulation of mineralizing fluids leading to goethite precipitation during 20 My. Even though no precipitation rates are published for massive botryoidal goethite, the values obtained here are consistent with precipitation rates estimated between 0.4 and 6.7 mm/Ma for supergene colloform cryptomelane, on the basis of K-Ar and  $^{40}\text{Ar}/^{39}\text{Ar}$  dating (e.g. Vasconcelos et al., 1994; Hénocque et al., 1998; Li et al., 2007b; Li et al., 2007a).

The fracture-filling 1) 18FAR02 at Far West presents an average age of  $64 \pm 4$  Ma, 2) 18TIF20 at Tifersine provides an average age of  $57 \pm 3$  Ma, and 3) 18PL25, 15PL02 and 18PL02B at Plateaux site respectively give average ages of  $71 \pm 4$  Ma,  $74 \pm 4$  Ma, and  $82 \pm 5$  Ma. The greater dispersion of ages and eU values of vein-filling goethite results from the random extraction of aliquots in these samples, without targeting single generations.

### 6.2.3.b Composition of the mineralizing fluids

In this study,  $\delta\text{D}$ - $\delta^{18}\text{O}$  data indicate that goethite did not precipitate in equilibrium with pure meteoric waters (Yapp 2000) and suggest the potential influence of fluid/rock interactions processes (Fig. 6.2.3). Dissolution/precipitation of carbonates, which notoriously concentrate  $^{18}\text{O}$  in their structure, may indeed induce isotopic exchanges leading to the higher  $\delta^{18}\text{O}$  ratio of mineralizing fluids (Garlick 1966; Dekoninck et al. 2018). Here, the dissolution of Imini host dolostones may have triggered the release of heavy oxygen and its incorporation in goethite, and consequently, be responsible for the wiping out of the usual  $^{18}\text{O}$  signal of supergene phases.

In addition, the youngest 18TIF20 sample deviates from others, with the highest U, Mn, Ba, Cu, As, Pb and Zn contents, the lowest Fe and V concentrations and distinct MnO, CaO and As concentrations (see Data Repository for additional details). These particular features, together with the joint decrease in (e)U and ages of all samples, and the depletion in U of the youngest generation of 18FAR02A (Fig. 6.2.2A), suggest the precipitation of goethite from an evolving mineralizing fluid. However, the local input of elements from a distinct fluid is also conceivable. The relatively high Ba-content of some Imini's goethite (up to 330 ppm) probably arises from the presence of barite within the ore beds and of Ba-ores in the eastern part of the district.

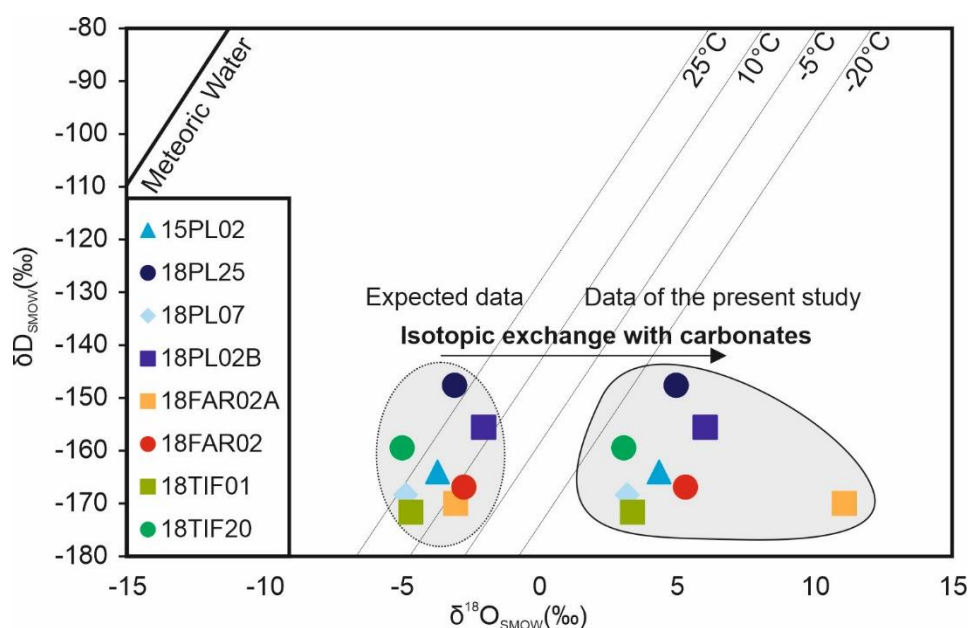


**Figure 6.2.3.**  $\delta D$  and  $\delta^{18}O$  data of Imini goethite. Temperature lines are calculated from (Yapp, 1987). The meteoric water (Craig, 1961) is given for reference.

### 6.2.3.c Paragenetic and geodynamical implications

Goethite (U-Th-Sm)/He ages of the present study are barely younger than Imini host rocks (100.5-89.8 Ma; Fig. 6.2.4), and younger, for many samples, than the pre-Senonian karstification. This suggests, along with  $\delta D$ - $\delta^{18}O$  data, the precipitation of Imini's goethite during or after diagenesis and dolomitization processes, as claimed for Mn oxides (Force et al. 1986; Thein 1990; Lalaoui et al. 1991; Gutzmer et al. 2006; Dekoninck et al. 2016a). The (U-Th-Sm)/He ages, coupled to macroscopic and microscopic observations, also reveal the crystallization of goethite before all Mn oxides (Fig. 6.2.1D). Therefore, Imini's Fe oxides should no longer be considered as resulting from recent surface processes, at the end of the paragenetic sequence – as proposed in Dekoninck et al. (2016) – but inserted between the diagenetic processes and the Mn ores. According to Gutzmer et al. (2006) and references therein, the formation of Mn ores arises from the Late Turonian regression that allowed exposure and erosion of carbonates and development of a karstic surface. The concentration of botryoidal goethite exclusively in the upper mineralized level is probably also related to this significant early karstification (Force et al. 1986). The subaerial carbonates exposure may ensue from the Late Cretaceous initiation of the High Atlas doming identified by Froitzheim (1984) and Leprêtre et al. (2018). The low precipitation rates of goethite imply that the water table altitude remained relatively stable during a long period and thereby correlate with this slow orogenic process. The cavity-filling goethite likely records weathering associated to fluids percolation and migration associated with the doming ( $D_0$  phase in Fig. 6.2.3). The coincidence of the 70-50 Ma fracture-filling goethite with the late- or post-orogenic period suggests that fractures appeared at the end of the doming and were promptly filled with goethite precipitating from fluids of evolved compositions, or from remobilizations (Fig. 6.2.3). The quite common sequential precipitation of Fe and Mn oxides usually arises from environments that become increasingly oxidizing with time (Verhaert et al. 2018). In this way, a stronger oxidation phase probably followed the precipitation of goethite, favoring the crystallization of extensive Mn ores.



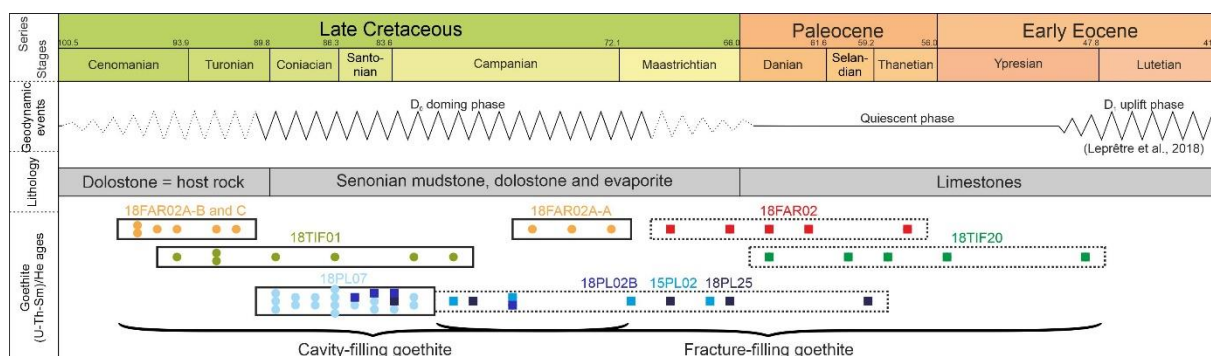


**Figure 6.2.4.** Schematic diagram highlighting time-relations between geodynamic events defined in the High Atlas (Leprêtre et al., 2018), the stratigraphic units defined in the Imini district, and the (U-Th-Sm)/He ages obtained for goethite. The cavity and fracture filling samples are framed by black continuous and dotted rectangles, respectively.

## 6.2.4 Conclusions

The combination of: i) the well-arranged botryoidal texture, ii) the relatively large crystallites (> 100 nm) and iii) the scarcity of contaminants/disturbances of the crystal lattice of Imini's goethite led to limited He diffusive losses with time and yields highly reproducible (U-Th-Sm)/He ages that corroborate the reliability and applicability of this dating method. At Imini, the early stages of mineralization were obviously characterized by the precipitation of large amounts of botryoidal goethite, from fluids isotopically modified by host carbonates. The consistency between the 90-70 Ma colloform filling of dissolution cavities with the geodynamic evolution of the Atlas suggests that surface deformation (partly) controls the precipitation of goethite.

## 6.2.5 Data Repository – Supplementary material

### 6.2.5.a Samples and analytical methods

#### Sampling strategy

Respectively nineteen, twenty and thirty-four samples of iron mineralization were collected in three ore deposits of the Imini Mn district: 1) Far West, 2) Tifersine, 3) Plateaux (see Fig. 1A, 1B for location information). Imini Mn ores are concentrated in three stratabound layers defined as C<sub>1</sub>, C<sub>2</sub> and C<sub>3</sub> (Fig. 1B) (Gutzmer et al. 2006). Layers C<sub>1</sub> and C<sub>2</sub> contain the economic Mn-ore composed of pyrolusite, mainly (Gutzmer et al. 2006). Hollandite group minerals, goethite and minor hematite are concentrated in the uppermost C<sub>3</sub> layer (Gutzmer et al. 2006; Dekoninck et al. 2016a). Botryoidal goethite is the most common iron phase at Imini, and is restricted to the C<sub>3</sub> mineralized level, in the western part of the district. Rare poorly crystallized hematite and goethite are also found in C<sub>2</sub> and C<sub>3</sub> layers. Goethite does not replace the dolomitic host rock, and is not substituted by later Mn-oxides. The choice of dating goethite from this district is based on the following criteria:

- 1) the existence of studies and publications on the petrology and paragenesis of the principal Mn-mineralization (Gutzmer et al. 2006; Dekoninck et al. 2016a, b),
- 2) the provision of large amounts of massive and fairly pure botryoidal goethite,
- 3) the presence of K-bearing Mn-oxides such as cryptomelane, their potential <sup>40</sup>Ar/<sup>39</sup>Ar dating and comparison with (U-Th-Sm)/He ages,
- 4) the district location, at the junction of the High Atlas and Anti-Atlas, constitutes an opportunity to investigate relations between geodynamic events and the formation of ore deposits.



Hand-sized samples have been collected in ore dumps (Fig. 6.2.5A), veins/fractures in outcrops (Fig. 6.2.5B), and in cavities in galleries (Fig. 6.2.5C, 6.2.5D). Different types of iron mineralization have been selected on the field, and analyzed in order to select samples that are most suitable for (U-Th-Sm)/He dating and  $\delta D$ - $\delta O$  analyses (Table 6.2.1, Fig. 6.2.6). Botryoidal goethite samples were estimated to be as the purest and best crystallized materials and were thus further examined.



**Figure 6.2.5.** Field pictures of Imini district. (A) Far West site ore dumps. (B) Botryoidal goethite filling fractures and forming thin veins, at Tifersine site (sample 18TIF20). (C) Mine gallery at the Plateaux site. (D) Large botryoidal goethite filling cavities at the Plateaux site (sample 18PL07).

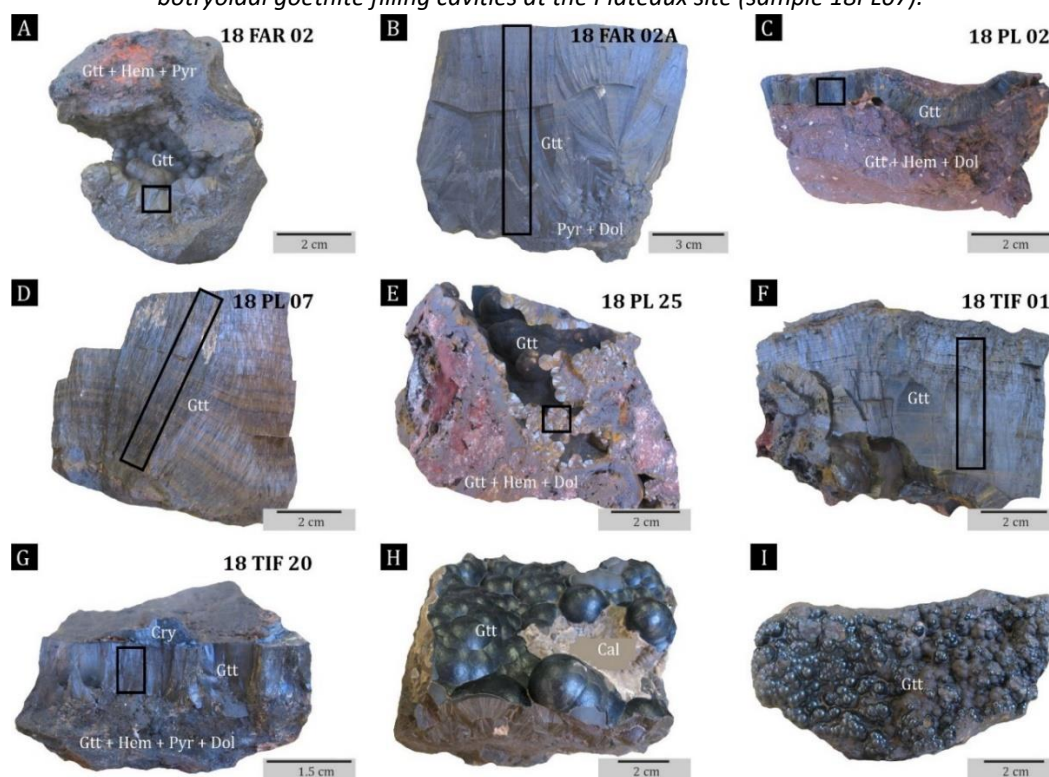


**Figure 6.2.6.** Pictures of botryoidal goethite samples, highlighting the distinction between goethite filling thin fractures (A, C, E, G) and large goethite filling cavities (B, D, F, H, I) (Gtt = goethite; Hem = hematite; Cry = cryptomelane). The black frame indicates the area sampled for (U-Th-Sm)/He dating and isotopic analyses. Goethite featured in figures H and I did not undergo (U-Th-Sm)/He dating, nor isotopic analyses.

**Table 6.2.1. Summary of information and performed analyses of Imini goethite.**

Sample	Description	Location		Elevation	XRD	SEM	Geochemical analyses	Isotopic analyses	(U-Th-Sm)/He dating
		Lat (°N)	Long (°W)	(m)					
Far West									
18FAR02	massive botryoidal goethite	31°2'29"	7°27'57"	1711	x	x	x	x	x
18FAR02A	massive botryoidal goethite	31°2'29"	7°27'57"	1711	x	x	x	x	x
18FAR02B	massive botryoidal goethite	31°2'29"	7°27'57"	1711	x	x			
18FAR02C	powdery hematite and goethite	31°2'29"	7°27'57"	1711	x		x		
18FAR03	massive botryoidal goethite	31°2'29"	7°27'57"	1711	x	x			
18FAR07X	massive botryoidal goethite	31°1'12"	7°28'6"	1739	x	x	x		
18FAR15	massive botryoidal goethite	31°1'12"	7°28'6"	1739	x	x			
18FAR17	botryoidal goethite	31°1'12"	7°28'6"	1739	x	x			
18FAR18	botryoidal goethite	31°1'12"	7°28'6"	1739	x	x			
Tifersine									
18TIF01	massive botryoidal goethite	31°2'45"	7°27'21"	1674	x	x	x	x	x
18TIF05	thin botryoidal goethite vein	31°2'45"	7°27'21"	1674	x	x	x		
18TIF12	mixed Mn oxides and goethite	31°2'27"	7°27'18"	1654	x				
18TIF16	brechified goethite	31°2'27"	7°27'18"	1654	x				
18TIF20	thin botryoidal goethite vein	31°2'27"	7°27'18"	1654	x	x	x	x	x
Plateaux									
15PL02	massive botryoidal goethite	31°1'35"	7°29'31"	1763	x	x	x	x	x
18PL02A	powdery hematite and goethite	31°1'27"	7°29'3"	1766	x				
18PL02B	thin botryoidal goethite vein	31°1'27"	7°29'3"	1766	x	x	x	x	x
18PL07	massive botryoidal goethite	31°1'27"	7°29'3"	1766	x	x	x	x	x
18PL07B	massive botryoidal goethite	31°1'27"	7°29'3"	1766	x	x			
18PL20	thin botryoidal goethite vein	31°1'27"	7°29'3"	1766	x	x			
18PL25	thin botryoidal goethite vein	31°1'27"	7°29'3"	1766	x	x	x	x	x
18PL27	massive botryoidal goethite	31°1'27"	7°29'3"	1766	x	x	x		
Note: All samples are associated to Mn ores, and are hosted by Cenomanian-Turonian dolomites.									

*Note:* All samples are associated to Mn ores, and are hosted by Cenomanian-Turonian dolomites.

## Petrological characterization

X-Ray diffraction has been carried out on nine samples from Far West, five from Tifersine, and eight from Plateaux (Table 6.2.1). A Philips Analytical X-ray diffractometer (Malvern Panalytical, Spectris, Egham, United Kingdom) with a Cu anticathode was used to identify the major mineral phases (University of Namur, Belgium). Eight, three, and seven polished sections, from Far West, Tifersine, and Plateaux, respectively, have been observed on a Zeiss Axiophot reflection microscope (Carl Zeiss AG, Oberkochen, Germany), and with a Jeol JSM-7500F scanning electron microscope (SEM) (JEOL, Tokyo, Japan) coupled to an energy dispersive electron spectrometer (EDS) (Table 6.2.1) (University of Namur, Belgium). For each site, the sample that provided the largest cross-section of the most numerous generations has been observed with a Zeiss Sigma 300 FEG scanning electron microscope (Carl Zeiss AG, Oberkochen, Germany) equipped with two Bruker EDS detectors (Bruker Corporation, Massachusetts, USA) (University of Liège, Belgium).

## Geochemical characterization

Geochemical analyses have been performed on four samples from Far West, three from Tifersine, and five from Plateaux, in Activation Laboratories (Ancaster, ON, Canada) (Table 6.2.1). Rare Earth and major elements were respectively analyzed by Fusion Mass Spectrometry (FUS-MS; Perkin Elmer Sciex Elan 9000 ICP-MS; Sciex AB, Singapore) and Fusion Inductively Coupled Plasma Optical Emission Spectrometry (FUS-ICP; Varian Vista 735 ICP; Agilent, Santa Clara, CA, USA). Trace elements were

quantified by FUS-MS, with the exception of V, Sr, Zr, Ba, Sc and Be, which were occasionally determined by FUS-ICP. FeO was quantified by titration, following the method of Wilson (1955).

### **Stable isotope geochemistry**

The oxygen ( $\delta^{18}\text{O}$ ) and hydrogen ( $\delta\text{D}$ ) isotopic compositions have been determined on two samples of botryoidal goethite of Far West (18FAR02 and 18FAR02A), two of Tifersine (18TIF01 and 18TIF20), and four of Plateaux (15PL02, 18PL02B, 18PL07, 18PL25), at the Institute of Earth Surface Dynamics of the University of Lausanne (Switzerland) (Table 6.2.1). Hydrogen and oxygen isotopic compositions were measured with a Finnigan MAT 253 gas source mass spectrometer (Thermo Fisher Scientific, Waltham, USA) and are reported in permil (‰) in Table 6.2.5, in the typical  $\delta$ -notation relative to the Vienna Standard Mean Ocean Water (VSMOW). According to the method defined by Vennemann et al. (2001), the oxygen isotope compositions were obtained using a  $\text{CO}_2$ -laser fluorination line. Between 2 and 3 mg of goethite, crushed from individual grains, were loaded onto small Pt sample holders. After several cycles of pre-fluorination of the chamber, samples were heated with a  $\text{CO}_2$ -laser to yield  $\text{O}_2$ , in the presence of pure  $\text{F}_2$  that acts as a reagent. After purification of the gas, the extracted  $\text{O}_2$  was introduced into the inlet of the mass spectrometer. Replicate oxygen isotope analyzes of the LS-1 quartz standard (in-house-reference material of Lausanne, quartz 18.1‰) gave an average value of  $18.10 \pm 0.24\text{‰}$  for  $\delta^{18}\text{O}$ . The hydrogen isotope composition and water content of goethite were determined with a zero blank auto-sampler and a High-Temperature Conversion Elemental Analyzer (TC-EA) (Thermo Fisher Scientific, Waltham, USA), according to the method of Bauer and Vennemann (2014), using between 2 and 3 mg of goethite. In-house reference materials of biotite (G1;  $\delta\text{D} = -62 \pm 0.8\text{‰}$ ) and kaolinite (K-17;  $\delta\text{D} = -125 \pm 0.9\text{‰}$ ) were used to calibrate the measured isotopic compositions (Bauer and Vennemann, 2014). All the measurements of samples and standards were replicated, but only their average values are reported in Table 6.2.5.

### **(U-Th-Sm)/He dating**

(U-Th-Sm)/He data have been determined on eight pure and well crystallized cm-sized botryoidal goethite samples (Fig. 6.2.6B, 6.2.6D, 6.2.6F) at the GEOPS laboratory of the Paris Saclay University (France). Goethite filling thin fractures were grinded to keep  $\sim 500\text{ }\mu\text{m}$  long fragments (needles) that were cleaned in distilled water in an ultrasonic bath, and later rinsed with pure ethanol. The clean fragments were selected by handpicking under a binocular microscope, on the basis of their homogeneity, coherence and limited porosity. Five aliquots were selected for each sample originating from thin veins (18FAR02, 18TIF20, 15PL02, 18PL02B, 18PL25). For large-size goethite samples (18FAR02A, 18TIF01, and 18PL07), a Dremel tool with titanium pins was used to extract fragments from three different layers of crystallization, from sawed smooth surfaces. Each of the very thin growth bands represents one event of goethite precipitation: the grains dated by the (U-Th-Sm)/He method may contain not only one, but several successive generations of goethite, as observed by Heim et al. (2006). For the large samples 18FAR02A and 18TIF01, a total of nine aliquots of three goethite bands were sampled, while 18 aliquots originate from three generations of the very large sample 18PL07. Each aliquot (0.02-0.08 mg) was measured, photographed, encapsulated into a  $1\times 1\text{mm}$  niobium tube (purity 99.9%) and weighted. Tubes containing goethite fragments were placed in a vacuum chamber, on a 49-cells plate, along with Durango apatite fragments. Encapsulated samples were degassed using a diode Ytterbium laser under vacuum for 30 minutes, at a temperature below  $1000\text{ }^\circ\text{C}$ , in order to reach the thermal activation and diffusion of He without losing U and Th. This heating step was once or twice repeated, until all  $^4\text{He}$  was degassed. Then, the gas was mixed with a known amount of  $^3\text{He}$ , in a purification line. He was separated from most  $\text{H}_2\text{O}$ ,  $\text{CO}_2$ ,  $\text{H}_2$  and Ar using three liquid nitrogen-cooled traps of activated charcoal, a titanium sponge trap heated at  $\sim 850^\circ\text{C}$  and a SAES 701 getter. Helium isotopes ( $^3\text{He}$  and  $^4\text{He}$ ),  $\text{H}_2\text{O}$ ,  $\text{CO}_2$ ,  $\text{H}_2$ , and Ar were measured with a Pfeiffer Prisma Quadrupole

mass spectrometer (Allard et al. 2018). After degassing, aliquots were extracted from the vacuum chamber. Tubes were transferred into 5 mL Savillex Teflon-capped vials, followed by 50  $\mu\text{L}$  of 5N  $\text{HNO}_3$  containing  $^{235}\text{U}$  (~4 ppb),  $^{230}\text{Th}$  (~4 ppb) and  $^{149}\text{Sm}$  (~4 ppb), 50  $\mu\text{L}$  of 5N  $\text{HNO}_3$ , 400  $\mu\text{L}$  of 40% concentrated  $\text{HCl}$ , and two drops of 38%  $\text{HF}$ . The tightly closed vials were heated at  $\sim 100^\circ\text{C}$  overnight. The vials were placed on a hot plate during two hours for complete evaporation. A 1.9 mL dose of 1N  $\text{HNO}_3$  was added to the solution, to set the Fe content to 100 ppm. The solution was heated at  $100^\circ\text{C}$  for two hours. After cooling, 1.5 mL of the solution was taken and diluted with 1N  $\text{HNO}_3$  to reach a total volume of 3 mL. Finally,  $^{238}\text{U}$ ,  $^{232}\text{Th}$ , and  $^{147}\text{Sm}$  contents were determined by using an ELEMENT XR Thermofisher Scientific high-resolution mass spectrometer. An analytical error of 5% at  $1\sigma$  is expected for the two-step analysis based on Durango apatite dating performed at the same time.

Goethite precipitation rates are estimated for the three large samples, by representing the distance between dated growth bands of goethite as a function of ages (Fig. 2). The angular coefficient of the regression line represents the rate of precipitation. This calculation provides an average value for the whole sample, and does not take into consideration internal variations such as the relation between the thickness of each generation and the time needed for its precipitation.

### 6.2.5.b Additional results and interpretations

#### Characterization

The X-ray diffractograms of Imini botryoidal samples yield narrow, sharp and symmetrical peaks indicating the presence of goethite and suggesting a high degree of crystallinity. The examination of polished sections under the microscopes confirms that botryoidal goethite is constituted of cohesive small crystals with homogeneous elementary concentrations. The high level of homogeneity of the successive layers/generations of Imini botryoidal goethite is highlighted by SEM observations (Fig. 6.2.8). The fluctuating colors of these layers (Fig. 2, 6.2.6B, 6.2.6C, 6.2.6E) are due to variations of porosity (Fig. 6.2.8G). Scarce Mn-oxides of the hollandite group occur in fractures (Fig. 6.2.8B, 6.2.8C, 6.2.8D, 6.2.8F, 6.2.8H) and cavities (Fig. 6.2.8G, 6.2.8H) of goethite, or as a coating on the last goethite generation (Fig. 6.2.6D, 6.2.8D). These phases are never found between successive goethite layers. Hematite is occasionally present at the contact between goethite and the dolomitic host rock (Fig. 6.2.8I), or at the growth center of goethite (Fig. 6.2.8A). Small rare barite grains are noticed in sample 18TIF20. The size of goethite crystallites has been examined with the SEM, in the secondary electrons mode. The width of goethite needles, which is the smallest dimension, always exceed 100 nm (Fig. 6.2.7).

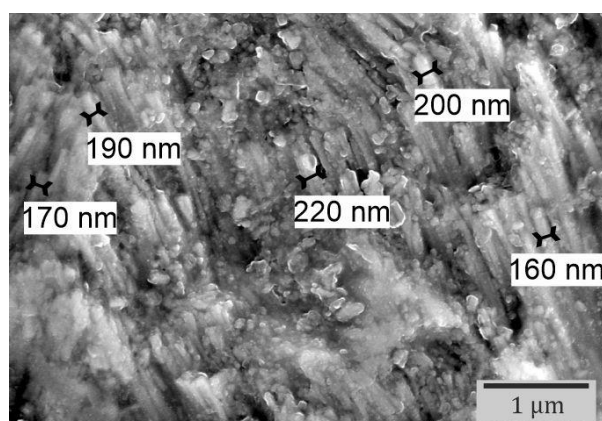


**Figure 6.2.7.** SEM microphotograph of sample 18PL07 in secondary electrons mode. The size of Imini goethite crystallites exceeds 100 nm.

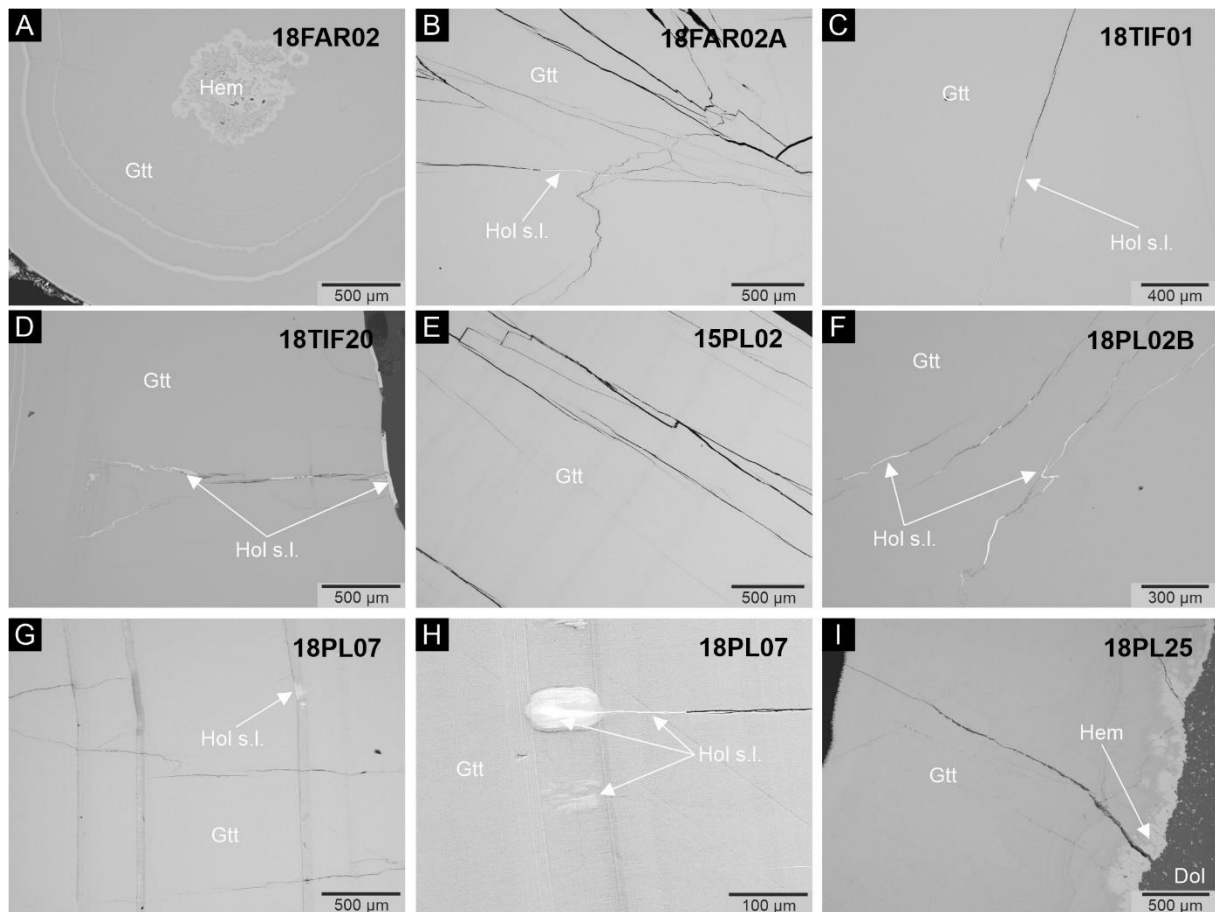


**Figure 6.2.8.** SEM microphotographs of the most representative samples, in back scattered electron mode (Gtt = goethite; Hem = hematite; Hol s.l. = hollandite sensu lato).

Imini goethite samples present quite homogeneous major, minor and trace elements concentrations as observed in Tables 6.2.2, 6.2.3 and 6.2.4. Their very low and close REE contents (total REE content does not exceed 20 ppm) and moderate minor elements concentrations attest of their likeliness (Fig. 6.2.9A, 6.2.9B). Tifersine samples, and more particularly goethite 18TIF20, present slightly different contents in Ba, As, Pb, Zn, and Cu than their Far West and Plateaux counterparts (Fig. 6.2.9B, Table 6.2.4). The enrichment in Ba is most probably related to the precipitation of barite in cavities of more porous goethite layers. The existence of barite has already been noticed by Dekoninck et al. (2016a). Tifersine samples probably derive from fluids containing more base metals than others, probably acquired by fluid-rock interactions. Figure 6.2.9C illustrates the discrepancy between 18TIF20 that is richer in As and all other samples, which fall into the same Cu vs. As contents domain.

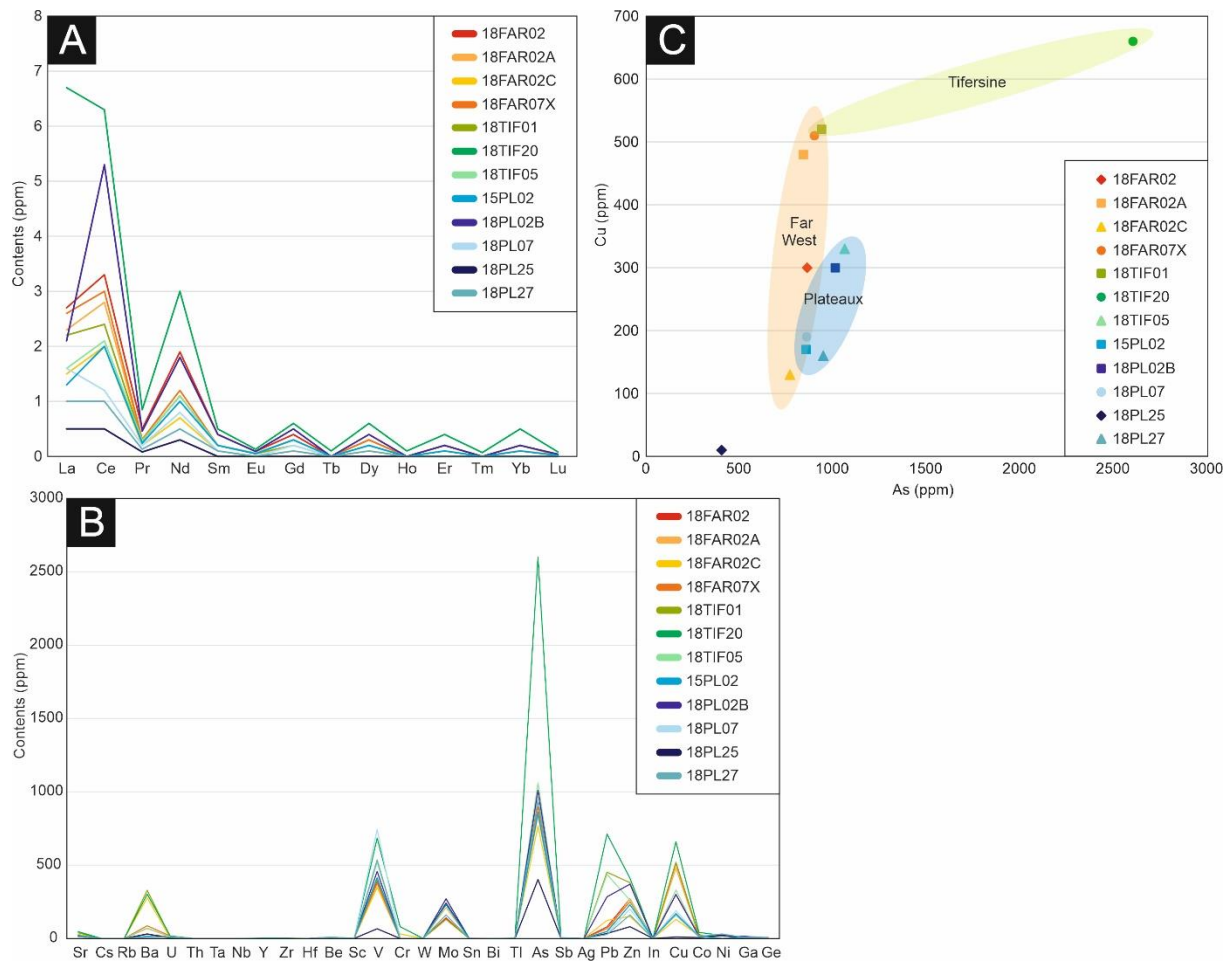


**Figure 6.2.9.** Geochemical data of Far West, Tifersine, and Plateaux samples. (A) Rare earth elements patterns; (B) Trace elements patterns; (C) Cu contents as a function of As contents.

**Table 6.2.2. Results of geochemical analyses for major elements.**

Sample number	FeO	SiO <sub>2</sub>	Al <sub>2</sub> O <sub>3</sub>	Fe <sub>2</sub> O <sub>3</sub>	MnO	MgO	CaO	Na <sub>2</sub> O	K <sub>2</sub> O	TiO <sub>2</sub>	P <sub>2</sub> O <sub>5</sub>	LOI	Total
	(%)	(%)	(%)	(%)	(%)	(%)	(%)	(%)	(%)	(%)	(%)	(%)	(%)
<u>Far West</u>													
18FAR02	<0.1	2.67	0.15	84.55	0.350	0.76	0.13	0.02	<0.01	<0.001	0.14	11.24	100.0
18FAR02A	<0.1	3.05	0.16	82.79	0.413	0.78	0.14	0.03	<0.01	0.001	0.16	11.63	99.2
18FAR02C	<0.1	2.69	0.37	87.02	0.526	0.38	0.16	0.02	0.01	0.001	0.11	7.50	98.8
18FAR07X	<0.1	2.99	0.18	82.73	0.381	0.80	0.13	0.03	<0.01	<0.001	0.20	11.65	99.1
<u>Tifersine</u>													
18TIF01	<0.1	3.02	0.19	83.09	0.778	0.77	0.19	0.03	0.01	0.002	0.18	11.56	99.8
18TIF20	<0.1	3.09	0.47	80.13	1.205	0.95	0.49	0.04	0.01	0.003	0.36	11.84	98.6
18TIF05	<0.1	2.36	0.05	84.97	0.386	0.78	0.40	0.03	<0.01	<0.001	0.24	11.52	100.7
<u>Plateaux</u>													
15PL02	<0.1	2.45	0.09	83.07	0.229	0.77	0.55	0.03	<0.01	<0.001	0.19	11.74	99.2
18PL02B	<0.1	2.72	0.44	83.36	0.335	0.93	0.17	0.04	<0.01	0.002	0.28	11.86	100.1
18PL07	<0.1	2.24	<0.01	84.80	0.276	0.71	0.26	0.04	<0.01	<0.001	0.19	11.69	100.2
18PL25	<0.1	1.87	<0.01	85.32	0.079	0.70	0.29	0.05	<0.01	<0.001	0.11	10.82	99.3
18PL27	<0.1	2.18	<0.01	85.26	0.176	0.71	0.17	0.02	<0.01	<0.001	0.08	11.48	100.1

**Table 6.2.3. Results of geochemical analyses for Rare Earth Elements.**

Sample number	La	Ce	Pr	Nd	Sm	Eu	Gd	Tb	Dy	Ho	Er	Tm	Yb	Lu
	(ppm)	(ppm)	(ppm)	(ppm)	(ppm)	(ppm)	(ppm)	(ppm)	(ppm)	(ppm)	(ppm)	(ppm)	(ppm)	(ppm)
<u>Far West</u>														
18FAR02	2.7	3.3	0.5	1.9	0.4	0.09	0.4	<0.1	0.3	<0.1	0.2	<0.01	0.1	0.02
18FAR02A	2.3	2.8	0.3	1.1	0.2	0.06	0.3	<0.1	0.3	<0.1	0.2	<0.01	0.2	0.02
18FAR02C	1.5	2.0	0.2	0.7	0.1	<0.01	0.1	<0.1	0.1	<0.1	<0.1	<0.01	<0.1	0.01
18FAR07X	2.6	3.0	0.3	1.2	0.2	0.05	0.3	<0.1	0.3	<0.1	0.2	<0.01	0.2	0.03
<u>Tifersine</u>														
18TIF01	2.2	2.4	0.3	1.1	0.2	0.05	0.2	<0.1	0.2	<0.1	0.1	<0.01	<0.1	0.01
18TIF20	6.7	6.3	0.9	3.0	0.5	0.13	0.6	0.1	0.6	0.1	0.4	0.07	0.5	0.08
18TIF05	1.6	2.1	0.3	1.1	0.2	0.06	0.3	<0.1	0.2	<0.1	0.1	<0.01	<0.1	0.01
<u>Plateaux</u>														
15PL02	1.3	2.0	0.2	1.0	0.2	0.05	0.3	<0.1	0.2	<0.1	0.1	<0.01	0.1	0.02
18PL02B	2.1	5.3	0.5	1.8	0.4	0.09	0.5	<0.1	0.4	<0.1	0.2	<0.01	0.2	0.04
18PL07	1.6	1.2	0.2	0.8	0.1	<0.01	0.2	<0.1	0.2	<0.1	<0.1	<0.01	<0.1	0.01
18PL25	0.5	0.5	0.1	0.3	<0.1	<0.01	<0.1	<0.1	<0.1	<0.1	<0.1	<0.01	<0.1	<0.01
18PL27	1.0	1.0	0.1	0.5	0.1	<0.01	0.1	<0.1	0.1	<0.1	<0.1	<0.01	<0.1	<0.01



**Table 6.2.4. Results of geochemical analyses for minor elements.**

Sample number	Sr	Cs	Rb	Ba	U	Th	Ta	Nb	Y	Zr	Hf	Be	Sc	V	Cr	W	Mo	Sn	Bi	Tl	As	Sb	Ag	Pb	Zn	In	Cu	Co	Ni	Ga	Ge
(ppm)																															
Far West																															
18FAR02	19	<0.1	<1	28	9.5	<0.05	<0.01	<0.2	<0.5	<1	<0.1	7	<1	391	<20	<0.5	140	<1	<0.1	0.3	859	1.5	<0.5	79	270	<0.1	300	26	<20	10	4
18FAR02A	21	<0.1	<1	68	12.2	<0.05	<0.01	<0.2	<0.5	<1	<0.1	7	<1	351	<20	<0.5	210	<1	<0.1	0.4	839	2.9	<0.5	49	270	<0.1	480	18	<20	8	7
18FAR02C	27	<0.1	<1	276	3.2	<0.05	<0.01	<0.2	<0.5	2	<0.1	3	<1	347	30	<0.5	130	<1	<0.1	0.7	767	4.0	<0.5	123	150	<0.1	130	19	<20	4	9
18FAR07X	21	<0.1	<1	86	16.5	<0.05	<0.01	<0.2	<0.5	<1	<0.1	9	<1	376	<20	<0.5	240	<1	<0.1	0.3	898	2.6	<0.5	67	250	<0.1	510	20	20	11	7
Tifersine																															
18TIF01	38	<0.1	<1	329	11.4	<0.05	<0.01	<0.2	<0.5	<1	<0.1	6	<1	403	<20	<0.5	130	<1	<0.1	0.9	936	3.4	<0.5	452	380	<0.1	520	24	<20	8	6
18TIF20	46	<0.1	<1	302	16.6	<0.05	<0.01	<0.2	<0.5	3	<0.1	8	1	684	80	<0.5	230	<1	<0.1	2.0	2600	4.0	<0.5	712	410	<0.1	660	41	20	12	6
18TIF05	20	<0.1	<1	71	11.7	<0.05	<0.01	<0.2	<0.5	<1	<0.1	8	<1	519	<20	<0.5	270	<1	<0.1	0.3	1060	2.5	<0.5	437	260	<0.1	330	14	20	9	5
Plateaux																															
15PL02	17	<0.1	<1	14	7.9	<0.05	<0.01	<0.2	<0.5	<1	<0.1	7	<1	416	<20	1.0	230	<1	<0.1	<0.1	853	1.5	<0.5	47	230	<0.1	170	14	<20	7	4
18PL02B	19	<0.1	<1	13	9.5	<0.05	<0.01	<0.2	<0.5	<1	<0.1	8	<1	457	<20	<0.5	270	1	<0.1	0.3	1010	2.2	<0.5	284	370	<0.1	300	15	20	14	4
18PL07	17	<0.1	<1	15	10.3	<0.05	<0.01	<0.2	<0.5	<1	<0.1	9	<1	744	<20	<0.5	230	<1	<0.1	<0.1	856	4.0	<0.5	33	200	<0.1	190	15	30	7	7
18PL25	12	<0.1	<1	31	1.6	<0.05	<0.01	<0.2	<0.5	<1	<0.1	3	<1	66	<20	<0.5	240	<1	<0.1	<0.1	402	1.7	<0.5	34	80	<0.1	10	6	20	2	6
18PL27	13	<0.1	<1	8	9.0	<0.05	<0.01	<0.2	<0.5	<1	<0.1	6	<1	536	<20	<0.5	160	<1	<0.1	<0.1	945	4.7	<0.5	27	160	<0.1	160	12	30	6	6

## Stable isotope geochemistry

The water proportion of Imini goethite varies between 10.46% (18FAR02) and 11.41% (18PL02B) (Table 6.2.5). The isotopic hydrogen compositions are quite homogeneous and fluctuate between 156‰ (18PL02B) and 172‰ (18TIF01) (Table 6.2.5). The oxygen isotopic compositions are consistent, with the exception of sample 18FAR02A that provides a much higher  $\delta^{18}\text{O}$  value (11.09‰) (Table 6.2.5, Fig. 3). No particular reason could be found to explain this divergence. The  $\delta^{18}\text{O}$  values of the other samples range between 3.07 (18TIF20) and 6.03 (18PL02B) (Table 6.2.5). Imini goethite  $\delta\text{D}$ - $\delta^{18}\text{O}$  data gather around a temperature line of  $-35^\circ\text{C}$  in the diagram of Yapp (1987) (Fig. 3; Table 6.2.5). Such low temperatures are unreasonable for the precipitation of goethite in equilibrium with surficial meteoric waters. If  $\delta\text{D}$  values fall within an expected range,  $\delta\text{O}^{18}$  compositions are strongly shifted to the right of the temperature lines in equilibrium with the meteoric water line (MWL) defined by Craig (1961), which might indicate modification of the mineralizing fluid (Fig. 3). The fluids involved in goethite precipitation were in disequilibrium with meteoric waters. Fluid/rock interactions processes, such as the dissolution/precipitation of minerals, might lead to isotopic exchanges between mineralizing fluids and host rocks. Here, the dissolution of carbonates, which are known to concentrate  $^{18}\text{O}$  in their structure (Garlick 1966), is probably responsible for the  $\delta^{18}\text{O}$  shift, as observed by Dekoninck et al. (2018) for goethite and kaolinite in Tunisia. Heavy oxygen might have been released in meteoric fluids after the dissolution of Imini host rock and incorporated in goethite. This early diagenesis process might have wiped out the usual depletion in  $^{18}\text{O}$  of supergene phases.

**Table 6.2.5.** Oxygen and Hydrogen isotopic compositions of Imini goethite.

Sample number	H <sub>2</sub> O (wt%)	$\delta\text{D}_{\text{VSMOW}}$ (‰)	$\delta^{18}\text{O}_{\text{VSMOW}}$ (‰)
<u>Far West</u>			
18FAR02	10.48	-167	5.31
18FAR02A	11.03	-170	11.09
<u>Tifersine</u>			
18TIF01	11.02	-172	3.39
18TIF20	11.08	-159	3.07
<u>Plateaux</u>			
15PL02	11.06	-164	4.35
18PL02B	11.35	-156	6.03
18PL07	11.03	-168	3.19
18PL25	10.56	-148	4.98

## (U-Th-Sm)/He dating

Fifty-six (U-Th-Sm)/He data have been produced from eight samples; data are reported in table 6.2.6. The data and their interpretation can be found in the main text of the article. The gathering of all raw ages on a frequency distribution chart suggests the existence of two distinct populations of botryoidal goethite at Imini (Fig. 6.2.10). Most ages converge around 80-90 Ma, but a second peak is observed around 60-70 Ma (Fig. 6.2.10). The oldest generation corresponds, to a certain extent, to the large goethite samples that precipitated in cavities of the host rock. The second generation of goethite roughly matches with fracture-filling goethite in Far West, Tifersine and Plateaux sites.

The particularly reproducible fifty-six (U-Th-Sm)/He ages of the present study are characterized by a very low dispersion: 3.5% for Durango apatite instead of the usual 4-4.5%, and 3.6% for goethite rather than the common >6%. The error associated to He diffusive losses is estimated to represent a maximum of 5% of the ages, including analytical issues. This value is much lower than the one usually estimated in previous studies (Shuster et al. 2005; Vasconcelos et al. 2013; Monteiro et al. 2014; Riffel et al. 2016; Allard et al. 2018). The high reproducibility of our ages arises from the direct precipitation

of goethite in fractures and cavities (Fig. 6.2.5, 6.2.6), the very well-arranged botryoidal texture (Fig. 6.2.6, 6.2.8), the near non-existence of inclusions and contaminant minerals, the quite large dimensions of crystallites that ensures an efficient He retention (the smallest dimension always exceeds 100 nm; Fig. 6.2.7), the very low contents in elements (Fig. 6.2.9) suggesting only few substitutions and, consequently, few disturbances in the crystal lattice. The rare combination of all these parameters, in goethite, probably led to very limited He diffusive losses, in comparison with previous studies. The well-considered sampling and the extensive characterization led to the dating of the most ideal material, i.e. remarkably pure, homogeneous and well crystallized goethite. Figure 6.2.11 compares the effective uranium values (eU) and the ages of Imini goethite samples, and highlights an almost linear relation between both parameters, exception made of sample 18TIF20. The oldest samples own the highest eU, and *vice versa*. This probably implies that Imini's goethite precipitated from evolving mineralizing fluids characterized with a declining U concentration. The very low Th and Sm contents of Imini goethite have almost no influence on ages and eU, which thus mostly depend on U concentrations.

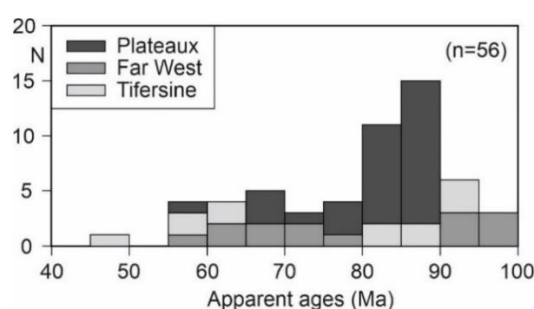


**Figure 6.2.10.** Distribution of Imini goethite (U-Th-Sm)/He ages from Far West, Tifersine, and Plateaux sites.

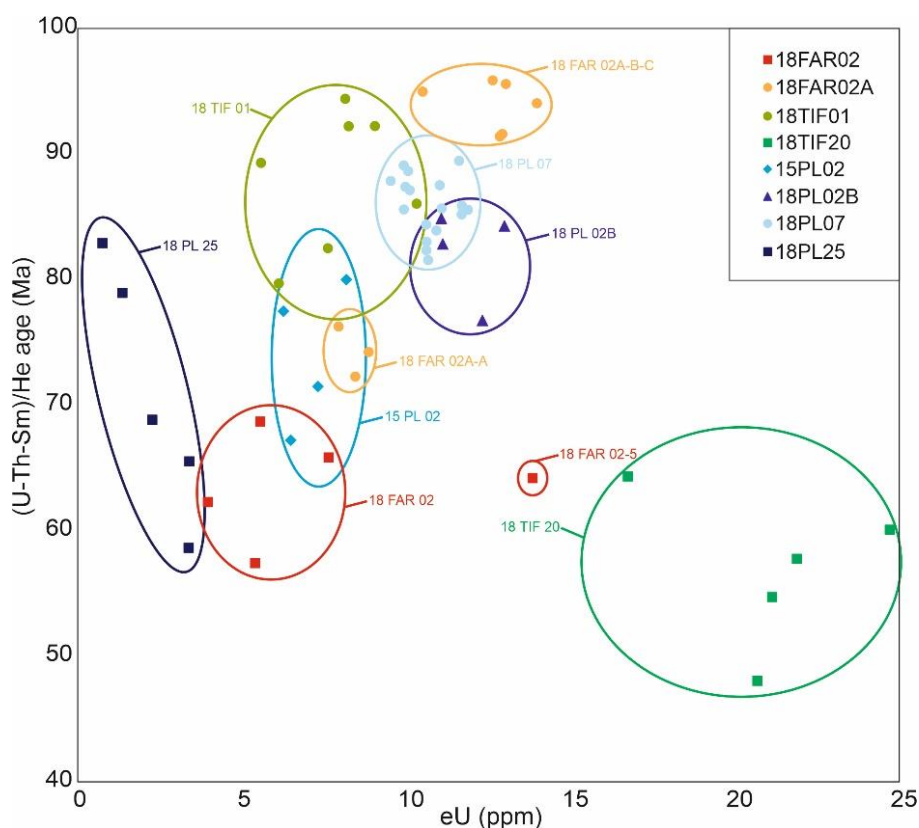


**Figure 6.2.11.** He ages as a function of the effective uranium (eU) contents, for all dated samples of Far West, Tifersine, and Plateaux sites.

**Table 6.2.6. Imini goethite (U-Th-Sm)/He data.**

Sample number	<sup>4</sup> He	± s	<sup>238</sup> U	<sup>232</sup> Th	<sup>147</sup> Sm	Weight	<sup>4</sup> He	± s	<sup>238</sup> U	<sup>232</sup> Th	<sup>147</sup> Sm	eU	Th/U	Th/Sm	Uncorrected age and error	Average age	Standard deviation	Corrected age* and error**
	(ccSTP)	(ccSTP)	(ng)	(ng)	(ng)	(mg)	(nccSTP/g)	(nccSTP/g)	(ppm)	(ppm)	(ppm)	(ppm)			(Ma)	(Ma)		(Ma)
<u>Far West</u>																		
18FAR02AA-1	1.19E-09	1.19E-11	0.13	0.01	0.00	0.02	79453	795	8.6	0.9	0.15	9	0.11	6.21	74 ± 4			76 ± 4
18FAR02AA-2	1.90E-09	1.90E-11	0.20	0.01	0.00	0.03	73209	732	7.9	0.3	0.03	8	0.04	9.40	76 ± 5	74	2.0	79 ± 4
18FAR02AA-3	9.60E-10	9.60E-12	0.11	0.00	0.00	0.01	73837	738	8.4	0.3	0.05	8	0.03	6.00	72 ± 4			74 ± 4
18FAR02AB-1	2.65E-09	2.65E-11	0.23	0.01	0.00	0.02	120550	1206	10.4	0.3	0.04	10	0.03	5.82	95 ± 6			98 ± 5
18FAR02AB-2	1.99E-09	1.99E-11	0.18	0.01	0.00	0.01	141987	1420	12.8	0.4	0.07	13	0.03	5.06	91 ± 5	93	2.0	94 ± 5
18FAR02AB-3	1.57E-09	1.57E-11	0.14	0.00	0.00	0.01	143108	1431	12.8	0.4	0.14	13	0.03	2.98	92 ± 5			94 ± 5
18FAR02AC-1	2.26E-09	2.26E-11	0.19	0.00	0.00	0.02	150593	1506	13.0	0.2	0.03	13	0.01	5.83	96 ± 6			98 ± 5
18FAR02AC-2	1.43E-09	1.43E-11	0.13	0.00	0.00	0.01	158922	1589	13.9	0.3	0.06	14	0.02	4.16	94 ± 6	95	1.0	97 ± 5
18FAR02AC-3	1.90E-09	1.90E-11	0.16	0.01	0.00	0.01	146352	1464	12.4	0.8	0.08	13	0.07	10.34	96 ± 6			99 ± 5
18FAR02-1	9.12E-10	9.12E-12	0.11	0.00	0.00	0.02	60803	608	7.6	0.3	0.11	8	0.04	3.00	66 ± 4			68 ± 3
18FAR02-2	7.76E-10	7.76E-12	0.10	0.01	0.00	0.03	29829	298	3.9	0.2	0.07	4	0.06	3.27	62 ± 4			64 ± 3
18FAR02-3	4.86E-10	4.86E-12	0.06	0.03	0.00	0.01	37418	374	4.9	1.9	0.29	5	0.39	6.71	57 ± 3	64	4.2	59 ± 3
18FAR02-4	1.01E-09	1.01E-11	0.12	0.01	0.00	0.02	46133	461	5.5	0.3	0.06	6	0.05	4.75	69 ± 4			71 ± 4
18FAR02-5	1.50E-09	1.50E-11	0.19	0.01	0.00	0.01	107457	1075	13.7	0.6	0.14	14	0.04	4.28	64 ± 4			66 ± 3
<u>Tifersine</u>																		
18TIF01A-1	5.30E-10	5.30E-12	0.05	0.02	0.00	0.01	58879	589	5.5	2.4	0.31	6	0.43	7.78	80 ± 5			82 ± 4
18TIF01A-2	8.35E-10	8.35E-12	0.08	0.01	0.00	0.01	75927	759	7.3	1.2	0.26	8	0.17	4.79	82 ± 5	84	4.9	85 ± 4
18TIF01A-3	2.71E-09	2.71E-11	0.25	0.00	0.00	0.05	60218	602	5.5	0.1	0.03	6	0.02	3.98	89 ± 5			92 ± 5
18TIF01B-2	1.72E-09	1.72E-11	0.16	0.01	0.00	0.02	107313	1073	10.2	0.4	0.06	10	0.04	5.58	86 ± 5	86	0.0	89 ± 4
18TIF01C-1	1.93E-09	1.93E-11	0.17	0.00	0.00	0.02	92018	920	8.2	0.1	0.09	8	0.02	1.62	92 ± 6			95 ± 5
18TIF01C-2	1.71E-09	1.71E-11	0.15	0.01	0.00	0.02	100828	1008	8.9	0.4	0.07	9	0.05	5.94	92 ± 6	93	1.3	95 ± 5
18TIF01C-3	1.58E-09	1.58E-11	0.14	0.01	0.00	0.02	92920	929	8.0	0.5	0.07	8	0.06	7.49	94 ± 6			97 ± 5
18TIF20-1	1.32E-09	1.32E-11	0.22	0.01	0.00	0.01	120093	1201	20.5	0.9	0.14	21	0.05	6.77	48 ± 3			49 ± 2
18TIF20-2	5.31E-09	5.31E-11	0.80	0.01	0.00	0.04	139829	1398	21.1	0.1	0.06	21	0.01	2.31	55 ± 3			56 ± 3
18TIF20-3	1.56E-09	1.56E-11	0.20	0.01	0.00	0.01	130216	1302	16.6	0.6	0.14	17	0.03	4.12	64 ± 4	57	6.1	66 ± 3
18TIF20-4	1.19E-08	1.19E-10	1.70	0.01	0.01	0.08	152874	1529	21.8	0.2	0.08	22	0.01	2.16	58 ± 3			59 ± 3
18TIF20-5	1.62E-09	1.62E-11	0.21	0.05	0.01	0.01	179469	1795	23.4	5.4	0.98	25	0.23	5.55	60 ± 4			62 ± 3
<u>Plateaux</u>																		
18PL07A-1	4.90E-09	4.90E-11	0.45	0.01	0.00	0.04	125525	1255	11.6	0.2	0.06	12	0.01	2.49	89 ± 5			92 ± 5
18PL07A-2	8.54E-09	8.54E-11	0.83	0.00	0.00	0.07	120329	1203	11.7	0.0	0.03	12	0.00	0.80	85 ± 5	87	2.3	88 ± 4
18PL07A-3	8.38E-09	8.38E-11	0.81	0.00	0.00	0.07	121417	1214	11.7	0.1	0.03	12	0.00	1.98	86 ± 5			88 ± 4
18PL07B-1	3.26E-09	3.26E-11	0.33	0.01	0.00	0.03	105155	1052	10.6	0.3	0.03	11	0.03	11.22	82 ± 5			84 ± 4
18PL07B-2	2.10E-09	2.10E-11	0.20	0.00	0.00	0.02	116610	1166	11.0	0.1	0.03	11	0.01	3.26	88 ± 5	85	3.0	90 ± 5
18PL07B-3	1.97E-09	1.97E-11	0.19	0.01	0.00	0.02	122852	1229	11.8	0.4	0.05	12	0.03	6.94	86 ± 5			88 ± 4
18PL07C-1	2.53E-09	2.53E-11	0.24	0.00	0.00	0.03	101191	1012	9.5	0.1	0.03	10	0.01	4.76	88 ± 5	87	1.2	90 ± 5

18PL07C-2	3.18E-09	3.18E-11	0.31	0.01	0.00	0.03	102720	1027	9.9	0.2	0.04	10	0.02	5.25	86 ± 5			88 ± 4
18PL07C-3	2.56E-09	2.56E-11	0.24	0.00	0.00	0.02	106462	1065	10.1	0.2	0.03	10	0.02	5.08	87 ± 5			90 ± 4
18PL07D-1	4.54E-09	4.54E-11	0.45	0.00	0.00	0.04	110750	1107	10.9	0.1	0.02	11	0.01	3.54	84 ± 5	83	1.1	86 ± 4
18PL07D-3	6.02E-09	6.02E-11	0.60	0.01	0.00	0.06	105642	1056	10.6	0.2	0.04	11	0.02	4.86	82 ± 5			85 ± 4
18PL07E-1	1.58E-09	1.58E-11	0.15	0.00	0.00	0.02	105397	1054	9.9	0.3	0.06	10	0.03	5.20	87 ± 5			90 ± 5
18PL07E-2	3.90E-09	3.90E-11	0.38	0.00	0.00	0.04	108227	1082	10.6	0.1	0.05	11	0.01	2.73	84 ± 5	85	2.2	87 ± 4
18PL07E-3	2.66E-09	2.66E-11	0.26	0.01	0.00	0.03	106560	1066	10.5	0.3	0.05	11	0.03	6.62	83 ± 5			85 ± 4
18PL07F-1	3.34E-09	3.34E-11	0.31	0.01	0.00	0.03	107809	1078	10.0	0.2	0.07	10	0.02	2.68	89 ± 5			91 ± 5
18PL07F-2	1.71E-09	1.71E-11	0.16	0.00	0.00	0.02	106855	1069	9.9	0.1	0.03	10	0.01	3.40	89 ± 5	88	1.9	92 ± 5
18PL07F-3	2.06E-09	2.06E-11	0.20	0.01	0.00	0.02	114687	1147	11.0	0.5	0.06	11	0.04	7.77	86 ± 5			88 ± 4
18PL25-1	8.85E-10	8.85E-12	0.12	0.03	0.00	0.04	23919	239	3.2	0.9	0.08	3	0.28	10.83	59 ± 4			60 ± 3
18PL25-2	1.23E-09	1.23E-11	0.14	0.01	0.00	0.07	18862	189	2.2	0.2	0.02	2	0.09	9.15	69 ± 4			71 ± 4
18PL25-3	4.56E-10	4.56E-12	0.05	0.02	0.00	0.02	26849	268	3.1	1.1	0.17	3	0.36	6.75	66 ± 4	71	9.9	67 ± 3
18PL25-4	3.84E-10	3.84E-12	0.04	0.00	0.00	0.05	7523	75	0.7	0.0	0.01	1	0.05	3.98	83 ± 5			85 ± 4
18PL25-5	5.95E-10	5.95E-12	0.06	0.00	0.00	0.05	12944	129	1.3	0.1	0.02	1	0.07	6.38	79 ± 5			81 ± 4
15PL02-1	1.05E-08	1.1E-10	1.29	0.01	n.a.	0.20	52666	527	6.5	0.0	n.a.	6	0.01	N.D.	67 ± 4			69 ± 3
15PL02-2	5.87E-09	5.9E-11	0.62	0.01	n.a.	0.10	58665	587	6.2	0.1	n.a.	6	0.01	N.D.	77 ± 5	74	5.8	80 ± 4
15PL02-3	1.64E-08	1.6E-10	1.90	0.01	n.a.	0.26	63228	632	7.3	0.0	n.a.	7	0.00	N.D.	71 ± 4			74 ± 4
15PL02-4	6.19E-08	6.19E-10	6.39	0.03	0.03	0.78	79100	791	8.2	0.0	0.04	8	0.00	0.77	80 ± 5			82 ± 4
18PL02B-2	1.12E-08	1.12E-10	1.10	0.00	0.00	0.09	132352	1324	13.0	0.0	0.06	13	0.00	0.46	84 ± 5			87 ± 4
18PL02B-3	6.34E-09	6.34E-11	0.63	0.01	0.00	0.06	111250	1113	11.1	0.2	0.06	11	0.01	2.63	83 ± 5	82	3.7	85 ± 4
18PL02B-4	4.66E-09	4.66E-11	0.44	0.07	0.04	0.04	113580	1136	10.7	1.7	0.94	11	0.16	1.77	85 ± 5			87 ± 4
18PL02B-5	3.65E-09	3.65E-11	0.36	0.14	0.02	0.03	114176	1142	11.2	4.4	0.50	12	0.39	8.89	77 ± 5			79 ± 4

\*A 3% correction is added to ages.

\*\*A 5 % error is considered.

N.D. = No data

### **6.3 Unraveling the potential relations between the formation of supergene ores and geodynamic in the Anti-Atlas and High Atlas (Morocco), by goethite (U-Th-Sm)/He dating**

This study focuses on three Cu-Pb-Zn-V ore deposits located in the Oriental High Atlas (Jbel Haouanit, Jbel Klakh and Jbel Rhals) and on four Cu(-As) deposits (Tazalaght, Agoujgal, Tassrirt, Tizert; Verhaert et al., in press; Poot et al., submitted) and three gossans (Assifid, Irkhs, Ighrem) situated in the Occidental Anti-Atlas, that all underwent weathering processes leading to the development of supergene profiles topped by iron (oxyhydr-)oxides. If the paragenetic sequence of these mineralization is well known and often published, the timing of precipitation of these ores remains poorly understood. The present study aims to provide clues to a better understanding of weathering processes and of the genesis of metallic ore deposits. The detailed petrological and geochemical characterization reveals the structure, composition and paragenetic relations of iron (oxyhydr-)oxides, while  $\delta D$ - $\delta^{18}O$  analyses refine our knowledge of the composition of the mineralizing fluids. The numerous (U-Th-Sm)/He goethite ages, together with analyses of stable isotopes bring concrete indications and restrictions on supergene mineralization in the regional geodynamic contexts. The present study also aims at testing of the applicability of (U-Th-Sm)/He method through dating iron (oxyhydr-)oxides on different types such as botryoidal goethite, goethite and hematite pseudomorphosing pyrite and siderite, “microcrystalline” goethite clusters and powdery goethite.

#### **6.3.1 Geological setting**

##### **6.3.1.a Anti-Atlas (Tazalaght, Agoujgal, Tassrirt, Irkhs, Tizert, Assifid and Ighrem sites)**

The Tazalaght, Agoujgal, Tassrirt, Irkhs, Tizert, Assifid and Ighrem sites are located in the Anti-Atlas, south to the Anti-Atlas Major Fault (AAMF) (Fig. 6.3.1A). Tazalaght Cu-deposit is situated at the eastern edge of the Aït Abdellah inlier, east of the Kerdous inlier, at an altitude of approximately 1800 m (Fig. 6.3.1B). The Paleoproterozoic basement of this hercynian anticlinal structure is unconformably overlain by Early-Middle Neoproterozoic quartzites and metapelites, Late Neoproterozoic ignimbrites and volcano-detrital rocks and is surrounded by Cambrian conglomeratic series (Massacrier 1980). The lithostratigraphic sequence of the deposit comprises, from base to top: Paleoproterozoic quartzites and conglomerates, Neoproterozoic conglomerates, the Cambrian “Base Serie” composed of a quartzitic breccia and alternating sandstones and siltstones, the “Tamjout dolomite”, and the “Inferior Limestone Series”. Numerous fractures, mostly NNW-SSE and NNE-SSW are identified in the cover formations (Asladay 2002; El Basbas et al. 2011). The Cu-mineralization occurs in the quartzite, Base Serie, and Tamjout dolomite. The ores underwent significant weathering leading to the formation of a thick supergene sequence above the primary sulfides. More information about the mineralogy and paragenesis of As-rich Tazalaght and Agoujgal ores can be found in Verhaert et al. (in press). The geodynamic setting of these sites is detailed in chapter 3.3 of the present thesis.

Agoujgal Cu- deposit lies at an altitude of 1300 m, at the southeastern angle of the Kerdous inlier, where it extends to the small Tafeltast inlier (Fig. 6.3.1B). The substratum of this ENE-WSW monoclinial structure moderately dipping to the SSE is composed of a slightly metamorphized eburnean granite dated at  $2046 \pm 3$  Ma by Hassenforder et al. (2001) and intersected by numerous basic dykes dated at  $1741 \pm 10$  Ma by Youbi et al. (2013). Early Cambrian transgressive series unconformably overlay the granitic basement, with, from base to top, alternating siltstones and sandstones of the “Base Serie”, the “Tamjout dolomite”, dolomitic sandstones, and the “Inferior Limestones” that are all crosscut by

N-S, E-W, and NE-SW fractures (Maddi et al. 2011). The Cu(-Ag) mineralization is found in all Cambrian cover facies; the development of the extensive oxidized mineralization results from weathering processes (Verhaert et al., in press).

The Tassrirt site is located at an altitude of 1800 m, at the eastern edge of the Kerdous inlier, in the Tassrirt massif, which is interpreted as a Late Proterozoic diapiric gneiss dome (Soulaïmani and Piqué 2004). The stratigraphic sequence of the area begins with a slightly metamorphized eburnean granite that intruded all preexistent structures, triggering the setting of foliated gneiss (Soulaïmani and Piqué 2004; Gasquet et al. 2008). Then, Neoproterozoic conglomerates are overlaid by the Adoudou Formation that hosts most of the primary sulfidic and secondary supergene Zn-Cu mineralization. This unit is composed, from base to top, by the “Base Serie” containing sandstones and siltstones, the “Superior Limestones”, and the rarer “Lie de Vin” dolostones and clays (Maloof et al. 2006).

The Irkhs site is located at the northern edge of the Tagrara d’Akka inlier, at an altitude of 1450 m. The stratigraphic sequence is strongly similar to that of Tazalaght and Agoujgal. This gossan is associated to scarce supergene Cu-phases but does not top supergene ores. The mineralization, hosted in the Cambrian “Inferior Limestones”, could be stratiform, as it seems to follow the stratification, but might also be associated to the presence of normal faults in the area.

The respectively 1000 and 1300 m high Tizert and Assifid gossans are located at the north of Ighrem inlier, while Assifid gossan is found at its south, at an altitude of 1700 m. The gossans are hosted by the Late Proterozoic-Cambrian “Inferior Limestones” and do not top any supergene ores. Tizert gossan is not related to the eponymous Cu-deposit, located 10 km to the south: its Fe mineralization is located at the bottom of the Tizert Oued valley, in strongly fractured limestones, in association with quartz-mineralized faults. Assifid gossan tops a non-mineralized sequence comprising the “Base serie” to the “Tamjout dolomite”. Ighrem gossan is found close to a large Jurassic dolerite dyke.

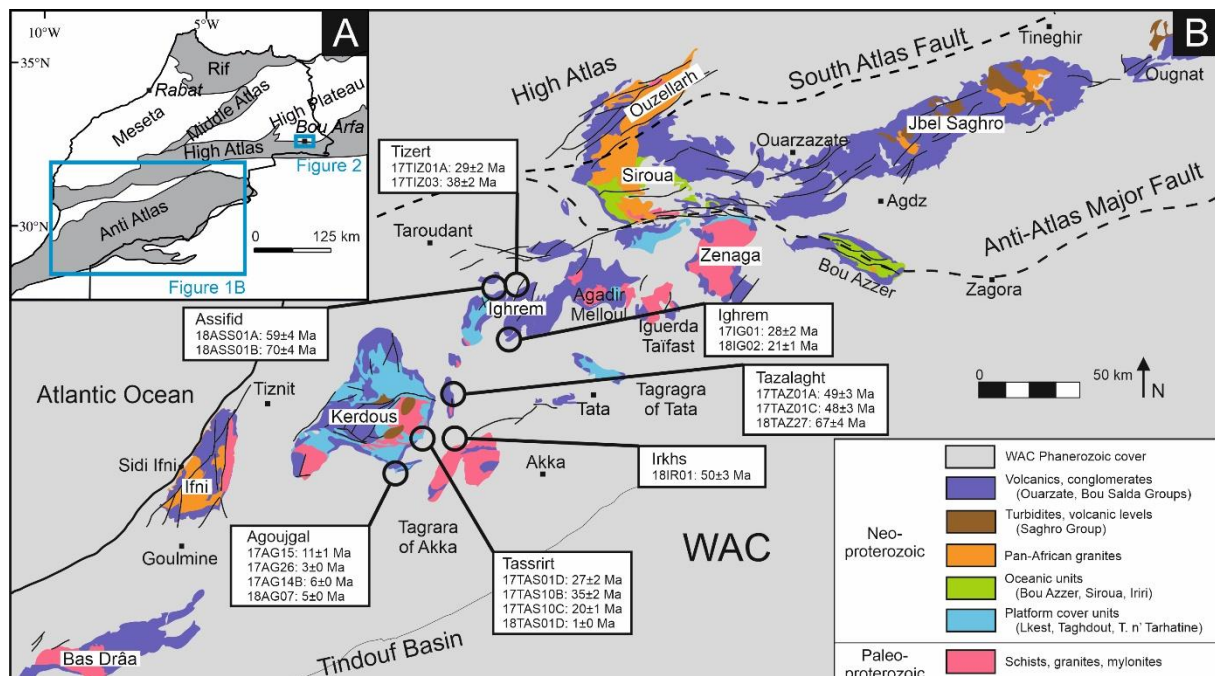


**Figure 6.3.1.** (A) Simplified geologic map of Morocco, with the studied areas framed in blue. (B) Geologic map of the Anti-Atlas providing the location and average goethite (U-Th-Sm)/He ages of Agoujgal, Tazalaght, Tassrirt, Irkhs, Assifid, Tizert, Ighrem, and Imi Omagha sites along the aligned Precambrian inliers (modified after Gasquet et al. 2008; Ikenne et al. 2017).



### 6.3.1.b High Atlas (Jbel Rhals, Jbel Haouanit and Jbel Klakh sites)

The Jbel Rhals, Jbel Haouanit and Jbel Klakh sites are located at the northern edge of the Oriental High Atlas, respectively at 20 km southward, 45 km westward and 28 km eastward of the city of Bou Arfa (Fig. 6.3.2). The basement formations of the area include Precambrian shales, conglomerates, sandstones and volcanic rocks (Chefchaoui et al. 1963). Cambrian to Visean rocks are represented by shales, quartzites and conglomerates with limestone beds (Chefchaoui et al. 1963). Permian to Triassic argillites are sealed by basalt flows, and covered by Liassic to Cretaceous dolomitized limestones, marls and conglomeratic series (Chefchaoui et al. 1963). These formations are overlaid by recent sediments, sand, alluvium and silt (Chefchaoui et al. 1963). E-W, NE-SW and WNW-ESE faults affect the Triassic to Cretaceous sequence (Chefchaoui et al. 1963). The several meters thick Jbel Rhals Fe-Mn-Cu ores lie in Paleozoic shales topped by Permian-Triassic basalts, at an altitude of 1200 – 1300 m. The mineralogy and paragenesis of these ores are defined in Verhaert et al. (2018). The Pb-Zn and Cu-V ores of Jbel Haouanit deposit are located at 1150 – 1250 meters of altitude, while the Cu ores of Jbel Klakh lie at an altitude of 1300 – 1500 m. In both deposits, the ores are concentrated in 0.1 millimeter to 20 centimeters wide veins hosted by strongly fractured and moderately folded Jurassic dolomitized rocks. The Jbel Klakh and Jbel Haouanit mineralogy and paragenesis are described in Verhaert et al. (2017). The geodynamic setting of these sites is detailed in chapter 3.2 of the present thesis.

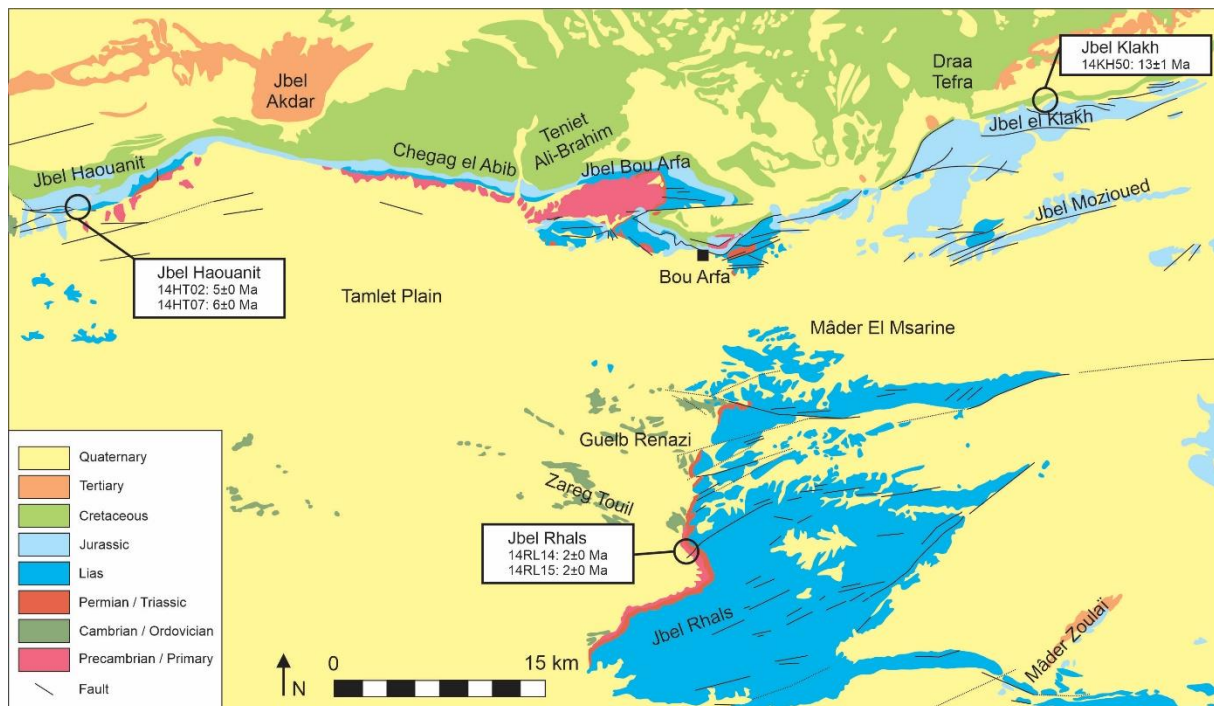


**Figure 6.3.2.** Geologic map of the Bou Arfa district in the Oriental High Atlas, providing the location and average goethite (U-Th-Sm)/He ages of Jbel Haouanit, Jbel Klakh, and Jbel Rhals sites (modified after Chefchaoui et al. 1963).

### 6.3.2 Materials and analytical methods

Sixty-four samples of iron (oxyhydr-)oxides have been collected during three field campaigns, in March 2014 (samples labelled 14XX00), May 2017 (samples labelled 17XX00) and March 2018 (samples labelled 18XX00). Ten samples originate from three sites in the oriental High Atlas: Jbel Rhals, Jbel Haouanit, and Jbel Klakh. Fifty-four samples have been collected from nine sites in the Anti-Atlas: Agoujgal, Tazalaght, Tassirt, Tizert, Ighrem, Assifid, Irkhs, Imi Omagha, and Est Akka. Selected samples

precipitated in gossans associated or not with supergene metal deposits (Fig. 6.3.3A), in pseudomorphose of a precursor mineral phase (Fig. 6.3.3B, 6.3.3C), as botryoidal phases (Fig. 6.3.3D, 6.3.3E) or as microcrystalline phases (Fig. 6.3.3F, 6.3.3G). Table 6.3.1 summarizes the information for all samples, including their location and the analyses performed as part of the present study.

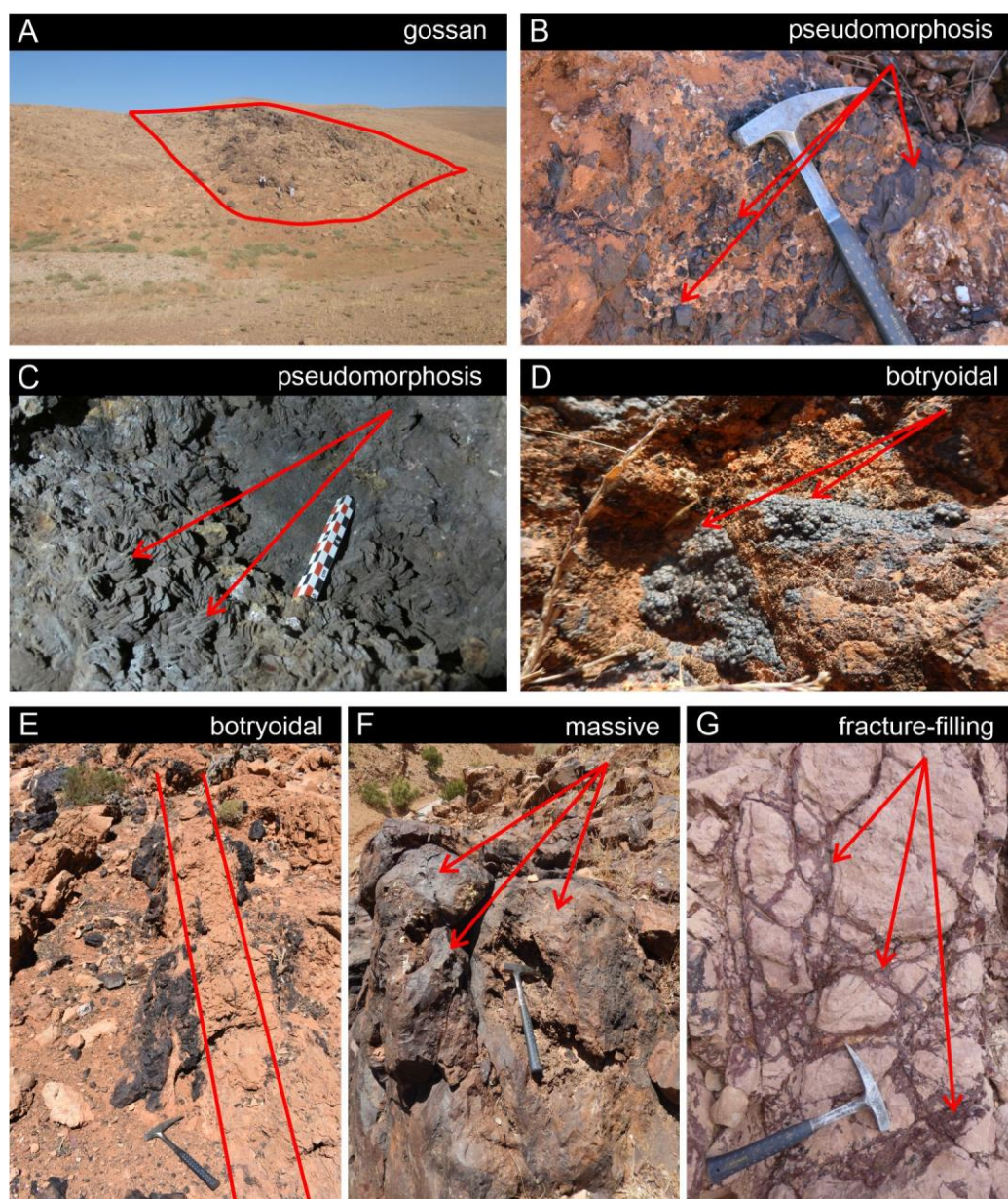


**Figure 6.3.3.** Field pictures illustrating the various analyzed and dated goethite forms. (A) Ighrem: goethite in limestone, in a gossan; (B) Tazalaght: goethite pseudomorphosing pyrite in quartzite; (C) Jbel Rhals: goethite pseudomorphosing siderite, in shales; (D) Tizert: botryoidal goethite in limestone; (E) Irkhs: stratabound botryoidal goethite in dolostone; (F) Tizert: massive microcrystalline goethite in limestone; (G) Jbel Klakh: goethite filling fractures in dolostone.

As previously pointed out by Vasconcelos (1999) for the dating of Mn oxides, the successful dating of supergene materials strongly depends on the careful selection of samples on the field, their subsequent thorough macroscopic and microscopic characterization in the laboratories and the thoughtful integration of results in their geological context. From the sixty-four samples pre-selected on the field, only twenty-four have been selected for (U-Th-Sm)/He dating. Forty samples have been rejected. A first selection has been made on the basis of the macroscopic aspect of samples: visibly

impure samples are discarded. X-ray diffraction has been then carried out on fifty-nine samples with a Philips Analytical X-ray diffractometer to identify the major mineral phases that must be goethite and/or hematite. A third and last selection has been based on the observation of sixty-five polished sections of the remaining set of samples, with a Zeiss Axiophot reflection microscope (Carl Zeiss AG, Oberkochen, Germany) and a Jeol JSM-7500F scanning electron microscope (SEM) (JEOL, Tokyo, Japan) coupled to an energy dispersive electron spectrometer (EDS). The aim of this last stage is to retain only pure, datable samples that should deliver clean ages of precipitation. Particular attention is thus paid to discard samples that present one of the following characteristics: 1) presence of powdery, poorly crystallized or excessively porous phases; 2) variation of phases at a small scale, *e.g.* rim vs center of pseudomorphs; 3) mixing of (several generations of) hematite and goethite; 4) mixing with potentially datable such as Mn oxides, malachite, mottramite; 5) omnipresence of quartz, clays, calcite, dolomite; 6) presence of gangue minerals such as apatite, zircon and rutile; 7) presence of lamellar crystals (only concerns hematite); 8) presence of small crystallites (<100nm); 9) limited amount of datable material and undersized fragments. The presence of powdery, poorly crystallized or excessively porous phases is highly problematic since these poorly He-retentive phases potentially experienced significant He losses and are disintegrated during cleaning. Furthermore, the concentration of silicates and carbonates in iron (oxyhydr-)oxides, even if these minerals are (probably) not He-retentive, is not ideal, even if the occurrence of a few crystals is tolerated. Tests have been performed on lamellar hematite; obviously, these very thin crystals are not sufficiently He-retentive and must be avoided.

(U-Th-Sm)/He data have been obtained for twenty-four samples at the GEOPS laboratory of the Paris Sud University (France). Goethite samples were grinded to keep 500  $\mu\text{m}$  to 1 mm long fragments that were cleaned in distilled water in an ultrasonic bath, and later rinsed with pure ethanol. The fragments were selected by handpicking under a binocular microscope, on the basis of their homogeneity, coherence and limited porosity. Each aliquot was measured, photographed, encapsulated in niobium envelopes or tubes (purity 99.9%) and weighted. Encapsulated samples were placed in a vacuum chamber, along with Durango apatite fragments. Aliquots were degassed using a diode Ytterbium laser under vacuum for 30 minutes, at a temperature below 1000  $^{\circ}\text{C}$ , in order to reach the thermal activation and diffusion of He without losing U and Th. This heating step was once or twice repeated, until all  $^4\text{He}$  was degassed. Then, the gas was mixed with a known amount of  $^3\text{He}$ , in a purification line. He was separated from most  $\text{H}_2\text{O}$ ,  $\text{CO}_2$ ,  $\text{H}_2$  and Ar using three liquid nitrogen-cooled traps of activated charcoal, a titanium sponge trap heated at  $\sim 850^{\circ}\text{C}$  and a SAES 701 getter. Helium isotopes ( $^3\text{He}$  and  $^4\text{He}$ ),  $\text{H}_2\text{O}$ ,  $\text{CO}_2$ ,  $\text{H}_2$ , and Ar were measured with a Pfeiffer Prisma Quadrupole mass spectrometer (Allard et al. 2018). After degassing, aliquots were extracted from the vacuum chamber. Tubes were transferred into 5 mL Savillex Teflon-capped vials, followed by 50  $\mu\text{L}$  of 5N  $\text{HNO}_3$  containing  $^{235}\text{U}$  ( $\sim 4$  ppb),  $^{230}\text{Th}$  ( $\sim 4$  ppb) and  $^{149}\text{Sm}$  ( $\sim 4$  ppb), 50  $\mu\text{L}$  of 5N  $\text{HNO}_3$ , 400  $\mu\text{L}$  of 40% concentrated HCl, and two drops of 38% HF. The tightly closed vials were heated at  $\sim 100^{\circ}\text{C}$  overnight. The vials were placed on a hot plate during two hours for complete evaporation. A 1.9 mL dose of 1N  $\text{HNO}_3$  was added to the solution, to set the Fe content to 100 ppm. The solution was heated at  $100^{\circ}\text{C}$  for two hours. After cooling, 1.5 mL of the solution was taken and diluted with 1N  $\text{HNO}_3$  to reach a total volume of 3 mL. Finally,  $^{238}\text{U}$ ,  $^{232}\text{Th}$ , and  $^{147}\text{Sm}$  contents were determined by using an ELEMENT XR Thermofisher Scientific high-resolution mass spectrometer. An analytical error of 5% at  $1\sigma$  is expected for the two-step analysis based on Durango apatite dating performed at the same time.

Geochemical analyses have been performed on forty samples, in Activation Laboratories (Ancaster, ON, Canada). REE (Rare Earth Elements) and most of the trace elements (Cs, Pb, U, Th, Ta, Nb, Hf, Cr, W, Mo, Sn, Bi, Tl, Sb, Pb, In, Ga, Ge, Co, Ni, Cu, Zn, As, Rb, Nb, Ag) have been analyzed by Fusion Mass Spectrometry (FUS-MS) (Perkin Elmer Sciex Elan 9000 ICP-MS; Sciex AB, Singapore); Sr, Ba, Zr, Be, Sc, V, and Y contents have been quantified by Fusion Inductively Coupled Plasma Optical Emission



Spectrometry (FUS-ICP) (Varian Vista 735 ICP; Agilent, Santa Clara, CA, USA). Major elements have been analyzed by FUS-ICP (Panalytical Axios Advanced XRF; PANalytical, Almelo, The Netherlands), and FeO has been quantified by titration. For samples containing high contents of Mo, As, Pb, Zn, Cu and Co, analyses have been carried out with Fusion Inductively Coupled Plasma Sodium Peroxide Oxidation (FUS-Na<sub>2</sub>O<sub>2</sub>), and results quantified in percentages rather than in ppm.

The oxygen ( $\delta^{18}\text{O}$ ) and hydrogen ( $\delta\text{D}$ ) isotopic compositions have been determined on eighteen samples, at the Institute of Earth Surface Dynamics of the University of Lausanne (Switzerland). Hydrogen and oxygen isotopic compositions were measured with a Finnigan MAT 253 gas source mass spectrometer (Thermo Fisher Scientific, Waltham, USA) and are reported in permil (‰) in Table 6.3.6, in the typical  $\delta$ -notation relative to the Vienna Standard Mean Ocean Water (VSMOW). According to the method defined by Vennemann et al. (2001), the oxygen isotope compositions were obtained using a CO<sub>2</sub>-laser fluorination line. Between 2 and 3 mg of goethite, crushed from individual grains, were loaded onto small Pt sample holders. After several cycles of pre-fluorination of the chamber, samples were heated with a CO<sub>2</sub>-laser to yield O<sub>2</sub>, in the presence of pure F<sub>2</sub> that acts as a reagent. After purification of the gas, the extracted O<sub>2</sub> was introduced into the inlet of the mass spectrometer. Replicate oxygen isotope analyzes of the LS-1 quartz standard (in-house-reference material of Lausanne, quartz 18.1‰) gave an average value of  $18.10 \pm 0.24\text{‰}$  for  $\delta^{18}\text{O}$ . The hydrogen isotope composition and water content of goethite were determined with a zero-blank auto-sampler and a High-Temperature Conversion Elemental Analyzer (TC-EA) (Thermo Fisher Scientific, Waltham, USA), according to the method of Bauer and Vennemann (2014). In-house reference materials of biotite (G1;  $\delta\text{D} = -62 \pm 0.8\text{‰}$ ) and kaolinite (K-17;  $\delta\text{D} = -125 \pm 0.9\text{‰}$ ) were used to calibrate the measured isotopic compositions (Bauer and Vennemann 2014). All the measurements of samples and standards were replicated, but only their average values are reported in Table 6.3.6.

**Table 6.3.1. Summary of all analyses performed on iron (oxyhydr-)oxides samples.**

Sample number	Description	Location		Elevation (m)	XRD	SEM	Geochem. analyses	Isotopic analyses	(U-Th) /He dating	Reason of rejection for dating
		Lat (°N)	Long (°W)							
<u>Jbel Rhals - altitude 1300 m - Cu-Fe-Mn ores hosted by Paleozoic shists</u>										
14RL14	pseudomorphose of siderite, by goethite	32°20'41"	1°58'40"	1220	x	x	x	x	x	Omnipresence of gangue minerals
14RL15	pseudomorphose of siderite, by goethite	32°20'41"	1°58'40"	1220	x	x		x	x	
14RL17	pseudomorphose of siderite, by goethite	32°20'41"	1°58'40"	1220	x	x				
<u>Jbel Haouanit - Cu-Pb-Zn-V ores in Jurassic dolostones</u>										
14HAO04	microcrystalline goethite in a fracture	32°34'42"	2°26'21"	1182	x	x				Impure and poorly crystallized material
14HAO05	microcrystalline goethite in a fracture	32°34'34"	2°26'17"	1135	x	x				Impure and poorly crystallized material
14HT02	microcrystalline goethite associated to mottramite	32°35'27"	2°26'21"	1338	x	x		x	x	
14HT07	microcrystalline goethite associated to mottramite	32°35'27"	2°26'21"	1338	x	x	x	x	x	
<u>Jbel Klakh - altitude 1500 m - Cu ores in Jurassic dolostones</u>										
14KH11	hematite plating on fault filling materials	32°37'07"	1°41'19"	1451	x	x				Undersized material containing gangue minerals
14KH50	microcrystalline goethite filling fractures with Mn oxides	32°37'09"	1°41'10"	1447	x	x		x	x	
14KH52	microcrystalline goethite in a fracture	32°37'08"	1°41'12"	1444	x	x				Omnipresence of quartz and gangue minerals in a powdery material
<u>Agoujgal - altitude 1300 m - Cu-As-Pb ores in Late Proterozoic sandstones, dolostones and siltstones</u>										
17AG09B	microcrystalline massive goethite	29°23'37"	9°01'12"	1321	x	x	x			Mixing of excessively porous hematite-goethite generations
17AG14A	pseudomorphose of pyrite, by goethite (and hematite)	29°23'36"	9°01'17"	1320	x	x				Omnipresence of quartz in a poorly crystallized material
17AG14B	pseudomorphose of pyrite, by goethite (and hematite)	29°23'36"	9°01'17"	1320	x	x	x	x	x	
17AG14D	pseudomorphose of pyrite, by goethite (and hematite)	29°23'36"	9°01'17"	1320	x	x	x			Omnipresence of quartz and gangue minerals in a poorly crystallized material
17AG14E	pseudomorphose of pyrite, by goethite (and hematite)	29°23'36"	9°01'17"	1320	x	x				Omnipresence of gangue minerals in mixed hematite-goethite generations
17AG14F	pseudomorphose of pyrite, by goethite (and hematite)	29°23'36"	9°01'17"	1320	x	x				Omnipresence of gangue minerals in mixed hematite-goethite generations
17AG14G	pseudomorphose of pyrite, by goethite (and hematite)	29°23'36"	9°01'17"	1320	x	x	x			Omnipresence of gangue minerals in mixed hematite-goethite generations
17AG15	pseudomorphose of pyrite, by goethite (and hematite)	29°23'36"	9°01'17"	1320	x	x	x	x	x	

17AG25A	fine botryoidal goethite layer associated to powdery goethite	29°23'28"	9°01'24"	1289	x	x	x			Powdery material
17AG26	fine botryoidal goethite layer associated to mottramite	29°23'28"	9°01'24"	1289	x	x	x	x	x	
18AG07	fine botryoidal goethite layer associated to mottramite	29°23'29"	9°01'25"	1280	x	x	x	x	x	
<u>Tazalaght - altitude 1700 m - Cu-As ores in Late Proterozoic quartzites, sandstones, dolostones and siltstones</u>										
17TAZ01A	pseudomorphose of pyrite, by goethite (and hematite)	29°42'60"	8°42'42"	1828	x	x	x	x	x	
17TAZ01C	fine botryoidal goethite layer	29°42'60"	8°42'42"	1828	x	x	x			x
17TAZ03	Powdery goethite and Mn-oxides	29°42'60"	8°42'42"	1828	x	x	x			Omnipresence of gangue minerals in poorly crystallized material
17TAZ15	pseudomorphose of pyrite, by goethite (and hematite)	29°44'47"	8°43'13"	1858			x			Mixing of several hematite-goethite generations
17TAZ16	pseudomorphose of pyrite, by goethite (and hematite)	29°44'47"	8°43'13"	1858			x			Mixing of several hematite-goethite generations
17TZ04B	Hematite	29°45'35"	8°43'46"	1872			x			Platy hematite composed of undersized crystallites
18TAZ23	microcrystalline goethite associated to calcite	29°44'47"	8°43'13"	1859	x	x	x			Omnipresence of quartz in a poorly crystallized material
18TAZ25	pseudomorphose of pyrite, by goethite (and hematite)	29°43'00"	8°42'48"	1830	x	x	x			Mixing of several hematite-goethite generations
18TAZ26	microcrystalline goethite	29°43'00"	8°42'48"	1830	x	x	x			Omnipresence of quartz in an excessively porous material
18TAZ27	fine botryoidal goethite layer	29°43'00"	8°42'48"	1830	x	x	x	x	x	
<u>Tassirt - altitude 1800 m - Cu-Zn ores in Late Proterozoic - Cambrian limestones, siltstones and sandstones</u>										
17TAS01D	pseudomorphose of pyrite, by goethite (and hematite)	29°35'11"	8°53'01"	1774	x	x				x
17TAS07	powdery iron (oxyhydr)-oxides	29°35'11"	8°53'01"	1774	x	x	x			Poorly crystallized material
17TAS10A	pseudomorphose of pyrite, by goethite (and hematite)	29°35'14"	8°53'04"	1792						Omnipresence of quartz and gangue minerals in mixed hematite-goethite generations
17TAS10B	pseudomorphose of pyrite, by goethite (and hematite)	29°35'14"	8°53'04"	1792	x	x	x			x
17TAS10C	pseudomorphose of pyrite, by goethite (and hematite)	29°35'14"	8°53'04"	1792	x	x	x			x
17TAS10D	pseudomorphose of pyrite, by goethite (and hematite)	29°35'14"	8°53'04"	1792						Omnipresence of quartz and gangue minerals in mixed hematite-goethite generations
18TAS01B	massive microcrystalline goethite	29°35'14"	8°53'04"	1792	x	x	x			Omnipresence of quartz and gangue minerals in mixed hematite-goethite generations
18TAS01D	fine botryoidal goethite layer	29°35'11"	8°53'01"	1774	x	x	x	x	x	
18TAS02	botryoidal hematite	29°35'11"	8°53'01"	1774	x	x	x			Omnipresence of gangue minerals and clays
18TAS03	botryoidal hematite	29°35'13"	8°53'05"	1793	x	x	x			Omnipresence of gangue minerals and clays
18TAS04	botryoidal hematite	29°35'13"	8°53'05"	1793	x	x				Omnipresence of gangue minerals and clays
18TAS07	pseudomorphose of pyrite, by goethite (and hematite)	29°35'13"	8°53'05"	1793	x	x	x			Omnipresence of quartz and gangue minerals in mixed hematite-goethite generations
18TAS11	powdery iron (oxyhydr)-oxides	29°35'13"	8°53'05"	1793	x	x	x			Poorly crystallized material

18TAS78	powdery iron (oxyhydr-)oxides	29°35'14"	8°53'03"	1786	x	x	x		Poorly crystallized material
<u>Tizert - altitude 1000 m - gossan in Late Proterozoic limestones</u>									
17TIZ01A	microcrystalline massive goethite	30°18'19"	8°25'02"	1009	x	x	x	x	
17TIZ01B	microcrystalline massive mixed goethite and hematite	30°18'19"	8°25'02"	1009	x	x	x		Mixing of several hematite-goethite generations
17TIZ01C	microcrystalline massive mixed goethite and hematite	30°18'19"	8°25'02"	1009	x	x			Excessively porous material
17TIZ01D	microcrystalline massive mixed goethite and hematite	30°18'19"	8°25'02"	1009	x	x			Mixing of several hematite-goethite generations
17TIZ03	fine botryoidal goethite layer	30°18'19"	8°25'02"	1009	x	x	x	x	Mixing of several hematite-goethite generations
17TIZ05	fine botryoidal goethite layer	30°18'19"	8°25'02"	1009	x	x			Omnipresence of gangue minerals in undersized fragments
17TIZ06	powdery iron (oxyhydr-)oxides	30°18'19"	8°25'02"	1009	x	x	x		Poorly crystallized material
<u>Ighrem - altitude 1700 m - gossan in Late Proterozoic limestones</u>									
17IG01	large botryoidal goethite layer	30°01'41"	8°26'19"	1668	x	x	x	x	x
18IG02	large botryoidal goethite layer	30°01'41"	8°26'18"	1669	x	x	x	x	x
18IG03	pseudomorphose of pyrite, by goethite (with hematite)	30°01'41"	8°26'18"	1669	x	x	x		Omnipresence of quartz and calcite in mixed hematite-goethite generations
<u>Assifid - altitude 1300 m - Cu ores Late Proterozoic - Cambrian limestones</u>									
18ASS01A	large botryoidal goethite layer	30°15'11"	8°31'08"	1290	x	x	x	x	x
18ASS01B	large botryoidal goethite layer	30°15'11"	8°31'08"	1290	x	x	x	x	x
18ASS02	pseudomorphose of pyrite, by goethite and hematite	30°15'11"	8°31'08"	1290	x	x	x		Omnipresence of quartz and calcite in mixed hematite-goethite generations
18ASS03	microcrystalline massive goethite	30°15'11"	8°31'08"	1290	x	x	x		Mixing of several hematite-goethite generations
<u>Irkhs - altitude 1450 m - Cu ores in in Late Proterozoic dolostones</u>									
18IR01	large botryoidal goethite layer	29°31'56"	8°43'40"	1436	x	x	x	x	x
18IR02	large botryoidal goethite	29°31'53"	8°43'40"	1426	x	x	x		Omnipresence of quartz in an excessively porous material
18IR04	botryoidal goethite brecciated by calcite	29°31'53"	8°43'40"	1426	x	x			Omnipresence of calcite in undersized fragments
18IR05	microcrystalline massive goethite	29°31'53"	8°43'40"	1426	x	x			Excessively porous material
18IR07	pseudomorphose of pyrite, by goethite and hematite	29°31'53"	8°43'40"	1426	x	x	x		Mixing of excessively porous hematite-goethite generations



### 6.3.3 Results

#### 6.3.3.a Mineralogical characterization

On the field, careful consideration has been given to the selection of iron (oxyhydr-)oxides that may be classified in three categories reflecting their environment of formation: 1) pseudomorphose of a precursor mineral such as pyrite (Fig. 6.3.3B, 6.3.4A-6.3.4E) or siderite (Fig. 6.3.3C, 6.3.4F), 2) microcrystalline phases (Fig. 6.3.3F, 6.3.3G, 6.3.4G-6.3.4J) and 3) botryoidal phases (Fig. 6.3.3D, 6.3.3E, 6.3.4K-6.3.4O).

In the Anti-Atlas samples, millimetric to centimetric scaled pyrite pseudomorphs (17TAZ01A, 17AG14B, 7AG15, 17TAS01D, 17TAS10B, 17TAS10C) are mostly dodecahedral (Fig. 6.3.4A, 6.3.4B, 6.3.4C), but cubic forms also occur (Fig. 6.3.4D, 6.3.4E). Scanning electron microscope observations reveal that the structure and composition of these completely weathered samples originating from different sites are very similar (Fig. 6.3.4A-6.3.4E). Their mineralogy is usually not homogeneous at the scale of the pseudomorphose, and more pronounced variations occur between the rim and the center of the figures (Fig. 6.3.4A). Whereas only goethite was initially expected to be found in these samples, mixed generations of goethite and hematite are mostly present in the entire pseudomorphs (Fig. 6.3.4C). Hydration and dehydration processes are most probably responsible for the replacement of hematite by goethite, and the other way around. These structures commonly host gangue minerals such as quartz, rutile, apatite, zircon, inherited from the host rocks during the epigenesis of pyrite (Fig. 6.3.4B, 6.3.4C). In the High Atlas, the studied pseudomorphs (Fig. 6.3.3F; 14RL14, 14RL15) display the replacement of siderite by goethite along previous cleavage planes (Fig. 6.3.4F; see Verhaert et al., 2018 for more details). Pyrolusite is sometimes present, but gangue minerals are scarcely hosted by goethite. The crystallites of sample 14RL15 reach 50 nm in width and between 200 and 800 nm in length.

Microcrystalline samples encompass several subcategories including 1) goethite associated with supergene mineral phases such as mottramite  $\text{PbCu}(\text{VO}_4)(\text{OH})$  (samples 17AG26, 14HT02 and 14HT07; Fig. 6.3.4G, 6.3.4H, 6.3.5H, 6.3.5I), 2) massive clusters of goethite and minor hematite (sample 17TIZ01A; Fig. 6.3.4I) and 3) goethite and hematite filling fractures and faults (sample 14KH50; Fig. 6.3.4J, 6.3.5J). Samples 14HT02, 14HT07 and 14KH50 are already characterized in Verhaert et al. (2017). Goethite associated with mottramite (and rarely minor malachite) is well crystallized, devoid of gangue minerals and contaminants although its mixing with other supergene phases such as carbonates or the above-named vanadate, which are potentially datable phases, might be an issue for further investigation (Fig. 6.3.4H, 6.3.5H). Only the purest zones of goethite in these samples are selected for dating. The smallest dimension of goethite crystallites strongly varies but remain larger than 200 nm. The well crystallized goethite of 17TIZ01A encloses a few quartz grains (less than 5%) and rare apatite crystals. Sample 14KH50 features the filling of fractures in dolostone by very thin generations of microcrystalline goethite seldom associated with Mn oxides (Fig. 6.3.4J, 6.3.5J).

Botryoidal iron (oxyhydr-)oxide samples collected in the Anti-Atlas have been considered last (samples 17TAZ01C, 18TAZ27, 18AG07, 18TAS01D, 17TIZ03, 17IG01, 18IG02, 18ASS01A, 18ASS01B, 18IR01; Fig. 6.3.4K-6.3.4O; 6.3.5K-6.3.5R). They are all composed of successive concentric generations of very pure goethite that is almost completely devoid of contaminants. Only sample 18AG07 encloses mottramite crystals between goethite layers, indicating their concurrent precipitation (Fig. 6.3.5M). Hematite is rarely present in botryoidal goethite, but can locally form most likely due to dehydration processes (Fig. 6.3.5K). Quartz sometimes occur as a late supergene phase filling cavity (Fig. 6.3.5K, 6.3.5O), but is easy to separate from goethite. No inherited gangue minerals have been observed in botryoidal goethite. The center of botryoidal structures has never been considered for dating as it obviously

encloses inherited minerals and host rock pieces. Ighrem (Fig. 6.3.4N, 6.3.5P), Irkhs (Fig. 6.3.4O, 6.3.5R) and Assifid (Fig. 6.3.5Q) botryoidal goethite samples are the purest in the set (Figs. 6.3.5P-6.3.5R). The smallest dimension of their crystallites always exceeds 100 nm.

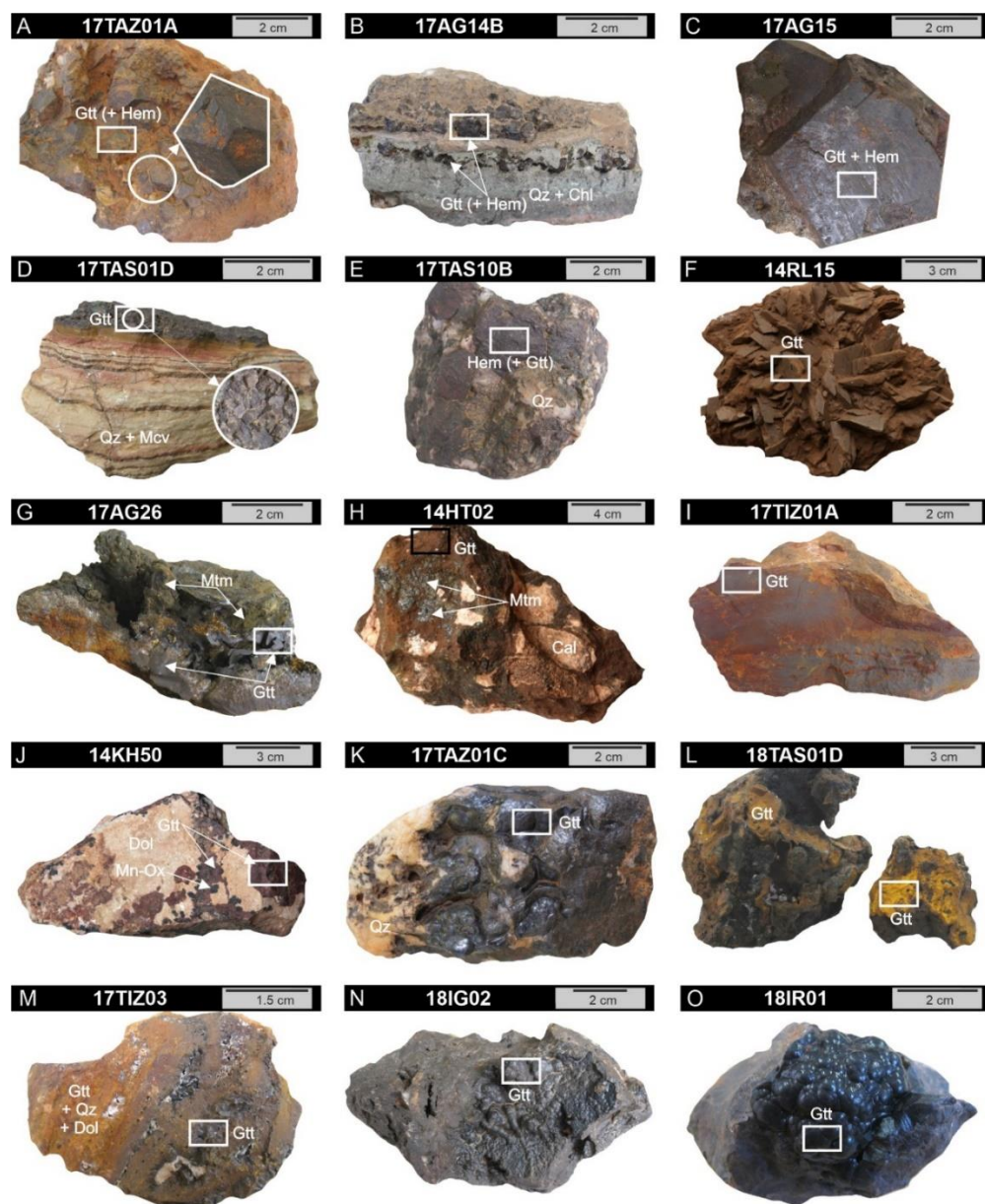


**Figure 6.3.4.** Representative samples pictures of Tazalaght (A, K), Agoujgal (B, C, G), Tassirt (D, E, L), Jbel Rhals (F), Jbel Haouanit (H), Tizert (I, M), Jbel Klakh (J), Ighrem (N), Irkhs (O). Black frames indicate the sampling area for (U-Th-Sm)/He dating. (A) Goethite (and minor hematite) pseudomorphosing euhedral pyrite, in Late Proterozoic quartzite; (B, C) goethite (and minor hematite) pseudomorphosing stratabound euhedral pyrite in Late Proterozoic sandy dolostone; (D, E) goethite (and minor hematite) pseudomorphosing stratabound euhedral pyrite, in Late Proterozoic sandstone; (F) goethite pseudomorphosing siderite in Paleozoic schists; (G) microcrystalline goethite associated with supergene mottramite, in Late Proterozoic sandy dolostone; (H) microcrystalline goethite associated with supergene calcite and mottramite in Jurassic dolostone; (I) microcrystalline goethite in Late Proterozoic limestone; (J) goethite filling fractures with Mn-oxides in Jurassic dolostone; (K) botryoidal goethite in Late Proterozoic quartzite; (L) botryoidal goethite in Late Proterozoic sandstone; (M) fine vein of botryoidal goethite in massive microcrystalline goethite, associated to quartz and dolomite, in Late Proterozoic limestone; (N, O) botryoidal goethite in Late Proterozoic dolostone/limestone (L; (Gtt = goethite; Mtt = mottramite; Cal = calcite; Dol = dolomite; Mn-Ox = Mn-oxides; Qz = quartz; Chl = chlorite; Hem = hematite; Mcv = muscovite).

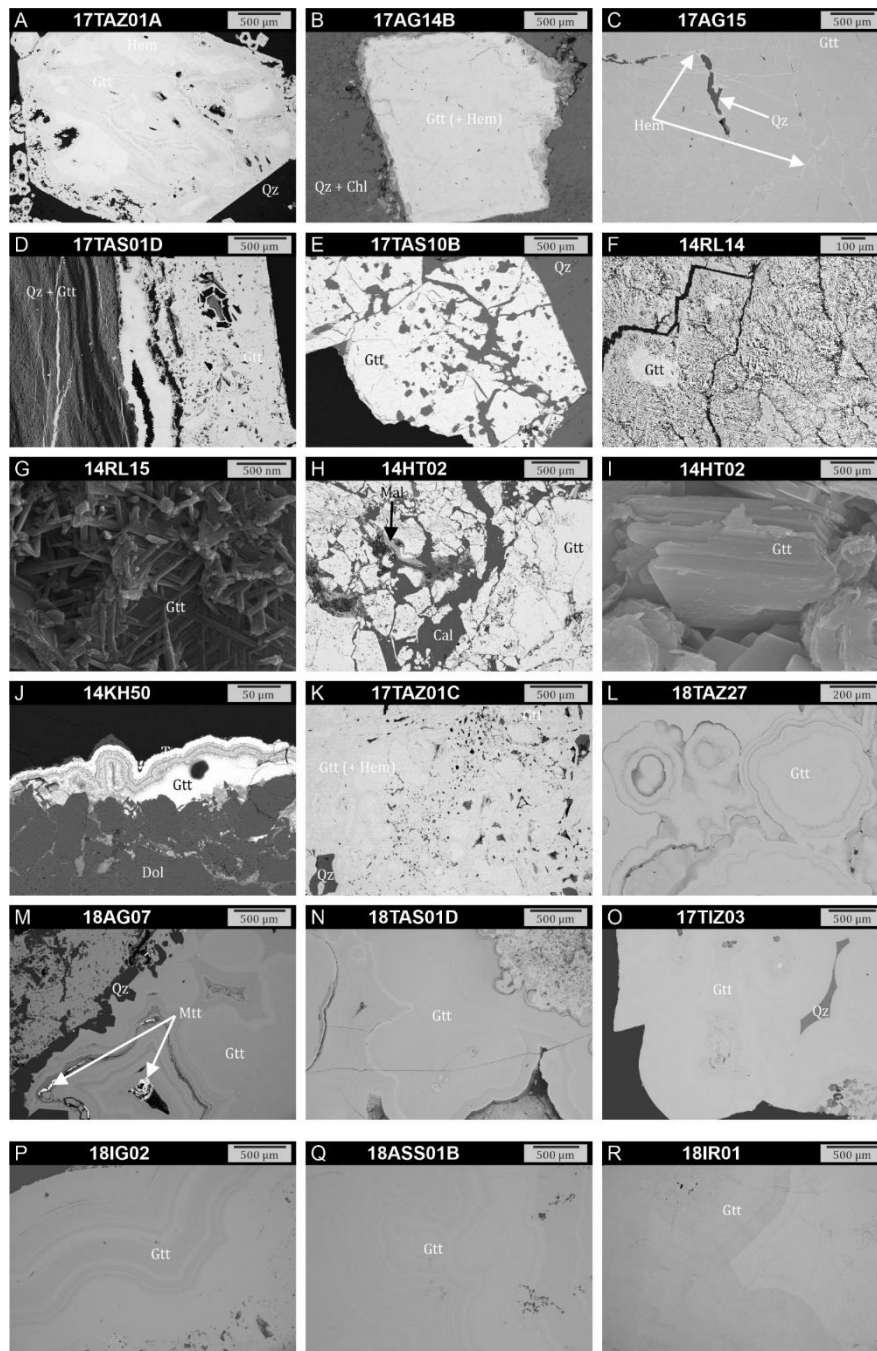


**Figure 6.3.5.** Representative samples SEM pictures in backscattered electrons mode (A-F, H, J-R) and in secondary electrons mode (G, I), of Tazalaght (A, K, L), Agoujgal (B, C, M), Tassrirt (D, E, N), Jbel Rhals (G), Jbel Haouanit (H, I), Jbel Klakh (J), Tizert (O), Ighrem (P), Assifid (Q), Irkhs (R). (A) Goethite and hematite pseudomorphosing euhedral pyrite in a quartz gangue; (B) Goethite, with minor hematite, pseudomorphosing cubic pyrite in a quartz and chlorite gangue; (C) Goethite, with minor hematite in fractures, pseudomorphosing cubic pyrite; (D) Goethite pseudomorphosing stratabound euhedral pyrite; (E) Goethite pseudomorphosing euhedral pyrite, in a quartz gangue; (F, G) Goethite pseudomorphosing siderite; (H, I) Microcrystalline goethite brecciated by calcite and associated with mottramite and malachite; (J) Successive generations of goethite in a fracture in dolomite; (K) Goethite and hematite pseudomorphosing euhedral pyrite in a quartz gangue; (L) Successive fine generations of botryoidal goethite; (M) Successive generations of botryoidal goethite precipitating along with mottramite and quartz; (N) Successive generations of botryoidal goethite precipitating along with mottramite and quartz; (O-R) Large successive layers of pure botryoidal goethite (Gtt = goethite; Mtt = mottramite; Cal = calcite; Dol = dolomite; Qz = quartz; Chl = chlorite; Hem = hematite).

### 6.3.3.b Geochemical characterization

The major elements contents of all iron (oxyhydr-)oxides presented above mostly depend on the type of rock hosting the gossan (Table 6.3.2). The influence of carbonate rocks is, for instance, visible for samples 17TAS10B and 17TAS10C, which show the highest CaO contents (Table 6.3.2). Sample 14RL14 obviously contains some pyrolusite since its Mn content reaches 10% (Table 6.3.2).

Some elements labelled as minor in Table 6.3.3 could have been considered as major elements, since their concentrations sometimes exceed the percent. Minor elements concentrations mostly fluctuate according to their environment of formation: since most samples originate from deposits mined for Cu, they concentrate chalcophile elements such as Cu, As, Pb, Zn, Co and Mo (Table 6.3.3, Fig. 6.3.6). The high concentrations in As (up to 0.75%) are related, for the Anti-Atlas samples, to the common presence of arsenates in the ore of the deposits (Table 6.3.3, Fig. 6.3.6) (Verhaert et al., in press). Contents in U always exceed those in Th, except for the pyrite-pseudomorphosing 17AG15 that probably contain inherited gangue minerals (Table 6.3.3). The relatively high concentrations in V (up to 1800 ppm) most likely arise from the common presence of mottramite grains in iron (oxyhydr-)oxides of the Anti-Atlas (Table 6.3.3, Fig. 6.3.6). Interestingly, a slight discrepancy is observed between botryoidal and pyrite-pseudomorphosing samples that concentrate more significantly Cu, Co, Mo and As (Fig. 6.3.7A, 6.3.7B). The composition of microcrystalline iron (oxyhydr-)oxides and powdery samples are closer to pseudomorphosing and botryoidal samples, respectively (Fig. 6.3.6C, 6.3.6D). The tendency curves featuring REE of botryoidal and pseudomorphosing (oxyhydr-)oxides are similar (Fig. 6.3.6A, 6.3.6B). All samples present higher contents in LREE than MREE and HREE (Table 6.3.4). However, slight differences are distinguishable when contents are normalized to the PAAS (Fig. 6.3.7). Botryoidal samples present very similar, flat curves, with small negative Ce anomalies (Fig. 6.3.7A). Pyrite-pseudomorphosing samples curves are more variable than their botryoidal counterparts, with marked negative Ce anomalies (Fig. 6.3.7B). The siderite-pseudomorphosing goethite sample displays a strongly different trend with a marked depletion in LREE (Fig. 6.3.7B). Microcrystalline samples curves are even more fluctuating, with positive and negative Ce anomalies (Fig. 6.3.7C). Powdery goethite plots dissimilarly, with marked LREE enrichments (Fig. 6.3.7D).

The water proportion of iron (oxyhydr-)oxides here varies between 6.94% (17AG14B) and 13.58% (18TAS01D) (Table 6.3.5). The isotopic hydrogen compositions fluctuate between 133‰ (18TAS01D) and 162‰ (14RL15) (Table 6.3.5, Fig. 6.3.8). The oxygen isotopic compositions are consistent and range between -5.17 (14RL15) and 0.41 (18TAS01D), with the exception of sample 18IR01 that provides a much higher  $\delta^{18}\text{O}$  value (6.17‰) (Table 6.3.5, Fig. 6.3.8). The High Atlas and Anti-Atlas iron (oxyhydr-)oxides  $\delta\text{D}$ - $\delta^{18}\text{O}$  data gather around a temperature line of 25°C in the diagram of Yapp (1987) (Fig. 6.3.8). For sample 18IR01,  $\delta^{18}\text{O}$  value is strongly shifted to the right of the temperature lines in equilibrium with the meteoric water line (MWL) defined by Craig (1961) (Fig. 6.3.8). Curiously, a divergence is observed between pyrite- and siderite-pseudomorphosing and botryoidal samples: pseudomorphosing samples present lower  $\delta^{18}\text{O}$  and  $\delta\text{D}$  values than botryoidal goethite which are much more scattered (Fig. 6.3.8).

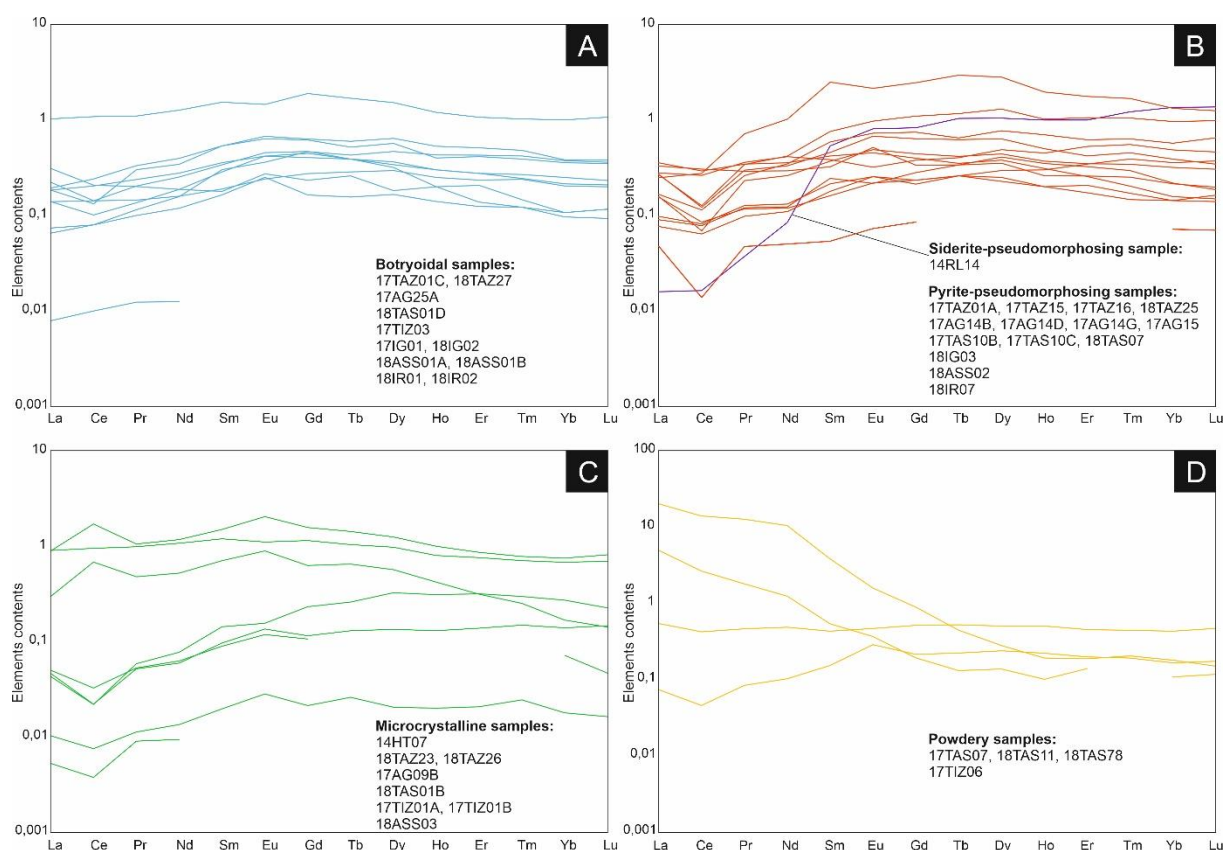


**Figure 6.3.6.** REE contents, normalized to the PAAS, of samples gathered by type: (A) botryoidal; (B) siderite- and pyrite-pseudomorphosing; (C) microcrystalline; (D) powdery samples.

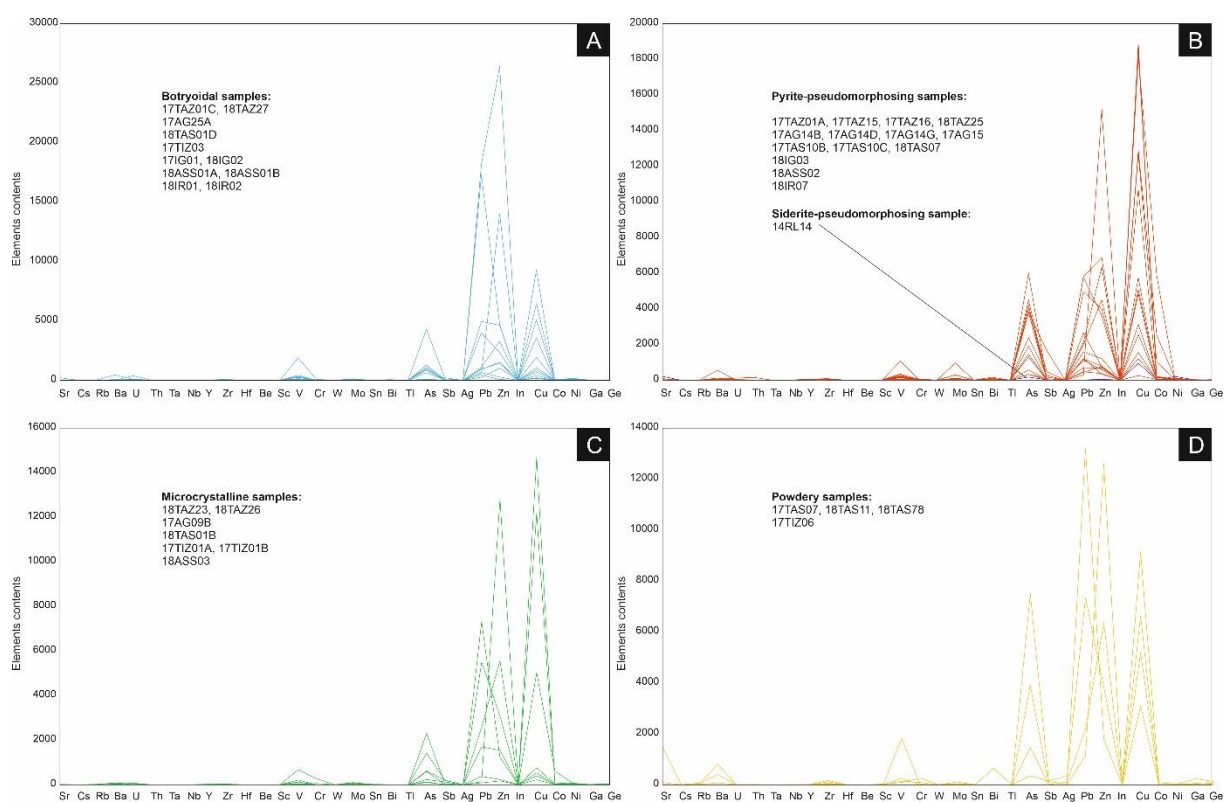


**Figure 6.3.7.** "Minor" elements contents of samples gathered by type: (A) botryoidal; (B) siderite- and pyrite-pseudomorphosing; (C) microcrystalline; (D) powdery samples.

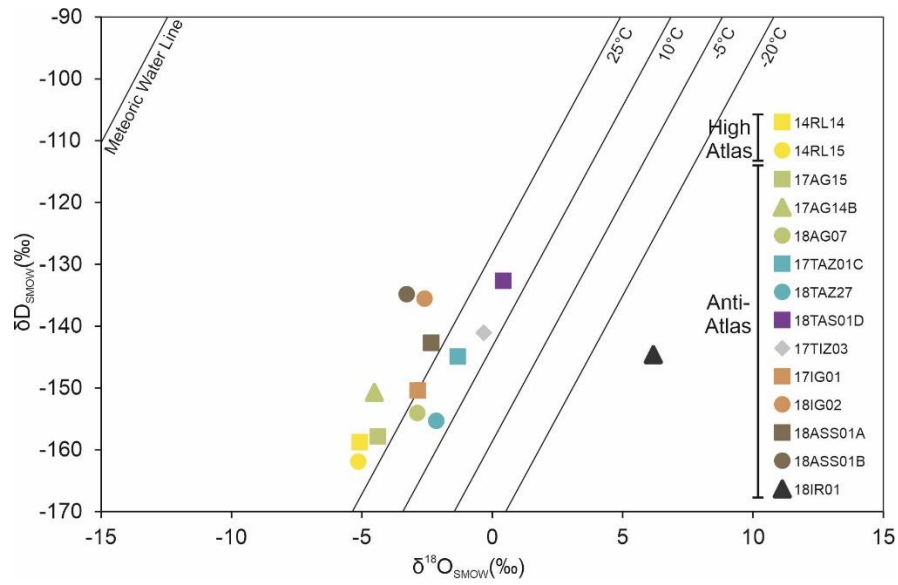


**Figure 6.3.8.**  $\delta D$  and  $\delta^{18}O$  data of goethite. Temperature lines are calculated from (Yapp 1987). The meteoric water (Craig 1961) is given for reference.



**Table 6.3.2. Results of geochemical analyses for major elements.**

Sample number	FeO	SiO <sub>2</sub>	Al <sub>2</sub> O <sub>3</sub>	Fe <sub>2</sub> O <sub>3</sub>	MnO	MgO	CaO	Na <sub>2</sub> O	K <sub>2</sub> O	TiO <sub>2</sub>	P <sub>2</sub> O <sub>5</sub>	LOI	Total
Unit	(%)	(%)	(%)	(%)	(%)	(%)	(%)	(%)	(%)	(%)	(%)	(%)	(%)
Detection Limit	0.1	0.01	0.01	0.01	0.001	0.01	0.01	0.01	0.01	0.001	0.01	0.01	0.01
14 RL 14	N.A.	4.44	0.19	69.85	10.330	0.54	0.36	0.01	0.04	0.010	0.17	12.60	98.54
17 AG 09B	N.A.	1.64	0.17	57.24	0.051	0.25	19.52	<0.01	<0.01	0.001	0.15	18.20	97.25
17 AG 14B	N.A.	6.26	0.96	75.57	2.834	0.95	0.52	0.02	N.A.	0.131	0.13	9.26	96.65
17 AG 14D	N.A.	5.16	0.48	80.98	0.044	0.79	0.39	0.02	0.01	0.098	0.17	10.46	98.62
17 AG 14G	N.A.	6.35	1.35	81.39	0.027	0.19	0.27	0.03	<0.01	0.240	0.38	7.63	97.87
17 AG 15	N.A.	2.58	0.03	84.55	0.058	0.19	0.19	N.A.	N.A.	0.133	0.09	10.42	98.24
17 AG 25A	N.A.	3.16	<0.01	78.28	0.023	0.07	0.10	<0.01	<0.01	0.008	0.73	11.16	93.56
17 TAZ 01A	N.A.	4.27	0.20	83.77	0.023	0.29	0.20	N.A.	N.A.	0.004	0.17	10.40	99.34
17 TAZ 01C	N.A.	5.57	0.10	83.38	0.070	0.04	0.06	N.A.	N.A.	0.002	0.05	11.04	100.30
17 TAZ 15	N.A.	2.90	0.14	87.77	0.201	<0.01	0.14	<0.01	<0.01	0.001	0.06	5.88	97.10
17 TAZ 16	N.A.	2.41	0.14	87.75	0.177	0.58	1.01	<0.01	<0.01	0.002	0.06	5.51	97.66
17 TZ 04B	1.6	1.95	0.04	93.26	0.021	<0.01	0.02	0.01	<0.01	1.946	<0.01	0.07	99.01
18 TAZ 23	0.1	5.14	0.25	60.27	0.141	0.25	11.41	<0.01	<0.01	0.001	0.09	17.05	94.70
18 TAZ 25	0.5	2.44	0.21	85.39	0.037	0.38	0.28	0.02	<0.01	<0.01	0.09	10.49	99.89
18 TAZ 26	N.A.	10.64	0.10	78.79	0.011	0.06	0.04	<0.01	0.02	0.003	0.02	9.55	99.33
18 TAZ 27	0.3	3.53	1.05	81.86	0.019	0.30	0.12	N.A.	N.A.	0.004	0.12	11.31	98.64
17 TAS 07	N.A.	48.87	9.16	26.94	0.008	0.79	0.16	0.09	3.01	0.471	0.70	6.89	97.09
17 TAS 10B	0.3	4.65	0.19	85.00	0.033	0.25	2.66	0.01	0.01	0.004	0.23	5.64	99.01
17 TAS 10C	N.A.	4.44	0.51	76.23	0.027	0.23	2.68	0.01	0.05	0.009	0.23	11.58	96.03
18 TAS 01B	0.4	6.48	1.93	78.12	0.105	0.05	0.13	0.01	0.41	0.062	0.19	9.16	97.09
18 TAS 01D	N.A.	7.70	5.76	65.29	0.029	0.22	0.63	0.03	0.80	0.097	2.95	13.44	96.95
18 TAS 02	N.A.	15.24	9.59	49.87	2.362	0.14	0.97	0.04	0.86	0.062	2.01	13.01	94.16
18 TAS 07	N.A.	3.78	0.28	79.92	0.061	0.37	1.33	0.03	0.03	0.005	0.18	9.76	95.76
18 TAS 11	1.9	4.23	1.30	50.81	0.092	0.55	2.61	0.18	3.80	0.413	1.89	23.73	91.72
18 TAS 78	0.2	7.73	2.19	67.55	0.084	0.96	2.43	0.05	0.35	0.112	0.20	13.64	95.52
17 TIZ 01A	N.A.	4.22	0.18	89.71	0.012	N.A.	0.23	N.A.	N.A.	0.001	0.05	5.05	99.42



17 TIZ 01B	N.A.	28.12	2.69	37.82	0.010	0.52	13.36	0.01	0.99	0.112	0.07	13.81	97.52
17 TIZ 03	N.A.	9.11	0.30	75.95	0.022	0.09	0.60	N.A.	0.04	0.011	0.10	10.21	96.47
17 TIZ 06	N.A.	52.90	2.05	19.52	0.020	0.40	10.62	<0.01	0.70	0.079	0.04	10.57	96.92
17 IG 01	N.A.	4.61	0.21	79.82	0.058	0.06	0.21	N.A.	0.02	0.005	0.18	13.32	98.52
18 IG 02	N.A.	4.41	0.50	80.98	0.028	0.11	0.26	N.A.	N.A.	0.009	0.26	12.10	98.68
18 IG 03	0.1	6.14	0.27	79.22	0.040	0.30	1.02	<0.01	0.02	0.009	0.32	10.97	98.42
18 ASS 01A	N.A.	4.74	0.06	80.78	0.028	0.07	0.08	0.01	N.A.	0.002	0.09	11.72	97.59
18 ASS 01B	N.A.	3.96	0.36	82.71	0.021	0.04	0.10	N.A.	0.03	0.008	0.04	12.99	100.30
18 ASS 02	N.A.	2.84	0.25	84.46	0.036	0.19	0.38	0.02	<0.01	0.004	0.11	9.43	97.73
18 ASS 03	0.8	1.45	<0.01	90.98	0.016	0.03	0.09	<0.01	<0.01	0.001	0.09	5.34	98.89
18 IR 01	N.A.	1.36	0.26	95.92	0.020	0.04	0.08	N.A.	0.01	N.A.	0.01	2.77	100.50
18 IR 02	N.A.	6.61	1.46	77.77	0.032	0.35	0.87	0.02	0.34	0.056	0.06	11.02	98.59
18 IR 07	0.1	2.68	0.05	87.11	0.012	0.22	0.16	<0.01	<0.01	0.002	0.05	7.93	98.33

---

*N.A.= non-analyzed, under the detection limit*

---

**Table 6.3.3. Results of geochemical analyses for minor elements.**

Sample number	Sr	Cs	Rb	Ba	U	Th	Ta	Nb	Y	Zr	Hf	Be	Sc	V	Cr	W	Mo	Sn	Bi	Tl	As	Sb	Ag	Pb	Zn	In	Cu	Co	Ni	Ga	Ge
Unit	(ppm)																														
Detection limit	2	0.5	2	2	0.1	0.1	0.1	1	1	2	0.2	1	1	5	20	1	2	1	0.4	0.1	5	0.5	0.5	5	30	0.2	10	1	20	1	1
14 RL 14	205	<0.5	<2	45	29.3	<0.1	<0.1	<1	61	<2	<0.2	<1	<1	34	20	1	74	<1	<0.4	<0.1	168	22.7	<0.5	9	50	1.4	950	8	200	30	2
17 AG 09B	18	<0.5	<2	13	3.2	0.4	<0.1	<1	15	3	<0.2	2	4	118	<20	<1	4	17	1.4	<0.1	589	8.9	<0.5	376	230	14.2	1.47*	3	<20	2	1
17 AG 14B	75	<0.5	<2	552	9.5	1.0	0.1	3	44	87	1.7	5	9	140	30	5	0.096*	<1	95.9	0.1	1910	2.5	1.0	2650	740	0.2	1.82*	0.589*	60	5	1
17 AG 14D	15	<0.5	<2	49	37.3	8.1	0.1	2	29	54	1.2	5	14	345	20	2	37	<1	62.3	<0.1	0.6*	13.6	0.6	437	760	0.2	1.29*	0.253*	100	2	1
17 AG 14G	83	<0.5	<2	46	19.5	5.2	0.3	5	14	74	1.8	3	12	330	40	8	11	1	159.0	<0.1	1300	7.6	0.7	468	370	0.7	1.89*	30	<20	4	3
17 AG 15	11	<0.5	<2	52	108.0	149.0	0.1	2	50	26	0.3	5	14	180	30	3	0.03*	<1	26.3	<0.1	0.38*	8.1	<0.5	1120	580	<0.2	1.27*	0.102*	50	1	1
17 AG 25A	4	<0.5	<2	8	379.0	<0.1	<0.1	1	15	13	<0.2	2	<1	332	20	2	98	<1	1.2	<0.1	0.43*	0.021*	<0.5	1.82*	2.64*	29.9	3570	7	<20	7	15
17 TAZ 01A	7	<0.5	<2	9	6.0	0.3	<0.1	<1	13	9	0.2	3	2	275	<20	1	71	<1	2.7	<0.1	321	19.8	<0.5	698	680	<0.2	1210	30	120	2	2
17 TAZ 01C	2	<0.5	<2	<2	8.8	0.2	<0.1	<1	20	2	<0.2	3	4	72	<20	<1	23	<1	0.5	<0.1	101	1.4	<0.5	258	1020	<0.2	210	45	100	<1	1
17 TAZ 15	6	<0.5	<2	32	17.6	0.1	<0.1	<1	12	44	0.6	2	5	159	<20	1	91	3	5.6	1.0	0.38*	0.165*	5.8	4980	3990	0.9	1.07*	144	100	4	3
17 TAZ 16	5	<0.5	<2	49	7.4	<0.1	<0.1	<1	7	44	0.3	2	3	132	<20	<1	70	<1	8.3	0.7	0.4*	0.047*	4.9	5770	3620	3.8	5080	206	60	2	4
18 TAZ 23	9	<0.5	<2	30	7.1	0.4	<0.1	<1	23	26	0.6	2	11	122	<20	<1	28	<1	<0.4	0.1	0.062*	198.0	1.3	2580	5570	<0.2	5030	612	60	3	<1
18 TAZ 25	7	<0.5	<2	36	20.1	0.1	<0.1	<1	<1	20	<0.2	3	<1	232	60	2	0.011*	<1	5.3	<0.1	325	81.6	<0.5	1580	1210	<0.2	1550	16	70	2	3
18 TAZ 26	3	<0.5	<2	28	4.1	<0.1	<0.1	<1	<1	<2	<0.2	<1	<1	<5	60	1	93	21	5.8	<0.1	104	8.5	2.4	85	170	<0.2	220	11	30	<1	2
18 TAZ 27	7	<0.5	<2	22	13.0	3.0	<0.1	<1	9	84	1.5	10	<1	283	<20	<1	0.013*	<1	57.7	<0.1	1070	132.0	<0.5	4950	4630	<0.2	860	39	150	3	2
17 TAS 07	90	4.1	68	398	9.0	8.7	0.6	9	7	171	5	1	4	140	90	3	38	5	9.6	0.3	1460	10.5	0.0105*	2180	6360	0.3	5170	0	<20	58	19
17 TAS 10B	26	<0.5	<2	112	9.8	0.2	<0.1	<1	8	19	<0.2	1	<1	49	20	<1	29	9	1.3	<0.1	3800	167.0	1.5	2000	4490	0.4	3130	38	30	2	24
17 TAS 10C	8	<0.5	<2	36	15.0	0.2	0.1	<1	9	14	<0.2	<1	1	36	30	<1	48	3	3.0	<0.1	4200	6.0	1.1	2120	6350	1.8	1.85*	40	120	5	26
18 TAS 01B	9	0.7	13	90	8.9	1.3	<0.1	2	19	20	0.7	1	3	19	<20	<1	14	<1	1.5	0.3	131	<0.5	0.9	137	1.28*	<0.2	1.22*	87	40	3	2
18 TAS 01D	210	0.8	21	458	75.3	1.9	0.1	3	27	26	0.8	3	2	12	40	<1	5	<1	2.0	0.1	91	0.6	0.8	624	1.4*	<0.2	9280	13	60	4	<1
18 TAS 02	690	1.1	20	563	40.8	10.3	<0.1	2	16	20	0.6	2	18	218	260	<1	39	<1	<0.4	0.8	1950	<0.5	7.7	15	9280	9.4	2.7*	0.123*	50	14	4
18 TAS 07	15	<0.5	<2	111	7.4	0.2	<0.1	<1	13	24	0.2	<1	9	70	40	2	21	13	3.1	<0.1	0.45*	5.5	1.5	286	1.52*	2	4870	26	50	2	5
18 TAS 11	1473	<0.5	23	809	8.0	12.0	0.4	6	2	114	2.4	<1	25	90	260	7	0.011*	4	645.0	0.2	0.75*	162.0	0.0334*	7330	3840	30.3	9140	80	30	232	125
18 TAS 78	15	0.5	10	79	2.9	1.0	0.1	2	11	57	1.5	<1	3	248	<20	3	42	1	4.0	<0.1	0.39*	3.6	1.1	1140	1.26*	<0.2	6630	10	20	7	3
17 TIZ 01A	3	<0.5	<2	26	73.3	<0.1	<0.1	<1	1	<2	<0.2	<1	2	43	<20	1	100	<1	0.8	<0.1	1420	200.0	5.2	5500	3090	<0.2	530	11	60	4	29
17 TIZ 01B	18	0.5	20	76	49.6	1.3	0.1	2	6	33	0.8	1	2	208	<20	1	60	2	<0.4	0.2	231	124.0	6.6	7320	1230	<0.2	400	4	0	17	48

17 TIZ 03	7	<0.5	<2	12	106.0	0.2	<0.1	<1	4	5	0.2	2	2	141	<20	<1	27	<1	<0.4	0.1	967	52.7	1.3	<i>1.73*</i>	4700	<0.2	1060	38	170	3	6
17 TIZ 06	11	0.5	14	72	9.6	1.1	0.1	1	7	30	0.6	2	2	1820	20	2	36	7	0.4	0.3	356	128.0	27.6	<i>1.32*</i>	1780	0.8	3080	8	20	20	77
17 IG 01	5	<0.5	<2	<2	11.4	0.1	<0.1	<1	12	19	0.2	4	3	416	<20	1	14	<1	<0.4	0.1	866	11.3	<0.5	959	1420	<0.2	5110	63	70	3	1
18 IG 02	7	<0.5	<2	7	16.9	0.2	<0.1	<1	10	10	<0.2	3	2	1884	80	1	53	1	<0.4	0.2	1280	15.1	<0.5	<i>0.398*</i>	2340	<0.2	6440	68	60	2	3
18 IG 03	11	<0.5	<2	28	4.9	0.2	<0.1	<1	8	28	0.2	6	3	200	60	1	92	<1	4.5	<0.1	1450	16.3	0.8	<i>0.119*</i>	790	<0.2	5750	70	80	3	1
18 ASS 01A	4	<0.5	<2	<2	59.9	<0.1	<0.1	<1	7	<2	<0.2	6	1	240	<20	<1	5	<1	<0.4	<0.1	884	7.1	<0.5	<i>0.11*</i>	3270	<0.2	1910	65	50	6	5
18 ASS 01B	4	<0.5	<2	<2	27.5	0.1	<0.1	<1	3	<2	<0.2	3	<1	34	<20	<1	2	<1	<0.4	<0.1	1290	2.0	<0.5	<i>0.0909*</i>	1540	<0.2	670	43	50	1	<1
18 ASS 02	16	<0.5	<2	21	32.4	0.1	<0.1	<1	5	16	0.3	8	1	1067	40	2	<i>0.029*</i>	1	1.2	<0.1	<i>0.24*</i>	<i>0.026*</i>	4.9	<i>0.582*</i>	6870	2.3	2560	50	100	28	6
18 ASS 03	9	<0.5	<2	6	19.2	<0.1	<0.1	<1	<1	<2	<0.2	3	<1	674	270	2	89	7	<0.4	<0.1	<i>0.23*</i>	43.2	2.2	<i>0.17*</i>	1550	<0.2	760	29	70	3	9
18 IR 01	23	<0.5	<2	67	2.3	0.3	<0.1	<1	<1	<2	<0.2	<1	<1	52	<20	<1	6	13	2.7	<0.1	641	27.1	<0.5	<i>0.0437*</i>	70	<0.2	160	3	<20	1	9
18 IR 02	13	<0.5	8	38	78.1	0.9	<0.1	<1	6	30	0.7	2	3	22	<20	1	20	<1	2.6	<0.1	66	16.3	<0.5	<i>0.0657*</i>	270	<0.2	400	29	40	3	<1
18 IR 07	12	<0.5	<2	47	34.2	<0.1	<0.1	<1	<1	18	<0.2	2	1	195	60	3	79	<1	3.9	<0.1	564	14.9	<0.5	<i>0.12*</i>	340	<0.2	250	40	60	2	5

Note: Values in italics and marked by a star correspond to contents in %. The detection limit is fixed at 0.01% for As, Pb and Zn, at 0.002% for Co, at 0.005% for Cu and Mo.

*N.A.= non-analyzed.*

**Table 6.3.4. Results of geochemical analyses for Rare Earth Elements.**

Sample number	La	Ce	Pr	Nd	Sm	Eu	Gd	Tb	Dy	Ho	Er	Tm	Yb	Lu
Unit	(ppm)	(ppm)	(ppm)	(ppm)	(ppm)	(ppm)	(ppm)	(ppm)	(ppm)	(ppm)	(ppm)	(ppm)	(ppm)	(ppm)
Detection limit	0.1	0.1	0.05	0.1	0.1	0.05	0.1	0.1	0.1	0.1	0.1	0.05	0.1	0.01
14 RL 14	<0.1	<0.1	0.04	0.1	0.5	0.81	0.8	1.0	1.0	1.0	1.0	1.22	1.4	1.37
17 AG 09B	<0.1	<0.1	0.06	0.1	0.1	0.16	0.2	0.3	0.3	0.3	0.3	0.30	0.3	0.23
17 AG 14B	0.6	0.6	0.71	0.9	1.4	1.65	1.9	1.7	1.8	1.5	1.5	1.40	1.4	1.30
17 AG 14D	0.3	0.1	0.34	0.4	0.8	0.97	1.1	1.2	1.3	1.0	1.1	1.05	1.0	0.98
17 AG 14G	0.3	0.3	0.36	0.4	0.4	0.32	0.4	0.4	0.5	0.5	0.5	0.55	0.5	0.46
17 AG 15	0.2	0.3	0.72	1.0	2.5	2.15	2.5	3.0	2.8	2.0	1.8	1.68	1.3	1.25
17 AG 25A	0.1	0.1	0.11	0.2	0.3	0.36	0.5	0.4	0.5	0.4	0.4	0.42	0.4	0.36
17 TAZ 01A	0.2	0.1	0.23	0.3	0.4	0.49	0.4	0.4	0.4	0.4	0.3	0.34	0.3	0.30
17 TAZ 01C	0.2	0.2	0.33	0.4	0.5	0.67	0.6	0.6	0.6	0.5	0.5	0.48	0.4	0.38
17 TAZ 15	0.3	0.1	0.30	0.3	0.5	0.68	0.6	0.6	0.6	0.5	0.4	0.45	0.4	0.34
17 TAZ 16	0.3	0.3	0.29	0.3	0.3	0.52	0.3	0.3	0.4	0.3	0.3	0.25	0.2	0.20
17 TZ 04B	<0.1	<0.1	0.01	<0.1	0.0	0.02	<0.1	<0.1	<0.1	<0.1	<0.1	<0.05	<0.1	0.02
18 TAZ 23	0.9	1.7	1.06	1.2	1.5	2.05	1.6	1.4	1.3	1.0	0.9	0.78	0.8	0.81
18 TAZ 25	0.1	0.1	0.13	0.1	0.2	0.25	0.2	0.3	0.3	0.2	0.2	0.17	0.1	0.16
18 TAZ 26	<0.1	<0.1	0.01	<0.1	<0.1	<0.05	<0.1	<0.1	<0.1	<0.1	<0.1	<0.05	<0.1	0.02
18 TAZ 27	0.2	0.1	0.30	0.3	0.5	0.64	0.6	0.5	0.6	0.4	0.4	0.39	0.4	0.35
17 TAS 07	20.1	13.9	12.58	10.4	3.8	1.57	0.9	0.4	0.3	0.2	0.2	0.20	0.2	0.15
17 TAS 10B	0.1	0.1	0.12	0.1	0.2	0.22	0.3	0.3	0.4	0.4	0.3	0.30	0.2	0.19
17 TAS 10C	0.4	0.3	0.34	0.4	0.4	0.45	0.4	0.4	0.4	0.3	0.3	0.20	0.2	0.15
18 TAS 01B	0.9	1.0	0.99	1.1	1.2	1.11	1.1	1.0	1.0	0.8	0.8	0.71	0.7	0.70
18 TAS 01D	1.0	1.1	1.10	1.3	1.5	1.45	1.9	1.7	1.5	1.2	1.1	1.02	1.0	1.07
18 TAS 02	0.9	1.1	1.38	1.5	1.9	2.47	1.1	0.9	0.8	0.6	0.8	0.90	1.1	1.23
18 TAS 07	0.2	0.1	0.26	0.3	0.6	0.73	0.7	0.6	0.8	0.7	0.6	0.63	0.6	0.65
18 TAS 11	4.9	2.6	1.79	1.2	0.5	0.36	0.2	0.1	0.1	0.1	0.1	<0.05	0.1	0.12
18 TAS 78	0.5	0.4	0.46	0.5	0.4	0.46	0.5	0.5	0.5	0.5	0.4	0.44	0.4	0.47
17 TIZ 01A	<0.1	<0.1	0.01	<0.1	<0.1	0.03	<0.1	<0.1	<0.1	<0.1	<0.1	0.02	<0.1	0.02
17 TIZ 01B	<0.1	<0.1	0.05	0.1	0.1	0.14	0.1	0.1	0.1	0.1	0.1	0.15	0.1	0.15
17 TIZ 03	0.1	0.1	0.10	0.1	0.2	0.25	0.2	0.2	0.2	0.1	0.1	0.12	0.1	0.09
17 TIZ 06	0.1	<0.1	0.08	0.1	0.2	0.28	0.2	0.2	0.2	0.2	0.2	0.19	0.2	0.17
17 IG 01	0.2	0.1	0.14	0.2	0.2	0.24	0.3	0.3	0.3	0.3	0.2	0.24	0.2	0.20
18 IG 02	0.1	0.1	0.14	0.2	0.3	0.42	0.4	0.4	0.4	0.3	0.3	0.24	0.2	0.21
18 IG 03	0.2	0.1	0.12	0.1	0.2	0.22	0.2	0.3	0.3	0.3	0.3	0.39	0.4	0.37

18 ASS 01A	0.1	0.1	0.20	0.3	0.3	0.45	0.5	0.4	0.3	0.2	0.2	0.15	0.1	0.12
18 ASS 01B	0.3	0.2	0.20	0.2	0.2	0.27	0.2	0.3	0.2	0.2	0.1	0.12	0.1	0.12
18 ASS 02	0.1	0.1	0.10	0.1	0.2	0.25	0.2	0.3	0.2	0.2	0.2	0.15	0.1	0.14
18 ASS 03	0.1	<0.1	0.05	0.1	0.1	0.12	0.1	<0.1	0.1	<0.1	0.1	<0.05	0.1	0.05
18 IR 01	<0.1	<0.1	0.01	<0.1	<0.1	<0.05	<0.1	<0.1	<0.1	<0.1	<0.1	<0.05	<0.1	<0.01
18 IR 02	0.2	0.2	0.24	0.3	0.4	0.42	0.4	0.4	0.3	0.3	0.3	0.27	0.3	0.23
18 IR 07	<0.1	<0.1	0.05	0.1	0.1	0.07	0.1	<0.1	0.1	<0.1	0.1	<0.05	0.1	0.07

**Table 6.3.5.** Oxygen and hydrogen isotopic compositions of goethite.

Sample number	H <sub>2</sub> O (wt%)	$\delta D_{VSMOW}$ (‰)	$\delta^{18}O_{VSMOW}$ (‰)
14RL14	11.06	-159	-5.09
14RL15	13.96	-162	-5.17
14HT02	2.48	-100	7.83
14HT07	2.55	-106	5.09
14KH50	14.43	-157	13.11
17AG15	8.76	-158	-4.40
17AG26	3.00	-122	-11.24
17AG14B	6.94	-151	-4.53
18AG07	10.87	-154	-2.88
17TAZ01C	10.94	-145	-1.33
18TAZ27	10.74	-155	-2.15
18TAS01D	13.58	-133	0.41
17TIZ03	11.02	-141	-0.33
17IG01	12.44	-150	-2.86
18IG02	12.36	-136	-2.60
18ASS01A	11.20	-143	-2.34
18ASS01B	11.22	-135	-3.29
18IR01	11.26	-145	6.17

### 6.3.3.c (U-Th-Sm)/He data

Considering all dated samples of the present study, GHe (goethite (U-Th-Sm)/He) ages strongly vary from one sample to another (Table 6.3.6). GHe ages range between 0 and 80 Ma (Fig. 6.3.9). However, ages range differently according to their origin: High Atlas samples present young GHe ages fluctuating between 0 and 25 Ma, while much more scattered GHe ages of the Anti-Atlas samples range from 0 to 80 Ma (Fig. 6.3.9). It may be noted that while botryoidal iron (oxyhydr-)oxides are scattered between 0 to 80 Ma, pseudomorphosing samples seem to concentrate around younger GHe ages, from 0 and 55 Ma. Moreover, botryoidal and microcrystalline samples provide much more reproducible GHe ages than pseudomorphosing samples. For instance, at Tassrirt, pseudomorphosing sample 17TAS10B ranges between 16 and 51 Ma, while botryoidal sample 18TAS01D GHe ages vary between 0 and 1 Ma.

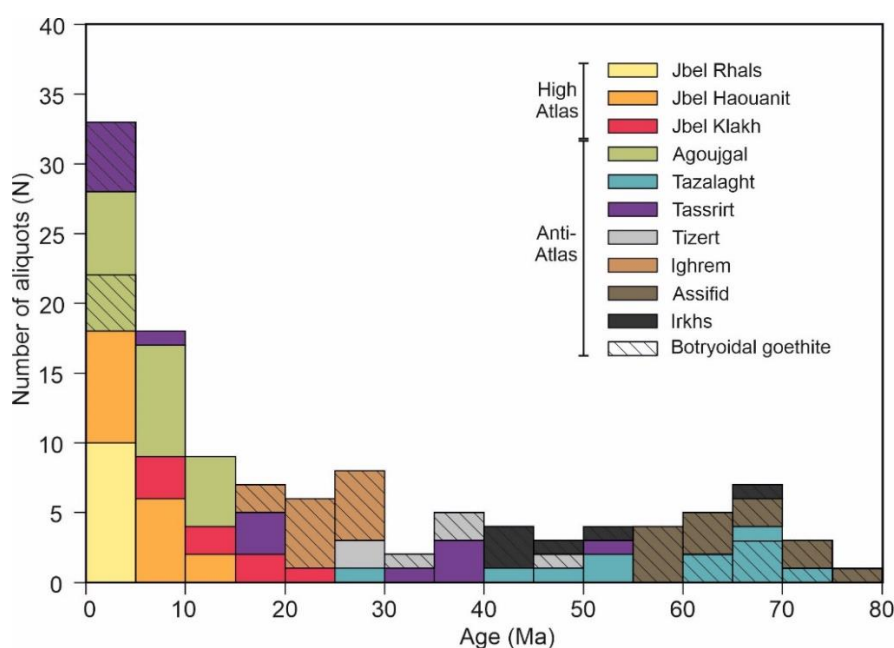


**Figure 6.3.9.** Distribution of goethite (U-Th-Sm)/He ages. The hatched zones correspond to botryoidal goethite aliquots.

For some samples, GHe ages are very reproducible whereas for other samples, GHe vary from one aliquot to another (Table 6.3.6). In the High Atlas, the siderite-pseudomorphosing goethite of Jbel Rhals site present young and strongly reproducible GHe ages ranging between 1 and 3 Ma (Table 6.3.6, Fig. 6.3.9). GHe ages of the Jbel Haouanit microcrystalline goethite associated with supergene mottramite are well reproducible and can be grouped in two categories: most aliquots fall into the 3-7 Ma category, while two aliquots show GHe ages of 12-13 Ma (Table 6.3.6, Fig. 6.3.9). At Jbel Klakh, goethite filling a fracture gives strongly scattered GHe ages fluctuating between 7 and 26 Ma (Table 6.3.6, Fig. 6.3.9). In the Anti-Atlas, at Agoujgal, goethite pseudomorphosing pyrite provides scattered GHe ages ranging between 1 and 16 Ma (Table 6.3.6, Fig. 6.3.9). The GHe ages of Agoujgal botryoidal goethite associated or not with supergene mottramite are reproducible and extend between 2 and 7 Ma (Table 6.3.6, Fig. 6.3.9). At Tazalaght, the pyrite pseudomorphosing sample gives strongly scattered older GHe ages between 28 and 74 Ma (Table 6.3.6, Fig. 6.3.9). Tazalaght botryoidal goethite samples present more reproducible GHe ages between 44 and 58 Ma, and 69 and 79 Ma (Table 6.3.6, Fig. 6.3.9). The pyrite-pseudomorphosing iron (oxyhydr-)oxides of Tassrirt provide scattered GHe ages extending between 10 and 56 Ma (Table 6.3.6, Fig. 6.3.9). The botryoidal sample of Tassrirt, however, delivers very young and reproducible GHe ages approximating 1 Ma (Table 6.3.6, Fig. 6.3.9). Tizert microcrystalline and botryoidal iron (oxyhydr-)oxides provide fairly reproducible GHe ages ranging between 30 and 51 Ma (Table 6.3.6, Fig. 6.3.9). Ighrem, Assifid and Irkhs botryoidal goethite GHe ages

are particularly well reproducible, with fluctuations between 21 and 31 Ma, 63 and 84 Ma, and 47 and 57 Ma with an exception at 76 Ma (Table 6.3.6, Fig. 6.3.9). On the field, no physical variations were observed between samples from these three sites.

No direct relation is observed between GHe ages and eU values (Fig. 6.3.10), at the contrary of Imini goethite ages (Verhaert et al., submitted). However, while botryoidal samples present more scattered eU values than GHe ages, pseudomorphosing samples show the reverse trend (Fig. 6.3.10). Samples 17TIZ01A and 17AG26 are particularly rich in U (Table 6.3.6). No direct relation is highlighted between GHe ages and the altitude of sampling, if all samples are considered (Fig. 6.3.11). However, a linear correlation is observed for part of the samples, particularly for the High Atlas samples and the Anti-Atlas pseudomorphosing and microcrystalline samples (Fig. 6.3.11). Except for Tizert, Assifid and Irkhs samples, GHe ages of iron (oxyhydr-)oxides appear to increase with the altitude of sampling (Fig. 6.3.11). The correlation line that may be traced on the basis of this alignment is characterized by a slope of 12m/Ma and a 0.7  $R^2$  (Fig. 6.3.11).

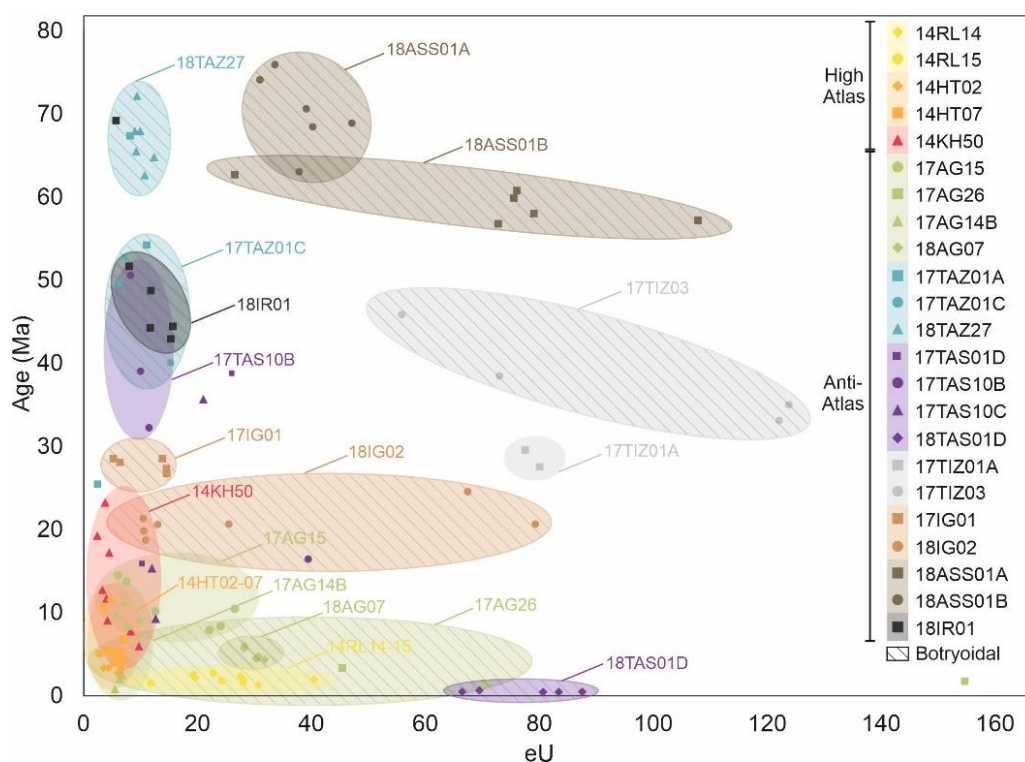


**Figure 6.3.10.** (U-Th-Sm)/He ages as a function of the effective uranium values (eU). The hatched zones correspond to botryoidal goethite aliquots.



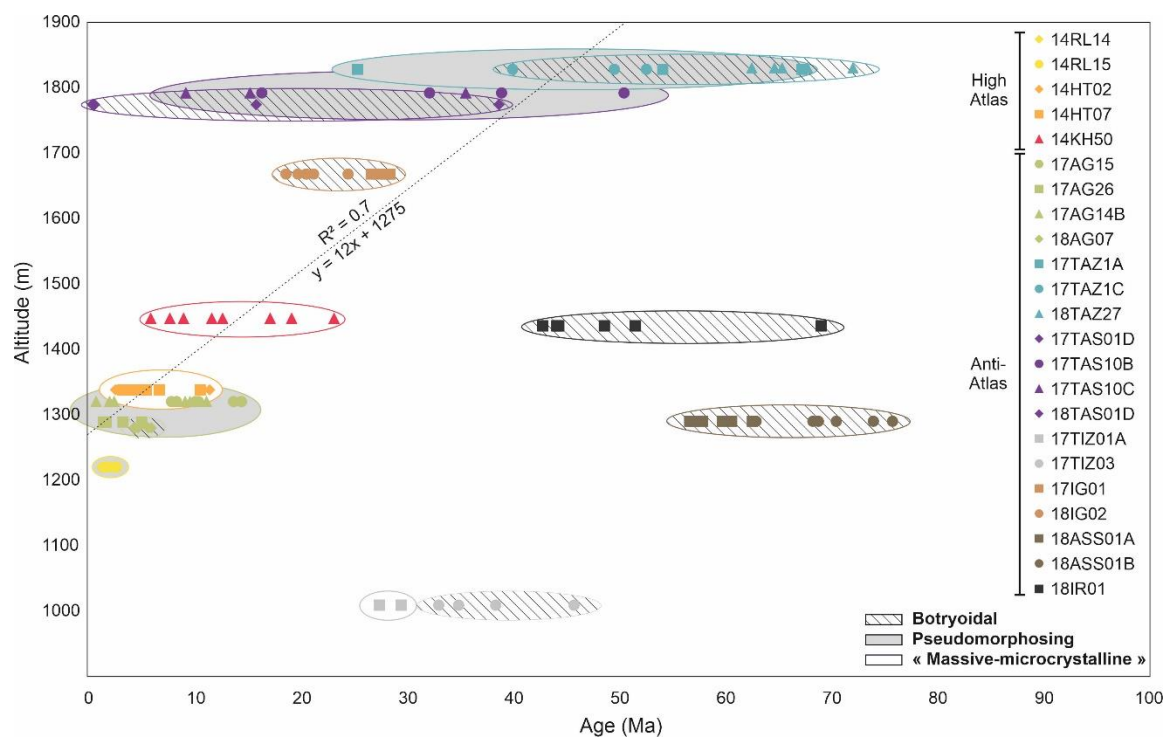


**Figure 6.3.11.** (U-Th-Sm)/He ages as a function of altitude. The hatched and gray zones correspond to botryoidal and pseudomorphosing goethite aliquots, respectively.

**Table 6.3.6.** Goethite (U-Th-Sm)/He data.

Samples nature	Sample Number	<sup>4</sup> He	± s	<sup>238</sup> U	<sup>232</sup> Th	<sup>147</sup> Sm	weight	<sup>4</sup> He	± s	<sup>238</sup> U	<sup>232</sup> Th	<sup>147</sup> Sm	eU	Th/U	Th/Sm	Raw age	± s	Corr. age*	± s**
		(ccSTP)	(ccSTP)	(ng)	(ng)	(ng)	(mg)	(nccSTP/g)	(nccSTP/g)	(ppm)	(ppm)	(ppm)	(ppm)			(Ma)	(Ma)	(Ma)	(Ma)
<u>Jbel Rhals - altitude 1300 m - Cu-Fe-Mn ores hosted by Paleozoic shists</u>																			
Pseudomorph ose of siderite	14RL14-1	1.28E-09	1.28E-11	5.25	0.02	N.D.	0.13	9866	99	40.4	0.1	N.D.	40	0.00	N.D.	2	0	2	0
	14RL14-4	8.25E-10	8.25E-12	3.14	0.01	N.D.	0.16	5155	52	19.6	0.1	N.D.	20	0.00	N.D.	2	0	2	0
	14RL14-5	1.96E-09	1.96E-11	6.87	0.01	N.D.	0.25	7854	79	27.5	0.0	N.D.	28	0.00	N.D.	2	0	3	0
	14RL14-6	4.36E-09	4.36E-11	17.58	0.11	0.30	0.63	6914	69	27.9	0.2	0.47	28	0.01	0.35	2	0	2	0
	14RL14-7	3.94E-09	3.94E-11	24.65	0.01	1.12	0.81	4892	49	30.6	0.0	1.39	31	0.00	0.01	1	0	1	0
	14RL15-1	4.34E-10	4.34E-12	2.35	0.01	N.D.	0.20	2170	22	11.7	0.1	N.D.	12	0.01	N.D.	2	0	2	0
	14RL15-2	1.08E-09	1.08E-11	4.84	0.02	N.D.	0.20	5396	54	24.2	0.1	N.D.	24	0.00	N.D.	2	0	2	0
	14RL15-3	7.06E-10	7.06E-12	3.64	0.01	N.D.	0.13	5431	54	28.0	0.1	N.D.	28	0.00	N.D.	2	0	2	0
	14RL15-4	1.13E-09	1.13E-11	3.40	0.02	0.05	0.15	7536	75	22.7	0.1	0.32	23	0.01	0.36	3	0	3	0
	14RL15-6	3.66E-09	3.66E-11	11.79	0.01	0.13	0.61	5980	60	19.3	0.0	0.21	19	0.00	0.05	3	0	3	0
<u>Jbel Haouanit - altitude 1300 m - Cu-Pb-Zn-V ores in Jurassic dolostones</u>																			
Microcrystalline, associated with motttramite	14HT02-1	3.93E-09	3.93E-11	2.38	1.82	N.D.	0.60	6545	65	4.0	3.0	N.D.	5	0.77	N.D.	12	1	13	1
	14HT02-2	2.46E-09	2.46E-11	3.37	2.33	N.D.	0.72	3419	34	4.7	3.2	N.D.	5	0.69	N.D.	5	0	6	0
	14HT02-3	1.07E-09	1.07E-11	1.51	2.51	N.D.	0.29	3695	37	5.2	8.7	N.D.	7	1.66	N.D.	4	0	5	0
	14HT02-5	2.15E-09	2.15E-11	4.51	3.40	1.38	1.53	1407	14	2.9	2.2	0.90	3	0.75	2.46	3	0	4	0
	14HT02-6	1.89E-09	1.89E-11	3.93	2.90	1.29	1.08	1751	18	3.6	2.7	1.20	4	0.74	2.24	3	0	4	0
	14HT02-7	3.29E-09	3.29E-11	7.14	6.52	1.99	1.33	2472	25	5.4	4.9	1.49	7	0.91	3.28	3	0	3	0
	14HT02-8	4.19E-09	4.19E-11	5.00	5.39	1.38	0.98	4269	43	5.1	5.5	1.41	6	1.08	3.90	6	0	6	0
	14HT02-9	2.84E-09	2.84E-11	7.07	5.73	2.01	1.41	2013	20	5.0	4.1	1.43	6	0.81	2.84	3	0	3	0
	14HT02-10	3.71E-09	3.71E-11	6.08	6.07	1.58	1.31	2834	28	4.7	4.6	1.20	6	1.00	3.85	4	0	4	0
	14HT07-1	1.59E-09	1.59E-11	1.99	1.54	N.D.	0.58	2741	27	3.4	2.6	N.D.	4	0.77	N.D.	6	0	6	0
Microcrystalline, associated with motttramite	14HT07-2	9.28E-10	9.28E-12	1.27	0.92	N.D.	0.32	2899	29	4.0	2.9	N.D.	5	0.72	N.D.	5	0	6	0
	14HT07-3	1.31E-09	1.31E-11	0.88	0.57	N.D.	0.29	4512	45	3.0	2.0	N.D.	4	0.65	N.D.	11	1	12	1
	14HT07-5	5.39E-09	5.39E-11	5.33	5.13	2.25	0.93	5777	58	5.7	5.5	2.41	7	0.96	2.28	7	0	7	0
	14HT07-6	3.80E-09	3.80E-11	6.44	5.50	2.55	1.45	2624	26	4.4	3.8	1.76	5	0.85	2.15	4	0	4	0
	14HT07-8	3.10E-09	3.10E-11	4.12	3.45	1.76	0.80	3880	39	5.2	4.3	2.20	6	0.84	1.96	5	0	6	0
	14HT07-10	2.57E-09	2.57E-11	4.10	3.61	1.45	0.81	3176	32	5.1	4.5	1.80	6	0.88	2.49	4	0	5	0
	14HT07-10	2.57E-09	2.57E-11	4.10	3.61	1.45	0.81	3176	32	5.1	4.5	1.80	6	0.88	2.49	4	0	5	0
<u>Jbel Klakh - altitude 1500 m - Cu ores in Jurassic dolostones</u>																			
Filling fractures with Mn oxides	14KH50-1	5.50E-09	5.50E-11	1.64	1.32	N.D.	0.52	10582	106	3.2	2.5	N.D.	4	0.80	N.D.	23	1	26	2
	14KH50-2	4.47E-09	4.47E-11	1.91	0.96	N.D.	0.48	9306	93	4.0	2.0	N.D.	4	0.50	N.D.	17	1	19	1
	14KH50-3	1.76E-09	1.76E-11	0.77	1.58	N.D.	0.35	5025	50	2.2	4.5	N.D.	3	2.05	N.D.	13	1	14	1
	14KH50-4	3.80E-09	3.80E-11	2.92	2.27	0.24	0.83	4572	46	3.5	2.7	0.29	4	0.78	9.43	9	1	10	1
	14KH50-7	7.91E-09	7.91E-11	8.96	8.42	0.61	1.13	7000	70	7.9	7.4	0.54	10	0.94	13.86	6	0	7	0
	14KH50-8	6.28E-09	6.28E-11	3.58	3.56	0.74	1.11	5675	57	3.2	3.2	0.66	4	0.99	4.84	12	1	13	1

		14KH50-9	5.03E-09	5.03E-11	1.76	1.65	0.26	0.91	5523	55	1.9	1.8	0.29	2	0.94	6.25	19	1	21	1	
		14KH50-10	6.16E-09	6.16E-11	5.61	3.89	0.25	0.80	7744	77	7.1	4.9	0.31	8	0.69	15.62	8	0	9	1	
Agouigal - altitude 1300 m - Cu-As-Pb ores in Late Proterozoic sandstones, dolostones and siltstones																					
Fine	botryoidal layer associated with	Pseudomorphose of pyrite	17AG15-1	1.28E-08	1.28E-10	7.26	0.02	0.34	1.21	10563	106	6.0	0.0	0.28	6	0.00	0.06	15	1	16	1
			17AG15-2	1.35E-08	1.35E-10	8.06	0.04	0.20	1.08	12468	125	7.5	0.0	0.18	7	0.00	0.20	14	1	15	1
			17AG15-3	2.56E-08	2.56E-10	20.76	0.03	0.20	1.65	15540	155	12.6	0.0	0.12	13	0.00	0.15	10	1	11	1
			17AG15-4	2.88E-08	2.88E-10	22.70	0.13	0.33	0.86	33630	336	26.5	0.1	0.39	27	0.01	0.38	10	1	12	1
			17AG15-5	1.76E-08	1.76E-10	18.34	0.02	0.18	0.83	21157	212	22.0	0.0	0.21	22	0.00	0.14	8	0	9	1
			17AG15-6	1.68E-08	1.68E-10	16.53	0.04	0.36	0.69	24399	244	24.0	0.1	0.52	24	0.00	0.12	8	1	9	1
		Pseudomorphose of pyrite	17AG26-1	1.33E-07	1.33E-09	620.23	0.01	0.29	4.01	33176	332	154.7	0.0	0.07	155	0.00	0.05	2	0	2	0
			17AG26-2	6.72E-08	6.72E-10	165.30	0.04	0.13	3.64	18474	185	45.4	0.0	0.04	45	0.00	0.33	3	0	4	0
			17AG26-3	4.70E-08	4.70E-10	260.03	0.02	0.21	3.69	12734	127	70.5	0.0	0.06	70	0.00	0.11	1	0	2	0
			17AG26-6	8.92E-09	8.92E-11	14.37	0.01	2.26	5.22	1709	171	2.8	0.0	0.43	3	0.00	0.00	5	0	6	0
Fine botryoidal layer associated with mottamite		17AG14B-1	1.49E-09	1.49E-11	5.86	0.14	0.63	0.93	1599	16	6.3	0.2	0.68	6	0.02	0.22	2	0	2	0	
		17AG14B-2	1.03E-08	1.03E-10	9.94	0.39	1.06	1.30	7889	79	7.6	0.3	0.82	8	0.04	0.37	8	1	9	1	
		17AG14B-3	4.77E-09	4.77E-11	4.26	0.05	0.39	0.43	11091	111	9.9	0.1	0.90	10	0.01	0.14	9	1	10	1	
		17AG14B-4	9.40E-09	9.40E-11	6.87	0.15	0.76	0.95	9890	99	7.2	0.2	0.80	7	0.02	0.19	11	1	12	1	
		17AG14B-5	2.68E-09	2.68E-11	8.72	0.16	0.81	1.29	2075	21	6.8	0.1	0.63	7	0.02	0.20	3	0	3	0	
		17AG14B-6	4.33E-09	4.33E-11	3.67	0.07	0.43	0.65	6662	67	5.7	0.1	0.66	6	0.02	0.17	10	1	11	1	
		17AG14B-7	2.92E-10	2.92E-12	2.95	0.07	0.35	0.54	541	5	5.5	0.1	0.64	5	0.02	0.19	1	0	1	0	
Fine botryoidal layer associated with mottamite		18AG07-1	2.07E-09	2.07E-11	3.78	0.01	0.72	0.13	16529	0	30.2	0.1	5.76	30	0.00	0.01	5	0	5	0	
		18AG07-2	1.53E-09	1.53E-11	2.63	0.01	0.57	0.09	17807	0	30.6	0.1	6.60	31	0.00	0.02	5	0	5	0	
		18AG07-3	1.32E-09	1.32E-11	1.81	0.00	0.42	0.06	20635	0	28.2	0.1	6.59	28	0.00	0.01	6	0	7	0	
		18AG07-4	1.00E-09	1.00E-11	1.87	0.02	0.37	0.06	16953	0	31.7	0.3	6.34	32	0.01	0.05	4	0	5	0	
		18AG07-5	1.10E-09	1.10E-11	2.01	0.02	0.43	0.07	16652	0	30.4	0.3	6.56	30	0.01	0.04	5	0	5	0	
		18AG07-6	1.66E-09	1.66E-11	2.39	0.01	0.56	0.09	19575	0	28.1	0.1	6.54	28	0.00	0.01	6	0	6	0	
Tazalaght - altitude 1700 m - Cu-As ores in Late Proterozoic sandstones, dolostones and siltstones																					
Pseudo morphose of pyrite	Fine botryoidal layer	17TAZ1A-1	1.05E-07	1.05E-09	15.60	1.35	0.30	1.44	72608	726	10.8	0.9	0.21	11	0.09	4.54	54	3	60	4	
		17TAZ1A-2	9.57E-09	9.57E-11	3.07	0.10	1.17	1.27	7537	75	2.4	0.1	0.92	2	0.03	0.09	25	2	28	2	
		17TAZ1A-4	7.76E-08	7.76E-10	9.51	0.05	0.27	1.17	66358	664	8.1	0.0	0.23	8	0.01	0.19	67	4	74	5	
		17TAZ1C-1	1.47E-07	1.47E-09	23.02	0.13	1.60	3.20	45990	460	7.2	0.0	0.50	7	0.01	0.08	53	3	58	4	
		17TAZ1C-2	1.24E-07	1.24E-09	20.53	0.21	1.76	3.21	38585	386	6.4	0.1	0.55	6	0.01	0.12	50	3	55	3	
		17TAZ1C-3	1.00E-07	1.00E-09	20.67	0.12	0.30	1.36	73869	739	15.2	0.1	0.22	15	0.01	0.40	40	2	44	3	
		18TAZ27-1	5.39E-09	5.39E-11	0.60	0.25	0.02	0.07	73896	1	8.2	3.4	0.31	9	0.42	10.96	68	4	75	5	
		18TAZ27-2	3.85E-09	3.85E-11	0.40	0.18	0.02	0.05	81894	1	8.5	3.8	0.32	9	0.45	11.93	72	4	79	5	
		18TAZ27-3	4.23E-09	4.23E-11	0.48	0.23	0.02	0.06	72946	1	8.3	3.9	0.31	9	0.48	12.90	66	4	72	5	
		18TAZ27-4	2.32E-09	2.32E-11	0.28	0.09	0.01	0.02	96822	1	11.5	3.7	0.43	12	0.32	8.64	65	4	71	4	
		18TAZ27-5	4.55E-09	4.55E-11	0.50	0.22	0.02	0.06	81309	1	9.0	3.9	0.33	10	0.43	11.72	68	4	75	5	
		18TAZ27-6	7.15E-09	7.15E-11	0.85	0.37	0.03	0.09	81251	1	9.7	4.2	0.32	11	0.44	13.38	63	4	69	4	

Tassart - altitude 1800 m - Cu-Zn ores in Late Proterozoic - Cambrian limestones, siltstones and sandstones

Pseudo morphology of pyrite	17TAS1D-1	8.79E-08	8.79E-10	18.63	0.28	0.24	0.72	122017	1220	25.9	0.4	0.34	26	0.02	1.17	39	2	43	3
	17TAS1D-2	6.86E-08	6.86E-10	31.26	18.41	3.17	3.49	19666	197	9.0	5.3	0.91	10	0.59	5.82	16	1	18	1
Pseudo morphology of pyrite	17TAS10B-1	8.82E-08	8.82E-10	22.56	0.10	0.23	1.97	44764	448	11.4	0.1	0.12	11	0.00	0.45	32	2	36	2
	17TAS10B-2	4.81E-08	4.81E-10	10.13	0.18	0.09	1.02	47183	472	9.9	0.2	0.08	10	0.02	2.12	39	2	43	3
Pseudo morphology of pyrite	17TAS10B-3	5.88E-08	5.88E-10	9.57	0.12	0.15	1.17	50246	502	8.2	0.1	0.13	8	0.01	0.81	51	3	56	3
	17TAS10B-4	4.09E-08	4.09E-10	20.42	0.28	2.05	0.52	78575	786	39.3	0.5	3.95	39	0.01	0.14	16	1	18	1
Pseudo morphology of pyrite	17TAS10C-3	7.25E-08	7.25E-10	16.77	0.12	0.21	0.80	90676	907	21.0	0.1	0.27	21	0.01	0.56	36	2	39	2
	17TAS10C-4	7.38E-09	7.38E-11	6.54	0.13	0.06	0.52	14202	142	12.6	0.2	0.12	13	0.02	2.06	9	1	10	1
Pseudo morphology of pyrite	17TAS10C-5	2.09E-08	2.09E-10	11.19	0.28	0.23	0.94	22247	222	11.9	0.3	0.24	12	0.03	1.24	15	1	17	1
	18TAS01D-2	1.78E-10	1.78E-12	3.08	0.02	0.01	0.04	4802	0	83.3	0.5	0.22	83	0.01	2.24	0	0	1	0
Fine botryoidal layer	18TAS01D-3	1.16E-10	1.16E-12	2.02	0.01	0.00	0.03	4633	0	80.6	0.2	0.10	81	0.00	2.13	0	0	1	0
	18TAS01D-5	1.27E-10	1.27E-12	2.09	0.03	0.01	0.02	5276	0	87.2	1.3	0.23	88	0.01	5.56	0	0	1	0
Fine botryoidal layer	18TAS01D-6	2.20E-10	2.20E-12	2.71	0.01	0.00	0.04	5644	0	69.4	0.3	0.11	69	0.00	2.35	1	0	1	0
	18TAS01D-7	1.03E-10	1.03E-12	1.72	0.03	0.00	0.03	3969	0	66.2	1.1	0.18	66	0.02	5.98	0	0	1	0

Tizert - altitude 100 m - Cu ores in Late Proterozoic limestones

Micro crystalline	17TIZ1A-2	3.68E-07	3.68E-09	110.42	0.04	0.01	1.38	266892	2669	80.0	0.0	0.01	80	0.00	3.11	28	2	30	2
	17TIZ1A-3	6.58E-07	6.58E-09	183.68	0.07	0.03	2.37	277583	2776	77.5	0.0	0.01	78	0.00	2.59	30	2	33	2
Botryoidal	17TIZ3-1	2.94E-07	2.94E-09	69.32	0.04	0.03	0.56	524747	5247	123.8	0.1	0.05	124	0.00	1.57	35	2	39	2
	17TIZ3-3	1.81E-07	1.81E-09	45.16	0.08	0.03	0.37	489700	4897	122.1	0.2	0.09	122	0.00	2.44	33	2	36	2
Botryoidal	17TIZ3-5	1.98E-07	1.98E-09	42.49	0.00	0.04	0.58	340223	3402	73.0	0.0	0.06	73	0.00	0.11	39	2	42	3
	17TIZ3-6	2.50E-07	2.50E-09	45.03	0.00	0.05	0.81	309935	3099	55.8	0.0	0.06	56	0.00	0.08	46	3	51	3

Ighrem - altitude 1700 m - Late Proterozoic sandstones and siltstones

Large botryoidal layers	17IG01-1	1.97E-08	1.97E-10	5.77	0.07	0.13	0.91	21635	216	6.3	0.1	0.15	6	0.01	0.51	28	2	31	2
	17IG01-3	1.75E-08	1.75E-10	5.06	0.01	0.18	0.98	17855	179	5.2	0.0	0.18	5	0.00	0.05	29	2	31	2
Large botryoidal layers	17IG01-4	4.05E-08	4.05E-10	12.24	0.01	0.02	0.84	48032	480	14.5	0.0	0.02	15	0.00	0.47	27	2	30	2
	17IG01-5	4.56E-08	4.56E-10	14.06	0.01	0.02	0.97	47243	472	14.6	0.0	0.02	15	0.00	0.26	27	2	29	2
Large botryoidal layers	17IG01-6	5.73E-08	5.73E-10	16.58	0.01	0.01	1.20	47732	477	13.8	0.0	0.01	14	0.00	0.70	29	2	31	2
	18IG02-1	1.53E-09	1.53E-11	0.61	0.01	0.01	0.02	63717	1	25.4	0.4	0.51	25	0.02	0.75	21	1	23	1
Large botryoidal layers	18IG02-2	1.43E-09	1.43E-11	0.57	0.01	0.01	0.04	32464	0	13.0	0.1	0.14	13	0.01	0.99	21	1	23	1
	18IG02-4	1.11E-09	1.11E-11	0.46	0.00	0.01	0.04	25336	0	10.5	0.1	0.17	11	0.01	0.42	20	1	22	1
Large botryoidal layers	18IG02-5	1.49E-08	1.49E-10	5.95	0.00	0.09	0.08	198341	2	79.3	0.0	1.18	79	0.00	0.04	21	1	23	1
	18IG02-6	2.04E-09	2.04E-11	0.90	0.01	0.02	0.08	24576	0	10.8	0.1	0.22	11	0.01	0.46	19	1	21	1
Large botryoidal layers	18IG02-7	3.41E-09	3.41E-11	1.15	0.00	0.01	0.02	200601	2	67.4	0.2	0.73	67	0.00	0.32	25	1	27	2
	18IG02-8	6.48E-10	6.48E-12	0.25	0.00	0.00	0.02	27006	0	10.4	0.1	0.19	10	0.01	0.64	21	1	23	1

Assifid - altitude 1300 m - Late proterozoic dolostones

Large botryoidal layers	18ASS01A-1	4.81E-08	4.81E-10	6.54	0.01	0.04	0.09	559305	6	76.0	0.1	0.44	76	0.00	0.21	61	4	67	4
	18ASS01A-2	2.78E-08	2.78E-10	3.95	0.01	0.02	0.05	555101	6	79.0	0.1	0.36	79	0.00	0.31	58	3	64	4
Large botryoidal layers	18ASS01A-3	1.37E-08	1.37E-10	1.89	0.00	0.01	0.03	547345	5	75.5	0.2	0.46	75	0.00	0.35	60	4	66	4

Large botryoidal layers	18ASS01A-4	1.94E-08	1.94E-10	2.80	0.01	0.02	0.03	747184	7	107.8	0.2	0.66	108	0.00	0.33	57	3	63	4
	18ASS01A-5	1.01E-08	1.01E-10	1.32	0.00	0.00	0.05	201252	2	26.5	0.1	0.09	27	0.00	0.74	63	4	69	4
	18ASS01A-6	2.80E-08	2.80E-10	4.07	0.00	0.02	0.06	500261	5	72.7	0.1	0.42	73	0.00	0.21	57	3	63	4
	18ASS01B-1	1.20E-08	1.20E-10	1.45	0.01	0.01	0.04	333215	3	40.2	0.2	0.32	40	0.01	0.69	68	4	75	5
	18ASS01B-2	2.52E-08	2.52E-10	2.81	0.01	0.05	0.09	277460	3	30.9	0.2	0.57	31	0.01	0.28	74	4	82	5
	18ASS01B-3	5.01E-09	5.01E-11	0.59	0.00	0.00	0.02	334129	50	39.0	0.3	0.20	39	0.01	1.50	71	4	78	5
	18ASS01B-4	9.42E-09	9.42E-11	1.12	0.03	0.02	0.02	392634	4	46.7	1.4	0.64	47	0.03	2.26	69	4	76	5
	18ASS01B-5	5.48E-09	5.48E-11	0.71	0.04	0.01	0.02	288665	3	37.3	2.2	0.27	38	0.06	8.15	63	4	69	4
	18ASS01B-6	4.63E-09	4.63E-11	0.50	0.01	0.00	0.02	308478	3	33.4	0.5	0.31	34	0.02	1.72	76	5	84	5
<u>Irkhs - altitude 1450 m - Cu ores in Cambrian Inferior Limestones</u>																			
Large botryoidal layers	18IR01-1	4.77E-09	4.77E-11	0.91	0.01	0.00	0.06	79515	1	15.2	0.2	0.07	15	0.01	3.05	43	3	47	3
	18IR01-2	3.00E-09	3.00E-11	0.55	0.02	0.00	0.05	62514	1	11.6	0.5	0.06	12	0.04	8.01	44	3	49	3
	18IR01-3	1.14E-09	1.14E-11	0.14	0.00	0.00	0.02	47437	0	5.6	0.1	0.10	6	0.03	1.39	69	4	76	5
	18IR01-5	3.79E-09	3.79E-11	0.70	0.02	0.00	0.05	84161	1	15.5	0.4	0.06	16	0.02	6.06	44	3	49	3
	18IR01-6	1.11E-09	1.11E-11	0.19	0.01	0.00	0.02	69643	1	11.7	0.6	0.09	12	0.05	6.63	49	3	54	3
	18IR01-7	6.98E-10	6.98E-12	0.11	0.00	0.00	0.01	49847	0	7.9	0.2	0.17	8	0.02	1.15	52	3	57	4

\*A 10% correction is added to ages.

\*\*A 15 % error is considered.

N.D. = No data

### 6.3.4 Discussion

Testing the (U-Th-Sm)/He dating method on different types of iron (oxyhydr-)oxides emphasizes several points.

#### 6.3.4.a Selection and characterization of most reliable samples for (U-Th-Sm)/He dating

SEMs are judged as the best tool to select the purest material for (U-Th-Sm/He) dating and to eliminate undatable samples. X-Ray diffraction only brings preliminary results on major phases (>5%) without regard for the structures and textures and is mostly used as a pre-sorting solution. It is obvious from the data presented above that botryoidal goethite samples are of much better quality for (U-Th-Sm)/He dating than pyrite-pseudomorphosing iron (oxyhydr-)oxides. Microcrystalline goethite samples are in the middle rank, along with the siderite-pseudomorphosing samples, while powdery samples are in no way datable. The heterogeneity of pyrite-pseudomorphosing iron (oxyhydr-)oxides, along with the interspersing of several generations of hematite and goethite and the common inheritance of tiny gangue minerals such as zircon and apatite, are all factors that contribute to give strong preference to the much purer and better crystallized botryoidal goethite samples.

The concentration of nearly all samples around the 25°C line on the  $\delta^{18}\text{O}$ - $\delta\text{D}$  diagram is concordant with the hypothesis of their formation in supergene environments, in equilibrium with meteoric waters (Fig. 6.3.8). The location of sample 18IR01 in the negative temperatures area is most probably related to the presence of carbonates in the analyzed aliquots (Fig. 6.3.8). Fluid/rock interactions processes, such as the dissolution/precipitation of minerals, might indeed lead to isotopic exchanges between mineralizing fluids and host rocks. Here, the dissolution of carbonates, which are known to concentrate  $^{18}\text{O}$  in their structure (Garlick, 1966), is probably responsible for the  $\delta^{18}\text{O}$  shift, as observed by Dekoninck et al. (2018) for goethite and kaolinite in Tunisia and by Verhaert et al. (submitted) in goethite in Moroccan (Imini). Heavy oxygen might have been released in meteoric fluids after the dissolution of Irkhs host rock and incorporated into goethite. This early diagenesis process might have wiped out the usual depletion in  $^{18}\text{O}$  of supergene phases

The reproducibility of GHe ages presented here is variable: it is best for botryoidal iron (oxyhydr-)oxides and youngest samples. Poor GHe ages replication within the same pyrite-pseudomorphosing sample could be attributed to the presence of previously undetected numerous generations of goethite and hematite, and/or to the presence of other datable phases in the analyzed goethite aliquot, such as Mn oxides and mottramite. The relatively rare occurrence of mottramite in aliquots of samples 14HT02, 14HT07, 17AG26 and 18AG07 may contribute to scattered GHe ages, such as at Jbel Haouanit. As previously stated by Boni et al. (2007), supergene vanadates such as descloizite, which is the Zn-analog of mottramite, are datable with the (U-Th)/He method and yield representative results. Here, since mottramite and goethite are paragenetically coeval, as suggested by the successive overlapping of their different generations (Fig. 6.3.5M), their concurrent dating is not a major issue.

No relation could be highlighted between GHe ages and: 1) the category of samples (botryoidal vs pseudomorphs), 2) the sampling localization, 3) the host rock age, and/or 4) the inliers hosting the sampling sites. However, the formation of botryoidal goethite spreads over 80 Ma, while that of pyrite-pseudomorphosing samples is focused on 55 Ma. The formation of goethite is also much more recent in the High Atlas (Cenozoic only; 0-25 Ma) than in the Anti-Atlas (0-80 Ma). In the High Atlas, the Cenozoic pseudomorphose of Jbel Rhals siderite is very recent and concentrated within a short time, indicating the rapid *in situ* replacement of siderite by goethite and minor pyrolusite, as already suggested in Verhaert et al. (2018). The remarkable reproducibility of these Late Pliocene – Pleistocene

GHe ages results from the complete absence of inherited gangue minerals in these pseudomorphs (Fig. 6.3.5F). At Jbel Haouanit, the late Miocene to Pliocene nearly coeval precipitation of goethite and mottramite is also very recent; the formation of mottramite probably slightly preceded that of goethite (Fig. 6.3.4H), resulting in moderately driven up ages.

#### **6.3.4.b Composition of fluids and mineralizing events**

In general, where both pseudomorphosing and botryoidal iron (oxyhydr-)oxides were dated, botryoidal and microcrystalline goethite are younger, found in small amounts and usually in thin layers. Where only botryoidal samples were dated, goethite is concentrated in considerable amounts and thick layers, and present much older ages. These divergences could be related to environmental conditions prevailing at the time of precipitation. The precipitation of the thick and older layers of botryoidal goethite of Ighrem, Tizert, Assifid and Irkhs is most probably related to the circulation of mineralizing fluids over several millions of years, at each site, whereas the formation of the young and thin botryoidal goethite layers of Agoujgal and Tassirt is rather linked to the very local and time-limited circulation of late mineralizing fluids, probably at the end of supergene processes. The nearly absence of pyrite-pseudomorphosing samples at Ighrem, Tizert, Assifid and Irkhs supports this hypothesis: the pseudomorphosing iron (oxyhydr-)oxides were either dissolved and reprecipitated, or never formed due to the repetitive passage of leaching fluids in a (moderately) humid environment. At the contrary, the coexistence of pseudomorphosing and very young botryoidal samples at Agoujgal and Tassirt further reinforces the hypothesis of local environmental variations.

Geochemical and isotopic analyses also strengthen these assertions. Major elements present in iron (oxyhydr-)oxides mostly depend on the nature of the host rock. For instance, carbonate-hosted samples such as those originating from Irkhs typically present higher contents in Ca than quartzite-hosted samples (Table 6.3.2). “Minor” elements depend more on the environment of precipitation. The preferential concentration of Cu, Co, Mo and As in pyrite-pseudomorphosing samples suggests that their formation was probably coeval with the precipitation of other supergene phases such as malachite and Cu-arsenates, for example at Tazalaght and Agoujgal (Fig. 6.3.6), while the precipitation of the very young botryoidal goethite would be related to late supergene processes. Enrichment of As is also related to the adsorption of this element by iron (oxyhydr-)oxides, in the form of arsenate or  $\text{FeAsO}_4$ , in oxic environments (Farmer and Lovell 1986). The typical concentration of U in iron (oxyhydr-)oxides ensues from their high specific surface and the subsequent important adsorption capacity, but also from the neoformation of discrete minerals at the contact with the mineralizing fluids (Kamineni et al. 1986; Koppi et al. 1996; Nicaise et al. 1996; De Putter et al. 2002). Enrichment in U but depletion in Th of iron (oxyhydr-)oxides is a typical supergene trend and is related to a selective U vs. Th mobilization during weathering processes. In supergene fluids, immobile Th is retained in weathering-resistant minerals or incorporated in rapidly precipitating minerals while soluble and mobile U is preferentially leached and accumulated in neoformed minerals such as iron (oxyhydr-)oxides (Pagel et al. 1990; Nicaise et al. 1996; De Putter et al. 2002; Verhaert et al. 2018). Botryoidal goethite present flat REE curves while pseudomorphs are characterized with variable REE contents and greater variations in negative Ce anomalies indicating fluctuations in the oxidizing-reducing conditions (Fig. 6.3.6). The adsorption of LREE and the common presence of LREE phosphates in powdery samples is responsible for their enrichment in these elements. At the contrary, the presence of HREE phosphates in Jbel Rhals siderite-pseudomorphosing samples (Verhaert et al. 2018) accounts for the divergent LREE-HREE contents. The only noteworthy feature observed in Fig. 6.3.6 is the slightly and marked negative Ce anomaly of botryoidal and pseudomorphosing samples, respectively. Ce anomalies result from the oxidation of this element to  $\text{Ce}^{4+}$  and to its subsequent decoupling from other REE that maintain their trivalent ionic states and are leached by fluids (Bau and Dulski 1996). As oxidation to



tetravalent Ce is restricted to strongly oxidizing environments, and is usually observed in the most weathered part of the profiles, typically for Fe-Mn oxyhydroxides (Ludden and Thompson 1979; Pracejus et al. 1990; Cotten et al. 1995), the negative anomalies observed here substantiate the formation of such samples in weathering environments characterized with pH values above 5 units (Brookins 1988; Leybourne et al. 2006). The absence of relation between eU values and GHe ages of all samples (Fig. 6.3.10) confirms the absence of joint mineralizing fluids leading to the precipitation of iron (oxyhydr-)oxides and of a single precipitation event. However, the discrepancy between the two types of iron (oxyhydr-)oxides supports the above hypothesis. The strongly scattered eU,  $\delta^{18}\text{O}$  and  $\delta\text{D}$  values but concentrated GHe ages of botryoidal samples indicate their precipitation from mineralizing fluids of evolving and fluctuating compositions. The contrasting little scattered eU,  $\delta^{18}\text{O}$  and  $\delta\text{D}$  values of pyrite-pseudomorphosing samples confirms the *in situ* pseudomorphose over long periods, with the stable U contents only depending on the initial U concentration of pyrite.

Another indication of the precipitation of botryoidal goethite from evolving fluids and of the *in situ* formation of pyrite is the divergence between the scattered  $\delta^{18}\text{O}$  and  $\delta\text{D}$  values of botryoidal goethite contrasting with the very similar values of pseudomorphosing samples.

### 6.3.4.c Role of geodynamic during weathering periods

#### High Atlas

The progressive filling of a fracture at Jbel Klakh involved the precipitation of numerous generations of goethite and obviously staggered over several millions of years between Late Oligocene and Miocene (Fig. 6.3.5J). These High Atlas GHe ages are consistent with the polyphased Cenozoic deformation phases (noted D<sub>1</sub> to D<sub>3</sub>) related to convergence processes between Africa and Europe, defined in the High Atlas by Leprêtre et al. (2015, 2018). GHe ages obtained for Jbel Rhals, Jbel Haouanit and Jbel Klakh samples effectively correlate with the second and third erosional phases of Leprêtre et al. (2018), extending in Early-Middle Miocene (D<sub>2</sub>) and Late Pliocene-Quaternary (D<sub>3</sub>), respectively. As suggested by these authors, the most recent uplift phase (D<sub>3</sub>) is responsible for most of the Cenozoic topographic building of the High Atlas, and thus for bringing rocks to the surface by large upward movements. The concordance between GHe ages and these uplift phases highlights the relation between uplifts, weathering processes and thus supergene ore formation. Evidences of iron (oxyhydr-)oxides formation in relation with the first Cenozoic erosional phase (D<sub>1</sub>) of Leprêtre et al. (2018) could not be highlighted here. This may be attributed to the localization of the studied deposits at the extreme west boundary of the High Atlas of the belt, where the initial steps of the deformation could have been delayed or less marked.

#### Anti-Atlas

In the Anti-Atlas, one would have expected to obtain similar ages for iron (oxyhydr-)oxides originating from the very similar Agoujgal and Tazalaght supergene deposits, but this is not the case. Only young ages are acquired for Agoujgal samples; the spread of pyrite-pseudomorphosing ages in Miocene and Pleistocene is due to the progressive replacement of pyrite by several generations of goethite and hematite, in accordance with the environmental conditions (Fig. 6.3.5B, 6.3.5C). The precipitation of Agoujgal microcrystalline and botryoidal goethite is more recent (Late Miocene – Pliocene) and characterized by much more various U concentrations. At Tazalaght, the formation of iron (oxyhydr-)oxides is much older; the precipitation of botryoidal goethite extends in Late Cretaceous, and Late Paleocene to Early Eocene, while the vastly expanded and unreproducible GHe ages of pseudomorphs would indicate precipitation processes between Upper Cretaceous and Late Oligocene. The Pleistocene botryoidal goethite of Tassirt is again much younger than the strongly scattered

Paleogene-Miocene ages of pyrite-pseudomorphosing mixed hematite and goethite (Fig. 6.3.5E). At Tizert, both microcrystalline and botryoidal goethite provided reproducible Paleogene ages. At Ighrem, Assifid and Irkhs, botryoidal goethite present reproducible ages, in the Late Eocene-Early Miocene, Late Cretaceous – Early Paleocene, and in Early Eocene, respectively; no relation could be highlighted between these GHe ages and the geographic position of samples. The absence of relation between GHe ages and the position of the studied deposits or gossans tends to suggest that if climatic conditions were generally similar at this scale of the Anti-Atlas, they may have experienced differential deformation arising from their variable geodynamic features. As pointed out by Choulet et al. (2014), the differential deformation, either between inliers or in a same inlier, directly impact the local amount of uplift and erosion, and also controls the water table level and the ability to concentrate metals. Differential deformation could thus be responsible, here, for the strongly varying ages between the studied Anti-Atlas sites. Recurrent alternation of wet and dry periods could have accentuated the trend described above.

At the contrary of the High Atlas where goethite was sampled within a 50 km-radius area presenting a relatively homogenous geology, iron (oxyhydr-)oxides originating from the Anti-Atlas were collected in different inliers presenting various geologic histories, over more than 100 km. The relatively poor GHe ages concordance between Anti-Atlas samples could be attributed to this geographical and geological scattering of samples and to differential deformation (see above). However, GHe are broadly consistent with the end of exhumation episodes recently described in the Moroccan Atlas. First, the Late Cretaceous to Paleocene ages of Assifid, Tazalaght and Irkhs iron (oxyhydr-)oxides are coeval with the end of the wide-scale Late Cretaceous deformation phase ( $D_0$ ) reported by Gouiza et al. (2017) and Seht et al. (2018) in the northwestern Anti-Atlas, by Froitzheim (1984), Domènech et al. (2016) and Leprêtre et al. (2018) in the High Atlas, by Hafid et al. (2006) in the Moroccan offshore, and by Khomsi et al. (2016) in Tunisia. Gouiza et al. (2017) illustrate the existence of major vertical movements through Mesozoic and Cenozoic times in the Anti-Atlas, indicating than the effects of Atlantic and Tethys Oceans rifting and drifting extended beyond their presumed margins, since the belt has for a long time only been interpreted as of Variscan age. More precisely, they demonstrate on the basis of AFT and AHe ages (Sebti et al. 2009; Ruiz et al. 2011; Seht 2014; Gouiza et al. 2017) that, between Late Cretaceous and Cenozoic, in the entire Anti-Atlas, and possibly, Morocco, basement rocks were slowly brought to the surface to their present-day elevation after experiencing 2 – 3.5 km of exhumation. Even if, in the Anti-Atlas, the Cenozoic precipitation of iron (oxyhydr-)oxides in response to uplifts and weathering, and consequently, the deformation itself, seems less concentrated in episodes but more expressed as a wide-scale deformation, the Cenozoic GHe ages obtained in this study for the Anti-Atlas also correlate, to a certain extent, with the beginning and/or end of deformation phases observed by Leprêtre et al. (2015, 2018). The Late Eocene – Early Miocene GHe ages of Tassirt, Ighrem and Tizert iron (oxyhydr-)oxides correlate with the end of the  $D_1$  phase (Leprêtre et al. 2018). The Late Miocene – Quaternary ages of Agoujgal and Tassirt goethite correspond to the end of the  $D_2$  phase and to the beginning of the final  $D_3$  major pulse of Leprêtre et al. (2018).

The correspondence between GHe ages presented in this paper and exhumation episodes described above, as well in the Anti-Atlas as in the High Atlas, suggests that the formation of iron (oxyhydr-)oxides in relation with weathering processes could ensue from, and be driven by, exhumation phases (Fig. 6.3.12).

Significant lack of fit between our GHe ages and Cenozoic: 1) warmest climatic periods in North Africa (Late Paleocene- Early Eocene Thermal Maximum; Stott and Kennett, 1990), or 2) wet/humid periods (Late Pleistocene African Humid Period (Pokras and Mix 1987; DeMenocal et al. 2000), Late Tortonian

– Messinian Zeit Wet Phase (Griffin 2002)), or 3) more arid times (Pliocene-Pleistocene; Feakins and DeMenocal, 2010) suggests that weathering processes are moderately regulated by temperatures and precipitations. These observations match with the conclusions of De Putter et al. (2015), Fontaine et al. (2020) and De Putter and Ruffet (2020), which suggested that the formation of supergene ores in Central Africa directly mainly results from tectonics, while climatic controls are of second-order. The relative alignment of pseudomorphosing samples on an age vs. altitude graph, at the contrary of the botryoidal goethite of Tizert, Assifid and Irkhs ties in with the idea of various precipitation processes (Fig. 6.3.11). The *in situ* pseudomorphose of pyrite and siderite is probably directly related with the altitude of the initial sulfide and consequently to eventual exhumation process, but also to the climatic conditions and fracturing (Fig. 6.3.12). On the contrary, the formation of botryoidal goethite from fluids that can percolate *per descensum* before precipitation is not *in situ* process linked to the altitude of an initial mineral: such minerals may not align on a linear age vs altitude plot (Fig. 6.3.11).

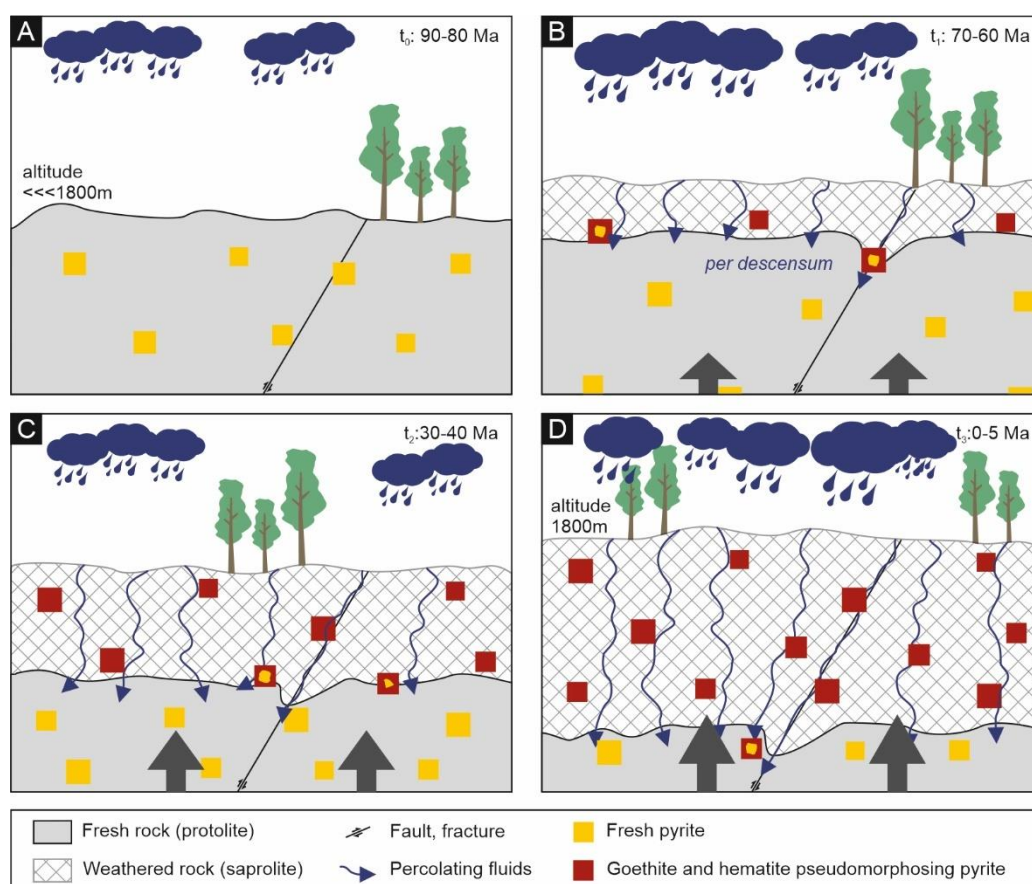


**Figure 6.3.12.** Sketch highlighting the relation between geodynamic conditions in the studied areas and the pseudomorphosis of pyrite by iron (oxyhydr-)oxides.

### 6.3.5 Conclusion

Twenty-four samples from three ore deposits of the High Atlas (Jbel Rhals, Jbel Haouanit and Jbel Klakh) and nine sites of the Anti-Atlas (Tazalaght, Agoujgal, Tassrirt, Tizert, Ighrem, Assifid, Irkhs) were dated with the (U-Th-Sm)/He method. We concluded that botryoidal goethite are the best samples for (U-Th-Sm)/He dating since their pure composition allows the obtention of representative results, while pseudomorphosing samples are the worst because of their common intermixed goethite and hematite generations. Microcrystalline samples are in the middle rank and powdery iron (oxyhydr-)oxides are in no way datable. Various divergences between botryoidal and pseudomorphosing samples characteristics (textures,  $\delta^{18}\text{O}$ ,  $\delta\text{D}$ , eU, minor elements contents) highlight and confirm their different formation processes: pseudomorphs formed *in situ*, while the precipitation of botryoidal goethite, either as old thick layers or as very recent thin layers, implicates the circulation of mineralizing fluids.

The formation of iron (oxyhydr-)oxides in the High Atlas may be linked to two Cenozoic uplift phases already defined in the Atlas (Leprêtre et al. 2015). Similarly, the formation of pseudomorphosing and botryoidal iron (oxyhydr-)oxides in the Anti-Atlas match with Late Cretaceous and Cenozoic uplift phases (Leprêtre et al. 2015; Gouiza et al. 2017). Our data therefore suggest that the formation of supergene mineralization, and particularly of iron (oxyhydr-)oxides, could ensue from, and be driven by, exhumation phases. It is consequently proposed that the exhumation of preexisting mineralization and/or of host rocks is a key process required for the formation of supergene ore deposits and gossans. Differential deformation between studied sites is tentatively suggested as a hypothesis to explain the absence of relation between iron (oxyhydr-)oxides sampling localization and GHe ages. Understanding weathering requires thus an integration not only of geochemical and climatic features, but also of geodynamic features.

## 6.4 K-Ar dating of Moroccan alunite

This chapter focuses on the dating of alunite. These distinct analyses have been carried out to provide more information on the timing of weathering and oxidation processes in the supergene deposits presented in chapter 6.3, and to tentatively confirm the relation between supergene mineralization and geodynamic events. Additionally, this study aims at combining GHe and alunite K-Ar ages of samples collected in the same deposits in order to compare the results of both the methods.

Alunite is a relatively common mineral in supergene profiles and has been dated successively with the K-Ar and  $^{40}\text{Ar}/^{39}\text{Ar}$  methods to constrain the timing of oxidation in copper deposits of Chile, Peru, North America (see Sillitoe and Mckee 1996, Alpers and Brimhall 1988, Vasconcelos 1999, Sillitoe 2019 and references therein). However, despite its widespread distribution and local abundances in supergene profiles, relatively little research has been conducted on dating supergene alunite from Morocco.

### 6.4.1 Geologic context

See chapter 6.3.1 and Fig. 6.4.1 and 6.4.2 for localization of samples.

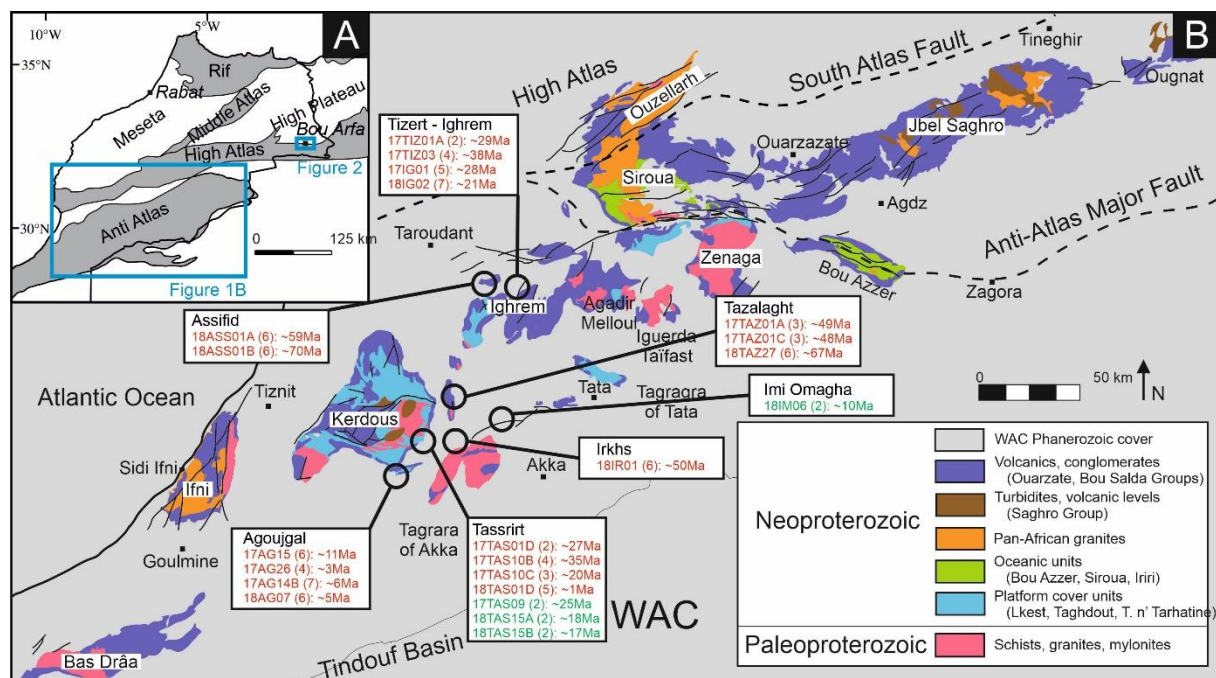


**Figure 6.4.1.** (A) Simplified geologic map of Morocco, with the studied areas framed in blue. (B) Geologic map of the Anti-Atlas providing the location and average goethite (U-Th-Sm)/He (red) and alunite K-Ar (green) ages of Agoujal, Tazalaght, Tassart, Irkhs, Assifid, Tizert, Ighrem, and Imi Omagha sites along the aligned Precambrian inliers (modified after Gasquet et al. 2008; Ikenne et al. 2017).

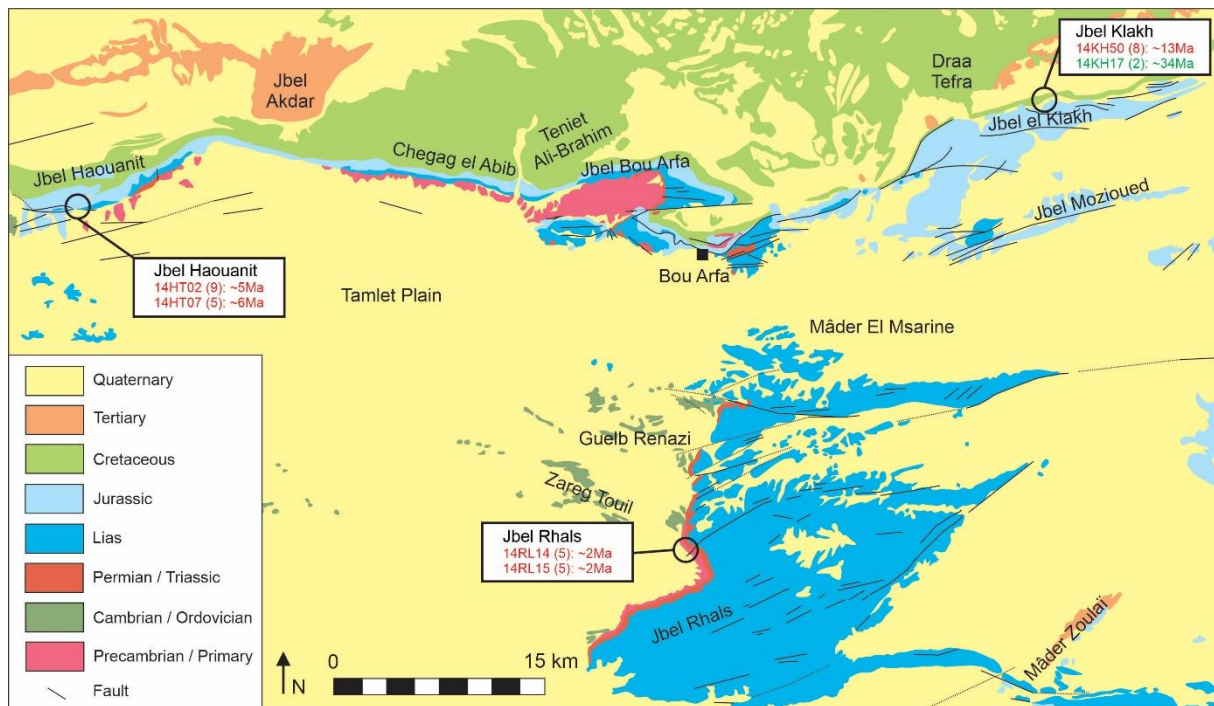


**Figure 6.4.2.** Geologic map of the Bou Arfa district in the Oriental High Atlas, providing the location and average goethite (U-Th-Sm)/He (red) and alunite K-Ar (green) ages of Jbel Haouanit, Jbel Klakh, and Jbel Rhals sites (modified after Chefchaouni et al. 1963).

### 6.4.2 Methodology

Five samples collected at Jbel Klakh (14KH17), Tassrirt (17TAS09, 18TAS15A, 18TAS15B) and Imi Omagha (18IM06) were selected. The material for dating was collected from the central parts of the irregularly distributed veinlets to avoid contamination by other K-bearing phases such as muscovite inherited from the host rock. Whole rock X-ray diffraction has been carried on all five samples with a Philips Analytical X-ray diffractometer to identify the major mineral phase that must be alunite. Polished sections of 17TAS09, 18TAS15A, 18TAS15B and 18IM06 have been observed with a Jeol JSM-7500F scanning electron microscope (SEM) (JEOL, Tokyo, Japan) coupled to an energy dispersive electron spectrometer (EDS) to verify the absence of contaminants such as muscovite.

Samples submitted for K-Ar whole rock analysis in the Activation Laboratories (Actlabs, Ontario, Canada) were first crushed to fragments. Two analyses were performed for each sample. At Actlabs, analyses are carried out according to the following protocol. Aliquots are weighted into Al container, loaded into sample system of extraction unit, and degassed at ~100°C during two days to remove surface gases. Argon is extracted in a double vacuum furnace at 1700°C. The determination of radiogenic argon content is carried out twice on a MI-1201 IG mass-spectrometer by isotope dilution method with  $^{38}\text{Ar}$  as spike, which is introduced to the sample system prior to each extraction. The extracted gases are cleaned up in two step purification system. Then pure Ar is introduced into the custom-built magnetic sector mass spectrometer (Reinolds type). Each test is done twice to ensure the consistency of the results. Two globally accepted standards are measured for  $^{38}\text{Ar}$  spike calibration: Bern 4M Muscovite ( $18.6 \pm 0.4$  Ma) (or P-207 Muscovite) and 1/65 "Asia" rhyolite matrix ( $262.7 \pm 1.0$  Ma). For K analysis, aliquot of the sample is weighted into a graphite crucible with lithium metaborate/tetraborate flux and fused using a LECO induction furnace. The fusion bead is dissolved with acid. Standards, blanks and sample are analyzed on an ICP Spectrometer. For age calculations, international values of constants are used as follow:  $^{40}\text{K}\lambda_e = 0.581 \cdot 10^{-10} \text{y}^{-1}$ ,  $^{40}\text{K} \lambda_\beta = 4.962 \cdot 10^{-10} \text{y}^{-1}$ ,  $^{40}\text{K} = 0.01167$  (at.%).



### 6.4.3 Results

Sample 14KH17 is composed of pure white powdery alunite (Fig. 6.4.3A). Sample 17TAS09 consists dominantly of alunite, but minor muscovite, quartz and fraipontite are also present (Fig. 6.4.3B). Only the white powdery section of the sample, almost pure alunite, was selected for dating (Fig. 6.4.3B). Samples 18TAS15A and 18TAS15B are light green massive cryptocrystalline, “porcelaneous” alunite that contains minor interstitial kaolinite and goethite (Fig. 6.4.3C). The purest areas were selected for dating (Fig. 6.4.3C). Sample 18IM06 is an almost pure white cryptocrystalline alunite, with minor dolomite (Fig. 6.4.3D).

This chapter reports ten new K-Ar ages for five supergene alunite (Table 6.4.1). For the five samples, the reproducibility between the two dated aliquots is remarkable. In the High Atlas, Jbel Klakh alunite provides ages of  $35.5 \pm 0.7$  and  $31.4 \pm 0.7$  Ma. In the Anti-Atlas, Tassirt white alunite is dated at  $25.1 \pm 0.5$  and  $24.9 \pm 0.4$  Ma, while the green-tinted porcelaneous alunite provide ages of  $18.2 \pm 0.4$ ,  $18.6 \pm 0.3$ ,  $16.7 \pm 0.4$  and  $17.1 \pm 0.3$  Ma. The Imi Omagha alunite is the youngest, with ages of  $9.8 \pm 0.2$  and  $9.6 \pm 0.2$  Ma.

**Table 6.4.1.** Alunite K-Ar data.

Sample Number	K (%)	$\pm s$ (%)	$^{40}\text{Ar}_{\text{rad}}$ (nl/g)	$\pm s$ (%)	$^{40}\text{Ar}_{\text{air}}$ %	Age (Ma)	$2\sigma$ (Ma)
<u>Jbel Klakh</u>							
14KH17-1	5.90	0.06	14.68	0.07	18.3	<b>35.5</b>	<b>0.7</b>
14KH17-2	5.96	0.06	13.09	0.04	12.5	<b>31.4</b>	<b>0.7</b>
<u>Tassirt</u>							
17TAS09-1	6.58	0.07	11.54	0.04	18.5	<b>25.1</b>	<b>0.5</b>
17TAS09-2	6.58	0.07	11.43	0.12	22.6	<b>24.9</b>	<b>0.4</b>
18TAS15A-1	7.29	0.08	9.26	0.03	10.9	<b>18.2</b>	<b>0.4</b>
18TAS15A-2	7.38	0.08	9.51	0.10	15.0	<b>18.6</b>	<b>0.3</b>
18TAS15B-1	7.15	0.07	8.30	0.03	15.8	<b>16.7</b>	<b>0.4</b>
18TAS15B-2	7.24	0.08	8.53	0.11	15.7	<b>17.1</b>	<b>0.3</b>
<u>Imi Omagha</u>							
18IM06-1	6.92	0.07	4.72	0.02	31.5	<b>9.8</b>	<b>0.2</b>
18IM06-2	6.86	0.07	4.58	0.08	28.4	<b>9.6</b>	<b>0.2</b>

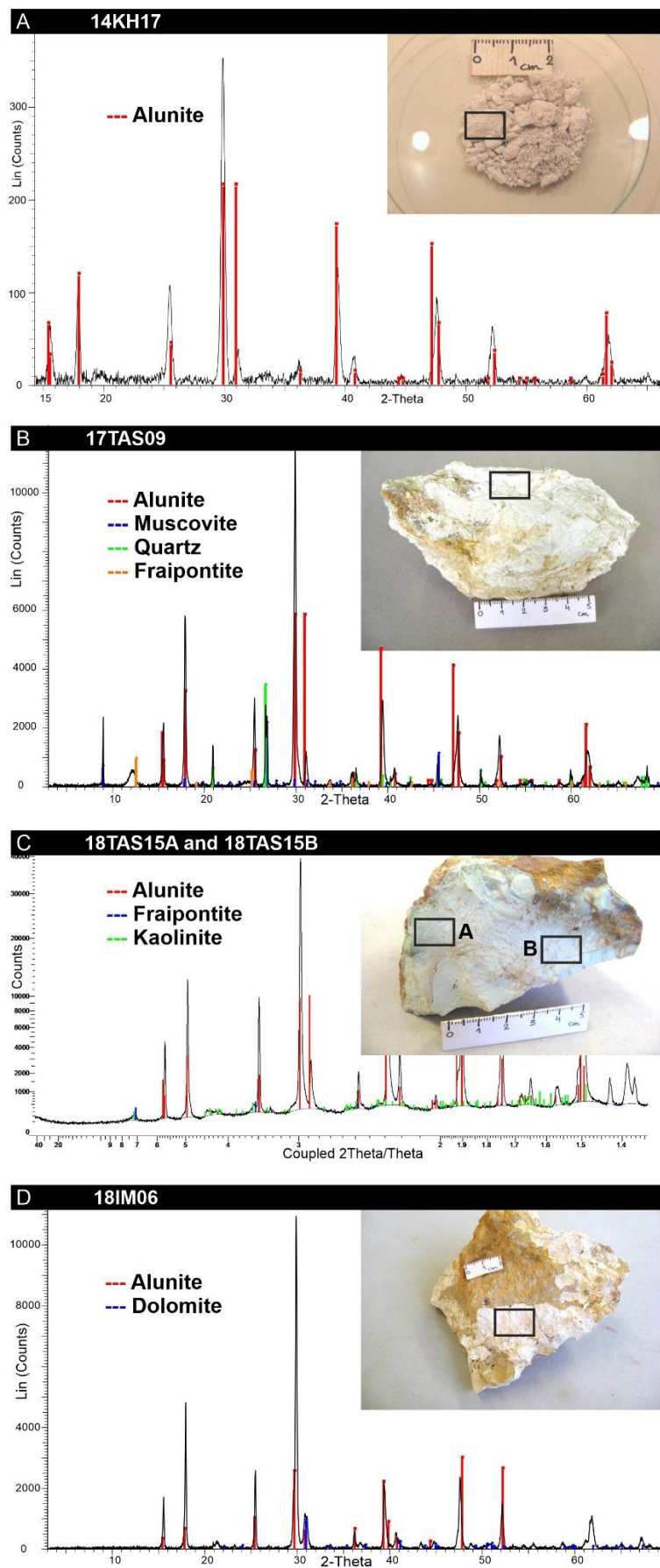


**Figure 6.4.3.** XRD diagrams and pictures of the five alunite samples dated with K-Ar method.



#### 6.4.4 Discussion

Since alunite forms under acidic conditions (Hemley et al. 1969), it is mostly found in areas where abundant pyrite is undergoing oxidation, in or beneath gossans dominated by iron (oxyhydr-)oxides or jarosite (Nordstrom 1982; Bladh 1982). Following Ague and Brimhall (1989), alunite formation ceases once pyrite oxidation stops. At Jbel Klakh, Tassirt and Imi Omagha, the initial presence of hypogene pyrite is attested by the numerous pseudomorphoses of this sulfide and the large iron (oxyhydr-)oxides amounts in their gossan (e.g. 6.1.4A, 6.1.4D, 6.1.4E, 6.1.4K). Therefore, it could be inferred that alunite formation results from the oxidation of pyrite in these deposits. The intimate association of alunite with other supergene mineral phases (goethite, hematite, fraipontite) also confirms its supergene formation in the oxidized or leached zone, and discredits its presence as the result of inheritance from precursor sulfide zones (as suggested by Alpers and Brimhall 1988 in the Central Andes). Substitution of  $\text{Fe}^{3+}$  and  $\text{Cu}^{2+}$  for some  $\text{Al}^{3+}$  in the alunite structure probably gave rise to the light green coloration of 18TAS15A and 18TAS15B (Alpers et al. 1992). Once precipitated, alunite is relatively stable in the presence of meteoric water in the surficial environment; it may be however unstable when exposed to saline groundwater (Vasconcelos 1999). Therefore, the presence of alunite in weathering profiles is interpreted to record a transition toward arid conditions (Alpers and Brimhall 1988; Bird et al. 1990; Vasconcelos 1999). Here, at Jbel Klakh, Tassirt and Imi Omagha, there is no evidence of dissolution and recrystallization processes.

The ten K-Ar ages provided in this study are relatively coeval with the GHe ages obtained for the deposits. At Jbel Klakh, Late Eocene alunite is about 10 Ma older than the Miocene goethite. This divergence could ensue from the environment of formation of the dated samples: the alunite is associated with other supergene mineral phases, whereas the goethite is found in a fracture that could have been filled later than the main supergene mineralization. Another explanation of this divergence could be that (locally), during the early weathering steps, evaporative concentration of supergene solutions may have played a role in supergene alunite formation (Long et al. 1992). Arid conditions indeed result in a restricted dilution of supergene fluids, and hence lower pH values and greater sulfate activities promoting the precipitation of alunite. At Tassirt, the ~25 and ~17-18 Ma ages of alunite slightly correspond with the previously acquired scattered GHe ages. Since the iron (oxyhydr-)oxides dated with the (U-Th-Sm)/He method presented several problems of contaminations (see chapter 6.3), such correspondences must be viewed cautiously. However, the Late Oligocene – Early Miocene K-Ar ages are consistent with the similar ages of several aliquots of goethite pseudomorphosing pyrite, at Tassirt. This may suggest that the oxidation of pyrite and the precipitation of alunite under low pH conditions was rapidly followed by the formation of iron (oxyhydr-)oxides at Tassirt, thanks to a rapid neutralization through host rock dissolution. Another argument for this hypothesis is the intimate association of alunite and iron (oxyhydr-)oxides at Tassirt, and the absence of other sulfates resulting from pyrite oxidation. All ionic sulfur must have been rapidly involved in alunite formation. This would confirm that the supergene alunite radiometric ages effectively date the oxidation of pyrite concentrations, as suggested, among others, by Vasconcelos (1999) and Sillitoe (2019). At Imi Omagha, no (U-Th-Sm)/He analyses have been carried out, despite the presence of (pyrite- pseudomorphosing) iron (oxyhydr-)oxides. However, these very young Tortonian ages match with young ages obtained for iron (oxyhydr-)oxides at Agoujgal deposit, and corroborate the hypothesis of significant Late Miocene weathering processes.

The matching of the Late Eocene K-Ar ages of Jbel Klakh with the  $D_1$  uplift phase of Leprêtre et al. (2018), and of the Tassirt Late Oligocene – Early Miocene ages with the early steps of the  $D_2$  deformation phase supports the previously discussed hypothesis of supergene mineralization in relation with geodynamic events. Again, differential deformation between studied sites is tentatively

proposed to explain the absence of relation between alunite K-Ar ages. Further K-Ar dating of alunite samples collected in the High Atlas and Anti-Atlas of Morocco are necessary to ascertain these hypotheses.

## 6.5 New (U-Th)/He dating of mixed and polyphase alteration processes in the vertebrate-bearing Nefza-Sejnane polymetallic mining district (Tunisia)

The mining district of Nefza-Sejnane contains numerous ores and raw materials deposits, including the oxidized Zn–Pb Sidi Driss and vertebrate-bearing Douahria Sedex deposits (Decrée et al. 2008), the halloysite-bearing iron deposit of Tamra Formation (Decrée et al. 2008, 2010b; Moussi et al. 2011; Dekoninck et al. 2018), the LREE-U breccia of Oued Belif (Decrée et al. 2013), and kaolinitic clays of the late Oligocene Numidian Flysch Formation (Chargui et al. 2018; Moussi et al. 2020) (Fig. 6.5.1, 6.5.2). From Miocene times, these deposits experienced successive circulations of Fe-rich fluids of mixed meteoric and hydrothermal origins. The hydrothermal activity ensues from relatively high geothermic gradient and Miocene magmatic rocks of the area (Jallouli et al. 2003). Using geochemical arguments, Decrée et al. (2014) demonstrated that emplacement of magmatic rocks has enhanced hydrothermal fluid circulations, leading to the deposition of polymetallic mineralization. Alternatively, significant periods of weathering are confirmed by i) pedogenesis on sediments located within small basins such as in Tamra basin and the deposition of the subaerial Tamra Formation (Decrée et al. 2008), and ii) late supergene fluids leading to the formation of botryoidal or euhedral goethite (Decrée et al. 2013; Dekoninck et al. 2018). The nature and role of meteoric circulations in metal enrichment of the area has already been stressed by Decrée et al. (2008, 2010) and discussed by Dekoninck et al. (2018) using  $\delta D$  and  $\delta^{18}O$  on halloysite-kaolinite and Fe (oxyhydr)-oxides, and by Decrée et al. (2008c) using iron isotopes and chemical composition of Fe-(oxi)hydroxides. However, refined ages of these meteoric influences in this area are still lacking, jeopardizing the regional integration of the ore formation. Furthermore, the Douahria Fe-deposit contains the famous “Pikermian” vertebrate fauna, including a rhinocerotid, a giraffid, and an anthracotheriid originally described by Roman and Solignac (1934) in a ferruginous crust. Here we provide, for the first time in Tunisia, new (U-Th)/He ages on goethite (GHe ages) associated with weathering processes in the vertebrate-bearing Nefza-Sejnane polymetallic mining district. Matched with previous data, these new investigations allow us to discuss i) the influences of meteoric fluids in the formation of ore deposits in this main mining district of Tunisia, and ii) the role of geodynamic and climatic parameters in weathering processes, at a regional scale. Moreover, we propose a global revision of the mammalian assemblage, aiming at providing updated taxonomic assignments for the concerned remains, and at discussing their biostratigraphical outputs, in order to further confront GHe ages and paleontological dating.

### 6.5.1. Geological setting

The Nefza-Sejnane mining district is located in the Tellian “Nappe Zone” of Northern Tunisia (Fig. 6.5.1, 6.5.2). The district is characterized by the occurrence of late Cenozoic mineral deposits, overlying a substratum comprising folded marls Albian to late Priabonian in age, and Chattian-Burdigalian Numidian Flysch Formation (Riahi et al. 2010), present as thrust sheets in the Tellian “Nappe Zone” (Rouvier 1994). The regional felsic sub-volcanic rocks emplaced between  $12.9 \pm 0.5$  Ma and  $8.2 \pm 0.4$  Ma (Serravallian to Tortonian; e.g. Jallouli et al. 2003), while basaltic flows of the Zouara basin (Fig. 6.5.2) were dated between  $8.4 \pm 0.4$  Ma and  $6.4 \pm 0.15$  Ma (Rouvier 1977). The Ghardimaou-Cap Serrat (G-CS) sinistral fault zone (Rouvier 1977), a major regional structure guiding Alpine tectonics at the tectonic plate scale, and the regional N80°E lineaments controlled the magmatism and subsequent mineralization (Fig. 6.5.1, 6.5.2; Decrée et al. 2016). The first notable mineralization event in the area was associated to a major brecciation episode and led to the formation of the ring-shaped Oued Belif LREE-U hematite breccia (Decrée et al. 2013). The origin of this breccia is most likely related to the mixing of magmatic-hydrothermal fluids and basinal (evaporite) brines. K-Fe alteration event, slightly predating the main mineralization, is dated at  $9.2 \pm 0.25$  Ma using K-Ar method on K-feldspars (Decrée

et al. 2013). The main LREE-U mineralization is coeval with a major episode of brecciation, most likely associated to the emplacement of the Oued Belif rhyolite intrusion. The remaining voids are filled with goethite, which, in some areas, is mixed with kaolinite and Ba-Mn oxide. The two Sedex deposits (Sidi Driss and Douahria; Fig. 6.5.2) are attributed to formation by thermally-driven circulating fluids related to magmatism and reactivation of shear zones during late Miocene extension in small basins (Decrée et al. 2016). The Pb-Zn ore of Sidi Driss is correlated with the stratified Fe-ore of Douahria, which yielded a large mammalian assemblage, late Miocene in age (e.g. Guérin 1966; Geraads 1989; Harris et al. 2010). The Tamra basin, unconformably overlying the Sidi Driss basin, is the host for iron mineralization in the form of a 50 m thick succession (Tamra Formation) of iron hydroxide-bearing sediments together with kaolinite-halloysite lenses (Decrée et al. 2008; Moussi et al. 2011; Dekoninck et al. 2018). Previous dating on hollandite  $[\text{Ba}(\text{Mn}^{4+}, \text{Mn}^{2+})_8\text{O}_{16}]$  and coronadite  $[\text{Pb}(\text{Mn}^{4+}, \text{Mn}^{2+})_8\text{O}_{16}]$  of the Tamra mine yielded Pliocene K-Mn ages (Decrée et al. 2010). The dated K-Mn oxides relate to mineralizing events closely connected with hydrothermal circulation and leaching of underlying mineralization of the Sidi Driss Pb-Zn Sedex type deposit (Decrée et al. 2010; Dekoninck et al. 2018). At Tamra, the  $\delta\text{D}$  and  $\delta^{18}\text{O}$  of halloysite-kaolinite are not in equilibrium with the potential Mio-Pliocene meteoric fluids, confirming that they could be related to fluid-rock interactions with the underlying ores, marls and/or skarns (Dekoninck et al. 2018). Late mineralization of galena, pyrite and siderite in sub-vertical fractures cut the whole sequence of the district and are associated with a new hydrothermal event, still active in the area with numerous hot springs from 35°C up to 70°C and regional thermal gradients up to 100°C/km (Jallouli et al. 2003). Recent circulation of hydrothermal fluids is moreover evidenced by K-Ar dating of adularia around c. 0 in the Oued Belif breccia (Decrée et al. 2013).

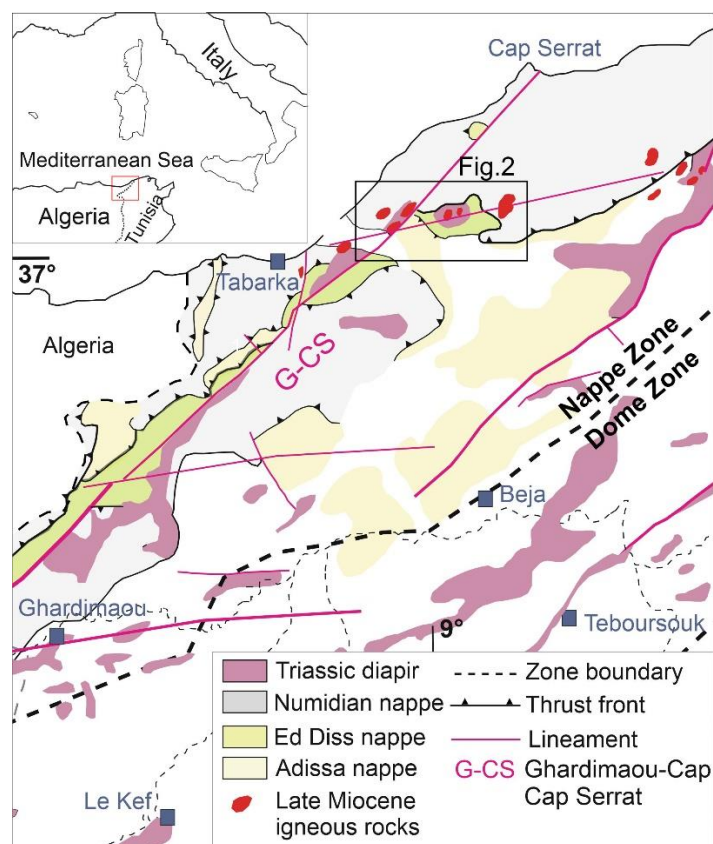


**Figure 6.5.1.** Tectonic map of central and northern Tunisia, showing the location of the studied area (modified after Rouvier 1985; Bouaziz et al. 2002; Decrée et al. 2016; Dekoninck et al. 2018).

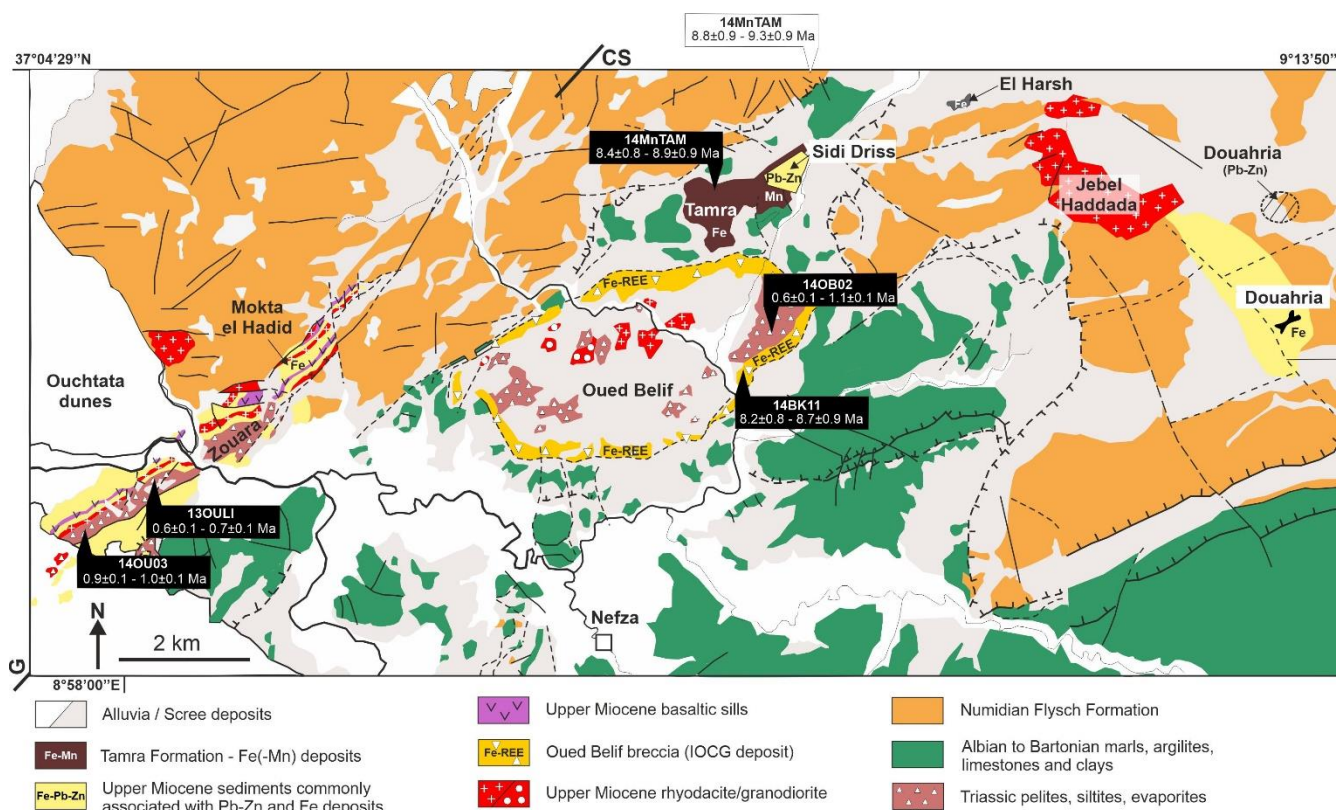


**Figure 6.5.2.** Simplified geologic map of the Nefza-Sejnane district, Tunisia (modified after Decrée et al. 2013), showing the location and (U-Th)/He corrected ages of the supergene goethite. G-CS = Ghardimaou Cap Serrat sinistral fault zone.

### 6.5.2. Materials and methods

Samples of iron (oxyhydr-)oxides were collected in the Tamra Fe-mine, the Boukhchiba Fe-mine, the Oued Belif LREE-U breccia, and the Ouchtata area-Zouara basin (Fig. 6.5.2; Table 6.5.1). Sample 14MnTAM was collected in the upper part of the Tamra mine, within the manganiferous zone (Decrée et al. 2010). It contains pure, well crystallized goethite with botryoidal texture (Fig. 6.5.3A-6.5.3B), associated to pedogenesis of the Tamra Formation (Dekoninck et al. 2018). The 14TAM07 sample, also collected in the Tamra mine, show a mixture of goethite and hematite, with potential influences of both weathering and hydrothermal origins, as attested by the occurrence of hematite and Mn(Pb)oxides (Fig. 6.5.3C-6.5.3D). The 13NEFZA sample, also collected in the Tamra mine, corresponds to Fe-indurations of the intermediate part of the sequence defined by Decrée et al. (2008). This sample contains hematite and displays hydrothermal influences according to  $\delta D$  and  $\delta^{18}O$  data from Dekoninck et al. (2018) for samples CP04-3 and CP04-35 (very similar to sample 13NEFZA). The 14BK11 sample comes from a mineralized vein in the Boukhchiba Fe-mine (Fig. 6.5.2), clearly cross-cutting the LREE-U iron-bearing breccia described in Decrée et al. (2013). The sample contains very pure, well-crystallized and homogeneous goethite (Fig. 6.5.3E-6.5.3F), that precipitated in equilibrium with meteoric waters (Dekoninck et al. 2018). The 14OU03 and the 13OULI samples were collected in the Ouchtata area (Fig. 6.5.2). They consist on several generations of goethite pseudomorphosing grains of pyrite of the Triassic sediments. "Ouchtata" sample in Dekoninck et al. (2018), similar to 13OULI sample, was associated to meteoric fluids by the latter authors. Sample 14OB02 was collected in mineralized vein of the Oued Belif locality. It contains goethite, mixed with euhedral quartz and K-feldspars (Fig. 6.5.3G-6.5.3H). The goethite of this sample was considered as supergene (below the water table) by Decrée et al. (2013). The isotopic data of this sample are logically away from the meteoric equilibrium water line (Dekoninck et al. 2018), due to mixing with quartz and K-feldspars. Ferruginous crust from the



mammal-bearing Douahria site was also sampled in order to perform (U-Th)/He dating. The latter, however, contains large amounts of mixed hydrothermal Fe-Mn phases, and could thus not be analyzed with the (U-Th)/He method.

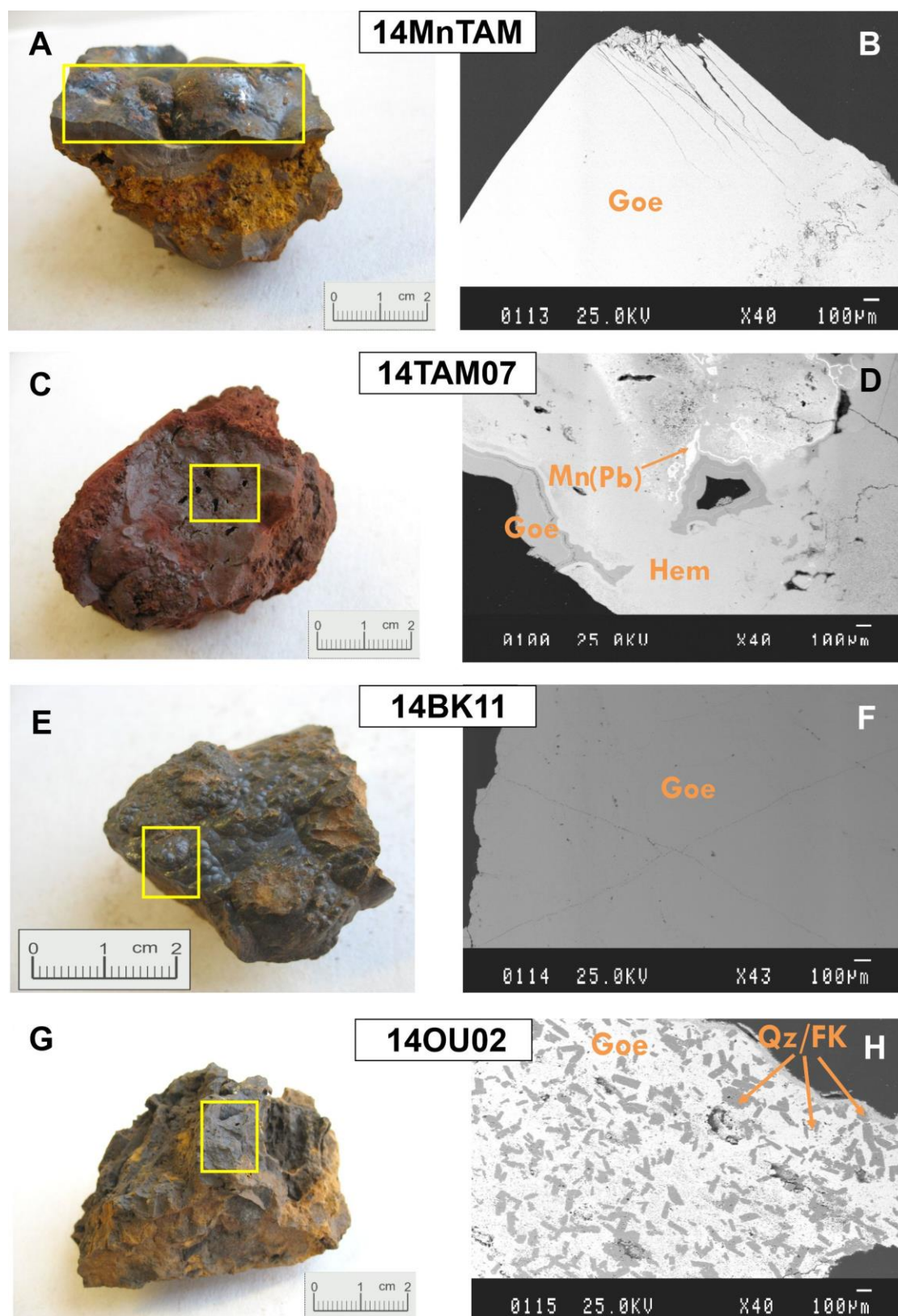


**Figure 6.5.3.** Samples of studied goethite and SEM microphotograph in back scattered electrons mode, showing the pure character of supergene goethite of samples 14MnTAM and 14BK11.

The mineralogy of samples was characterized using an X-ray Panalytical X'Pert Pro and a Philips diffractometer (CuK $\alpha$  radiation), and a JEOL JXA-8600 SUPERPROBE scanning electron microscope (SEM) coupled to an energy dispersive electron spectrometer (EDS).

The (U-Th)/He dating method relies on the  $^4\text{He}$  production, ejection and accumulation inside the crystal structure during alpha decay of the radioactive U-Th chains (Farley 2002). The (U-Th)/He age is determined by measuring the total He content of the samples and in a second step, the total U and Th content. (U-Th)/He ages were obtained in the GEOPS laboratory (University Paris-Sud, Orsay, France) for three aliquots per sample, except for 14BK11 where only two aliquots were analyzed. For samples composed of several iron (oxyhydr-)oxides generations, the purest zones were selected to avoid the obtention of erroneous and meaningless ages. First, fragments manually extracted from the hand-sized samples were cleaned using an ultrasonic bath and rinsed with milli-Q water and ethanol. Aliquots were handpicked under a binocular microscope, weighed and encapsulated into niobium envelopes (purity 99.9 %). Fragments with a length exceeding 0.5 mm and a weight around 0.5 mg for 14OU03 sample and ranging between 6 and 18 mg for other samples were selected. Each encapsulated sample was degassed using a diode Ytterbium laser under vacuum for thirty minutes at temperatures below 1000°C. This procedure was repeated until all  $^4\text{He}$  was degassed. The  $^4\text{He}$  gas was mixed in the purification line with a known amount of  $^3\text{He}$ , and purified. Helium isotopes ( $^3\text{He}$  and  $^4\text{He}$ ) were measured with a Pfeiffer Prisma Quadrupole mass spectrometer to ensure the purity of the analytical gas (see Allard et al. 2018, for more details). After degassing, samples were extruded from the envelopes directly into 5 mL Teflon-capped vials for complete dissolution. Firstly, 100 mL of 5M  $\text{HNO}_3$  containing a known amount of  $^{230}\text{Th}$  and  $^{235}\text{U}$  was introduced in each vial followed by 200 mL of 30% HCl, and a few drops of 38% HF. Vials were closed and heated up to 70°C overnight. Solutions were evaporated at 180°C to concentrate the sample. If samples were not completely dissolved, the procedure of adding HCl and HF was repeated. Secondly, 5 mL of 5M  $\text{HNO}_3$  was added to the final solution that was heated for one hour at 100°C. The solution was diluted with 1M  $\text{HNO}_3$  to set the iron content at 100 ppm. The U and Th measurements were undertaken by using a quadrupole ICP-QMS series<sup>II</sup> CCT Thermo-Electron at LSCE (Gif sur Yvette, France). The analytical error for He and U-Th measurements is 5% at 1 $\sigma$ .

The fossil specimens illustrated here were collected at the Douahria Fe deposit, and are stored in the Paleontological Collection of the University Lyon 1-Villeurbanne (FSL).

### **6.5.3. Results**

Table 6.5.1 shows the (U-Th)/He data on goethite collected in the Nefza-Sejnane district. Most of the prepared samples are pure goethite. Two samples (14TAM07 and 13NEFZA) present a mixture of goethite with other hydrothermal phases such as hematite and a Mn-Pb oxide (see Fig. 6.5.3D), and another sample (14OU02) a mixture of goethite-quartz and K-feldspars (Fig. 6.5.3H). All samples present homogeneous effective uranium ( $e\text{U}=\text{U}+0.24\text{Th}$ ) contents ranging from 0.5 to 7 ppm, and most samples have similar Th/U ratios around 0.01-0.2. Only one sample is characterized by a significantly higher Th/U ratio of  $1.7\pm 0.1$  (14TAM07, Table 6.5.1). The variability in the Th/U ratio, which may be used to trace differences in iron oxide populations or the presence of inclusions (Monteiro et al. 2014; Riffel et al. 2016), confirms the relatively high content of hematite in sample 14TAM07. The raw (U-Th)/He ages range from  $0.5\pm 0.03$  to  $8.1\pm 0.4$  Ma, and are mostly homogeneous per sample. No correction of alpha ejection has been considered here, because the mean alpha stopping distance of the ejected He in iron oxides and hydroxides ranging from 14 to 16  $\mu\text{m}$  (Ketcham et al. 2011), is small compared to the samples size (circa 0.5 mm). On the other hand, as He can be lost by diffusion due to



the polycrystalline nature of the samples (see Ault et al. 2019 for a review), here we correct He losses by applying a 10% correction on the He age and a 10% error (Table 6.5.1). For example, Vasconcelos et al. (2013), Monteiro et al. (2014), Riffel et al. (2016) applied a 5 to 30% correction for goethite (U-Th)/He ages based on diffusion data measured directly on the dated crystals. In this study, we used a 10 % correction on the raw ages and apply an additional error of 10%, allowing to estimate He losses by diffusion that represents the sum of the analytical error and the error on He diffusion loss estimation (Table 6.5.1). This correction will not significantly change the ages interpretation but will be used in the following discussion, as it better reflects crystallization ages. The reproducibility of He ages obtained for Tamra and Boukchiba goethite is better than the 10% error estimated to account for He diffusion processes, which gives good confidence in the present data. However, the consideration of a 10% error is preferred to account for potential He diffusion error. With this He correction, the oldest episode, around ~8.5 Ma, is recorded in Tamra and Boukchiba. The earliest episode, younger than ~1 Ma, is recorded in Ouchtata, Belif and Tamra (Table 1). In summary, most of the present (U-Th)/He ages are well reproducible (Table 6.5.1), highlighting two main episodes of supergene goethite formation with mean ages of  $8.6 \pm 0.9$  Ma, and  $0.8 \pm 0.2$  Ma (Table 6.5.1, Fig. 6.5.4).

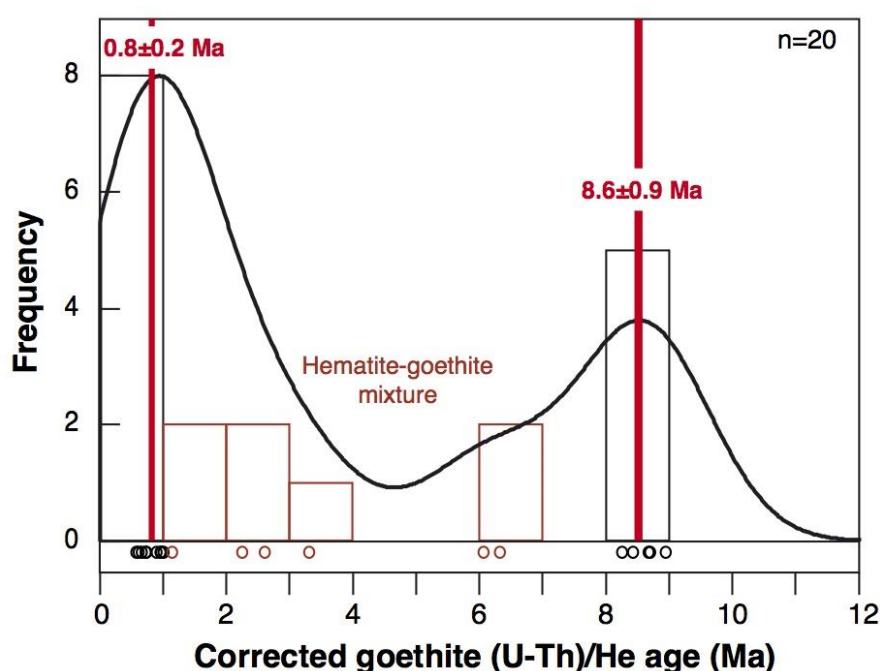


**Figure 6.5.4.** Goethite corrected (U-Th)/He histogram age. The two main crystallisation phases at  $8.6 \pm 0.9$  Ma and  $0.8 \pm 0.2$  Ma are also reported. For hematite-goethite mixed samples, (U-Th)/He ages range between the two main weathering phases.

**Table 6.5.1.** Sampling site, geological characterization and (U-Th)/He data of analysed samples. N.A. = not analyzed.

Geological caracterization					(U-Th)/He data												
Label	Location	Geological context	Mineralogy	Interpretation $\delta D$ - $\delta^{18}O$ Dekoninck et al. (2018)	Label	weight (mg)	$4He$ (nccSTP/g)	$\pm s$ (nccSTP/g)	U (ppm)	Th (ppm)	eU (ppm)	Th/U	Raw age (Ma)	$\pm s$ (Ma)	Age (Ma) + 10%	$\pm$ 10% (Ma)	
14BK11	Boukhchiba	Fe ore	Euhedral goethite in vein	In equilibrium with meteoric waters	14BK-11-A	10.4	1517	30	1.7	0.02	1.7	0.01	7.5	0.4	8.2	0.8	
					14BK-11-B	13.3	1892	38	1.9	0.23	2.0	0.12	7.9	0.4	8.7	0.9	
14MnTAM	Tamra	Tamra Fe ore (Decrée et al., 2008)	Botroydal goethite in Mn zone	In equilibrium with meteoric waters	14MN-TAM-A	6.6	1039	21	1.1	0.02	1.1	0.02	8.1	0.4	8.9	0.9	
					14MN-TAM-B	17.9	671	13	0.7	0.02	0.7	0.03	7.9	0.4	8.7	0.9	
					14MN-TAM-C	9.7	984	20	1.1	0.04	1.1	0.04	7.7	0.4	8.4	0.8	
14TAM07	Tamra	Tamra Fe ore (Decrée et al., 2008)	Goethite-hematite poorly cristallized, rich in Mn, mixing of several phases	In equilibrium with meteoric waters	14TAM-07-A	11.0	210	4	0.4	0.73	0.6	1.81	3.0	0.2	3.3	0.3	
					14TAM-07-B	12.3	371	7	0.4	0.72	0.6	1.86	5.5	0.3	6.1	0.6	
					14TAM-07-C	13.7	381	8	0.4	0.63	0.6	1.57	5.7	0.3	6.3	0.6	
13NEFZA	Tamra	Tamra Fe ore (Decrée et al., 2008)	Goethite-hematite in vein	N.A (similar and close to samples CP04-3 and CP04-35, not in equilibrium with meteoric waters)	13NEFTA-A	11.4	165	3	0.6	0.06	0.6	0.11	2.4	0.1	2.6	0.3	
					13NEFTA-B	7.6	56	1	0.5	0.03	0.5	0.07	0.9	0.0	1.0	0.1	
					13NEFTA-C	11.5	225	4	0.9	0.06	0.9	0.07	2.0	0.1	2.3	0.2	
14OU03	Ouchtata	Weathered Triassic	Goethite - Pseudomorphose of pyrite	N.A.	14OU03-1	0.9	230	5	2.3	0.02	2.3	0.01	0.8	0.0	0.9	0.1	
					14OU03-2	0.5	202	4	1.9	0.06	1.9	0.03	0.9	0.0	0.9	0.1	
					14OU03-3	0.5	400	8	3.8	0.05	3.8	0.01	0.9	0.0	1.0	0.1	
13OULI	Ouchtata	Weathered Triassic	Euhedral goethite	sample "Ouchtata" in Dekoninck et al. (2018), in equilibrium with meteoric waters	13OULI-A	11.4	149	3	1.8	0.02	1.8	0.01	0.7	0.0	0.7	0.1	
					13OULI-B	8.6	120	2	1.9	0.03	1.9	0.02	0.5	0.0	0.6	0.1	
					13OULI-C	9.1	129	3	1.8	0.03	1.8	0.02	0.6	0.0	0.7	0.1	
14OB02	Oued Belif	Breccia (Decree et al., 2013)	Euhedral goethite close to quartz and K-feldspars	Unknown for pure goethite. Isotopic values contaminated by quartz and feldspars	14OB-02-A	7.3	547	11	6.7	1.08	7.0	0.16	0.7	0.0	0.7	0.1	
					14OB-02-B	12.7	359	7	2.8	0.34	2.9	0.12	1.0	0.1	1.1	0.1	
					14OB-02-C	9.2	332	7	4.7	0.86	4.9	0.18	0.6	0.0	0.6	0.1	

#### **6.5.4. Discussion**

##### **6.5.4.a (U-Th)/He age significance using petrographic examination of goethite**

Most of the studied samples show pure and well-crystallized supergene goethite, allowing us to obtain, for the first time in Tunisia, direct robust dating of two periods of major meteoric fluid circulation at  $8.6 \pm 0.9$  Ma and  $0.8 \pm 0.2$  Ma. The ages between these two main episodes reflect the mixture of goethite with contaminating other mineral phases. The 14TAM07 sample clearly shows a mixture of goethite and hematite, with several phases of crystallization and potential contamination by Mn-Fe phases (Fig. 6.5.3D). This mixture most likely explains the large variation observed in (U-Th)/He ages, from  $3.3 \pm 0.3$  Ma to  $6.3 \pm 0.6$  Ma, ranging within the potential mixing of the two main episodes ( $\sim 8.6$  and  $\sim 0.8$  Ma). A similar interpretation is proposed for the 13NEFZA sample, with (U-Th)/He ages ranging from  $1.0 \pm 0.1$  Ma to  $2.6 \pm 0.3$  Ma. All these observations confirm that a refined petrographic examination and a precise methodology of sampling are required for reliable (U-Th)/He results on supergene goethite. Alternatively, we observed that sample 14OB02, constituted of goethite with quartz and K-feldspars, provides similar (U-Th)/He ages ( $0.6 \pm 0.1$  to  $1.1 \pm 0.1$  Ma) than other samples. This suggests that (U-Th)/He method is not affected by potential mixing of goethite with quartz and K-feldspars, the latter classically having a relatively poor content in U, Th, Sm, He.

##### **6.5.4.b Age of the meteoric Fe-fluids in the Nefza-Sejnane district**

The new (U-Th)/He data highlight the circulation in two episodes of Fe-rich meteoric fluids in the Nefza-Sejnane district, at  $8.6 \pm 0.9$  Ma and  $0.8 \pm 0.2$  Ma.

##### **Late Tortonian weathering event ( $8.6 \pm 0.9$ Ma)**

The oldest (U-Th)/He ages (mean age of  $8.6 \pm 0.9$  Ma) are obtained for goethite samples from Tamra and Boukchiba localities. The Tamra Formation, deposited during a regional extensional tectonic regime (Bouaziz et al. 2002), consists of successive sedimentary sequences (Decrée et al. 2008). Each sedimentary sequence results from (1) sedimentation of iron-rich inherited material, and (2) *in situ* pedogenesis and iron concentration without evidence of a precursor hydrothermal event. This clearly confirms that meteoric fluids were associated to Fe-(oxi)hydroxides formation in the area. In this context, extensional regime has provided the geological drains (fractures, faults, ...) allowing the fluids to percolate within sediments, as it has been previously suggested for numerous weathering profiles in various areas (e.g. De Putter et al. 2015; Verhaert et al., in press). The 14MnTAM sample, showing GHe ages between  $8.9 \pm 0.9$  Ma and  $8.4 \pm 0.8$  Ma (Table 6.5.1), is clearly related to weathering due to i) its botryoidal texture (Fig. 6.5.3A) and ii) the  $\delta D$  and  $\delta^{18}O$  data highlighting its formation in equilibrium with meteoric waters (Dekoninck et al. 2018). This relatively old age may also be associated to pedogenesis recognized during the deposition of the sequence (Decrée et al. 2008). This episode of weathering is likewise recognized at Boukchiba, where the GHe ages of 14BK11 range from  $8.7 \pm 0.9$  Ma to  $8.2 \pm 0.8$  Ma, which is consistent with those of sample 14MnTAM. The Boukchiba site also experienced weathering, as attested by  $\delta D$  and  $\delta^{18}O$  data on the same sample of goethite in equilibrium with meteoric waters (Dekoninck et al. 2018), during late Tortonian period, but was not affected by syndepositional pedogenesis of the subaerial Tamra Formation. The pure goethite of sample 14BK11 (Fig. 6.5.3E-6.5.3F), located in a vein cross-cutting the Oued Belif breccia, clearly postdates the major LREE-U mineralization event associated to the brecciation event stressed by Decrée et al. (2013). Then, the late Tortonian weathering period is observed in the syndepositional

pedogenesis of the Tamra Formation (sample 14MnTAM) and in the surrounding brecciated rocks, suggesting at least a local event of weathering.

#### **Late Pleistocene weathering event ( $0.8\pm0.2$ Ma)**

The 14OU03, 13OULI and 14OB02 samples, located at various localities in the district (see Fig. 6.5.2, Table 6.5.1), present consistent GHe ages, ranging from  $1.0\pm0.1$  Ma to  $0.6\pm0.1$  Ma, highlighting that meteoric Fe-fluids circulated during a late episode around  $0.8\pm0.2$  Ma in the Nefza-Sejnane district.

#### **Stratigraphic frame of the Nefza-Sejnane district**

This new (U-Th)/He dating refines the stratigraphic frame of the Nefza-Sejnane district, especially from Tortonian to Pleistocene periods (Fig. 6.5.5).

The entire nappe pile is cut by shallow-level, Serravallian to early Tortonian intrusive rocks. The felsic rocks of the whole district are dated between  $12.9\pm0.2$  Ma and  $8.2\pm0.4$  Ma (see a detailed review in Decrée et al. 2016). In the Zouara basin (Fig. 6.5.2), the transitional basalt sills outcropping at Mokta el-Hadid have been dated at  $8.4\pm0.4$  Ma (Bellon 1976), and at  $6.9\pm0.3$  and  $6.4\pm0.15$  Ma (Rouvier 1977). The reliability of some of these ages is however discussed/questioned by Decrée et al. (2016). Anyway, a widespread bimodal magmatism, late Miocene in age, has occurred in the whole district.

The age of the Tamra Formation was not precisely known but was supposedly Mio-Pliocene or younger according to the 1:50,000 geological map of Nefza (Rouvier 1977, 1994). Our new dating refines the age of the Tamra succession. The deposition of the Tamra sediments is globally coeval to the oldest GHe age associated to synsedimentary pedogenesis, i.e.  $8.6\pm0.9$  Ma, suggesting that the Tamra Formation is late Tortonian in age. In this period, meteoric waters may have played a role in the precipitation of halloysite and kaolinite and/or destabilization of primary clays in the Tamra ore, associated to mixing of deep hot saline fluids, related to a thermally driven circulation (Dekoninck et al. 2018). It confirms that the Tamra Formation experienced polyphased and mixed hydrothermal/meteoric fluid circulations, as already stressed by Decrée et al. (2008).

The Tamra iron mine sediments overlay the Sidi Driss sediments (Fig. 6.5.5), the latter correlated with the Douahria sediments on the basis of i) regional lithological similitudes, ii) the presence of volcanoclastic intercalations in the Douahria and Sidi Driss sequences, including cinerites (Decrée et al. 2008, 2014), and iii) their similar gastropod fauna (Pallary 1901; Bank and Menkhirst 2009). The Sidi Driss and Douahria sediments were attributed to Late Miocene (Messinian?) by Decrée et al. (2008). Our data suggest a minimal Tortonian age for these sediments, close or coeval to the end of the magmatic activity of the area (Fig. 6.5.5). This is in good agreement with the isotopic results of Decrée et al. (2014), demonstrating that metals of the Nefza-Sejnane deposits were supplied by the regional magmatic and sedimentary rocks. Interestingly, Decrée et al. (2008) observed that the oxidized Sidi Driss and Douahria sulfide ore deposits, close to the Tamra and Boukchiba localities where a late Tortonian meteoric fluid circulation is highlighted by our new data, are hosted within carbonate lenses initially composed of Fe–Mn-enriched dedolomite. The dedolomitisation is a well-known process that usually takes place when dolomite comes into contact with meteoric fluids (e.g. Sanz-Rubio et al. 2001). There, concurrent with an Mg loss, a Fe–Mn gain led to formation of Fe–Mn carbonates, or of pure calcite (in the absence of Fe–Mn gain). In Sidi Driss and Douahria, dedolomitisation is observed in the first stage of the ore sequence, before the early replacement by barite and celestite (Decrée et al., 2008) and could be related to the late Tortonian episode of weathering recognized at Tamra (Fig. 6.5.5).

In the Nefza-Sejnane district, the late Tortonian episode of weathering was followed by circulation(s) of hydrothermal fluids, leading to the precipitation of nontronite and talc observed in several localities of the district and dated at  $6.2 \pm 0.4$  Ma (Ben Abdallah et al. 2013). Neoformation of nontronite and talc is observed mainly in i) the basaltic flows of Mokhta El Hadid (Zouara basin), and ii) the Triassic material and Miocene rhyodacite of Oued Belif (Fig. 6.5.2, 6.5.5). These hydrothermal circulations are most likely associated to the mineralization of Pb-Zn sulfides, barite, celestite and fluorite at Sidi Driss and Douahria. Mn oxides constitute another milestone for the district. Decrée et al. (2010) stressed that hydrothermal enrichment was superimposed on the weathering conditions found in the Tamra sequence, leading to the formation of first, hollandite, romanechite and Sr-cryptomelane, dated at  $4.7 \pm 0.1$  Ma by  $^{40}\text{Ar}$ - $^{39}\text{Ar}$  dating, and then coronadite, chalcophanite, and amorphous Mn-oxides at  $3.35 \pm 0.07$  Ma. Hydrothermal circulations were confirmed by Dekoninck et al. (2018), studying the  $\delta\text{D}$  and  $\delta^{18}\text{O}$  isotopes of kaolinite-halloysite, not in equilibrium with meteoric waters. Our new data show that a late Tortonian weathering phase predates the Messinian-Pliocene hydrothermal episodes leading to the formation of Mn oxides, Pb-Zn sulfides, barite, celestite and fluorite.

A late Pleistocene weathering period has been established by our new (U-Th)/He analyses. This recent meteoric fluid circulation is most probably responsible for the late occurrence of anglesite and iron oxide at Sidi Driss and Douahria (Decrée et al. 2008). The meteoric fluids associated to this recent weathering event affected the whole district, and are most likely responsible for the numerous weathering profiles observed in the area, including in the superficial part of the Albian-Priabonian marls, and in the Numidian Flysch Formation leading to the formation of kaolinitic industrial clays (Moussi et al. 2011, 2020; Chargui et al. 2018).

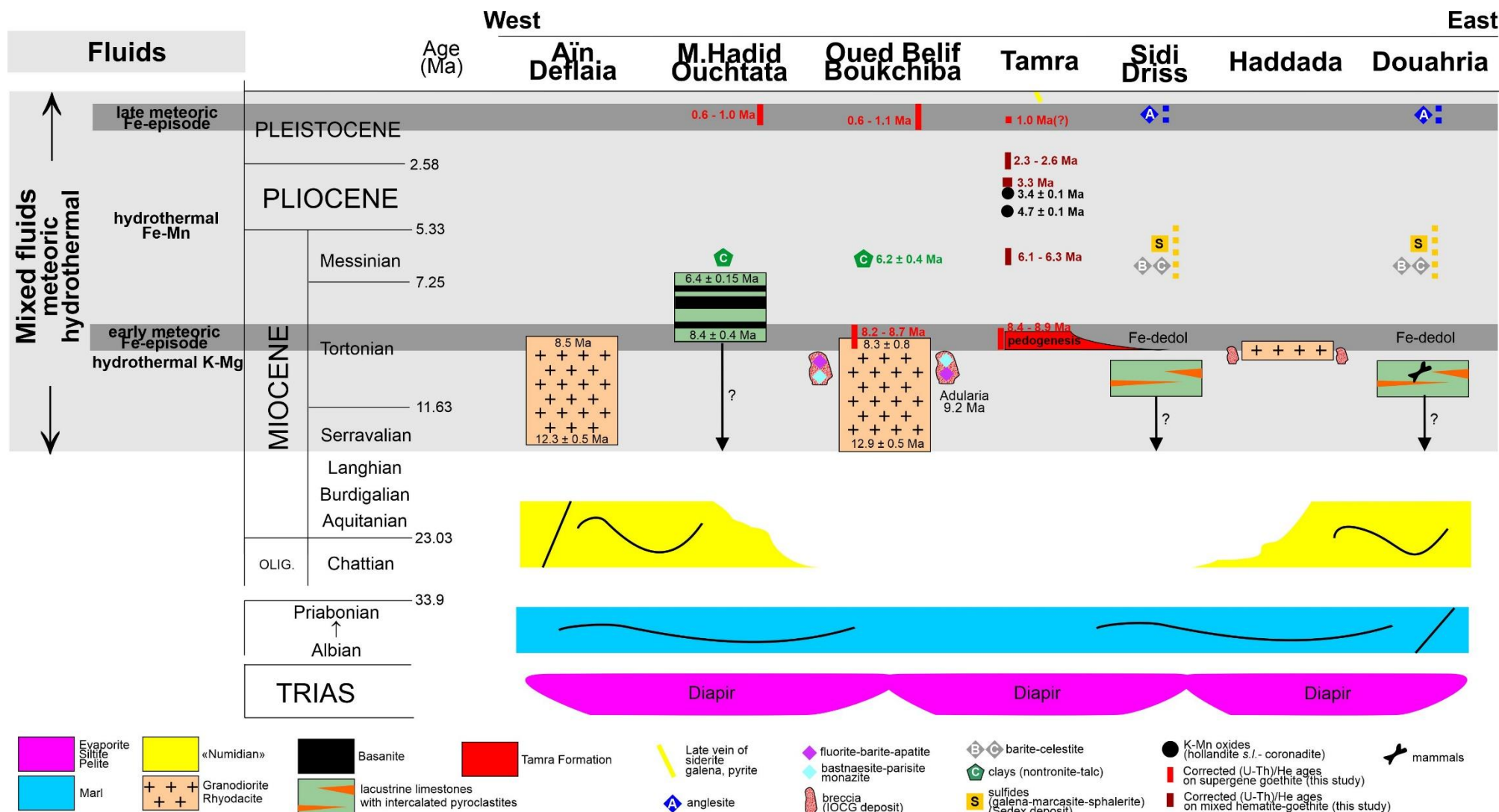


**Figure 6.5.5.** Stratigraphic frame of the Nefza-Sejnane district (Tunisia), including the new (U-Th)/He data on Fe (oxyhydr-)oxides. In red: data on supergene goethite; in purple: data on mixed hydrothermal-meteoric hematite-goethite. Olig. = Oligocene.

## Significance of the weathering periods at a regional scale

The suitable conditions for the development of significant weathering profiles generally consider a combination of slow large-scale tectonic movement and (sub)tropical climate. At a regional scale, new ages of weathering periods provide relevant constraints to unravel the role of i) the geodynamic/tectonic setting as exposure to weathering depends on exhumation (uplift) creating a hydrodynamic gradient for the transit of meteoric fluids, and ii) the climate as water is needed for the percolation of meteoric fluids and the subsequent formation of secondary minerals such as goethite. Our new data highlight two periods - late Tortonian and late Pleistocene - of weathering in the Nefza-Sejnane district. Interestingly, these periods were previously regarded as weathering events in Tunisia (Garnit et al. 2018). Studying the C-O stable isotopes of numerous non-sulfide Zn-Pb Tunisian deposits, these authors concluded that weathering leading to the formation of the Tunisian supergene deposits proceeded in the middle to late Miocene interval and at Pliocene-Quaternary, both periods corresponding to two distinct Alpine tectonic pulses that produced the exhumation of sulfides ores. The new (U-Th)/He data refine the previously suggested periods of weathering in Tunisia. Large-scale, vertical, positive movements were able to produce sulfide uncapping and weathering processes, by creating a gradient for the percolation of meteoric fluids. In the last decade, the temporal link between uplift-related exhumation and weathering periods at a regional scale has been documented by several studies, in various geological contexts. Using  $^{40}\text{Ar}$ - $^{39}\text{Ar}$  method on cryptomelane in Mn ores of Democratic Republic of Congo, De Putter et al. (2015), followed by De Putter and Ruffet (2020) and Fontaine et al. (2020), highlighted successive periods of weathering since late Cretaceous and concluded that tectonics accounts for most of the recognized supergene ore formation episodes, controlled by vertical lithospheric movements that are ultimately responsible for alternating stages of landscape stability and erosion. Tectonics is there regarded as the first-order control for supergene ore formation in Central Africa, over the last 80 Myr. Similarly, in Ardenne area (Western Europe), a recent synthesis of weathering periods showed that the uplift of the Ardenne was most probably the main factor triggering the development of weathering mantles, together with the increasing seasonality and high precipitation (Dekoninck et al. 2019). In Morocco, weathering periods are most likely associated to some of the four main Atlasic geodynamic events, as attested in recent geodynamic and ore deposits studies (Choulet et al. 2014; Verhaert et al. 2017; Dekoninck et al. 2020). In Tunisia, Alpine compressional movements may have caused marked slow and large-scale (at least regional) uplifts, preventing deposition of coeval sediments, except in local extensional basin, such as in Tamra and Zouara basins. Then, the studied area must be regarded as an elevated zone during late Tortonian and late Pleistocene, favoring the formation of weathering profiles. In Iberian Pyrite Belt (Southern Spain), preliminary ages of different parts of the gossans using  $^{40}\text{Ar}$ - $^{39}\text{Ar}$  techniques show that at least two stages of oxidation took place at 7–8 Ma and about 1–2 Ma (Velasco et al. 2013), quite coeval to the new GHe ages in Tunisia. This may suggest that the late Tortonian and late Pleistocene are Mediterranean regional periods of weathering. Further studies in Atlasic and Mediterranean domains are however requested to refine the nature/scale/role of this uplift-related weathering, assuming the available age record is complete.

Climate has also been regarded as an important parameter of weathering periods because sufficient water supply is needed for weathering processes (Maher and Chamberlain 2014). The late Pleistocene is marked by wet climate in North Africa (“African Humid Period”; e.g. DeMenocal et al. 2000). The Tortonian climate was presumably humid to subhumid around the Mediterranean Sea, while the hinterland was dryer (Gladstone et al. 2007; Pound et al. 2011; Quan et al. 2014), as it is the case today. During the late Tortonian, North Africa experienced a turnover from dry to wet climate, initiating the “Zeit Wet Phase” of the Messinian (Griffin 2002). Conversely, our GHe ages do not match Cenozoic warmest climates in the studied area. Comparing these climatic conditions with the weathering



periods obtained by our new data supports that warm climate is a second-order control, whereby wet climatic conditions are necessary to ensure percolation of meteoric fluids. The relatively high precipitation during the late Tortonian and late Pleistocene can provide water to the weathering system, when differential uplift movements generate the weathering gradient for the progression of meteoric fluids.

### Revision and refined age of the mammalian fauna in the Douahria Fe-deposit

Our new GHe ages refines the stratigraphy of classical fossils from the Douahria Fe-deposit. The fossils comprise two land snail species (*Helix (Iberus) fossulata* and *Helix (Archelix) solignaci*; Roman and Solignac 1934; Guérin 1966) and large mammal remains. The latter elements were discovered in a ferruginous crust cropping out in the Fe-deposit at Douahria (Roman and Solignac 1934; Fig. 6.5.2). The concerned vertebrate remains were then assigned to taxa of both eastern Mediterranean (the rhinocerotid "*Rhinoceros pachygnathus*" (= *Ceratotherium neumayri*, Osborn, 1900; sensu Antoine and Sarac 2005) and the giraffid "*Helladotherium duvernoyi*" and Asian affinities (the anthracotheriid "*Merycopotamus dissimilis*"), further indicating a latest Miocene age ("Pontian", roughly coinciding with the Messinian standard age, i.e. 7.24–5.33 Ma; Hilgen et al. 2012). Historically, this paleontological assemblage provided the first argument for assigning a late Neogene age to the Nefza-Sejnane ore deposits (Singer and Solignac, 1934). The taxonomic assignment of the rhinocerotid was later revised by Guérin (1966), who named the new species *Diceros douariensis* after the remains from Douahria.

The stratified Fe-ore of Douahria is stratigraphically correlated with the *Sedex-type* Pb-Zn-ore of Sidi Driss related to thermally-driven fluid circulations (Decrée et al. 2008). From biostratigraphical and biogeographical perspectives, the Douahria gastropod assemblage has a late Neogene signature, at a Maghreb scale (late Miocene–Pliocene; Pallary 1901; Bank and Menhorst 2009), but it allows for no further precision. Only a late Miocene age of these fossils is in agreement with our (U-Th)/He dating of the Fe-fluids (ferruginous crust) of the area, suggesting that the first episode of ferruginous crust containing the fossils is late Tortonian in age ( $8.6 \pm 0.9$  Ma – see above).

A systematic revision of the mammalian fauna from Douahria may provide a better age constraint. The giraffid from Douahria was first referred to as "*Helladotherium duvernoyi*", a short-necked sivatheriine species originally described by Gaudry and Lartet (1856) at Pikermi, a classic late Miocene vertebrate locality from Greece (dated around the Tortonian–Messinian transition, at 7.5–7 Ma; for review, see Bohme et al. 2017). The concerned dental and postcranial remains were recently reassigned to the longer-ranged sivatheriine *Sivatherium hendeyi*, documenting the late Miocene–early Pliocene interval in Africa (11.6–4 Ma; Harris et al. 2010; Werdelin 2010). The Douahria anthracotheriid was originally assigned by Roman and Solignac (1934) to the Asian species "*Merycopotamus dissimilis*", of late Miocene–earliest Pleistocene range (7.8–2.4 Ma; Lihoreau et al. 2007). In their revision of African anthracotheriids, Holroyd et al. (2010) and Lihoreau et al. (2014) consider that the referred specimens from Africa belong to *Libycosaurus* instead. Dental features and moderate dimensions further closely match those of *Libycosaurus anisae* (Black 1972), known to range the latest middle–early late Miocene interval in East and North Africa (~12–10 Ma; Holroyd et al. 2010; Lihoreau et al. 2014). Aside from Douahria, this species has been recognized in Central Tunisia (Bled Douarah, Beglia Formation, early late Miocene; Holroyd et al. 2010) and Southern Tunisia (El Ziz, late Miocene). The two-horned rhinocerotine rhinocerotid *Diceros douariensis* was named by Guérin (1966) on the basis of the abundant craniomandibular and postcranial material from Douahria. Guérin (2000) proposed an age of 9.5 Ma for the latter locality, based on biostratigraphic correlations with the Djebel Krechel el Artsouma (Central Tunisia) and other circum-Mediterranean occurrences of *D. douariensis*. Geraads (2010) later reassigned this species to *Ceratotherium* and considered that

specimens from As Sahabi, Northern Libya (latest Miocene; 6.2–5.33 Ma) were also probably assignable to *Ceratotherium douariense*, thus significantly extending upward its stratigraphic range (i.e., 9.5–5.33 Ma). From a morpho-anatomical perspective, this species has the closest affinities with *Ceratotherium neumayri* (Osborn, 1900), a conspicuous element of eastern Mediterranean faunas throughout the late Miocene (e.g., Antoine and Sarac 2005; Antoine et al. 2012).

Direct re-examination of the specimens in the Lyon University collection led to the unexpected recognition of a second rhinocerotid taxon at Douahria. Most rhinocerotid remains do belong to *C. douariense*, as typified by the adult skull FSL 16749 (holotype; Fig. 6.5.6A-6.5.6B). Nevertheless, the juvenile skull FSL 16752 (Fig. 6.5.6C-6.5.6F), previously defined as the paratype of “*Diceros douariensis* Guérin, 1966”, has cranial and dental characteristics discarding any referral to a two-horned rhinocerotine, such as the presence of a concave dorsal profile and a rounded nasal notch (Fig. 6.5.6C), of laterally projected orbits (Fig. 6.5.6D), of a lingual wall on upper premolars (Fig. 6.5.6E), of sagittally elongated molars with an ectoloph undulated in occlusal view, and the abundance of cement filling the valleys of cheek teeth (Fig. 6.5.6F). These features are diagnosing middle and early late Miocene elasmotheriine rhinocerotids from Eurasia and Africa, i.e. the ones retaining non-ever-growing teeth (Antoine 2002, 2003; Handa et al. 2017). The juvenile skull FSL 16752 cannot be assigned to any known elasmotheriine species, notably as documented in Africa (i.e., *Kenyatherium bishopi* Aguirre & Guérin, 1974; *Ougandatherium napakense* Guérin & Pickford, 2003; *Victoriaceros kenyensis* Geraads et al., 2016; *Samburuceros ishidai* Handa et al. 2017; and references therein). It is most likely documenting a new species the formal description of which is far beyond the scope of the current work. Accordingly, no precise biostratigraphical age can be formally inferred from this occurrence, as usual regarding new taxa. Yet, given its evolutionary stage among elasmotheriine rhinocerotids (Antoine 2002, 2003), a late middle to early late Miocene age can be suspected for the first appearance of this taxon. Independently, the Douahria assemblage can be refined at ~11.6–10 Ma, thanks to the concurrent range of the bothriodontine anthracotheriid *Libycosaurus anisae* (Black 1972) and of the sivatheriine giraffid *Sivatherium hendeyi* (Harris 1976) documenting the 12–10 and 11.6–4 Ma interval, respectively. This stratigraphical range as inferred for Douahria is further compatible with its rhinocerotid components. A Tortonian age is thus supported here for the Douahria mammalian assemblage. Accordingly, deposition of the Douahria fossils may have occurred in (early) Tortonian, just prior to the circulation of the meteoric fluids, here dated late Tortonian ( $8.6 \pm 0.9$  Ma) by (U-Th)/He method. No long gap is necessarily to be suspected between both the events.

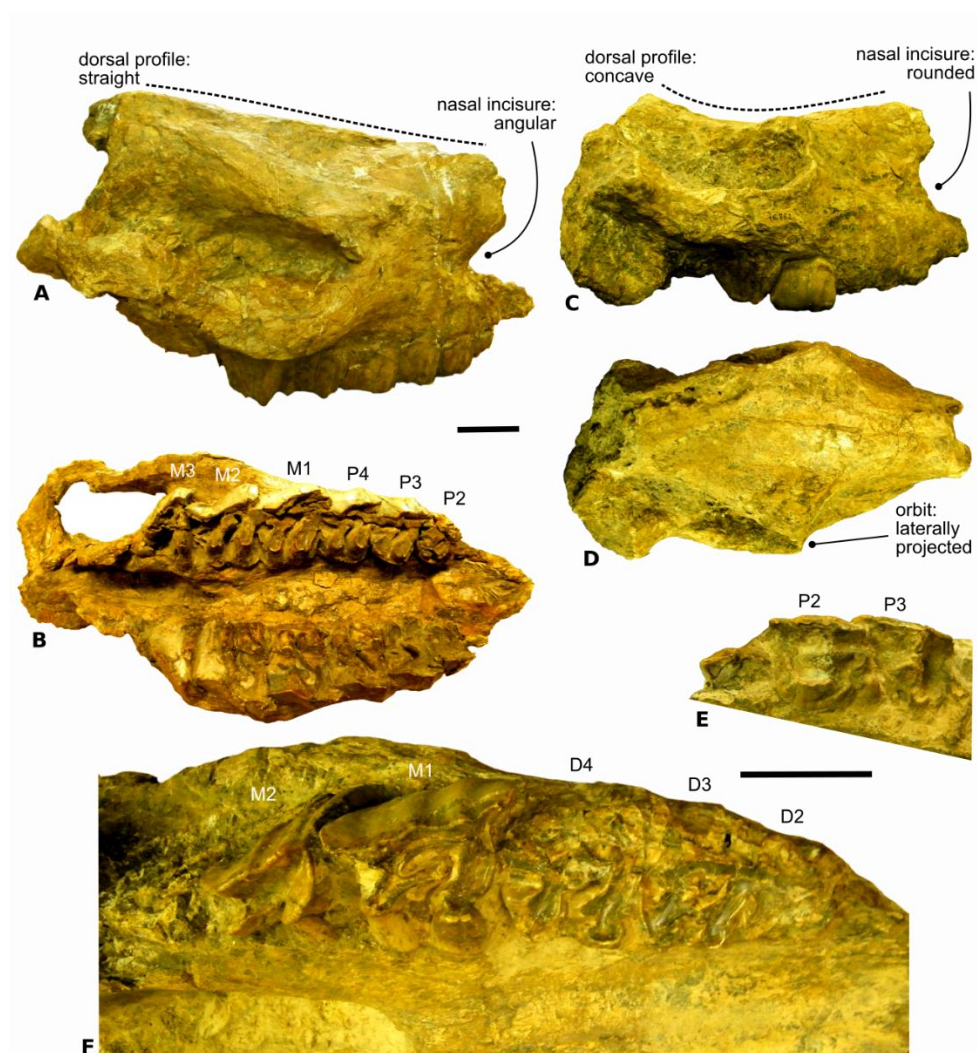


**Figure 6.5.6.** Selected rhinocerotid remains from the early Tortonian Douahria fossil locality, Tunisia. A-B, *Ceratotherium douariense* (Guérin 1966), adult skull FSL 16749 (holotype). A, right lateral view; B, palatine view, with left and right dental series (premolars [P2-P4] and molars [M1-M3]). C-F, Unidentified elasmotheriine, juvenile skull FSL 16752 (formerly paratype of *C. douariense*). C, right lateral view; D, dorsal view; E, detailed occlusal view of the left dental series, with emerging 2nd and 3rd premolars (P2-P3); F, detailed occlusal view of the right dental series, with decidual teeth (D2-D4) and functional 1st and 2nd permanent molars (M1-M2). Scale bars = 5 cm.

### 6.5.5. Conclusion

The new (U-Th)/He data in the vertebrate-bearing Nefza-Sejnane polymetallic district highlight that:

- i) meteoric fluids circulate during late Tortonian ( $8.6 \pm 0.9$  Ma) and late Pleistocene ( $0.8 \pm 0.2$  Ma), confirming the polyphased and mixed (hydrothermal/meteoric) fluid circulations in the district and their role for mineralization,
- ii) these events of meteoric fluid circulations refine the ages previously suggested for weathering periods in Tunisia, confirming that (U-Th)/He on rigorously sampled and well characterized (using petrography and  $\delta D$ - $\delta^{18}O$  analyses) goethite is a very powerful method in order to decipher weathering periods,
- iii) these periods are coeval with geodynamic events and relatively wet climates in North Africa, confirming a temporal link between weathering events and both regional tectonics and humid periods, as already stressed by other studies in other areas.

Matched with previous stratigraphic data, our new results refine the chronological frame of the district, allowing the integration of the numerous deposits (Pb, Zn, Fe, Mn, LREE, U, clays). As a consequence, the deposition of the Douahria fossils in a ferruginous crust, here taxonomically revisited, occurred no long prior to the late Tortonian circulation of the meteoric Fe-fluids, here dated by (U-Th)/He method.

## 6.6 Conclusions: implications of Moroccan/Tunisian GHe and alunite K-Ar ages

From all (U-Th-Sm)/He ages acquired during this PhD thesis, several conclusions may be drawn. The selection and preliminary **characterization of samples** are of the greater influence on ages. **Botryoidal** goethite samples should be preferentially dated since their pure composition and remarkable crystallization enable a quantitative He retention, and the acquisition of the most reproducible, representative and accurate ages. **Microcrystalline** and **pyrite-pseudomorphosing** iron (oxyhydr-)oxides provide variably scattered ages, while **powdery** iron (oxyhydr-)oxides are in no way datable.

**$\delta^{18}\text{O}$ - $\delta\text{D}$  isotopic analyses** are ideally suited to distinguish samples that precipitated in supergene or hydrothermal environments, and thus provide additional elements to interpretations of GHe ages. However, when considering such discussions, it must be considered that fluid/rock interactions processes may degrade the supergene  $\delta^{18}\text{O}$ - $\delta\text{D}$  signal. Major, minor and Rare Earth elements contents also provide useful information regarding the precipitation processes.

Since **highly reproducible** numerous ages requiring **few corrections** were obtained for sample 18PL07 (Imini, Morocco – see Chapter 6.2) thanks to its purity, homogeneity, and efficient crystallization, this sample is now tested as a **standard** for goethite (U-Th-Sm)/He dating at the University of Paris-Sud. Sample 14MnTAM (Tunisia – see Chapter 6.5) is similarly undergoing tests to be developed as a laboratory standard.

The correspondences between GHe ages, alunite K-Ar ages and geodynamic events, highlighted at several locations of the High Atlas, Anti-Atlas and in Tunisia, suggests that the formation of iron (oxyhydr-)oxides in relation with **weathering processes** could ensue from, and be driven by, **exhumation phases**. However, these potential relations also raise several questions. The first interrogation is regarding whether these correlations reflects direct relations, or whether these are purely coincidental, due to **spacetime causalities**. At Imini, a duality appears between cavity-filling goethite that likely records weathering associated with a Late Cretaceous doming (e.g. Froitzheim 1984; Leprêtre et al. 2018), and with the Early Paleogene fracture-filling goethite that is in the line with the late- or post-orogenic period. In Bou Arfa area, GHe ages are consistent with the second and third erosional events (Early-Middle Miocene ( $D_2$ ) and Late Pliocene-Quaternary ( $D_3$ )) of the polyphased Cenozoic deformation defined by Leprêtre et al. (2015, 2018). In the occidental Anti-Atlas, the Late Cretaceous to Paleocene ages of Assifid, Tazalaght and Irkhs iron (oxyhydr-)oxides are coeval with the end of the wide-scale Late Cretaceous deformation phase ( $D_0$ ). Cenozoic GHe ages obtained for the Anti-Atlas also correlate, to a certain extent, with the beginning and/or end of deformation phases observed by Leprêtre et al. (2015, 2018). The Late Eocene – Early Miocene GHe ages of Tassrirt, Ighrem and Tizert correlate with the end of the  $D_1$  phase, while the Late Miocene – Quaternary ages of Agoujgal and Tassrirt correspond to the end of the  $D_2$  phase and to the beginning of the final  $D_3$  major pulse of Leprêtre et al. (2018). The Late Tortonian and Late Pleistocene GHe ages of Tamra area are also coeval with weathering and geodynamic events in Tunisia (middle to late Miocene and Pliocene-Quaternary; Garnit et al. 2018). On the basis of all these ages and on the correspondences established not only at the Atlas-scale, but on a large-scale possibly for Maghreb, **geodynamics are regarded as a major parameter for supergene mineralization** from Late Cretaceous, as it already was suggested in Central Africa by De Putter et al. (2015), De Putter and Ruffet (2020) and Fontaine et al. (2020), among others. However, the development of significant weathering profiles also requires rainfalls, since sufficient **water** is needed for the migration of meteoric fluids and the subsequent formation of secondary minerals. The lack of direct correspondence between GHe ages and (sub)tropical climates in North Africa suggests that the temperature does not have a strong influence on the development of

weathering profiles but does not prejudice the fact that the **climatic precipitations** are of a major importance in supergene processes.

CHAPTER VII  
GENERAL CONCLUSIONS  
AND PERSPECTIVES

---



## Chapter 7

### General conclusions and perspectives

<b>7.1 Characterization of supergene mineralization and profiles</b>	<b>p. 252</b>
<b>7.2 Dating supergene processes</b>	<b>p. 253</b>
7.2.1 <i>Advances in the (U-Th-Sm)/He methodology</i>	<i>p. 253</i>
7.2.2 <i>Relation between geodynamics and weathering processes</i>	<i>p. 254</i>
<b>7.3 Perspectives</b>	<b>p. 255</b>
7.3.1 <i>Application of the (U-Th-Sm)/He method in supergene environments</i>	<i>p. 255</i>
7.3.2 <i>Relation between weathering and geodynamic processes at the Maghreb scale</i>	<i>p. 255</i>
7.3.3 <i>Towards etchplanation mapping in Maghreb as previously defined in Europe? European weathering mantles and geodynamics</i>	<i>p. 255</i>

In this last chapter, I propose a summary of the general conclusions that may be drawn from the present PhD thesis, first about the characterization of supergene ore deposits, and secondly about the dating of weathering processes in Northern Africa. Perspectives about the future works that could be undertaken in relation with these subjects are ultimately discussed.

## 7.1 Characterization of supergene mineralization and profiles

The six supergene ore deposits characterized in this thesis share several common features, even if they all present a number of particularities, especially Jbel Rhals mineralization which is a peculiar case (see chapter 5). First, processes involved in the formation of such mineralization are similar and start with the **oxidation and dissolution of hypogene minerals**: base metal sulfides at Jbel Klakh, Jbel Haouanit, Tazalaght, Agoujgal and Tizert, and probably siderite at Jbel Rhals. The following **mobilization and recombination** of ions and ligands enable the formation of a wide assortment of phases.

Secondly, the **vertical distribution** of weathering zones composed of the **hypogene zone** (sulfides such as chalcopryite, pyrite, tennantite, galena, sphalerite), **cementation zone** (sulfide such as bornite, digenite, chalcocite, djurleite, covellite), **oxidized zone** (*i.e.* malachite, azurite, brochantite, olivenite, chenevixite), and **leached zone** (iron (oxyhydr-)oxides, mottramite, quartz, calcite), is particularly emphasized in the Cu deposits of Jbel Klakh, Tazalaght and Tizert, but moderately at the Cu and Pb deposits of Agoujgal and Jbel Haouanit, respectively (see chapters 5.1, 5.3, 5.4). The armoring of galena by weathering products jeopardizing further weathering is particularly limiting the formation of such zonation; mineral variations are mostly restricted at the scale of the minerals (see chapter 5.1). At Tazalaght and Agoujgal, tennantite samples also recorded the transition from the fresh ore (tennantite), the cementation zone (chalcocite), the oxidation zone (arsenates and malachite), and finally the gossan (goethite and hematite) in single hand specimens presenting **boxwork textures**, reflecting the evolution of fluid-rock interactions with time (see chapter 5.3). The absence of such vertical zoning at Jbel Rhals ensues from its polyphased surimposed metallogenic history, and potentially implies the much lower position of the water table level jeopardizing the formation of sulfides that requires reducing environmental conditions (see chapter 5.2).

Finally, the **influence of the host rock and hypogene mineralization** nature on supergene processes is highlighted in the carbonate-hosted Jbel Klakh, Jbel Haouanit, Agoujgal, Tizert deposits and the silicate-hosted Jbel Rhals and Tazalaght deposits. The first four exhibit a broad panel of oxidized mineral phases that precipitate after an efficient **neutralization of the acidic fluids** by host rock dissolution. This rapid and efficient neutralization, where both carbonate minerals and chlorite were involved, is responsible for the particular abundance of homogeneous Cu carbonates at Tizert, which is a major advantage for potential mining and has led to its qualification as a “giant” copper deposit (see chapter 5.4). The high porosity of the dolomitized host rocks also played an important role by providing cavities of different dimensions for supergene mineralization. However, at Tazalaght and Jbel Rhals, no such efficient neutralization was enabled by the quartzitic host rock, limiting the variety of the secondary mineral assemblage.

However, the **mineralogical and chemical contents** of the six above named supergene ores deposits present variations that are related to the leaching and concentration, by substitution or adsorption, of elements during weathering processes. For instance, the vanadate mottramite is ubiquitous in all six deposits, indicating the common circulation of V-rich fluids in supergene environments. Though, the source of vanadium is still a matter of debate. The concentration of U and REE in iron (oxyhydr-)oxides is also a typical of all six deposits, while the enrichment in Ge and Ag of Jbel Haouanit calamine

products, in LREE of Jbel Klakh alunite, and in Ag of Agoujgal secondary sulfides are distinctive patterns of given locations.

## 7.2 Dating supergene processes

### *7.2.1 Advances in the (U-Th-Sm)/He methodology*

The first conclusion of this subchapter ties up with the outcome of Vasconcelos (1999) for the dating of Mn oxides, implying that the successful dating of supergene materials strongly depends on the **careful selection of samples** on the field, their subsequent **thorough characterization** in the laboratories and the **thoughtful integration** of results in their geological context. Detailed macroscopic and microscopic investigation of datable material indeed enables to avoid dating contaminated and impure samples and allows the acquisition of accurate and meaningful ages (see chapters 6.1 and 6.3). On the field, much attention must be paid to the environment of formation of iron (oxyhydr-)oxides, i.e. if they precipitated in veins, fractures, faults, cavities, by pseudomorphose or by impregnation of host rocks. A first selection must be undertaken on the basis of the macroscopic aspect of samples: visibly impure samples such as powdery samples and or samples composed of inseparable mixed phases must be discarded. A second scan, using X-ray diffraction aims at verifying the major composition of samples. A last selection involves the observation with reflection optical microscopes and scanning electronic microscopes of the remaining set of samples to retain only pure, datable samples and to reject those containing powdery or poorly crystallized phases, excessively porous phases, variations of mineralogy at a very small scale (e.g. in pseudomorphs), mixed several generations, mixed with other potentially datable phases, quartz, clays, carbonates, presence of inherited gangue minerals, too small crystals and crystallites. Poorly He-retentive phases that potentially experienced significant He losses are thus discarded. **SEMs** are judged to be the best tool to select the purest material for (U-Th-Sm/He) dating with regard for the structures and textures, and to eliminate undatable samples.

The **testing and dating of iron (oxyhydr-)oxides pseudomorphosing pyrite** from several deposits in Morocco highlight several issues: 1) absence of homogeneity at the scale of the crystal, 2) presence of mixed successive generations of goethite and hematite due to the stepwise replacement of the sulfide and to hydration and dehydration processes, 3) inheritance of tiny gangue minerals from the host rock leading to the obtention of completely erroneous ages (see chapters 6.1 and 6.3). Therefore, iron (oxyhydr-)oxides pseudomorphosing pyrite should not be considered for (U-Th-Sm)/He dating. Alternatively, the testing of **botryoidal goethite** from the High Atlas and Anti-Atlas of Morocco, which is the purest material, provided surprisingly good and reproducible ages (see chapter 6.2). Hence, botryoidal goethite is regarded as the **ideal material for (U-Th-Sm)/He dating**. The dating of the very pure and well-crystallized goethite of Imini that probably suffered very limited He diffusive losses with time demonstrated the high reliability and applicability of this method. **Microcrystalline goethite** samples delivered reasonable ages as long as they were not mixed with (potentially) datable phases such as Mn oxides, mottamite and malachite, and are thus viewed as a **second choice** when botryoidal goethite samples are not available (see chapter 6.3).

Geochemical features such as the major, minor elements and REE concentrations, the oxygen and hydrogen stable isotopes and the effective uranium contents are to be considered as useful tools to **constrain the conditions** of precipitation of iron (oxyhydr-)oxides, for instance, from hydrothermal fluids, circulating supergene fluids, or *in situ*, and to provide additional elements to interpretations of GHe ages (see chapters 6.2 and 6.3).

### **7.2.2 Relation between geodynamics and weathering processes**

A relation between iron (oxyhydr-)oxides and their **feasibility to record uplift/doming periods** is suggested by observations in the High Atlas and Anti-Atlas (see chapters 6.2 and 6.3) but also in Tunisia (see chapter 6.5). The formation of supergene mineralization, and particularly of iron (oxyhydr-)oxides, could thus ensue from, and be driven by, exhumation phases. Hence, it is proposed that the exhumation of preexisting mineralization and/or of host rocks is a key process required for the formation of supergene ore deposits and gossans.

In the **Oriental High Atlas**, the formation of iron (oxyhydr-)oxides correlate with the second and third erosional phases of Leprêtre et al. (2018), Early-Middle Miocene ( $D_2$ ) and Late Pliocene-Quaternary ( $D_3$ ), respectively (see chapter 6.3). At **Imini, in the Central High Atlas**, the dating of botryoidal goethite and its consistency with the Cenomanian-Turonian host rock age enabled the revision of the paragenetic sequence previously proposed. Moreover, the precipitation of such important amounts of botryoidal goethite could be related to the Late Cretaceous ( $D_0$ ) initiation of the High Atlas doming identified by Froitzheim (1984) and Leprêtre et al. (2018) (see chapter 6.2). Similarly, evidences of broad consistence between GHe ages of pseudomorphosing and botryoidal iron (oxyhydr-)oxides and the end of the Cretaceous deformation phase ( $D_0$ ), of the  $D_1$  and  $D_2$  phases, and with the beginning of the final  $D_3$  major pulse of Leprêtre et al. (2015, 2018) could be highlighted in the **Occidental Anti-Atlas**. The assumption of differential deformation between the Anti-Atlas inliers or in a same inlier is made to explain the surprising absence of relation between GHe ages and the position of the studied gossans (see chapter 6.3). As pointed out by Choulet et al. (2014), such phenomenon indeed directly impacts the local amount of uplift and erosion and controls the water table level and the ability to concentrate metals. The matching of the few alunite K-Ar ages with the  $D_1$  and the early steps of the  $D_2$  deformation phase corroborate the previous hypothesis (see chapter 6.4). It is proposed that the quite older ages of alunite over goethite relate to their divergent conditions of precipitation. Similar interpretations are suggested in the **Tunisian Nefza-Sejnane polymetallic district**, where GHe ages indicate the circulation of meteoric fluids during late Tortonian and late Pleistocene, periods that experienced “regional” geodynamic activity, confirming the relation with geodynamic events recorded in the area (see chapter 6.5).

On the basis of all these ages and on the correspondences established not only at the Atlas-scale, but on a large-scale possibly for Maghreb, for instance for the wide-scale Late Cretaceous deformation phase ( $D_0$ ) reported by Gouiza et al. (2017) and Sehrt et al. (2018) in the northwestern Anti-Atlas, by Froitzheim (1984), Domènech et al. (2016) and Leprêtre et al. (2018) in the High Atlas, by Hafid et al. (2006) in the Moroccan offshore, and by Khomsi et al. (2016) in Tunisia, **geodynamics, and in particular long-wave vertical movements** that do not lead to massive erosion but **generate weathering gradients necessary for the progression/percolation of meteoric fluids**, are regarded as the **first-order control for supergene mineralization** from Late Cretaceous. The influence of **climatic parameters, i.e. temperature and precipitations**, which was not extensively investigated during this thesis, is still a matter of debate. The preliminary conclusions drawn in the last chapter tends to corroborate the hypothesis of De Putter et al. (2015), Fontaine et al. (2020) and De Putter and Ruffet (2020) in Central Africa, implying that weathering processes are mostly regulated by tectonics, while climatic parameters play a secondary role. Here, significant lack of fit between GHe ages and warm Cenozoic (sub)tropical climates in North Africa suggests that the development of weathering profiles is **slightly influenced by the temperature**, which acts mainly on the kinetic of reactions. However, the development of supergene profiles requires water for the percolation of meteoric fluids and the subsequent formation of secondary minerals such as goethite. The second climatic factor, the

precipitations, is thus also of a major importance in the formation of supergene mineralization. It remains to be determined to what extent **eustatism** has a role in weathering processes.

## 7.3 Perspectives

### ***7.3.1 Application of the (U-Th-Sm)/He method in supergene environments***

The current testing of the sample 18PL07 (**Imini**, Morocco – see Chapter 6.2) as a **potential standard** for GHe dating, at the GEOPS laboratory (University Paris-Saclay), based on the highly reproducible ages obtained during this thesis, would be a major advance in the field of dating supergene goethite. Until now, only Durango apatite is used to calibrate the results. Similarly, sample 14MnTAM (**Tunisia** – see Chapter 6.5) is also considered as a potential standard, and tested to ensure its adequacy in this mission. Further (U-Th-Sm)/He tests should be performed in order to better constrain **He retention** in iron (oxyhydr-)oxides, *i.e.* in relation with the size of dated fragments, for instance.

### ***7.3.2 Relation between weathering and geodynamic processes at the Maghreb scale***

Interrogations regarding the relations potentially highlighted in the Moroccan Atlas (and Northern Tunisia) between weathering processes and uplift/doming events remain, since these could also result from purely coincidental correlations. To resolve this uncertainty, **further dating** of supergene mineral phases collected in the Moroccan Atlas is required. Supplementary (U-Th-Sm)/He dating on botryoidal (or microcrystalline) goethite collected **in the High Atlas and Anti-Atlas of Morocco** could strengthen the above hypotheses.

To confirm the above assumptions and examine the subject in depth, **further dating**, using other mineral phases and based on other dating methods, is required. Since botryoidal iron (oxyhydr-)oxides typically form ultimately in the supergene sequence, their precipitation is probably delayed from the initial uplift and doming events. Dating mineral phases that precipitate earlier in the sequence, such as **alunite**, could bring relevant information regarding weathering processes timing. In this study, the comparison of GHe and K-Ar ages enables the observation of **encouraging similarities** between ages (chapter 6.4). However, further K-Ar dating of alunite samples is necessary to ascertain these relations. Other phases precipitating late in the weathering sequence could be similarly considered, to confirm GHe ages and infirm the potentiality of spacetime causalities. Among these methods, are: 1) the K/Ar and  $^{40}\text{Ar}$ - $^{39}\text{Ar}$  dating of **Mn oxides**, even if datable K-bearing Mn oxides are quite rare in supergene base metal (Cu, Pb, Zn) deposits, 2) the U-Pb dating on **calcite**, which is abundant in supergene environments, 3) (U-Th)/He dating on the ubiquitous and goethite-associated vanadate **mottramite**, as suggested by Boni et al. (2007) for its Zn-analog, descloizite. In this way, the  $^{40}\text{Ar}$ - $^{39}\text{Ar}$  dating of cryptomelane in the Imini district would provide additional inputs to the discussion led in chapter 6.2.

Finally, to confirm the proposed relation between the precipitation of supergene (oxyhydr-)oxides and tectonics at the scale of Maghreb, and to bring important aspects and complement this discussion, dating **should be extended geographically**. To extend this study to entire Morocco and, even better, to the **Maghreb area** that shares a common alpine deformation, additional research should be undertaken in other geological settings. Regardless of the method, dating should be extended geographically to the numerous supergene deposits and gossans located in the **Central Anti-Atlas, the Moroccan Rif, the Algerian Tell, and the Algerian and Tunisian Saharian Atlas**. Similarly, the investigation of the relations between supergene mineralization and long-wave vertical movements related to the alpine orogeny in Morocco could be extended to the **entire alpine area** since recent ages

obtained in the Belgium Ardenne area and in western Europe massifs show correlations between the development of weathering mantles and uplift (e.g. Hautmann and Lippolt 2000; Dekoninck et al. 2019).

### ***7.3.3 Towards etchplanation mapping in Maghreb as previously defined in Europe? European weathering mantles and geodynamics***

In order to better constrain the link between crustal vertical movements, climatic factors, and the formation of weathering profiles in the entire Maghreb, a thorough characterization of weathering mantles and the dating of supergene mineral phases collected in such profiles, as it has been carried out in Belgium by Demoulin et al. (2018) (see annexe 8.14), would enable the intensive investigation and reconstruction of the area geomorphology. Applying the methodology presented in Demoulin et al. (2018) to the Maghreb area would also bring essential information for the prospection of supergene ore deposits.

## CHAPTER VIII

### APPENDICES

---



## Chapter 8

### Appendices

<b>8.1 Characterization and genesis of Cu-Pb-Zn-V supergene ore deposits in the Oriental High Atlas (Bou Arfa, Morocco) – extended abstract Geologica Belgica (2016)</b>	<b>p. 261</b>
<b>8.2 Characterization and genesis of Cu-Pb-Zn-V supergene ore deposits in the Oriental High Atlas (Bou Arfa, Morocco) – abstract PhD day UNITER (2016)</b>	<b>p. 262</b>
<b>8.3 The contribution of a Europe-Maghreb cooperation for a better prospection of the mining district of Bou Arfa (Morocco): Supergene Fe-Mn-Cu mineralization at Jbel Rhals – abstract Resources and Innovative Geology (2016)</b>	<b>p. 263</b>
<b>8.4 Characterization and genesis of Pb-Zn-Cu-V supergene ore deposits in the Oriental High Atlas (Bou Arfa, Morocco) – abstract Atlas Georesources International Congress (2017)</b>	<b>p. 264</b>
<b>8.5 Implications of the occurrence of mottramite (PbCu[VO<sub>4</sub>]) in the Jbel Haouanit Cu-Pb-Zn-V supergene ore deposit (Eastern High Atlas, Morocco) – abstract First West African Craton and Margins International Workshop (2017)</b>	<b>p. 265</b>
<b>8.6 Chronology of weathering periods by supergene goethite (U-Th)/He dating in the Oriental High Atlas, Morocco – abstract Goldschmidt (2017)</b>	<b>p. 266</b>
<b>8.7 Genesis of the mottramite bearing Jbel Haouanit Cu-Pb-Zn-V supergene ore deposit (Eastern High Atlas, Morocco) – extended abstract SGA (2017)</b>	<b>p. 267</b>
8.7.1. <i>Introduction</i>	<i>p. 267</i>
8.7.2. <i>Geological setting</i>	<i>p. 267</i>
8.7.3. <i>Materials and analytical methods</i>	<i>p. 268</i>
8.7.4. <i>Results and discussion</i>	<i>p. 268</i>
8.7.5. <i>Conclusion: weathering profile in the ore</i>	<i>p. 272</i>
<b>8.8 (U-Th)/He dating of goethite from the gossan of Moroccan supergene ore deposits – abstract Resources for Future Generations (2018)</b>	<b>p. 273</b>
<b>8.9 REE-U-Th-As enrichment in iron (hydr-)oxides from supergene ore deposits of the High Atlas and Anti-Atlas (Morocco) – abstract Conference of the Geological Society of Africa (2018)</b>	<b>p. 274</b>
<b>8.10 The unexpected presence of supergene Cu-Pb-Ca-Zn-Fe arsenates and vanadates in Agoujgal Cu-mine (Anti-Atlas, Morocco) – abstract Geologica Belgica (2018)</b>	<b>p. 275</b>
<b>8.11 Late Miocene to Quaternary mixed hydrothermal/weathering processes in the Nefza-Sejnane polymetallic mining district (Tunisia) viewed by new goethite (U-Th)/He dating – abstract Réunion des Sciences de la Terre (2018)</b>	<b>p. 277</b>
<b>8.12 (U-Th)/He dating of goethite from the gossan of Moroccan supergene deposits – abstract ILEE Research Day (2019)</b>	<b>p. 278</b>
<b>8.13 Expert's report: petrography, mineralogy and geochemistry of the Tazalaght, Agoujgal, Tassrirt and Tizert-Ighrem sites (collaboration UNamur - Managem company)</b>	<b>p. 279</b>
<b>8.14 Erosion surfaces in the Ardenne-Oesling and their associated kaolinic weathering mantle – book chapter (2018)</b>	<b>p. 280</b>
8.14.1 <i>Weathering mantles</i>	<i>p. 281</i>
8.14.1.a <i>Geographical and geological setting</i>	<i>p. 281</i>
8.14.1.b <i>Characterization and dating of key Ardennian saprolites</i>	<i>p. 282</i>

Transinne	p. 284
Bihain	p. 285
Morialmé	p. 287
Beez	p. 287
<i>8.14.2 Erosion surfaces in the Ardenne and Oesling</i>	<i>p. 288</i>
8.14.2.a Geographical and geological setting	p. 288
8.14.2.b Shape and characteristic of an erosion surface	p. 289
8.14.2.c Identifying an erosion surface	p. 290
8.14.2.d Erosion surfaces of the Hautes Fagnes plateau	p. 291
8.14.2.e Dating a surface	p. 296
8.14.2.f The whole picture: stepped surfaces of the Ardenne-Oesling	p. 297
<i>8.14.3 Erosion surfaces, tectonic uplift and denudation rates in the Ardenne-Oesling</i>	<i>p. 298</i>
<i>8.14.4 Conclusion</i>	<i>p. 301</i>
<b>8.15 Localization of collecting sites and samples</b>	<b>p. 302</b>

Ten abstracts and two extended abstracts published in conferences proceedings and presented during congresses are compiled in this chapter.

Subchapter 8.1 presents an extended abstract (Characterization and genesis of Cu-Pb-Zn-V supergene ore deposits in the Oriental High Atlas (Bou Arfa, Morocco)) published in 2016 in the framework of the Master Day of Geologica Belgica (Brussels, Belgium), in volume 19/3-4, pp. 303-304, and co-authored by **Michèle Verhaert**, Alain Bernard and Johan Yans.

Subchapter 8.2 presents an abstract (Characterization and genesis of Cu-Pb-Zn-V supergene ore deposits in the Oriental High Atlas (Bou Arfa, Morocco)) published in 2016 in the framework of the PhD Day of UNITER (Brussels, Belgium), authored by **Michèle Verhaert**.

Subchapter 8.3 presents an abstract (The contribution of a Europe-Maghreb cooperation for a better prospection of the mining district of Bou Arfa (Morocco): Supergene Fe-Mn-Cu mineralization at Jbel Rhals) published in 2016 in the framework of the Resources and Innovative Geology congress (Montpellier, France), co-authored by **Michèle Verhaert**, Alain Bernard, Augustin Dekoninck, Gaëtan Rochez, Ludovic Lafforgue and Johan Yans.

Subchapter 8.4 presents an abstract (Characterization and genesis of Pb-Zn-Cu-V supergene ore deposits in the Oriental High Atlas (Bou Arfa, Morocco)) published in 2017 in the framework of the Atlas Georesources International Congress (Hammamet, Tunisia), co-authored by **Michèle Verhaert**, Alain Bernard, Augustin Dekoninck, Ludovic Lafforgue, Omar Saddiqi and Johan Yans.

Subchapter 8.5 presents an abstract (Implications of the occurrence of mottramite ( $\text{PbCu}[\text{VO}_4]$ ) in the Jbel Haouanit Cu-Pb-Zn-V supergene ore deposit (Eastern High Atlas, Morocco)) published in 2017 in the framework of the First West African Craton and Margins International Workshop (Dakhla, Morocco), co-authored by **Michèle Verhaert**, Alain Bernard, Augustin Dekoninck, Omar Saddiqi and Johan Yans.

Subchapter 8.6 presents an abstract (Chronology of weathering periods by supergene goethite (U-Th)/He dating in the Oriental High Atlas, Morocco) published in 2017 in the framework of the Goldschmidt congress (Paris, France), co-authored by **Michèle Verhaert**, Cécile Gautheron, Alain Bernard, Augustin Dekoninck, Yves Missenard and Johan Yans.

Subchapter 8.7 presents an extended abstract (Genesis of the mottramite bearing Jbel Haouanit Cu-Pb-Zn-V supergene ore deposit (Eastern High Atlas, Morocco)) published in 2017 in the framework of the SGA congress (Québec, Canada), co-authored by Johan Yans, **Michèle Verhaert** and Augustin Dekoninck.

Subchapter 8.8 presents an abstract ((U-Th)/He dating of goethite from the gossan of Moroccan supergene ore deposits) published in 2018 in the framework of the Resources for Future Generations congress (Vancouver, Canada), co-authored by **Michèle Verhaert**, Cécile Gautheron, Alain Bernard and Johan Yans.

Subchapter 8.9 presents an abstract (REE-U-Th-As enrichment in iron (hydr-)oxides from supergene ore deposits of the High Atlas and Anti-Atlas (Morocco)) published in 2018 in the framework of the 17th Conference of the Geological Society of Africa (Aveiro, Portugal), co-authored by **Michèle Verhaert**, Lhou Maacha, Mohamed Zouhair, Atman Madi and Johan Yans.

Subchapter 8.10 presents an abstract (The unexpected presence of supergene Cu-Pb-Ca-Zn-Fe arsenates and vanadates in Agoujgal Cu-mine (Anti-Atlas, Morocco)) published in 2018 in the framework of the Geologica Belgica congress (Leuven, Belgium), co-authored by **Michèle Verhaert**,

Lhou Maacha, Atman Madi, Abdelaziz Elbasbas, Mohamed Elharkaty, Abdellah Oummouch, Lahcen Oumohou and Johan Yans.

Subchapter 8.11 presents an abstract (Late Miocene to Quaternary mixed hydrothermal/weathering processes in the Nefza-Sejnane polymetallic mining district (Tunisia) viewed by new goethite (U-Th)/He dating) published in 2018 in the framework of the Réunion des Sciences de la Terre congress (Lille, France), co-authored by **Michèle Verhaert**, Cécile Gautheron, Fakher Jamoussi, Béchir Moussi, Hedi-Ridha Chafthar, Sophie Decrée, Nouri Hatira, Augustin Dekoninck and Johan Yans.

Subchapter 8.12 presents an abstract ((U-Th)/He dating of goethite from the gossan of Moroccan supergene deposits) published in 2019 in the framework of the ILEE Research Day (Namur, Belgium), co-authored by **Michèle Verhaert**, Cécile Gautheron, and Johan Yans.

Subchapter 8.13 presents an expert's report drawn up in 2017 for Managem, by **Michèle Verhaert** and Johan Yans, about the petrography, mineralogy and geochemistry of the Tazalaght, Agoujgal, Tassrirt and Tizert-Ighrem sites. The entire export is not displayed to protect the confidentiality of the information.

Subchapter 8.14 presents a book chapter: "Landscapes and Landforms of Belgium and Luxembourg" entitled "Erosion Surfaces in the Ardenne–Oesling and Their Associated Kaolinic Weathering Mantle" authored by Alain Demoulin, François Barbier, Augustin Dekoninck, **Michèle Verhaert**, Gilles Ruffet, Christian Dupuis and Johan Yans, and published in 2018. This chapter presents the long-term geomorphology of the Paleozoic Ardenne–Oesling massif of Southern Belgium and deals with its recording of several phases of weathering.

Subchapter 8.15 gathers the GPS coordinates of the samples studied during this thesis.

## **8.1 Characterization and genesis of Cu-Pb-Zn-V supergene ore deposits in the Oriental High Atlas (Bou Arfa, Morocco) – extended abstract Geologica Belgica (2016)**

Renewed interest has been shown to supergene ore deposits over the last years, due to their high metal contents, their easier extraction process, their softened host rocks, and their location close to the surface.

The deposits of Jbel Klakh (Cu) and Jbel Haouanit (Pb-Zn) are located at the northern edge of the Oriental High Atlas (Morocco). This intracontinental mountain belt is the result of two major events: the Triassic-Liassic rifting and opening of the Atlantic and Tethys Oceans, and the Cenozoic uplift caused by the convergence of the African and Iberian plates. The mineralized veins are hosted in dolostones of Jurassic age.

The Jbel Klakh deposit is characterized by the succession, from the bottom to the top, of four zones defined by mineral assemblages: the primary sulfides in the protolite, the secondary sulfides in the cementation zone, the oxidized minerals in the saprolite, and the iron (hydr-)oxides in the laterite. Three phases of weathering and of supergene mineralization have been identified. The hypogene sulfides (mostly chalcopyrite) are first replaced by secondary sulfides (bornite, digenite, chalcocite, covellite), when reduced and acidic conditions are prevalent. Later, as the environment became more oxidizing and neutral, thanks to the dissolution (buffering) of the carbonate host rocks, malachite, azurite and other oxidized minerals formed by recombination of metallic cations and ligands originating from the dissolved host rocks and oxidized sulfides. Finally, late calcite and dolomite precipitated under neutral conditions. Iron (hydr-)oxides (goethite, hematite) have been precipitating along the whole sequence.

Typical calamine minerals are observed at Jbel Haouanit; three steps of weathering are also considered. The hypogene galena is firstly replaced by anglesite in locally acidic environments. Cerussite precipitates later, at the same time as sphalerite is weathered in smithsonite, under oxidizing conditions. Smithsonite is often rapidly replaced by hydrozincite. Again, late calcite and dolomite are the last minerals to precipitate, and iron (hydr-)oxides are found in the whole sequence. Occurrences of Cu minerals and of a Cu-Pb-Zn vanadate (mottramite) have also been observed close to the Pb-Zn mineralization.

A relation may be established between these weathering phases and the tectonic and climatic evolution of the High Atlas. The precipitation of the hypogene sulfides is most probably related to the Triassic rifting. The hypogene ores and their host rocks were exposed to the oxidizing atmospheric conditions and precipitations during the Cenozoic uplift(s), leading to their weathering. During this period, the alternation of long arid and short wet periods may have provided the optimal conditions for the concentration of metals in solution and the precipitation of massive supergene ores.

## **8.2 Characterization and genesis of Cu-Pb-Zn-V supergene ore deposits in the Oriental High Atlas (Bou Arfa, Morocco) – abstract PhD day UNITER (2016)**

Renewed interest has been shown to supergene ore deposits over the last years, due to their high metal contents, their easier extraction process, their softened host rocks, and their location close to the surface.

The deposits of Jbel Klakh (Cu) and Jbel Haouanit (Pb-Zn) are located at the northern edge of the Oriental High Atlas (Morocco). This intracontinental mountain belt is the result of two major events: the Triassic-Liassic rifting and opening of the Atlantic and Tethys Oceans, and the Cenozoic uplift caused by the convergence of the African and Iberian plates. The mineralized veins are hosted in dolostones of Jurassic age.

The Jbel Klakh deposit is characterized by the succession, from the bottom to the top, of four zones defined by mineral assemblages: the primary sulfides in the protolite, the secondary sulfides in the cementation zone, the oxidized minerals in the saprolite, and the iron (hydr-)oxides in the laterite. Three phases of weathering and of supergene mineralization have been identified. The hypogene sulfides (mostly chalcopyrite) are first replaced by secondary sulfides (bornite, digenite, chalcocite, covellite), when reduced and acidic conditions are prevalent. Later, as the environment became more oxidizing and neutral, thanks to the dissolution (buffering) of the carbonate host rocks, malachite, azurite and other oxidized minerals formed by recombination of metallic cations and ligands originating from the dissolved host rocks and oxidized sulfides. Finally, late calcite and dolomite precipitated under neutral conditions. Iron (hydr-)oxides (goethite, hematite) have been precipitating along the whole sequence.

Typical calamine minerals are observed at Jbel Haouanit; three steps of weathering are also considered. The hypogene galena is firstly replaced by anglesite in locally acidic environments. Cerussite precipitates later, at the same time as sphalerite is weathered in smithsonite, under oxidizing conditions. Smithsonite is often rapidly replaced by hydrozincite. Again, late calcite and dolomite are the last minerals to precipitate, and iron (hydr-)oxides are found in the whole sequence. Occurrences of Cu minerals and of a Cu-Pb-Zn vanadate (motttramite) have also been observed close to the Pb-Zn mineralization. A relation may be established between these weathering phases and the tectonic and climatic evolution of the High Atlas. The precipitation of the hypogene sulfides is most probably related to the Triassic rifting. The hypogene ores and their host rocks were exposed to the oxidizing atmospheric conditions and precipitations during the Cenozoic uplift(s), leading to their weathering. During this period, the alternation of long arid and short wet periods may have provided the optimal conditions for the concentration of metals in solution and the precipitation of massive supergene ores.

### **8.3 The contribution of a Europe-Maghreb cooperation for a better prospection of the mining district of Bou Arfa (Morocco): Supergene Fe-Mn-Cu mineralization at Jbel Rhals – abstract Resources and Innovative Geology (2016)**

The Jbel Rhals massif is located at the northern edge of the Oriental High Atlas. Several phases of uplift were recorded in this intracontinental mountain belt during the Cenozoic period (Leprêtre et al. 2015). The Jbel Rhals ores are hosted in Paleozoic schists overlaid by Permo-Triassic basalts and Lower Jurassic dolostones. New prospections are currently ongoing, aiming for Cu ores. The slaty host rock is strongly fractured, and the overlying basalts are heavily weathered. In the most weathered basalts, layers of various composition seem to be the result of a successive preferential weathering: quartz and clay-rich layers are considered to be the weathering residues of feldspars, while goethite and pyrolusite-rich layers would result from the weathering of ferromagnesian minerals (Macaire and Perruchot 1988; Kamel et al. 1996; Hamidi et al. 1997; Dekayir and El-Maataoui 2001). The dissolution of the former minerals resulted in the formation of cavities that were rapidly filled by a mixture of clays and Fe-Mn oxihydroxides. Two types of mineralized veins are observed: large veins of goethite and fine veins of malachite. In the larger veins, goethite is mainly observed as pseudomorphoses of primary rhombohedral crystals; dendritic pyrolusite often developed at their surface and in some cavities. The basalts intrusion may have affected the underlying host rocks, and the circulation of related fluids may be considered as the source of hydrothermal mineral phases (Daoudi and Pot de Vin 2002). A hypothesis consists of the hydrothermal formation of siderite after this intrusion, in the underlying rocks. Siderite is unstable under oxidizing conditions, and may have been weathered in iron oxihydroxides, during the exhumation and fracturing of the series (Kholodov and Butuzova 2008). The presence of later pyrolusite is consistent with this hypothesis, as siderite often contains high proportions of Mn, which may be released during weathering. Moreover, small crystals of chalcopyrite, pyrite and galena are often found with hydrothermal siderite (Kholodov and Butuzova 2008), and were observed in goethite. Concentric structures of central goethite rimmed by pyrolusite are common in this deposit, and pyrolusite is characterized by a stronger negative Ce anomaly than goethite. This attests of the successive formation of goethite and later of pyrolusite, when conditions became more oxidizing and less acidic, after buffering of the acidity by some host rock (chlorites and carbonates) dissolution. The concretionary and collomorphic structures probably represent the infilling of cavities by various successive generations of fluids. The occurrence of clays, quartz, and K-Ca-Mg-Al-Fe microcrystalline silicates indicates the percolation of Si-rich fluids in the host rock. The general enrichment in REE and Y is related to the presence of REE-phosphates (monazite and xenotime), in quartz and goethite. The later calcite veins contain fine malachite laths and some Cu-Fe-Ni-Mn-minerals, and cut the larger goethite veins. Their precipitation seems to result from a much later circulation of fluids, different from those associated with the Fe-Mn mineralization. Finally, sulfates (jarosite, melanterite, ferricopiapite) were observed on some walls of extracting galleries. Their recent formation is due to the mining and indicates locally strongly acid and oxidizing conditions.

## **8.4 Characterization and genesis of Pb-Zn-Cu-V supergene ore deposits in the Oriental High Atlas (Bou Arfa, Morocco) – abstract Atlas Georesources International Congress (2017)**

The interesting potential of supergene ore deposits lead, over the last years, to a revival of interest for these mineralizations. Their relatively high metal and REE (Rare Earth Elements) content, combined to their relatively easy extraction process related to the softened host rocks and the near-surface situation, make them economically interesting, in particular since prices and demand of metals and REE for new technologies increase.

Here we consider two deposits located at the northern edge of the Moroccan Oriental High Atlas, close to the town of Bou Arfa: Jbel Klakh (Cu) and Jbel Haouanit (Pb-Zn). The mineralogical and geochemical properties of the mineralizations of both sites are different, but the processes responsible for their formation are quite similar. In both cases, mineralized veins are hosted in Jurassic dolostones, and precipitation of supergene minerals is related to the neutralization of acidic fluids during host rock dissolution.

Weathering of Jbel Klakh hypogene ore generated the formation of four mineralogical zones, from base to top: the hypogene zone or protolite (chalcopryrite, pyrite), the secondary sulfides enrichment zone or cementation zone (bornite, digenite, chalcocite, djurleite, covellite), the oxidized zone or saprolite (malachite, azurite, brochantite ...), and the leached zone or laterite (goethite, hematite).

A clear mineral paragenesis is identified at Jbel Haouanit. Hypogene galena is mainly replaced by cerussite, while anglesite occurs in acidic microenvironments. Sphalerite is weathered to smithsonite, which is later replaced by hydrozincite. Occurrences of copper minerals (chalcocite, malachite) and mottramite veins are also observed 2 km away from the Pb-Zn mine; they indicate that Cu, Pb, V bearing fluids also circulated through Jurassic host rocks at Jbel Haouanit.

A relation may be proposed between the weathering and the geodynamic and climatic evolution of the High Atlas. Two major events gave rise to this intracontinental mountain belt: 1) the Triassic-Liassic rifting and opening of the Atlantic and Tethys Oceans, and 2) the Cenozoic tectonic inversion and uplift caused by the convergence of the African and Iberian plates. Precipitation of hypogene sulfides is thought to be related to Triassic rifting. The uplift of the belt provoked the exhumation of hypogene ores and Jurassic host rocks to oxidizing atmospheric conditions and meteoric waters, which most likely led to their weathering. The Cenozoic climate of this region is characterized by an alternation of long arid and short wet periods, which may have provided the optimal conditions for the precipitation of massive supergene ores.



## **8.5 Implications of the occurrence of mottramite ( $\text{PbCu}[\text{VO}_4]$ ) in the Jbel Haouanit Cu-Pb-Zn-V supergene ore deposit (Eastern High Atlas, Morocco) – abstract First West African Craton and Margins International Workshop (2017)**

The Jbel Haouanit deposit, hosted in dolomitized Jurassic limestones, is located at the Northern edge of the Oriental High Atlas (Morocco). The deposit is known for the Pb Zn main mine that was exploited during the first half of the 20<sup>th</sup> century (until 1954), providing 150. 000 tons of ore. Handcrafted excavations are currently exploited 2.5 km away from the principal mine, for Cu and Cu Pb V ores.

The primary sulfides of Jbel Haouanit, galena, sphalerite, pyrite, and chalcopyrite, underwent weathering processes leading to the precipitation of typical supergene minerals. Carbonates are the predominant secondary phases at Jbel Haouanit, leading to neoformation of calamine (typical lead and zinc weathering minerals) minerals). The carbonates result from the buffering of the fluids acidity associated to the oxidation of sulfides, through the dissolution of the dolomitic host rocks. Galena is successively replaced by anglesite and cerussite, sphalerite is weathered in to smithsonite, which is subsequently replaced by hydrozincite, and pyrite is pseudomorphosed in hematite and goethite. The weathering of chalcopyrite successively leads to the precipitation of chalcocite, covellite, malachite, and goethite. Small grains of barite, copper lead sulfosalts and phosphoarsenates are disseminated in the ore. Mottramite  $\text{PbCu}[\text{VO}_4]$  is observed in veins in the cementation zone, as euhedral crystals surrounded by (ferriferous) calcite and dolomite. Malachite also contains numerous small crystals of mottramite. The occurrence of copper minerals and mottramite at Jbel Haouanit indicates that Cu, Pb, V bearing fluids also circulated through the Jurassic host rocks. Mottramite is typically found in the southern part of Africa (Namibia, Angola, Zambia) in oxidized zones of vanadium bearing supergene deposits, but it may also be abundant around Cu sulfides ores (Boni et al. 2007, and references therein). This vanadate forms at low temperatures (40-50°C), in arid, acidic and slightly reduced environments, such as the boundary between the phreatic and vadose zones (Takahashi 1960; Boni et al. 2007). Jbel Haouanit mottramite shows a positive Ce anomaly suggesting its neoformation in relation with Eh variations (Leybourne et al. 2000). The slight enrichment in LREE (Light Rare Earth Elements), compared to HREE (Heavy Rare Earth Elements), also indicates that mottramite precipitated from slightly more acidic fluids than the other supergene minerals, where LREE are further soluble than HREE (De Putter et al. 1999). Vanadium is initially restricted in minor quantities in the primary sulfides (e.g. galena) and in the host dolostone of Jbel Haouanit, at the range of 5-10 ppm. When the host rock is weathered, V is released with other ions. It is probably transported as a calcium metavanadate ( $\text{Ca}[\text{VO}_3]_2$ ) far away from its source before precipitation by recombination with metal cations in favourable environments (van der Westhuizen et al. 1989). Following Boni et al. (2007), the released Ca may then react with bicarbonate ions to form dolomite and calcite. All the Jbel Haouanit samples are V rich, and “bulk” calamine rocks are also enriched in this metal compared to galena, suggesting that V bearing fluids have percolated in the whole deposit, and that mottramite may result from the same weathering step as the other secondary minerals. Once formed, mottramite does not seem to undergo further weathering. Note that descloizite, the Zn analogue of mottramite, was not found in this deposit.

The High Atlas was built in several steps, the two most dominant being the Mesozoic rifting and the Cenozoic tectonic inversion and uplift. Three major episodes of Cenozoic uplift are defined by Leprêtre et al. (2015) in the eastern High Atlas: late Eocene, early to middle Miocene, and late Pliocene to Quaternary. Neoformation of mottramite, as the other supergene minerals, should be associated to these geodynamic events (as proposed by Choulet et al. 2014).

## **8.6 Chronology of weathering periods by supergene goethite (U-Th)/He dating in the Oriental High Atlas, Morocco – abstract Goldschmidt (2017)**

The application of (U-Th)/He dating to iron oxihydroxides recently renewed the interest in supergene ore deposits chronology. The (U-Th)/He method is based on the accumulation of  $^4\text{He}$  produced during the alpha decay of U and Th that are usually contained in traces in various minerals, and offers the potential to date supergene minerals over a range of timescales, up to hundreds of Ma. Goethite and hematite, especially, are ubiquitous in supergene deposits and precipitate in surface conditions that are favorable for slow He diffusion and thus He retention over geological ages, which makes them ideal candidates for (U-Th)/He dating.

To better understand the development of supergene profiles, we have performed goethite (U-Th)/He dating on samples collected in the Oriental High Atlas (Morocco), in the oxidized Pb-Zn-Cu-V-Fe ore deposits of Jbel Haouanit, Jbel Klakh, and Jbel Rhals. The Jbel Klakh and Jbel Rhals samples respectively yielded reproducible ages of ca. 15-20 and 1.5-2.5 Ma. Jbel Haouanit results show some variations, with ages of ca. 4-5.5 and 10.5-11.5 Ma. We speculate that these variations could be related to the polycrystalline structure of these samples and/or to the continued growth of these minerals through contact with groundwater long after initial precipitation. These new ages correlate with geodynamical events recently defined by Leprêtre et al. (2015) in the High Atlas during the Cenozoic: 1) late Eocene, 2) early to middle Miocene, and 3) Pliocene to present. Our data in the Moroccan High Atlas do confirm that goethite (U-Th)/He dating is a reliable tool to date the weathering processes/periods, and that this method may be useful for dating mineralizations related to recent crustal movements.

## **8.7 Genesis of the mottramite bearing Jbel Haouanit Cu-Pb-Zn-V supergene ore deposit (Eastern High Atlas, Morocco) – extended abstract SGA (2017)**

The Jbel Haouanit ore deposit, hosted in dolomitized Jurassic limestones, is located in the Oriental High Atlas (Morocco). Pb-Zn mineralizations have been exploited in an ancient underground mine, while Cu-Pb-V occurrences are currently mined in handmade (“artisanal”) excavations. The primary sulfides of Jbel Haouanit, galena, sphalerite, pyrite, and chalcopyrite, underwent weathering processes leading to the precipitation of typical supergene minerals, mainly carbonates. Their formation was allowed by the buffering of the fluids acidity associated with the oxidation of sulphides, through the dissolution of the dolomitic host rocks. The paragenetic sequence is rather simple: galena has been successively replaced by anglesite and cerussite, sphalerite has been weathered in smithsonite, which was later replaced by hydrozincite, and pyrite has been pseudomorphosed in hematite and goethite. The weathering of chalcopyrite successively leads to the precipitation of chalcocite, covellite, malachite, and goethite. Late iron oxyhydroxides are mainly found at the top of the deposit. Occurrences of mottramite indicate that V rich fluids have circulated in the deposits. The presence of secondary sulfides (galena, covellite) and mottramite is related to local fluctuations of the hydrostatic level.

### ***8.7.1. Introduction***

Morocco hosts a wide range of supergene deposits distributed along the High Atlas and the Anti-Atlas. The renewal of interest in these ore deposits, leading to new exploration and mining projects, has been induced by the rise of metal prices since the 2000s, the introduction of modern prospecting tools, and the increasing demand for metals for new technologies. Moreover, supergene metal deposits are easier and faster accessible and extractable than the primary minerals, and their metals and REE contents are typically higher (Reich and Vasconcelos 2015).

Here we focus on the Jbel Haouanit deposit, located close to the Moroccan city of Bou Arfa. The deposit is mostly known for its Pb Zn mine that was exploited during the first half of the 20th century (until 1954), providing 150 000 tons of ore. Handcrafted excavations are currently exploited 2.5km away from the principal mine, for Cu and Cu-Pb-V ores. The purposes of this study are to 1) characterize the supergene mineral assemblages, 2) establish a mineral inventory, 3) identify the parageneses, and 4) propose a genetic model that includes the various mineralizations of the deposit, while giving some particular attention to the uncommon Cu Pb V occurrences.

### ***8.7.2. Geological setting***

The Jbel Haouanit mine is located at the northern edge of the Oriental High Atlas (Fig. 8.7.1). This intracontinental mountain belt was built in several steps, the two most dominant being the Mesozoic rifting and the Cenozoic tectonic inversion and uplift. The rifting, lasting from Permian to Middle Jurassic, has been induced by the break up of Pangaea and the opening of the Tethys and Atlantic Oceans. The Late Cretaceous opening of the Atlantic Ocean modified the drifting direction of the African plate from heading E to NE, and made it converge with the Iberian (Eurasian) plate, triggering the basin inversion and generating fracturing, folding and sometimes detachment of the Mesozoic and Cenozoic cover units from the Variscan basement (e.g. Frizon de Lamotte et al. 2000, and references therein). In the studied area, three major episodes of Cenozoic uplift are defined by Leprêtre et al. (2015): late Eocene, early to middle Miocene, and late Pliocene to Quaternary. The paroxysmal compressional phase happened during Pliocene. These crustal processes coupled with a high asthenospheric heat flow are responsible for the current topography of the Atlas Chain (Missenard et al. 2006).

The Pb-Zn, Cu and Cu-Pb-V ores of Jbel Haouanit are hosted in Jurassic dolomitized series most likely Dogger in age, between Aalenian and Bathonian (Chefchaoui et al. 1963; Fig. 1). These limestones are strongly fractured, moderately folded, and lie unconformably on the Paleozoic schist basement. Numerous faults affect the Triassic, Jurassic and Cretaceous strata of the Bou Arfa region, in the E W, NE SW, and WNW ESE directions; a major E-W oriented fault may be observed close to the main mine (Chefchaoui et al. 1963; Fig. 8.7.1).

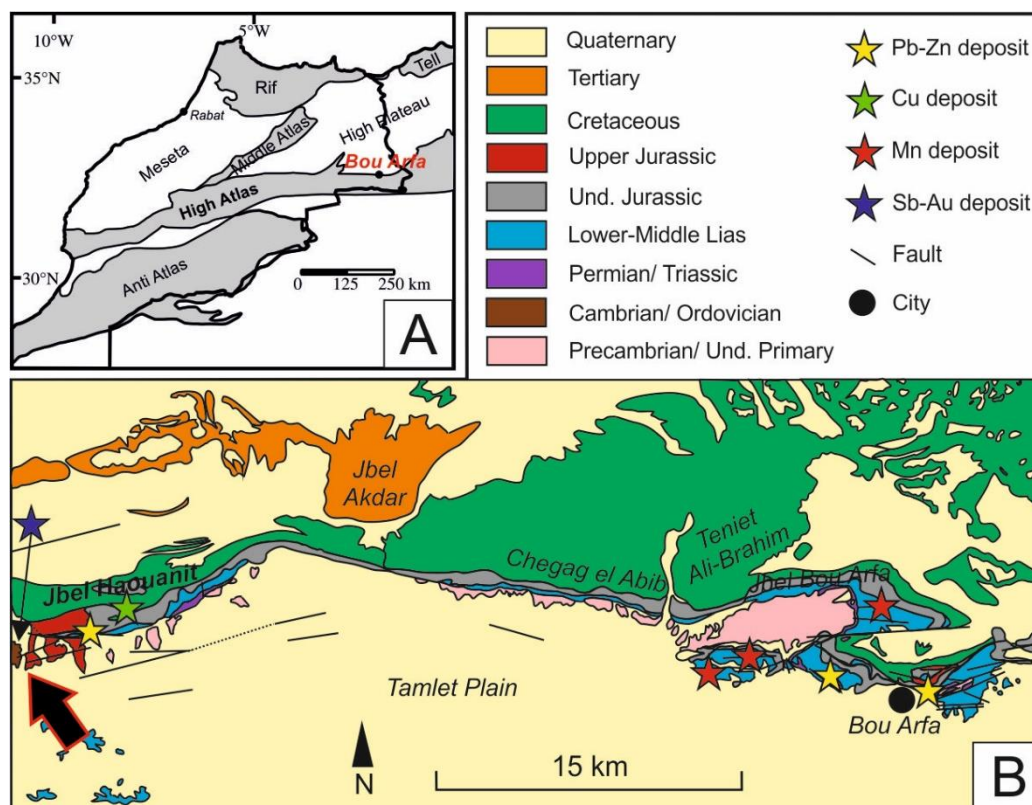


**Figure 8.7.1.** (A) Simplified geologic map of Morocco showing the location of Bou Arfa. (B) Synthetic geologic map of the Bou Arfa region showing the location of the Jbel Haouanit ore deposit in undetermined Jurassic dolostones (modified zoom of the geologic map of Chefchaoui et al., 1963).

### 8.7.3. Materials and analytical methods

Field observation has been complemented by a multidisciplinary approach (transmission and reflection optical microscopy, XRD (X-Ray Diffraction), SEM (Scanning Electron Microscopy), geochemistry) for the mineralogical characterization.

### 8.7.4. Results and discussion

#### 8.7.4.a Host rock

The Jurassic host rock consists of a xenotopic recrystallized matrix of microcrystalline dolomite punctuated by rare iron oxyhydroxides, which results from the replacement of the primary limestone by dolomite. The presence of carbonates in the host rock has been of a major importance during the weathering, as it enabled the buffering of the fluids acidity and the precipitation of secondary minerals.

#### 8.7.4.b Cu and Cu-Pb-V mineralization

The copper ores mined in the small (“artisanal”) excavations consist of highly brecciated chalcocite successively weathered in covellite and malachite, associated to botryoidal goethite (Fig. 8.7.2A, 8.7.3).

Ore veins are 0.5 to 5 centimeters wide. Chalcopyrite and pyrite are thought to be the primary sulfides: the circulation of acidic, Cu-rich fluids in the deposit triggers the replacement of chalcopyrite in chalcocite, and the remobilization and precipitation of iron in goethite (Fig. 8.7.3). Covellite then replaces the highly fractured chalcocite, from the edges to the center, when fluids become less enriched in Cu (Fig. 8.7.2A, 8.7.3). Malachite finally replaces both chalcocite and covellite, by recombination of dissolved copper and bicarbonate ions (Fig. 8.7.2A, 8.7.3).

Covellite often contains acanthite inclusions that are typically found in supergene oxidation zones, associated with low temperature secondary sulfides (Ramdohr 1980). Small grains of partly oxidized pyrite, barite, copper-lead sulfosalts and phospho-arsenates are disseminated in the ore. Malachite also contains numerous small crystals of mottramite, a Cu-Pb hydrated vanadate.

Some excavations exhibit veins containing euhedral crystals of mottramite surrounded by (ferriferous) calcite and dolomite (Fig. 8.7.2B). Mottramite is typically found in oxidized zones of vanadium-bearing supergene deposits, but may also be abundant within/around Cu-sulfides ores. It is observed in the southern part of Africa (Namibia, Angola, Zambia) (Boni 2007, and references herein). This vanadate forms at low temperatures (40–50°C), in arid (Takahashi 1960), acidic and slightly reduced environments, such as the boundary between the phreatic and vadose zones (Boni et al. 2007).

Jbel Haouanit mottramite shows a positive Ce anomaly, suggesting its neoformation in relation with Eh variations (Leybourne et al. 2000). The slight enrichment in LREE (Light Rare Earth Elements), compared to HREE (Heavy Rare Earth Elements) in mottramite, also indicates that this mineral may have precipitated from slightly more acidic fluids than the other supergene minerals, where LREE are more soluble than HREE (De Putter et al. 1999).

Vanadium was initially restricted in minor quantities in the primary sulfides (e.g. galena) and in the host dolostone of Jbel Haouanit, in the range of 5–10 ppm. V was released with other ions during weathering. It was probably transported as calcium metavanadate ( $\text{Ca}[\text{VO}_3]_2$ ) far away from its source (van der Westhuizen et al. 1989) and precipitated by recombination with metal cations in favourable environments. Following Boni et al. (2007), the released Ca may then have reacted with bicarbonate ions to form dolomite and calcite.

All the Jbel Haouanit samples are V-rich, and Calamine rocks are also enriched in this metal compared to galena, suggesting that V-bearing fluids may have percolated in the whole deposit, and that mottramite may result from the same weathering step as the other secondary minerals. Once formed, mottramite does not seem to undergo further weathering. Note that descloizite, the Zn analogue of mottramite, was not found in this deposit.

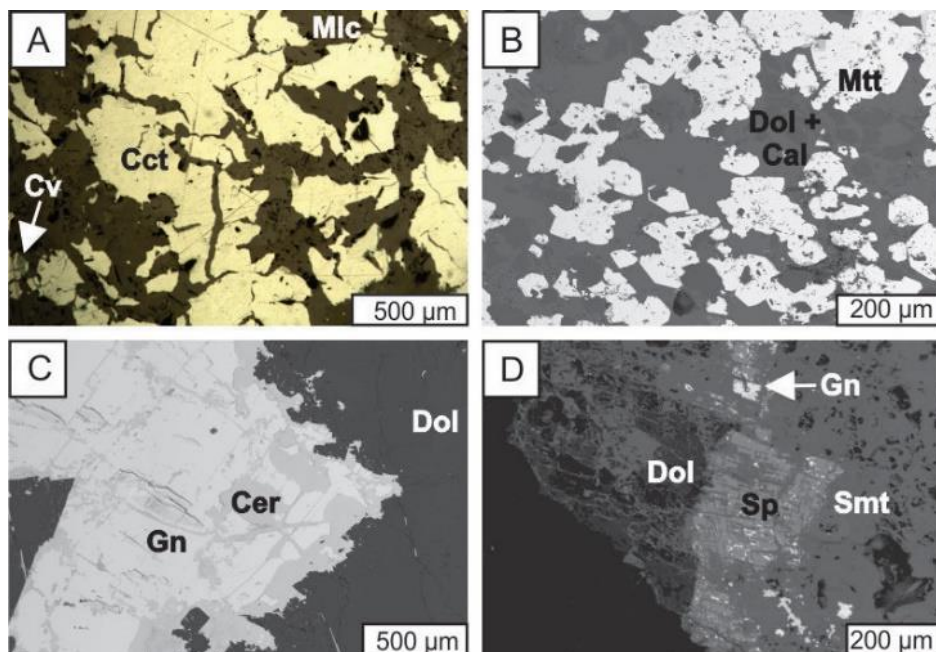


**Figure 8.7.2.** Representative samples of the Jbel Haouanit deposit: reflected light photomicrograph (A), and SEM microphotographs in backscattered electrons mode (B, C, D). (A) Lattice of chalcocite (Cct), covellite (Cv) and malachite (Mlc); (B) mottramite (Mtt) surrounded by dolomite and calcite (Cal); (C) weathering of galena (Gn) in cerussite (Cer), surrounded by dolomite (Dol); (D) sphalerite (Sp) weathered in smithsonite (Smt), close to galena and dolomite.

Minerals	Sedimentation + diagenesis	Hypogene mineralization	Supergene mineralization
Limestone	●		
Dolomite I	●		
Sphalerite		●	
Galena I		●	
Pyrite		●	
Chalcopyrite		●	
Chalcocite			●
Galena II			●
Covellite			●
Mottramite			●
Anglesite			●
Hematite			●
Goethite			●
Malachite			●
Cerussite			●
Smithsonite			●
Calcite			●
Dolomite II			●
Hydrozincite			●

**Figure 8.7.3.** Tentative paragenetic sequence for the Jbel Haouanit deposit.

#### 8.7.4.c Pb-Zn mineralization

In the Pb-Zn ore, mineralized veins are 1 millimeter to 20 centimeters wide, and mostly contain galena surrounded by lead and zinc weathering minerals (here designated as calamine; Fig. 8.7.2C). The principal primary sulfide observed in the ore is galena, but pyrite and sphalerite were likely initially present, as their weathering products (relics and pseudomorphs) are found in significant quantities (Fig. 8.7.3). The supergene mineral assemblage resulting from the weathering of these sulfides, under slightly acidic and oxidizing conditions, is dominated by carbonates. The predominant position of cerussite suggests a low acidity of the mineralizing fluids, due to an efficient buffering of the acidity by dissolution of the carbonated host rocks.

Galena has been weathered to anglesite and cerussite: anglesite is found in fractures and cleavages, whereas cerussite also surrounds galena (Fig. 8.7.2C, 8.7.3). This divergence is related to the stability domains of these minerals: cerussite is stable under slightly acidic to basic conditions ( $\text{pH} > 5$ ), whereas anglesite usually forms in acidic environments ( $\text{pH} < 5$ ), where sulfate ions activity is high. These last specific conditions are typically found close to weathering-ongoing pyrite that causes locally substantial drops of pH, or in favorable microenvironments as fractures and cleavages. With increase of pH, anglesite is replaced by cerussite (Reichert 2007). At Jbel Haouanit, covellite is often observed at the contact between galena and cerussite/anglesite, and secondary galena is found in cavities, close to cerussite. The occurrence of these secondary sulfides suggests that, locally, slightly reduced conditions prevailed or that the environment was fluctuating between oxidizing and reduced conditions due to local variations of the hydrostatic level (Choulet et al. 2014).

Weathering of sphalerite in smithsonite began along cleavages and fractures, and later affected the whole crystal (Fig. 8.7.2D, 8.7.3). Smithsonite is only stable at pH lower than 7, and high  $\text{CO}_2$  partial pressures, typically observed in percolating fluids that are not in equilibrium with the atmospheric  $\text{CO}_2$ . At the end of the weathering processes, when  $\text{CO}_2$  pressure turned to atmospheric values, smithsonite became unstable and has been replaced by more stable hydrozincite (Reichert 2007). Smithsonite encloses anhedral inclusions of acanthite that are responsible for a remarkable enrichment in Ag (up to 450-550 ppm). The lack of Zn silicates at Jbel Haouanit indicates that the mineralizing fluids did not contain significant amounts of Si, which is quite rare in calamine deposits, but consistent with the low content in detritic elements of the host rock dolostone.

Small crystals of pyrite have been pseudomorphosed in iron oxyhydroxides: hematite and goethite are respectively observed at the center and external rim of the pseudomorphs. Goethite precipitates under acidic conditions, whereas hematite forms under more neutral pH conditions (Fig. 8.7.3; Jönsson et al. 2006 and references therein); goethite often replaces hematite. Iron oxyhydroxides are the most enriched in REE, and are characterized by the highest contents in immobile elements, which is related to their low solubility and their in-situ precipitation. Large veins of hematite, goethite, and late (ferriferous) dolomite and calcite also surround the Pb-Zn ores.

The relative resistivity of galena to weathering, in comparison with the other sulfides, and its subsistence among the supergene mineralizations, is related to the geochemical behaviour of Pb. Because Pb is an immobile element, galena is replaced in situ by its quite insoluble weathering products that precipitate directly around the sulfide, creating an armoring protecting galena from further weathering and oxidation by (partially) hindering contact with the oxidizing agents (Reichert 2007). As



Zn ions are particularly mobile under acidic conditions, sphalerite does not have such a protective layer, and is totally weathered.

Calamine samples and galena are rich in Ge (up to 16.5 ppm): in the sulfide, this enrichment is due to the common substitution, involving elements such as Fe, Cu, Ag, to Zn (Cook et 2009). When sphalerite is oxidized, Ge is released and may then accumulate in calamine samples (here particularly in smithsonite), by substituting Zn. All samples are also enriched in U, which is a typical supergene pattern.

### 8.7.5. Conclusion: weathering profile in the ore

Clear parageneses are easily identified at Jbel Haouanit. The hypogene galena has been successively replaced by anglesite and cerussite, whereas sphalerite has been weathered in smithsonite and hydrozincite. The occurrence of copper minerals and mottramite indicates that Cu, Pb, V bearing fluids have also circulated through the Jurassic host rocks. As shown in Figure 8.7.4, the weathering of the hypogene sulfides led to the formation of several mineralogical zones: the primary sulfides zone (chalcopryrite, pyrite, galena, sphalerite), the secondary sulfides zone (chalcocite, covellite, mottramite), the oxidized ores zone (cerussite, anglesite, smithsonite, hydrozincite, malachite, mottramite, iron oxyhydroxides), and the leached zone (iron oxyhydroxides and late calcite and dolomite, principally). The secondary sulfides zone of the Pb-Zn deposit is quite reduced, in comparison to that of the Cu and Cu-Pb-V occurrences.

No dating has yet been performed on these supergene mineralizations, although it could bring very useful information on the refined chronology of this deposit. Geochronological data are also essential to insert supergene ore genesis in the climate and geodynamic evolution of the metallogenic province (i.e. relations between the supergene mineralizations and the Cenozoic High Atlas uplifts). For this purpose, (U-Th)/He chronology will be carried out on some supergene goethite and hematite.

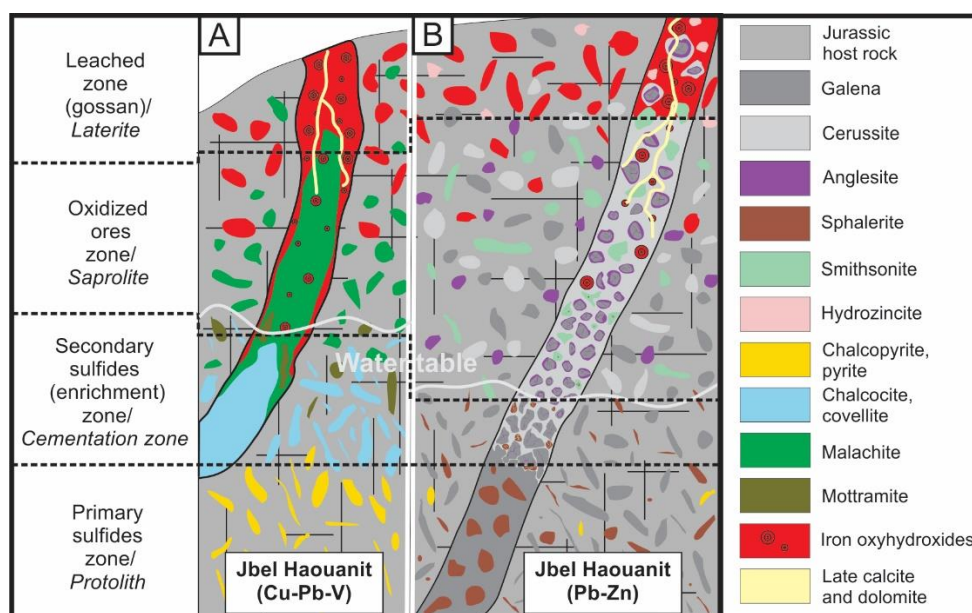


**Figure 8.7.4.** Schematic cross-sections (not at scale) showing the mineralogical zones of the Jbel Haouanit supergene ore deposits and the most common mineral phases; (A) Cu-Pb-V deposit of Jbel Haouanit, (B) Pb-Zn deposit of Jbel Haouanit (adapted after Robb 2005).



## **8.8 (U-Th)/He dating of goethite from the gossan of Moroccan supergene ore deposits – abstract Resources for Future Generations (2018)**

A wide range of supergene deposits are hosted in Morocco, principally in the High-Atlas and Anti-Atlas. They typically show a four-levels profile composed, from base to top, of the hypogene, cementation, oxidized, and leached (or gossan) zones. The formation of these supergene profiles is triggered by weathering processes of hypogene ores. The leached zone mainly contains iron (hydr-)oxides such as goethite, which is the most common and stable iron oxyhydroxide under atmospheric conditions.

Here we focus on the (U-Th)/He dating of goethite sampled in the Oriental High Atlas of Morocco. The (U-Th)/He method is particularly suitable for refining our knowledge of the formation of supergene deposits through dating of goethite, which is widely distributed in the deeply gossan zone. Goethite forms here by low temperature processes, under surface conditions that are favorable for reduced He diffusion and retention over geological ages.

We performed goethite (U-Th)/He dating on 18 aliquots collected in the oxidized Pb-Zn-Cu-V-Fe deposits of Jbel Haouanit, Jbel Klakh, and Jbel Rhals. Prior to dating, samples were investigated mineralogically and geochemically, with particular focus on mineral paragenesis, homogeneity, and textures. Samples preliminarily yielded three sets of uncorrected ages: 1.0-2.5, 3.0-6.0, and 10-20 Ma. These ages correlate with the two latest episodes of the alpine geodynamical events in the High Atlas: early to middle Miocene, and Pliocene to present. Our data indicate that the Pliocene-Recent phase is polyphased, with a first episode of goethite precipitation during early Pliocene, and a second during early Pleistocene. The scattering of the oldest ages, corresponding to the middle Miocene phase, is probably related to a more continued growth of these samples, through extended contact with groundwater.

## **8.9 REE-U-Th-As enrichment in iron (hydr-)oxides from supergene ore deposits of the High Atlas and Anti-Atlas (Morocco) – abstract Conference of the Geological Society of Africa (2018)**

Morocco hosts a wide range of supergene deposits principally located in the High Atlas and Anti-Atlas. The interest of mining these ores lies in their relatively high metal, including Rare Earth Elements (REE) content, and their rather easy extraction process related to their softened host rocks and near-surface distribution. The weathering of hypogene ores generates the formation of supergene profiles composed of, from base to top, the i) hypogene zone, ii) cementation zone, iii) oxidized zone, and iv) leached zone (or gossan). We focus here on the enrichment in particular elements of iron (hydr-)oxides such as goethite. Goethite is the most common and stable iron oxyhydroxyde under atmospheric conditions, and is thus widely observed in the gossan of supergene deposits. Several copper deposits from the districts of Bou Arfa (Oriental High Atlas) and Akka (Eastern Anti-Atlas, Kerdous and Ighrem inliers) are considered.

Twenty-six samples of goethite were analyzed to assess their concentrations in major and trace elements (including REE). The contents of major and trace elements in goethite are mostly depending on the nature of the host rocks (carbonates, shales, ...) and the type of the mineralized veins (Cu, Pb, Zn, ...) of the deposit, whereas the REE patterns show particular features related to the nature of the samples. Well-crystallized samples show higher values in LREE, whereas poorly crystalline powdery goethite is enriched in MREE. In comparison to the Post-Archean Australian Shale (PAAS), most samples present fractionated patterns, with slightly negative Ce anomalies and an enrichment in MREE and HREE.

Another important feature of iron (hydr-)oxides of both Bou Arfa and Akka districts is their high U and As content. The concentration of U and REE in iron (hydr-)oxides is a typical supergene trend. Enrichment in U and associated depletion in Th are related to a selective U vs Th mobilization during weathering processes. Soluble and mobile U is preferentially leached and accumulated in neoformed minerals, while immobile Th is retained in weathering-resistant minerals. The high REE and U contents in goethite are related to the large specific surface, the numerous cation exchange sites, the subsequent important adsorption capacity under acidic conditions, but also to the coprecipitation of minerals at the interface between iron (hydr-)oxides and fluids. Enrichment in As is related to the adsorption of this element by goethite, in the form of arsenate or  $\text{FeAsO}_4$ , in oxic environments. The fractionation of REE patterns reflects the precipitation of goethite from relatively acidic fluids, where LREE are more soluble than HREE, whereas the lack of fractionation is a consequence of neutral pH conditions, possibly related to a neutralization by carbonate host rock. The slightly negative Ce anomaly of most samples indicates that Fe (hydr-)oxides formed in an oxidizing environment. The rapid oxidation and subsequent precipitation of this element indeed triggers its decoupling from the other REEs that remain in solution.

## 8.10 The unexpected presence of supergene Cu-Pb-Ca-Zn-Fe arsenates and vanadates in Agoujgal Cu-mine (Anti-Atlas, Morocco) – abstract Geological Belgica (2018)

A large number of copper deposits are located in the Moroccan Anti-Atlas, particularly at the contact between Precambrian inliers and Cambrian-Adoudounian cover formations. The Agoujgal deposit is located at the southeastern border of the Kerdous inlier, and has been managed by the mining company Managem for its copper (~1%) and silver (~30g/t) ore.

The ores are hosted by Adoudounian silts, sandstones, dolomites, dolomitic sandstones and limestones, and are located on the top of a strongly altered and weathered porphyritic granite and volcanoclastic series. The mineralization is composed of hypogene Cu(-Co-As-Pb-Zn) sulfides that underwent significant weathering, leading to the formation of successive generations of secondary minerals. Supergene minerals are observed as filling of fractures and geodic cavities of the host rock, as impregnations of the gangue, and as *in situ* replacement of the primary mineralization. The usual vertical sequence of weathered copper deposits is not observed at Agoujgal, which may be related to the varying altitude of the weathering front, in accordance with the fracturing and folding of the host rocks. However, the typical paragenetic profile (primary sulfides – secondary sulphides – oxidized minerals – iron oxides or *gossan*) is clearly recognized.

Pyrite and chalcopyrite are the main primary sulfides; bornite ( $\text{Cu}_5\text{FeS}_4$ ), tennantite ( $\text{Cu}_6\text{Cu}_4(\text{Fe}, \text{Zn})_2\text{As}_4\text{S}_{13}$ ), cobaltite ( $\text{CoAsS}$ ), bismuthinite ( $\text{Bi}_2\text{S}_3$ ), acanthite ( $\text{Ag}_2\text{S}$ ), galena ( $\text{PbS}$ ), arsenopyrite ( $\text{FeAsS}$ ), matildite ( $\text{AgBiS}_2$ ), sphalerite ( $\text{ZnS}$ ), greenockite ( $\text{CdS}$ ) and kobellite ( $\text{Pb}_{22}\text{Cu}_4(\text{Bi}, \text{Sb})_{30}\text{S}_{69}$ ) are present in smaller proportions. The first step of weathering of chalcopyrite (and bornite) is the successive transformation in secondary sulfides such as bornite, chalcocite ( $\text{Cu}_2\text{S}$ ), djurleite ( $\text{Cu}_{31}\text{S}_{16}$ ) and covellite ( $\text{CuS}$ ). By substituting chalcopyrite and bornite, chalcocite and djurleite form a typical *chickenwire* texture in which they are successively replaced by goethite and malachite (Fig. 8.10.1A).

The Cu-oxidized mineralization is much diversified, with carbonates (malachite, azurite), oxides (cuprite, tenorite, goethite), vanadates (motttramite ( $\text{PbCu}(\text{VO}_4)(\text{OH})$ ), calcio-volborthite ( $\text{CaCu}(\text{VO}_4)(\text{OH})$ )), arsenates (conichalcite ( $\text{CaCu}(\text{AsO}_4)(\text{OH})$ ), olivenite ( $\text{Cu}_2\text{AsO}_4(\text{OH})$ )), and sulfates (brochantite ( $\text{Cu}_4\text{SO}_4(\text{OH})_6$ )). These oxidized minerals, in which intergrowths are very common (Fig. 8.10.1B), most probably all precipitated within a short period of time. Arsenates are mainly found close to the altered and weathered granite of the basement, but are also observed in smaller amounts in the entire deposit. Conichalcite sometimes replaces a primary mineral of which only the shapes of the crystals remain (Fig. 8.10.1C). In some samples, mimetite ( $\text{Pb}_5(\text{AsO}_4)_3\text{Cl}$ ) is weathered in a succession of various minerals including, among others, conichalcite, olivenite, calcio-duftite ( $(\text{Pb}, \text{Ca})\text{CuAsO}_4(\text{OH})$ ), motttramite, calcio-volborthite, Ca-Cu-, Ca-Zn-, and Ca-Fe- arsenates (Fig. 8.10.1D, 8.10.1E).

The proximity of Agoujgal granite probably enhanced the formation of hydrothermal polymetallic ores and later, the development of secondary minerals due to weathering. Base metals such as Cu, Pb, Zn, As, and V in the supergene minerals most probably derive from the primary sulfides and rocks. The arsenates result from the relative abundance of As-bearing minerals in the primary mineral association; tennantite is thought to be the most significant source of As. V is thought to be included in sulfides, such as galena and pyrite. During weathering, As and V are mobilized and recombined with available ions to be precipitated at favorable sites or barriers, such as the contact with the granite at

Agoujgal. Vanadates, i.e. mottramite, preferably precipitate under low Eh and acidic conditions arising from sulfides weathering. Cation substitutions and solid solutions are common in arsenates, which might explain the abundance of mixed Ca-Cu-Zn-Fe arsenates at Agoujgal. For instance, conichalcite and calcio-duftite form a solid solution and are often replacing one another. The successive transformation of mimetite in calcio-duftite and later in olivenite is related to a rise of the Cu content; the inverse replacement of olivenite by calcio-duftite is associated with local pH rises. The presence of conichalcite or olivenite depends on geochemical parameters: conichalcite prefers basic pH and low Eh conditions, whereas olivenite precipitates from more acid fluids that are characterized with a lower Cu- activity.

Iron (hydr-)oxides show different forms: powdery, as pseudomorphs of pyrite, and botryoidal. Hematite and goethite are mixed in all samples. Two generations of pyrite, one cubic and the other rhombododecaedral, are replaced by goethite and hematite in layers that follow the stratification (Fig. 8.10.1F). In these samples, goethite is observed at the center of the structures, and hematite at the edges, which could indicate dehydration processes. Late greenish Zn-calcite is cutting the entire sequence, sometimes leading to the formation of brecciated units.

Arsenates-bearing samples are rich in LREE, reaching ~900 ppm of La, ~1500 ppm of Ce, and ~500 ppm of Nd, which is consistent with the observation of monazite. Vanadates are slightly enriched in HREE, but values are not exceeding ~200 ppm. The As, Pb and Zn contents are particularly high for all the Agoujgal samples, and related to the presence of these elements in the primary (i.e. in sphalerite) and secondary (i.e. in smithsonite) mineralization. Arsenates are also rich in Bi (~1600 ppm) and Mo (~1000 ppm), and mottramite in Y (~1800 ppm).

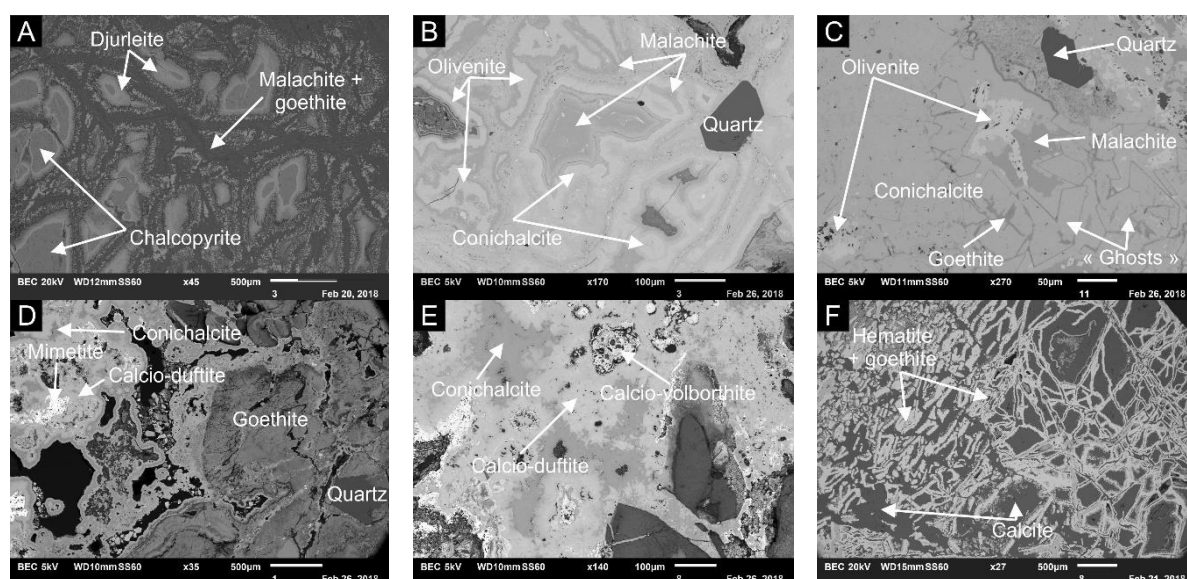


**Figure 8.10.1** SEM photomicrographs in backscattered electrons mode.

### **8.11 Late Miocene to Quaternary mixed hydrothermal/weathering processes in the Nefza-Sejnane polymetallic mining district (Tunisia) viewed by new goethite (U-Th)/He dating – abstract Réunion des Sciences de la Terre (2018)**

The Nefza polymetallic mining district is located in the Tellian "Nappe Zone" of northern Tunisia. The Cenozoic deposits overlay a basement made up of Albian-late Priabonian folded marls and Chattian-Burdigalian sandstones. Late Miocene felsic subvolcanic rocks and basaltic flows are regionally observed. New samples were collected for (U-Th)/He dating in the halloysite-Fe-Mn quarry of Tamra, the volcanic Fe-REE-U breccia of Oued Belif, and the Boukchiba and Ouchtata Fe localities, in order to constraint the hydrothermal and/or weathering episodes that affected this area and led to the formation of the various polymetallic deposits.

First, X-ray diffraction and scanning electron microscopy have been used to identify the mineral phases of twenty samples, and ensure a considered choice of mineralogically unmixed samples. Three samples of goethite were selected at Tamra (from a vein, associated to hematite, and close to the Mn ore), two at Ouchtata (pseudomorphosis of pyrite and from a vein), one at Boukchiba (from a vein), and one at Oued Belif (from a vein). (U-Th)/He raw ages have been corrected to compensate He diffusion by applying a 10% correction. Tamra samples yielded following ages: ~1-3, 3-6, and 8-9 Ma, whereas samples from Ouchtata and Oued Belif delivered ages of ~0.8 Ma. The Boukchiba sample presents ages of ~4 and ~9 Ma.

There were thus at least two episodes of Fe-rich fluids percolation in the Nefza district. The oldest episode (8-9 Ma), recorded at Tamra and Boukchiba, might be related to the Late Miocene magmatic activity and enhanced hydrothermalism. The latest episode (< 1 Ma), recorded at Ouchtata, Oued Belif, and Tamra, could correspond to goethite precipitation most likely linked to weathering. The 3 to 6 Ma ages of Boukchiba and Tamra probably represent a blend of the previously cited ages and of successive generations of goethite (and hematite, at Tamra). The 4.7 and 3.35 Ma  $^{40}\text{Ar}$ - $^{39}\text{Ar}$  ages obtained by Decrée et al. (2010) could be embedded within this sequence, with a precipitation of Mn-oxides between the two main episodes of Fe-(hydr-)oxides formation.

The (U-Th)/He dating confirms that the Fe-Mn mineralization of Tamra is the result of mixed synsedimentary pedogenesis processes and later hydrothermal and meteoric fluids circulation. The compiling of all the ages suggests the successive formation of hydrothermal goethite and hematite, Mn-oxides, and goethite related to weathering.

## 8.12 (U-Th)/He dating of goethite from the gossan of Moroccan supergene deposits – abstract ILEE Research Day (2019)

Numerous secondary (supergene) deposits are hosted in the Moroccan High-Atlas and Anti-Atlas. These deposits form when buried rocks and primary (hypogene) ore bodies are exposed at the Earth's surface and undergo the oxidation of sulfides and native metals, the dissolution of host rocks, and the reconcentration of (mainly metallic) elements. The weathering leads to the formation of four mineralogical zones, from base to top: the hypogene zone (primary sulfides such as chalcopyrite –  $\text{CuFeS}_2$ ), the cementation and enrichment zone (secondary sulfides such as chalcocite –  $\text{Cu}_2\text{S}$ ), the oxidized zone (oxides, carbonates, sulfates, silicates such as malachite –  $\text{Cu}_2\text{CO}_3(\text{OH})_2$ ), and the leached zone or gossan (iron (oxyhydr-)oxides).

The interesting potential of supergene ore deposits lies in their relatively high metal and Rare Earth Elements (REE) content, combined to their reasonably easy extraction process related to the softened host rocks and the near-surface situation. In the last decade, a renewed interest in these deposits is associated to the increase of metals and REE demand for new technologies. Supergene deposits are also of environmental interest, as they provide natural analogues for the dissolution (corrosion), transport, and subsequent deposition of metals in natural and man-made environments (e.g. the acid mine drainage processes).

Our knowledge about the formation of supergene deposits is refined through the (U-Th)/He dating of goethite ( $\text{FeOOH}$ ), which is the most common and stable iron oxihydroxide under atmospheric conditions, and which is widely distributed in the gossan zone. The method is based on the radioactive decay of U, Th, and Sm and on the release of  $^4\text{He}$  atoms at each chain reaction. The measurement of parent and daughter elements concentration gives access to the time elapsed since the crystallization of goethite. A wide set of goethite samples from various places of the High Atlas and Anti-Atlas have been dated in order to precise the adaptation of the (U-Th)/He method to this kind of material, and to verify the existence of a relation between the weathering and crystallization of supergene goethite, and geodynamic events defined in these mountain belts. For example, we could relate the precipitation of goethite in copper deposits located in the oriental High Atlas with several recent alpine uplifts.

**8.13 Expert's report: petrography, mineralogy and geochemistry of the Tazalaght, Agoujgal, Tassirt and Tizert-Ighrem sites (collaboration UNamur - Managem company)**



Rapport d'expertise :  
Sites de Tazalaght,  
Agoujgal, Tassirt,  
Tizert – Ighrem

Michèle VERHAERT, PhD student  
Johan YANS, Professeur

Mars 2018

## **8.14 Erosion surfaces in the Ardenne-Oesling and their associated kaolinic weathering mantle – book chapter (2018)**

It has long been recognized that erosion surfaces are a main component of the landscape in the southern part of Belgium and the northern Grand-Duchy of Luxembourg, where they impose the levelled horizons and extended flat areas characterizing the Paleozoic Ardenne–Oesling Plateau (Oesling, or Éislek in Luxembourgian, is the name given to the part of the Rhenish massif situated in the Grand-Duchy of Luxembourg). Bearing witness to the Mesozoic and Cenozoic geomorphological evolution of the region, they constitute the long-term frame in which incision of the Plio-Quaternary drainage network has not yet nibbled the pre-Quaternary heritage.

The Ardenne massif is famous for its well-preserved erosion surfaces, the so-called peneplains that W. Davis commented on already in the end of the nineteenth century (Davis 1896, 1899) after having visited the area with A. de Lapparent during one of his European travels. The age of the surfaces and the uplift history of the massif revealed by their arrangement, were already a subject of discussion. This testing by Davis of his normal cycle of erosion in the Ardennian landscape was possible because, ten years earlier, Gosselet (1888) had provided a very modern overview of the nature and age of the post-Paleozoic sediments sparsely preserved on the surfaces and had discussed the tectonic deformations implied by their distribution.

Many studies dealt with the Ardennian erosion surfaces in the first half of the twentieth-century, building on the Davis' theory or sometimes adapting it, such as (Baulig 1926), with his multifaceted Ardennian platform. However, it was a long time before one realized that these surfaces had been formed under climatic conditions totally different from those currently prevailing. Being the product of a long evolution under tropical conditions, they essentially respond to the etchplanation processes proposed by Wayland (1933), possibly flavored with features of the pedimentation model of King (1947), much more than to the normal erosion model of Davis (1899). Gullentops (1954) was probably the first to show real interest in the remnants of the weathering mantle often accompanying the old surfaces and to take advantage of them in his reconstruction of the long-term geomorphic history of the massif. Recently, qualitative observations gave way to quantitative data about the age of the Ardennian kaolinic saprolites, which bring additional support to the chronology of such reconstructions (Yans 2003; Thiry et al. 2006).

In this section, the geomorphic history of the Ardenne–Oesling massif will be reexplored through the analysis of four archetypal sites of the Ardenne. We first describe the deep weathering profile exposed at Transinne, in the last quarry active in kaolin exploitation in west-central Ardenne, for which we present new geochronological results. Then, moving to the eastern part of the Ardenne (Plateau des Tailles area, Bihain site), we provide a new Ar–Ar dating of the weathering profiles. The Hautes Fagnes Plateau, a recently uplifted area that has preserved several well-developed erosion surfaces of Cretaceous and Paleogene ages will also be described because it offers a condensed view of various modes of surface evolution. Finally, new dating of supergene minerals from the northern part of the Ardenne (Beez and Morialmé sites, Entre-Sambre-et-Meuse) will be discussed against the background of the Ardenne evolution.



### 8.14.1 Weathering mantles

#### 8.14.1.a Geographical and geological setting

Located in the southern part of Belgium, the Ardenne region geologically corresponds to the Ardenne allochthon, which is part of the Rheno-hercynian fold-and-thrust belt. Belanger et al. (2012) recently distinguished the following structural units, from north to south, across the Paleozoic of Belgium: the Brabant Massif and the base of its Devonian cover unaffected by the Variscan orogeny, the Brabant parautochthon, the Haine-Sambre-Meuse overturned thrust sheets (HSM-OTS) and the Ardenne allochthon where the Transinne and Bihain sites are located (Fig. 8.14.1). The third presented site, Morialmé, is situated in the Entre-Sambre-et-Meuse area, which is the northwestern part of the Ardenne allochthon, whereas the fourth one, Beez, is located in the HSM-OTS.

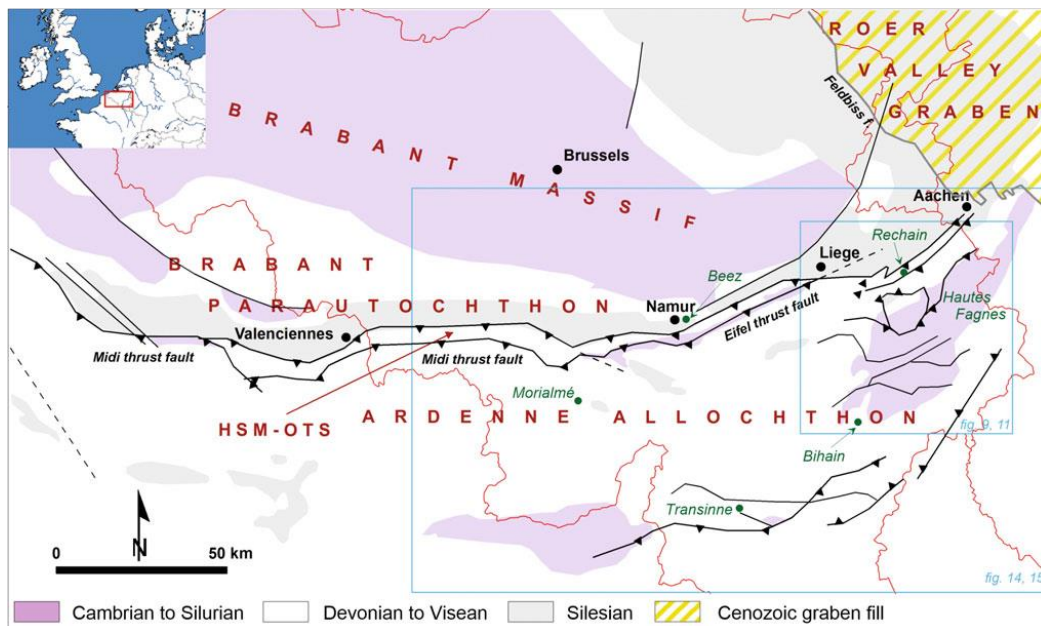


**Fig. 8.14.1** Main structural units of the Paleozoic in Belgium and Luxembourg (stripped of their Meso-Cenozoic cover in Middle and Low Belgium). Four units are distinguished within the Paleozoic basement (Brabant Massif, Brabant parautochthon, HSM-OTS: Haine-Sambre-Meuse overthrust sheets, and Ardenne allochthon). The Variscan front is marked by the Midi and Eifel thrust faults, from west to east. In the NE, up to 1.5-km-thick Cenozoic deposits were accumulated in the Roer Valley Graben. Green dots and names locate the sites mentioned in this chapter.

Thick saprolites are widespread in Belgium (e.g. Quesnel et al. 2002; Yans 2003; Dejonghe and Boni 2004; Dusar and Lagrou 2007). Yans (2003) highlighted at least ten areas that experienced period(s) of deep chemical weathering in Belgium. Fig. 8.14.2 provides an overview of those affected by weathering period(s) well constrained in time in and around the Ardenne, but additional areas with unconstrained timing of weathering may also be listed (e.g., Welkenraedt, Hautes Fagnes, Rocroi, northern part of the Mons Basin; (Yans 2013). The weathering led to the formation of saprolites up to 80- and 65 m-thick in the Brabant Massif and the Haute-Lesse area, respectively.

North of the Ardenne, the long phase of weathering and kaolinization that affected the Paleozoic basement of the Brabant Massif to depths reaching a maximum of 80 m started in the Early Cretaceous and continued up until the Cenomanian along the southern margin of the massif and the Santonian or later along its northern margin, depending on the local time of flooding and onset of subsequent marine sedimentation (Dusar and Lagrou 2007). The saprolites are widely preserved, with thickness



been removed by later erosion of the uplifted plateau and is only preserved in scattered places around the massif (e.g., at the Borne-de-Fer, French–Luxembourgian border; Théveniaut et al. 2007), where uninterrupted Mesozoic and Cenozoic tectonic stability strongly limited denudation. Elsewhere, only the saprolite sensu Nahon (1991), i.e., the bulk of the deeply weathered bedrock below the lateritic soil, is (partly) preserved. Depending on bedrock lithology, the neoformed minerals are essentially made of kaolinite, often poorly crystallized and mainly derived from the chlorite component of the Ardennian shales (Alexandre and Thorez 1995), and iron oxides and hydroxides. Quartz is the dominant residual mineral over sandstone and quartzitic bedrock. The saprolite retains the sedimentary and metamorphic structures of the parent rock, as exemplified by the Transinne outcrop, in west-central Ardenne, where stratification is clearly preserved in the weathered material (Fig. 8.14.3). The distribution of weathering depths may be highly unequal at the local scale over the Ardennian erosion surfaces because erosion led to the preservation of only the roots of the original weathering mantles and the weathering front is very irregular, mainly in relation with the variable degree of bedrock fracturing and the fracture geometry.

In order to improve the understanding and, especially, the chronology of the long-term geomorphic evolution of the Ardenne–Oesling, its erosion surface landscape and the associated kaolinic weathering mantles, we focused on four saprolite sampling sites in central Ardenne (Transinne in the Haute-Lesse area and Bihain in the Plateau des Tailles), the Entre-Sambre-et-Meuse (Morialmé), and the Haine-Sambre-Meuse overturned thrust sheets (Beez, a karst-controlled site near Namur). The dating of weathering periods is obviously very helpful for reconstructing the chronology of paleosurface development because, by definition, the erosion surface itself leaves few datable traces of its evolution. Moreover, it contributes to highlight the interplay between weathering and erosion processes, including the estimation of denudation rates and sediment budgets in the adjacent basins (e.g. De Putter et al. 2015).



**Fig. 8.14.3** View of the kaolinized Lochkovian shales and sandstones at Transinne (see location in Fig. 5.1) showing the preservation of the rock structures by the saprolite.



## Transinne

The Paleozoic basement of the Ardenne and adjacent areas experienced intense weathering during successive post-Variscan periods. These weathering phases generated kaolinic profiles that reach a depth of 65 m below the levelled plateau surface cut by the Transinne quarry at 445 m asl (Fig. 8.14.4). By contrast, outcrops in the nearby valley of the Haute Lesse expose fresh, though densely jointed bedrock at elevations of ~330 m. Discovered by Jérôme (1907), the kaolin has been mined since 1922 in this area and is now used for the cement and the ceramics industries. In Transinne, the mineralogy of the saprolite developed over Late Lochkovian shales and sandstones mainly consists of neoformed kaolinite, iron, and manganese oxides in various proportions, with residual illite and quartz (Dupuis et al. 1996; Yans 2003).



**Fig. 8.14.4** The Transinne quarry cuts into Lochkovian shales and sandstones outcropping on the Selandian erosion surface of western and central Ardenne, here at 445 m asl, exposing a ~65-m-thick mantle of deeply kaolinized rocks (© Google Earth 2015).

Weathered mantles may contain neoformed cryptomelane, a potassium-bearing Mn oxide with tunnel structure, and hollandite, its barium-bearing equivalent that may also include potassium cations. Belonging to the hollandite supergroup (Biagioni et al. 2013), both are suitable for radiometric dating using the K–Ar system. The  $^{39}\text{Ar}$ – $^{40}\text{Ar}$  and  $^{40}\text{K}$ – $^{40}\text{Ar}$  methods have been widely used on Mn oxides to date weathering periods around the world (e.g. Vasconcelos et al. 1995), including in Western Europe (e.g. Hautmann and Lippolt 2000; Dill et al. 2010). Dating hollandites and cryptomelanes of the Transinne section by these methods, Yans (2003) showed that the saprolite in Transinne is the result of polyphase weathering. K–Ar ages of hollandites in the upper part of the profile range between 120 and 135 Ma (Early Cretaceous), while Ar–Ar and K–Ar results consistently point to ages around 21 Ma (Early Miocene) for cryptomelanes from the basal part of the profile. Additional K–Ar ages on hollandites provided by Thiry et al. (2006) date the intermediate part of the profile to ~88–94 Ma (early Late Cretaceous). Moreover, paleomagnetic dating on iron (hydr)oxides sampled in the upper part of the Transinne profile yielded ages around 110–120 Ma, fully supporting the K–Ar ages obtained in that part of the profile (Yans 2003; Thiry et al. 2006). This vertical succession of ages is consistent with the long-term development of the weathering mantle by downward progression of the weathering front whenever the climatic and tectonic conditions were favourable to deep chemical weathering. The very old age of the upper part of the preserved profile underlines that Cenozoic denudation was almost zero in interior parts of the Ardennian erosion surfaces, and the ages obtained close to the weathering front suggest that the Early Miocene was the last period favourable to resumption of kaolinization in

the Ardennes. Finally, Pb–Pb dating of secondary U-bearing phosphates emplaced per descensum in fractures located just below the weathering front and probably closed since the time of phosphate precipitation might indicate active weathering as early as the Late Permian–Early Triassic, further confirming the antiquity of parts of the Ardennian landscape (Yans and Dupuis 2005). However, this dating requires further investigation because lead is very mobile during weathering.

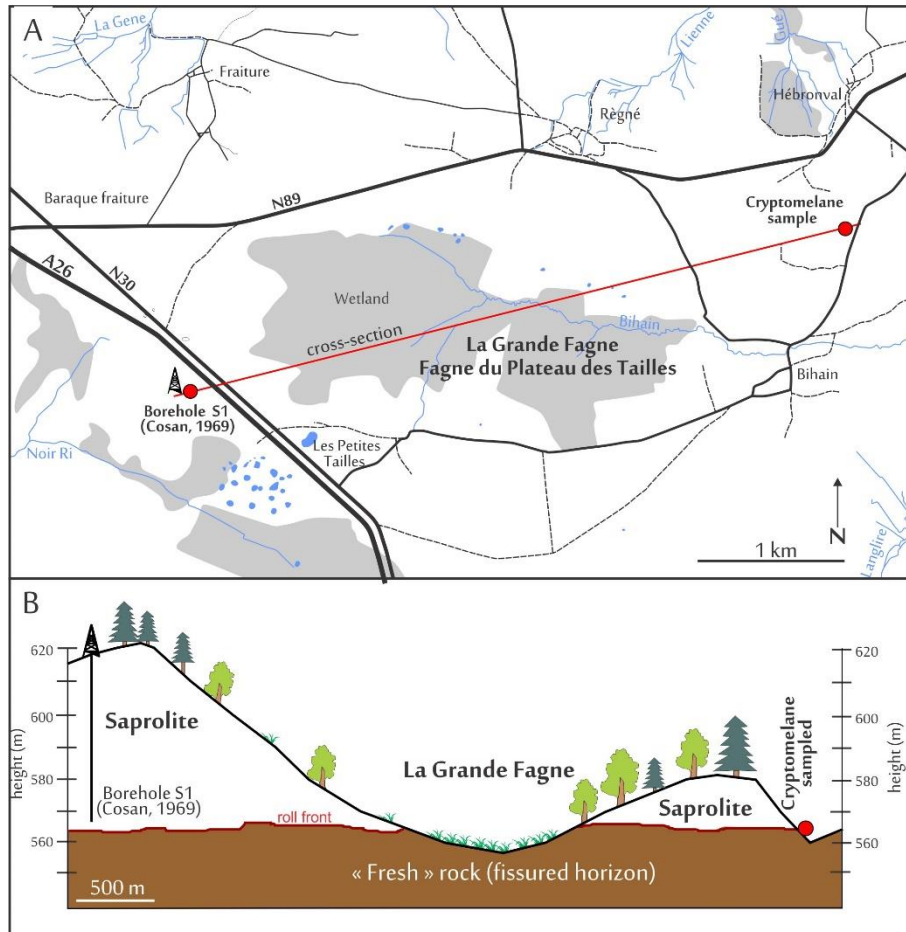


**Fig. 8.14.4 a.** Map of the Bihain site in the Plateau des Tailles (see location in ► Fig. 6.1), one of the few areas of central Ardennes-Eifel whose summits still bear witness to the pre-Senonian surface in a region where the Late Cretaceous topography was possibly never covered by marine transgressions. **b.** Weathering profile across the Plateau des Tailles. Note the location of the dated saprolite close to the weathering front (roll front) at 565 m asl, i.e., ~90 m below the summit surface of Cretaceous age.

## Bihain

Saprolite thicknesses of up to 50 m have also been recorded over phyllites and quartzites of the Cambrian, Revin Group, of the Stavelot massif, for instance in the Plateau des Tailles area (Fig. 8.14.5; Cosan 1969). At Bihain, a hamlet established at 580–600 m asl on a remnant of an Early Paleocene erosion surface (see below), the saprolite formed on the phyllites of the Ordovician Ottré Formation. Here too, weathering led to the neoformation of kaolinite, iron oxi-hydroxides and iron–manganese oxides (Fig. 8.14.6); Fransolet (1979) already identified the presence of cryptomelane in the lower part of the saprolite of this area. Recent  $^{40}\text{Ar}$ – $^{39}\text{Ar}$  dating of homogeneous cryptomelane and of a mixture of cryptomelane–lithiophorite suggests an Early Miocene age for the lower part of the weathered profile at Bihain (Fig. 8.14.7), consistent with findings in Transinne.

Of course, such ages obtained close to the weathering front do not preclude older period(s) of weathering for the upper parts of the profile. Interestingly, K–Ar dating of neoformed Mn oxides found

in deposits at the base of dissolution pockets within Dinantian limestones at Rechain, just north of NE Ardenne (Fig. 8.14.1), yielded ages between 88 and 95 Ma (Cenomanian to Santonian; Demoulin et al. 2010). These Late Cretaceous ages are in good agreement with the topographic position of the samples, situated very close beneath the trace of the pre-Cretaceous erosion surface emerging from below the nearby Cretaceous cover of the Herve Plateau. These deposits thus represent the westernmost extension of the continental sediments making the basal Hergenrath Member of the Late Cretaceous cover in the area, corresponding to a wealden-type lowland sedimentation contemporaneous with the deep weathering that took place farther inland (Demoulin et al. 2010).

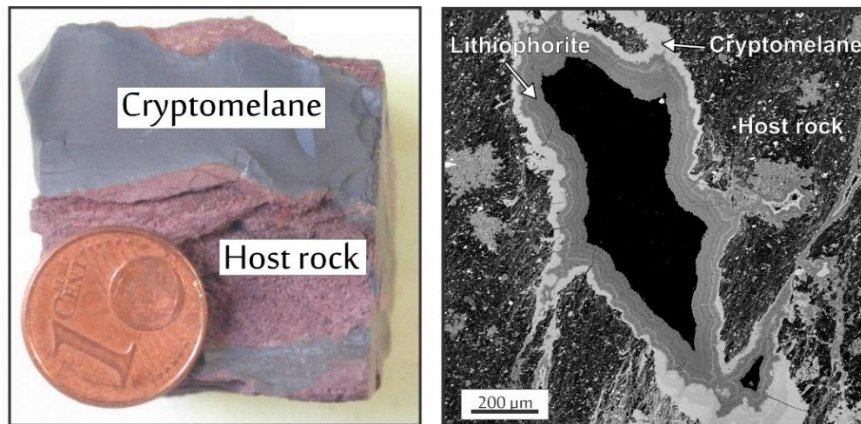


**Fig. 8.14.6 a.** Sample of cryptomelane of the Bihain quarry (collection of the Laboratory of Mineralogy, University of Liège, and courtesy A.-M. Fransolet). The host rock is an alternation of Ordovician quartzite and phyllite. **b.** SEM-EDS (Scanning Electron Microscopy with Energy Dispersive X-ray Spectroscopy) view of the mixture cryptomelane-lithiophorite in Bihain.

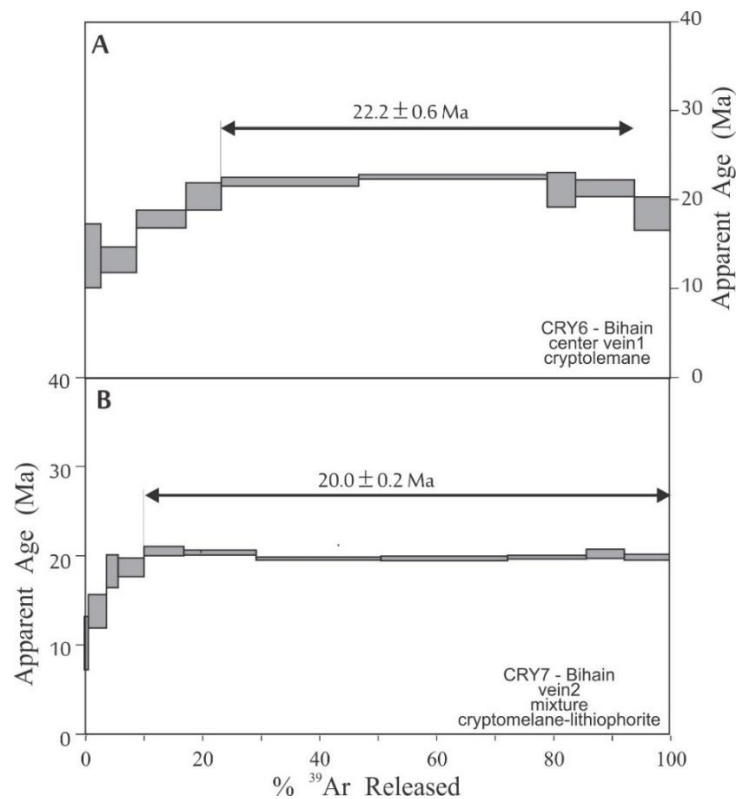


**Fig. 8.14.7**  $^{40}\text{Ar}$ - $^{39}\text{Ar}$  age spectra of the Bihain cryptomelane. **a.**  $^{40}\text{Ar}$ - $^{39}\text{Ar}$  age spectrum obtained for an homogeneous vein of cryptomelane, yielding a calculated plateau age of  $22.2 \pm 0.6$  Ma (70, 6% of  $^{39}\text{Ar}$  released). **b.**  $^{39}\text{Ar}$ - $^{40}\text{Ar}$  age spectrum of a mixture of cryptomelane and lithiophorite, yielding a calculated plateau age of  $20.0 \pm 0.2$  Ma (89, 8% of  $^{39}\text{Ar}$  released).

## Morialmé

The Morialmé weathering profile is located in the “Le Faya” quarry, at 260 m asl near Morialmé, in the Entre-Sambre-et-Meuse (ESEM). The quarry cuts the southern flank of an anticline and is mined for the brick industry. The saprolite was developed on micaceous slates of the Famennian Etroeungt and Ciney Formations, weathering processes being mainly kaolinite neoformation in the upper part of the profile and swelling clay formation in its lower part (Barbier et al. 2012). Although the degree of weathering is highly variable inside the quarry (Barbier et al. 2010), the top of the weathering profile still displays the alloterite (Barbier et al. 2012), i.e., the upper part of the profile that has undergone structure collapse and compaction (Wyns et al. 1999), showing that the profile top was quasi unaffected by erosion at the time of its burial under fluvial sediments in the Late Paleocene (Schuler et al. 1992) to Early Eocene (Fig. 8.14.8; Barbier et al. 2012). Two samples of hollandite from the lower middle part of the profile yielded K–Ar ages of  $53.3 \pm 2.3$  Ma and  $58.2 \pm 2.4$  Ma (Table 8.14.1; Barbier et al. 2010), confirming that weathering was still active just prior to this fluvial sedimentation episode at the Paleocene-Eocene transition. This sequence of events is also consistent with the Selandian age assigned by Demoulin (1995) to the erosion surface preserved in the western part of the Ardenne and ESEM, which continued to evolve during the Thanetian where it was not drowned by the Early Thanetian Sea.

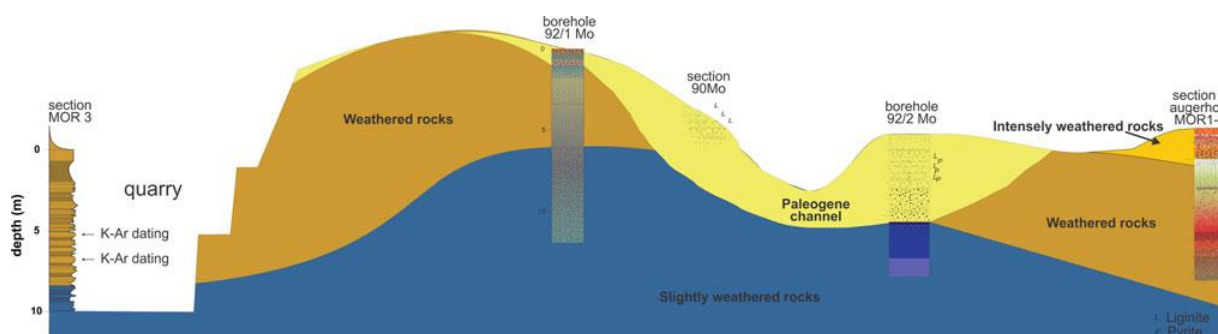


**Fig. 8.14.8** The weathering profile at Morialmé (see location in Fig. 8.14.1), with location of the samples for K–Ar dating on hollandite.

**Table 8.14.1** K–Ar dating results on hollandite in Morialmé and jarosite in Beez (see location in Fig. 8.14.1).

Location	Sample	K <sub>2</sub> O (%)	Ar (%)	<sup>40</sup> Ar (10 <sup>–6</sup> cm <sup>3</sup> /g)	Age (Ma ± 2σ)
Morialmé	08mori-oxmn1	0.52	17.38	0.9	$53.3 \pm 2.3$
	08mori-oxmn2	0.66	13	1.25	$58.2 \pm 2.4$
Beez	Jar-Beez-A	3.39	67.5	1.85	$16.5 \pm 0.8$
	Jar-Beez-B	1.92	18.25	1.05	$16.8 \pm 0.5$

## Beez

Cut into a bench at ~160 m asl along the northern valley side of the Meuse valley close to Namur, the Beez quarry exposes a cryptokarst developed in Visean limestones. In this karstic setting, possibly in relation with the circulation of acid fluids originating from pyrite leaching and oxidation in the overlying Namurian black shales, the weathering paragenesis includes neoformed halloysite, gibbsite, Fe and Mn (hydr)oxides, gypsum, and jarosite. Based on data from neighbouring cryptokarsts and saprolites, Bruyère et al. (2003) pointed to a possible Miocene age of this weathering. New K–Ar analyses performed on jarosite yielded ages of  $16.5 \pm 0.8$  and  $16.8 \pm 0.5$  Ma that confirm the Miocene timing of weathering in Beez (Table 8.14.1). One notes that these ages are somewhat younger than those obtained at the base of the Transinne and Bihain profiles. However, the weathering history at Beez

might have responded mainly to local geochemical (leaching of iron sulphides) and drainage conditions (karstic vertical transfer, possibly linked to the Meuse valley downcutting) and have a more limited climatic and geodynamic meaning than that assigned to the weathering mantles dated elsewhere in the Ardenne. Moreover, the unknown original depth of the cryptokarst makes it very difficult to relate this weathering episode with any contemporaneous topography.

Summarizing, the available age data for weathering mantles and residues in the Ardenne identify periods favourable to deep weathering that are in excellent agreement with those recognized in neighbouring areas throughout the Mesozoic and the Cenozoic, namely during the Early and early Late Cretaceous, the Late Paleocene, and the Early Miocene plus, to a lesser extent, the Late Permian-Early Triassic. As we will show in the next section, these periods fit also very well with the periods of planation and surface development inferred in the Ardenne from independent data, weathering and planation going hand in hand under conditions of warm humid climate and relative tectonic stability in regions where mean elevation is high enough to create the vadose zone required for effective leaching. It remains of course a possibility that further dating of weathering products may point to other phases of weathering, whose climatic/geodynamic meaning will have to be examined carefully in any case, avoiding to put too much emphasis on isolated occurrences linked to specific environments (e.g. karstic setting, water table fluctuation zone).

### ***8.14.2 Erosion surfaces in the Ardenne and Oesling***

#### **8.14.2.a Geographical and geological setting**

Beyond being famous for its unique periglacial features, the Hautes Fagnes Plateau of NE Ardenne (E Belgium) exposes remarkably well-preserved remnants of erosion surfaces of various Mesozoic and Cenozoic ages. Located at the tip of the recently uplifted Paleozoic Ardenne (e.g. Demoulin et al. 2009), this old erosional landscape of stepped surfaces dominates by ~400 m the Pays de Herve, the northern foreland of the massif, to which it connects by a narrow margin of moderately steep slopes drained by the Vesdre River flowing at its foot. While all slopes are covered by dense forests, the top of the plateau above 550 m bears extended moorland that enhances the flat character of the inherited topography, which is still only marginally affected by the Plio-Quaternary incision of rivers. This presence of large peat bogs is a specificity of the Hautes Fagnes Plateau, which is otherwise similar to all plateau areas of the Ardenne (and the nearby Eifel as well).

The Ardenne–Oesling massif belongs mostly to the Rheno-hercynian zone of the Variscan fold-and-thrust belt of middle Europe, the northern limit of the present-day plateau corresponding more or less to the Variscan front (Fig. 8.14.9). Structures inherited from the Caledonian orogeny and deformed again in Variscan times crop out along the axis of the uplifted massif, and especially in its northeastern part, resulting in a structurally complex basement wherein longitudinal ENE–WSW folds and thrust faults are cut by numerous NW–SE to NNW–SSE striking normal faults (Demoulin 1995). The Hautes Fagnes Plateau pertains almost entirely to the Cambrian-Ordovician Stavelot inlier, one of these inherited Caledonian structures aligned along the axis of the Ardenne anticlinorium and essentially made of variably erodible phyllites and very resistant quartzites. To the south of this anticlinorium, the bulk of the Ardenne Plateau corresponds to the Neufchâteau synclinorium, which mainly exposes fairly homogeneous Lower Devonian slates and where marked lithological contrasts arise only locally from intercalations of conglomerate or arkose formations. Such arkoses crop out for instance along the eastern limit of the Stavelot inlier, in the SE of the Hautes Fagnes area. To the north of the Ardenne anticlinorium, the northern part of the Ardenne allochthon corresponds to the Dinant synclinorium, where the slaty bedrock of the Ardenne s.s. gives way to alternating Middle Devonian to Lower Carboniferous sandstones, shales and limestones. These rocks define the particular landscapes of the



Famenne, a wide depression carved in Fammenian shales, and of the Condroz plateau, with alternating elongated ridges on sandstones and valleys cut in the limestones (Fig. 8.14.9). Scattered over the Condroz ridges and the flat summits of W and NE Ardenne, few remnants of loose sediments, mainly marine sand and clay-with flints, also attest that the massif was partly drowned by marine transgressions coming either from the north or the west during the Cretaceous and the Paleogene (e.g. Demoulin 2003).

Morphologically, the Ardenne represents a western annex to the Rhenish shield in the form of an E–W elongated relief whose flat summits gradually descend from elevations above 600 m in the east to 500–600 m in the central domain and below 400 m west of the Meuse valley. As a consequence, the transition from the massif to its N and S forelands, rather sharp in the east, is progressively less conspicuous westward and, would geology not witness its limit, the Ardenne goes imperceptibly into the Mesozoic cover of the Thiérache to the west. Except its SE confines drained by the Sûre River towards the Mosel and the Rhine, the Ardenne Plateau is drained by rivers of the Meuse basin that have incised 100- to 150-m-deep Plio-Pleistocene valleys through it (Rixhon and Demoulin 2018). Culminating at ~700 m asl, the Hautes Fagnes Plateau corresponds to the highest part of the massif.

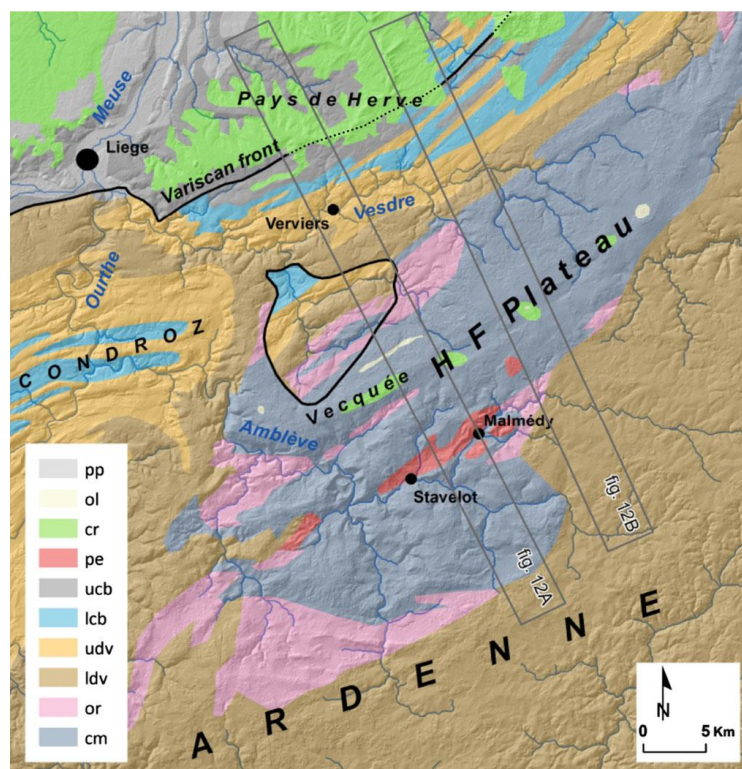


**Fig. 8.14.9** Simplified geological map of the Hautes Fagnes Plateau and surrounding areas in NE Ardenne (see location in Fig. 8.14.1) draped on a hillshade of the SRTM 3" digital elevation model. cm Cambrian or Ordovician. ldv Lower Devonian. udv Middle and Upper Devonian. lcb Lower Carboniferous. ucb Upper Carboniferous. pe Permian. cr Cretaceous. ol Oligocene. pp Plio-Pleistocene.

### 8.14.2.b Shape and characteristic of an erosion surface

Being remote descendants of etchplains formed under warm-humid conditions, the Ardennian erosion surfaces display a variable mix of extremely flat areas and more undulating topographies (Fig. 8.14.10). In principle, active etchplains are essentially flat and remarkably horizontal as long as a deep weathering mantle covers them uniformly, leaving only large-scale inselbergs that emerge abruptly from the surrounding surface and dominate it often by 100 or more meters (Thomas 1994). However,

when climatic conditions turn drier or cooler, it is common that the etchplain is stripped of part or all of its weathering mantle and that the weathering front becomes exposed. Being more sensitive to lithological and joint density contrasts, this front usually presents irregularities at all scales that appear then at the surface, forming topographic bumps from m- to dm-sized whalebacks to large subdued hilly reliefs up to a few tens of meters in height. This is the large-scale shape most usually shown by the Ardennian surfaces, in agreement with the patchy preservation of their associated weathering mantles, whose stripping probably mainly resulted from the drastic slowdown of weathering imposed by generally cooler conditions since the Oligocene. Recognising the weak relief currently displayed by the erosion surfaces is important in paleolandscape reconstructions because it prevents one from the temptation of distinguishing supposed surfaces vertically too close to each other.

### **8.14.2.c Identifying an erosion surface**

The most obvious criterion of surface identification is the overall geometry of individual levelled elements and ensembles of elements in the present landscape. However, it relies on the assumption that the envelope of part of the topography may correspond to one particular ancient erosion surface, which is sometimes questionable in regions with a complex history involving many episodes of planation and intervening deformation and degradation. Nevertheless, the reconstructed surfaces display in general, and especially in the Ardenne, a large-scale plane shape, more or less tilted, sometimes locally or regionally flexured, and displaying a relief amplitude in the order of 20–30 m (Demoulin 2006). Beyond post-planation deformation, two factors complicate such geometry-based surface reconstructions. The first one relates to the inherent relief of any erosion surface, especially when stripped of their weathering mantle. It implies that the reconstruction allows for a careful balance between topographic variations within a single-stage paleolandscape and close positions of successive surfaces in some areas, especially where differently tilted surfaces are intersecting each other. The second factor refers to the issue of defining the moment when a given surface ceases to evolve as such and begins to degrade, thus giving way to the formation of a new, distinct landscape. This comes to find a clear separation between pure acyclism and clear-cut morphogenetic cyclicity, whereas all transitions actually exist between these end-members in real landscape evolution (Klein, 1990).

Facing such difficulties, geometric reconstructions are advantageously supported by the analysis of the so-called correlative deposits. In particular, when geometry allows the connection of the exhumed part of a paleosurface with its counterpart buried as the base surface of a sedimentary cover in the massif's foreland, the very existence of the latter attests to an episode of aggradation, continental or marine, that clearly ended the previous planation stage and defines its specific topography. In such cases, there is most often a more or less extended transition zone where scattered remnants of the sedimentary cover confirm the position of the exhumed surface within the uplifted massif. In any case, as scarcely as it may be preserved, the sedimentary record is a key element in the analysis of erosional paleolandscapes. In this respect, next to sediments, the weathering mantle associated with the surfaces may also be helpful for distinguishing planation episodes, thanks to specific features such as depth, degree of preservation, secondary products (e.g. duricrusts) and, of course, dating of weathering profiles.



**Fig. 8.14.10** The pre-Senonian surface as it appears on top of the Hautes Fagnes Plateau, near Baraque Michel, underlain by a widespread peat cover that still locally overlies residual Cretaceous clay-with-flint and sand, and Oligocene marine sands. The faint ~8‰ slope to the north (toward the left of the photograph) was produced by post-Cretaceous tilting of N Ardenne (essentially in the very Early Paleogene, as all Cenozoic erosion surfaces are horizontal across central and northern Ardenne).

#### 8.14.2.d Erosion surfaces of the Hautes Fagnes plateau

The area whose successive paleolandscapes we describe in some detail corresponds to the Hautes Fagnes region s.l., which is made of the Hautes Fagnes massif s.s. (HFM), its western prolongation in the Vecquée ridge (VR), their northern margin, gently sloping toward the Plateau de Herve in the north, and the high plateau area to the SE of the HFM (Fig. 8.14.11). Mapping of the intricate erosion surfaces will be aided by the analysis of topographic swath profiles (Fig. 8.14.12).

The most conspicuous surface element is represented by the remarkably flat, almost horizontal plateau surface covering the HFM at >600 m asl and currently occupied by peat bogs and extensive heath that confer to the area its wild character and wide horizons (Fig. 7.10). In the east, this surface is dominated by a few subdued summits rising a few tens of meters above their surroundings. To the NW, it goes rather abruptly in a tilted and dissected surface that makes the margin of NE Ardenne. The forested interfluvies materialising the surface remnants slope regularly (by ~4 %) down to ~320 m asl, where they join the upper edge of the incised Plio-Quaternary valley of the Vesdre. On the opposite side of the HFM, steeper slopes rapidly lead down southeastward to another very regular, hardly dissected surface at 560–580 m asl, covered by pasture and interrupted by small wooded areas only where upper valley reaches of the Roer catchment begin to incise. Though essentially horizontal, this 560–580 m landscape element shows imperceptible slopes going up in a residual relief that culminates in the SE at ~690 m asl at the Weisser Stein (Fig. 8.14.12). On its southwest flank, the HFM displays a stepped descent toward the perfectly horizontal ridge of the Vecquée. Extending at 560–570 m asl for ~15 km to the SW and with a width of 0.5–1.5 km, the VR represents a distinct topographic element in the present landscape of the area. On the north, it is bordered by a ~120-m-high escarpment that links it to a lower surface well preserved on the interfluvies between the incised valleys of the Gileppe, the Hoëgne, and the Wayai. This surface, which skirts the western end of the ridge, is observed at elevations around 450 m at its foot, from where it slopes very gently (~0.6 %) toward NW. It includes extended levelled areas at 360–390 m asl between the villages of Theux, Sart-lez-Spa, and Jalhay (Figs. 8.14.11 and 8.14.13). On the south of the VR, a smaller, ~60-m-high escarpment leads down to a local

intramontane basin whose levelled bottom appears in the form of wide flat interfluvies at uniform elevations of 500–510 m asl. Centred on the area where weak rocks of the Permian graben of Malmédy crop out (Fig. 8.14.9), this erosional feature opens towards the massif's exterior in the west, where it is geometrically connected to the 450-m surface.

In the northern foreland of the massif, the Meso-Cenozoic sedimentary cover of the Pays de Herve offers an opportunity for reconstructing the profile of two paleosurfaces onto which transgressing seas encroached. The first one is the base surface of the Senonian deposits (the clays and sands of the basal Aachen Formation are dated to the Santonian), which shows a slight but consistent tilt of 1.4% towards NNW. Emerging at the topographic surface in the south of the Pays de Herve, it appears there in the form of large exhumed remnants, similarly tilted and preserving sands and clays of early Late Cretaceous age in solution pockets of the underlying Dinantian limestones (Demoulin et al. 2010). Prolonged southward toward the Hautes Fagnes summits, the 1.4% tilt angle connects the VR surface and the tilted surface on the northern flank of the HFM with the Senonian base surface in the Pays de Herve (Fig. 8.14.12). The second marker interface in the Meso-Cenozoic cover is the base surface of the sand formation that accumulated during the last marine transgression that covered the northern part of the Ardenne in the Oligocene (Rupelian?). Again, NNW–SSE sections of the cover indicate a minor (0.6%) but uniform NNW tilt of this interface that can easily be followed across the Vesdre valley to the 360–450-m surface in the massif, north of the VR, which shows exactly the same tilt in the same direction.

Finally, remnants of the Cretaceous sands and clay-with-flints and Oligocene marine sands scattered over the northern margin and summits of the Hautes Fagnes region provide additional evidence of the geometric connections established between the massif's erosion surfaces and their buried counterpart in the Pays de Herve. Discontinuous clay-with-flint, often overlying Aachen sand and gravel, are still widespread over the VR and the HFM and are found locally on the sloping surface leading up to the latter, especially southeast of Eupen (Fig. 8.14.11). Elsewhere, beyond rare occurrences of isolated reworked flints lying around on the 500-m surface south of the VR, the 360–450-m surface in the north and the 560–580-m surface in the south are completely devoid of Cretaceous sediments. By contrast, sparse deposits of Oligocene sands are mainly encountered all over the 360–450-m surface, while rarer remnants of this cover also exist next to, and sometimes over, Cretaceous sediments on the HFM summit and northern slope and on the VR.



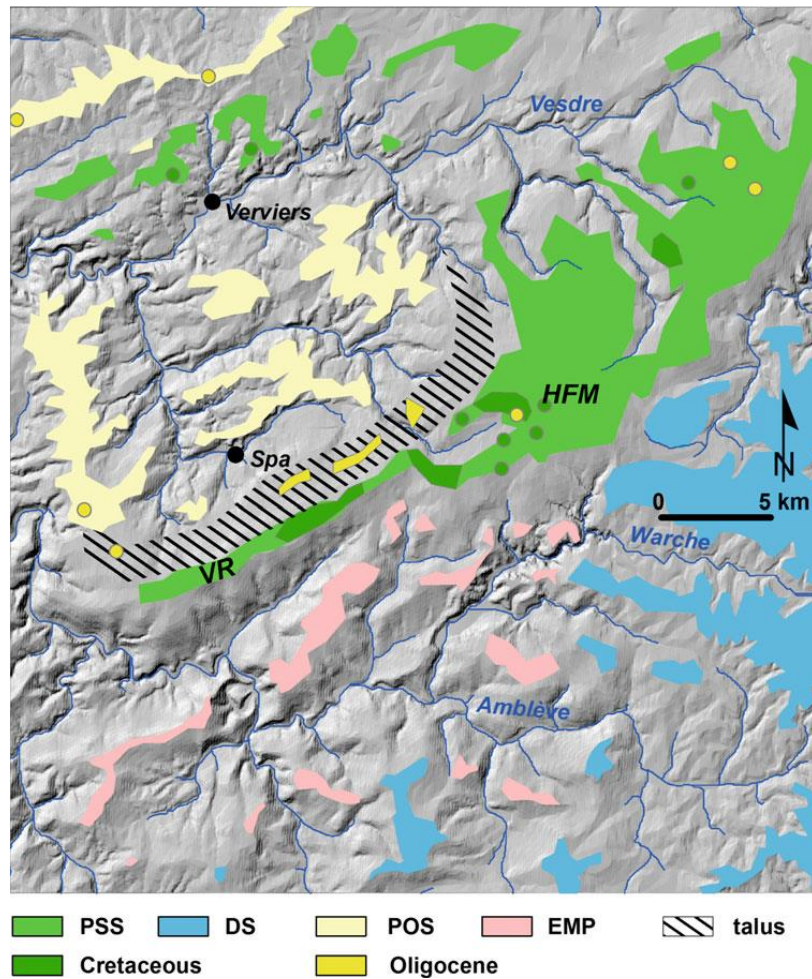


**Fig. 8.14.11** Map of the erosion surface remnants in the Hautes Fagnes area of NE Ardenne, draped on a hillshade of the SRTM 3'' digital elevation model. All flat interfluvies and broader plateau areas belong to pre-Quaternary topographies of various ages. PSS Pre-Senonian surface. DS Danian surface. POS Pre-Oligocene surface. EMP Early Miocene planation, developed in less resistant Permian conglomerates and Ordovician shales. Talus: ~100-m-high erosional riser between the pre-Senonian/Danian and the pre-Oligocene surfaces as it is preserved since it was carved in the regional topography during the Paleogene.

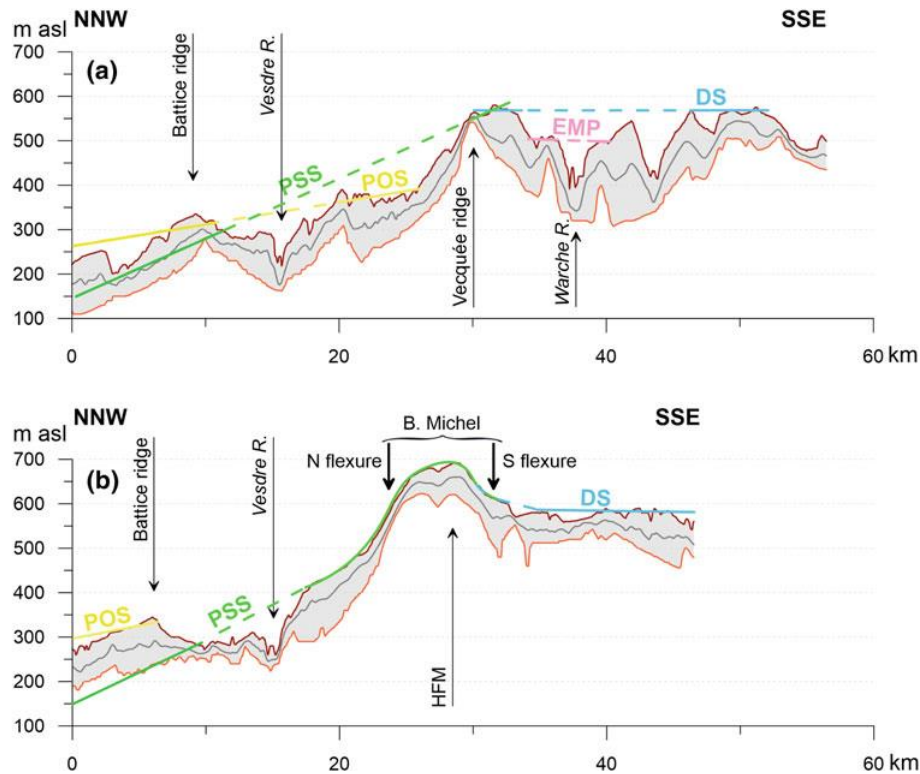


**Fig. 8.14.12** NNW-oriented 4-km-wide swath profiles (see location in ► Fig. 6.9; orange, grey, and ruby brown lines are for minimum, mean, and maximum elevations, respectively) showing the geometry of the erosion surfaces across the northern margin of NE Ardenne at the height of the Vecquée ridge (a) and the Hautes Fagnes Plateau (b), where the general tilt to north is complicated by post-Oligocene uplift of the Baraque Michel block inducing the flexure of the surfaces. PSS Pre-Senonian surface. DS Danian surface. POS Pre-Oligocene surface. EMP Early Miocene planation level. The trace of exhumed erosion surfaces obviously follows maximum elevation lines of the swath profiles. By contrast, north of the Vesdre valley, the pre-Senonian surface is still buried under a continuous Upper Cretaceous cover. Height exaggerated x30.

Integrating all these observations, one obtains the following consistent reconstruction of the successive paleosurfaces whose fingerprint is still visible in the present landscape (Fig. 8.14.11). The oldest preserved surface in the Hautes Fagnes area is pre-Senonian in age and includes the levelled summits of the region (VR and HFM) and also the tilted surface that makes the northern margin of the HFM and links it to its foreland east of a line joining Verviers to Malmédy (Fig. 8.14.12). The unity of this surface made of distinct topographic elements is demonstrated by the Cretaceous deposits that all of them still expose. However, the pre-Senonian surface underwent strong post-planation deformation during the Cenozoic, mainly in the form of a marked differential uplift of the HFM. Its overall geometry shows that the HFM block uplift was limited by flexures on its northern and southern sides (Fig. 8.14.12b), while a series of NNW-striking Variscan faults, reactivated in normal mode, accommodated the ~100 m height difference with the adjacent Vecquée ridge to the west.

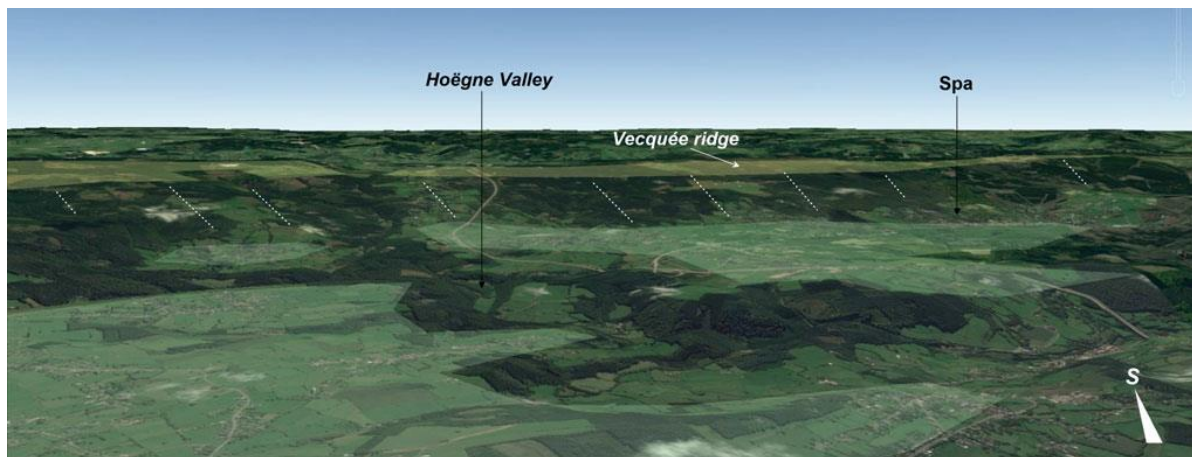


**Fig. 8.14.13** S-looking oblique aerial view of the pre-Oligocene surface (in light green transparency) developed at 350–400 m asl north of the Vecquée ridge, which represents the pre-Senonian surface, exhumed and reexposed since the Danian (in light yellow transparency). The erosional scarp between both surfaces (dotted white lines) clearly appears as a regional morphological feature. In the background, beyond the barely visible Early Miocene planation level developed in the Stavelot-Malmédy area, south of the Vecquée, the uniform horizon line shows the well-preserved Danian surface of central Ardenne. Scale the visible length of the Vecquée ridge is ~20 km. Elevation factor 2 (@ Google Earth 2015).

Even if they share the VR summit (Fig. 8.14.12), the 560–580-m surface to the SE of the HFM represents a planation episode different than that attested by the pre-Senonian surface. Indeed, with the exception of few residual reliefs such as the Weisser Stein, whose summits are probably hardly degraded isolated remnants of the pre-Senonian surface, the remarkable horizontality of the 560–580-m surface across the whole central Ardenne and nearby Eifel shows that it resulted from low-angle bevelling of the slightly tilted previous (pre-Senonian) topography, the intersection between both surfaces occurring along the VR (Fig. 8.14.12a). This interpretation is further supported by the absence of Cretaceous sediments on the 560–580-m surface south of the VR, where their complete removal (their former presence in this area being only proved by isolated clay-with-flints remains on the SE flank of the Weisser Stein) had to precede regradation of their base surface (regradation being the process of tending towards a new grade after a perturbation; Fairbridge 1968).

Finally, the last envelope surface of the topography locates a third nested paleolandscape that is chiefly associated with the 360–450-m surface developed in the north and west of the Hautes Fagnes region and prolonged inside the massif by the 500-m intramontane basin south of the VR. However, whereas remnants of the Oligocene sand cover scattered over the surface north of the VR attest that it was developed before the Oligocene transgression on the massif, the absence of corresponding deposits in the intramontane basin despite drowning of the VR by the Oligocene sea strongly suggests that this inward extension of the 360–450-m surface was carved in later times.

Separation between the different surfaces occurs in two ways. While the 560–580-m and, north of the Vesdre valley, the 360–450-m surfaces both cut at low angle the tilted older pre-Senonian surface, a well-developed 60- to 150-m-high erosion scarp, making the northern flank of the VR, separates them from each other (Fig. 8.14.12a). The erosional nature of this scarp, as opposed to the tectonic flexures limiting the uplifted HFM, is demonstrated by the fact that N–S sections north of the VR show no equivalent to this flexure in the older, uniformly tilted pre-Senonian surface (Fig. 8.14.12). The two types of surface separation suggest distinct erosional mechanisms. Low-angle bevelling is typical of

acyclic morphogenesis where surfaces temporally distinguished by their associated sedimentary record gradually regrade their predecessor under etchplanation regime in response to slow, low amplitude deformation. By contrast, erosional scarps signal morphogenic cyclicality, implying a combination of etchplanation and scarp retreat in response to more rapid, larger tectonic deformation with a significant component of en-bloc uplift.

### 8.14.2.e Dating a surface

It is clear from the Hautes Fagnes example that geometric relationships between paleosurfaces and their links to buried base surfaces within foreland sedimentary covers already provide powerful tools for unravelling the chronology of long-term geomorphology in erosional settings. Taking into account the various types of discontinuity that give rhythm to such a “surface stratigraphy” further allows inferences about the nature of the often tectonic triggers of morphogenesis.

The paleolandscape chronology is also aided by the analysis of correlative deposits preserved on the erosion surfaces. In the Ardenne–Oesling, the oldest sediments of Fig. 8.14.13 interest in this respect correspond to the band of Bunter sandstones (Lower Triassic) cropping out at the southern edge of the Oesling, and continuing eastward inside the massif into the N–S Eifel zone. More to the west, the Mesozoic deposits directly resting on the southern border of the Ardenne are younger, mainly Liassic, and ending with Turonian and Coniacian chinks at the limit between W Ardenne and Thierache (Fig. 8.14.14). The equivalent first post-Variscan sediments present on the northern side of the massif are Upper Cretaceous sands and chinks (weathered to clay-with-flint). Their outcrop zone is restricted to the Hautes Fagnes region in the NE (Bless and Felder 1989), where they nevertheless covered large areas inside the massif as witnessed by the clay-with-flint retrieved at Dalhem, east of the Weisser Stein (Fig. 8.14.14). Later, further seas which encroached upon the Ardenne are recorded during the Early Thanetian in the west, where Upper Thanetian continental sands also sparsely cover the western Rocroi Plateau, and during the Rupelian, when marine sands were deposited not only in the Hautes Fagnes but also over the whole Condroz Plateau and in the ESEM region (Fig. 8.14.14).

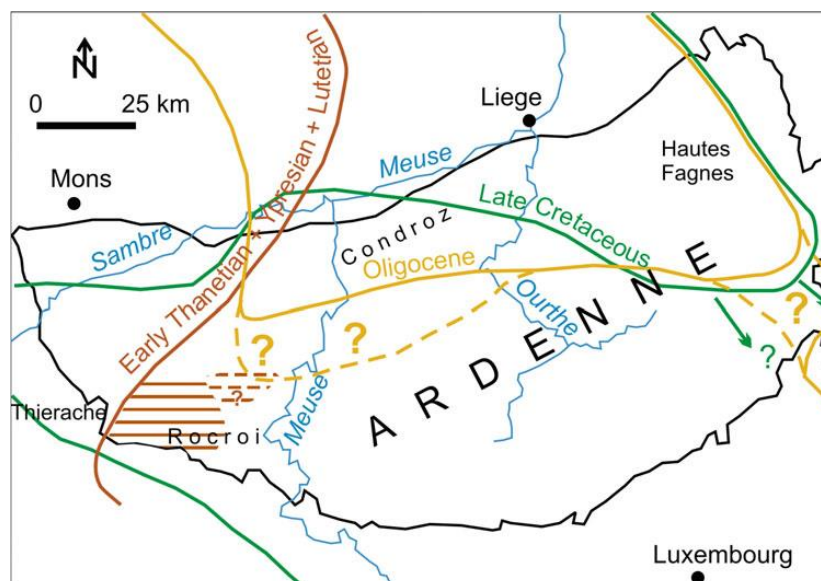


**Fig. 8.14.14** Map of the Mesozoic and Cenozoic marine transgressions over the Ardenne massif (modified after Demoulin (1995). Horizontal brown hatching denotes the area of occurrence of Upper Thanetian continental deposits.



Finally, as indicated in the first part of this chapter, dating techniques applied in the past two decades to minerals precipitated during weathering brought significant improvement in the appraisal of the age of erosional paleolandscapes in uplifted massifs, and especially in the Ardenne, by incorporating in the discussion quantitative information about the age of the associated weathering mantles. The next section brings a brief overview of the current understanding of the long-term geomorphic evolution in the Ardenne–Oesling at the light of this diverse, recently enlarged body of evidence.

#### **8.14.2.f The whole picture: stepped surfaces of the Ardenne-Oesling**

During Mesozoic and Cenozoic times, the Ardenne–Oesling underwent many phases of subaerial denudation, only interrupted by limited marine transgressions. The seas that drowned the margins of the massif came from E to SE in Triassic and Liassic times, from W during the Eocene and from N in the Early Oligocene. Only the Late Cretaceous sea probably submerged larger parts of central Ardenne. Seven generations of paleolandscape may be recognized (Fig. 8.14.15; Demoulin 1995, 2003). A pre-Triassic topography, mainly observed in W Eifel, where it displays a fairly animated relief (Junge 1987), also emerges from below the Triassic cover to form the slopes of the SE margin of the Oesling. It is continued westwards by the diachronic, so-called post-Hercynian peneplain, which constitutes the southern margin of the Ardenne, with interfluvies tilted by 1–3% to the south. In NE Ardenne, following a longer phase of post-Variscan denudation, the oldest paleosurface preserved as part of the modern landscape dates back to the Late Cretaceous. As stated above, remnants of this pre-Senonian surface are also preserved as the highest summits, at 650–700 m elevation, in the heart of the massif (Baraque Michel, Baraque Fraiture, Weisser Stein, Schneifel). Then, after the Late Cretaceous regression, acyclic erosion of the Ardenne–Oesling removed its Cretaceous cover almost completely and caused an extensive erosion surface to develop over northern and central Ardenne by regrading the pre-Cretaceous landscape during the Danian. Corresponding to the “surface supérieure” of Macar (1938), this Danian surface is now observed at altitudes of 560–580 m, going down slowly in the south to reach ~500 m asl along the southern border of the massif. In contrast with previous surfaces, it developed independently of any marine ingression and its age is primarily inferred from geometrical considerations and the derived “surface stratigraphy”. Another information is, however, provided by the Early Cretaceous radiometric ages obtained for the upper part of the weathering profile at Transinne, which roughly locates the weathering front at (modern) 450 m asl at 130 Ma, i.e., ~80 m lower than the trace of the Danian surface in the same location, suggesting that the Danian regradation of the pre-Cretaceous topography was minimal in this area.

The Danian surface represents the end product of the long-lasting acyclic evolution of the Ardenne–Oesling under conditions of prevailing tectonic stability during the Mesozoic. From the Middle Paleocene onwards, rather than regrading the older surfaces more or less uniformly and cutting them at low angle, new paleosurfaces developed at their expense by creating 50–170 m-high scarps that retreated inward, progressively nibbling the higher topography and producing a stepped landscape in response to more perceptible tilt of the massif. This happened so first on the western side of the massif, where the Danian landscape was replaced by a lower erosion surface during the Selandian, until this surface was buried by the Early Thanetian Sea in the west. In the east, it probably remained emerged and continued to evolve and proceed inward for some time, as attested by the 55 Ma radiometric age of the Morialmé weathering profile and the presence of Upper Thanetian continental sands scattered on the Rocroi Plateau (Fig. 8.14.15; Voisin 1981). At its eastern limit, east of the Meuse

valley, the Selandian surface abuts the Danian one through a ~70-m-high gently sloping erosional scarp.

Then, another phase of massif uplift caused new surfaces to develop along the northern and southern sides of the Ardenne–Oesling, new scarps separating them from the inner Selandian and Danian topographies. Such a Late Eocene surface (usually called “pre-Oligocene”) formed in N Ardenne, erasing the former landscape in part of the ESEM, in the Condroz, and along the NW slopes of the Hautes Fagnes before being sealed by the sand cover abandoned by the Rupelian sea. The scarp leading to the Danian surface is up to 170-m-high near Nassogne (Fig. 8.14.15). Likewise, south of the massif, active denudation and scarp retreat produced another well-developed surface with elevations around 300–420 m asl in the NE Paris basin and the Gutland area, prolonging eastward in the Moselle trough. While the age of this surface, Upper Eocene to Miocene, is still debated (E. and Baeckeroot 1947; Quesnel 2003; Demoulin 2006), its antiquity is not disputed, identifying the southern margin of the Ardenne –Oesling as a Tertiary erosional feature and disqualifying the assumption that it primarily resulted from the Plio-Quaternary differential uplift of the massif.

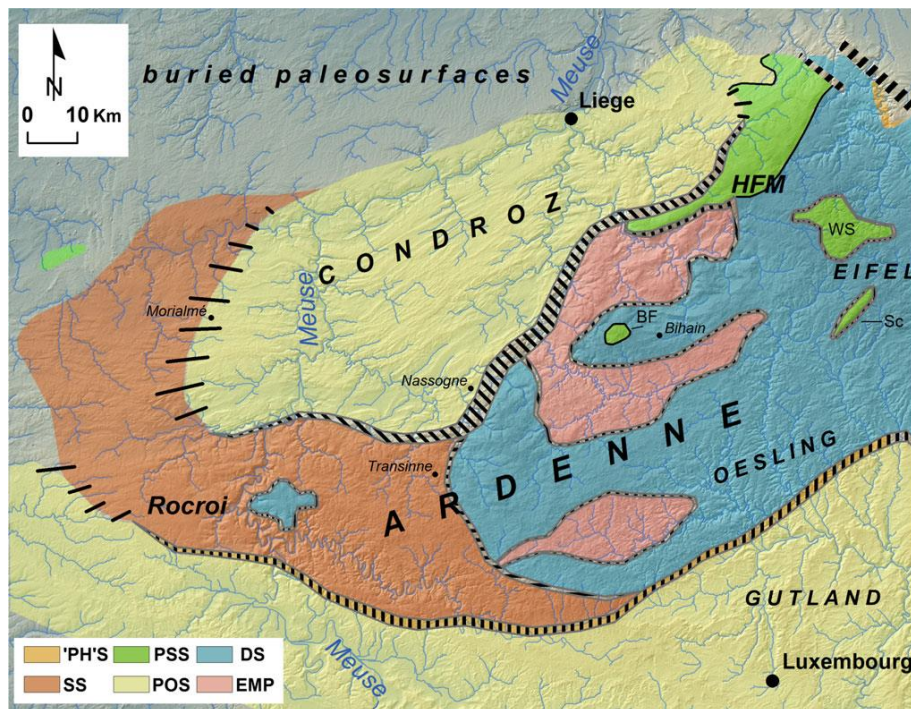


**Fig. 8.14.15** Map of the erosion surfaces of the Ardenne and its margins, draped on a hillshade of the SRTM 3'' digital elevation model. “PH”S. Post-Hercynian surface (including its more specific pre-Triassic variant in Luxembourg and north Eifel). PSS. Pre-Senonian surface. DS. Danian surface. SS. Selandian surface. POS. Pre-Oligocene surface. EMP. Early Miocene planation level. Thin hatching denotes erosional scarps between surfaces. In the west, the scarps between the Selandian and pre-Oligocene surfaces are progressively less conspicuous, finally giving way to a regradational type transition between the two surfaces (widely spaced black lines). Bold hatching (in top right corner of the map) is for fault scarps. BF Baraque Fauture. WS Weisser Stein. Sc Schneifel.

Finally, while the Paleogene sand covers were progressively removed from the younger surfaces, the Oligo-Miocene evolution of the massif’s interior was restricted to the development of intramontane planation basins of limited extent within the Danian topography, owing to climatic conditions generally less favourable to chemical weathering and etchplanation. These basins formed preferentially on

weaker bedrock, in relation with the main drainage axes of the massif, and open all to the west, where their base level corresponded to the top surface of the sand covers of the pre-Oligocene and Selandian surfaces (Fig. 8.14.15). Their Early Miocene age is consistently supported by the absence of Paleogene marine deposits and the evidence of a last phase of active bedrock kaolinization around 20 Ma from K–Ar and Ar–Ar dating of cryptomelanes at the base of the weathering mantle at Transinne and on the Plateau des Tailles (Bihain).

### ***8.14.3 Erosion surfaces, tectonic uplift and denudation rates in the Ardenne-Oesling***

Although paleosurface reconstruction is now often deemed superseded by developments in the thermochronological and cosmogenic nuclide approaches of long-term landscape evolution, the recent progress in the dating of weathering products allows for sounder such reconstructions, with important implications regarding the underlying tectonic evolution of the Ardennian erosional setting and the associated denudation volumes.

Beyond local tectonics such as the HFM block uplift, broad-scale differential deformation between the originally almost horizontal surfaces of different ages suggests that every particular uplift episode of the massif during the Cenozoic did not exceed a few hundred meters with respect to the forelands. For example, the difference of tilt between the pre-Senonian and Danian surfaces in NE Ardenne indicates a ~400-m-high broad upwarping of central Ardenne in the Early Paleocene, which however never raised the massif's heart to such elevations, as surface regradation more or less kept pace with uplift. The varying tilt angle of the external facets of the acyclic surface developed over Ardenne–Oesling, systematically larger for older facets, attest that this slow doming of the massif was a background trait of its tectonic behaviour during the Mesozoic.

The change for cyclic morphogenesis during the Selandian was probably related to more focused uplift of the massif, highlighted especially in N Ardenne by the contrast between horizontal topography in the massif's interior and abruptly, though weakly, tilted surfaces close to its margins. At least in the north, probably in relation with the dawn of the Lower Rhine rift activity, subdued doming thus gave way to more en-bloc, multiphased uplift. The cumulated heights of the erosional scarps that were consequently produced between the successive surfaces amount to ~200 m from Selandian to Rupelian times, while the surfaces deformation points to an additional few tens of meters of Neogene marginal tilt and the Plio-Quaternary component of en-bloc uplift may be estimated from river incision in the order of 150 m (Willems and Rodet 2018).

Paleosurface analysis and the dating of weathering products are also useful tools to assess the plausibility of long-term landscape evolution and denudation rates derived from thermochronology and cosmogenic nuclide data in regions of low to moderate uplift and elevation. In the Ardenne, thermochronological data are so far limited to fission track (FT), mainly on apatite (Glasmacher et al. 1998; Xu et al. 2009; Bour 2010) and led to a variety of interpretations. From the stand-alone analysis of their FT data, Xu et al. (2009) infer that slow exhumation prevailed in the Ardenne from 230 to 45 Ma, as indicated by cooling rates of 0.1–0.3 °C/Ma. Based on the usually used thermal gradient of 30 °C/km, this corresponds to denudation rates of 4–13 m/Ma. Then, from 45 Ma onwards, they model a phase of faster cooling (0.7–1.1 °C/Ma) that translates in denudation rates of 20–30 m/Ma, and suggest that an exhumation of 0.9–1.3 km would have occurred since the Middle Eocene. However, in

a thermal history modelling that does not call for a thick Upper Cretaceous cover over the Ardenne, this km-scale amount of Cenozoic exhumation is in contradiction with field data showing the preservation of Lower Cretaceous weathering products and Upper Cretaceous sediments on the Ardennian surfaces. In order to overcome such discrepancies between field data and FT inferences, Bour (2010) introduces in the modelling of his own FT data constraints imposed by the measured ages of the weathering mantle and the timing of marine transgressions upon the massif's margins. Consequently, following a long stay from 230 to 90 Ma in the [10–50 °C] domain not resolved by FT but most probably with insignificant denudation rates, his best-fit thermal histories display a heating episode indicating that the Upper Cretaceous sea would have buried the N Ardenne under a more than 1 km-thick sediment cover, succeeded by rapid cooling during the Cenozoic, which Bour (2010) interprets as the result of tectonic inversion and massif uplift. However, though consistent with Lower Cretaceous kaolinic weathering in central Ardenne and the observed burial under Upper Cretaceous chinks along the massif's northern margin, this thermal history faces another difficulty because the Thanetian marine cover directly resting on the Paleozoic basement of the ESEM's western confines and the 55-Ma age of weathering products at Morialmé imply that this thick Cretaceous cover should have been removed very rapidly in the beginning of the Paleocene, at rates of 100–150 m/Ma. Though not impossible per se, such rates would imply comparatively high Paleogene rock uplift rates in the Ardenne, which no other evidence supports. Independent information about the volume of the Late Cretaceous Ardennian cover is thus required, which might perhaps be derived from estimates of the fraction of reworked Cretaceous material included in the Selandian and Thanetian sediment covers surrounding the massif. While the apparent inconsistencies between paleosurface and paleoweathering observation on one hand, FT modelling results on the other hand, might refer to the use of inappropriate T°-depth profiles in the latter, they especially stress the importance of the former data type and the need for further efforts towards dating of weathered material, sediments, and exposed surfaces in slow evolving erosional settings, which the Ardenne massif represents.

Likewise, cosmogenic radionuclide (CRN) studies have yielded a lot of denudation estimates in uplifting massifs, and especially in the Ardenne (Schaller et al. 2002, 2004; Sougn ez 2012) and the Rhenish shield (Meyer et al. 2010), which, though indicative of shorter term denudation, are often compared to the long-term evolution of the massif. These estimates are obtained from measurements of cosmogenic <sup>10</sup>Be concentration in the quartz sand fraction of river bed loads, assumed to carry information on the average denudation rate in the river's catchment upstream of the sampling point. Most CRN estimates from Ardennian rivers fall in the range 20–80 mm/ky at least for the last 50 ky. However, as secular equilibrium is assumed in the calculation of CRN denudation rates and the climatic conditions of the last 50 ky are indeed representative of those of at least the last 1 My, this suggests that a rock slice 50–200 m-thick would have been removed from the massif just during the Quaternary, a figure hardly compatible with the preservation of >30-Ma-old loose sediments and kaolinized rocks over many levelled interfluvies. Moreover, Demoulin et al. (2009) showed that these rate estimates are much closer to the rates of valley incision since 0.7 Ma in the Ardenne, concluding that the CRN rate estimates in the massif are not representative of average denudation because the river bed load does not sample the extended horizontal remnants of the paleosurfaces where virtually no erosion takes place currently. Here again, the geomorphological reconstructions of paleolandscapes appear thus as a welcome counterweight to sometimes hasty conclusions derived from new techniques.

#### **8.14.4 Conclusion**

Praised by writers, celebrated by painters, the Ardenne's scenic landscapes have also been studied for more than a century by geoscientists. While several local names were chosen already in the nineteenth century, and are still often in use, to describe stages, especially of the Devonian System, of the international stratigraphic chart, geomorphologists studied the Ardennian relief as a well-preserved example of the long-term geomorphic features of temperate latitudes' old massifs, highlighting their typical evolution most probably under former warm, often wet, climatic conditions. Within the Ardenne, the Hautes Fagnes area, with its wild beauty, is certainly one of the best places to observe the general character of extended remnants of etchplains and unravel the complex relationships between regional tectonic deformation, continental weathering and relief development, and episodic marine transgressions leading to the present layout of variously intersecting or stepped paleosurfaces. The sections offered by the Transinne quarry and the Bihain outcrop across the deeply kaolinized bedrock of west- and north-central Ardenne are also key localities for observing the thick profile produced by long-lived chemical weathering, indispensable to etchplanation. In other words, the Ardenne–Oesling is not only a world-class area for its contribution to the history of the understanding of long-term landscape evolution in temperate regions (i.e., the typical setting of the Davisian “normal” geomorphic evolution) but also a remarkable example of how the geomorphic landscape record may be as powerful a tool as the geological rock record for reconstructing the long-term history of regions where continental, tectonically stable or weakly active regimes prevailed over 107–108 yr timescales. Moreover, the recent results presented in this overview reveal new perspectives for future research and advances, especially in the chronology of the Ardennian evolution and its meaning as a piece in the history of the large-scale foreland domain of the Alpine collision zone in Europe. Meanwhile, every rambler walking through the Ardenne plateau's wild scenery and deep forested valleys cannot keep from having a strong feeling of the grandeur and long time scale of the landscapes in which humans pass so quickly.

## 8.15 Localization of collecting sites and samples

**Table 8.15.** GPS coordinates of samples studied during this thesis.

Site	Samples	Latitude	Longitude
Jbel Klakh	14KH01 – 11	32°37'9.40"N	1°40'54.00"W
	14KH12 – 21	32°37'7.30"N	1°41'19.00"W
	14KH22 – 50	32°37'9.11"N	1°41'08.51"W
Jbel Haouanit	14HAO01 – 09	32°34'42.32"N	2°26'20.72"W
	14HAO10 – 13	32°34'33.56"N	2°26'17.44"W
	14HAO14 – 16	32°34'32.38"N	2°26'14.69"W
	14HAO17	32°34'31.98"N	2°26'18.07"W
	14HAO18	32°34'34.20"N	2°26'28.94"W
	14HAO19 – 20	32°34'34.66"N	2°26'38.15"W
	14HT01 – 03	32°35'26.76"N	2°25'21.26"W
	14HT04 – 17	32°35'19.63"N	2°25'03.62"W
	14HT18	32°34'34.30"N	2°26'23.00"W
	14HT19	32°34'35.60"N	2°26'16.50"W
Jbel Rhals	14RL01 – 17	32°20'41.14"N	1°58'39.94"W
	14RL18 – 21	32°20'45.21"N	1°58'30.45"W
	14RL22 – 23	32°20'44.63"N	1°58'25.79"W
	14RL24	32°20'45.20"N	1°58'24.60"W
	14RL25	32°20'43.62"N	1°58'22.13"W
Tazalaght	17TAZ01	29°42'59.5"N	8°42'42.0"W
	17TAZ02 – 05	29°44'52.8"N	8°43'26.1"W
	17TAZ06 – 11	29°44'53.8"N	8°43'24.0"W
	17TAZ12	29°44'53.5"N	8°43'22.3"W
	17TAZ13	29°44'51.4"N	8°43'18.7"W
	17TAZ14	29°44'51.2"N	8°43'17.5"W
	17TAZ15 – 16	29°44'47.7"N	8°43'13.3"W
	17TZ01	29°43'51.2"N	8°43'21.5"W
	17TZ02	29°45'46.0"N	8°43'33.5"W
	17TZ03	29°45'45.0"N	8°43'34.4"W
	17TZ04	29°45'33.4"N	8°43'46.4"W
	17TZ05 – 08	29°44'55.2"N	8°43'26.9"W
	17TZ09 – 10	29°44'53.5"N	8°43'24.7"W
	17TZ11 – 12	29°44'55.0"N	8°43'21.8"W
	17TZ13 – 14	29°44'53.4"N	8°43'12.8"W
	18TAZ01 – 08	29°44'52.6"N	8°43'13.5"W
	18TAZ09 – 12	29°44'52.9"N	8°43'18.8"W
	18TAZ13	29°44'53.7"N	8°43'19.8"W
	18TAZ14 – 21	29°44'51.5"N	8°43'19.8"W
	18TAZ22	29°44'48.4"N	8°43'13.0"W
	18TAZ23	29°44'47.4"N	8°43'13.0"W
	18TAZ25 – 27	29°42'59.5"N	8°42'42.0"W
Agoujgal	17AG01 – 08	29°23'36.5"N	9°01'12.8"W
	17AG09 – 19	29°23'36.2"N	9°01'17.5"W
	17AG20 – 27	29°23'29.1"N	9°01'24.2"W
	18AG01 – 13	29°23'28.9"N	9°01'17.1"W
	18AG14 – 25	29°23'40.03"N	9°01'15.74"W
Tasssirt	17TAS01 – 02	29°35'09.6"N	8°53'06.6"W
	17TAS03 – 11	29°35'09.3"N	8°53'06.7"W
	18TAS01 – 02	29°35'11.0"N	8°53'0.6"W
	18TAS03 – 05	29°35'13.4"N	8°53'4.8"W
	18TAS06	29°35'9.8"N	8°53'6.5"W
	18TAS07 – 08	29°35'9.8"N	8°53'6.5"W
	18TAS09 – 14	29°35'05.4"N	8°53'0.8"W

	18TAS15 – 16	29°35'3.8"N	8°53'0.0"W
	18TAS17 – 20	29°35'8.7"N	8°53'2.1"W
	18TAS30 – 41	29°35'12.77"N	8°53'1.14"W
	18TAS42 – 51	29°35'14.39"N	8°53'3.06"W
	18TAS52 – 53	29°35'12.3"N	8°53'4.5"W
	18TAS54 – 61	29°35'10.4"N	8°53'8.1"W
	18TAS70 – 74	29°35'46.68"N	8°52'45.67"W
	18TAS76 – 79	29°35'9.2"N	8°53'6.2"W
	18TAS80 – 83	29°35'8.8"N	8°53'2.2"W
	18TAS84 – 96	29°35'5.6"N	8°53'2.3"W
Tizert	17TIZ01 – 08	30°18'20.0"N	8°25'01.09"W
Ighrem	17IG01	30°01'41.0"N	8°26'19.5" W
	18IG01 – 03	30°01'41.3"N	8°26'19.2" W
Est Akka	18EA01 – 03	29°30'36.9"N	8°27'37.2"W
Irkhs	18IR01 – 07	29°31'52.7"N	8°43'39.7"W
Imi Omagha	18IM01 – 06	29°39'36.5"N	8°27'27.1"W
Assifid	18ASS01 – 04	30°15'11.76"N	8°31'08.77"W
Imini	18TIF01 – 03	31°04'58.99"N	7°45'58.35"W
	18TIF05 – 16	31°04'71.12"N	7°45'74.21"W
	18TIF17	31°04'11.71"N	7°45'47.64"W
	18TIF18 – 21	31°04'09.04"N	7°45'51.31"W
	18FAR01	31°01'17.84"N	7°46'81.61"W
	18FAR02 – 04	31°04'13.29"N	7°46'57.19"W
	18FAR 05 – 06	31°02'05.59"N	7°46'88.61"W
	18FAR07 – 08	31°02'00.25"N	7°46'84.39"W
	18FAR09 – 18	31°01'32.30"N	7°47'02.64"W
	18PL01-29	31°02'41.13"N	7°48'0.82"W



## CHAPTER IX

# REFERENCES

---

- Ague JJ, Brimhall GH (1989) Geochemical modeling of steady state fluid flow and chemical reaction during supergene enrichment of porphyry copper deposits. *Econ Geol* 84:506–528. doi: 10.2113/gsecongeo.84.3.506
- Aït Malek H, Gasquet D, Bertrand J-M, Jacques L (1998) Géochronologie U-Pb sur zircon de granitoïdes éburnéens et panafricains dans les boutonnières protérozoïques d'Igherm, du Kerdous et du Bas Drâa (Anti-Atlas occidental, Maroc). *Comptes Rendus l'Académie des Sci Paris - Sci la Terre* 237:819–826
- Alderton DHM, Pearce JA, Potts PJ (1980) Rare earth element mobility during granite alteration: Evidence from southwest England. *Earth Planet Sci Lett* 49:149–165. doi: 10.1016/0012-821X(80)90157-0
- Alexandre J, Thorez J (1995) Au secondaire et au tertiaire, l'Ardenne tropicale. L'altération des roches et les climats anciens. In: Demoulin A (ed) *L'Ardenne. Essai de Géographie physique*. Dépt de Géographie physique et Quaternaire, University of Liège, pp 53–67
- Alfieris D, Voudouris P, Spry PG (2013) Shallow submarine epithermal Pb-Zn-Cu-Au-Ag-Te mineralization on western Milos Island, Aegean Volcanic Arc, Greece: Mineralogical, geological and geochemical constraints. *Ore Geol Rev* 53:159–180. doi: 10.1016/j.oregeorev.2013.01.007
- Allard T, Gautheron C, Bressan Riffel S, et al (2018) Combined dating of goethites and kaolinites from ferruginous duricrusts. Deciphering the Late Neogene erosion history of Central Amazonia. *Chem Geol* 479:136–150. doi: 10.1016/j.chemgeo.2018.01.004
- Alpers CN, Brimhall GH (1988) Middle Miocene climatic change in the Atacama Desert, northern Chile: Evidence from supergene mineralization at La Escondida. *Bull Geol Soc Am* 100:1640–1656. doi: 10.1130/0016-7606(1988)100<1640:MMCCIT>2.3.CO;2
- Alpers CN, Rye RO, Nordstrom DK, et al (1992) Chemical, crystallographic and stable isotopic properties of alunite and jarosite from acid-Hypersaline Australian lakes. *Chem Geol* 96/1-2:203–226. doi: 10.1016/0009-2541(92)90129-S
- Anand RR, Paine M (2002) Regolith geology of the Yilgarn Craton, Western Australia: Implications for exploration. *Aust J Earth Sci* 49:3-162. doi: 10.1046/j.1440-0952.2002.00912.x
- Andrew-Jones DA (1968) The application of geochemical techniques to mineral exploration. *Color Sch Mines Bull* 11:1–31
- Annich M (2002) Gisement de Ouansimi. In: El Barodi B, Mouttaqi A, Annich M (eds) *Méthode et technique d'exploration minière et principaux gisements au Maroc*. pp 219–223
- Antoine P-O (2002) Phylogénie et évolution des Elasmotheriina (Mammalia, Rhinocerotidae). *Mémoires du Muséum Natl d'Histoire Nat* 188:359
- Antoine P-O (2003) Middle Miocene elasmotheriine Rhinocerotidae from China and Mongolia: taxonomic revision and phylogenetic relationships. *Zool Scr* 32:95–118. doi: 10.1046/j.1463-6409.2003.00106.x
- Antoine P-O, Orliac MJ, Albayrak E, et al (2012) A Rhinocerotid Skull Cooked-to-Death in a 9.2 Ma-old Ignimbrite Flow of South Central Anatolia, Turkey. *PLoS One* 7:1–12. doi: 10.1371/journal.pone.0049997
- Antoine P-O, Sarac G (2005) The late Miocene mammalian locality of Akkasdagi, Turkey: Rhinocerotidae. *Geodiversitas* 27:601–632
- Arndt NT, Ganino C (2012) *Metals and Society. An Introduction to Economic Geology*. Springer-Verlag, Berlin Heidelberg, 162 p. doi: 10.1007/978-3-642-22996-1

- Arndt NT, Ganino C (2010) Ressources minérales - Origine, nature et exploitation, Dunod. Paris
- Arrobas DL, Hund KL, McCornick MS, et al (2017) The growing role of minerals and metals for a low carbon future. World Bank, Washington DC, 117581
- Asladay A (2002) Gisement de Tazalaght. In: Barodi EB, Watanabe Y, Mouttaqi A, Annich M (eds) Méthodes et techniques d'exploration minière et principaux gisements au Maroc. BRPM, pp 215–219
- Asladay A, Barodi EB, Maacha L, Zinbi Y (1998) Les minéralisations cuprifères du Maroc. Chroniques des Rech Minières 531–532:29–44
- Ault AK, Gautheron C, King GE (2019) Innovations in (U–Th)/He, fission track, and trapped charge thermochronometry with applications to earthquakes, weathering, surface-mantle connections, and the growth and decay of mountains. *Tectonics* 3705–3739. doi: 10.1029/2018TC005312
- Ault AK, Reiners PW, Evans JP, Thomson SN (2015) Linking hematite (U–Th)/He dating with the microtextural record of seismicity in the Wasatch fault damage zone, Utah, USA. *Geology* 43:771–774. doi: 10.1130/G36897.1
- Ayarza P, Alvarez-Lobato F, Teixell A, et al (2005) Crustal structure under the central High Atlas Mountains (Morocco) from geological and gravity data. *Tectonophysics* 400/1–4:67–84. doi: 10.1016/j.tecto.2005.02.009
- Ayora C, Macías F, Torres E, Nieto JM (2015) Rare Earth Elements in Acid Mine Drainage. In: XXXV Reunión de la Sociedad Española de Mineralogía. pp 1–22
- Baele JM, Quesnel F, Dupuis C (2016) Silcrete in northern France and Belgium: a terrestrial record of surface environments under the influence of pyroclastic ash-falls. In: 5<sup>th</sup> International Geologica Belgica Meeting. Mons, Belgium, p 40
- Baidder L, Raddi Y, Tahiri M, Michard A (2008) Devonian extension of the Pan-African crust north of the West African craton, and its bearing on the Variscan foreland deformation: evidence from eastern Anti-Atlas (Morocco). *Geol Soc London, Spec Publ* 297:453–465. doi: 10.1144/sp297.21
- Balout H, Roques J, Gautheron C, et al (2017) Helium diffusion in pure hematite ( $\alpha$ -Fe<sub>2</sub>O<sub>3</sub>) for thermochronometric applications: A theoretical multi-scale study. *Comput Theor Chem* 1099:21–28. doi: 10.1016/j.comptc.2016.11.001
- Banfield JF (1989) Apatite Replacement and Rare Earth Mobilization, Fractionation, and Fixation During Weathering. *Clays Clay Miner* 37:113–127. doi: 10.1346/CCMN.1989.0370202
- Bank R, Menkhirst PMG (2009) A revised bibliography of the malacological papers of Paul Pallary. *Zool Meded* 83:537–546
- Barbarand J, Bour I, Pagel M, et al (2018) Post-Paleozoic evolution of the northern Ardenne Massif constrained by apatite fission-track thermochronology and geological data. *Bull la Société Géologique Fr.* doi: 10.1051/bsgf/2018015
- Barbier F, Prognon C, Quesnel F, et al (2010) Dating and weathering characterization of the Morialmé quarry (Entre-Sambre-et-Meuse, Belgium). In: 4<sup>th</sup> French congress on stratigraphy. Paris, France, p 18
- Barbier F, Quesnel F, Dupuis C, Yans J (2012) ). The late paleocene-early eocene interval as a potential period for weathering in Western Europe: the case of the Morialmé section (Belgium). In: 4<sup>th</sup> International Geologica Belgica Meeting. Brussels, Belgium, p 59
- Bau M, Dulski P (1996) Distribution of yttrium and rare-earth elements in the Penge and Kuruman iron-

- formations, Transvaal Supergroup, South Africa. *Precambrian Res* 79:37–55. doi: 10.1016/0301-9268(95)00087-9
- Bauer KK, Vennemann TW (2014) Analytical methods for the measurement of hydrogen isotope composition and water content in clay minerals by TC/EA. *Chem Geol* 363:229–240. doi: 10.1016/j.chemgeo.2013.10.039
- Baulig H (1926) Le relief de la Haute-Belgique. *Ann Geogr* 35. doi: 10.3406/geo.1926.8449
- Beaudoin B, André L, Péliissonnier H (1976) Action des eaux superficielles dans le gisement de manganèse d'Imini (Maroc). *Bull la Société Géologique Fr VIII*:95–100
- Belanger I, Delaby S, Delcambre B, et al (2012) Redéfinition des unités structurales du front varisque utilisées dans le cadre de la nouvelle Carte géologique de Wallonie (Belgique). *Geol Belgica* 15:169–175
- Belissant R, Boiron MC, Luais B, Cathelineau M (2014) LA-ICP-MS analyses of minor and trace elements and bulk Ge isotopes in zoned Ge-rich sphalerites from the Noailhac - Saint-Salvy deposit (France): Insights into incorporation mechanisms and ore deposition processes. *Geochim Cosmochim Acta* 126:518–540. doi: 10.1016/j.gca.2013.10.052
- Bellon N (1976) Séries magmatiques néogènes et quaternaires du pourtour de la Méditerranée occidentale comparées dans leur cadre géodynamique : implications géodynamiques. University Paris-Sud, France
- Ben Abdallah R, Medhioub M, Hatira N, et al (2013) Hydrothermal and meteoric alteration of Triassic materials in the Oued Belif structure (Nefza, Northern Tunisia). *Eur J Sci Res* 98:470–480
- Bennami M, Toto EA, Chakiri S (2001) Les chevauchements frontaux du Haut Atlas central marocain : styles structuraux et taux de raccourcissement différentiel entre les versants nord et sud. *Comptes Rendus l'Académie Sci* 333:241–247. doi:10.1016/S1251-8050(01)01628-7
- Benssaou M, Hamoumi N (2003) Le graben de l'Anti-Atlas occidental (Maroc) : contrôle tectonique de la paléogéographie et des séquences au Cambrien inférieur. *Comptes Rendus Geosci* 335:297–305. doi: 10.1016/s1631-0713(03)00033-6
- Bernal JP, Eggins SM, McCulloch MT, et al (2006) Dating of chemical weathering processes by in situ measurement of U-series disequilibria in supergene Fe-oxy/hydroxides using LA-MC-ICPMS. *Chem Geol* 235/1-2:76-94. doi: 10.1016/j.chemgeo.2006.06.009
- Bertorino G, Caredda AM, Zuddas P (1995) Weathering of Pb-Zn mine tailings in pH buffered environment. *Proceedings of the 8th International Symposium on Water-Rock Interaction*, pp 859–862
- Biagioni C, Capalbo C, Pasero M (2013) Nomenclature tunings in the hollandite supergroup. *Eur J Mineral* 25: . doi: 10.1127/0935-1221/2013/0025-2255
- Bigham JM, Murad E (1997) Mineralogy of ochre deposits formed by the oxidation of iron sulfide minerals. In: Bigham JM (ed) *Soils and Environment—Soil Processes from Mineral to Landscape Scale*. *Advances in Geoecology*, pp 193–225
- Bird MI, Chivas AR (1993) Geomorphic and palaeoclimatic implications of an oxygen-isotope chronology for Australian deeply weathered profiles. *Aust J Earth Sci* 40/4:345-358. doi: 10.1080/08120099308728086
- Bird MI, Chivas AR, McDougall I (1990) An isotopic study of surficial alunite in Australia 2. Potassium-argon geochronology. *Chem Geol Isot Geosci Sect* 80:133–145. doi: 10.1016/0168-9622(90)90022-5

- Blackburn TJ, Stockli DF, Walker JD (2007) Magnetite (U-Th)/He dating and its application to the geochronology of intermediate to mafic volcanic rocks. *Earth Planet Sci Lett* 259:360–371. doi: 10.1016/j.epsl.2007.04.044
- Bladh KW (1982) The formation of goethite, jarosite, and alunite during the weathering of sulfide-bearing felsic rocks. *Econ Geol* 77:176–184. doi: 10.2113/gsecongeo.77.1.176
- Bless MJM, Felder PJS (1989) Note on the Late Cretaceous of Hockai (Hautes Fagnes, NE Belgium). *Ann - Soc Geol Belgique* 112
- Bohme M, Spassov N, Ebner M, et al (2017) Messinian age and savannah environment of the possible hominin *Graecopithecus* from Europe. *PLoS One* 12:1–31. doi: 10.371/journal.pone.0177347
- Boni M, Giuseppina Balassone, Vernon Arseneau, Paul Schmidt (2009) The nonsulfide zinc deposit at Accha (Southern Peru): Geological and mineralogical characterization. *Econ Geol* 104:267–289. doi: 10.2113/gsecongeo.104.2.267
- Boni M, Large D (2005) Nonsulfide Zinc Mineralization in Europe: An Overview. *Econ Geol* 98:715–729. doi: 10.2113/98.4.715
- Boni M, Mondillo N (2015) The “Calamines” and the “Others”: The great family of supergene nonsulfide zinc ores. *Ore Geol Rev* 67:208–233. doi: 10.1016/j.oregeorev.2014.10.025
- Boni M, Terracciano R, Evans NJ, et al (2007) Genesis of vanadium ores in the Otavi Mountainland, Namibia. *Econ Geol* 102:441–469. doi: 10.2113/gsecongeo.102.3.441
- Bonnet NJ, Beauvais A, Arnaud N, et al (2014) First  $^{40}\text{Ar}/^{39}\text{Ar}$  dating of intense Late Palaeogene lateritic weathering in Peninsular India. *Earth Planet Sci Lett* 386:126–137. doi: 10.1016/j.epsl.2013.11.002
- Borg G (2009) The role of fault structures and deep oxidation in supergene base metal deposits. In: Titley SR (ed) *Supergene Environments, Processes and Products*, Economic G. pp 121–132
- Borisenko AS, Borovikov AA, Pavlova GG, et al (2013) Formation conditions of Hg-silver deposition at the Imiter deposit (Anti-Atlas, Morocco). In: *The 12<sup>th</sup> Biennial SGA Meeting*. Uppsala, Sweden
- Bouabdellah M, Margoum D (2016) Geology, Fluid Inclusions, and Geochemistry of the Aouli Sulphide-Fluorite-Barite Vein Deposit (Upper Moulouya District, Morocco) and Its Relationships to Pangean Rifting and Opening of the Tethys and Central Atlantic Oceans. In: Bouabdellah M, Slack JF (eds) *Mineral Deposits of North Africa*, Mineral Resource Reviews. Springer, ChamoniX, Switzerland, pp 291–305
- Bouabdellah M, Slack JF (2016) *Mineral Deposits of North Africa*. Springer International Publishing: Heidelberg, Germany
- Bouabdellah M, Zemri O, Jébrak M, et al (2016) Geology and Mineralogy of the El Hammam REE-Rich Fluorite Deposit (Central Morocco): A Product of Transtensional Pangean Rifting and Central Atlantic Opening. In: Bouabdellah M, Slack JF (eds) *Mineral Deposits of North Africa*, Mineral Resource Reviews2. Springer, ChamoniX, Switzerland, pp 307–324
- Boudzoumou F, Vandamme D, Affaton P, et al (2012) Evidence of a Permian remagnetization in the Neoproterozoic-Cambrian Adoudounian Formation (Anti-Atlas, Morocco). *Bull l’Institut Sci Sect Sci la Terre* 34:15–28
- Boulvain F, Belanger I, Delsate D, et al (2000) New lithostratigraphical, sedimentological, mineralogical and palaeontological data on the mesozoic of Belgian Lorraine : A progress report. *Geol Belgica* 3:3-33

- Bour I (2010) Histoire thermique des massifs ardennais et bohémien. Conséquences sur la dynamique de l'Europe de l'Ouest au Méso-Cénozoïque. University Paris-Sud, France
- Bourque H, Barbanson L, Sizaret S, et al (2015) A contribution to the synsedimentary versus epigenetic origin of the Cu mineralizations hosted by terminal Neoproterozoic to Cambrian formations of the Bou Azzer – El Gaara inlier: new insights from the Jbel Laassel deposit (Anti-Atlas, Morocco). *J African Earth Sci* 32:723–739
- Bowell RJ (2014) Hydrogeochemistry of the Tsumeb Deposit: implications for arsenate mineral stability. *Rev Mineral Geochemistry* 79:589–627. doi: 10.2138/rmg.2014.79.14
- Boyle DR (1997) Iodargyrite as an indicator of arid climatic conditions and its association with gold-bearing glacial tills of the Chibougamau - Chapais area, Quebec. *Can Mineral* 35:23–34
- Bracène R, Frizon de Lamotte D (2002) The origin of intraplate deformation in the Atlas system of western and central Algeria: From Jurassic rifting to Cenozoic-Quaternary inversion. *Tectonophysics*. doi: 10.1016/S0040-1951(02)00369-4
- Braun JJ, Pagel M, Muller JP, et al (1990) Cerium anomalies in lateritic profiles. *Geochim Cosmochim Acta* 54:781–795. doi: 10.1016/0016-7037(90)90373-S
- Brookins DG (1988) Eh-pH diagrams for geochemistry. Springer Berlin Heidelberg, Berlin, Heidelberg
- Brookins DG (1989) Aqueous geochemistry of rare earth elements. In: Lipin BR, McKay GA (eds.) *Geochemistry and Mineralogy of Rare Earth Elements*. *Rev Mineral Geochemistry* 21:201–225
- Brown DJ, Helmke PA, Clayton MK (2003) Robust geochemical indices for redox and weathering on a granitic laterite landscape in Central Uganda. *Geochim Cosmochim Acta* 67:2711–2723. doi: 10.1016/S0016-7037(03)00104-2
- Brown EH (1967) The greenschist facies in part of eastern Otago, New Zealand. *Contrib to Mineral Petrol* 14:259–292. doi: 10.1007/BF00373808
- BRPM (2002) Méthodes et techniques d'exploration minière et principaux gisements au Maroc
- Bruyère D, De Putter T, Perruchot A, Dupuis C (2003) Neogenesis of halloysite in cryptokarstic environments (Beez, Belgium): chemical modeling. In: 10<sup>th</sup> Conference of the European clay groups association. Modena, p 48
- Bruyère D, Putter T De, Decrée S, et al (2010) Miocene karsts and associated Fe–Zn-rich minerals in Aïn Khamouda (Central Tunisia). *J African Earth Sci* 57:70–78. doi: 10.1016/j.jafrearsci.2009.07.011
- Burkhard M, Caritg S, Helg U, et al (2006) Tectonics of the Anti-Atlas of Morocco. *Comptes Rendus Geosci* 338:11–24. doi: 10.1016/j.crte.2005.11.012
- Castor SB, Hendrick JB (2006) Rare Earth Elements. In: Kogel JE, Trivedi NC, Barker JM (eds) *Industrial Minerals and Rocks*. Society for Mining, Metallurgy and Exploration, Littleton, USA, pp 769–792
- Chargui H, Hajjaji W, Wouters J, et al (2018) Orange Selophenyl TGL dye fixation by modified kaolin. *Clay Miner* 53:271–287. doi: 10.1180/clm.2018.18
- Charrière A, Haddoumi H, Mojon PO (2005) Découverte de Jurassique supérieur et d'un niveau marin du Barrémien dans les «couches rouges» continentales du Haut Atlas central marocain: Implications paléogéographiques et structurales. *Comptes Rendus - Palevol* 4/5:385-394. doi: 10.1016/j.crpv.2005.04.009
- Chavez JR (2000) Supergene oxidation of copper deposits : zoning and distribution of copper oxide minerals. *Econ Geol* 41:10–21

- Chazan W (1954) Les gisements stratiformes plombo-zincifères de l'Infracambrien de l'Anti Atlas occidental. Notes Mémoires du Serv Géologique du Maroc 120:202
- Chefchaoui YC, Diouri M, Choubert G (1963) Carte géologique du Haut Atlas oriental, feuilles Bou Arfa, Iche, Talzaga et Figuig. Notes Mémoires du Serv Géologique du Maroc 158
- Cheilietz A, Gasquet D, Filali F, et al (2010) A Late Triassic  $^{40}\text{Ar}/^{39}\text{Ar}$  age for the El Hammam high-REE fluorite deposit (Morocco): Mineralization related to the Central Atlantic Magmatic Province. *Miner Depos* 45:323–329. doi: 10.1007/s00126-010-0282-y
- Choubert G, Fauve-Muret A (1962) Evolution du domaine atlasique marocain depuis les temps paléozoïques. In: Durand-Delga (ed) Livre à la mémoire du Professeur Paul Fallot. Société Géologique de France, Paris
- Choulet F, Charles N, Barbanson L, et al (2014) Non-sulfide zinc deposits of the moroccan High Atlas: Multi-scale characterization and origin. *Ore Geol Rev* 56:115–140. doi: 10.1016/j.oregeorev.2013.08.015
- Choulet F, Richard J, Boiron M-C, et al (2019) Distribution of trace elements in willemite from the Belgium non-sulphide deposits. *Eur J Mineral* 31:983–997. doi: 10.1127/ejm/2019/0031-2871
- Ciantia MO, Castellanza R (2016) Modelling weathering effects on the mechanical behaviour of rocks. *Eur J Environ Civ Eng* 20:1054–1082. doi: 10.1080/19648189.2015.1030086
- Clauer N, Leblanc M (1977) Implications stratigraphiques d'une étude géochronologique rubidium-strontium sur métasédiments précambriens de Bou Azzer (Anti Atlas marocain). Notes Mémoires du Serv Géologique du Maroc 268:7–12
- Clavel M, Leblanc M (1971) Liaison entre tectonique et minéralisation cuprifère dans les dolomies infracambriennes de la région du Jbel N'Zourk (Anti-Atlas central, Maroc). Notes Mémoires du Serv Géologique du Maroc 237:229–232
- Cocker MD (2012) Lateritic, supergene rare earth element (REE) deposits. In: 48<sup>th</sup> Annual Forum on the Geology of Industrial Minerals. Arizona Geological Survey, Scottsdale, USA, pp 1–20
- Cocker MD (2014) Lateritic, supergene rare earth element (REE) deposits. In: Paper AGSS (ed) Proceedings of the 48th Annual Forum on the Geology of Industrial Minerals. pp 1–18
- Commission E (2014) Report on critical raw materials for the EU
- Cook NJ, Ciobanu CL, Pring A, et al (2009) Trace and minor elements in sphalerite: A LA-ICPMS study. *Geochim Cosmochim Acta* 73:4761–4791. doi: 10.1016/j.gca.2009.05.045
- Coppin F, Berger G, Bauer A, et al (2002) Sorption of lanthanides on smectite and kaolinite. *Chem Geol* 182:57–68. doi: 10.1016/S0009-2541(01)00283-2
- Coppola V, Boni M, Gilg HA, et al (2008) The “calamine” nonsulfide Zn-Pb deposits of Belgium: Petrographical, mineralogical and geochemical characterization. *Ore Geol Rev* 33:187–210. doi: 10.1016/j.oregeorev.2006.03.005
- Cornell RM, Schwertmann U (2003) The Iron Oxides. Wiley-VCH Verlag GmbH & Co. KGaA, Weinheim
- Cosan Y (1969) Etude géologique de sondages au Plateau des tailles. Mémoires du Serv Géologique Belgique 32
- Cotten J, Le Dez A, Bau M, et al (1995) Origin of anomalous rare-earth element and yttrium enrichments in subaerially exposed basalts: Evidence from French Polynesia. *Chem Geol* 119:115–138. doi: 10.1016/0009-2541(94)00102-E



- Cotter-Howells J (1996) Lead phosphate formation in soils. *Environ Pollut* 93:9–16 . doi: 10.1016/0269-7491(96)00020-6
- Cotter-Howells JD, Champness PE, Charnocky JM, Pattrick RAD (1994) Identification of pyromorphite in mine-waste contaminated soils by ATEM and EXAFS. *Eur J Soil Sci* 45:393–402. doi: 10.1111/j.1365-2389.1994.tb00524.x
- Craig H (1961) Isotopic variations in meteoric waters. *Science* (80) 133:1702–1703
- Crank J (1975) The mathematics of diffusion. 2nd Edn. Oxford Univ. Press
- Danišík M, Evans NJ, Ramanaidou ER, et al (2013) (U-Th)/He chronology of the Robe River channel iron deposits, Hamersley Province, Western Australia. *Chem Geol* 354:150–162. doi: 10.1016/j.chemgeo.2013.06.012
- Daoudi L, Pot de Vin JL (2002) Effets thermique et hydrothermal de la coulée de basalte triasico-liasique sur les argiles du bassin d'Argana (Maroc). *Comptes Rendus Geosci* 334:463–468. doi: 10.1016/S1631-0713(02)01765-0
- Davis A, Drexler JW, Ruby M V., Nicholson A (1993) Micromineralogy of mine wastes in relation to lead bioavailability, Butte, Montana. *Environ Sci Technol* 27:1415–1425. doi: 10.1021/es00044a018
- Davis W (1896) The Seine, the Meuse and the Moselle. *Natl Geogr Mag* 89:228–238
- Davis W (1899) The peneplain. *Am Geol* 23:207–239
- Dawood YH, Abd El-Naby HH, Sharafeldin AA (2004) Influence of the alteration processes on the origin of uranium and europium anomalies in trachyte, central Eastern Desert, Egypt. *J Geochemical Explor* 88:15–27. doi: 10.1016/S0375-6742(03)00210-3
- De Putter T, André L, Bernard A, et al (2002) Trace element (Th, U, Pb, REE) behaviour in a cryptokarstic halloysite and kaolinite deposit from Southern Belgium: importance of “accessory” mineral formation for radioactive pollutant trapping. *Appl Geochemistry* 17:1313–1328. doi: 10.1016/S0883-2927(02)00022-7
- De Putter T, Charlet J-MM, Quinif Y (1999) REE, Y and U concentration at the fluid-iron oxide interface in late cenozoic cryptodolines from Southern Belgium. *Chem Geol* 153:139–150. doi: 10.1016/S0009-2541(98)00156-9
- De Putter T, Mees F, Decrée S, Dewaele S (2010) Malachite, an indicator of major Pliocene Cu remobilization in a karstic environment (Katanga, Democratic Republic of Congo). *Ore Geol Rev* 38:90–100. doi: 10.1016/j.oregeorev.2010.07.001
- De Putter T, Ruffet G (2020) Supergene manganese ore records 75 Myr-long Campanian to Pleistocene geodynamic evolution and weathering history of the Central African Great Lakes Region – Tectonics drives, climate assists. *Gondwana Res* 83:96–117. doi: 10.1016/j.gr.2020.01.021
- De Putter T, Ruffet G, Yans J, Mees F (2015) The age of supergene manganese deposits in Katanga and its implications for the Neogene evolution of the African Great Lakes Region. *Ore Geol Rev* 71:350–362. doi: 10.1016/j.oregeorev.2015.06.015
- Decrée S, De Putter T, Yans J, et al (2008) Iron mineralisation in Mio-Pliocene sediments of the Tamra iron mine (Nefza mining district, Tunisia): Mixed influence of pedogenesis and hydrothermal alteration. *Ore Geol Rev* 33:397–410. doi: 10.1016/J.OREGEOREV.2007.02.001
- Decrée S, Deloule É, Ruffet G, et al (2010a) Geodynamic and climate controls in the formation of Mio–Pliocene world-class oxidized cobalt and manganese ores in the Katanga province, DR Congo. *Miner Depos* 45:621–629. doi: 10.1007/s00126-010-0305-8

- Decrée S, Marignac C, Abidi R, et al (2016) Tectonomagmatic Context of Sedex Pb–Zn and Polymetallic Ore Deposits of the Nappe Zone Northern Tunisia, and Comparisons with MVT Deposits in the Region. In: Mineral deposits of North Africa. Springer International Publishing, pp 497–525
- Decrée S, Marignac C, De Putter T, et al (2013) The Oued Belif hematite-rich breccia: A Miocene iron oxide Cu–Au–(U–REE) deposit in the Nefza mining district, Tunisia. *Econ Geol* 108:1425–1457. doi: 10.2113/econgeo.108.6.1425
- Decrée S, Marignac C, De Putter T, et al (2008) Pb–Zn mineralization in a Miocene regional extensional context: The case of the Sidi Driss and the Douahria ore deposits (Nefza mining district, northern Tunisia). *Ore Geol Rev* 34:285–303. doi: 10.1016/j.oregeorev.2008.01.002
- Decrée S, Marignac C, Liégeois J-P, et al (2014) Miocene magmatic evolution in the Nefza district (Northern Tunisia) and its relationship with the genesis of polymetallic mineralizations. *Lithos* 192–195:240–258. doi: 10.1016/j.lithos.2014.02.001
- Decrée S, Ruffet G, Putter T De, et al (2010b) Mn oxides as efficient traps for metal pollutants in a polyphase low-temperature Pliocene environment: A case study in the Tamra iron mine, Nefza mining district, Tunisia. *J African Earth Sci* 57:249–261. doi: 10.1016/j.jafrearsci.2009.08.005
- Dejonghe L, Boni M (2004) The “Calamine-type” zinc-lead deposits in Belgium and West Germany: a product of Mesozoic paleoweathering processes. *Geol Belgica* 8:3–14
- Dekayir A, El-Maataoui M (2001) Mineralogy and geochemistry of supergene alteration of an alkali basalt from the Middle Atlas, Morocco. *J African Earth Sci* 32:619–633. doi: 10.1016/S0899-5362(02)00045-3
- Dekoninck A, Bernard A, Barbarand J, et al (2016a) Detailed mineralogy and petrology of manganese oxyhydroxide deposits of the Imini district (Morocco). *Miner Depos* 52:1049–1064. doi: 10.1007/s00126-015-0590-3
- Dekoninck A, Leprêtre R, Saddiqi O, et al (2016b) The high-grade Imini manganese district - karst-hosted deposits of Mn oxides and oxyhydroxides. In: Bouabdellah M, Slack JF (eds) Mineral deposits of North Africa. Springer International Publishing, pp 575–594
- Dekoninck A, Monié P, Blockmans S, et al (2019) Genesis and  $^{40}\text{Ar}/^{39}\text{Ar}$  dating of K–Mn oxides from the Stavelot Massif (Ardenne, Belgium): new insights on Oligocene to Pliocene weathering periods in Europe. *Ore Geol Rev* 115:103–191. doi: 10.1016/j.oregeorev.2019.103191
- Dekoninck A, Moussi B, Vennemann T, et al (2018) Mixed hydrothermal and meteoric fluids evidenced by unusual H- and O-isotope compositions of kaolinite-halloysite in the Fe(–Mn) Tamra deposit (Nefza district, NW Tunisia). *Appl Clay Sci* 163:33–45. doi: 10.1016/j.clay.2018.07.007
- DeMenocal PB, Ortiz J, Guilderson T, et al (2000) Abrupt onset and termination of the African Humid Period: Rapid climate responses to gradual insolation forcing. *Quat Sci Rev* 19:347–361. doi: 10.1016/S0277-3791(99)00081-5
- Demoulin A (1995) Les surfaces d'érosion méso-cénozoïques en Ardenne-Eifel. *Bull la Société Géologique Fr* 166:573–585
- Demoulin A (2006) La néotectonique de l'Ardenne-Eifel et des régions avoisinantes. *Mémoires la CI des Sci Académie R Belgique* 25:252
- Demoulin A (2003) Paleosurfaces and residual deposits in Ardenne-Eifel: historical overview and perspectives. *Géologie la Fr* 1:17–21
- Demoulin A, Hallot E, Rixhon G (2009) Amount and controls of the Quaternary denudation in the Ardennes massif (western Europe). *Earth Surf Process Landforms* 34. doi: 10.1002/esp.1834

- Demoulin A, Quesnel F, Dupuis C, et al (2010) Cenomanian sands and clays north of the Vesdre valley: The oldest known Cretaceous deposits in Eastern Belgium. *Geol Belgica* 13:241-256
- Deng XD, Li JW, Shuster DL (2017) Late Mio-Pliocene chemical weathering of the Yulong porphyry Cu deposit in the eastern Tibetan Plateau constrained by goethite (U–Th)/He dating: Implication for Asian summer monsoon. *Earth Planet Sci Lett* 472:289–298. doi: 10.1016/j.epsl.2017.04.043
- Descostes M, Beaucaire C, Mercier F, et al (2002) Effect of carbonate ions on pyrite (FeS<sub>2</sub>) dissolution. *Bull la Soc Geol Fr* 173:265–270. doi: 10.2113/173.3.265
- Dill HG (2015) Supergene alteration of ore deposits: From nature to humans. *Elements* 11:311–316. doi: 10.2113/gselements.11.5.311
- Dill HG, Hansen B, Keck E, Weber B (2010) Cryptomelane: A tool to determine the age and the physical-chemical regime of a Plio-Pleistocene weathering zone in a granitic terrain (Hagendorf, SE Germany). *Geomorphology* 121. doi: 10.1016/j.geomorph.2010.05.004
- Dill HG, Techmer A, Botz R (2013) Copper-bearing encrustations: a tool for age dating and constraining the physical–chemical regime during the late Quaternary in the Wadi Araba, southern Jordan. *Int J Earth Sci* 102:1541–1561. doi: 10.1007/s00531-013-0877-5
- Dodson MH (1973) Closure temperature in cooling geochronological and petrological systems. *Contrib to Mineral Petrol* 40:259-274. doi: 10.1007/BF00373790
- Domènech C, de Pablo J, Ayora C (2002) Oxidative dissolution of pyritic sludge from the Aznalcóllar mine (SW Spain). *Chem Geol* 190:339–353. doi: 10.1016/S0009-2541(02)00124-9
- Domènech M, Teixell A, Stockli DF (2016) Magnitude of rift-related burial and orogenic contraction in the Marrakech High Atlas revealed by zircon (U–Th)/He thermochronology and thermal modeling. *Tectonics* 35:2609–2635. doi: 10.1002/2016TC004283
- Dong D, Nelson YM, Lion LW, et al (2000) Adsorption of Pb and Cd onto metal oxides and organic material in natural surface coatings as determined by selective extractions: new evidence for the importance of Mn and Fe oxides. *Water Res* 34:427–436. doi: 10.1016/S0043-1354(99)00185-2
- Du Dresnay R (1965) Notice géologique sur la région de Bou-Arfa. *Notes Mémoires du Serv Géologique du Maroc* 181
- Du LJ, Li B, Huang ZL, et al (2020) Mineralogy, Fluid Inclusion, and Hydrogen and Oxygen Isotope Studies of the Intrusion-Related Yangla Cu Deposit in the Sanjiang Region, SW China: Implications for Metallogenesis and Deposit Type. *Resour Geol* 70:28-49. doi: 10.1111/rge.12215
- Dupuis C (1979) Esquisse paléogéographique du Nord et du Nord-Ouest du Bassin de Paris au Paléocène et à l'Eocène inférieur. *Incidences structurales. Comptes Rendus l'Academie Sci Paris* 288:1587–1590
- Dupuis C, Charlet J-M, Dejonghe L, Thorez J (1996) Reconnaissance par carottage des paléaltérations kaolinisées mésozoïques de la Haute-Ardenne (Belgique). Le sondage de transinne (194E-495): premiers résultats. *Ann la Société Géologique Belgique* 119:91–109
- Dusar M, Lagrou D (2007) Cretaceous flooding of the Brabant Massif and the lithostratigraphic characteristics of its chalk cover in northern Belgium. *Geol Belgica* 10:27-38
- E. KC, Baeckeroot G (1947) Oesling et Gutland: morphologie du bassin Ardennais et Luxembourgeois de la Moselle. *Geogr J* 109. doi: 10.2307/1789913
- Ehlers TA, Farley KA (2003) Apatite (U–Th)/He thermochronometry: Methods and applications to problems in tectonic and surface processes. *Earth Planet Sci Lett* 206/1-2:1-14. doi:

- El Arabi EH, Diez JB, Broutin J, Esamoud R (2006) First palynological characterization of the Middle Triassic; implications for the first Tethysian rifting phase in Morocco. *Comptes Rendus - Geosci* 338:641–649. doi:10.1016/j.crte.2006.04.001
- El Basbas A, Aissa M, Ouguir H, et al (2011) La mine de Tazalarht (Anti-Atlas occidental). In: Michard A, Saddiqi O, Chalouan A, et al. (eds) *Notes et Mémoires du Service Géologique du Maroc : Les principales mines du Maroc*. pp 145–149
- El Basbas A, Aissa M, Ouguir H, Mahdoudi ML (2019) Ouansimi copper mineralization (Western Anti-Atlas, Morocco): Paragenetic sequence and circulation of gangue hosted paleofluids. *J African Earth Sci* 162. doi: 10.1016/j.jafrearsci.2019.103692
- El Harfi A, Guiraud M, Lang J (2006) Deep-rooted “thick skinned” model for the High Atlas Mountains (Morocco). Implications for the structural inheritance of the southern Tethys passive margin. *J Struct Geol* 28:1958–1976. doi: 10.1016/j.jsg.2006.08.011
- El Kochri A, Chorowicz J (1995) Oblique extension in the Jurassic trough of the central and eastern High Atlas (Morocco). *Can J Earth Sci* 33:84–92. doi: 10.1139/e96-009
- Emberger A, Pouit G (1966) Les minéralisations polymétalliques (Mn, Cu, Pb-Zn) dans les socles hercynien et précambrien et leurs couvertures au Maroc. *Notes Mémoires du Serv Géologique du Maroc* 188:115–122
- Evenson NS, Reiners PW, Spencer JE, Shuster DL (2014) Hematite and mn oxide (U-Th)/He dates from the buckskin-Rawhide detachment system, Western Arizona: Gaining insights into hematite (U-Th)/He systematics. *Am J Sci* 314:1373–1435. doi: 10.2475/10.2014.01
- Fairbridge R (1968) *Encyclopedia of earth science. Geomorphology*. Springer, Berlin Heidelberg
- Faivre D (2016) *Iron Oxides: From Nature to Applications*. Wiley-VCH, Weinheim. doi:10.1002/9783527691395
- Fanale FP, Kulp JL (1962) The helium method and the age of the Cornwall, Pennsylvania magnetite ore. *Econ Geol* 57:735–746
- Farley KA (2002) (U-Th)/He Dating: Techniques, Calibrations, and Applications. *Rev Mineral Geochemistry* 47:819–844. doi: 10.2138/rmg.2002.47.18
- Farley KA (2018) Helium diffusion parameters of hematite from a single-diffusion-domain crystal. *Geochim Cosmochim Acta* 231:117-129. doi: 10.1016/j.gca.2018.04.005
- Farley KA, Flowers RM (2012) (U-Th)/Ne and multidomain (U-Th)/He systematics of a hydrothermal hematite from eastern Grand Canyon. *Earth Planet Sci Lett* 359–360:131–140. doi: 10.1016/j.epsl.2012.10.010
- Farley KA, Wolf RW, Silver LT (1996) The effects of long alpha-stopping distances on (U-Th)/He ages. *Geochim Cosmochim Acta* 60:4223–4229. doi:10.1016/S0016-7037(96)00193-7
- Farmer JG, Lovell MA (1986) Natural enrichment of arsenic in Loch Lomond sediments. *Geochim Cosmochim Acta* 50:2059–2067. doi: 10.1016/0016-7037(86)90259-0
- Fauvelet E (1973) *Réflexions sur une liaison possible entre les minéralisations cuprifères et les roches plutoniques basiques hercyniennes dans l'Anti Atlas (Maroc)*. Collection Scientifique Internationale E. Raguin, Masson, Paris
- Feakins SJ, DeMenocal PB (2010) Global and African Regional Climate during the Cenozoic. In: Werdelin L, Sanders WJ (eds) *Cenozoic Mammals of Africa*. University of California Press, pp 45–56

- Feng XH, Zhai LM, Tan WF, et al (2007) Adsorption and redox reactions of heavy metals on synthesized Mn oxide minerals. *Environ Pollut* 147:366–373 . doi: 10.1016/j.envpol.2006.05.028
- Fodor R V., Frey FA, Bauer GR, Clague DA (1992) Ages, rare-earth element enrichment, and petrogenesis of tholeiitic and alkalic basalts from Kahoolawe Island, Hawaii. *Contrib to Mineral Petrol* 110:442–462. doi: 10.1007/BF00344080
- Fontaine L, De Putter T, Bernard A, et al (2020) Complex mineralogical-geochemical sequences and weathering events in the supergene ore of the Cu–Co Luiswishi deposit (Katanga, D.R. Congo). *J African Earth Sci* 161:103674. doi: 10.1016/j.jafrearsci.2019.103674
- Force ER, Back W, Spiker EC, Knauth LP (1986) A ground-water mixing model for the origin of the Imini manganese deposit (Cretaceous) of Morocco. *Econ Geol* 81:65–79. doi: 10.2113/gsecongeo.81.1.65
- Fransolet A (1979) Occurrences de lithiophorite, nsutite et cryptomélane dans le Massif de Stavelot, Belgique. *Ann la Société Géologique Belgique* 102:303–312
- Frizon de Lamotte D, Leturmy P, Missenard Y, et al (2009) Mesozoic and Cenozoic vertical movements in the Atlas system (Algeria, Morocco, Tunisia): An overview. *Tectonophysics* 475:9–28. doi: 10.1016/j.tecto.2008.10.024
- Frizon de Lamotte D, Saint Bezar B, Bracène R, Mercier E (2000) The two main steps of the Atlas building and geodynamics of the Western Mediterranean. *Tectonics* 19:740–761. doi: 10.1029/2000TC900003
- Frizon de Lamotte D, Zizi M, Missenard Y, et al (2008) The Atlas System. In: Michard A (ed) *Continental evolution: The geology of Morocco*, Springer-V. Springer-Verlag, Heidelberg, Germany, pp 133–202
- Froitzheim N (1984) Late Cretaceous vertical tectonics in the High Atlas SW' of Marrakech/Morocco - Reconstruction of tectonic movements in an early stage of the High Atlas orogenesis. *Neues Jarb fur Geol und Palaontologie - Monatshefte* 8:463–471
- Froitzheim N, Stets J, Wurster P (2005) Aspects of Western High Atlas tectonics. In: Jacobshagen VH, ed, *The Atlas System of Morocco. Lecture Notes in earth Sciences*, 15, Springer, berlin, Heidelberg, pp 219-244
- Frost RL, Xi Y, López A, et al (2014) The molecular structure of the vanadate mineral mottramite [PbCu(VO<sub>4</sub>)(OH)] from Tsumeb, Namibia - A vibrational spectroscopic study. *Spectrochim Acta - Part A Mol Biomol Spectrosc* 122:252–256. doi: 10.1016/j.saa.2013.11.086
- Gao ZL, Kwak TAP, Changkakoti A, et al (1995) Supergene ore and hypogene nonore mineralization at the Nagambie sediment-hosted gold deposit, Victoria, Australia. *Econ Geol* 90. doi: 10.2113/gsecongeo.90.6.1747
- Garasic V, Jurkovic I (2012) Geochemical characteristics of different iron ore types from the Southern Tomašica deposit, Ljubija NW Bosnia. *Geol Croat* 65:255–270. doi: 10.4154/gc.2012.18
- Garlick GD (1966) Oxygen isotope fractionation in igneous rocks. *Earth Planet Sci Lett* 1:361–368
- Garnit H, Boni M, Buongiovanni G, et al (2018) C-O stable isotopes geochemistry of Tunisian nonsulfide zinc deposits: a first look. *Minerals* 8:13. doi: 10.3390/min801001
- Garrels RM (1954) Mineral species as functions of pH and oxidation-reduction potentials, with special reference to the zone of oxidation and secondary enrichment of sulphide ore deposits. *Geochim Cosmochim Acta* 5:153–168. doi: 10.1016/0016-7037(54)90030-7

- Gasquet D, Ennih N, Liégeois J-P, et al (2008) The Pan-African Belt. In: Michard A, Saddiqi O, Chalouan A, Frizon de Lamotte D (eds) *Continental evolution: The geology of Morocco*. Lecture Notes in Earth Sciences, 116, Springer Verlag, Berlin, Heidelberg, pp 33–64
- Gasquet D, Levresse G, Cheilletz A, et al (2005) Contribution to a geodynamic reconstruction of the Anti-Atlas (Morocco) during Pan-African times with the emphasis on inversion tectonics and metallogenic activity at the Precambrian-Cambrian transition. *Precambrian Res* 140:157–182. doi: 10.1016/j.precamres.2005.06.009
- Gaudry A, Lartet E (1856) Sur les résultats des recherches paléontologiques entreprises dans l'Attique sous les auspices de l'Académie. *Comptes Rendus l'Academie Sci Paris* 43:271–274
- George L, Cook N, Ciobanu C (2017) Minor and trace elements in natural tetrahedrite-tennantite: Effects on element partitioning among base metal sulphides. *Minerals* 7:17–42. doi: 10.3390/min7020017
- Geraads D (1989) Vertébrés fossiles du Miocène supérieur du djebel krechem el artsouma (Tunisie centrale). *Comparaisons biostratigraphiques*. *Geobios* 22:777–801
- Giese P, Jacobshagen V (1992) Inversion tectonics of intracontinental ranges: High and Middle Atlas, Morocco. *Geol Rundschau* 81:249–259. doi: 10.1007/BF01764553
- Girard J-P, Freyssinet P, Chazot G (2000) Unraveling climatic changes from intraprofile variation in oxygen and hydrogen isotopic composition of goethite and kaolinite in laterites: an integrated study from Yaou, French Guiana. *Geochim Cosmochim Acta* 64:409–426. doi: 10.1016/S0016-7037(99)00299-9
- Gladstone R, Flecker R, Valdes P (2007) The Mediterranean hydrologic budget from a Late Miocene global climate simulation. *Palaeogeogr Palaeoclimatol Palaeoecol* 251:254–267. doi: 10.1016/j.palaeo.2007.03.050
- Glasmacher U, Zentilli M, Grist AM (1998) Apatite Fission Track Thermochronology of Paleozoic Sandstones and the Hill-Intrusion, Northern Linksrheinisches Schiefergebirge, Germany. In: Van den Haute P, de Corte F, eds, *Advances in Fission-Track Geochronology*, Springer, Dordrecht
- Göb S, Bau M, Markl G (2014) Chemical composition of waters in a former Cu-As mine: water–rock interaction, REE systematics and stability of secondary copper minerals. *Neues Jahrb für Mineral - Abhandlungen J Mineral Geochemistry* 192:11–32. doi: 10.1127/0077-7757/2014/0268
- Göb S, Wenzel T, Bau M, et al (2011) The redistribution of rare-earth elements in secondary minerals of hydrothermal veins, Schwarzwald, Southwestern Germany. *Can Mineral* 49:1305–1333. doi: 10.3749/canmin.49.5.1305
- Gołębiewska B (2005) Solid solution within vanadates and arsenates of the descloizite and the adelite groups from Rędziny (the Sudetes). *Mineral - Spec Pap* 25:85–88
- Gołębiewska B, Pieczka A, Franus W (2006) Olivenite-Adamite Solid Solution From Oxidation Zone in Rędziny (West Sudetes, Poland). *Mineralogia* 37:101–110. doi: 10.2478/v10002-007-0001-1
- Golebiewska B, Pieczka A, Rzepa G, et al (2010) Iodargyrite from Zalas (Cracow area, Poland) as an indicator of Oligocene-Miocene aridity in Central Europe. *Palaeogeogr Palaeoclimatol Palaeoecol* 296:130–137. doi: 10.1016/j.palaeo.2010.06.022
- Gomez F, Barazangi M, Bensaid M (1996) Active tectonism in the intracontinental Middle Atlas Mountains of Morocco: Synchronous crustal shortening and extension. *J Geol Soc London* 153:389–402. doi: 10.1144/gsjgs.153.3.0389
- Gomez F, Barazangi M, Demnati A (2000) Structure and Evolution of the Neogene Guercif Basin at the

- Junction of the Middle Atlas Mountains and the Rif Thrust Belt, Morocco. *Am Assoc Pet Geol Bull* 84/9:1340-1364. doi: 10.1306/a9673ea0-1738-11d7-8645000102c1865d
- Górecka E, Kozłowski A, Kibitlewski S (1996) The Silesian-Cracow Zn-Pb deposits, Poland: Considerations on ore-forming processes. *Pr - Panstw Inst Geol* 154:166-181
- Gouiza M, Charton R, Bertotti G, et al (2017) Post-Variscan evolution of the Anti-Atlas belt of Morocco constrained from low-temperature geochronology. *Int J Earth Sci* 106:593–616. doi: 10.1007/s00531-016-1325-0
- Griffin DL (2002) Aridity and humidity: Two aspects of the late Miocene climate of North Africa and the Mediterranean. *Palaeogeogr Palaeoclimatol Palaeoecol* 182:65–91. doi: 10.1016/S0031-0182(01)00453-9
- Guérin C (1966) *Diceros douariensis* nov. sp., un Rhinocéros du Mio-Pliocène de Tunisie du Nord. *Doc du Lab Géologie la Fac des Sci Lyon* 16:1–50
- Guérin C (2000) The Neogene rhinoceroses of Namibia. *Palaeontol africana* 36:119–138
- Guilbert JM, Park CF (1986) *The Geology of Ore Deposits*. W.H. Freeman and Company, New York
- Gullentops F (1954) Contributions à la chronologie du Pléistocène et des formes du relief en Belgique. *Mémoires de l'Institut de Géologie de l'Université de Louvain* 18:123–252
- Gutzmer J, Beukes NJ, Rhalimi M, Mukhopadhyay J (2006) Cretaceous karstic cave-fill manganese-lead-barium deposits of Imini, Morocco. *Soc Econ Geol* 101:385–405. doi: 10.2113/gsecongeo.101.2.385
- Hafid M, Zizi M, Bally AW, Ait Salem A (2006) Structural styles of the western onshore and offshore termination of the High Atlas, Morocco. *Comptes Rendus - Geosci* 338:50–64. doi: 10.1016/j.crte.2005.10.007
- Hamidi EM, Boulangé B, Colin F (1997) Altération d'un basalte triasique de la région d'Elhajeb, Moyen Atlas, Maroc. *J African Earth Sci* 24:141–151. doi: 10.1016/S0899-5362(97)00032-8
- Handa N, Nakatsukasa M, Kunitatsu Y, Nakaya H (2017) A new Elasmotheriini (Perissodactyla, Rhinocerotidae) from the upper Miocene of Samburu Hills and Nakali, northern Kenya. *Geobios* 50:197–209. doi: 10.1016/j.geobios.2017.04.002
- Hannigan RE, Sholkovitz ER (2001) The development of middle rare earth element enrichments in freshwaters: Weathering of phosphate minerals. *Chem Geol* 175:495–508. doi: 10.1016/S0009-2541(00)00355-7
- Hanor JS (2001) Barite-celestine geochemistry and environments of formation. *Reviews in Min and Geochem* 40:193-276. doi:10.2138/rmg.2000.40.4
- Harris DL, Lottermoser BG, Duchesne J (2003) Ephemeral acid mine drainage at the Montalbion silver mine, north Queensland. *Aust J Earth Sci* 50:797–809. doi: 10.1111/j.1440-0952.2003.01029.x
- Harris J, Soulounias N, Geraads D (2010) Giraffoidea. In: *Cenozoic Mammals of Africa*. University of California Press, Berkeley, pp 797–811
- Hassenforder B (1987) La tectonique panafricaine et varisque de l'Anti Atlas dans le massif de Kerdous (Maroc). *Université Louis Pasteur, Strasbourg*
- Hassenforder B, Roger J, Baudin T, et al (2001) Carte géologique du Maroc au 1/50000, feuille de Sidi Bou Addi, et notice explicative. *Notes Mémoires du Serv Géologique du Maroc* 414
- Hautmann S, Lippolt HJ (2000)  $^{40}\text{Ar}/^{39}\text{Ar}$  dating of central European K-Mn oxides - a chronological

- framework of supergene alteration processes during the Neogene. *Chemical Geology* 170:37-80. doi: 10.1016/S0009-2541(99)00241-7
- Hefferan K, Soulaïmani A, Samson SD, et al (2014) A reconsideration of Pan African orogenic cycle in the Anti-Atlas Mountains, Morocco. *J African Earth Sci* 98:34–46. doi:10.1016/j.jafrearsci.2014.03.007
- Heim JA, Vasconcelos PM, Shuster DL, et al (2006a) Dating paleochannel iron ore by (U-Th)/He analysis of supergene goethite, Hamersley province, Australia. *Geology* 34:173–176. doi: 10.1130/G22003.1
- Heim JA, Vasconcelos P V., Farley KA, et al (2006b) (U-Th)/He and  $^{40}\text{Ar}/^{39}\text{Ar}$  geochronology of weathering, Hamersley Province, Australia: Implications for weathering history and landscape evolution. In: *Goldschmidt Conference Abstract 2006*. p A240
- Helg U, Burkhard M, Caritg S, Robert-Charrue C (2004) Folding and inversion tectonics in the Anti-Atlas of Morocco. *Tectonics* 23:1–17. doi: 10.1029/2003TC001576
- Hemley JJ, Hostetler PB, Gude AJ, Mountjo WT (1969) Some stability relations of alunite. *Econ Geol.* doi: 10.2113/gsecongeo.64.6.599
- Hénocque O, Ruffet G, Colin F, Féraud G (1998)  $^{40}\text{Ar}/^{39}\text{Ar}$  dating of West African lateritic cryptomelanes. *Geochim Cosmochim Acta* 62:2739–2756. doi: 10.1016/S0016-7037(98)00185-9
- Herbert RB (1999) Sulphide oxidation in mine waste deposits, a review with emphasis on dysoxic weathering. Mitigation of the environmental impact from mining waste (MiMi), MiMi Print. Lulea, Sweden
- Herbig H-G, Trappe J (1994) Stratigraphy of the Subatlas Group (Maastrichtian - Middle Eocene, Morocco). *Newsletters Stratigr* 30/3:125-165. doi: 10.1127/nos/30/1994/125
- Heyl A V. (1964) Oxidized Zinc Deposits of the United States. *Geol Surv Bull* 1135:247 p. doi: 10.3133/b1135
- Hilgen FJ, Lourens LJ, Van Dam JA (2012) The Neogene period. In: Gradstein F, Ogg J, Schmitz M, Ogg G (eds) *The Geologic Time Scale 2012*. Elsevier, Boston, pp 923–878
- Hitzman MW, Reynolds NA, Sangster DF, et al (2003) Classification, Genesis, and Exploration Guides for Nonsulfide Zinc Deposits. *Econ Geol* 98:685–714. doi: 10.2113/gsecongeo.98.4.685
- Hofmann F, Reichenbacher B, Farley KA (2017) Evidence for >5 Ma paleo-exposure of an Eocene–Miocene paleosol of the Bohnerz Formation, Switzerland. *Earth Planet Sci Lett* 465:168–175. doi: 10.1016/j.epsl.2017.02.042
- Holroyd PA, Lihoreau F, Gunnell GF, et al (2010) Anthracotheriidae. In: Werdelin L (ed) *Cenozoic Mammals of Africa*. University of California Press, pp 843–851
- Holtzapffel T (1985) Les minéraux argileux; préparation, analyse diffractométrique et détermination. *Ann la Société Géologique du Nord* 12:136 p.
- Huminicki DMC, Rimstidt JD (2008) Neutralization of sulfuric acid solutions by calcite dissolution and the application to anoxic limestone drain design. *Appl Geochemistry* 23:148–165. doi: 10.1016/j.apgeochem.2007.10.004
- Ibough H, Hibti M, Amari K El (2013) La mine de Tansrift : un exemple de red beds crétacés du Haut Atlas central, Maroc. In: *3MA Colloque international Magmatisme, métamorphisme et minéralisations associées*. Marrakech, Maroc
- Ibough H, Mouguina EM (2011) Aguerd n ' Tazoult , une mine Zn-Pb du Haut Atlas central / Aguerd n '



- Tazoult , a Zn-Pb Mine in the Central High Atlas. In: Mouttaqi A, Rjimati L, Maacha L, et al (eds) Les principales mines du Maroc. Notes et Mémoires du Service géologique du Maroc, pp. 293-296
- Inegbenebor AI, Thomas JH, Williams PA (1989) The chemical stability of mimetite and distribution coefficients for pyromorphite–mimetite solid-solutions. *Mineral Mag* 53:363–371. doi: 10.1180/minmag.1989.053.371.12
- Iseppi M, Sevin B, Cluzel D, et al (2018) Supergene nickel ore deposits controlled by gravity-driven faulting and slope failure, Peridotite Nappe, New Caledonia. *Econ Geol* 113:53-544. doi: 10.5382/econgeo.2018.4561
- Jallouli C, Mickus K, Turki MM, Rihane C (2003) Gravity and aeromagnetic constraints on the extent of Cenozoic rocks within the Nefza-Tabarka region, northwestern Tunisia. *J Volcanol Geotherm Res* 122:51–68. doi: 10.1016/S0377-0273(02)00469-9
- Jambor JL, Nordstrom DK, Alpers CN (2000) Metal-sulfate salts from sulfide mineral oxidation. *Rev Mineral Geochemistry* 40:303–350. doi: 10.2138/rmg.2000.40.6
- Jérôme A (1907) De la découverte d'un gisement notable de kaolin en Ardenne. *Bull la Société Géologique Belgique* XXI:217–222
- Jönsson J, Jönsson J, Lövgren L (2006) Precipitation of secondary Fe(III) minerals from acid mine drainage. *Appl Geochemistry* 21:437–445. doi: 10.1016/j.apgeochem.2005.12.008
- Junge H (1987) Der Einfluss von Tektonik und eustatischen Meeresspiegelschwankungen auf die Ausbildung der Reliefgenerationen im Norden der Eifeler Nord-Süd-Zone. *Zeitschrift für Geomorphol* 65:35–84
- Kamel S, Bouabid R, Boulangé B, Colin F (1996) Paléooaltérations hydrothermale et supergène dans un basalte triasique du Moyen Atlas, Maroc. *J African Earth Sci* 23:225–235. doi: 10.1016/S0899-5362(96)00064-4
- Kamineneni DC, Chung CF, Dugal JJB, Ejeckam RB (1986) Distribution of uranium and thorium in core samples from the Underground Research Laboratory lease area, southeastern Manitoba, Canada. *Chem Geol* 54:97–111. doi: 10.1016/0009-2541(86)90074-4
- Kamona F, Friedrich G (1994) Die Blei-Zink-Lagerstätte Kabwe in Zentral Sambia. *Erzmetall* 47:34–44
- Kampf AR, Steele IM, Jenkins RA (2006) Phosphohedyphane,  $\text{Ca}_2\text{Pb}_3(\text{PO}_4)_3\text{Cl}$ , the phosphate analog of hedyphane: Description and crystal structure. *Am Mineral* 91:1909–1917. doi: 10.2138/am.2006.2268
- Karrat L, Perruchot A, Macaire JJ (1998) Weathering of a quaternary glass-rich basalt in Bakrit, Middle Atlas Mountains, Morocco. Comparison with a glass-poor basalt. *Geodin Acta* 11:205–215. doi: 10.1080/09853111.1998.11105320
- Keim MF, Markl G (2015) Weathering of galena: Mineralogical processes, hydrogeochemical fluid path modeling, and estimation of the growth rate of pyromorphite. *Am Mineral* 100:1584–1594. doi: 10.2138/am-2015-5183
- Keim MF, Staude S, Marquardt K, et al (2018) Weathering of Bi-bearing tennantite. *Chem Geol* 499:1–25. doi: 10.1016/j.chemgeo.2018.07.032
- Keim MF, Vaudrin R, Markl G (2016) Redistribution of silver during supergene oxidation of argentiferous galena: A case study from the Schwarzwald, SW Germany. *Neues Jahrb für Mineral - Abhandlungen J Mineral Geochemistry* 193:295–309. doi: 10.1127/njma/2016/0002

- Ketcham RA, Gautheron C, Tassan-Got L (2011) Accounting for long alpha-particle stopping distances in (U–Th–Sm)/He geochronology: Refinement of the baseline case. *Geochim Cosmochim Acta* 75:7779–7791. doi: 10.1016/J.GCA.2011.10.011
- Kholodov VN, Butuzova GY (2008) Siderite formation and evolution of sedimentary iron ore deposition in the Earth's history. *Geol Ore Depos* 50:299–319. doi: 10.1134/S107570150804003X
- Khomsy S, de Lamotte DF, Bédier M, Echihi O (2016) The Late Eocene and Late Miocene fronts of the Atlas Belt in eastern Maghreb: integration in the geodynamic evolution of the Mediterranean Domain. *Arab J Geosci* 9:650. doi: 10.1007/s12517-016-2609-1
- King L (1947) Landscape study in southern Africa. *Proc Geol Soc South Africa* 50:23–102
- Knight KB, Nomade S, Renne PR, et al (2004) The Central Atlantic Magmatic Province at the Triassic–Jurassic boundary: Paleomagnetic and  $^{40}\text{Ar}/^{39}\text{Ar}$  evidence from Morocco for brief, episodic volcanism. *Earth Planet Sci Lett* 228:143–160. doi: 10.1016/j.epsl.2004.09.022
- Kocourková E, Sracek O, Houzar S, et al (2011) Geochemical and mineralogical control on the mobility of arsenic in a waste rock pile at Dlouhá Ves, Czech Republic. *J Geochemical Explor* 110:61–73. doi: 10.1016/j.gexplo.2011.02.009
- Köhler SJ, Harouiya N, Chaïrat C, Oelkers EH (2005) Experimental studies of REE fractionation during water–mineral interactions: REE release rates during apatite dissolution from pH 2.8 to 9.2. *Chem Geol* 222:168–182. doi: 10.1016/J.CHEMGEO.2005.07.011
- Koppi AJ, Edis R, Field DJ, et al (1996) Rare earth element trends and cerium-uranium-manganese associations in weathered rock from Koongarra, Northern Territory, Australia. *Geochim Cosmochim Acta* 60:1695–1707. doi: 10.1016/0016-7037(96)00047-6
- Lafforgue L (2016) Place de la minéralisation de manganèse de Bou Arfa dans l'évolution méso-cénozoïque de l'oriental marocain. University Paris-Saclay, Orsay, France
- Lalaoui M-D, Beauchamp J, Sagon J-P (1991) Le gisement de manganèse de l'Imini (Maroc): un dépôt sédimentaire sur la ligne de rivage. *Chroniques des Rech Minières* 502:23–36
- Laville E, Pique A, Amrhar M, Charroud M (2004) A restatement of the Mesozoic Atlasic Rifting (Morocco). *J African Earth Sci* 38:145–153. doi: 10.1016/j.jafrearsci.2003.12.003
- Leprêtre R, Missenard Y, Barbarand J, et al (2018) Polyphased Inversions of an Intracontinental Rift: Case Study of the Marrakech High Atlas, Morocco. *Tectonics* 37:818–841. doi: 10.1002/2017TC004693
- Leprêtre R, Missenard Y, Saint-Bezar B, et al (2015) The three main steps of the Marrakech High Atlas building in Morocco: Structural evidences from the southern foreland, Imini area. *J African Earth Sci* 109:177–194. doi: 10.1016/j.jafrearsci.2015.05.013
- Lesavre A (1975) Le gisement de manganèse d'Imini (Maroc). Université Pierre et Marie Curie - Paris 6
- Leverett P, Mckinnon AR, Williams PA (2005) Supergene geochemistry of the Endeavor ore body, Cobar, NSW, and relationships to other deposits in the Cobar Basin. *Regolith , Ten years of CRC LEME: Proceedings of the CRC LEME Regional Symposia, november 2005, Adelaide and Canberra*, pp. 191–194
- Lewis AJ, Palmer MR, Sturchio NC, Kemp AJ (1997) The rare earth element geochemistry of acid-sulphate and acid-sulphate-chloride geothermal systems from Yellowstone National Park, Wyoming, USA. *Geochim Cosmochim Acta* 61:695–706. doi: 10.1016/s0016-7037(96)00384-5
- Leybourne MI, Goodfellow WD, Boyle DR, Hall GM (2000) Rapid development of negative Ce anomalies

- in surface waters and contrasting REE patterns in groundwaters associated with Zn–Pb massive sulphide deposits. *Appl Geochemistry* 15:695–723. doi: 10.1016/S0883-2927(99)00096-7
- Leybourne MI, Johannesson KH (2008) Rare earth elements (REE) and yttrium in stream waters, stream sediments, and Fe-Mn oxyhydroxides: Fractionation, speciation, and controls over REE + Y patterns in the surface environment. *Geochim Cosmochim Acta* 72:5962–5983. doi: 10.1016/j.gca.2008.09.022
- Leybourne MI, Peter JM, Layton-Matthews D, et al (2006) Mobility and fractionation of rare earth elements during supergene weathering and gossan formation and chemical modification of massive sulfide gossan. *Geochim Cosmochim Acta* 70:1091–1112. doi: 10.1016/j.gca.2005.11.003
- Li JW, Vasconcelos P, Duzgoren-Aydin N, et al (2007a) Neogene weathering and supergene manganese enrichment in subtropical South China: An  $^{40}\text{Ar}/^{39}\text{Ar}$  approach and paleoclimatic significance. *Earth Planet Sci Lett* 256:389–402. doi: 10.1016/j.epsl.2007.01.021
- Li JW, Vasconcelos P, Zhang W, et al (2007b) Timing and duration of supergene mineralization at the Xinrong manganese deposit, western Guangdong Province, South China: Cryptomelane  $^{40}\text{Ar}/^{39}\text{Ar}$  dating. *Miner Depos* 42:361–383. doi: 10.1007/s00126-006-0118-y
- Lihoreau F, Barry J, Blondel C, et al (2007) Anatomical revision of the genus *Merycopotamus* (Artiodactyla; Anthracotheriidae): its significance on late Miocene mammal dispersions in Asia. *Palaeontology* 50:503–524. doi: 10.1111/j.1475-4983.2006.00673.x
- Lihoreau F, Boisserie JR, Blondel C, et al (2014) Description and palaeobiology of a new species of *Libycosaurus* (Cetartiodactyla, Anthracotheriidae) from the Late Miocene of Toros-Menalla, northern Chad. *J Syst Palaeontol* 12:761–798. doi: 10.080/14772019.838609
- Lippolt HJ, Brander T, Mankopf NR (1998) An attempt to determine formation ages of goethites and limonites by (U-Th)/He dating. *Neues Jahrb fur Mineral Monatshefte* 11:505–528
- Lottermoser BG (1990) Rare-earth element mineralisation within the Mt. Weld carbonatite laterite, Western Australia. *Lithos* 24:151–167. doi: 10.1016/0024-4937(90)90022-S
- Ludden JN, Thompson G (1979) An evaluation of the behavior of the rare earth elements during the weathering of sea-floor basalt. *Earth Planet Sci Lett* 43:85–92. doi: 10.1016/0012-821X(79)90157-2
- Maacha L, Ennaciri O, El Ghorfi M, et al (2011a) Le cuivre oxydé du J. La'sal (boutonnière d'El Graara, Anti-Atlas central). In: Mouttaqi A, Rjimati EC, Maacha L, et al. (eds) *Les principales mines du Maroc. Notes et Mémoires du Service Géologique du Maroc*
- Maacha L, Ennaciri O, Saquaque A, Soulaïmani A (2011b) Un gîte prometteur : le cuivre du Jbel N'Zourk (Anti-Atlas central). In: Mouttaqi A, Rjimati EC, Maacha L, et al. (eds) *Les principales mines du Maroc. Notes et Mémoires du Service Géologique du Maroc*
- Macaire J, Perruchot A (1988) Transformations Géochimiques au Cours de l'Altération Météorique d'une Basanite Pliocène du Massif Central Français. *Geoderma* 41:287–314
- Macar P (1938) Contribution à l'étude géomorphologique de l'Ardenne. *Ann la Société Géologique Belgique* 61:187–217
- Maddi O, Baoutoul H, Maacha L, et al (2011) La mine d'Agjal au sud de Kerdous; considérations sur les gîtes stratoïdes de cuivre et argent de l'Anti Atlas occidental et central. In: Mouttaqi A, Rjimati L, Maacha L, et al. (eds) *Les principales mines du Maroc. Notes et Mémoires du Service Géologique du Maroc*
- Magalhães MCF, Pedrosa de Jesus JD, Williams PA (1988) The chemistry of formation of some

- secondary arsenate minerals of Cu(II), Zn(II) and Pb(II). *Mineral Mag* 52:679–690. doi: 10.1180/minmag.1988.052.368.12
- Maghfouri S, Hosseinzadeh MR, Rajabi A, Choulet F (2018) A review of major non-sulfide zinc deposits in Iran. *Geosci Front* 9:249–272. doi: 10.1016/j.gsf.2017.04.003
- Maier K, Chamberlain CP (2014) Hydrologic regulation of chemical weathering and the geologic carbon cycle. *Science* (80- ) 343:1502–1504. doi: 10.1126/science.1250770
- Makkoudi D (1995) Minéralisations Pb-Ba de M'fiss: étude géologique et contribution à la gîtologie des gisements du Tafilalet. University Mohammed V, Rabat, Morocco
- Maloof AC, Ramezani J, Bowring SA, et al (2010) Constraints on early Cambrian carbon cycling from the duration of the Nemakit-Daldynian-Tommotian boundary  $^{13}\text{C}$  shift, Morocco. *Geology* 38:623–623. doi: 10.1130/G30726.1
- Maloof AC, Schrag DP, Crowley JL, Bowring SA (2006) An expanded record of Early Cambrian carbon cycling from the Anti-Atlas Margin, Morocco. *Can J Earth Sci* 42:2195–2216. doi: 10.1139/e05-062
- Managem Group MM, Ennaciri A (2012) The Agjal Mine of Southern Kerdous ; Overview of the Stratabound Copper and Silver Deposits. Unpublished report
- Manceau A, Charlet L, Boisset MC, et al (1992) Sorption and speciation of heavy metals on hydrous Fe and Mn oxides. From microscopic to macroscopic. *Appl Clay Sci* 7:201–223. doi: 10.1016/0169-1317(92)90040-T
- Marcoux E, Nerci K, Branquet Y, et al (2015) Late-Hercynian intrusion-related gold deposits: An integrated model on the Tighza polymetallic district, central Morocco. *J African Earth Sci* 107:65–88. doi: 10.1016/j.jafrearsci.2015.01.011
- Margoum D, Bouabdellah M, Klugel A, et al (2015) Pangea rifting and onward pre-Central Atlantic opening as the main ore-forming processes for the genesis of the Aouli REE-rich fluorite–barite vein system, upper Moulouya district, Morocco. *J African Earth Sci* 108:22–39. doi: 10.1016/j.afrearsci.2015.03.021
- Markl G, von Blanckenburg F, Wagner T (2006) Iron isotope fractionation during hydrothermal ore deposition and alteration. *Geochim Cosmochim Acta* 70:3011–3030. doi: 10.1016/j.gca.2006.02.028
- Massacrier P (1980) Les boutonnières précambriennes d'Aït Abdellah-Alma et leur couverture Adoudounienne (Protérozoïque supérieur et terminal de l'Anti Atlas occidental, Maroc) : étude cartographique, lithostratigraphique et structurale. Aix Marseille I
- Mattauer M, Tapponnier P, Proust F (1977) Sur les mecanismes de formation des chaines intracontinentales; l'exemple des chaines atlasiques du Maroc. *Bull la Soc Geol Fr S7-XIX*:521–526. doi: 10.2113/gssgfbull.S7-XIX.3.521
- Maulana A, Yonezu K, Watanabe K (2014) Geochemistry of rare earth elements (REE) in the weathered crusts from the granitic rocks in Sulawesi Island, Indonesia. *J Earth Sci* 25:460–472. doi: 10.1007/s12583-014-0449-z
- McPhail DC, Summerhayes E, Welch S, Brugger J (2003) The geochemistry of zinc in the regolith. In: Roach IC (ed.) *Advances in Regolith. CRC Landsc Environ Miner Explor* 287–291
- Mees F, Stoops G (1999) Palaeoweathering of lower palaeozoic rocks of the Brabant Massif, Belgium: A mineralogical and petrographical analysis. *Geol J* 34-4:349–367. doi: 10.1002/(SICI)1099-1034(199911/12)34:4<349::AID-GJ830>3.0.CO;2-S

- Metcalf JR (2014) An Introduction to the Theory and Methods of ( U-Th )/ He Thermochronology. In 2014 Earthscope Institute: Geochronology in the Earth Sciences
- Meyer H, Hetzel R, Strauss H (2010) Erosion rates on different timescales derived from cosmogenic <sup>10</sup>Be and river loads: Implications for landscape evolution in the Rhenish Massif, Germany. *Int J Earth Sci* 99-2:395-412. doi: 10.1007/s00531-008-0388-y
- Michard A (1989) Rare earth element systematics in hydrothermal fluids. *Geochim Cosmochim Acta* 53:745–750
- Michard A, Hoepffner C, Soulaïmani A, Baidder L (2008) The Variscan Belt. In: Michard A, Saddiqi O, Chalouan A, Frizon de Lamotte D (eds) *Continental Evolution: The Geology of Morocco*. Springer Berlin, Heidelberg, pp 65–132
- Michard A, Saddiqi O, Missenard Y, et al (2017) Les grandes régions géologiques du Maroc; diversité et soulèvement d'ensemble. *Géologues* 197:4–12
- Miller R (2008) The geology of Namibia. *Geol Surv Namibia, Windhoek Namibia*
- Millman AP (1960) The descloizite-mottramite series of vanadates from Minas Do Lueca, Angola. *Am Mineral* 45:763–773
- Missenard Y, Zeyen H, de Lamotte DF, et al (2006) Crustal versus asthenospheric origin of relief of the Atlas mountains of Morocco. *J Geophys Res* 111:1–13. doi: 10.1029/2005JB003708
- Monteiro HS, Vasconcelos PM, Farley KA, et al (2014) (U-Th)/He geochronology of goethite and the origin and evolution of cangas. *Geochim Cosmochim Acta* 131:267–289. doi: 10.1016/j.gca.2014.01.036
- Morel GB, Setterholm DR (1997) rare earth elements in weathering profiles and sediments of Minnesota: implications for provenance studies. *J Sediment res* 67:105-115. doi: 10.1016/s0899-5362(00)00011-7
- Morey GB, Setterholm DR (1997) Rare earth elements in weathering profiles and sediments of Minnesota: implicatinos for provenance studies. *J Sediment Res* 67:105–115. doi: 10.1306/D4268504-2B26-11D7-8648000102C1865D
- Morland R, Webster AE (1998) Broken Hill lead-zinc-silver deposit. *Geol Aust Papuan New Guinean Mienral Depos* 619–626
- Mouguina EM, Daoudi L (2008) Pb-Zn mineralization of Ali ou Daoud area (Central High Atlas, Morocco): characterisation of deposit and relationships with the clay assemblages. *Estud Geológicos* 64:135–150. doi: 10.3989/egeol.08642.038
- Moussi B, Hajjaji W, Hachani M, et al (2020) Numidian clay deposits as raw material for ceramics tile manufacturing. *J African Earth Sci* 164:103775. doi: 10.1016/j.afrearsci.2020.103775
- Moussi B, Medhioub M, Hatira N, et al (2011) Identification and use of white clayey deposits from the area of Tamra (northern Tunisia) as ceramic raw materials. *Clay Miner* 46:165–175. doi: 10.1180/claymin.2011.046.1.165
- Mouttaqi A, Rjmati EC, Maacha L, et al (2011) Les principales mines du Maroc, Editions d. Royaume du Maroc, Ministère de l'Energie, des Mines; de l'Eau et de l'Environnement. 374p. ISSN 0374-9789
- Nahon D (1991) Introduction to the petrology of soils and chemical weathering. Wiley, New York
- Nesbitt HW, Wilson RE (1992) Recent chemical weathering of basalts. *Am. J. Sci.* 292:740–777

- Nicaise D, André L, Jedwab J, et al (1996) Neoformed LREE phosphates at the nanometer scale, in acid low temperature weathering: consequences in rare earth elements, uranium and thorium trapping. *Comptes Rendus l'Académie des Sci Paris* 323:113–120
- Nickel EH, Williams PA, Downes PJ, et al (2007) Secondary minerals in a tennantite boxwork from the Bali Lo prospect, Ashburton Downs, Western Australia. *Aust J Mineral* 13:31–39
- Nordstrom DK (1982) The effect of sulfate on aluminum concentrations in natural waters: some stability relations in the system  $\text{Al}_2\text{O}_3\text{-SO}_3\text{-H}_2\text{O}$  at 298 K. *Geochim Cosmochim Acta*. doi: 10.1016/0016-7037(82)90168-5
- Nriagu JO (2011) Formation and stability of base metal phosphates in soils and sediments. *Phosphate Miner* 318–329. doi: 10.1007/978-3-642-61736-2\_10
- Oukassou M, Saddiqi O, Barbarand J, et al (2013) Post-Variscan exhumation of the Central Anti-Atlas (Morocco) constrained by zircon and apatite fission-track thermochronology. *Terra Nov* 25:151–159. doi: 10.1111/ter.12019
- Oummouch A, Essaifi A, Zayane R, et al (2017) Geology and Metallogenesis of the Sediment-Hosted Cu-Ag Deposit of Tizert (Igherm Inlier, Anti-Atlas Copperbelt, Morocco). *Geofluids* 1–19. doi:10.1155/2017/7508484
- Pagel M, Braun J, Muller J (1990) Mécanismes de fractionnement géochimique des terres rares, de l'uranium et du thorium lors des altérations supergènes. In: Wackermann JM (ed) Séminaire ORSTOM 90: Organisation et Fonctionnement des Altérites et des Sols. Bondy, France, pp 219–226
- Paktunc D, Bruggeman K (2010) Solubility of nanocrystalline scorodite and amorphous ferric arsenate: Implications for stabilization of arsenic in mine wastes. *Appl Geochemistry* 25:674–683. doi: 10.1016/j.apgeochem.2010.01.021
- Palinkaš L, Damyanov ZK, Borojević Šoštarić S, et al (2016) Divergent drift of Adriatic-Dinaridic and Moesian carbonate platforms during the rifting phase witnessed by triassic MVT Pb-Zn and SEDEX deposits; a metallogenic approach. *Geol Croat* 69:75–78. doi: 10.4154/GC.2016.06
- Pallary P (1901) Sur les mollusques fossiles terrestres, lacustres et saumâtres de l'Algérie. *Mémoires la Société Géologique Fr* 22:1–213
- Pasava J (1994) Geochemistry and the role of anoxic sediments in the origin of the Imiter silver deposit in Morocco. *Vestn Ces Geol Ust* 69:1-11
- Pelletier RA (1930) The zinc, lead and vanadium deposit of Broken Hill, N. Rhodesia. *South African Miner Eng* 40:91
- Pidgeon RT (2003) Application of ( U-Th )/ He Geochronology To Date Hematite and Other Iron Minerals Produced During Weathering. In: Roach IC (ed) *Advances in Regolith: Proceedings of the CRC LEME Regional Regolith Symposia*, CRC LEME, pp 321–323
- Pidgeon RT, Brander T, Lippolt HJ (2004) Late Miocene (U+Th)-<sup>4</sup>He ages of ferruginous nodules from lateritic duricrust, Darling Range, Western Australia. *Aust J Earth Sci* 51:901–909. doi: 10.1111/j.1400-0952.2004.01094.x
- Pinney N, Morgan D (2013) Thermodynamics of Al-substitution in Fe-oxyhydroxides. *Geochim Cosmochim Acta* 120:514–530. doi: 10.1016/j.gca.2013.05.045
- Pique A, Dahmani M, Jeannette D, bahi L (1987) Permanence of structural lines in Morocco from Precambrian to present. *J African Earth Sci* 6: 247-256. doi: 10.1016/0899-5362(87)90066-2

- Pokras E, Mix AC (1987) Earth's precession cycle and Quaternary climatic change in tropical Africa. *Nature* 326:486–487. doi: 10.1038/326486a0
- Post JE (1999) Manganese oxide minerals: Crystal structures and economic and environmental significance. *Proc Natl Acad Sci* 96:3447–3454. doi: 10.1073/pnas.96.7.3447
- Pouit G (1966) Paléogéographie et répartition des minéralisations stratiformes de cuivre dans l'Anti Atlas occidental (Maroc). *Chroniques des Rech Minières* 34:279–289
- Pound MJ, Haywood AM, Salzmann U (2011) A Tortonian (Late Miocene, 11.61–7.25Ma) global vegetation reconstruction. *Palaeogeogr Palaeoclimatol Palaeoecol* 300:29–45. doi: 10.1016/j.palaeo.2010.11.029
- Pracejus B, Bolton BR, Frakes LA, Abbott M (1990) Rare-earth element geochemistry of supergene manganese deposits from Groote Eylandt, Northern Territory, Australia. *Ore Geol Rev* 5:293–314. doi: 10.1016/0169-1368(90)90035-L
- Quan C, Liu YS, Tang H, Utescher T (2014) Miocene shift of European atmospheric circulation from trade wind to westerlies. *Sci Rep* 4:5560. doi: 10.1038/srep05660
- Quesnel F (2003) Paleoweathering and paleosurfaces from northern and eastern France to Belgium and Luxembourg : geometry, dating and geodynamic implications. *Géologie la Fr Spec Conf "Paleoweathering Paleosurf Ardennes-Eifel Reg*
- Quesnel F, Dupuis C, Yans J, et al (2002) Paléosurfaces et paléoaltérations dans le Nord de la France et en Belgique. *Géologues* 133–134:40–43
- Radková AB, Jamieson H, Lalinská-Voleková B, et al (2017) Mineralogical controls on antimony and arsenic mobility during tetrahedrite-tennantite weathering at historic mine sites Špania Dolina-Piesky and L'ubietová-Svätodušná, Slovakia. *Am Mineral* 102:1091–1100. doi: 10.2138/am-2017-5616
- Ramdohr P (1980) *The Ore Minerals and their Intergrowths*. Pergamon Press, Oxford, UK
- Rasbury ET, Hanson GN, Meyers WJ, Saller AH (1997) Dating of the time of sedimentation using U-Pb ages for paleosol calcite. *Geochim Cosmochim Acta*. doi: 10.1016/S0016-7037(97)00043-4
- Reich M, Palacios C, Parada MA, et al (2008) Atacamite formation by deep saline waters in copper deposits from the Atacama Desert, Chile: Evidence from fluid inclusions, groundwater geochemistry, TEM, and <sup>36</sup>Cl data. *Miner Depos* 43:663–675. doi: 10.1007/s00126-008-0184-4
- Reich M, Vasconcelos PM (2015) Geological and Economic Significance of Supergene Metal Deposits. *Elements* 11:305–310. doi: 10.2113/gselements.11.5.305
- Reichert J (2007) A metallogenetic model for carbonate-hosted non-sulphide zinc deposits based on observations of Mehdi Abad and Irankuh, Central and Southwestern Iran. *Martin-Luther-Universität Halle-Wittenberg*
- Reichert J, Borg G (2008) Numerical simulation and a geochemical model of supergene carbonate-hosted non-sulphide zinc deposits. *Ore Geol Rev* 33:134–151. doi: 10.1016/j.oregeorev.2007.02.006
- Reiners PW (2009) Nonmonotonic thermal histories and contrasting kinetics of multiple thermochronometers. *Geochim Cosmochim Acta* 73:3612–3629. doi: 10.1016/j.gca.2009.03.038
- Renock D, Shuller-Nickles LC (2015) Predicting geologic corrosion with electrodes. *Elements* 11:331–336. doi: 10.2113/gselements.11.5.331
- Rhalmi M, Pascal A, El E, Chellai H (2000) Litho-biostratigraphie, diagenèse et paléogéographie au

- Cénomanién supérieur-Turonien inférieur des bassins sud-atlasiques marocains. *Géologie Alp* 76:135–149
- Rhalmi M, Pascal A, Lang J (1997) Contrôle séimentaire et diagénétique de la minéralisation manganésifère au cours du Crétacé supérieur dans la région d'Imini (Haut-Atlas central, Maroc). *Comptes Rendus l'Academie Sci - Ser Ila Sci la Terre des Planetes* 324:213–220
- Riahi S, Soussi M, Bou Khalfa K, et al (2010) Stratigraphy, sedimentology and structure of the Numidian flysch thrust belt in northern Tunisia. *J African Earth Sci* 57:109–126. doi: 10.1016/j.afrearsci.2009.07.016
- Riffel SB, Vasconcelos PM, Carmo IO, Farley KA (2016) Goethite (U–Th)/He geochronology and precipitation mechanisms during weathering of basalts. *Chem Geol* 446:18–32. doi: 10.1016/j.chemgeo.2016.03.033
- Riffel SB, Vasconcelos PM, Carmo IO, Farley KA (2015) Combined  $^{40}\text{Ar}/^{39}\text{Ar}$  and (U–Th)/He geochronological constraints on long-term landscape evolution of the Second Paran Plateau and its ruiniform surface features, Paran, Brazil. *Geomorphology* 233:52–63. doi: 10.1016/j.geomorph.2014.10.041
- Robb LJ (2005) Introduction to ore-forming processes. Blackwell Publishing Ltd, Oxford, UK
- Roman F, Solignac M (1934) Découverte d'un gisement de Mammifères pontiens à Douahria (Tunisie septentrionale). *Comptes Rendus l'Academie Sci Paris* 199:1649–1659
- Rose JHJ, Blade LV, Ross M (1958) Earthy monazite at Magnet Cove, Arkansas. *Am Mineral* 43:995–997
- Rouvier H (1994) Notice explicative de la carte géologique de la Tunisie au 1:50000 Nefza
- Rouvier H (1977) Géologie de l'extrême Nord-Tunisien: tectoniques et paléogéographie superposées à l'extrémité orientale de la chaîne Nord-Maghrebine. Université Pierre et Marie Curie - Paris VI
- Ruffet G, Innocent C, Michard A, et al (1996) A geochronological  $^{40}\text{Ar}/^{39}\text{Ar}$  and  $^{87}\text{Rb}/^{87}\text{Sr}$  study of K–Mn oxides from the weathering sequence of Azul, Brazil. *Geochim Cosmochim Acta* 60:2219–2232. doi: 10.1016/0016-7037(96)00080-4
- Ruiz GMHH, Sebt S, Negro F, et al (2011) From central Atlantic continental rift to Neogene uplift - western Anti-Atlas (Morocco). *Terra Nov* 23:35–41. doi: 10.1111/j.1365-3121.2010.00980.x
- Saddiqi O, El Haimer FZ, Michard A, et al (2009) Apatite fission-track analyses on basement granites from south-western Meseta, Morocco: Paleogeographic implications and interpretation of AFT age discrepancies. *Tectonophysics* 475/1:29–37. doi: 10.1016/j.tecto.2009.01.007
- Salahane A (1978) Etude géologique et métallogénique du gisement cuprifère du Jbel Klakh — Haut Atlas oriental (Maroc). *Notes Mémoires du Serv Géologique du Maroc* 40/275:147–237
- Sanematsu K, Moriyama T, Sotouky L, Watanabe Y (2011) Mobility of Rare Earth Elements in Basalt-Derived Laterite at the Bolaven Plateau, Southern Laos. *Resour Geol* 61:140–158 . doi: 10.1111/j.1751-3928.2011.00155.x
- Sangameshwar SR, Barnes HL (1983) Supergene processes in zinc-lead-silver sulfide ores in carbonates. *Econ Geol* 78:1379–1397. doi: 10.2113/gsecongeo.78.7.1379
- Sanz-Rubio E, Sanchez-Moral S, Canaveras JC, et al (2001) Calcitization of Mg–Ca carbonate and Ca sulphate deposits in a continental Tertiary Basin (Calatayud Basin, NE Spain). *Sediment Geol* 140:123–142. doi: 10.1016/S0037-0738(00)00175-5
- Sarih S (2008) Géodynamique et transferts sédimentaires des Bassins Liasiques Du Haut-Atlas Central (Maroc). University of Bourgogne, Dijon, France



- Schaller M, von Blanckenburg F, Hovius N, et al (2004) Paleoerosion rates from cosmogenic  $^{10}\text{Be}$  in a 1.3 Ma terrace sequence: Response of the river Meuse to changes in climate and rock uplift. *J Geol* 112. doi: 10.1086/381654
- Schaller M, von Blanckenburg F, Veldkamp A, et al (2002) A 30,000 yr record of erosion rates from cosmogenic  $^{10}\text{Be}$  in Middle European river terraces. *Earth Planet Sci Lett* 204:307–320. doi: 10.1016/S0012-821X(02)00951-2
- Schneider J, Boni M, Laukamp C, et al (2008) Willemite ( $\text{Zn}_2\text{SiO}_4$ ) as a possible Rb-Sr geochronometer for dating nonsulfide Zn-Pb mineralization: Examples from the Otavi Mountainland (Namibia). *Ore Geol Rev* 33:152–167. doi: 10.1016/j.oregeorev.2006.05.012
- Schuler M, Cavelier C, Dupuis C, et al (1992) The Paleogene of the Paris and Belgian Basins. Standard stages and regional stratotypes. *Cah Micropaléontol* 7:29–92
- Schumer BN, Stegen RJ, Barton MD, et al (2019) Mineralogical profile of supergene sulfide ore in the western copper area, Morenci mine, Arizona. *Can Mineral* 57:391–401. doi: 10.3749/canmin.1800020
- Schwellnus CM (1945) Vanadium deposits in the Otavi Mountains, southwest Africa. *South African J Geol* 48:49–73
- Scott K, Ashley P, Lawie D (2001) The geochemistry, mineralogy and maturity of gossans derived from volcanogenic Zn–Pb–Cu deposits of the eastern Lachlan Fold Belt, NSW, Australia. *J Geochemical Explor* 72:169–191. doi: 10.1016/S0375-6742(01)00159-5
- Scott KM (1987) Solid solution in, and classification of, gossan-derived members of the alunite-jarosite family, northwest Queensland, Australia. *Am Mineral* 72:178–187
- Seber D, Barazangi M, Tadili BA, et al (1996) Three-dimensional upper mantle structure beneath the intraplate Atlas and interplate Rif mountains of Morocco. *J Geophys Res Solid Earth* 101/B2:3125–3138. doi: 10.1029/95jb03112
- Sebti S, Saddiqi O, El Haimer FZ, et al (2009) Vertical movements at the fringe of the West African Craton: First zircon fission track datings from the Anti-Atlas Precambrian basement, Morocco. *Comptes Rendus - Geosci* 341:71–77. doi: 10.1016/j.crte.2008.11.006
- Sehrt M (2014) Variscan to Neogene long-term landscape evolution at the Moroccan passive continental margin (Tarfaya Basin and western Anti-Atlas). Heidelberg University
- Sehrt M, Glasmacher UA, Stockli DF, et al (2018) The southern Moroccan passive continental margin: An example of differentiated long-term landscape evolution in Gondwana. *Gondwana Res* 53:129–144. doi: 10.1016/J.GR.2017.03.013
- Sejkora J, Škovíra J, Čejka J, Plášil J (2009) Cu-rich members of the beudantite-segnitite series from the Krupka ore district, the Krušné Hory Mountains, Czech Republic. *J Geosci* 54:355–371. doi: 10.3190/jgeosci.055
- Shevade A V., Erickson L, Pierzynski G, Jiang S (2017) Formation and stability of substituted pyromorphite: A molecular modeling study. *J Hazard Subst Res* 3:1–12. doi: 10.4148/1090-7025.1020
- Short SA, Lowson RT, Ems J, David M. P (1989) Thorium-uranium disequilibrium dating of Late Quaternary ferruginous concretions and rinds. *Geochim Cosmochim Acta* 53/6:1379–1389. doi: 10.1016/0016-7037(89)90070-7
- Shuster DL, Farley KA (2005) Diffusion kinetics of proton-induced  $^{21}\text{Ne}$ ,  $^3\text{He}$ , and  $^4\text{He}$  in quartz. *Geochim Cosmochim Acta* 69:2349–2359. doi: 10.1016/j.gca.2004.11.002

- Shuster DL, Farley KA (2009) The influence of artificial radiation damage and thermal annealing on helium diffusion kinetics in apatite. *Geochim Cosmochim Acta* 73:183–196. doi: 10.1016/j.gca.2008.10.013
- Shuster DL, Farley KA, Vasconcelos PM, et al (2012) Cosmogenic  $^3\text{He}$  in hematite and goethite from Brazilian “canga” duricrust demonstrates the extreme stability of these surfaces. *Earth Planet Sci Lett* 329–330:41–50. doi: 10.1016/j.epsl.2012.02.017
- Shuster DL, Flowers RM, Farley KA (2006) The influence of natural radiation damage on helium diffusion kinetics in apatite. *Earth Planet Sci Lett* 249:148–161. doi: 10.1016/j.epsl.2006.07.028
- Shuster DL, Vasconcelos PM, Heim JA, Farley KA (2005) Weathering geochronology by (U-Th)/He dating of goethite. *Geochim Cosmochim Acta* 69:659–673. doi: 10.1016/j.gca.2004.07.028
- Sillitoe RH (2005) Supergene oxidized and enriched porphyry copper and related deposits. *Econ Geol One Hundredth Anniv Vol* 723–768. doi: 10.5382/AV100.22
- Sillitoe RH (2019) Supergene oxidation of epithermal gold-silver mineralization in the Deseado massif, Patagonia, Argentina: response to subduction of the Chile Ridge. *Miner Depos* 54:381–394. doi: 10.1007/s00126-018-0814-4
- Sillitoe RH, Mckee EH (1996) Age of Supergene oxidation and enrichment in the Chilean porphyry copper province. *Econ Geol* 91:164–179. doi: 10.2113/gsecongeo.91.1.164
- Skala G, Hollabaugh CL (2012) Goethite after siderite: the presence of goethite after siderite pseudomorphs in a pegmatic matrix from Lake George, Colorado. *Geol Soc Am* 44:6
- Sougnéz N (2012) Reconstruction of Quaternary landscape evolution based on  $^{10}\text{Be}$  denudation rates and tectonic uplift data in a moderate uplifted region (Ardennes Massif, Belgium). *Quat Int* 279–280. doi: 10.1016/j.quaint.2012.08.1519
- Soulaimani A, Bouabdelli M, Piqué A (2003) L’extension continentale au Néo-Protérozoïque supérieur-Cambrien inférieur dans l’Anti-Atlas (Maroc). *Bull la Soc Geol Fr* 174:83–92. doi: 10.2113/174.1.83
- Soulaimani A, Hefferan K (2017) Le Précambrien à la bordure nord du craton ouest-africain ( Anti-Atlas et Haut Atlas , Maroc ) Données générales. *Géologues* 194:33–36
- Soulaimani A, Michard A, Ouanaimi H, et al (2014) Late Ediacaran-Cambrian structures and their reactivation during the Variscan and Alpine cycles in the Anti-Atlas (Morocco). *J African Earth Sci* 98:94–112. doi: 10.1016/j.jafrearsci.2014.04.025
- Soulaimani A, Piqué A (2004) The Tasirt structure (Kerdous inlier, Western Anti-Atlas, Morocco): A late Pan-African transtensive dome. *J African Earth Sci* 39:247–255. doi: 10.1016/j.jafrearsci.2004.07.043
- Soulaimani A, Ouanaimi H, Saddiqi O, et al (2018) The Anti-Atlas Pan-African belt (Morocco): verview and pending questions. *Comptes Rendus - Geosci* 350:279–288. doi: 10.1016/j.crte.2018.07.002
- Stevko M, Ozdin D (2012) Supergene native silver and acanthite from the Jasenie-Soviansko base metals deposit, Nízke Tatry mts. (Slovak Republic). *Bull Mineral oddělení Národního Muz v Praze* 20:47–51
- Stott L, Kennett JP (1990) Antarctic Paleogene planktonic foraminifer biostratigraphy, ODP Leg 113, Sites 689 and 690. In: *Proceedings of the Ocean Drilling Program, Scientific Results* 113. pp 549–569
- Strutt RJ (1909) The accumulation of helium in geological time. *R Soc London Proc* 83:96–99
- Sverjensky DA (1984) Europium redox equilibria in aqueous solution. *Earth Planet Sci Lett* 67:70–78

- Szczerba M, Sawłowicz Z (2009) Remarks on the origin of cerussite in the Upper Silesian Zn-Pb deposits, Poland. *Mineralogia* 40:53–64. doi: 10.2478/v10002-009-0002-3
- Takahashi T (1960) Supergene alteration of zinc and lead deposits in limestone. *Econ Geol* 55:1083–1115. doi: 10.2113/gsecongeo.55.6.1083
- Taylor JH (1954) The lead-zinc-vanadium deposits at Broken Hill, northern Rhodesia. *Colon Geol Surv Bull* 4:335–365
- Taylor R (2011) *Gossans and leached cappings*. Springer-Verlag, Berlin Heidelberg
- Taylor SR, McLennan SM (1985) *The Continental Crust: Its composition and evolution; an examination of the geochemical record preserved in sedimentary rocks*. Oxford, UK
- Teixell A, Arboleya ML, Julivert M, Charroud M (2003) Tectonic shortening and topography in the central High Atlas (Morocco). *Tectonics* 22:1051–1064. doi: 10.1029/2002TC001460
- Teixell A, Ayarza P, Zeyen H, et al (2005) Effects of mantle upwelling in a compressional setting: The Atlas Mountains of Morocco. *Terra Nov* 17:456–461. doi: 10.1111/j.1365-3121.2005.00633.x
- Tesón E, Teixell A (2008) Sequence of thrusting and syntectonic sedimentation in the eastern Sub-Atlas thrust belt (Dadès and Mgoun valleys, Morocco). *Int J Earth Sci* 97:103–113. doi: 10.1007/s00531-006-0151-1
- Thein J (1990) Paleogeography and geochemistry of the “Cenomano-Turonian” formations in the manganese district of Imini (Morocco) and their relation to ore deposition. *Ore Geol Rev* 5:257–291. doi: 10.1016/0169-1368(90)90034-K
- Théveniaut H, Freyssinet P (1999) Paleomagnetism applied to lateritic profiles to assess saprolite and duricrust formation processes: The example of Mont Baduel profile (French Guiana). *Palaeogeogr Palaeoclimatol Palaeoecol* 148:209–231. doi: 10.1016/S0031-0182(98)00183-7
- Théveniaut H, Quesnel F, Wyns R, Hugues G (2007) Palaeomagnetic dating of the “Borne de Fer” ferricrete (NE France): Lower Cretaceous continental weathering. *Palaeogeogr Palaeoclimatol Palaeoecol* 253: . doi: 10.1016/j.palaeo.2007.01.010
- Thiry M, Quesnel F, Yans J, et al (2006) Continental France and Belgium during the early cretaceous: Paleoweatherings and paleolandforms. *Bull la Soc Geol Fr* 177. doi: 10.2113/gssgfbull.177.3.155
- Thomas M (1994) *Geomorphology in the tropics. A study of weathering and denudation in low latitudes*. Wiley, Winchester
- Thomas RJ, Chevallier LP, Gresse PG, et al (2002) Precambrian evolution of the Sirwa Window, Anti-Atlas Orogen, Morocco. *Precambrian Res* 118:1–57. doi: 10.1016/S0301-9268(02)00075-X
- Thomas RJ, Fekkak A, Ennih N, et al (2004) A new lithostratigraphic framework for the Anti-Atlas Orogen, Morocco. *J African Earth Sci* 39:217–226. doi: 10.1016/j.afrearsci.2004.07.046
- Tijani MB, Quajhain A (1992) Etude métallographique de la minéralisation de Tazalaght. *Bulletin d’analyse*, 92/5/1320, Rabat
- Torres-Alvarado IS, Pandarinath K, Verma SP, Dulski P (2007) Mineralogical and geochemical effects due to hydrothermal alteration in the Los Azufres geothermal field, Mexico. *Rev Mex Ciencias Geol* 24:15–24
- Torres Ruiz J (1983) Genesis and evolution of the Marquesado and adjacent ore deposits, Granada, Spain. *Econ Geol* 78:1657–1673
- Underhill JR, Partington MA (1993) Jurassic thermal doming and deflation in the North Sea:

- Implications of the sequence stratigraphic evidence. In: Petroleum Geology Conference Proceedings
- van der Westhuizen WA (1984) The nature, genesis and geochemistry of the supergene vanadium ores of the Otavi Mountain Land. University Orange Free State, Bloemfontein, South Africa
- van der Westhuizen WAA, Tordiffe EAWAW, de Bruijn H, Beukes GJJ (1989) The composition of descloizite-mottramite in relation to the trace-element distribution of Pb, Zn, Cu and V in the Otavi Mountain Land, South West Africa/Namibia. *J Geochemical Explor* 34:21–29. doi: 10.1016/0375-6742(89)90127-1
- Van Langendonck S, Muchez P, Dewaele S, et al (2013) Petrographic and mineralogical study of the sediment-hosted Cu-Co ore deposit at Kambove West in the central part of the Katanga Copperbelt (DRC). *Geol Belgica* 16:91–104
- Vasconcelos PM (1999) K-Ar and  $^{40}\text{Ar}/^{39}\text{Ar}$  geochronology of weatehring processes. *Annu Rev Earth Planet Sci* 27:183–229. doi: 10.1146/annurev.earth.27.1.183
- Vasconcelos PM, Heim JA, Farley KA, et al (2013)  $^{40}\text{Ar}/^{39}\text{Ar}$  and (U-Th)/He -  $^4\text{He}/^3\text{He}$  geochronology of landscape evolution and channel iron deposit genesis at Lynn Peak, Western Australia. *Geochim Cosmochim Acta* 117:283–312. doi: 10.1016/j.gca.2013.03.037
- Vasconcelos PM, Reich M, Shuster DL (2015) The paleoclimatic signatures of supergene metal deposits. *Elements* 11:317–322. doi: 10.2113/gselements.11.5.317
- Vasconcelos PM, Renne PR, Becker TA, Wenk HR (1995) Mechanisms and kinetics of atmospheric, radiogenic, and nucleogenic argon release from cryptomelane during  $^{40}\text{Ar}/^{39}\text{Ar}$  analysis. *Geochim Cosmochim Acta* 59: . doi: 10.1016/0016-7037(95)00126-3
- Vasconcelos PM, Renne PR, Brimhall GH, Becker TA (1994) Direct dating of weathering phenomena by  $^{40}\text{Ar}/^{39}\text{Ar}$  and K-Ar analysis of supergene K-Mn oxides. *Geochim Cosmochim Acta* 58:1635–1665. doi: 10.1016/0016-7037(94)90565-7
- Velasco F, Herrero JM, Suarez S, et al (2013) Supergene features and evolution of gossans capping massive sulphide deposits in the Iberian Pyrite Belt. *Ore Geol Rev* 53:181–203. doi: 10.1016/j.oregeorev.2013.01.008
- Vennemann TW, Morlok A, von Engelhardt W, Kyser K (2001) Stable isotope composition of impact glasses from the Nördlinger Ries impact crater, Germany. *Geochim Cosmochim Acta* 65:1325–1336. doi: 10.1016/S0016-7037(00)00600-1
- Verati C, Rapaille C, Féraud G, et al (2007)  $^{40}\text{Ar}/^{39}\text{Ar}$  ages and duration of the Central Atlantic Magmatic Province volcanism in Morocco and Portugal and its relation to the Triassic-Jurassic boundary. *Palaeogeogr Palaeoclimatol Palaeoecol* 244:308–325. doi: 10.1016/j.palaeo.2006.06.033
- Verhaert M, Bernard A, Dekoninck A, et al (2017) Mineralogical and geochemical characterization of supergene Cu–Pb–Zn–V ores in the Oriental High Atlas, Morocco. *Miner Depos* 52:1049–1068. doi: 10.1007/s00126-017-0753-5
- Verhaert M, Bernard A, Saddiqi O, et al (2018) Mineralogy and genesis of the polymetallic and polyphased low grade Fe-Mn-Cu ore of Jbel Rhals deposit (Eastern High Atlas, Morocco). *Minerals* 8:39. doi: 10.3390/min8020039
- Verhaert M, Madi A, El Basbas A, et al (in press) Genesis of As-Pb-rich supergene mineralization: the Tazalaght and Agoujgal Cu deposits (Moroccan Anti-Atlas Copperbelt). *Econ Geol*
- Verwoerd WJ (1953) The mineralogy and genesis of the lead-zinc-vanadium deposit of Abenab West in the Otavi mountains, South West Africa. Stellenbosch : Stellenbosch University

- Vink BW (1986) Stability relations of malachite and azurite. *Mineral Mag* 50:41–47. doi: 10.1180/minmag.1986.050.355.06
- Voisin L (1981) Analyse géomorphologique d'une région-type: l'Ardenne occidentale. Université de Lille
- Wadjinny A (1998) Le plomb au Maroc ; cas des districts de Touissit et Jbel Aouam. *Chroniques des Rech Minières* 531–532:9–28
- Walsh GJ, Benziane F, Aleinikoff JN, et al (2012) Neoproterozoic tectonic evolution of the Jebel Saghro and Bou Azzer–El Graara inliers, eastern and central Anti-Atlas, Morocco. *Precambrian Res* 216–219:23–62. doi: 10.1016/j.precamres.2012.06.010
- Walters G (1998) Broken Hill-type deposits. *AGSO J Aust Geol Geophys*
- Wartha RR, Schreuder CP (1992) Minerals resource series–vanadium., Ministry o. Geological Survey of Namibia, Windhoek, Namibia
- Wayland E (1933) Peneplains and some other erosional platforms. *Ann Rep Bull, Prot Uganda Geol Surv* 1:77–79
- Werdelin L (2010) Chronology of Neogene mammal localities. In: Werdelin L (ed) *Cenozoic Mammals of Africa*. University of California Press, Berkeley, pp 24–43
- Wernicke RS, Lippolt HJ (1994) Dating of vein Specularite using internal (U+Th)/<sup>4</sup>He isochrons. *Geophys Res Lett* 21:345–347. doi: 10.1029/94GL00014
- Widdowson M (2008) Laterite and Ferricrete. In: Nash DJ, McLaren SJ (eds) *Geochemical Sediments and Landscapes*. Blackwell Publishing Ltd, Oxford, UK, pp 45–94
- Wilson AD (1955) A new method for determination of ferrous iron in rocks and minerals. *Bull Geol Surv Gt Britain* 9:56–68
- Wolf RA (1997) Development of the (U-Th)/He Thermochronometer. California Institute of Technology, Pasadena, California
- Woodhead J, Hellstrom J, Maas R, et al (2006) U-Pb geochronology of speleothems by MC-ICPMS. *Quat Geochronol* 1:208–221. doi: 10.1016/j.quageo.2006.08.002
- Wyns R (2002) Climat, Eustatisme, Tectonique: Quels contrôles pour l'altération continentale exemple des séquences d'altération cénozoïques en France. *Bull Inf Bass Paris*
- Wyns R, Gourry J, Baltassat J, Lebert F (1999) Caractérisation multiparamètre des horizons de subsurface (0–100 m) en contexte de socle altéré. *Pangea* 31 (32):51–54
- Xu C, Mansy JL, van den Haute P, et al (2009) Late- and post-Variscan evolution of the Ardennes in France and Belgium: Constraints from apatite fission-track data. *Geol Soc Spec Publ* 324. doi: 10.1144/SP324.13
- Xu T (2001) Modeling multiphase non-isothermal fluid flow and reactive geochemical transport in variably saturated fractured rocks: 2. Applications to supergene copper enrichment and hydrothermal flows. *Am J Sci* 301:34–59. doi: 10.2475/ajs.301.1.34
- Yans J (2003) An overview of the saprolites of Belgium and their potential kaolinitic supplies to Mesozoic and Cenozoic sediments. *Géologie la Fr* 1:33–37
- Yans J (2013) Gestion durable des ressources minérales wallonnes: pistes de réflexions en vue d'une meilleure intégration de la problématique. In: *Actes du 1er congrès interdisciplinaire du développement durable*. Namur, pp 195–206

- Yans J, Dupuis C (2005) Timing of saprolitisation in the Haute-Lesse area (Belgium). *Geophys Res Abstr* 7:7064
- Yapp CJ (1990) Oxygen isotopes in iron (III) oxides. *Chem Geol* 85:329–335. doi: 10.1016/0009-2541(90)90010-5
- Yapp CJ (2000) Climatic implications of surface domains in arrays of  $\delta D$  and  $\delta^{18}O$  from hydroxyl minerals: Goethite as an example. *Geochim Cosmochim Acta* 64:2009–2025. doi: 10.1016/S0016-7037(00)00347-1
- Yapp CJ (1987) Oxygen and hydrogen isotope variations among goethites ( $\alpha$ -FeOOH) and the determination of paleotemperatures. *Geochim Cosmochim Acta* 51:355–364. doi: 10.1016/0016-7037(87)90247-X
- Yapp CJ, Pedley MD (1985) Stable hydrogen isotopes in iron oxides—II. variations among natural goethites. *Geochim Cosmochim Acta* 49:487–495. doi: 10.1016/0016-7037(85)90040-7
- Yong R, Zheng L (1993) The characteristics of adsorption and desorption of Rare Earth Elements by the main types of soils of China. *J Chinese Rare Earth Soc* 11
- Youbi N, Kouyaté D, Söderlund U, et al (2013) The 1750 Ma magmatic event of the west African craton (Anti-Atlas, Morocco). *Precambrian Res* 236:106–123. doi: 10.1016/j.precamres.2013.07.003
- Youbi N, Martins LT, Munhá JM, et al (2003) The Late Triassic-Early Jurassic Volcanism of Morocco and Portugal in the Framework of the Central Atlantic Magmatic Province: An Overview. In: Hames WE, McHone JG, Renne PR, Ruppel C (eds) *The Central Atlantic Province; insights from fragments of Pangea*. American Geophysical union, pp 179–207
- Zabinski W (1960) Mineralogical characteristics of oxidation zone of Cracovian-Silesian Zn-Pb ore deposits. *Pr Geol* 1:1–99
- Zammit CM, Shuster JP, Gagen EJ, Southam G (2015) The geomicrobiology of supergene metal deposits. *Elements* 11:337–342. doi: 10.2113/gselements.11.5.337
- Zeitler PK, Herczeg AL, McDougall I, Honda M (1987) U-Th-He dating of apatite: A potential thermochronometer. *Geochim Cosmochim Acta* 51/10:2865–2868. doi: 10.1016/0016-7037(87)90164-5
- Zheng Z, Lin C (1996) The behaviour of Rare-Earth Elements (REE) during weathering of granites in Southern Guangxi, China. *Chinese J Geochemistry* 15:344–352
- Ziegler JF (1977) *Helium: Stopping powers and ranges in all elemental matter*. Pergamon Press, New York
- Ziegler JF, Ziegler MD, Biersack JP (2010) SRIM - The stopping and range of ions in matter (2010). *Nucl Instruments Methods Phys Res Sect B Beam Interact with Mater Atoms* 268:1818–1823. doi: 10.1016/j.nimb.2010.02.091

